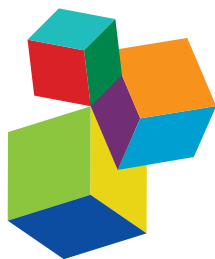


FUNCTIONALIZED INORGANIC SEMICONDUCTOR NANOMATERIALS: CHARACTERIZATION, PROPERTIES, AND APPLICATIONS

EDITED BY: Kezhen Qi, Rengaraj Selvaraj and Liwei Wang
PUBLISHED IN: Frontiers in Chemistry and Frontiers in Materials





frontiers

Frontiers eBook Copyright Statement

The copyright in the text of individual articles in this eBook is the property of their respective authors or their respective institutions or funders. The copyright in graphics and images within each article may be subject to copyright of other parties. In both cases this is subject to a license granted to Frontiers.

The compilation of articles constituting this eBook is the property of Frontiers.

Each article within this eBook, and the eBook itself, are published under the most recent version of the Creative Commons CC-BY licence.

The version current at the date of publication of this eBook is CC-BY 4.0. If the CC-BY licence is updated, the licence granted by Frontiers is automatically updated to the new version.

When exercising any right under the CC-BY licence, Frontiers must be attributed as the original publisher of the article or eBook, as applicable.

Authors have the responsibility of ensuring that any graphics or other materials which are the property of others may be included in the CC-BY licence, but this should be checked before relying on the CC-BY licence to reproduce those materials. Any copyright notices relating to those materials must be complied with.

Copyright and source acknowledgement notices may not be removed and must be displayed in any copy, derivative work or partial copy which includes the elements in question.

All copyright, and all rights therein, are protected by national and international copyright laws. The above represents a summary only. For further information please read Frontiers' Conditions for Website Use and Copyright Statement, and the applicable CC-BY licence.

ISSN 1664-8714

ISBN 978-2-88966-332-3

DOI 10.3389/978-2-88966-332-3

About Frontiers

Frontiers is more than just an open-access publisher of scholarly articles: it is a pioneering approach to the world of academia, radically improving the way scholarly research is managed. The grand vision of Frontiers is a world where all people have an equal opportunity to seek, share and generate knowledge. Frontiers provides immediate and permanent online open access to all its publications, but this alone is not enough to realize our grand goals.

Frontiers Journal Series

The Frontiers Journal Series is a multi-tier and interdisciplinary set of open-access, online journals, promising a paradigm shift from the current review, selection and dissemination processes in academic publishing. All Frontiers journals are driven by researchers for researchers; therefore, they constitute a service to the scholarly community. At the same time, the Frontiers Journal Series operates on a revolutionary invention, the tiered publishing system, initially addressing specific communities of scholars, and gradually climbing up to broader public understanding, thus serving the interests of the lay society, too.

Dedication to Quality

Each Frontiers article is a landmark of the highest quality, thanks to genuinely collaborative interactions between authors and review editors, who include some of the world's best academicians. Research must be certified by peers before entering a stream of knowledge that may eventually reach the public - and shape society; therefore, Frontiers only applies the most rigorous and unbiased reviews. Frontiers revolutionizes research publishing by freely delivering the most outstanding research, evaluated with no bias from both the academic and social point of view. By applying the most advanced information technologies, Frontiers is catapulting scholarly publishing into a new generation.

What are Frontiers Research Topics?

Frontiers Research Topics are very popular trademarks of the Frontiers Journals Series: they are collections of at least ten articles, all centered on a particular subject. With their unique mix of varied contributions from Original Research to Review Articles, Frontiers Research Topics unify the most influential researchers, the latest key findings and historical advances in a hot research area! Find out more on how to host your own Frontiers Research Topic or contribute to one as an author by contacting the Frontiers Editorial Office: researchtopics@frontiersin.org

FUNCTIONALIZED INORGANIC SEMICONDUCTOR NANOMATERIALS: CHARACTERIZATION, PROPERTIES, AND APPLICATIONS

Topic Editors:

Kezhen Qi, Shenyang Normal University, China

Rengaraj Selvaraj, Sultan Qaboos University, Oman

Liwei Wang, Guangxi University, China

Citation: Qi, K., Selvaraj, R., Wang, L., eds. (2021). Functionalized Inorganic Semiconductor Nanomaterials: Characterization, Properties, and Applications. Lausanne: Frontiers Media SA. doi: 10.3389/978-2-88966-332-3

Table of Contents

- 05 Editorial: Functionalized Inorganic Semiconductor Nanomaterials: Characterization, Properties, and Applications**
Kezhen Qi, Rengaraj Selvaraj and Liwei Wang
- 08 The Multiple Promotion Effects of Ammonium Phosphate-Modified Ag_3PO_4 on Photocatalytic Performance**
Qin Liu, Na Li, Zheng Qiao, Wenjuan Li, Linlin Wang, Shuao Zhu, Zhihong Jing and Tingjiang Yan
- 20 Accelerating Photocatalytic Hydrogen Production and Pollutant Degradation by Functionalizing $g\text{-C}_3\text{N}_4$ With SnO_2**
Amir Zada, Muhammad Khan, Muhammad Nasimullah Qureshi, Shu-yuan Liu and Ruidan Wang
- 28 SiO_2 Coated on ZnO Nanorod Arrays With UV-Durable Superhydrophobicity and Highly Transmittance on Glass**
Hong Li, Xinyan Zou, Hongyan Wei, Qiang Li, Qiang Gao, Qinzhuang Liu and Jinfeng Zhang
- 35 One-Step Microwave Synthesis of Micro/Nanoscale LiFePO_4 /Graphene Cathode With High Performance for Lithium-Ion Batteries**
Shulong Liu, Ping Yan, Haibin Li, Xiaobo Zhang and Wei Sun
- 45 Facile and Efficient Fabrication of Bandgap Tunable Carbon Quantum Dots Derived From Anthracite and Their Photoluminescence Properties**
Jianbo Jia, Yue Sun, Yaojie Zhang, Quanrun Liu, Jianliang Cao, Guangxu Huang, Baolin Xing, Chuanxiang Zhang, Lina Zhang and Yijun Cao
- 55 Fabrication and Characterization of Calcium-Phosphate Lipid System for Potential Dental Application**
Ningxin Zhu, Dan Wang, Fei Xie, Man Qin, Zhiqiang Lin and Yuanyuan Wang
- 64 Volatile Organic Compounds Gas Sensors Based on Molybdenum Oxides: A Mini Review**
Jingxuan Wang, Qu Zhou, Shudi Peng, Lingna Xu and Wen Zeng
- 71 Metal Oxides-Based Semiconductors for Biosensors Applications**
Ionel Șerban and Alexandru Enesca
- 79 Study on Preparation and Properties of InN Films on Self-Supporting Diamond Substrates Under Different Nitrogen Flows**
Shuaijie Wang, Fuwen Qin, Yizhen Bai and Dong Zhang
- 87 Flower-Like ZnO Nanorods Synthesized by Microwave-Assisted One-Pot Method for Detecting Reducing Gases: Structural Properties and Sensing Reversibility**
Abdullah Aljaafari, Faheem Ahmed, Chawki Awada and Nagih M. Shaalan
- 98 Mini-Review: Mixed Ionic–Electronic Charge Carrier Localization and Transport in Hybrid Organic–Inorganic Nanomaterials**
Mariano Romero, Dominique Mombrú, Fernando Pignanelli, Ricardo Faccio and Alvaro W. Mombrú
- 109 ZnO Nanomaterials: Current Advancements in Antibacterial Mechanisms and Applications**
Shengjie Jiang, Kaili Lin and Ming Cai

- 114** *Study and Analysis of Removing the Carbon Deposition on the Inner Surface of a Turbo-Shaft by Chemically Assisted Magnetic Grinding*
Hui Xu, Renke Kang, Xianglong Zhu, Lijuan Liu, Leilei Wang and Yan Chen
- 126** *Hydrothermal Synthesis of Flake-Flower NiO and Its Gas Sensing Performance to CO*
Guochao Qian, Qingjun Peng, Dexu Zou, Shan Wang and Bing Yan
- 134** *Fluorescence Resonant Energy Transfer-Based Quantum Dot Sensor for the Detection of Calcium Ions*
Shreya Ghosh, Yinghua Chen, Anne George, Mitra Dutta and Michael A. Stroschio
- 143** *Formulation of Mesoporous Silica Nanoparticles for Controlled Release of Antimicrobials for Stone Preventive Conservation*
Alessandro Presentato, Francesco Armetta, Alberto Spinella, Delia Francesca Chillura Martino, Rosa Alduina and Maria Luisa Saladino
- 154** *Size Dependent Photocatalytic Activity of ZnO Nanosheets for Degradation of Methyl Red*
Abdullah Aljaafari



Editorial: Functionalized Inorganic Semiconductor Nanomaterials: Characterization, Properties, and Applications

Kezhen Qi^{1*}, Rengaraj Selvaraj^{2*} and Liwei Wang^{3*}

¹ Institute of Catalysis for Energy and Environment, College of Chemistry and Chemical Engineering, Shenyang Normal University, Shenyang, China, ² Department of Chemistry, College of Science, Sultan Qaboos University, Muscat, Oman, ³ School of Marine Sciences, Guangxi University, Nanning, China

Keywords: functionalized inorganic semiconductors, nanocrystals, photocatalysis, quantum dots, nanorods, biosensors

Editorial on the Research Topic

Functionalized Inorganic Semiconductor Nanomaterials: Characterization, Properties, and Applications

OPEN ACCESS

Edited and reviewed by:

Jie He,
University of Connecticut,
United States

*Correspondence:

Kezhen Qi
kqzh2003@allyun.com
Rengaraj Selvaraj
rengaraj@squ.edu.om
Liwei Wang
20160214@gxu.edu.cn

Specialty section:

This article was submitted to
Nanoscience,
a section of the journal
Frontiers in Chemistry

Received: 13 October 2020

Accepted: 20 October 2020

Published: 11 November 2020

Citation:

Qi K, Selvaraj R and Wang L (2020)
Editorial: Functionalized Inorganic
Semiconductor Nanomaterials:
Characterization, Properties, and
Applications. *Front. Chem.* 8:616728.
doi: 10.3389/fchem.2020.616728

Nanotechnology involves studying and working with matter on a nanoscale, which provides the ability to work at the atomic level and molecular level to create large structures with fundamentally new molecular organization. The field of nanotechnology presents an exciting and rapid expansion of research area that crosses the barriers among physics, chemistry, biology, life, and engineering sciences. Nanostructure materials generally called nanomaterials are the materials having at least one dimension between 1 and 100 nm. These materials exhibit novel and significantly improved physical, chemical, and biological properties, phenomena, and processes due to their nanoscale size (Liu et al., 2019; Marzouqi et al., 2019; Qi et al., 2019a,b).

The functionalized semiconductor based nanomaterials with different morphologies and compositions have been successfully applied for numerous applications (Wang et al., 2018; Qi et al., 2020b). Depending on their size and shape, the physical, chemical, electrical, and optical properties of the functionalized nanomaterials are different as compared to their bulk structures (Ruqaishy et al., 2018; Qi et al., 2020a). Because of their small size, the nanomaterials have large surface area and high surface/volume ratio (Al-Fahdi et al., 2019). This high surface/volume ratio is one of the reasons that nanomaterials have superior chemical and physical properties such as large surface energy, reactivity, solubility and low melting point as compared to their bulk counter-parts (Yu et al., 2007; Qi et al., 2018; Hayat et al., 2019). Decreasing size of the material causes an increase in surface area. The functional properties of nanomaterials depend mainly on their unique structures, which can be classified into three levels namely, the microscale, mesoscale, and particle scale.

In this Research Topic, we present a collection of original research and review articles focussing on different aspects of functionalized inorganic semiconductor nanomaterials, including modified Ag₃PO₄ semiconductors for improved photocatalytic performance (Liu Q. et al.), hydrogen production and pollutant degradation by functionalizing g-C₃N₄ with SnO₂ (Zada et al.), SiO₂ coated ZnO nanorod arrays for UV-durable super hydrophobicity (Li et al.), synthesis of micro/nanoscale LiFePO₄/Graphene for lithium-ion batteries (Liu S. et al.), facile and efficient fabrication of bandgap tunable carbon Quantum Dots (Jia et al.), Calcium-phosphate lipid system

for potential dental application (Zhu et al.), VOC gas sensors based on molybdenum oxide (Wang J. et al.; Wang S. et al.), metal oxides—based semiconductors for biosensors (Serban and Enesca), ZnO nanorods for detecting reducing gases (Aljaafari et al.), ZnO nanomaterials: Current advancements in antibacterial mechanisms (Jiang et al.), quantum dot sensor for the detection of calcium ions (Ghosh et al.), mixed electronic and ionic charge carrier localization and transport (Romero et al.), and mesoporous silica nanoparticles for controlled release of antimicrobials for stone preventive conservation (Presentato et al.). We have also highlighted that how state of the art theoretical and experimental approaches are leading to better understanding of semiconducting materials and improved design of novel functional semiconducting materials.

The contribution of Qian et al. concerns an effect of ammonium phosphate—modified Ag_3PO_4 on photocatalytic performance. The authors demonstrated a novel one-pot surface modification route by using ammonium phosphate solutions to improve the photocatalytic performance of Ag_3PO_4 . It was found that ammonium phosphate played multiple promotion roles in favoring the formation of metallic Ag nanoparticles and providing the negative electrostatic field on the surface of Ag_3PO_4 photocatalysts, which consequently promoted the separation efficiency of photoinduced electron-hole pairs, enhanced selective adsorption of cationic dye, and increased concentration of reactive oxygen species. This work provides an alternative route to boost the photocatalytic activity of Ag_3PO_4 .

The work of Zada et al. investigated the functionalization of g- C_3N_4 with SnO_2 for the photocatalytic hydrogen production and degradation of pollutants. This work is emphasized to overcome energy crises and environmental pollution. The authors synthesized g- C_3N_4 nanosheets and coupled them with SnO_2 nanoparticles. The enhanced photoactivities were attributed to the better charge separation as the excited electrons thermodynamically transferred from g- C_3N_4 to SnO_2 as had been confirmed from photoluminescence spectra, steady state surface photovoltage spectroscopic measurement, and formed hydroxyl radicals. It is believed that this work would provide a feasible route to synthesize photocatalysts for improved energy production and environmental purification.

The contribution of Li et al. developed vertically aligned ZnO nanorod arrays with large area through chemical hydrothermal process. Ultra-thin SiO_2 shell film was deposited on ZnO nanorod arrays through PLD, and subsequently modified by stearic acid. This $\text{SiO}_2/\text{ZnO}/\text{glass}$ structure exhibited well UV-durable super hydrophobicity and high transmittance. These properties have important applications in solar cells.

Liu S. et al. prepared $\text{LiFePO}_4/\text{graphene}$ composites by packing LiFePO_4 nanoparticles in the micron graphene sheets by one-step microwave heating technique. The introduction of graphene did not affect the structure of LiFePO_4 as the nanoparticles were surrounded by the graphene sheets and the micron structure guarded the stability of the material. The electrochemical analysis reveal that the $\text{LiFePO}_4/\text{graphene}$ composites have excellent high-rate performance and cycling life.

The outstanding electrochemical performance, as well as the fast and efficient method, make this technology commercially viable.

Jia et al. developed a facile, fast, and green method to prepare bandgap tunable CQDs solely from anthracite. The bandgap change of the as-prepared CQDs could be achieved by simply controlling the concentration of H_2O_2 . The morphology, size and PL properties of the as-prepared CQDs indicated that the blue luminescence might be originated from the intrinsic emission, but the yellow and green luminescence might be originated from the extrinsic emission due to the new energy states created by the oxygen-containing functional groups inside the band gap of CQDs. This novel strategy for fabricating optically tunable CQDs from coal is highly promising for the high-end application of coal.

The work of Zhu et al. investigates the calcium-phosphate lipid system for potential dental application. Aljaafari research group successfully synthesized ZnO nanorods using a domestic microwave-assisted synthesis method and showed a smooth surface morphology and wurtzite hexagonal structure. They concluded that the fabricated ZnO NRs using the microwave method was very sensitive to CH_4 and CO , where the sensitivity toward these two gases was very high compared to H_2 gas. The smooth surface of nanorods could also be used as a high operating temperature sensor.

Jiang et al. (2020) studied the antibacterial properties, mechanism, and application prospects of ZnO nanoparticles. The excellent biocompatibility, photochemical stability, and other characteristics of ZnO nanoparticles make it suitable for antibacterial activity. They concluded that doping with other metals or non-metallic materials to enhance the selectivity for pathogenic microorganisms and reduce the toxic effect of tissue cells might exert more extensive biomedical potentials for ZnO nanoparticles.

Ghosh et al. developed a simple optical aptasensor for the detection of calcium ions. The sensor had been found to have high specificity for calcium ions in comparison to other metal ions like sodium, magnesium, and potassium. The molecular apta-beacons also demonstrated successful endocytosis and FRET-based calcium ion detection in osteocyte cells when conjugated with a cell-penetrating peptide (DSS).

We hope this Research Topic will attract readers, providing novel literature insights, synergistic research ideas, and enthusiasm in research and studies.

AUTHOR CONTRIBUTIONS

All authors listed have made a substantial, direct and intellectual contribution to the work, and approved it for publication.

FUNDING

This research was supported by Liaoning Revitalization Talents Program (XLYC1807238), Liaoning BaiQianWan Talents Program, Shenyang Revitalization Talents Program.

REFERENCES

- Al-Fahdi, T., Al Marzouqi, F., Kuvarega, A. T., Mamba, B. B., Al Kindy, S. M., et al. (2019). Visible light active CdS@TiO₂ core-shell nanostructures for the photodegradation of chlorophenols. *J. Photochem. Photobiol. A Chem.* 374, 75–83. doi: 10.1016/j.jphotochem.2019.01.019
- Hayat, A., Ur Rahman, M., Khan, I., Khan, J., Sohail, M., Yasmeen, H., et al. (2019). Conjugated electron donor-acceptor hybrid polymeric carbon nitride as a photocatalyst for CO₂ reduction. *Molecules* 24:1779. doi: 10.3390/molecules24091779
- Jiang, S., Lin, K., and Cai, M. (2020). ZnO nanomaterials: current advancements in antibacterial mechanisms and applications. *Front. Chem.* 8:580. doi: 10.3389/fchem.2020.00580
- Liu, M., Wageh, S., Al-Ghamdi, A. A., Xia, P., Cheng, B., Zhang, L., et al. (2019). Quenching induced hierarchical 3D porous g-C₃N₄ with enhanced photocatalytic CO₂ reduction activity. *Chem. Commun.* 55, 14023–14026. doi: 10.1039/C9CC07647F
- Marzouqi, F. A., Kim, Y., and Selvaraj, R. (2019). Shifting of the band edge and investigation of charge carrier pathways in the CdS/g-C₃N₄ heterostructure for enhanced photocatalytic degradation of levofloxacin. *N. J. Chem.* 43, 9784–9792. doi: 10.1039/C9NJ01782H
- Qi, K., Li, Y., Xie, Y., Liu, S. Y., Zheng, K., Chen, Z., et al. (2019a). Ag loading enhanced photocatalytic activity of g-C₃N₄ porous nanosheets for decomposition of organic pollutants. *Front. Chem.* 7:91. doi: 10.3389/fchem.2019.00091
- Qi, K., Liu, S. Y., Chen, Y., Xia, B., and Li, G. D. (2018). A simple post-treatment with urea solution to enhance the photoelectric conversion efficiency for TiO₂ dye-sensitized solar cells. *Solar Energy Mater. Solar Cells* 183, 193–199. doi: 10.1016/j.solmat.2018.03.038
- Qi, K., Lv, W., Khan, I., and Liu, S. Y. (2020a). Photocatalytic H₂ generation via CoP quantum-dot-modified g-C₃N₄ synthesized by electroless plating. *Chin. J. Catal.* 41, 114–121. doi: 10.1016/S1872-2067(19)63459-5
- Qi, K., Xie, Y., Wang, R., Liu, S. Y., and Zhao, Z. (2019b). Electroless plating Ni-P cocatalyst decorated g-C₃N₄ with enhanced photocatalytic water splitting for H₂ generation. *Appl. Surface Sci.* 466, 847–853. doi: 10.1016/j.apsusc.2018.10.037
- Qi, K., Xing, X., Zada, A., Li, M., Wang, Q., Liu, S. Y., et al. (2020b). Transition metal doped ZnO nanoparticles with enhanced photocatalytic and antibacterial performances: experimental and DFT studies. *Ceramics Int.* 46, 1494–1502. doi: 10.1016/j.ceramint.2019.09.116
- Ruqaishy, M. A., Al Marzouqi, F., Qi, K., Liu, S. Y., Karthikeyan, S., Kim, Y., et al. (2018). Template-free preparation of TiO₂ microspheres for the photocatalytic degradation of organic dyes. *Korean J. Chem. Eng.* 35, 2283–2289. doi: 10.1007/s11814-018-0122-9
- Wang, S., Kuang, P., Cheng, B., Yu, J., and Jiang, C. (2018). ZnO hierarchical microsphere for enhanced photocatalytic activity. *J. Alloys Comp.* 741, 622–632. doi: 10.1016/j.jallcom.2018.01.141
- Yu, J., Zhang, L., Cheng, B., and Su, Y. (2007). Hydrothermal preparation and photocatalytic activity of hierarchically sponge-like macro-/mesoporous titania. *J. Phys. Chem. C* 111, 10582–10589. doi: 10.1021/jp0707889

Conflict of Interest: The authors declare that the research was conducted in the absence of any commercial or financial relationships that could be construed as a potential conflict of interest.

Copyright © 2020 Qi, Selvaraj and Wang. This is an open-access article distributed under the terms of the Creative Commons Attribution License (CC BY). The use, distribution or reproduction in other forums is permitted, provided the original author(s) and the copyright owner(s) are credited and that the original publication in this journal is cited, in accordance with accepted academic practice. No use, distribution or reproduction is permitted which does not comply with these terms.



The Multiple Promotion Effects of Ammonium Phosphate-Modified Ag_3PO_4 on Photocatalytic Performance

Qin Liu¹, Na Li^{2*}, Zheng Qiao¹, Wenjuan Li¹, Linlin Wang¹, Shuao Zhu¹, Zhihong Jing¹ and Tingjiang Yan^{1*}

¹ The Key Laboratory of Life-Organic Analysis, College of Chemistry and Chemical Engineering, Qufu, China, ² Qufu Normal University Library, Qufu Normal University, Qufu, China

OPEN ACCESS

Edited by:

Kezhen Qi,
Shenyang Normal University, China

Reviewed by:

Kai Dai,
Huaibei Normal University, China
Yang Qu,
Heilongjiang University, China

*Correspondence:

Na Li
chessmantj@163.com
Tingjiang Yan
tingjiangn@163.com

Specialty section:

This article was submitted to
Nanoscience,
a section of the journal
Frontiers in Chemistry

Received: 23 October 2019

Accepted: 02 December 2019

Published: 24 December 2019

Citation:

Liu Q, Li N, Qiao Z, Li W, Wang L,
Zhu S, Jing Z and Yan T (2019) The
Multiple Promotion Effects of
Ammonium Phosphate-Modified
 Ag_3PO_4 on Photocatalytic
Performance. *Front. Chem.* 7:866.
doi: 10.3389/fchem.2019.00866

Phosphate (PO_4^{3-}) modification of semiconductor photocatalysts such as TiO_2 , C_3N_4 , BiVO_4 , and etc. has been shown positive effect on the enhancement of photocatalytic performance. In the present study, we demonstrate a novel one-pot surface modification route on Ag_3PO_4 photocatalyst by ammonium phosphate $[(\text{NH}_4)_3\text{PO}_4]$, which combines PO_4^{3-} modification with ammonium (NH_4^+) etching to show multiple effects on the structural variation of Ag_3PO_4 samples. The modified Ag_3PO_4 photocatalysts exhibit much higher photocatalytic performance than bare Ag_3PO_4 for the degradation of organic dye solutions under visible light irradiation. It is indicated that the NH_4^+ etching favors the surface transition from Ag_3PO_4 to metallic Ag nanoparticles, resulting in the fast capture of photogenerated electrons and the followed generation of $\text{O}_2^{\cdot-}$ radicals. The strongly adsorbed PO_4^{3-} on the Ag_3PO_4 surfaces can further provide more negative electrostatic field, which improves the separation of photogenerated electron-hole pairs by inducing the holes to directly flow to the surface and then enhances the formation of reactive $\cdot\text{OH}$ radicals. Furthermore, the photocatalytic performance of the modified Ag_3PO_4 photocatalysts can be optimized by monitoring the concentration of $(\text{NH}_4)_3\text{PO}_4$ that is 1 mM.

Keywords: ammonium phosphate, surface modification, Ag_3PO_4 , metallic Ag, reactive species

INTRODUCTION

In recent years, photocatalytic technology has received widespread attention in wastewater treatment and energy development. At present, although titanium dioxide is the most widely used photocatalyst, the wide band energy, and the recombination of the photogenerated electron-hole limit its application (Asahi et al., 2001; Yan et al., 2014a; Qi et al., 2016, 2018). Many new semiconductor materials have then developed in recent years, such as ZnO (Qi et al., 2017), CdS (Jing and Guo, 2006; Dai et al., 2018), WO_3 (Liu et al., 2019), Ag_2WO_4 (Macedo et al., 2018), BiVO_4 (Wang et al., 2018, 2019; Song et al., 2019), AgCl (Han et al., 2011), C_3N_4 (Guo et al., 2019; Huo et al., 2019; Qi et al., 2019), etc. In 2010, Yi et al. (2010) reported that Ag_3PO_4 has noticeable absorption in the UV-visible spectral range, which can utilize visible light to oxidize water to produce oxygen and degrade organic contaminants to purify water resources. However, the photo-corrosion phenomenon and the low photocatalytic efficiency due to the fast recombination of photogenerated carriers restrict the wide application of Ag_3PO_4 (Martin et al., 2015).

Accordingly, several attempts have been proposed to enhance its photocatalytic activity and improve the photostability with some success, such as morphology and/or size control (Dong et al., 2013, 2014; Li et al., 2014; Krungchanuchat et al., 2017), metal deposition (Liu et al., 2012; Yan et al., 2014b; Lin et al., 2019), coupling with other semiconductors to form Z-scheme heterostructures (Chen et al., 2017; Wang et al., 2017; Li et al., 2019; Zhang et al., 2019).

Surface modification can be an alternative route to boost the photocatalytic performance by changing the charge transfer pathways that typically take place at the surfaces of photocatalysts (Zhao et al., 2008; Li et al., 2015). Many researchers have been reported that anions such as F^- , PO_4^{3-} , and SO_4^{2-} can greatly change the interfacial and surface chemistry of pristine photocatalysts like TiO_2 , BiPO_4 , Fe_2O_3 , C_3N_4 , etc. and enhance the photocatalytic performance (Park and Choi, 2004; Mohapatra and Parida, 2006; Kim and Choi, 2007; Korosi et al., 2007; Parida et al., 2008). Among them, PO_4^{3-} anions (phosphate) are known to exhibit a strong ability to adsorb onto the surfaces of semiconductor photocatalysts by substituting surface hydroxyl groups. Jing et al. have demonstrated that the photocatalytic activity for water oxidation over phosphate-modified TiO_2 was notably improved because the negative charges on the TiO_2 surface resulting from the phosphate groups ($-\text{Ti}-\text{O}-\text{P}-\text{O}^-$) promoted the charge separation (Jing et al., 2012a,b). The surface phosphate modification can also significantly enhance the reactive oxygen species and therefore prolong the photogenerated charge carrier lifetime and improve the separation efficiency (Liu et al., 2014; Min et al., 2014). For instance, Li and co-workers have demonstrated that the surface hydroxyl concentration of the phosphate-modified BiPO_4 samples is increased and responsible for the generation of more hydroxyl radicals to participate in the methylene orange (MO) degradation. As the aforementioned, Ag_3PO_4 photocatalyst suffers from serious photo corrosion issues due to the reduction of Ag_3PO_4 into metallic Ag by photogenerated electrons. The metallic Ag nanoparticles can also be formed by the reaction of Ag^+ in Ag_3PO_4 with the thermally excited electrons along with the creation of structural defects (oxygen and/or silver vacancies) during the thermal annealing process (Yan et al., 2016). Our recent work further showed that the composition and morphology of Ag_3PO_4 can be tuned using ammonia solution etching, which mentions that the strong interaction between surface Ag atoms and ammonia aroused that the surface Ag atoms spontaneous dissolution, resulting in the face-selective etching over Ag_3PO_4 dodecahedron and the formation of $\text{Ag}/\text{Ag}_3\text{PO}_4$ photocatalyst (Zhai et al., 2016). Inspiration by the promotion effect of surface modification on the reported photocatalysts and the structural instability of Ag_3PO_4 , it is expected that the simultaneous modification by phosphate and ammonia etching on Ag_3PO_4 could alter its structure and induce positive effects on the photogenerated charge separation and the reactive species.

In this work, we developed a one-pot surface modification route by using ammonium phosphate [$(\text{NH}_4)_3\text{PO}_4$] to achieve the multiple promotion effects on structural variation and photocatalytic performance of Ag_3PO_4 . The pristine Ag_3PO_4 was synthesized by the precipitation method and modified

by a general immersion process in different concentrations of $(\text{NH}_4)_3\text{PO}_4$ solutions, followed by a thermal annealing process. The chemical etching occurs on the surface of Ag_3PO_4 and induces the formation of Ag^0 nanoparticles due to the strong coordination interaction between Ag^+ and NH_4^+ ion, which can act as electrons acceptors to promote the separation of charge carriers and favor the formation of reactive O_2^- species. Meanwhile, the enrichment in the negative electrostatic field formed by the surface bounded PO_4^{3-} is favorable for the selective adsorption of cationic dyes, the fast transfer of holes to surfaces and the formation of $\cdot\text{OH}$ radicals. Accordingly, the multiple effect of surface modification of Ag_3PO_4 by $(\text{NH}_4)_3\text{PO}_4$ contributes to the enhanced photocatalytic activity and stability toward organic dye solutions.

EXPERIMENTAL

Preparation of Ag_3PO_4 and Ammonium Phosphate-Modified Ag_3PO_4 Samples

All the involved chemicals were purchased from the Shanghai reagent company and used without further purification. Pure Ag_3PO_4 was prepared by the reported precipitation method at room temperature (Yan et al., 2014c). 0.3 g of the as-prepared Ag_3PO_4 samples were put into the aqueous ammonium phosphate solution (50 mL) with different concentrations (0.5 mM, 1 mM, 5 mM, 10 mM), and the suspension was stirred for 5 h to allow the adsorption and chemical modification on the surface. The ammonium phosphate-modified Ag_3PO_4 samples were collected by centrifugation and dried in an oven at 60°C , followed by the thermal annealing in air at 300°C for 3 h in a muffle furnace. The corresponding products were denoted as 0.5P-AP, 1P-AP, 5P-AP, and 10P-AP, respectively. As a reference, the bare Ag_3PO_4 was also annealed in air at 300°C for 3 h and denoted as AP.

Characterizations

X-ray diffraction patterns (XRD) were collected on a Rigaku MinFlex II equipped with Cu K irradiation ($\lambda = 0.15406$ nm). Raman spectra of the samples were recorded on a Renishaw Invia Raman microscope. The morphology of the samples was investigated with a field emission scanning electron microscope (FE-SEM) (JEM-2100). X-ray photoelectron spectroscopy (XPS) analysis was conducted on an ESCALAB 250 photoelectron spectroscopy (Thermo Fisher Scientific) at 3.0×10^{10} mbar with monochromatic Al K radiation ($E = 1,486.2$ eV). Fourier transform infrared spectroscopy (FTIR) analysis was carried out by a Nicolet NeXUS 470. UV-visible diffuse reflectance spectra (DRS) of the powders were performed on a Cary 500 Scan Spectrophotometer (Varian, USA) over a range of 200–800 nm, with BaSO_4 as a reflectance standard. The Brunauer-Emmett-Teller (BET) surface area test was performed on an Auto Chem II surface area analyzer. The charge on the surface (Zeta) of the sample particles in the aqueous solution ($\text{pH} = 7$) is determined by a Nano ZS ZEN3600-type particle size analyzer. The photoluminescence (PL) spectra were obtained by using an F-4600 Fluorescence spectrophotometer with an excitation wavelength of 380 nm. Photoelectrochemical measurements were measured using the Chi660D electrochemical work station and

a 300 W Xe lamp equipped with cutoff filters ($400 \text{ nm} < \lambda < 800 \text{ nm}$) as light source. The photocurrent response was detected on an electrochemical workstation (CHI660E, China) using a standard three-electrode cell with a working electrode (as-prepared photocatalyst), a platinum wire as a counter electrode, and an AgCl electrode as a reference electrode in Na_2SO_4 solution (0.1 M). All electrochemical potentials are reported vs. NHE.

Photocatalytic Activity Test

Photocatalytic process were executed in an aqueous solution at room temperature. A 300W Xe lamp equipped with cutoff filters ($400 \text{ nm} < \lambda < 800 \text{ nm}$) was employed as the irradiation source. Typically, 80 mg specimen as the photocatalyst was dispersed into 80 mL of methyl orange (MO) solution (10 ppm). The suspension was kept stirring in dark condition for 30 min by a blender to establish an adsorption-desorption equilibrium between photocatalyst and MO molecules. Three milliliter of the suspension sample was taken at regular intervals during the process of irradiation and remove the photocatalysts by centrifugation. The residual concentration of the MO dye was detected by the UV-Vis spectrophotometer. The degradation rate is expressed as C/C_0 , where C_0 is the initial concentration of dye, and C represents the corresponding concentration at a certain time interval. The photocatalytic performance of bare Ag_3PO_4 and modified Ag_3PO_4 was also estimated by the decomposing dye of rhodamine B (RhB) and methylene blue (MB) under the same condition. Stability is an important and essential property of the photocatalyst, after each catalytic reaction, the final suspension was centrifuged and the solids photocatalyst obtained by centrifugation were washed by water several times and dried at 60°C to obtain a regenerated catalyst which was used to catalyze a new dye solution under the same photocatalytic process.

RESULTS AND DISCUSSION

Figure 1 shows the XRD patterns of the as-prepared Ag_3PO_4 and the ammonium phosphate-modified Ag_3PO_4 samples. All the XRD patterns of bare Ag_3PO_4 (AP) can be readily indexed

to body-centered cubic structure Ag_3PO_4 (JCPDS no. 06-0505) (Zhang et al., 2014). The intense and sharp XRD diffraction peaks suggest the bare Ag_3PO_4 is highly crystallized. Upon surface modification with ammonium phosphate, the main cubic structure of the modified samples has remained. However, as compared to bare AP, the diffraction peaks of the modified samples show a gradual left shift with increasing the concentration of ammonium phosphate solution. Our previous studies have shown that the surface Ag atoms are easily dissolved from the silver-contained compound after ammonia etching, due to the strong coordination interaction between Ag^+ and NH_3 driving the formation of $\text{Ag}(\text{NH}_3)_2^+$ complex ions (Zhai et al., 2016), which would arouse the structural condensation and reset of Ag_3PO_4 cells and thereby the separation of interior Ag atoms out from the Ag_3PO_4 supercell, responsible to the formation of metallic Ag nanoparticles. In the present study, it is noted that a new diffraction peak appeared at 38.1° in the modified samples (1P-AP, 5P-AP, and 10P-AP) which assigned to (111) plane of Ag^0 (JCPDS no. 65-2871). Thus, ammonium phosphate can function as a chemical etchant in favoring the formation of new Ag/ Ag_3PO_4 solid surfaces with distinct structure and composition for Ag_3PO_4 . The structural variation of Ag_3PO_4 upon ammonium phosphate modification is further investigated by Raman spectra (**Figure S1**). For bare AP, the weak peak at 71 cm^{-1} can be attributed to the external translational and rotational modes associated with the $[\text{PO}_4]$ group (Costa et al., 2018), while the strong peak at 909 cm^{-1} is assigned to the PO_4^{3-} symmetric stretching vibration (Sharma et al., 2017). The intensity of these two peaks shows obvious increase after ammonium phosphate modification especially at high concentration, suggesting the strong chemical interaction between ammonium phosphate and Ag_3PO_4 particles.

The morphology of the Ag_3PO_4 samples before and after surface modification was investigated by SEM (**Figure 2**). We can observe that the bare Ag_3PO_4 is assembled from a plurality of irregular sphere-like particles with obvious fracture surface and several micrometers in size. Meanwhile, many inter-crossed aggregates with a size of ca. 150 nm are observed on the smooth

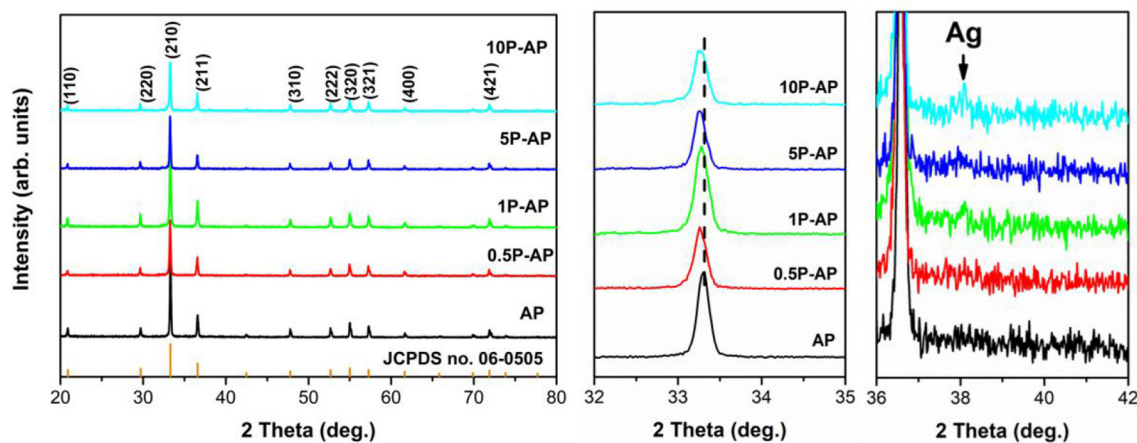


FIGURE 1 | XRD patterns of Ag_3PO_4 and ammonium phosphate-modified Ag_3PO_4 samples.

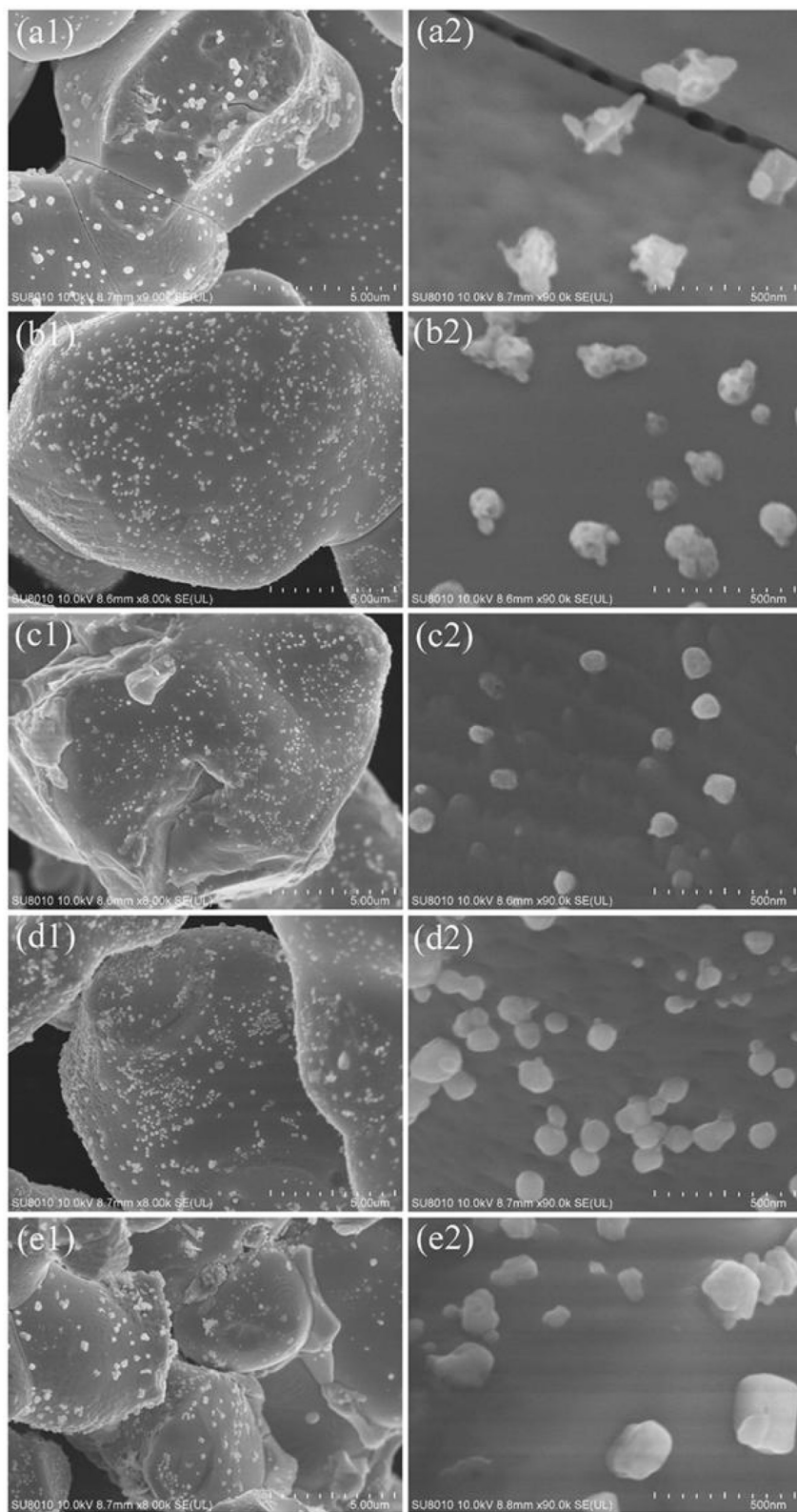


FIGURE 2 | SEM images of bare Ag_3PO_4 (**a1,a2**) and ammonium phosphate-modified Ag_3PO_4 samples: 0.5P-AP (**b1,b2**), 1P-AP (**c1,c2**), 5P-AP (**d1,d2**), and 10P-AP (**e1,e2**).

surfaces of sintered Ag_3PO_4 particles. These aggregates can be attributed to the formation of Ag^0 by thermal decomposition of Ag_3PO_4 during thermal annealing (Yan et al., 2016, 2017). As for the modified Ag_3PO_4 samples, it is obvious that the morphology and the smooth surface of Ag_3PO_4 crystals are kept original while the size and distribution of Ag nanoparticles are quite different. When the concentration of ammonium phosphate is 0.5 mM, the size of the Ag nanoparticles decreases markedly and their distribution improves greatly as compared to that on bare Ag_3PO_4 . This should be due to the strong mutual effect between NH_4^+ and Ag^+ on the surface and the continuous out-diffusion of Ag nanoparticles. With increasing the concentration of ammonium phosphate to 1 mM, the chemical etching of surface Ag^+ is proceeded, resulting in the formation of nearly monodispersed Ag nanoparticles which have a diameter around 60 nm instead of aggregates on the Ag_3PO_4 surfaces. The higher concentration of ammonium phosphate (5 and 10 mM) further promotes the formation of Ag nanoparticles but with particle growth into ca. 200 nm. The surface modification results in a slight decrease in BET surface area for the as-obtained Ag_3PO_4 samples (for example, $3.6 \text{ m}^2 \text{ g}^{-1}$ for AP and $3.0 \text{ m}^2 \text{ g}^{-1}$ for 1P-AP) (Table S1) which might be due to the cover of Ag^0 nanoparticles on the surface of Ag_3PO_4 crystals.

XPS spectra were shown in Figure 3 which invested the surface compositions and chemical states of Ag_3PO_4 after modified by ammonium phosphate. Figure 3A show that the samples before and after ammonium phosphate modification are mainly composed of Ag, O, and P elements. The high-resolution XPS spectrum of Ag3d (Figure 3B) indicates two characteristic peaks corresponding to Ag $3d_{5/2}$ and Ag $3d_{3/2}$. The peaks of

Ag $3d_{3/2}$ and Ag $3d_{5/2}$ can be further divided into two different peaks at 374.6, 374.08 eV and 368.6, 368.05 eV, respectively. The peaks at 374.6 and 368.6 eV can be ascribed Ag^0 , while the peaks at 374.08 and 368.05 eV are associated with Ag^+ ions (Ma et al., 2014; Mao et al., 2018). The calculated percentage composition of Ag^0 for AP and 1P-AP samples is 2.06 and 4.61%, respectively, which indicates that surface modification promotes the decomposition of Ag_3PO_4 into metallic Ag, in good agreement with the XRD and SEM results. The O 1s core level XPS spectra (Figure 3C) could be matched into two peaks at 530.6 and 532.2 eV, which can be assigned to oxides (O_2^-) and hydroxyl groups (OH), respectively (Dai et al., 2011; Teng et al., 2013). It is noted that the concentration of surface OH of 1P-AP sample increases significantly after surface modification, which could be attributed to the strong dissociation of H_2O and binding affinity of phosphate on the Ag_3PO_4 surface (Chong et al., 2016). The P 2p in both samples (Figure 3D) is located at 132.5 eV, confirming the valence state of P^{5+} in PO_4^{3-} (Wang et al., 2013; Zhang et al., 2019). From the XPS results, we can determine the actual content of $(\text{NH}_4)_3\text{PO}_4$ in the 10P-AP sample to be 10.1%, quite consistent with the theoretical value (10.0%) (Table S2). All these results prove that ammonium phosphate modification promotes the formation of Ag/ Ag_3PO_4 heterostructures and the strong adsorption of NH_4^+ and PO_4^{3-} species on the surface of the samples.

The strong interaction of phosphate on Ag_3PO_4 surface can be supported by FTIR. As shown in Figure 4A, the vibration peaks at 556 and $1,020 \text{ cm}^{-1}$ can be assigned to the asymmetrical and symmetrical stretching of PO_4^{3-} (Xie et al., 2015; Cruz et al., 2019) while a broad absorption band centered at $1,428 \text{ cm}^{-1}$ is

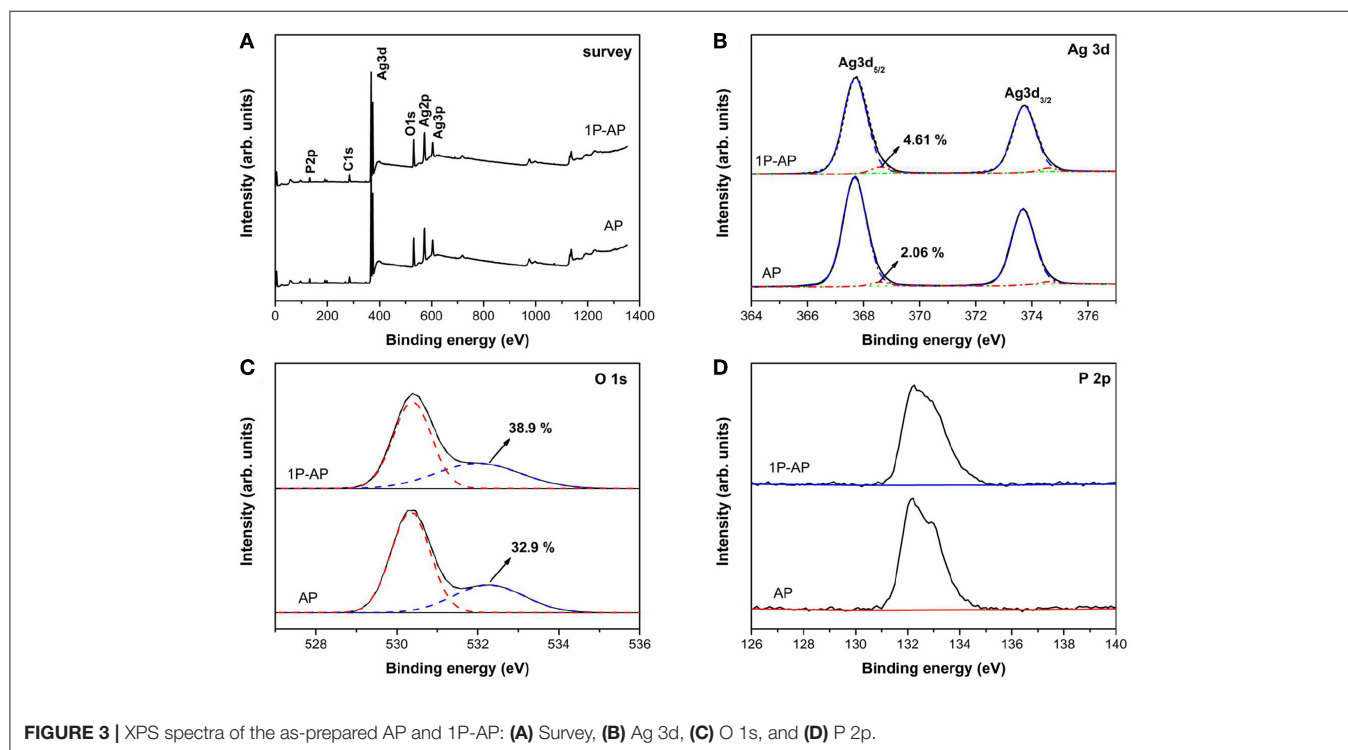


FIGURE 3 | XPS spectra of the as-prepared AP and 1P-AP: (A) Survey, (B) Ag 3d, (C) O 1s, and (D) P 2p.

assigned to the synergistic effect of P-O stretching vibration and PO_4^{3-} symmetric stretching vibrations (Liang et al., 2012). The intensity of all these peaks is gradually enhanced by increasing the concentration of ammonium phosphate, suggesting the strong binding affinity of PO_4^{3-} to the Ag_3PO_4 surfaces. Moreover, the peak at $3,440\text{ cm}^{-1}$ that is related to the hydroxyl stretching vibration is also enhanced upon surface modification. However, when the concentration of ammonium phosphate is too high to 10 mM, the hydroxyl stretching vibration shows a slight decrease in intensity, which might be because more PO_4^{3-} are strongly adsorbed onto the surfaces of Ag_3PO_4 by substituting surface hydroxyl groups (Xie et al., 2015). As expected, the strong binding affinity of PO_4^{3-} and hydroxyl groups to the Ag_3PO_4 surfaces would induce the surface negative electrostatic field of the as-obtained samples. **Figure 4B** depicts the Zeta potential of AP and 1P-AP samples in solutions at pH = 7. It is obvious that the Zeta potential for 1P-AP is -29.78 mV , more negative than that of bare AP (-21.34 mV). The increased surface-carried negative charge of Ag_3PO_4 after surface modification may improve the selective adsorption of cationic dye and accelerate the migrate of photogenerated holes to the surface, responsible to the obvious enhancement of photocatalytic activity.

The UV-Vis DRS spectra of bare Ag_3PO_4 and the modified Ag_3PO_4 samples are shown in **Figure 5A**. We can observe that the bare Ag_3PO_4 exhibits the broad solar light absorption in the wavelength range of $<530\text{ nm}$, and the corresponding band gap

energy is 2.48 eV . Surface modification has slightly enhanced the absorption in the UV-Vis spectral range but does not induce the change of band gap energy as well as the sample color (**Figure S2**). Moreover, it is observed that the modified samples show increasing light absorption intensity in the range of $530\text{--}800\text{ nm}$, which can be due to the plasmonic effect of newly formed Ag nanoparticles on the Ag_3PO_4 surfaces (Shen et al., 2018). The room-temperature PL spectra of the related samples are further shown in **Figure 5B**. All the samples display a strong emission peak located at around 560 nm , which can be considered as a result of the recombination of photogenerated electrons and holes of Ag_3PO_4 (Tian et al., 2017). It is interesting to note that the overall emission intensity of the modified samples is significantly decreased, especially for the 1P-AP sample. This indicates that the recombination of photogenerated carriers is effectively inhibited by surface modification because the newly generated Ag nanoparticles would act as electrons capture and the bounded PO_4^{3-} and hydroxyl groups provide negative electrostatic field in favoring the transfer of holes, conducting to boost photocatalytic activity.

The photocatalytic performance of bare Ag_3PO_4 and the modified Ag_3PO_4 photocatalysts were initially evaluated by decomposing MO dye which as a model pollutant in solution under visible light irradiation. As shown in **Figure 6A**, all the as-obtained Ag_3PO_4 samples before and after surface modification have almost no adsorption on the anionic dye

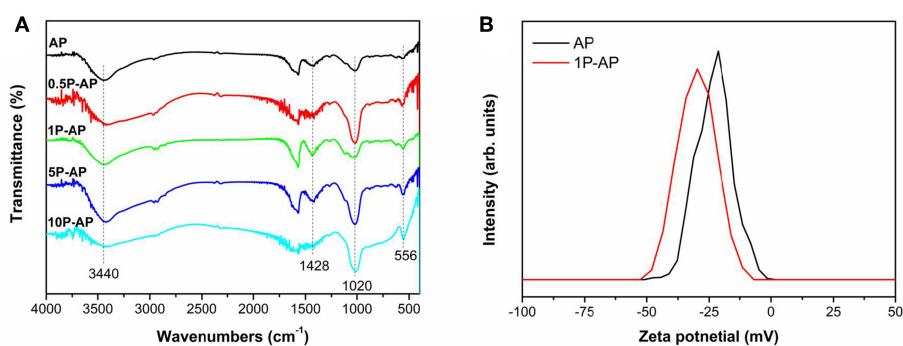


FIGURE 4 | (A) FTIR spectra and **(B)** Zeta potential of bare Ag_3PO_4 and ammonium phosphate-modified Ag_3PO_4 samples.

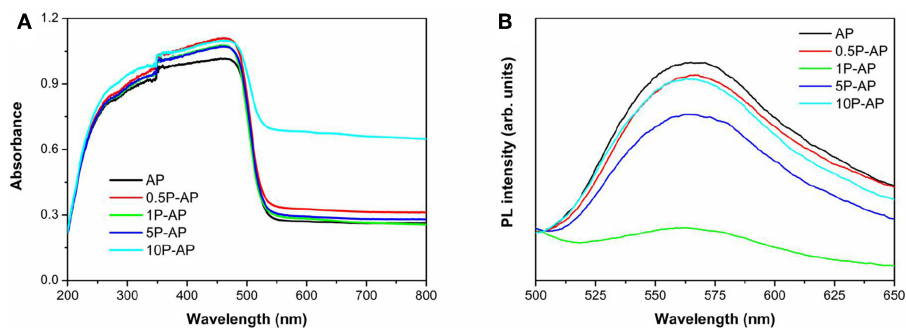
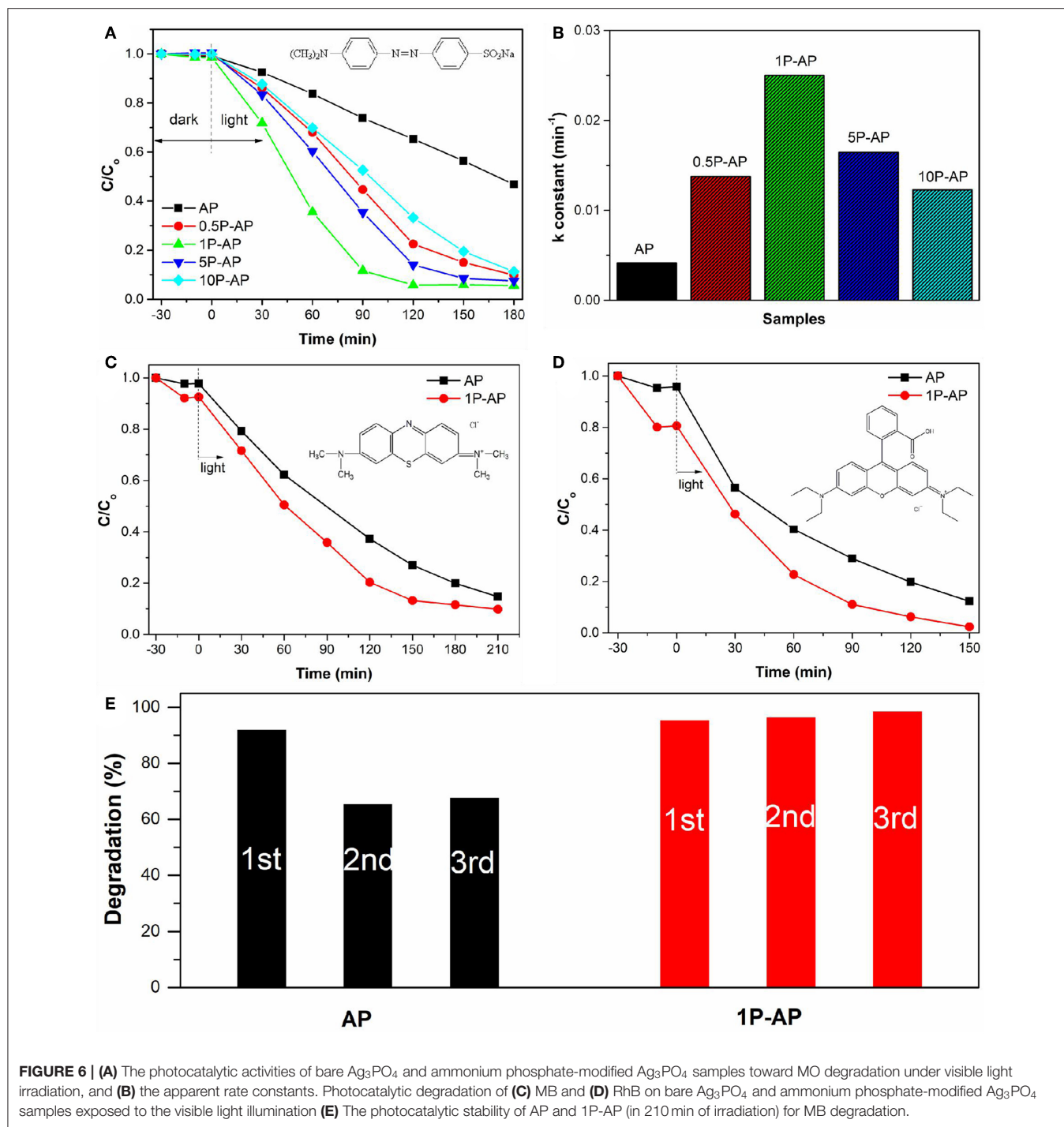


FIGURE 5 | (A) UV-Vis diffuse reflectance spectra and **(B)** room temperature PL spectra of bare Ag_3PO_4 and ammonium phosphate-modified Ag_3PO_4 samples.



MO, which might be because of the low BET surface area and the surface-carried negative charge of the samples. Bare Ag_3PO_4 (AP) could degrade MO into small molecules attributed to its high oxidation capacity; almost 35% of MO is decolorized within 120 min under light illumination. As compared, the photocatalytic performance of the modified Ag_3PO_4 was improved significantly and was highly dependent on the concentration of ammonium phosphate. Among them, the 1P-AP sample showed the highest activity and could degrade

almost 95% of MO within the same reaction period. Moreover, it was found that the photodegradation curves of MO dye were fitted by pseudo-first-order reaction kinetics. **Figure 6B** gives the corresponding rate constant of various samples. Clearly, the modified samples exhibited much higher rates than the bare Ag_3PO_4 while the 1P-AP sample had the highest rate constant, about 5 times that of the AP sample. In view of the improved photocatalytic performance of Ag_3PO_4 after surface modification, we extended the test for the other two cationic

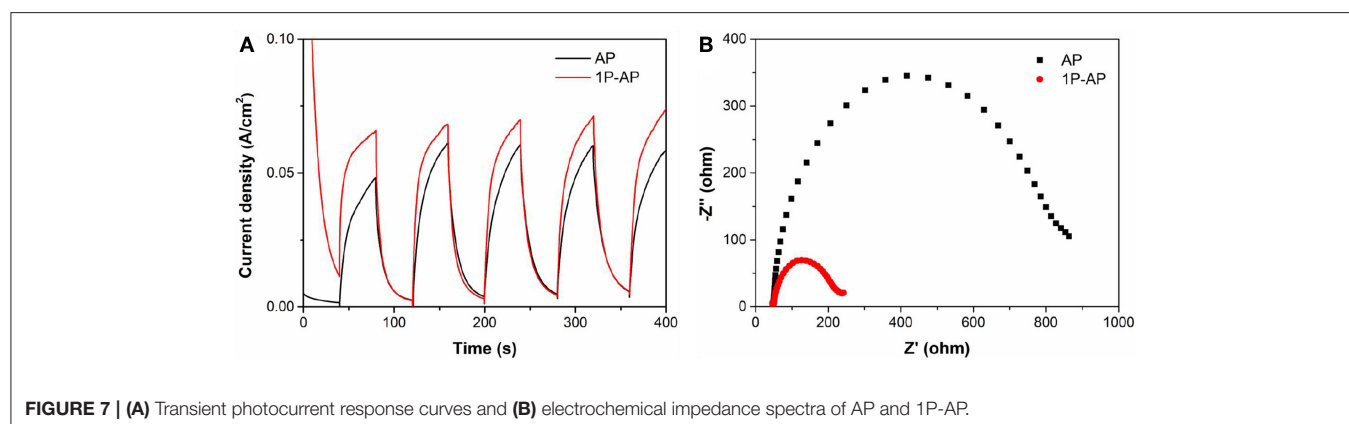
dyes MB and RhB (**Figures 6C,D**). As expected, bare Ag_3PO_4 had visible adsorption for these two dyes and the modified samples exhibited enhanced adsorption because of the more negative electrostatic field provided by phosphate modification. In addition, the modified 1P-AP sample showed much higher degradation for both MB and RhB than AP, suggesting the alternative route to boost the photocatalytic performance of Ag_3PO_4 by surface modification.

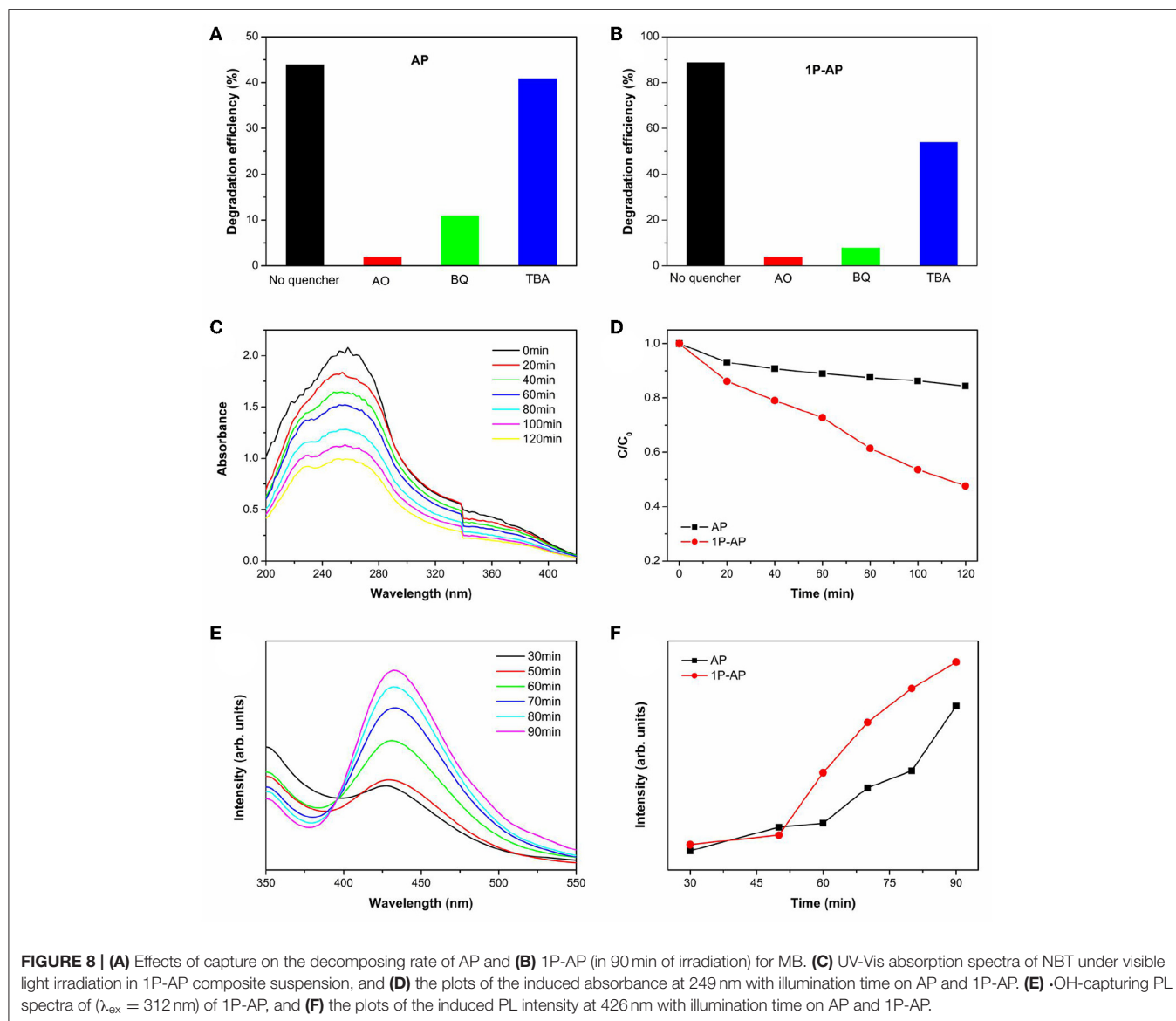
In addition to the photocatalytic activity, the modified Ag_3PO_4 samples also displayed improved activity stability with respect to the bare sample. As shown in **Figure 6E**, after three cycles, the photocatalytic activity of AP was reduced by 30% while 1P-AP did not show any significant loss of photocatalytic activity for the degradation of MB. The excellent photocatalytic stability of 1P-AP sample can be attributed to the formation of Ag/ Ag_3PO_4 heterostructures during the continuous photocatalytic experiments, as evidenced by the XRD and SEM characterizations of the used catalysts (**Figures S3, S4**). In particular, the modification of Ag_3PO_4 with $(\text{NH}_4)_3\text{PO}_4$ can remarkably inhibit the decomposition of Ag_3PO_4 into metallic Ag, resulting in the highly active and stable Ag/ Ag_3PO_4 heterostructures.

According to what we have observed and discussed above, the enhanced photocatalytic performance of Ag_3PO_4 photocatalyst after surface modification can be mainly attributed to the newly formed Ag nanoparticles and the strongly bounded PO_4^{3-} groups, rather than the effects of particle size and surface area. Many researchers have reported that the usually formed Ag^0 nanoparticles distributed on the surface of Ag-based photocatalysts can function as electron acceptors to accelerate the charge segregation due to the high Schottky barrier at the interface of metal/semiconductor, inducing efficient interfacial charge transfer (Yan et al., 2014b). It is also indicated that the phosphate modification could promote the transfer of photogenerated holes to the surface of photocatalysts driven by the negative electrostatic field, leading to an improved charge separation (Xie et al., 2015). Accordingly, the synergetic effect of Ag nanoparticles and surface negative electrostatic field makes separation of charge carriers more efficient and inhibits their recombination. Thus, the transient photocurrent and electrochemical impedance tests were investigated to prove

that (**Figures 7A,B**). As expected, the ammonium phosphate-modified sample shows a larger photocurrent and a smaller curvature radius of impedance than the bare Ag_3PO_4 . These results are also consistent with the above-mentioned PL spectra (**Figure 5B**), in which the modified samples show a lower emission peak than the bare sample, and the 1P-AP sample exhibits the lowest PL emission peak.

On the other hand, it is suggested that the surface modification by phosphate offers an attractive advantage to integrate with complex surface topologies, contribute to the forming of reactive oxygen substance (Zhong and Gamelin, 2010; Seabold and Choi, 2011; Zhong et al., 2011). As a consequence, it is necessary to probe the main active substance during photocatalysis on the Ag_3PO_4 photocatalysts to disclose the improved photocatalytic performance. We can observe that the decomposition efficiency of MB over bare Ag_3PO_4 after adding various scavengers (**Figure 8A**). The addition of benzoquinone (BQ) and oxalic acid ammonia (AO) significantly restrained the photocatalytic performance of bare Ag_3PO_4 , which indicates that $\text{O}_2^{\cdot-}$ and h^+ are the main active species over bare Ag_3PO_4 in photocatalysis, consistent with the reported results (Yan et al., 2014b; Zhai et al., 2016). As compared, it is observed from **Figure 8B** that the degradation of MB by the modified Ag_3PO_4 after BQ and AO addition is also significantly restrained, indicating that $\text{O}_2^{\cdot-}$ and h^+ are also the main active substances of modified Ag_3PO_4 ; meanwhile, the degradation activity was also inhibited after the addition of tertbutyl alcohol (TBA), indicating that $\cdot\text{OH}$ can also serve as active species in 1P-AP. It should be noticed that the 1P-AP sample suffered more suppression by the addition of BQ than AP, suggesting the more contribution of $\text{O}_2^{\cdot-}$ in 1P-AP by the increased amount of metallic Ag nanoparticle. The presence of $\text{O}_2^{\cdot-}$ radicals can be confirmed by a nitroblue tetrazolium (NBT) probe method (Yan et al., 2015). As shown in **Figure 8C**, the characteristic peak at 259 nm shows a gradual decrease in intensity with prolonging irradiation time, suggesting the reaction between NBT and $\text{O}_2^{\cdot-}$ radicals, indirectly evidencing the presence of $\text{O}_2^{\cdot-}$ radicals. In particular, under the same conditions, 1P-AP can produce more $\text{O}_2^{\cdot-}$ radicals than AP sample (**Figure 8D**), coinciding with the activity trend and the results of BQ quenching. Moreover, driven by the strong

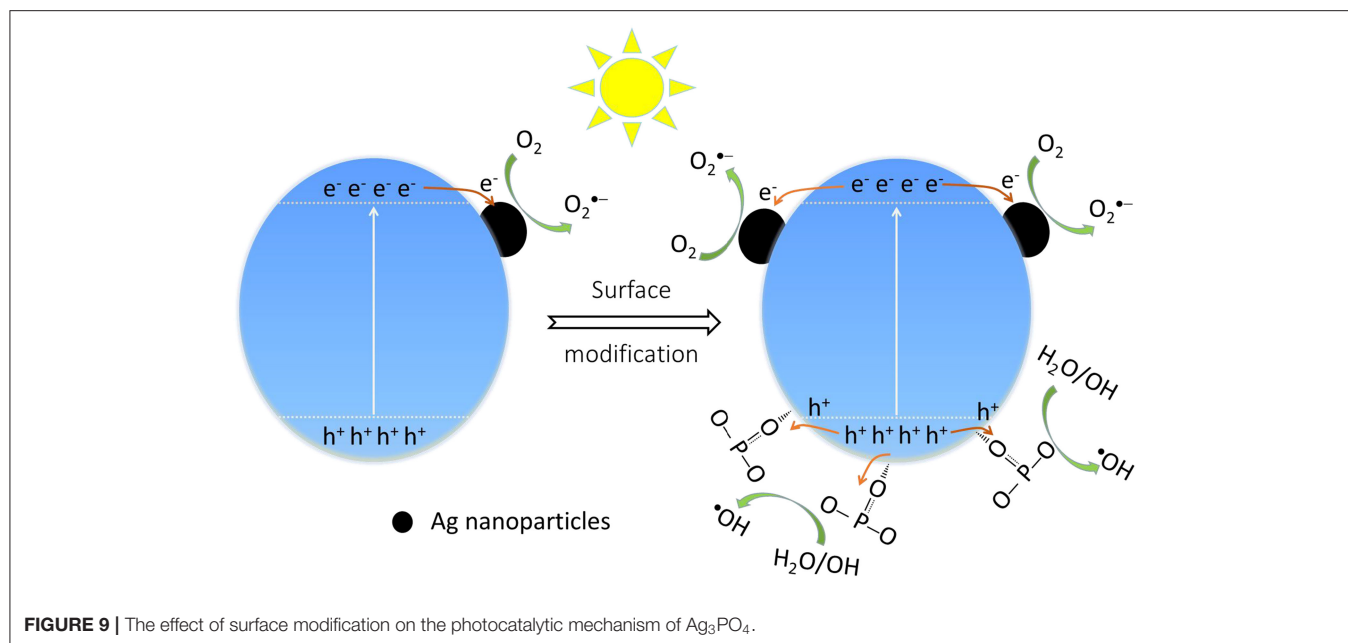




bound ability of PO_4^{3-} and the induced negative electrostatic field, photogenerated holes would migrate to the surface of 1P-AP and react with hydroxyl groups to form $\cdot\text{OH}$. The increased reactive $\cdot\text{OH}$ can be further supported by the measure of photoluminescence technique with terephthalic acid (PL-TA). The results in **Figure 8E** indicates that a significant PL emission peak located at around 426 nm is observed, which is monotonously increased against the irradiation time, evidencing the formation of $\cdot\text{OH}$ radicals in the photocatalysis. As shown in **Figure 8F**, under the same irradiation time, the 1P-AP sample displays much higher PL intensity than AP, demonstrating the high amount of generated $\cdot\text{OH}$ radicals on the modified photocatalyst. As a consequence, surface modification of Ag_3PO_4 favors the efficient charge of photogenerated electrons and holes to Ag nanoparticles and bounded OH groups, respectively, facilitating more charge carriers to produce

various reactive oxygen substance and participation in the photocatalysis (**Figure 9**).

The photocatalytic activity of modified Ag_3PO_4 is also dependent on the concentration of ammonium phosphate, which has an obvious effect on the size and distribution of Ag nanoparticles as well as the anion groups bounded on the Ag_3PO_4 surfaces. For example, at a moderate concentration (1 mM), the nearly monodispersed Ag nanoparticles with small size construct a good heterostructure interface with Ag_3PO_4 , accelerating the transfer of electron-hole pairs and producing highly reactive $\text{O}_2^{\cdot-}$; while the surface modification at high concentration (10 mM) would induce more Ag nanoparticles but they are highly aggregated and grow into larger particles, therefore contribute to a negative effect on the photocatalytic activity. At the same time, the more adsorbed PO_4^{3-} would also substitute the surface



OH groups, possibly reducing the chance of direct holes reacting with surface hydroxyl groups to generate reactive $\cdot\text{OH}$ radicals.

To further distinguish the single role of NH_4^+ and PO_4^{3-} in promotion of photocatalytic performance of Ag_3PO_4 , two control catalysts that were modified with NH_4NO_3 and Na_3PO_4 , and followed by the thermal treatment process were prepared and denoted as $1\text{NH}_4\text{NO}_3\text{-AP}$ and $1\text{Na}_3\text{PO}_4\text{-AP}$, respectively. As shown from the XRD results (Figure S5), the (210) peak of $1\text{NH}_4\text{NO}_3\text{-AP}$ displays a left shift as compared with bare AP, indicating the separation of silver ions from the crystal lattice driven by the strong coordination of NH_4^+ , in good agreement with the results of ammonium etching (Zhai et al., 2016). In the case of $1\text{Na}_3\text{PO}_4\text{-AP}$, there is no obvious change in the XRD peaks as compared with bare AP, but the photocatalytic activity increased obviously (Figure S6), which indicates the positive effect of PO_4^{3-} . Moreover, we can observe that the activity trend follows the order of $1(\text{NH}_4)_3\text{PO}_4\text{-AP} > 1\text{Na}_3\text{PO}_4\text{-AP} \approx 1\text{NH}_4\text{NO}_3\text{-AP} > \text{bare Ag}_3\text{PO}_4$, strongly supporting the multiple roles of ammonium phosphate in promotion the photocatalytic performance of Ag_3PO_4 .

CONCLUSION

We have developed a one-pot surface modification route by using ammonium phosphate solutions to improve the photocatalytic performance of Ag_3PO_4 . It was found that ammonium phosphate plays the multiple promotion roles in favoring the formation of metallic Ag nanoparticles and providing the negative electrostatic field on the surface of Ag_3PO_4 photocatalysts, which consequently promote the separation efficiency of photoinduced electron-hole pairs,

enhance the selective adsorption of cationic dye, and increase the concentration of reactive oxygen species. This work provides an alternative route to boost the photocatalytic activity of Ag_3PO_4 and can spread to design and fabricate other potential Ag-based photocatalytic materials.

DATA AVAILABILITY STATEMENT

The datasets generated for this study are available on request to the corresponding author.

AUTHOR CONTRIBUTIONS

QL and ZQ conducted the catalysts preparation. QL, LW, and SZ performed the activity test. NL, ZJ, and WL discussed the mechanism part. QL, NL, and TY conceived the project and co-wrote the manuscript. The manuscript was written through collective contributions from all authors. All authors approved the final version of the manuscript.

ACKNOWLEDGMENTS

This work was supported by the National Natural Science Foundation of China (21872081), Natural Science Foundation of Shandong Province (ZR2016BM04), and China Postdoctoral Science Foundation (2015M572011 and 2017T100494).

SUPPLEMENTARY MATERIAL

The Supplementary Material for this article can be found online at: <https://www.frontiersin.org/articles/10.3389/fchem.2019.00866/full#supplementary-material>

REFERENCES

- Asahi, R., Morikawa, T., Ohwaki, T., Aoki, K., and Taga, Y. (2001). Visible-light photocatalysis in nitrogen-doped titanium oxides. *Science* 293, 269–271. doi: 10.1126/science.1061051
- Chen, F., Yang, Q., Li, X. M., Zeng, G. M., Wang, D. B., Niu, C. G., et al. (2017). Hierarchical assembly of graphene-bridged Ag₃PO₄/Ag/BiVO₄ (040) Z-scheme photocatalyst: an efficient, sustainable and heterogeneous catalyst with enhanced visible-light photoactivity towards tetracycline degradation under visible light irradiation. *Appl. Catal. B Environ.* 200, 330–342. doi: 10.1016/j.apcatb.2016.07.021
- Chong, R. F., Cheng, X. X., Wang, B. Y., Li, D. L., Chang, Z. X., and Zhang, L. (2016). Enhanced photocatalytic activity of Ag₃PO₄ for oxygen evolution and Methylene blue degeneration: effect of calcination temperature. *Int. J. Hydrogen Energy* 41, 2575–2582. doi: 10.1016/j.ijhydene.2015.12.061
- Costa, T. M. S., Lima, M. S., Cruz, J. F., Silva, L. J., Santos, R. S., and Luz, G. E. (2018). Synthesis, characterization, and photocatalytic activity of Ag₃PO₄/SBA-15 in ciprofloxacin degradation under polychromatic irradiation. *J. Photochem. Photobiol. A* 364, 461–471. doi: 10.1016/j.jphotochem.2018.06.039
- Cruz, J. F., Costa, T. M. S., Lima, M. S., Silva, L. J., Santos, R. S., Cavalcante, L. S., et al. (2019). Effect of different synthesis methods on the morphology, optical behavior, and superior photocatalytic performances of Ag₃PO₄ sub-microcrystals using white-light-emitting diodes. *J. Photochem. Photobiol. A* 377, 14–25. doi: 10.1016/j.jphotochem.2019.03.031
- Dai, G. P., Yu, J. G., and Liu, G. (2011). Synthesis and enhanced visible-light photoelectrocatalytic activity of p-n junction BiOI/TiO₂ nanotube arrays. *J. Phys. Chem. C* 115, 7339–7346. doi: 10.1021/jp200788n
- Dai, K., Lv, J. L., Zhang, J. F., Zhu, G. P., Geng, L., and Liang, C. H. (2018). Efficient visible-light-driven splitting of water into hydrogen over surface-fluorinated anatase TiO₂ nanosheets with exposed {001} facets/layered CdS-diethylenetriamine nanobelts. *ACS Sustain. Chem. Eng.* 6, 12817–12826. doi: 10.1021/acssuschemeng.8b02064
- Dong, L. H., Wang, P., Wang, S., Lei, P. H., and Wang, Y. J. (2014). A simple way for Ag₃PO₄ tetrahedron and tetrapod microcrystals with high visible-light-responsive activity. *Mater. Lett.* 134, 158–161. doi: 10.1016/j.matlet.2014.07.094
- Dong, P. Y., Wang, Y. H., Li, H. H., Li, H., Ma, X. L., and Han, L. L. (2013). Shape-controllable synthesis and morphology-dependent photocatalytic properties of Ag₃PO₄ crystals. *J. Mater. Chem. A* 1, 4651–4656. doi: 10.1039/c3ta00130j
- Guo, F., Li, M., Ren, H., Huang, X., Shu, K., Shi, W., et al. (2019). Facile bottom-up preparation of Cl-doped porous g-C₃N₄ nanosheets for enhanced photocatalytic degradation of tetracycline under visible light. *Sep. Purif. Technol.* 228:115770. doi: 10.1016/j.seppur.2019.115770
- Han, L., Wang, P., Zhu, C., Zhai, Y., and Dong, S. (2011). Facile solvothermal synthesis of cube-like Ag@AgCl: a highly efficient visible light photocatalyst. *Nanoscale* 3, 2931–2935. doi: 10.1039/c1nr10247h
- Huo, Y., Zhang, J. F., Dai, K., Li, Q., Lv, J. L., Zhu, G. P., et al. (2019). All-solid-state artificial Z-scheme porous g-C₃N₄/Sn₂S₃-DETA heterostructure photocatalyst with enhanced performance in photocatalytic CO₂ reduction. *Appl. Catal. B Environ.* 241, 528–538. doi: 10.1016/j.apcatb.2018.09.073
- Jing, D., and Guo, L. (2006). A novel method for the preparation of a highly stable and active CdS photocatalyst with a special surface nanostructure. *J. Phys. Chem. B* 110, 11139–11145. doi: 10.1021/jp060905k
- Jing, L. Q., Cao, Y., Cui, H. Q., Durrant, J. R., Tang, J. W., Liu, D. N., et al. (2012b). Acceleration effects of phosphate modification on the decay dynamics of photo-generated electrons of TiO₂ and its photocatalytic activity. *Chem. Commun.* 48, 10775–10777. doi: 10.1039/c2cc34973f
- Jing, L. Q., Zhou, J., Durrant, J. R., Tang, J. W., Liu, D. N., and Fu, H. G. (2012a). Dynamics of photogenerated charges in the phosphate modified TiO₂ and the enhanced activity for photoelectrochemical water splitting. *Energ. Environ. Sci.* 5, 6552–6558. doi: 10.1039/c2ee03383f
- Kim, H., and Choi, W. (2007). Effects of surface fluorination of TiO₂ on photocatalytic oxidation of gaseous acetaldehyde. *Appl. Catal. B Environ.* 69, 127–132. doi: 10.1016/j.apcatb.2006.06.011
- Korosi, L., Papp, S., Bertoti, I., and Dekany, I. (2007). Surface and bulk composition, structure, and photocatalytic activity of phosphate-modified TiO₂. *Chem. Mater.* 19, 4811–4819. doi: 10.1021/cm070692r
- Krunghanuchat, S., Ekthammathat, N., Phruangrat, A., Thongtem, S., and Thongtem, T. (2017). High UV-visible photocatalytic activity of Ag₃PO₄ dodecahedral particles synthesized by a simple hydrothermal method. *Mater. Lett.* 201, 58–61. doi: 10.1016/j.matlet.2017.04.131
- Li, X. Z., Wu, K. L., Dong, C., Xia, S. H., Ye, Y., and Wei, X. W. (2014). Size-controlled synthesis of Ag₃PO₄ nanorods and their high-performance photocatalysis for dye degradation under visible-light irradiation. *Mater. Lett.* 130, 97–100. doi: 10.1016/j.matlet.2014.05.069
- Li, Y., Wang, Y. W., Huang, Y., Cao, J. J., Ho, W. K., Lee, S. C., et al. (2015). Controllable synthesis of phosphate-modified BiPO₄ nanorods with high photocatalytic activity: surface hydroxyl groups concentrations effects. *RSC Adv.* 5, 99712–99721. doi: 10.1039/C5RA20189F
- Li, Z., Wang, X., Zhang, J. F., Liang, C. H., Lu, L. H., and Dai, K. (2019). Preparation of Z-scheme WO₃(H₂O)_{0.333}/Ag₃PO₄ composites with enhanced photocatalytic activity and durability. *Chin. J. Catal.* 40, 326–334. doi: 10.1016/S1872-2067(18)63165-1
- Liang, Q. H., Shi, Y., Ma, W. J., Li, Z., and Yang, X. M. (2012). Enhanced photocatalytic activity and structural stability by hybridizing Ag₃PO₄ nanospheres with graphene oxide sheets. *Phys. Chem. Chem. Phys.* 14, 15657–15665. doi: 10.1039/c2cp42465g
- Lin, J. J., Sun, T., Li, M. B., Yang, J. X., Shen, J. N., Zhang, Z. Z., et al. (2019). More efficiently enhancing photocatalytic activity by embedding Pt within anatase-rutile TiO₂ heterophase junction than exposing Pt on the outside surface. *J. Catal.* 372, 8–18. doi: 10.1016/j.jcat.2019.02.019
- Liu, C., Jing, L. Q., He, L. M., Luan, Y. B., and Li, C. M. (2014). Phosphate-modified graphitic C₃N₄ as efficient photocatalyst for degrading colorless pollutants by promoting O₂ adsorption. *Chem. Commun.* 50, 1999–2001. doi: 10.1039/c3cc47398h
- Liu, X., Zhai, H., Wang, P., Zhang, Q., Wang, Z., Liu, Y., et al. (2019). Synthesis of a WO₃ photocatalyst with high photocatalytic activity and stability using synergetic internal Fe³⁺ doping and superficial Pt loading for ethylene degradation under visible-light irradiation. *Catal. Sci. Technol.* 9, 652–658. doi: 10.1039/C8CY02375A
- Liu, Y. P., Fang, L., Lu, H. D., Li, Y. W., Hu, C. Z., and Yu, H. G. (2012). One-pot pyridine-assisted synthesis of visible-light-driven photocatalyst Ag/Ag₃PO₄. *Appl. Catal. B Environ.* 115, 245–252. doi: 10.1016/j.apcatb.2011.12.038
- Ma, J. F., Zou, J., Li, L. Y., Yao, C., Kong, Y., Cui, B. Y., et al. (2014). Nanocomposite of attapulgite-Ag₃PO₄ for Orange II photodegradation. *Appl. Catal. B Environ.* 144, 36–40. doi: 10.1016/j.apcatb.2013.06.029
- Macedo, N. G., Gouveia, A. F., Roca, R. A., Assis, M., Gracia, L., Andres, J., et al. (2018). Surfactant-mediated morphology and photocatalytic activity of alpha-Ag₂WO₄ material. *J. Phys. Chem. C* 122, 8667–8679. doi: 10.1021/acs.jpcc.8b01898
- Mao, S., Bao, R., Fang, D., and Yi, J. H. (2018). Facile synthesis of Ag/AgX (X = Cl, Br) with enhanced visible-light-induced photocatalytic activity by ultrasonic spray pyrolysis method. *Adv. Powder Technol.* 29, 2670–2677. doi: 10.1016/j.apt.2018.07.016
- Martin, D. J., Liu, G. G., Moniz, S. J. A., Bi, Y. P., Beale, A. M., Ye, J. H., et al. (2015). Efficient visible driven photocatalyst, silver phosphate: performance, understanding and perspective. *Chem. Soc. Rev.* 44, 7808–7828. doi: 10.1039/C5CS00380F
- Min, Y. L., Qi, X. F., Xu, Q. J., and Chen, Y. C. (2014). Enhanced reactive oxygen species on a phosphate modified C₃N₄/graphene photocatalyst for pollutant degradation. *CrystEngComm* 16, 1287–1295. doi: 10.1039/c3ce41964a
- Mohapatra, P., and Parida, K. M. (2006). Photocatalytic activity of sulfate modified titania: decolorization of methylene blue in aqueous solution. *J. Mol. Catal. A Chem.* 258, 118–123. doi: 10.1016/j.molcata.2006.05.002
- Parida, K. M., Sahu, N., Biswal, N. R., Naik, B., and Pradhan, A. C. (2008). Preparation, characterization, and photocatalytic activity of sulfate-modified titania for degradation of methyl orange under visible light. *J. Colloid Interf. Sci.* 318, 231–237. doi: 10.1016/j.jcis.2007.10.028
- Park, H., and Choi, W. (2004). Effects of TiO₂ surface fluorination on photocatalytic reactions and photoelectrochemical behaviors. *J. Phys. Chem. B* 108, 4086–4093. doi: 10.1021/jp036735i
- Qi, K. Z., Cheng, B., Yu, J. G., and Ho, W. K. (2017). Review on the improvement of the photocatalytic and antibacterial activities of ZnO. *J. Alloy. Comp.* 727, 792–820. doi: 10.1016/j.jallcom.2017.08.142
- Qi, K. Z., Liu, S. Y., and Qiu, M. (2018). Photocatalytic performance of TiO₂ nanocrystals with/without oxygen defects. *Chin. J. Catal.* 39, 867–875. doi: 10.1016/S1872-2067(17)62999-1

- Qi, K. Z., Liu, S. Y., Selyaraj, R., Wang, W., and Yan, Z. X. (2019). Comparison of Pt and Ag as co-catalyst on g-C₃N₄ for improving photocatalytic activity: experimental and DFT studies. *Desalin. Water Treat.* 153, 244–252. doi: 10.5004/dwt.2019.24079
- Qi, K. Z., Selvaraj, R., Al Fahdi, T., Al-Kindy, S., Kim, Y., Wang, G. C., et al. (2016). Enhanced photocatalytic activity of anatase-TiO₂ nanoparticles by fullerene modification: a theoretical and experimental study. *Appl. Surf. Sci.* 387, 750–758. doi: 10.1016/j.apsusc.2016.06.134
- Seabold, J. A., and Choi, K. S. (2011). Effect of a Cobalt-based oxygen evolution catalyst on the stability and the selectivity of photo-oxidation reactions of a WO₃ photoanode. *Chem. Mater.* 23, 1105–1112. doi: 10.1021/cm1019469
- Sharma, M., Mohapatra, P. K., and Bahadur, D. (2017). Improved photocatalytic degradation of organic dye using Ag₃PO₄/MoS₂ nanocomposite. *Front. Mater. Sci.* 11, 366–374. doi: 10.1007/s11706-017-0404-x
- Shen, Y. Z., Zhu, Z. D., Wang, X. G., Khan, A., Gong, J. Y., and Zhang, Y. R. (2018). Synthesis of Z-scheme g-C₃N₄/Ag/Ag₃PO₄ composite for enhanced photocatalytic degradation of phenol and selective oxidation of gaseous isopropanol. *Mater. Res. Bull.* 107, 407–415. doi: 10.1016/j.materresbull.2018.08.017
- Song, M. T., Wu, Y. H., Xu, C., Wang, X. J., and Su, Y. G. (2019). Synergistic effects of multi-active sites in silver modified Bi degrees-BiVO₄ toward efficient reduction of aromatic nitrobenzene. *J. Hazard. Mater.* 368, 530–540. doi: 10.1016/j.jhazmat.2019.01.083
- Teng, W., Li, X. Y., Zhao, Q. D., and Chen, G. H. (2013). Fabrication of Ag/Ag₃PO₄/TiO₂ heterostructure photoelectrodes for efficient decomposition of 2-chlorophenol under visible light irradiation. *J. Mater. Chem. A* 1, 9060–9068. doi: 10.1039/c3ta11254c
- Tian, J., Yan, T. J., Qiao, Z., Wang, L. L., Li, W. J., You, J. M., et al. (2017). Anion-exchange synthesis of Ag₂S/Ag₃PO₄ core/shell composites with enhanced visible and NIR light photocatalytic performance and the photocatalytic mechanisms. *Appl. Catal. B Environ.* 209, 566–578. doi: 10.1016/j.apcatb.2017.03.022
- Wang, J., Song, Y., Hu, J., Li, Y., Wang, Z., Yang, P., et al. (2019). Photocatalytic hydrogen evolution on P-type tetragonal zircon BiVO₄. *Appl. Catal. B Environ.* 251, 94–101. doi: 10.1016/j.apcatb.2019.03.049
- Wang, Y. F., Li, X. L., Wang, Y. W., and Fan, C. M. (2013). Novel visible-light AgBr/Ag₃PO₄ hybrids photocatalysts with surface plasma resonance effects. *J. Solid State Chem.* 202, 51–56. doi: 10.1016/j.jssc.2013.03.013
- Wang, Z. L., Hu, T. P., Dai, K., Zhang, J. F., and Liang, C. H. (2017). Construction of Z-scheme Ag₃PO₄/Bi₂WO₆ composite with excellent visible-light photodegradation activity for removal of organic contaminants. *Chin. J. Catal.* 38, 2021–2029. doi: 10.1016/S1872-2067(17)62942-5
- Wang, Z. L., Lv, J. L., Zhang, J. F., Dai, K., and Liang, C. H. (2018). Facile synthesis of Z-scheme BiVO₄/porous graphite carbon nitride heterojunction for enhanced visible-light-driven photocatalyst. *Appl. Surf. Sci.* 430, 595–602. doi: 10.1016/j.apsusc.2017.06.093
- Xie, M. Z., Bian, J., Humayun, M., Qu, Y., Feng, Y. J., and Jing, L. Q. (2015). The promotion effect of surface negative electrostatic field on the photogenerated charge separation of BiVO₄ and its contribution to the enhanced PEC water oxidation. *Chem. Commun.* 51 2821–2823. doi: 10.1039/C4CC08835B
- Yan, T. J., Guan, W. F., Cui, L. T., Xu, Y. Q., and Tian, J. (2015). Immobilization of cadmium ions to synthesis hierarchical flowerlike cadmium phosphates microspheres and their application in the degradation of organic pollutants under light irradiation. *RSC Adv.* 5, 43756–43764. doi: 10.1039/C5R A07224G
- Yan, T. J., Guan, W. F., Li, W. J., and You, J. M. (2014c). Ag₃PO₄ photocatalysts loaded on uniform SiO₂ supports for efficient degradation of methyl orange under visible light irradiation. *RSC Adv.* 4, 37095–37099. doi: 10.1039/C4RA06135G
- Yan, T. J., Guan, W. F., Tian, J., Wang, P., Li, W. J., and You, J. M. (2016). Improving the photocatalytic performance of silver phosphate by thermal annealing: influence of acetate species. *J. Alloy. Compd.* 680, 436–445. doi: 10.1016/j.jallcom.2016.04.142
- Yan, T. J., Guan, W. F., Xiao, Y., Tian, J., Qiao, Z., Zhai, H. S., et al. (2017). Effect of thermal annealing on the microstructures and photocatalytic performance of silver orthophosphate: the synergistic mechanism of Ag vacancies and metallic Ag. *Appl. Surf. Sci.* 391, 592–600. doi: 10.1016/j.apsusc.2016.03.095
- Yan, T. J., Yuan, R. S., Li, W. J., and You, J. M. (2014a). Origin of superior photocatalytic activity in rutile TiO₂ hierarchical microspheres: the dominate role of “microcavity” structure. *Appl. Catal. A Gen.* 478, 204–210. doi: 10.1016/j.apcata.2014.04.013
- Yan, T. J., Zhang, H. W., Liu, Y. P., Guan, W. F., Long, J. L., Li, W. J., et al. (2014b). Fabrication of robust M/Ag₃PO₄ (M = Pt, Pd, Au) Schottky-type heterostructures for improved visible-light photocatalysis. *RSC Adv.* 4, 37220–37230. doi: 10.1039/C4RA06254J
- Yi, Z. G., Ye, J. H., Kikugawa, N., Kako, T., Ouyang, S. X., Stuart-Williams, H., et al. (2010). An orthophosphate semiconductor with photooxidation properties under visible-light irradiation. *Nat. Mater.* 9, 559–564. doi: 10.1038/nmat2780
- Zhai, H. S., Yan, T. J., Wang, P., Yu, Y., Li, W. J., You, J. M., et al. (2016). Effect of chemical etching by ammonia solution on the microstructure and photocatalytic activity of Ag₃PO₄ photocatalyst. *Appl. Catal. A Gen.* 528, 104–112. doi: 10.1016/j.apcata.2016.10.003
- Zhang, L., He, Y., Zhu, L., Jiao, Z. L., Deng, W. Z., Pu, C. P., et al. (2019). Alkyl phosphate modified graphene oxide as friction and wear reduction additives in oil. *J. Mater. Sci.* 54, 4626–4636. doi: 10.1007/s10853-018-03216-7
- Zhang, S. N., Zhang, S. J., and Song, L. M. (2014). Super-high activity of Bi³⁺ doped Ag₃PO₄ and enhanced photocatalytic mechanism. *Appl. Catal. B Environ.* 152, 129–139. doi: 10.1016/j.apcatb.2014.01.020
- Zhao, D., Chen, C. C., Wang, Y. F., Ji, H. W., Ma, W. H., Zang, L., et al. (2008). Surface modification of TiO₂ by phosphate: effect on photocatalytic activity and mechanism implication. *J. Phys. Chem. C* 112, 5993–6001. doi: 10.1021/jp712049c
- Zhong, D. K., Choi, S., and Gamelin, D. R. (2011). Near-complete suppression of surface recombination in solar photoelectrolysis by “Co-Pi” catalyst-modified W:BiVO₄. *J. Am. Chem. Soc.* 133, 18370–18377. doi: 10.1021/ja207348x
- Zhong, D. K., and Gamelin, D. R. (2010). Photoelectrochemical water oxidation by cobalt catalyst (“Co-Pi”)/alpha-Fe₂O₃ composite photoanodes: oxygen evolution and resolution of a kinetic bottleneck. *J. Am. Chem. Soc.* 132, 4202–4207. doi: 10.1021/ja908730h

Conflict of Interest: The authors declare that the research was conducted in the absence of any commercial or financial relationships that could be construed as a potential conflict of interest.

Copyright © 2019 Liu, Li, Qiao, Li, Wang, Zhu, Jing and Yan. This is an open-access article distributed under the terms of the Creative Commons Attribution License (CC BY). The use, distribution or reproduction in other forums is permitted, provided the original author(s) and the copyright owner(s) are credited and that the original publication in this journal is cited, in accordance with accepted academic practice. No use, distribution or reproduction is permitted which does not comply with these terms.



Accelerating Photocatalytic Hydrogen Production and Pollutant Degradation by Functionalizing g-C₃N₄ With SnO₂

Amir Zada², Muhammad Khan³, Muhammad Nasimullah Qureshi⁴, Shu-yuan Liu^{5,6*} and Ruidan Wang^{1*}

¹ Institute of Catalysis for Energy and Environment, College of Chemistry and Chemical Engineering, Shenyang Normal University, Shenyang, China, ² Department of Chemistry, Abdul Wali Khan University Mardan, Mardan, Pakistan, ³ School of Materials Science and Engineering, Northwestern Polytechnical University, Xi'an, China, ⁴ Department of Chemistry, University of Swabi, Swabi, Pakistan, ⁵ Department of Pharmacology, Shenyang Medical College, Shenyang, China, ⁶ Key Laboratory for Photonic and Electronic Bandgap Materials, Ministry of Education, College of Physics and Electronic Engineering, Harbin Normal University, Harbin, China

OPEN ACCESS

Edited by:

Liwei Wang,
Guangxi University, China

Reviewed by:

Zhenyi Zhang,
Dalian Nationalities University, China
Qin Li,
South-Central University for
Nationalities, China

*Correspondence:

Shu-yuan Liu
liushuyuan@symc.edu.cn
Ruidan Wang
wangruidan1980@163.com

Specialty section:

This article was submitted to
Nanoscience,
a section of the journal
Frontiers in Chemistry

Received: 12 November 2019

Accepted: 26 December 2019

Published: 18 February 2020

Citation:

Zada A, Khan M, Qureshi MN, Liu S
and Wang R (2020) Accelerating
Photocatalytic Hydrogen Production
and Pollutant Degradation by
Functionalizing g-C₃N₄ With SnO₂.
Front. Chem. 7:941.
doi: 10.3389/fchem.2019.00941

Energy crises and environmental pollution are two serious threats to modern society. To overcome these problems, graphitic carbon nitride (g-C₃N₄) nanosheets were fabricated and functionalized with SnO₂ nanoparticles to produce H₂ from water splitting and degrade 2-chlorophenol under visible light irradiation. The fabricated samples showed enhanced photocatalytic activities for both H₂ evolution and pollutant degradation as compared to bare g-C₃N₄ and SnO₂. These enhanced photoactivities are attributed to the fast charge separation as the excited electrons transfer from g-C₃N₄ to the conduction band of SnO₂. This enhanced charge separation has been confirmed by the photoluminescence spectra, steady state surface photovoltage spectroscopic measurement, and formed hydroxyl radicals. It is believed that this work will provide a feasible route to synthesize photocatalysts for improved energy production and environmental purification.

Keywords: g-C₃N₄, SnO₂, photocatalysis, hydrogen production, organic pollutant

INTRODUCTION

Exhaustion of hydrocarbon fuels and addition of toxic and hazardous materials from agricultural, medicinal, dyes, and cosmetic industries to the environment have resulted in increased pressure on the scientific community to address these problems adequately. A number of methods have been chalked out such as cracking of hydrocarbons and thermal splitting of water at elevated temperature to get H₂ (future fuel). However, these methods require highly costly and controlled operational environment and huge labor under normal conditions. On the other hand, different pollutants removal technologies such as adsorption, coagulation, and electrochemical methods have their own shortcomings and did not receive much popularity in the purification of the environment (Zhao et al., 2015; Gautam et al., 2016; Li et al., 2016; Ali et al., 2018b; Wang et al., 2018; Ali S. et al., 2019). Therefore, modern techniques are urgently required to address energy and environmental issues properly with the least operational cost and time.

Photocatalysis has opened a brilliant chapter to realize the energy crises and environmental issues. The photocatalysts have shown their remarkable influence in the production of H₂ from water, production of hydrocarbon fuels from CO₂, and removal of pollutants from air and

wastewater with minimum cost and least working labor (Singh et al., 2017; Li et al., 2018a,b; Qu et al., 2018; Ullah et al., 2019; Xu et al., 2019a). Although different photocatalysts such as TiO_2 , ZnO , and ZrO_2 have been widely utilized, there are some typical problems such as activeness only under ultraviolet (UV) light and fast recombination of photogenerated charges (Raizada et al., 2017; Qi et al., 2018a,b, 2020a). Since visible light contributes a major portion to electromagnetic radiations, therefore, photocatalysts active under visible light are more effective and efficient. Graphitic carbon nitride, $\text{g-C}_3\text{N}_4$, is a promising polymeric photocatalyst with a band gap of 2.7 eV. Its conduction band (CB) and valence band (VB) have characteristic abilities to reduce water and oxidize organic pollutants, respectively (Qi et al., 2019a,b). Its metal-free nature is of particular importance as its release to the environment does not produce harmful threats to the aquatic animals and plants (Nie et al., 2018; Ran et al., 2018; Fu et al., 2019; Liu M. et al., 2019). However, low surface area and poor excited charge separation capability of this photocatalyst is still a marked question on its utilization for fuel production and organic oxidation (Dong et al., 2019; Liu Y. et al., 2019; Zhu et al., 2019c; Qi et al., 2020b). Therefore, these problems need to be tackled in future generation of semiconductor photocatalysis.

SnO_2 is an excellent UV responsive metal oxide photocatalyst with a band gap of 3.5 eV. Its excellent stability and tunable optical properties make it a suitable candidate for photocatalysis, solar cells, and gas sensors. More interestingly, its CB is situated at a suitable position below the CB of $\text{g-C}_3\text{N}_4$ and thermodynamically acts as a sink to accept the excited electrons from $\text{g-C}_3\text{N}_4$ during photocatalysis (Jana and Mondal, 2014; Xu et al., 2018a; Qi et al., 2019c,d). Therefore, its heterojunctional combination with $\text{g-C}_3\text{N}_4$ will significantly improve excited charge separation for enhanced photocatalysis.

In this work, we coupled SnO_2 nanoparticles with $\text{g-C}_3\text{N}_4$ to form different ratio composites and applied for the photocatalytic production of H_2 and 2-chlorophenol (2-CP) degradation under visible light, keeping in view to excite only $\text{g-C}_3\text{N}_4$ and use SnO_2 as excited charge acceptor. The optimized composite ($6\text{SnO}_2/\text{g-C}_3\text{N}_4$) showed much improved photoactivities for H_2 production and pollutant degradation compared to bare SnO_2 and $\text{g-C}_3\text{N}_4$. These activities are solely attributed to the better charge separation in the composites.

EXPERIMENTAL PART

Preparation of $\text{g-C}_3\text{N}_4$

Polymeric $\text{g-C}_3\text{N}_4$ was prepared from dicyandiamide. A given amount of dicyandiamide was taken in crucible and heated at 550°C in a muffle furnace for 4 h at the rate of $2^\circ\text{C}/\text{min}$. After the completion of the heating duration, the cooled sample was grinded into fine powder and used for further study.

Preparation of SnO_2 Nanoparticles

Chloride salt of Sn(IV) was dissolved in water, and the solution was made basic with the help of NaOH solution under vigorous stirring. During addition of NaOH , the solution initially became milky and then became clear with the addition of more NaOH .

Finally, when the pH reached about 12, the solution was taken in an autoclave and heated at 220°C for 10 h in oven. The obtained white powder was purified three times with distilled water, dried in the oven overnight, and then calcined at 450°C for 1 h at the rate of $5^\circ\text{C}/\text{min}$.

Preparation of $\text{SnO}_2/\text{g-C}_3\text{N}_4$ Composites

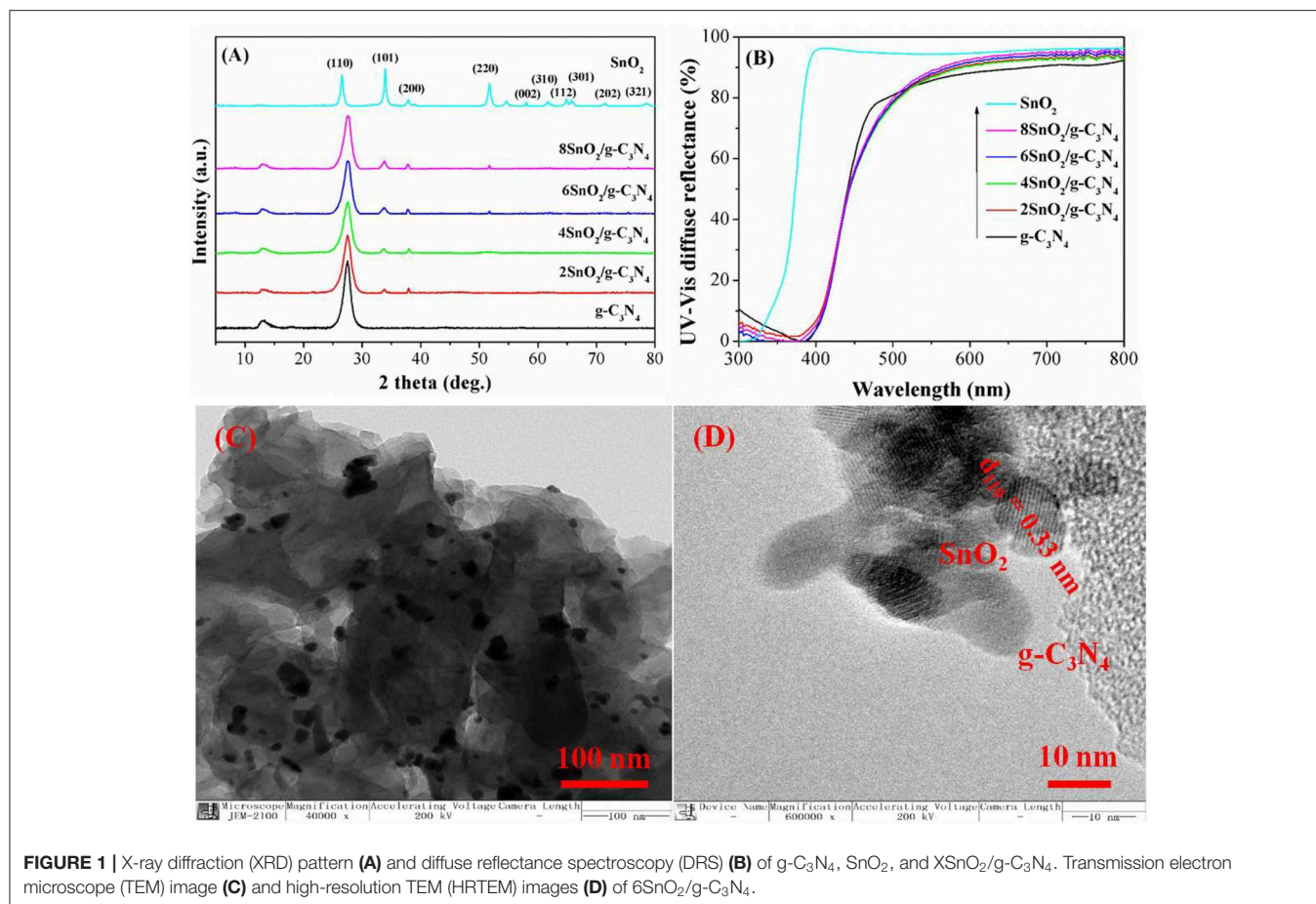
Composites containing different mass percent of SnO_2 and $\text{g-C}_3\text{N}_4$ ($\text{SnO}_2/\text{g-C}_3\text{N}_4$) were prepared by taking appropriate amounts of SnO_2 and $\text{g-C}_3\text{N}_4$ in water-methanol mixture containing 1 ml of concentrated HNO_3 . Each mixture was vigorously stirred under heating at 80°C till the whole solvent was evaporated. After that, each mixture was dried in the oven overnight and then calcined at 450°C for 1 h. The as prepared composites were represented by $\text{XSnO}_2/\text{g-C}_3\text{N}_4$ where "X" shows the percent amount (2, 4, 6, and 8%) of SnO_2 in the given composite.

Characterization Techniques

The prepared samples were passed through different characterization techniques to confirm the formation of heterojunctional composites. The X-ray diffraction (XRD) technique was used to determine the crystalline structure of the samples with the help of Bruker D8 Advance diffractometer using CuK_α radiation. The oxidation states of the constituent elements of the composites were examined by means of X-ray photoelectron spectroscopy (XPS) employing X-ray from mono-Al source with the help of a Kratos-Axis Ultra DLD apparatus. The obtained binding energies were calibrated with the binding energy of adventitious C-atom which is 284.55 eV. The microscopic structure was further revealed with the help of transmission electron microscope (TEM) and high-resolution TEM (HRTEM) operating at 200 kV. The optical properties were confirmed with the help of UV diffuse reflectance spectra, by taking BaSO_4 as a reference, measured with a Shimadzu UV-2550 spectrophotometer. The photoluminescence (PL) spectrum of each sample was realized with the help of spectrofluorophotometer (Perkin-Elmer LS55) at a 390-nm excitation wavelength. The steady state surface photovoltage spectroscopic (SS-SPS) measurement of each sample was carried in a controlled atmosphere employing a homemade equipment possessing a lock-in amplifier (SR830) synchronized with a light chopper (SR540). Each sample was first thoroughly grinded and then kept between two indium tin oxide (ITO) glass electrodes in an atmosphere-controlled sealed container. Radiations from a 500-W Xe lamp (CHF XQ500W, Global Xe lamp power) were passed through a double-prism monochromator (SBP300) to get a monochromatic light.

Evaluation of Photoactivity for Water Splitting

Water splitting photocatalysis was carried out with the help of an online H_2 production unit (Perfectlight, Beijing, Lab Solar III). About 0.1 g photocatalyst was taken in a glass-made reaction cell, and 100-ml aqueous solution of methanol (20% V/V) was added. The apparatus was first deaerated with the help of a vacuum pump to remove any traces of O_2 and CO_2 dissolved



in aqueous solution. The mixture was irradiated under visible light (wavelength > 420 nm) coming from a 300-W Xe lamp under vigorous stirring. The produced gases were analyzed after each hour with the help of a gas chromatograph (7,900, TCD, molecular sieve 5 Å, N_2 carrier, Tec comp.).

Evaluation of Photoactivity for Pollutant Degradation

The photoactivities were further studied by selecting 2-CP as a pollutant. About 0.2 g of powder sample was mixed with 50 ml of aqueous solution (25 mg/L) of 2-CP and exposed to a 150-W (GYZZ20) Xe lamp under visible light (wavelength > 420 nm). Before being exposed to light, each sample was first kept in complete dark for 30 min to attain adsorption–desorption equilibrium. The concentration of the pollutant was checked after each hour with the help of a Shimadzu UV-2550 spectrometer.

Evaluation of Hydroxyl Radicals ($\cdot\text{OH}$)

About 0.05 g powder sample was mixed with 50 ml of aqueous solution of coumarin (0.001 M) and exposed to a 150-W (GYZZ20) Xe lamp under visible light (wavelength > 420 nm). Before exposure to light, each sample was first kept in complete dark for 30 min to attain adsorption–desorption equilibrium. After each hour, the amount of formed 7-hydroxycoumarin was

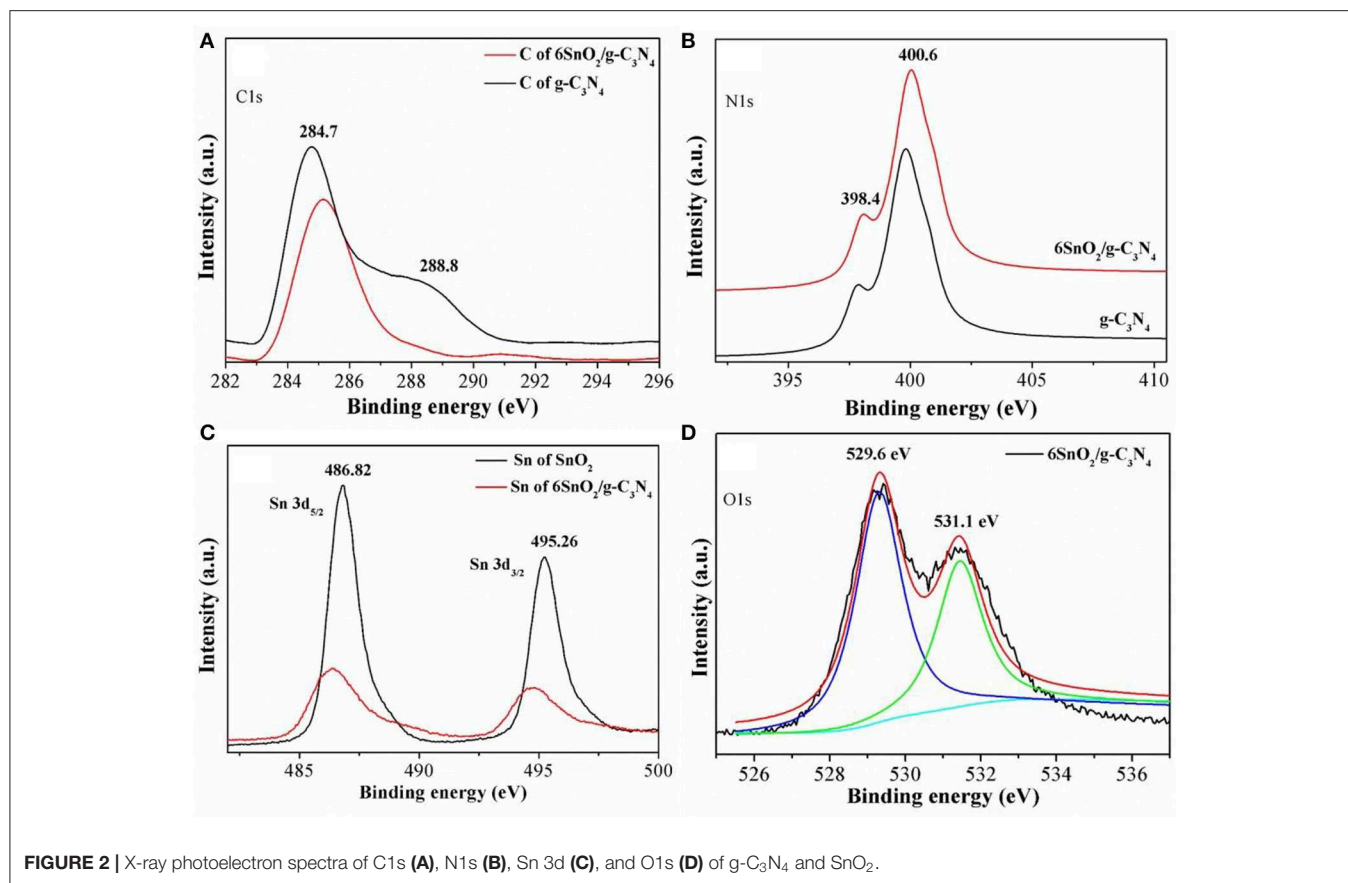
checked at 390-/460-nm excitation/emission wavelengths with the help of a spectrofluorophotometer (Perkin-Elmer LS55).

RESULT AND DISCUSSION

Structural Characterization

The crystal structure study of the pure $g\text{-C}_3\text{N}_4$ shows two characteristic diffraction peaks at 13.04 and 27.31° as shown in **Figure 1A**. The former peak is due to the interplanar stacking of the aromatic rings in conjugation while the later peak is related to the interlayer structural units (Liu et al., 2017; Guan et al., 2018; Xu et al., 2018b, 2019b). Similarly, pure SnO_2 shows diffraction peaks at 26.2 , 33.8 , 37.3 , 51.2 , 57.2 , 61.1 , 63.81 , 64.77 , 71.38 , and 78.27° , which can be, respectively, indexed to (110), (101), (200), (220), (002), (310), (112), (301), (202), and (321) planes of tetragonal SnO_2 nanoparticles (Mahjouri et al., 2020; Shokrzadeh et al., 2020). Interestingly, all the composite samples show the two characteristic peaks of $g\text{-C}_3\text{N}_4$ at 13.04 and 27.31° and SnO_2 peaks at 33.8 , 37.3 , and 51.2° . However, the diffraction peak at 13.04° has been decreased progressively as the amount of SnO_2 is increased, indicating that SnO_2 nanoparticles are well packed in the nanosheets of $g\text{-C}_3\text{N}_4$.

The UV-vis diffused reflectance spectra of the samples are shown in **Figure 1B**. As can be seen, $g\text{-C}_3\text{N}_4$ and SnO_2 ,



respectively, show optical thresholds at 475 and 360 nm, corresponding to band gaps of 2.61 and 3.45 eV, respectively. Although the composite samples show the same optical thresholds at 475 and 360 nm, their light absorption has been slightly decreased as SnO₂ is a wide-band-gap semiconductor and its coupling with g-C₃N₄ slightly decreases light absorption (Zhang et al., 2018; Zada et al., 2019a; Zhu et al., 2019a,b).

The TEM image of composite shows uniform distribution of small SnO₂ nanoparticles of about 10-nm size on the surface of g-C₃N₄ as shown in **Figure 1C**. The HRTEM image shows the lattice fringes of 0.33-nm interplanar distance corresponding to the (110) plane of SnO₂ (**Figure 1D**). This shows that both g-C₃N₄ and SnO₂ are in close contact with each other to intensify the charge separation for better photoactivities.

The oxidation states of different elements in the samples were determined using XPS measurements, and the results are shown in **Figure 2**. The obtained binding energies were calibrated with the binding energy of the adventitious carbon atom with a binding energy value of 284.55 eV. It is obvious that C1s in pure g-C₃N₄ shows two XPS peaks at binding energies of 284.7 and 288.2 eV (**Figure 2A**). These peaks are attributed to the sp² hybridized C-atoms, respectively, bonded with N-atom of the aromatic ring and NH₂ group linking different aromatic rings. Similarly, the XPS binding energies of N1s in pure g-C₃N₄ are composed of two parts at 398.4 and 400.6 eV and are, respectively, contributed by sec. and ter. N-atoms (**Figure 2B**) (Raziq et al.,

2016; Li Q. et al., 2019). The XPS peaks of Sn in pure SnO₂ are deconvoluted into two parts at 486.82 and 495.26 eV, which are, respectively, contributed by Sn3d_{5/2} and Sn3d_{3/2} and show that Sn is present in +4 oxidation state in the nanocomposite (**Figure 2C**) (Li H. et al., 2019). When g-C₃N₄ nanosheets are coupled with SnO₂ nanoparticles, the C1s and N1s peaks are slightly shifted toward the low-energy side while those of Sn are shifted toward the high-energy side. The binding energies of O1s in **Figure 2D** are contributed at 529.6 and 531.1 eV, which are, respectively, contributed by the lattice O-atom and adsorbed oxygen molecules. The redistribution of charge density in both components of the nanocomposite indicates that both g-C₃N₄ and SnO₂ are present in close contact with each other for improved charge separation.

Photocatalytic Activity

The photoactivities of composites were first evaluated by splitting water under visible light (wavelength > 420 nm) in the presence of methyl alcohol. As shown in the **Figure 3A**, the H₂ production activity of pure SnO₂ is negligible under visible light irradiation. However, pure g-C₃N₄ produces about 10 μmol of H₂ in 1 h under the stipulated conditions. Interestingly, these H₂ photoactivities are significantly enhanced when both g-C₃N₄ and SnO₂ are coupled to form heterojunctional composites. Further, photoactivities are increased along with the increase in the amount of SnO₂ nanoparticles and the highest activities are

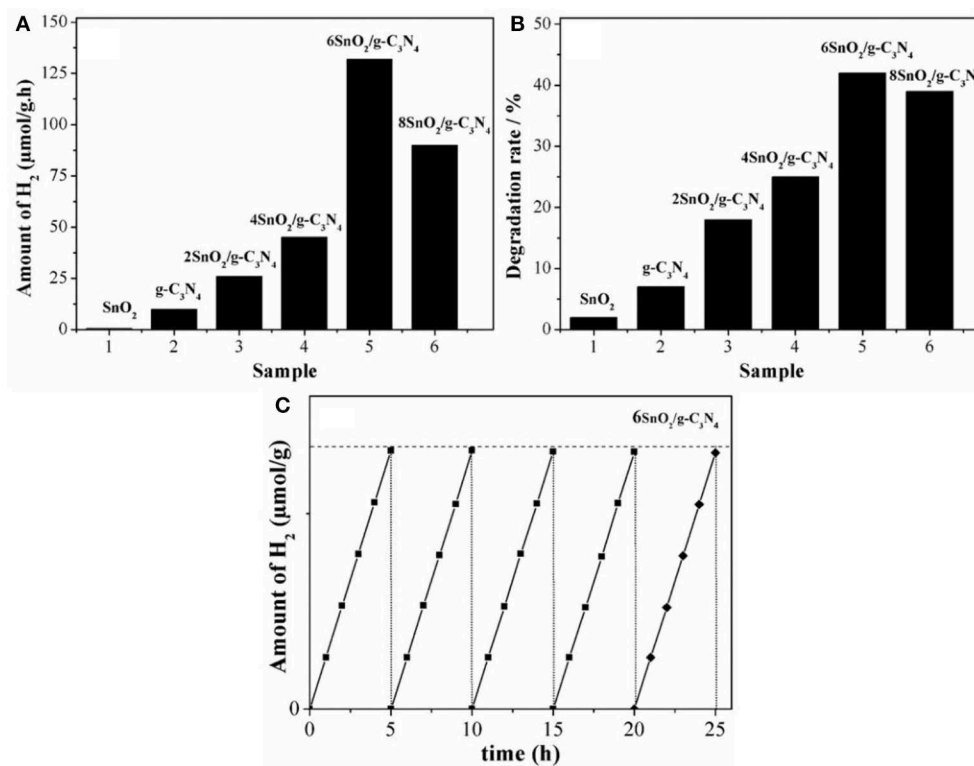


FIGURE 3 | Photoactivities for H₂ evolution (A), 2-CP degradation (B) of pure g-C₃N₄, and XSnO₂/g-C₃N₄ and stability test of 6SnO₂/g-C₃N₄ (C).

contributed by 6SnO₂/g-C₃N₄ sample, which are 132 μmol/h. However, further increase in the amount of SnO₂ decreases H₂ production as SnO₂ is a wide-band-gap semiconductor and it covers most surface of the g-C₃N₄ to prevent absorption of visible-light photons. These enhanced H₂ activities are solely attributed to the improved charge separation in the composites by transferring excited electrons from g-C₃N₄ to SnO₂ for the reduction of water. We further extended the photoactivities by measuring the degradation of 2-CP under visible-light (wavelength > 420 nm) irradiation. Again, the degradation performance of pure SnO₂ is very low due to its high-band-gap nature. The composite materials showed much improved photoactivities, and the optimized 6SnO₂/g-C₃N₄ sample showed 42% degradation activities under the given conditions as shown in **Figure 3B**. We also carried out the stability test of the optimized sample for five consecutive cycles, each cycle composed of a 5-h run. It is obvious from **Figure 3C** that there is no detectable decrease in the H₂ production activities, indicating that the optimized sample is very stable.

Charge Separation

The improved photoactivities of the composites compared to pure g-C₃N₄ are attributed to the extended charge separation. In order to determine it, we carried out PL spectra, keeping excitation λ at 390 nm. It is clear from **Figure 4A** that g-C₃N₄

gives intense peak at 470 nm, indicating poor charge separation. However, the intensities of the composites are progressively decreased as the amount of SnO₂ nanoparticles is increased, and the optimized sample shows relatively low PL peak, indicating excellent charge separation in it (Zhang et al., 2015; Ali et al., 2016; Lu et al., 2018; Ali N. et al., 2019; Ali S. et al., 2019). The relatively low intensities of PL peaks indicate enhanced charge separation and are responsible for improved photoactivities.

We further extended the charge separation experiments by measuring the atmosphere-controlled steady state surface photovoltage spectra (SS-SPS), and the results are shown in **Figure 4B**. As evident, g-C₃N₄ shows very low SPS intensity. However, the SPS peak intensities are much improved when both g-C₃N₄ and SnO₂ are coupled and the optimized 6SnO₂/g-C₃N₄ sample shows the highest peak intensity. Since high is the intensity of the SPS peak, high is the charge separation (Zada et al., 2018, 2019a,b); therefore, we can say that the composites impart enhanced charge separation and contributing to the improved photoactivities.

We also measured the hydroxyl radical (·OH) activities of the fabricated samples by doing coumarin fluorescent experiments under visible-light irradiation. Since ·OH is the major contributor to charge separation during photocatalysis and react with coumarin to form 7-hydroxycoumarin; therefore, the higher the intensity of coumarin fluorescent peak, the higher is the charge separation. As can be seen from **Figure 4C**, pure

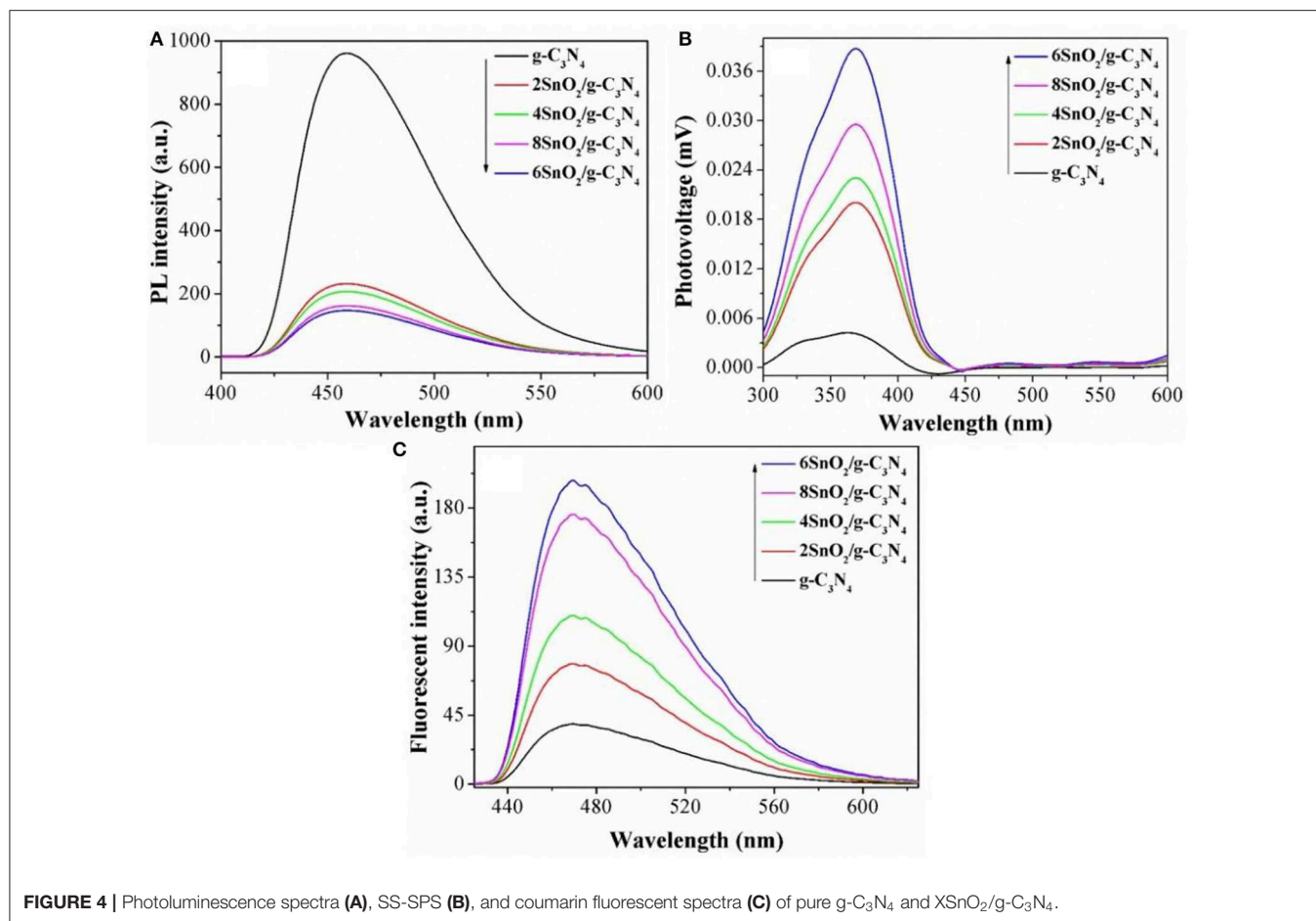


FIGURE 4 | Photoluminescence spectra (A), SS-SPS (B), and coumarin fluorescent spectra (C) of pure $g\text{-C}_3\text{N}_4$ and $X\text{SnO}_2/g\text{-C}_3\text{N}_4$.

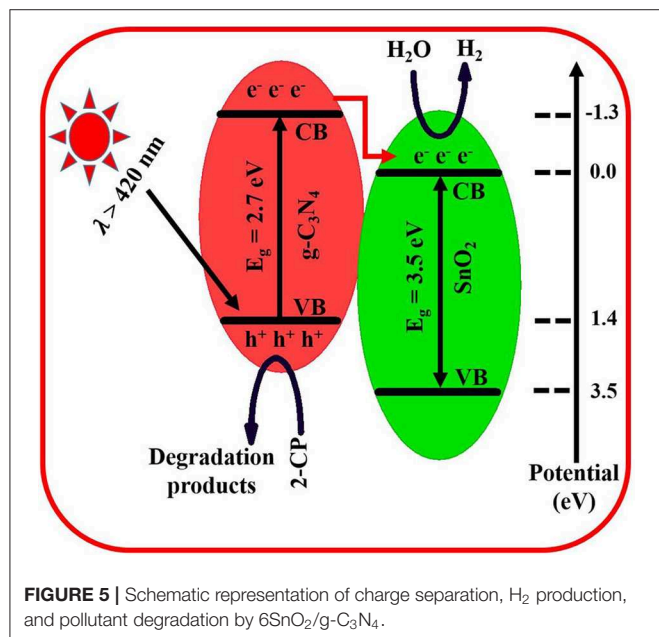


FIGURE 5 | Schematic representation of charge separation, H_2 production, and pollutant degradation by $6\text{SnO}_2/g\text{-C}_3\text{N}_4$.

$g\text{-C}_3\text{N}_4$ gives very low peak, which shows its inherited low charge separation. However, the $\cdot\text{OH}$ radical activities are considerably improved when both $g\text{-C}_3\text{N}_4$ and SnO_2 are coupled, indicating

improved charge separation and hence extended photoactivities (Ali et al., 2018a; Yasmeen et al., 2019a).

DISCUSSION

The improved charge separation in the prepared composite results in the enhanced H_2 production and 2-CP degradation. This enhanced charge separation has been schematically shown in **Figure 5**. The band gap of $g\text{-C}_3\text{N}_4$ is about 2.7 eV and absorbs visible-light photons (Raziq et al., 2015, 2017). Its CB present at -1.3 eV is most suitable for H_2 production and superoxide generation which require reduction potential of 0.00 and -0.33 eV, respectively. Its VB is present at 1.4 eV (Yasmeen et al., 2019b). On the other side, the band gap of SnO_2 is 3.5 eV, and its CB is present below the CB of $g\text{-C}_3\text{N}_4$ (Zada et al., 2016). Under visible-light irradiation, only $g\text{-C}_3\text{N}_4$ is excited, and electrons jumped to its CB, leaving positive holes in the VB. Since the excited electrons have a very short lifetime; therefore, they jumped to the CB of SnO_2 to achieve some stability for a while. Here these electrons reduce water into H_2 while the holes in VB of $g\text{-C}_3\text{N}_4$ are solely left to carryout oxidation of alcohol. In case of 2-CP degradation, these positive holes either directly oxidize pollutants or undergo the formation of more reactive species such as hydroxyl-free radicals, which then finally degrade the target pollutant into simple CO_2 and water (Zada et al., 2018).

CONCLUSION

In order to overcome energy crises and environmental pollution, here, we synthesized g-C₃N₄ nanosheets and coupled them with SnO₂ nanoparticles. The optimized composite of 6SnO₂/g-C₃N₄ produced about 132 μmol of H₂ from water in 1 h and degraded 42% 2-CP pollutant under visible-light irradiation as compared to the photoactivities of bare g-C₃N₄ and SnO₂. These enhanced photoactivities are attributed to the better charge separation as the excited electrons thermodynamically transfer from g-C₃N₄ to SnO₂ as has been confirmed from photoluminescence spectra, steady state surface photovoltage spectroscopic measurement, and formed hydroxyl radicals. It is believed that this work would provide a feasible route to synthesize photocatalysts for improved energy production and environmental purification.

REFERENCES

- Ali, A., Hussain, Z., Arain, M. B., Shah, N., Khan, K. M., Gulab, H., et al. (2016). Development of microwave assisted spectrophotometric method for the determination of glucose. *Spectrochim. Acta Mol. Biomol. Spectrosc.* 153, 374–378. doi: 10.1016/j.saa.2015.07.104
- Ali, N., Awais, K. T., Ul-Islam, Khan, M. A., Shah, S. J., and Zada, A. (2018b). Chitosan-coated cotton cloth supported copper nanoparticles for toxic dye reduction. *Int. J. Biol. Macromol.* 111, 832–838. doi: 10.1016/j.ijbiomac.2018.01.092
- Ali, N., Zada, A., Zahid, M., Ismail, A., Rafiq, M., Riaz, A., et al. (2019). Enhanced photodegradation of methylene blue with alkaline and transition-metal ferrite nanophotocatalysts under direct sun light irradiation. *J. Chin. Chem. Soc.* 66, 402–408. doi: 10.1002/jccs.201800213
- Ali, S., Li, Z., Chen, S., Zada, A., Khan, I., Khan, I., et al. (2019). Synthesis of activated carbon-supported TiO₂-based nano-photocatalysts with well recycling for efficiently degrading high-concentration pollutants. *Catal. Today* 335, 557–564. doi: 10.1016/j.cattod.2019.03.044
- Ali, W., Ullah, H., Zada, A., Alamgir, M. K., Muhammad, W., Ahmad, M. J., et al. (2018a). Effect of calcination temperature on the photoactivities of ZnO/SnO₂ nanocomposites for the degradation of methyl orange. *Mater. Chem. Phys.* 213, 259–266. doi: 10.1016/j.matchemphys.2018.04.015
- Dong, D., Yan, C., Huang, J., Lu, N., Wu, P., Wang, J., et al. (2019). An electron-donating strategy to guide the construction of MOF photocatalysts toward cocatalyst-free highly efficient photocatalytic H₂ evolution. *J. Mater. Chem. A* 7, 24180–24185. doi: 10.1039/C9TA06141J
- Fu, J., Xu, Q., Low, J., Jiang, C., and Yu, J. (2019). Ultrathin 2D/2D WO₃/g-C₃N₄ step-scheme H₂-production photocatalyst. *Appl. Catal. B Environ.* 243, 556–565. doi: 10.1016/j.apcatb.2018.11.011
- Gautam, S., Shandilya, P., Singh, V. P., Raizada, P., and Singh, P. (2016). Solar photocatalytic mineralization of antibiotics using magnetically separable NiFe₂O₄ supported onto graphene sand composite and bentonite. *J. Water Process Eng.* 14, 86–100. doi: 10.1016/j.jwpe.2016.10.008
- Guan, W., Zhang, Z., Tian, S., and Du, J. (2018). Ti₄O₇/g-C₃N₄ for visible light photocatalytic oxidation of hypophosphite: effect of mass ratio of Ti₄O₇/g-C₃N₄. *Front. Chem.* 6:313. doi: 10.3389/fchem.2018.00313
- Jana, S., and Mondal, A. (2014). Fabrication of SnO₂/α-Fe₂O₃, SnO₂/α-Fe₂O₃-PB heterostructure thin films: enhanced photodegradation and peroxide sensing. *ACS Appl. Mater. Interfaces* 6, 15832–15840. doi: 10.1021/am5030879
- Li, F., Wangyang, P., Zada, A., Humayun, M., Wang, B., and Qu, Y. (2016). Synthesis of hierarchical Mn₂O₃ microspheres for photocatalytic hydrogen production. *Mater. Res. Bull.* 84, 99–104. doi: 10.1016/j.materresbull.2016.07.032
- Li, H., Zhang, B., Wang, X., Zhang, J., An, T., Ding, Z., et al. (2019). Heterostructured SnO₂-SnS₂@C embedded in nitrogen-doped graphene as

DATA AVAILABILITY STATEMENT

The raw data supporting the conclusions of this article will be made available by the authors, without undue reservation, to any qualified researcher.

AUTHOR CONTRIBUTIONS

All authors listed have made a substantial, direct and intellectual contribution to the work, and approved it for publication.

FUNDING

This work was supported by the Doctoral Scientific Research Foundation of Liaoning Province (20170520011) and Project of Education Office of Liaoning Province (LQN201712).

- a robust anode Material for lithium-ion batteries. *Front. Chem.* 7:339. doi: 10.3389/fchem.2019.00339
- Li, Q., Shi, T., Li, X., Lv, K., Li, M., Liu, F., et al. (2018a). Remarkable positive effect of Cd(OH)₂ on CdS semiconductor for visible-light photocatalytic H₂ production. *Appl. Catal. B Environ.* 229, 8–14. doi: 10.1016/j.apcatb.2018.01.078
- Li, Q., Xia, Y., Yang, C., Lv, K., Lei, M., and Li, M. (2018b). Building a direct Z-scheme heterojunction photocatalyst by ZnIn₂S₄ nanosheets and TiO₂ hollow spheres for highly-efficient artificial photosynthesis. *Chem. Eng. J.* 349, 287–296. doi: 10.1016/j.cej.2018.05.094
- Li, Q., Zhao, T., Li, M., Li, W., Yang, B., Qin, D., et al. (2019). One-step construction of Pickering emulsion via commercial TiO₂ nanoparticles for photocatalytic dye degradation. *Appl. Catal. B Environ.* 249, 1–8. doi: 10.1016/j.apcatb.2019.02.057
- Liu, C., Raziq, F., Li, Z., Qu, Y., Zada, A., and Jing, L. (2017). Synthesis of TiO₂/g-C₃N₄ nanocomposites with phosphate-oxygen functional bridges for improved photocatalytic activity. *Chin. J. Catal.* 38, 1072–1078. doi: 10.1016/S1872-2067(17)62850-X
- Liu, M., Wageh, S., Al-Ghamdi, A. A., Xia, P., Cheng, B., Zhang, L., et al. (2019). Quenching induced hierarchical 3D porous g-C₃N₄ with enhanced photocatalytic CO₂ reduction activity. *Chem. Commun.* 55, 14023–14026. doi: 10.1039/C9CC07647F
- Liu, Y., Zhang, Z., Fang, Y., Liu, B., Huang, J., Miao, F., et al. (2019). IR-Driven strong plasmonic-coupling on Ag nanorices/W₁₈O₄₉ nanowires heterostructures for photo/thermal synergistic enhancement of H₂ evolution from ammonia borane. *Appl. Catal. B Environ.* 252, 164–173. doi: 10.1016/j.apcatb.2019.04.035
- Lu, N., Zhang, Z., Wang, Y., Liu, B., Guo, L., Wang, L., et al. (2018). Direct evidence of IR-driven hot electron transfer in metal-free plasmonic W₁₈O₄₉/Carbon heterostructures for enhanced catalytic H₂ production. *Appl. Catal. B Environ.* 233, 19–25. doi: 10.1016/j.apcatb.2018.03.073
- Mahjouri, S., Nasab, M. K., Kazemi, E. M., Divband, B., and Movafeghi, A. (2020). Effect of Ag-doping on cytotoxicity of SnO₂ nanoparticles in tobacco cell cultures. *J. Hazard. Mater.* 381:121012. doi: 10.1016/j.jhazmat.2019.121012
- Nie, N., Zhang, L., Fu, J., Cheng, B., and Yu, J. (2018). Self-assembled hierarchical direct Z-scheme g-C₃N₄/ZnO microspheres with enhanced photocatalytic CO₂ reduction performance. *Appl. Surf. Sci.* 441, 12–22. doi: 10.1016/j.apsusc.2018.01.193
- Qi, K., Li, Y., Xie, Y., Liu, S., Zheng, K., Chen, Z., et al. (2019a). Ag loading enhanced photocatalytic activity of g-C₃N₄ porous nanosheets for decomposition of organic pollutants. *Front. Chem.* 7:91. doi: 10.3389/fchem.2019.00091
- Qi, K., Liu, S., Chen, Y., Xia, B., and Li, G. (2018b). A simple post-treatment with urea solution to enhance the photoelectric conversion efficiency for TiO₂ dye-sensitized solar cells. *Sol. Energy Mater. Sol. Cells* 183, 193–199. doi: 10.1016/j.solmat.2018.03.038

- Qi, K., Liu, S., and Qiu, M. (2018a). Photocatalytic performance of TiO₂ nanocrystals with/without oxygen defects. *Chin. J. Catal.* 39, 867–875. doi: 10.1016/S1872-2067(17)62999-1
- Qi, K., Liu, S., Selvaraj, R., Wang, W., and Yan, Z. (2019b). Comparison of Pt and Ag as co-catalyst on g-C₃N₄ for improving photocatalytic activity: experimental and DFT studies. *Desalination Water Treat.* 153, 244–252. doi: 10.5004/dwt.2019.24079
- Qi, K., Liu, S., Wang, R., Chen, Z., and Selvaraj, R. (2019c). Pt/g-C₃N₄ composites for photocatalytic H₂ production and ·OH formation. *Desalination Water Treat.* 154, 312–319. doi: 10.5004/dwt.2019.24068
- Qi, K., Lv, W., Khan, I., and Liu, S. (2020a). Photocatalytic H₂ generation via CoP quantum-dot-modified g-C₃N₄ from electroless plating synthesis. *Chin. J. Catal.* 41, 114–121. doi: 10.1016/S1872-2067(19)63459-5
- Qi, K., Xie, Y., Wang, R., Liu, S., and Zhao, Z. (2019d). Electroless plating Ni-P cocatalyst decorated g-C₃N₄ with enhanced photocatalytic water splitting for H₂ generation. *Appl. Surf. Sci.* 466, 847–853. doi: 10.1016/j.apsusc.2018.10.037
- Qi, K., Xing, X., Zada, A., Li, M., Wang, Q., Liu, S., et al. (2020b). Transition metal doped ZnO nanoparticles with enhanced photocatalytic and antibacterial performances: experimental and DFT studies. *Ceram. Int.* 46, 1494–1502. doi: 10.1016/j.ceramint.2019.09.116
- Qu, Y., Sun, N., Humayun, M., Zada, A., Xie, Y., Tang, J., et al. (2018). Improved visible-light activities of nanocrystalline CdS by coupling with ultrafine NbN with lattice matching for hydrogen evolution. *Sustainable Energy Fuels* 2, 549–552. doi: 10.1039/C7SE00610A
- Raizada, P., Kumari, J., Shandilya, P., and Singh, P. (2017). Kinetics of photocatalytic mineralization of oxytetracycline and ampicillin using activated carbon supported ZnO/ZnWO₄ nanocomposite in simulated wastewater. *Desalination Water Treat.* 79, 204–213. doi: 10.5004/dwt.2017.20831
- Ran, J., Guo, W., Wang, H., Zhu, B., Yu, J., and Qiao, S. (2018). Metal-free 2D/2D phosphorene/g-C₃N₄ Van der Waals heterojunction for highly enhanced visible-light photocatalytic H₂ production. *Adv. Mater.* 30, 1800128. doi: 10.1002/adma.201800128
- Raziq, F., Li, C., Humayun, M., Qu, Y., Zada, A., Yu, H., et al. (2015). Synthesis of TiO₂/g-C₃N₄ nanocomposites as efficient photocatalysts dependent on the enhanced photogenerated charge separation. *Mater. Res. Bull.* 70, 494–499. doi: 10.1016/j.materresbull.2015.05.018
- Raziq, F., Qu, Y., Humayun, M., Zada, A., Yu, H., and Jing, L. (2017). Synthesis of SnO₂/B-P codoped g-C₃N₄ nanocomposites as efficient cocatalyst-free visible-light photocatalysts for CO₂ conversion and pollutant degradation. *Appl. Catal. B Environ.* 201, 486–494. doi: 10.1016/j.apcatb.2016.08.057
- Raziq, F., Qu, Y., Zhang, X., Humayun, M., Wu, J., Zada, A., et al. (2016). Enhanced cocatalyst-free visible-light activities for photocatalytic fuel production of g-C₃N₄ by trapping holes and transferring electrons. *J. Phys. Chem. C* 120, 98–107. doi: 10.1021/acs.jpcc.5b10313
- Shokrzadeh, L., Mohammadi, P., Mahmoudian, M. R., Basirun, W. J., and Bahreini, M. (2020). L-glycine-assisted synthesis of SnO₂/Pd nanoparticles and their application in detection of biodeteriorating fungi. *Mater. Chem. Phys.* 240:122172. doi: 10.1016/j.matchemphys.2019.122172
- Singh, P., Gautam, S., Shandilya, P., Priya, B., Singh, V. P., and Raizada, P. (2017). Graphene bentonite supported ZnFe₂O₄ as superparamagnetic photocatalyst for antibiotic degradation. *Adv. Mater. Lett.* 8, 229–238. doi: 10.5185/amlett.2017.1467
- Ullah, M., Nazir, R., Khan, M., Khan, W., Shah, M., Afridi, S. G., et al. (2019). Effective removal of heavy metals from water by activated carbon adsorbents of Albizia lebeck and Melia azedarach seed shells. *Soil Water Res.* 15, 30–37. doi: 10.17221/212/2018-SWR
- Wang, J., Qin, C., Wang, H., Chu, M., Zada, A., Zhang, X., et al. (2018). Exceptional photocatalytic activities for CO₂ conversion on Al-O bridged g-C₃N₄/α-Fe₂O₃ Z-scheme nanocomposites and mechanism insight with isotopes. *Appl. Catal. B Environ.* 221, 459–466. doi: 10.1016/j.apcatb.2017.09.042
- Xu, B., Zada, A., Wang, G., and Qu, Y. (2019a). Boosting the visible-light photoactivities of BiVO₄ nanoplates by doping Eu and coupling CeO_x nanoparticles for CO₂ reduction and organic oxidation. *Sust. Energy Fuels* 3, 3363–3369. doi: 10.1039/C9SE00409B
- Xu, D., Cheng, B., Wang, W., Jiang, C., and Yu, J. (2018a). Ag₂CrO₄/g-C₃N₄/graphene oxide ternary nanocomposite Z-scheme photocatalyst with enhanced CO₂ reduction activity. *Appl. Catal. B Environ.* 231, 368–380. doi: 10.1016/j.apcatb.2018.03.036
- Xu, Q., Zhu, B., Cheng, B., Yu, J., Zhou, M., and Ho, W. (2019b). Photocatalytic H₂ evolution on graphdiyne/g-C₃N₄ hybrid nanocomposites. *Appl. Catal. B Environ.* 255:117770. doi: 10.1016/j.apcatb.2019.117770
- Xu, Q., Zhu, B., Jiang, C., Cheng, B., and Yu, J. (2018b). Constructing 2D/2D Fe₂O₃/g-C₃N₄ direct Z-scheme photocatalysts with enhanced H₂ generation performance. *Sol. PRL* 2:1800006. doi: 10.1002/solr.201800006
- Yasmeen, H., Zada, A., Li, W., Xu, M., and Liu, S. (2019b). Suitable energy platform of Bi₂WO₆ significantly improves visible-light degradation activity of g-C₃N₄ for highly toxic diuron pollutant. *Mater. Sci. Semicond. Process.* 102:104598. doi: 10.1016/j.mssp.2019.104598
- Yasmeen, H., Zada, A., and Liu, S. (2019a). Dye loaded MnO₂ and chlorine intercalated g-C₃N₄ coupling impart enhanced visible light photoactivities for pollutants degradation. *J. Photochem. Photobiol. A Chem.* 380:111867. doi: 10.1016/j.jphotochem.2019.111867
- Zada, A., Ali, N., Subhan, F., Anwar, N., Shah, M. I. A., Ateeq, M., et al. (2019a). Suitable energy platform significantly improves charge separation of g-C₃N₄ for CO₂ reduction and pollutant oxidation under visible-light. *Prog. Nat. Sci. Mat. Int.* 29, 138–144. doi: 10.1016/j.pnsc.2019.03.004
- Zada, A., Humayun, M., Raziq, F., Zhang, X., Qu, Y., Bai, L., et al. (2016). Exceptional visible-light-driven cocatalyst-free photocatalytic activity of g-C₃N₄ by well-designed nanocomposites with plasmonic Au and SnO₂. *Adv. Energy Mater.* 6:1601190. doi: 10.1002/aenm.201601190
- Zada, A., Muhammad, P., Ahmad, W., Hussain, Z., Ali, S., Khan, M., et al. (2019b). Surface plasmonic-assisted photocatalysis and optoelectronic devices with noble metal nanocrystals: design, synthesis, and applications. *Adv. Funct. Mater.* 6:1906744. doi: 10.1002/adfm.201906744
- Zada, A., Qu, Y., Ali, S., Sun, N., Lu, H., Yan, R., et al. (2018). Improved visible-light activities for degrading pollutants on TiO₂/g-C₃N₄ nanocomposites by decorating SPR Au nanoparticles and 2,4-dichlorophenol decomposition path. *J. Hazard. Mater.* 342, 715–723. doi: 10.1016/j.jhazmat.2017.09.005
- Zhang, Z., Huang, J., Zhang, M., Yuan, Q., and Dong, B. (2015). Ultrathin hexagonal SnS₂ nanosheets coupled with g-C₃N₄ nanosheets as 2D/2D heterojunction photocatalysts toward high photocatalytic activity. *Appl. Catal. B Environ.* 163, 298–305. doi: 10.1016/j.apcatb.2014.08.013
- Zhang, Z., Jiang, X., Liu, B., Guo, L., Lu, N., Wang, L., et al. (2018). IR-driven ultrafast transfer of plasmonic hot electrons in nonmetallic branched heterostructures for enhanced H₂ generation. *Adv. Funct. Mater.* 30:1705221. doi: 10.1002/adma.201705221
- Zhao, X., Zhang, J., Wang, B., Zada, A., and Humayun, M. (2015). Biochemical synthesis of Ag/AgCl nanoparticles for visible-light-driven photocatalytic removal of colored dyes. *Materials* 8, 2043–2053. doi: 10.3390/ma8052043
- Zhu, B., Cheng, B., Zhang, L., and Yu, J. (2019a). Review on DFT calculation of s-triazine-based carbon nitride. *Carbon Energy* 1, 32–56. doi: 10.1002/cey2.1
- Zhu, B., Wageh, S., Al-Ghamdi, A. A., Yang, S., Tian, Z., and Yu, J. (2019b). Adsorption of CO₂, O₂, NO and CO on s-triazine-based g-C₃N₄ surface. *Catal. Today* 335, 117–127. doi: 10.1016/j.cattod.2018.09.038
- Zhu, Y., Zhang, Z., Lu, N., Hua, R., and Dong, B. (2019c). Prolonging charge-separation states by doping lanthanide-ions into {001}/{101} facets-coexposed TiO₂ nanosheets for enhancing photocatalytic H₂ evolution. *Chin. J. Catal.* 40, 413–423. doi: 10.1016/S1872-2067(18)63182-1

Conflict of Interest: The authors declare that the research was conducted in the absence of any commercial or financial relationships that could be construed as a potential conflict of interest.

Copyright © 2020 Zada, Khan, Qureshi, Liu and Wang. This is an open-access article distributed under the terms of the Creative Commons Attribution License (CC BY). The use, distribution or reproduction in other forums is permitted, provided the original author(s) and the copyright owner(s) are credited and that the original publication in this journal is cited, in accordance with accepted academic practice. No use, distribution or reproduction is permitted which does not comply with these terms.



SiO₂ Coated on ZnO Nanorod Arrays With UV-Durable Superhydrophobicity and Highly Transmittance on Glass

Hong Li^{1,2,3}, Xinyan Zou¹, Hongyan Wei¹, Qiang Li^{1,2}, Qiang Gao¹, Qinzhuang Liu^{1,2} and Jinfeng Zhang^{1*}

¹ School of Physics and Electronic Information, Huaibei Normal University, Huaibei, China, ² School Key Laboratory of Green and Precise Synthetic Chemistry and Applications, Ministry of Education, Huaibei Normal University, Huaibei, China,

³ Information College, Huaibei Normal University, Huaibei, China

ZnO nanorod arrays were fabricated on glass through hydrothermal way. Then a thin SiO₂ film was covered on ZnO nanorod arrays using pulsed laser deposition (PLD) technique, and modified by stearic acid. It was found that SiO₂ film only had slight effects on the contact angle and transmittance of ZnO nanorod arrays. However, it had brought a huge improvement in the UV durability of superhydrophobic ZnO nanorod arrays. The results showed that the water contact angle remains constantly at 160.5° even UV irradiation time exceeded 50 h when the deposition time of PLD was about 10 min. This structure with UV-durable superhydrophobicity and highly transmittance on glass substrate can be served as front materials in solar cells.

Keywords: ZnO nanorod arrays, superhydrophobicity, solar cell, PLD, UV durability

INTRODUCTION

Superhydrophobic surfaces have won considerable attentions because of its important application in self-cleaning, corrosion resistance, microfluidic systems and so on (Maghsoudi et al., 2019; Qu et al., 2019; Lv et al., 2020; Zhu et al., 2020). Rough micro-nano surface and lower surface energy are responsible for the formation of superhydrophobic surface (Shchukin et al., 2006; Wang et al., 2015; Velayi and Norouzbeigi, 2018). Many methods have been adopted to manufacture superhydrophobic surface (Darmanin and Guittard, 2011; Li and Guo, 2019; Zhang et al., 2020). ZnO is a common material used to prepare superhydrophobic surface. The reason is that it is not only rich in raw materials but also the morphology is easy to adjust through various methods (Zang, 2018; Aydemir et al., 2019; Wang et al., 2019).

As dust accumulates on the glass surface, the efficiency of solar cells will be reduced by nearly half (Elminir et al., 2006). It is of great importance to design a self-cleaning surface for solar cells. In addition to this property, prepared film must have good transmittance in the range of sunlight as well as being UV-durable (Park et al., 2011). Nanostructure ZnO has high visible transmittance due to its high band gap. Compared with TiO₂, the electron mobility in ZnO is higher, which can reduce the electron transfer time in the film (de Jongh and Vanmaekelbergh, 1996). In addition, ZnO and its doping have been widely used in solar cells (Shen et al., 2019), pressure-sensitive devices (Chen et al., 2016), and transparent conductive electrodes (Sharmma et al., 2017) due to its excellent photoelectric performance. Gao et al. (2011) fabricated highly transparent and superhydrophobic ZnO nanorod arrays on glass. It was found that this film had minimal impact on

OPEN ACCESS

Edited by:

Rengaraj Selvaraj,
Sultan Qaboos University, Oman

Reviewed by:

Alex Tawanda Kuvarega,
University of South Africa, South Africa
Sreejith Karthikeyan,
United Arab Emirates University,
United Arab Emirates
Younghun Kim,
Kwangwoon University, South Korea

*Correspondence:

Jinfeng Zhang
jfzhang@chnu.edu.cn

Specialty section:

This article was submitted to
Nanoscience,
a section of the journal
Frontiers in Chemistry

Received: 26 November 2019

Accepted: 03 February 2020

Published: 20 February 2020

Citation:

Li H, Zou X, Wei H, Li Q, Gao Q, Liu Q
and Zhang J (2020) SiO₂ Coated on
ZnO Nanorod Arrays With UV-Durable
Superhydrophobicity and Highly
Transmittance on Glass.
Front. Chem. 8:101.
doi: 10.3389/fchem.2020.00101

solar cell. However, the superhydrophobic surfaces formed by ZnO micro-nano structure are easy to lose their superhydrophobicity under sunlight because of photooxidative ability (Li et al., 2013). The wettability switch under UV irradiation from superhydrophobicity to superhydrophilicity on the surface of ZnO is caused by photochemical reactions (Feng et al., 2004).

SiO₂ is a material of ceramics with excellent electrical insulation performance (Wang et al., 2009). Furthermore, SiO₂ can easily form cross-linked chains and react with hydroxyl groups on the surface of ZnO (Al-Asbahi, 2017). Therefore, SiO₂ can be acted as UV-resistant material to form UV-durable superhydrophobicity. It is reported that the SiO₂ is covered on ZnO nanorod arrays to form UV-durable superhydrophobic surface (Li et al., 2019). SiO₂ film can be prepared through various techniques (Xue et al., 2013). Compared to these techniques, pulsed laser deposition (PLD) is a superior method for the growth of oxide film and it has many advantages, such as high deposition rate, low substrate temperature, precise stoichiometry, easily controlled thickness and so on (Nikov et al., 2019). SiO_x thin layer was fabricated on the surface of isolated multi-walled carbon nanotubes through PLD and the thickness can be precisely controlled (Ikuno et al., 2003). SiO₂ thin film was prepared on different substrate in the case of O₂. It was found that the transmittance of the 400-nm-thick films was 95% at a 500 nm wavelength (Okosh et al., 2002).

SiO₂ films were deposited on ZnO nanorod arrays through PLD method and modified by stearic acid. The results showed that superhydrophobicity of SiO₂/ZnO/glass remained stable even after prolonged UV irradiation. In addition, the light transmittance reached 85% in the visible region. Thus, the SiO₂/ZnO/glass with superhydrophobicity and high transmittance may provide an effective application in solar cells.

EXPERIMENTS

Preparation of ZnO Seed Layer on Glass

C₄H₆O₄Zn·2H₂O was dissolved in ethanol at room temperature. The concentration and volume of C₄H₆O₄Zn·2H₂O solution was 0.005 M and 100 ml, respectively. The solution was stirred for 2 h to form a stable suspension. The length, width and thickness of the Corning 7059 glass were 4 cm, 4 cm, and 1 mm, respectively. Glasses were sequentially cleaned by hydrochloric acid, acetone before being dried at room temperature. The solution was dropped onto the surface of glasses by straw and waited for the ethanol to evaporate. This process was repeated for six times. Finally glasses were annealed in muffle furnace at 350°C for 30 min.

Preparation of ZnO Nanorod Arrays

Three glass substrates were suspended vertically in three sealed beakers which containing 8 mM zinc nitrate hydrate 200 ml and 8 mM hexamethylenetetramine 200 ml. The three bakers were heated at 95°C in furnace with 2, 4, and 6 h, respectively. The glass substrates were then rinsed with deionized water and dried in the air.

Deposition of SiO₂ Film

ZnO nanorod arrays were coated by SiO₂ film through PLD with $\lambda = 248$ nm KrF. The base pressure was 10⁻⁴ Pa. During the preparation of the sample, the O₂ was introduced into the chamber. The pulse frequency, operating pressure and laser energy density were 5 Hz, 5 Pa, and 1.8 J/cm², respectively. The deposition time was 5 and 10 min. The distance between the silica dioxide target and the substrate was 45 cm.

Hydrophobization of Samples With Stearic Acid

Both SiO₂ coated and uncoated ZnO nanorod arrays were immersed in ethanol solution of stearic acid (8 mM, C₁₈H₃₆O₂) 100 ml for about 24 h at room temperature.

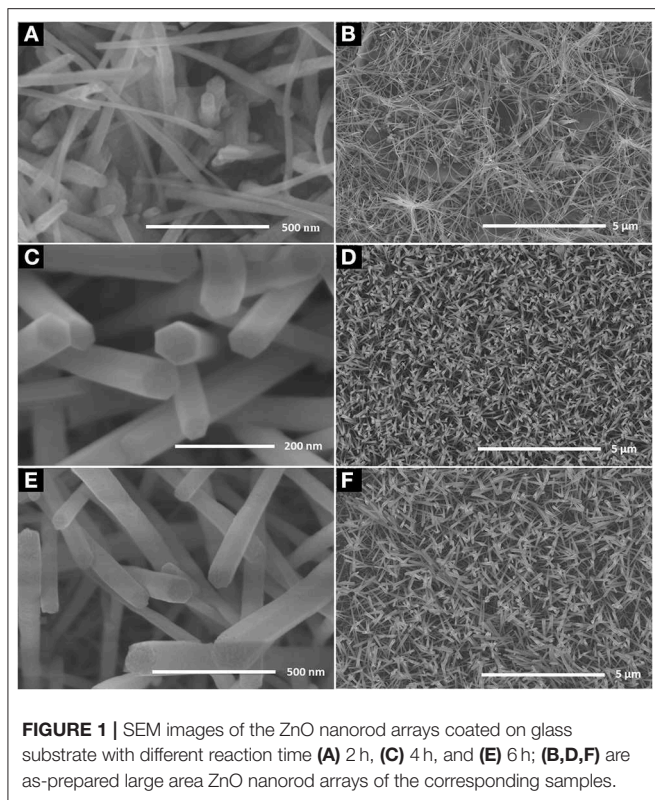
Characterization of Sample

Surface morphology, diffraction signal and water contact angle were performed by field-emission scanning electron microscope (SEM, JEOL, JSM-6610LV), X-ray diffractometer (XRD, XDAL-3000), High resolution transmission electron microscope (HRTEM, JEOL, JEM-2100) and contact angle measuring instrument (JC2000C1). The surface composition and photoluminescence spectrum of films were carried by Fourier transform infrared (FTIR, FP-6500) spectrometer and spectrofluorometer (FLS920 325 nm). The transmittance of the films was measured by ultraviolet-vis spectrometer (UV-Vis, Lambda-950). The ultraviolet light was provided by the 300 W mercury lamp (CEL-LAM300, 50 mW cm⁻², maximum light intensity at 365 nm). The distance between the light source and the sample was 30 cm.

RESULTS AND DISCUSSION

Figure 1 shows the SEM images of ZnO nanorod arrays prepared on glass with different reaction times. When reaction time is 2 h (**Figures 1A,B**), the diameter of ZnO nanorod is small, and some ZnO nanorod entangled with each other. It is shown in **Figures 1C,D**, the diameter is bigger and about 40–60 nm when reaction time is 4 h. in addition, ZnO nanorod stood nearly perpendicularly on the glass and the number of ZnO nanorod is about 36 roots μm^{-2} . With the increase of reaction time, the diameter and number of ZnO nanorod is about 150 nm and 10 roots μm^{-2} , respectively. The X-ray diffraction patterns of ZnO nanorod arrays with reaction time of 4 h were shown in **Figure 2**. Compared with the peaks of (100), (101), (102), (110), (103), (112), and (202), the intensity of (002) peak is much stronger than that of the others, showing that the ZnO nanorod arrays are c-axis oriented. In the formation of ZnO nanostructure under hydrothermal conditions, the growth velocities are $V_{[0001]} > V_{[01\bar{1}0]} > V_{[00\bar{1}1]}$, resulting in the formation of six-prism ZnO nanorod (Liu et al., 2009). As reaction time increases, ZnO nanorod exhibits increased diameter. In addition, their surfaces will become a little rougher due to dissolution. This can be confirmed in the **Figures 1E,F**.

Figure 3 shows the water contact angle on the ZnO nanorod arrays with different reaction time. The water contact angles on ZnO nanorod arrays modified by stearic acid are about 133.3°.



160.5°, and 149.1°, respectively. Wettability of ZnO nanorod arrays can be explained by the Cassie equation (Cassie and Baxter, 1944)

$$\cos \theta^* = -1 + f_1(1 + \cos \theta)$$

Where θ is water contact angle of smooth glass, θ^* is water contact angle of ZnO nanorod arrays, and f_1 is surface fraction of solid. As shown in **Figure 1A**, the surface roughness is small because the diameter of ZnO nanorod is small and lodging on the glass substrate. And the water contact angle is smaller. It can be estimated from **Figures 1C,E** that the f_1 values are about 0.15 and 0.36, respectively. A lot of air can be trapped among ZnO nanorod and acted as a barrier to diminish the contact between water and ZnO nanorod. Based on the above data, the ZnO nanorod arrays with reaction time of 4 h are selected as the research object for the following experiment.

ZnO nanorod arrays are coated with a thin SiO₂ film by pulsed laser deposition (PLD) technique and modified by stearic acid. Surface morphology and wettability on this surface unchanged and are the same as **Figure 1** and **Figure 3B**. This shows that the thickness of SiO₂ film is so thin that it negligibly changes the morphology of ZnO nanorod arrays. The X-ray diffraction patterns of SiO₂ shell on ZnO nanorod arrays are the same as **Figure 2** and there are no characteristic peaks of SiO₂. This shows that the amount of SiO₂ is very small or exists in amorphous state. In order to prove the presence of SiO₂, the elements analysis of SiO₂ shell on ZnO nanorod arrays is carried out

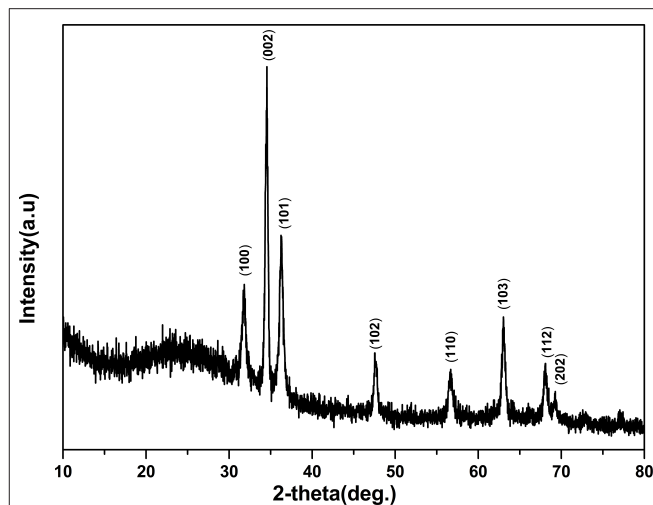


FIGURE 2 | X-ray diffraction patterns of the ZnO nanorod arrays coated on glass substrate with reaction times 4 h.

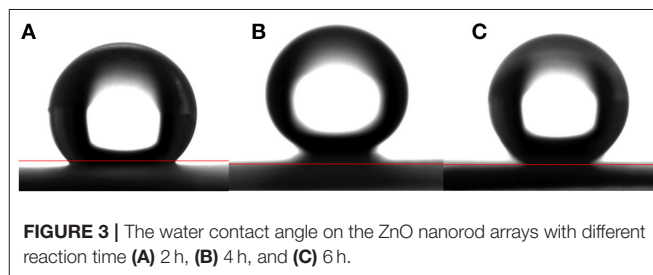
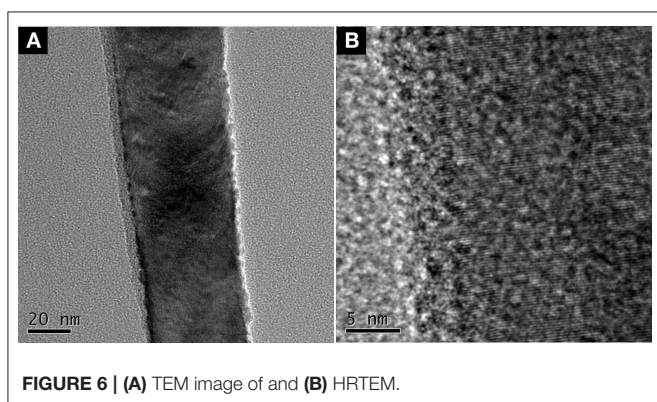
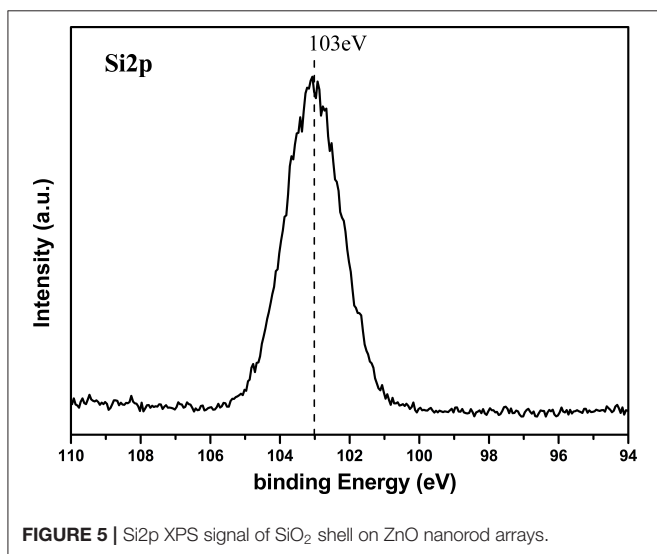
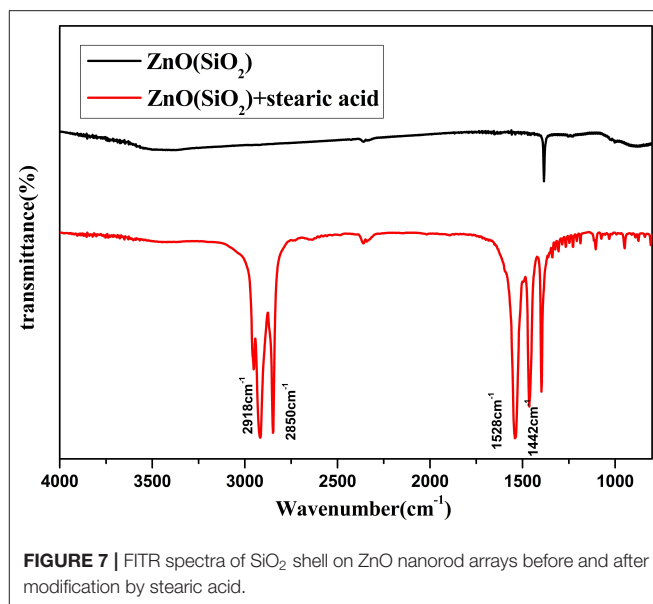
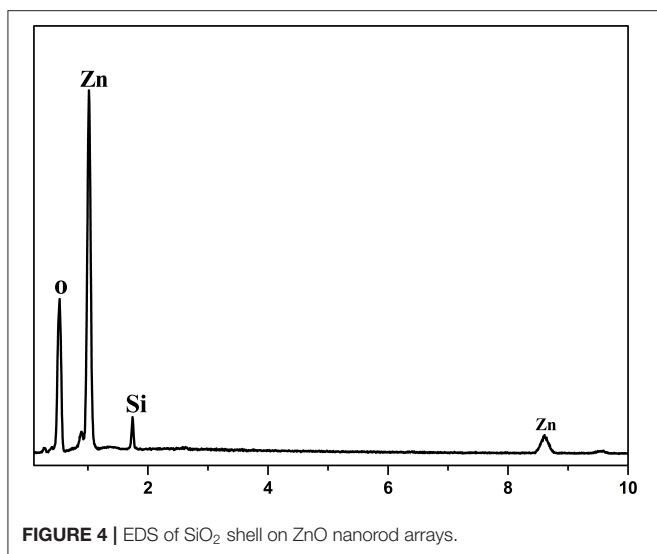


FIGURE 3 | The water contact angle on the ZnO nanorod arrays with different reaction time (A) 2 h, (B) 4 h, and (C) 6 h.

with energy dispersive spectrum (EDS). **Figure 4** exhibits the elements of prepared sample consisted of O, Zn and Si. To judge the deposition film, X-ray photoelectron spectroscopy (XPS) analyses with an Mg K α X-ray source is used. It can be seen in **Figure 5** that the position of Si 2p is 103 eV. This shows that the deposition film is SiO₂. **Figure 6** shows the TEM image of ZnO nanorods. A dense shell of SiO₂ is observed to coat the surface of ZnO nanorods (**Figures 6A,B**) and the thickness is about 5 nm. These show that the surface of ZnO nanorods is coated by SiO₂ film.

Figure 7 illustrates Fourier transform infrared (FTIR) spectra of SiO₂ coated on ZnO nanorod arrays before and after modification by stearic acid. Two absorption peaks at 2,918 and 2,850 cm⁻¹ are the antisymmetric and symmetric stretching vibration of methyl and methylene. Two absorption peaks at 1,528 and 1,442 cm⁻¹ are the stretching vibrations of -COOH- in the CH₃(CH₂)₁₆COO- group (Meth and Sukenik, 2003). This shows that stearic acid has been successfully assembled on the surface of sample.

ZnO is a kind of material with good photocatalytic properties and has a strong oxidation capacity (Zhang et al., 2004). It is known that photo-generated electron-hole pairs under UV irradiation in ZnO react with oxygen and water, producing hydroxyl radicals (Sun et al., 2001). So it can completely



decompose organic compounds modified on the surface of ZnO eventually to carbon dioxide and water. **Figure 8A** shows that the water contact angle on ZnO nanorod arrays under

UV irradiation for 2 h. the contact angle is about 16.1°. This shows that the wettability of ZnO nanorod arrays changes from superhydrophobicity to hydrophilicity. **Figures 8B,C** shows the water contact angle on SiO₂/ZnO/glass structure under UV irradiation for 4 h with 5 and 10 min deposition time. The water contact angles are about 143.2° and 160.5°, respectively. This indicates that SiO₂ can effectively protect the superhydrophobic surface of ZnO nanorod arrays.

Figure 9 illustrates the further relationship about the change of the water contact angle on SiO₂/ZnO/glass structure under UV irradiation. The water contact angle on bare ZnO nanorod arrays decreased quickly to 0° in 3 h. When the deposition time is 5 min, the water contact on SiO₂/ZnO/glass structure only decreased from 160.5° to 92.8° in 50 h. The water contact even nearly unchanged when the deposition time is extended to 10 min. The valence of SiO₂ is far lower and conduction band is higher than ZnO, respectively. Electron-hole pairs generated in ZnO are hard to get through barrier between ZnO and SiO₂, as a result, electron-hole pairs are difficult to react with stearic acid modified on the surface of SiO₂. This is the primary reason for the formation of UV-durable superhydrophobic surface. Electron-hole pairs will have to recombine with each other to generate photoluminescence through radiative transition, leading to the increase in the intensity of UV emission. The photoluminescence spectra of samples were performed by FLS 920 using excitation of 325 nm. **Figure 10** gives the photoluminescence spectra of bare ZnO and SiO₂ coated on ZnO with deposition of 10 min. It can be proved that the intensity of UV emission of SiO₂ coated on ZnO is stronger than bare ZnO. In addition, Si-O bonds in SiO₂ readily react with hydroxyl radicals on the surface of ZnO (Wu et al., 2007), as a result, ultra-thin SiO₂ shell film deposited through PLD is essential to the formation of UV-durable superhydrophobic surface.

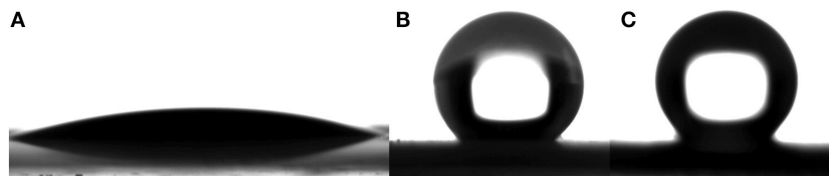


FIGURE 8 | (A) is water contact angle on the surface of bare ZnO nanorod arrays after exposure to UV for 2 h. (B,C) are water contact angle on the surface of SiO₂ shell on ZnO nanorod arrays with deposition times 5 and 10 min after exposure to UV for 4 h. All the samples were modified by stearic acid.

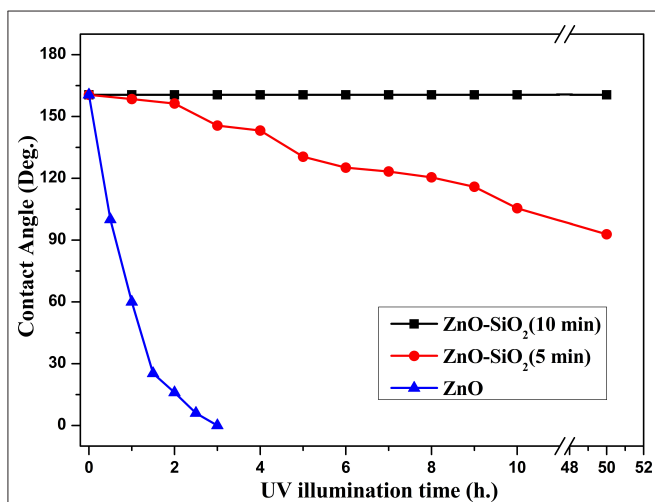


FIGURE 9 | The relationship between deposition time of SiO₂ shell modified by stearic acid and water contact angle under UV illumination.

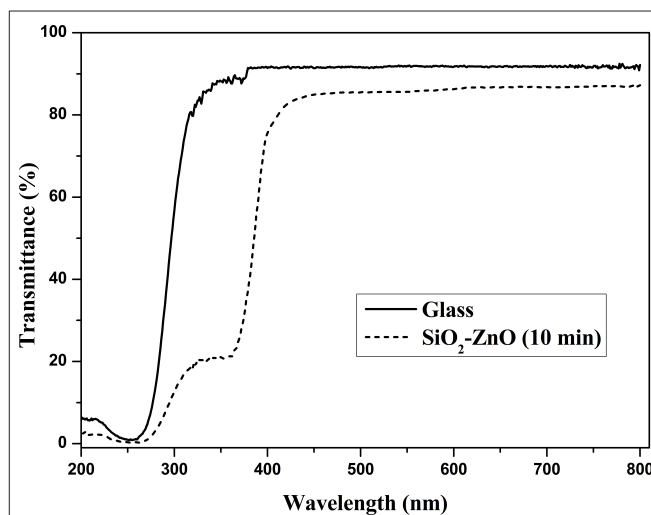


FIGURE 11 | Transmittance spectra of SiO₂ shell on ZnO nanorod arrays and bare glass.

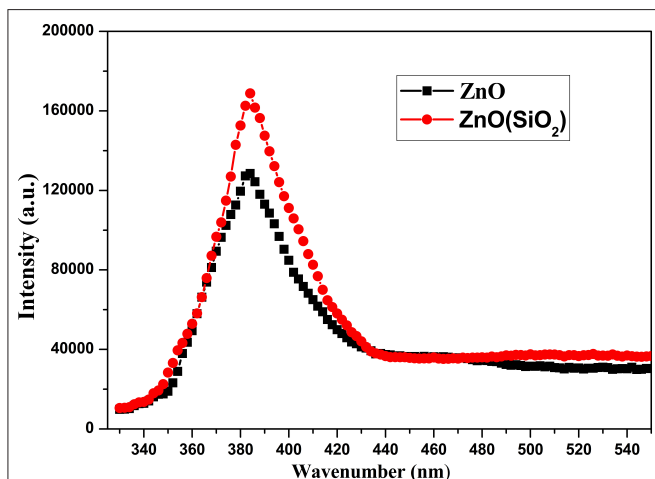


FIGURE 10 | Photoluminescence spectra of bare ZnO and SiO₂ coated on ZnO with deposition of 10 min.

High transmittance is the basic requirement for the front electrode materials in solar cells. ZnO nanostructure has good transmittance in visible and infrared region due to high band gap of 3.2 eV. The thickness of SiO₂ film is so thin that the effect

on the surface morphology and water contact angle is negligible. Figure 11 gives the transmittance spectra of SiO₂ shell on ZnO nanorod arrays and bare glass. It can be shown that transmittance is around 85% when wavelength ranges from 400 to 800 nm and with a small transmittance loss compared to bare glass. This loss in transmittance is acceptable compared to a loss of nearly half the efficiency due to dust.

CONCLUSION

A large area of vertically aligned ZnO nanorod arrays was prepared through chemical hydrothermal process. Ultra-thin SiO₂ shell film was deposited on ZnO nanorod arrays through PLD, and subsequently modified by stearic acid. This SiO₂/ZnO/glass structure exhibited well UV-durable superhydrophobicity and highly transmittance. These properties can have important applications in solar cells.

DATA AVAILABILITY STATEMENT

The datasets generated for this study are available on request to the corresponding author.

AUTHOR CONTRIBUTIONS

HW, QLi, QLi, XZ and QG participated in the discussion and gave useful suggestions. The manuscript was composed by HL and JZ. All authors read and approved the final manuscript.

REFERENCES

- Al-Asbahi, B. A. (2017). Influence of anatase titania nanoparticles content on optical and structural properties of amorphous silica. *Mater. Res. Bull.* 89, 286–291. doi: 10.1016/j.materresbull.2017.01.004
- Aydemir, G., Utlu, G., and Cetinel, A. (2019). Growth and characterization of ZnO nanostructures on porous silicon substrates: effect of solution temperature. *Chem. Phys. Lett.* 737:136827. doi: 10.1016/j.cplett.2019.136827
- Cassie, A. B. D., and Baxter, S. (1944). Wettability of porous surfaces. *Trans Faraday Soc.* 40, 546–551.
- Chen, M. X., Pan, C. F., Zhang, T. P., Li, X. Y., Liang, R. R., and Wang, Z. L. (2016). Tuning light emission of a pressure-sensitive silicon/ZnO nanowires heterostructure matrix through piezo-phototronic effects. *ACS Nano* 10, 6074–6079. doi: 10.1021/acsnano.6b01666
- Darmanin, T., and Guittard, F. (2011). Superhydrophobic fiber mats by electrodeposition of fluorinated poly(3,4-ethyleneoxythiophene). *J. Am. Chem. Soc.* 133, 15627–15634. doi: 10.1021/ja205283b
- de Jongh, P., and Vanmaekelbergh, D. (1996). Trap-limited electronic transport in assemblies of nanometer-size TiO₂ particles. *Phys. Rev. Lett.* 77, 3427–3430. doi: 10.1103/PhysRevLett.77.3427
- Elminir, H. K., Ghitas, A. E., Hamid, R. H., El-Hussairly, F., Beheary, M. M., Abdel-Moneim, K. M. (2006). Effect of dust on the transparent cover of solar collectors. *Energy Convers. Manage.* 47, 3192–3203. doi: 10.1016/j.enconman.2006.02.014
- Feng, X., Feng, L., Jin, M., Zhai, J., Jiang, L., and Zhu, D. (2004). Reversible superhydrophobicity to super-hydrophilicity transition of aligned ZnO nanorod films. *J. Am. Chem. Soc.* 126, 62–63. doi: 10.1021/ja038636o
- Gao, Y. Q., Gereige, L., Ei Labban, A., Cha, D., Isimjan, T. T., and Beaujuge, P. M. (2011). Highly transparent and UV-resistant superhydrophobic SiO₂-coated ZnO nanorod arrays. *ACS Appl. Mater. Interfaces* 3, 3152–3156. doi: 10.1021/am405513k
- Ikuno, T., Katayama, M., Kamada, K., Honda, S., Lee, J. G., and Oura, K. (2003). Insulator-coated carbon nanotubes synthesized by pulsed laser deposition. *Jpn. J. Appl. Phys.* 42, 1356–1358. doi: 10.1143/JJAP.42.L1356
- Li, H., Lu, H. Y., Liu, S. L., Li, Q., and Liu, Q. Z. (2019). SiO₂ shell on ZnO nanoflake arrays for UV-durable superhydrophobicity on Al substrate. *Mater. Res. Bull.* 114, 85–89. doi: 10.1016/j.materresbull.2019.02.022
- Li, H., Zheng, M. J., Liu, S. D., Ma, L., Zhu, C. Q., and Xiong, Z. Z. (2013). Reversible surface wettability transition between superhydrophobicity and superhydrophilicity on hierarchical micro/nanostructure ZnO mesh films. *Surf. Coat. Technol.* 224, 88–92. doi: 10.1016/j.surfcoat.2013.03.004
- Li, Z. H., and Guo, Z. G. (2019). Bioinspired surfaces with wettability for antifouling application. *Nanoscale* 11, 22636–22663. doi: 10.1039/C9NR05870B
- Liu, X., H., Afzaal, M., Ramasamy, K., O'Brien, P., and Akhtar, J. (2009). Synthesis of ZnO hexagonal single-crystal slices with predominant (0001) and (000-1) facets by poly(ethylene glycol)-assisted chemical bath deposition. *J. Am. Chem. Soc.* 131, 15106–15107. doi: 10.1021/ja906992s
- Lv, L., Liu, H., Zhang, W., Chen, J. Y., and Liu, Z. Z. (2020). Facile UV-curable fabrication of robust, anti-icing superhydrophobic coatings based on polyurethane. *Mater. Lett.* 258:126653. doi: 10.1016/j.matlet.2019.126653
- Maghsoodi, K., Momen, G., Jafari, R., and Farzaneh, M. (2019). Rigorous testing to assess the self-cleaning properties of an ultra-water-repellent silicone rubber surface. *Surf. Coat. Technol.* 374, 557–568. doi: 10.1016/j.surfcoat.2019.05.073

FUNDING

This work was supported by the Natural Science Foundation (Nos. 11974127, 51973078) and the Natural Science Foundation of Anhui Province (No: 1808085ME140), the Program for excellent young talents in College and University (No. gxyq2018162).

- Meth, S., and Sukenik, C. N. (2003). Siloxane-anchored thin films on silicon dioxide-modified stainless steel. *Thin Solid Films* 425, 49–58. doi: 10.1016/S0040-6090(02)01296-8
- Nikov, R. G., Dikovska, A. O., Avdeev, G. V., Amoroso, S., Ausanio, G., and Nedyalkov, N. N. (2019). PLD fabrication of oriented nanowires in magnetic field. *Appl. Surf. Sci.* 471, 368–374. doi: 10.1016/j.apsusc.2018.12.030
- Okosh, M., Kusaaki, M., and Inoue, N. (2002). Pulsed laser deposition of SiO₂ thin films with dimethylpolysiloxane targets. *Jpn. J. Appl. Phys.* 42, 1395–1399. doi: 10.1143/JJAP.41.1395
- Park, Y. B., Im, H., Im, M., and Choi, Y. K. (2011). Self-cleaning effect of highly water-repellent microshell structures for solar cell applications. *J. Mater. Chem.* 21, 633–636. doi: 10.1039/C0JM02463E
- Qu, J., Yang, Y. L., Yang, S. S., Hu, D. H., and Qiu, H. H. (2019). Droplet impingement on nano-textured superhydrophobic surface: experimental and numerical study. *Appl. Surf. Sci.* 491, 160–170. doi: 10.1016/j.apsusc.2019.06.104
- Sharma, V., Kumar, P., Kumar, A., Surbhi, Asokan, K., and Sachdev, K. (2017). High-performance radiation stable ZnO/Ag/ZnO multilayer transparent conductive electrode. *Sol. Energ. Mat. Sol. C* 169, 122–131. doi: 10.1016/j.solmat.2017.05.009
- Shchukin, D. G., Zheludkevich, M., Yasakau, K., Lamaka, S., Ferreira, M. G. S., and Mohwald, H. (2006). Layer-by-layer assembled nanocontainers for self-healing corrosion protection. *Adv. Mater.* 18, 1672–1678. doi: 10.1002/adma.200502053
- Shen, X. N., Yang, M., Zhang, C., Qiao, Z. X., Wang, H., and Tang, C. C. (2019). Utilizing magnetron sputtered AZO-ITO bilayer structure as transparent conducting oxide for improving the performance of flexible CIGS solar cell. *Superlattice. Microst.* 123, 251–256. doi: 10.1016/j.spmi.2018.09.001
- Sun, R. D., Nakajima, A., Fujishima, A., Watanabe, T., and Hashimoto, K. (2001). Photoinduced surface wettability conversion of ZnO and TiO₂ thin films. *J. Phys. Chem. B* 105, 1984–1990. doi: 10.1021/jp002525j
- Velayi, E., and Norouzbegi, R. (2018). Annealing temperature dependent reversible wettability switching of micro/nano structured ZnO superhydrophobic surfaces. *Appl. Surf. Sci.* 441, 156–164. doi: 10.1016/j.apsusc.2018.02.005
- Wang, L. B., Zhao, Y. Y., Zheng, K. S., She, J. C., Deng, S. Z., Xu, N. S., et al. (2019). Fabrication of large-area ZnO nanowire field emitter arrays by thermal oxidation for high-current application. *Appl. Surf. Sci.* 484, 966–974. doi: 10.1016/j.apsusc.2019.04.169
- Wang, L. L., Zhang, X. T., Fu, Y., Li, B., and Liu, Y. C. (2009). Bioinspired preparation of ultrathin SiO₂ shell on ZnO nanowire array for ultraviolet-durable superhydrophobicity. *Langmuir* 25, 13619–13624. doi: 10.1021/la901998p
- Wang, N., Xiong, D., Deng, Y., Shi, Y., and Wang, K. (2015). Mechanically robust superhydrophobic steel surface with anti-icing, UV-durability, and corrosion resistance properties. *ACS Appl. Mater. Interfaces* 7, 6260–6272. doi: 10.1021/acsami.5b00558
- Wu, Y. L., Tok, A. I. Y., Boey, F. Y. C., Zeng, X. T., and Zhang, X. H. (2007). Surface modification of ZnO nanocrystals. *Appl. Surf. Sci.* 253, 5473–5479. doi: 10.1016/j.apsusc.2006.12.091
- Xue, C. H., Yin, W., Zhang, P., Zhang, J., Ji, P. T., and Jia, S. T. (2013). UV-durable superhydrophobic textiles with UV-shielding properties by introduction of ZnO/SiO₂ core/shell nanorods on PET fibers and Hydrophobization. *Colloids Surf. A Physicochem. Eng. Aspects* 427, 7–12. doi: 10.1016/j.colsurfa.2013.03.021
- Zang, Z. (2018). Efficiency enhancement of ZnO/Cu₂O solar cells with well oriented and micrometer grain sized Cu₂O films. *Appl. Phys. Lett.* 112:042106. doi: 10.1063/1.5017002

- Zhang, J. C., Chen, F. Z., Lu, Y., Zhang, Z. T., Liu, J. Y., Chen, Y., et al. (2020). Superhydrophilic–superhydrophobic patterned surfaces on glass substrate for water harvesting. *J. Mater. Lett.* 55, 498–508. doi: 10.1007/s10853-019-04046-x
- Zhang, X. T., Sato, O., and Fujishima, A. (2004). Water ultrarepellency induced by nanocolumnar ZnO surface. *Langmuir* 20, 6065–6067. doi: 10.1021/la049471f
- Zhu, H. B., Hu, W. H., Zhao, S. P., Zhang, X., Pei, L., Zhao, G. Z., et al. (2020). Flexible and thermally stable superhydrophobic surface with excellent anti-corrosion behavior. *J. Mater. Sci.* 55, 2215–2225. doi: 10.1007/s10853-019-04050-1

Conflict of Interest: The authors declare that the research was conducted in the absence of any commercial or financial relationships that could be construed as a potential conflict of interest.

Copyright © 2020 Li, Zou, Wei, Li, Gao, Liu and Zhang. This is an open-access article distributed under the terms of the Creative Commons Attribution License (CC BY). The use, distribution or reproduction in other forums is permitted, provided the original author(s) and the copyright owner(s) are credited and that the original publication in this journal is cited, in accordance with accepted academic practice. No use, distribution or reproduction is permitted which does not comply with these terms.



One-Step Microwave Synthesis of Micro/Nanoscale LiFePO₄/Graphene Cathode With High Performance for Lithium-Ion Batteries

Shulong Liu^{1*}, Ping Yan², Haibin Li¹, Xiaobo Zhang¹ and Wei Sun¹

¹ School of Physics and Electronic Information/Information College, Huaibei Normal University, Huaibei, China, ² School of Life Science, Huaibei Normal University, Huaibei, China

OPEN ACCESS

Edited by:

Kezhen Qi,
Shenyang Normal University, China

Reviewed by:

Jian Zhang,
Wuhan University of
Technology, China
Qi Long Guo,
Northwest University for
Nationalities, China

*Correspondence:

Shulong Liu
liushulong0314@163.com

Specialty section:

This article was submitted to
Nanoscience,
a section of the journal
Frontiers in Chemistry

Received: 26 December 2019

Accepted: 04 February 2020

Published: 25 February 2020

Citation:

Liu S, Yan P, Li H, Zhang X and Sun W
(2020) One-Step Microwave
Synthesis of Micro/Nanoscale
LiFePO₄/Graphene Cathode With
High Performance for Lithium-Ion
Batteries. *Front. Chem.* 8:104.
doi: 10.3389/fchem.2020.00104

In this study, micro/nanoscale LiFePO₄/graphene composites are synthesized successfully using a one-step microwave heating method. One-step microwave heating can simplify the reduction step of graphene oxide and provide a convenient, economical, and effective method of preparing graphene composites. The structural analysis shows that LiFePO₄/graphene has high phase purity and crystallinity. The morphological analysis shows that LiFePO₄/graphene microspheres and micron blocks are composed of densely aggregated nanoparticles; the nanoparticle size can shorten the diffusion path of lithium ions and thus increase the lithium-ion diffusion rate. Additionally, the graphene sheets can provide a rapid transport path for electrons, thus increasing the electronic conductivity of the material. Furthermore, the nanoparticles being packed into the micron graphene sheets can ensure stability in the electrolyte during charging and discharging. Raman analysis reveals that the graphene has a high degree of graphitization. Electrochemical analysis shows that the LiFePO₄/graphene has an excellent capacity, high rate performance, and cycle stability. The discharge capacities are 166.3, 156.1, 143.0, 132.4, and 120.9 mAh g⁻¹ at rates of 0.1, 1, 3, 5, and 10 C, respectively. The superior electrochemical performance can be ascribed to the synergy of the shorter lithium-ion diffusion path achieved by LiFePO₄ nanoparticles and the conductive networks of graphene.

Keywords: LiFePO₄/graphene composite, micro/nanoscale, one step, microwave synthesis, electrochemical performance

INTRODUCTION

Energy and materials, important pillars of the modern developing society, are closely related to human civilization. Rechargeable lithium-ion batteries, an environmentally friendly and new green energy, have wide applicability in the fields of energy storage and transportation (Song et al., 2018). The ever-increasing demand for high current charge-discharge capability, high energy density, and long service life has driven the development of the lithium battery industry (Zhou et al., 2019). Olivine phase lithium iron phosphate (LiFePO₄) is one of the focused cathode materials in lithium-ion batteries (Padhi et al., 1997a,b). It has many superior properties, such as that Fe is low-cost and environmentally benign, that the covalently bonded PO₄ groups make the chemical properties more stable and prolong service lifetime, and that it has a high theoretical capacity (170 mAhg⁻¹)

and flat voltage plateau (3.45 V vs. Li/Li⁺). However, LiFePO₄ materials have some drawbacks, such as inferior electronic conductivity (ca. 10⁻⁹–10⁻¹⁰ Scm⁻¹) as well as slow one-dimensional lithium ion diffusion, which is a formidable obstacle to the high performance of lithium-ion batteries (Goodenough and Kim, 2010; Dathar et al., 2011). A considerable number of methods have been adopted with the aim of alleviating the above shortcomings. These methods can be categorized into two main classes: particle size control (Prosini et al., 2003; Zhao et al., 2016) and conductive material coating (Chang et al., 2019; Han et al., 2019; Ma et al., 2019; Tao et al., 2019).

Small particle size can decrease the migration distance of lithium ions from the interior to the surface and increase the diffusion rate (Lim et al., 2008; Hai et al., 2019; Li et al., 2019; Xiao et al., 2019). Various techniques, including solid-state reaction (Zheng et al., 2008), sol-gel (Zhang et al., 2011) hydrothermal (Kiyoshi et al., 2008; Chang et al., 2014), co-precipitation (Park et al., 2003; Wang et al., 2013), and microwave heating (Wang et al., 2007; Beninati et al., 2008; Guo et al., 2010), are adopted to control particle size. Moreover, surface coating with conductive material can increase the electronic conductivity between particles (Wang et al., 2010; Fathollahi et al., 2015; Ahn et al., 2019) and provide paths in all directions for the fast transmission of electrons (Wang et al., 2009; Jang et al., 2011; Fan et al., 2014). Graphene with high electrical conductivity has been adopted to improve the cycling stability and rate capability of cathode material (Ding et al., 2010; Zhou et al., 2011; Shi et al., 2012; Tang et al., 2012; Chen et al., 2018; Wang et al., 2018). Ding et al. (2010) prepared nano-structured LiFePO₄/graphene using co-precipitation and sintering at 700°C for 18 h under argon flow. Shi et al. (2012) prepared graphene-wrapped LiFePO₄/C using a microwave-assisted hydrothermal method, followed by sintering at 600°C for 2 h under H₂/Ar flow. Zhou et al. (2011) first synthesized LiFePO₄ nanoparticles by a hydrothermal method and then synthesized LiFePO₄/graphene from LiFePO₄ nanoparticles and graphene oxide nanosheets by spray-drying and annealing processes. Tang et al. (2012) synthesized LiFePO₄/graphene by mixing three-dimensional graphene prepared by chemical vapor deposition and LiFePO₄ prepared by solid-state reaction in a N-methyl pyrrolidinone (NMP) suspension. The above experimental methods are very complicated, and most of them require long-term high-temperature treatment and atmosphere protection, which lead to high energy consumption and cost. Additionally, the graphene and active materials agglomerate easily and distribute unevenly. Therefore, simplifying the preparation technology and obtaining a product with a small and homogeneous distribution remain great challenges for preparing LiFePO₄/graphene composites. Microwave heating is a convenient, economical, and environmentally friendly route for the preparation of graphene composites in a way that addresses the deficiency of graphene modification. Microwave heating can simplify the reduction step of graphene oxide, as, due to the microwave-absorbing properties of graphene oxide, microwave irradiation can restore it into graphene directly without any reductive agent and atmosphere.

In this work, micro/nanoscale LiFePO₄/graphene composites are synthesized successfully using a one-step microwave heating method. The synthesis technique has a decisive influence on the structure, morphology, and electrochemical properties of the LiFePO₄ product. Microwave synthesis can save synthesis time; this is because the raw material can absorb microwave energy by itself and convert electromagnetic energy into heat and internal molecular kinetic energy, thus improving the diffusion coefficient and accelerating the reaction rate. Meanwhile, microwave synthesis can lower the synthesis temperature; this is because the electromagnetic field decreases the activation energy of the reaction. Therefore, microwave heating is a rapid and effective synthetic method for preparing a product with small particle size. Furthermore, unlike in complex, multi-step preparation processes, microwave irradiation can restore the graphene oxide into graphene directly without any reductive agent and atmosphere. The synthesized micro/nanoscale LiFePO₄/graphene composites with fine particle size and uniform distribution can decrease the migration distance of lithium ions from the interior to the surface and increase the diffusion rate. Meanwhile, graphene wrapping of the surface of LiFePO₄ particles can guarantee that the electrons migrate to the active sites quickly. Controlling the particle size and coating with graphene play important roles in the electrochemical performance. The effects of graphene and microwave irradiation on the electrochemical performance of LiFePO₄/graphene cathode materials for lithium-ion batteries are further investigated.

EXPERIMENTAL

Preparation of Materials

FeSO₄·7H₂O (99%), LiOH·H₂O (95%), H₃PO₄ (85%), ethylene glycol, and sucrose were purchased from Sinopharm Chemical Reagent Co. Ltd. Graphene oxide was synthesized from natural graphite powder (325 mesh) using a modified Hummers' method (Kovtyukhova et al., 1999; Stankovich et al., 2007).

The LiFePO₄/graphene and LiFePO₄/C composites were synthesized via the following steps. FeSO₄·7H₂O and H₃PO₄ were dissolved in a mixed solution of de-ionized water and ethylene glycol, and GO suspension was added to the solution. Next, a mixture of LiOH·H₂O aqueous solution and GO suspension was added into the mixed solution under constant stirring. The molar ratio of Li:Fe:P is 3:1:1. After stirring for 3 h, the solution was evaporated at 80°C for 12 h. Meanwhile, a separate sample was prepared with the GO suspension replaced by sucrose as the source of carbon, and the previous steps were repeated. Finally, the precursors obtained were pressed into pellets, and then the pellets were placed inside a quartz crucible with a cover to prevent air oxidation. The quartz crucible was put in the middle of the domestic microwave oven, and the precursors were radiated by microwave for 10 min with a maximum power of 1,500 W and a frequency of 2.45 GHz. After microwave irradiation, LiFePO₄/graphene and LiFePO₄/C composites were obtained, respectively.

Characterization Techniques

The structures of LiFePO₄/graphene and LiFePO₄/C composites were investigated using an X-ray diffractometer (X'pert PRO, Panalytical, Holland) with Cu K α radiation operated at 40 kV and 40 mA. The contents of graphene and carbon in the LiFePO₄/graphene and LiFePO₄/C composites were calculated from TG-DSC (STA449F3, NETZSCH, Germany), which was carried out from room temperature to 700°C under an air atmosphere at a rate of 10°C min⁻¹. The morphologies of LiFePO₄/graphene composites were observed using a scanning electron microscope (SEM, JSM-IT300 at 20 kV) and transmission electron microscopy (TEM, JEM2100F Japan at 200 kV). The Raman spectra of LiFePO₄/graphene and LiFePO₄/C composites were recorded from 100 to 3,200 cm⁻¹ on a Renishaw Raman microprobe (INVIA, China) using a 514.5 nm argon-ion laser at room temperature.

Cell Fabrication and Electrochemical Measurement

The electrochemical behaviors of the LiFePO₄/graphene and LiFePO₄/C composites were evaluated with 2,025 coin-type batteries. The cathode electrodes were prepared by mixing 80 wt% active materials (LiFePO₄/graphene or LiFePO₄/C) and 10 wt% carbon black (TIMCAL) with 10 wt% polytetrafluoroethylene (PTFE, Aldrich) in isopropyl alcohol solution (99.5%, Aldrich). A uniform slurry was formed and pasted onto Al foils, dried at 120°C for 12 h, and then cut into circular electrodes with a diameter of 10 mm. Lithium metal (99.9%, Alfa-Aesar) was used as the anode, Celgard polypropylene (Celgard 2400) as the separator, and 1M LiPF₆ dissolved in ethylene carbonate and dimethyl carbonate (with a 1:1 volume ratio) as the electrolyte (MERCK KGaA, Germany). The cells were assembled in an argon-filled glove box (Etelux Lab2000, China). Cells were charged and discharged at room temperature using a LAND-CT2001A battery cycler (Wuhan, China) within the voltage range of 2.7–4.2 V (vs. Li⁺/Li). Cyclic voltammetry (CV) was performed with an Auto Potentiostat 30 system at a scan rate of 0.1 mVs⁻¹ between 2.5 and 4.2 V. Electrochemical impedance spectroscopy (EIS) profiles were obtained at the same open-circuit voltage by applying a 5-mV amplitude of the AC voltage with the frequency ranging from 100 kHz to 0.01 Hz.

RESULTS AND DISCUSSION

Phase Structural Analysis

The phase constitution and crystal structure of the synthetic LiFePO₄/graphene and LiFePO₄/C composites are here investigated. XRD patterns of the composites are shown in **Figure 1**. It can be seen that there is no noticeable difference between LiFePO₄/graphene and LiFePO₄/C composites. All the sharp diffraction peaks corresponding to the (200), (101), (210), (011), (111), (211), (301), (311), (121), (410), (221), (401), (112), (222), and (123) planes can be indexed to the orthorhombic olivine-type structure LiFePO₄ with the Pnma space group (JCPDS card No. 83-2092) (Wang et al., 2009, 2010), and no excess impurity peaks are observed. The results

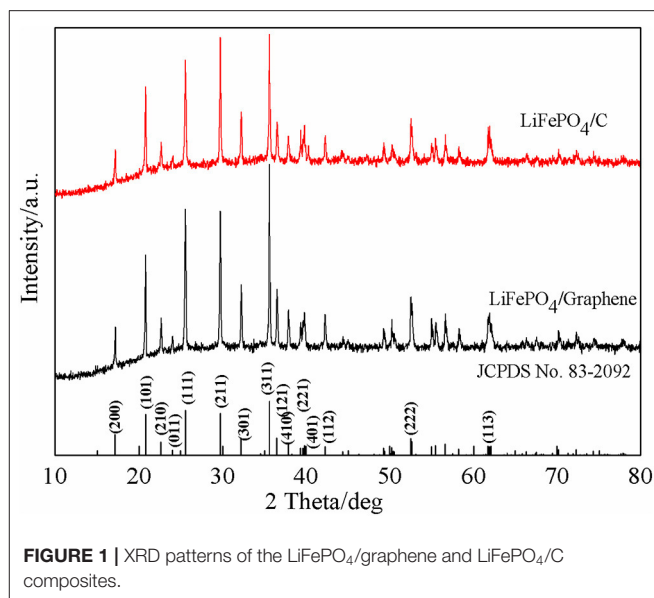


FIGURE 1 | XRD patterns of the LiFePO₄/graphene and LiFePO₄/C composites.

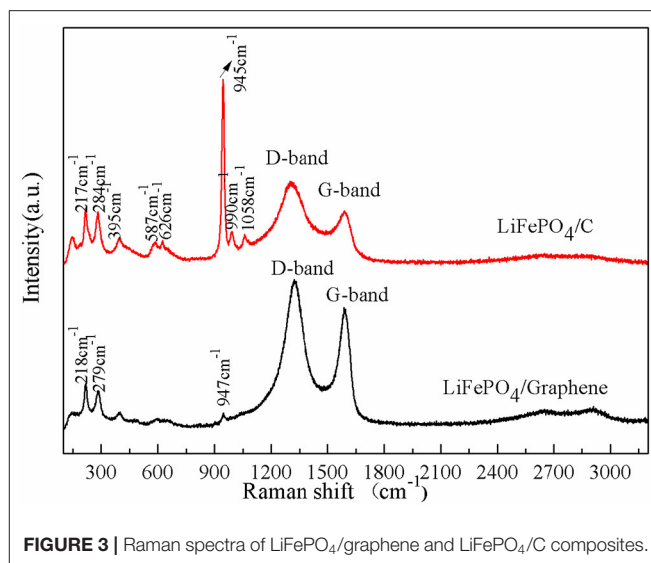
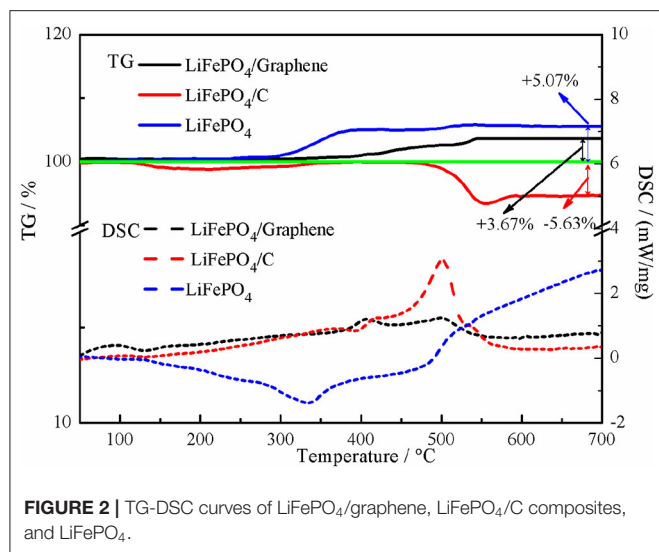
manifest that the synthetic composites have high crystallinity and purity; this is mainly because microwave synthesis has the advantage of increasing the crystallinity and purity of products. The diffraction pattern of LiFePO₄/graphene shows that no diffraction peak of graphene oxide (at around 12°) is observed, proving that the graphene oxide has already been reduced into graphene directly without any reducing agent or atmosphere. This is mainly because the graphene oxide with a large amount of oxygen functional groups on the surface that can absorb microwaves easily, and electromagnetic energy is converted into heat and molecular kinetic energy; the reactive oxygen groups are then exfoliated, and, finally, the graphene oxide is restored into graphene. Also, the introduction of graphene has no effect on the structure of LiFePO₄. Moreover, the diffraction pattern of LiFePO₄/C shows no diffraction peaks corresponding to residual carbon, indicating that the carbon decomposed from sucrose in the sample exists in an amorphous state.

TG-DSC Analysis

TG-DSC measurement data is used to estimate the graphene and carbon content in the LiFePO₄/graphene and LiFePO₄/carbon composites, as shown in **Figure 2**. The pure LiFePO₄ can be completely oxidized to Li₃Fe₂(PO₄)₃ and Fe₂O₃ under air flow, and the total weight gain is about 5.07% in theory (Belharouak et al., 2005; Bai et al., 2015). For LiFePO₄/graphene and LiFePO₄/carbon composites, in the temperature range of 400–600°C, the graphene and carbon are oxidized to CO₂ gas, so the amounts of graphene and carbon in the LiFePO₄/graphene and LiFePO₄/carbon composites are about 1.40 and 10.70%, respectively.

Raman Analysis

Raman scattering spectroscopy was employed to recognize the chemical structure of the LiFePO₄/graphene and LiFePO₄/C composites; the results are shown in **Figure 3**. The main vibration



modes include internal modes attributable to PO₄³⁻ anions and external modes attributable to the coupled motion of Fe²⁺ and PO₄³⁻ (Markevich et al., 2011). The modes at 990, 1,058, and 945 cm⁻¹ correspond to the anti-symmetric (ν₃) and symmetric (ν₁) stretching of the P-O bonds. The modes at 626 and 587 cm⁻¹ correspond to the symmetric (ν₂) and anti-symmetric (ν₄) bending of the O-P-O angles. The mode at 395 cm⁻¹ corresponds to the lithium cage and oxygen ion breathing cage. The modes in the 100–300 cm⁻¹ range are induced by translation of Fe and coupled translation and vibration of Fe and PO₄³⁻ (Burba and Frech, 2004; Wu et al., 2013). Moreover, there are two obvious D band peaks at around 1,310 cm⁻¹ and a G band at around 1,590 cm⁻¹ (Tuinstra and Koenig, 1970). The D band is induced by a disordered and defective carbon structure in the crystal plane of the short-order *sp*² and *sp*³ carbon. The G band is assigned to the in-plane bond-stretching motion of *sp*² carbon atoms. The intensity ratio of the D and G bands (*I*_D/*I*_G) is inversely proportional to the degree of graphitization of carbon materials. The *I*_D/*I*_G in LiFePO₄/graphene composites is 1.18, while the *I*_D/*I*_G in LiFePO₄/C composites is 1.43. This implies that the graphene has a higher degree of graphitization than the carbon decomposed from sucrose. The higher the degree of graphitization, the better the conductivity of the carbon. A high degree of graphitization is favorable for electron transfer and improves the electrochemical performance of the cathode. Additionally, the strong signals of the graphene (D band and G band) weaken and override the bands of LiFePO₄ in the high-frequency region.

Morphological Analysis

SEM images of the graphene oxide and LiFePO₄/graphene are shown in Figures 4A–F. Figure 4A shows that the micron-scale graphene oxide sheets aggregate into petal shapes; these sheets can provide implantation sites for the adhesion of reaction particles. Figures 4B,C clearly shows that the LiFePO₄/graphene composites are composed of micron-scale spheres and blocks

with average dimensions of ~2 μm. In Figures 4D–F, it can be clearly observed that these LiFePO₄/graphene microspheres and micron blocks are composed of densely aggregated nanoparticles. This structure forms because the self-heating effect induced by the microwave heating can greatly shorten the reaction time, and the graphene wrapping the surface of LiFePO₄ particles can inhibit the growth of grains. Under the action of graphene, the nanoparticles assembled into microspheres and micron blocks. When the highly conductive electrolyte penetrates into the cathode material, the nanoparticles have a high specific surface area, which increases the contact area with the electrolyte. The nanoparticle size can shorten the diffusion paths of electrons and lithium ions and improve the conductivity of the cathode material significantly. Moreover, the micron structure formed by the aggregation of nanoparticles does not collapse during the process of lithium-ion intercalation and deintercalation, which ensures the stability of cathode material in the electrolyte. TEM and HRTEM images of the micron/nanoscale LiFePO₄/graphene composite are shown in Figures 4G,H. The ultrathin graphene sheets successfully form an effective conducting network and intrinsically bridge and intimately connect the active LiFePO₄ particles. Figure 4H indicates that the graphene sheets around LiFePO₄ are highly graphitic. The highly efficient and stable conducting network can give the material desirable electrochemical properties. In the energy spectrum, elements of P, O, Fe, and C are found, as shown in Figure 4I; Li cannot be detected because of its very low atomic weight.

The formation process of the LiFePO₄/graphene composites is illustrated in Figure 5. At the initial stage of the reaction, the chemical reaction follows a dissolution–precipitation mechanism. The iron ions, phosphate ions, and lithium ions in the solution react with each other and form agglomerated precipitate on the surface of the graphene oxide sheets, and a large number of active functional groups are adsorbed on the surface of graphene oxide. At the stage of microwave irradiation,

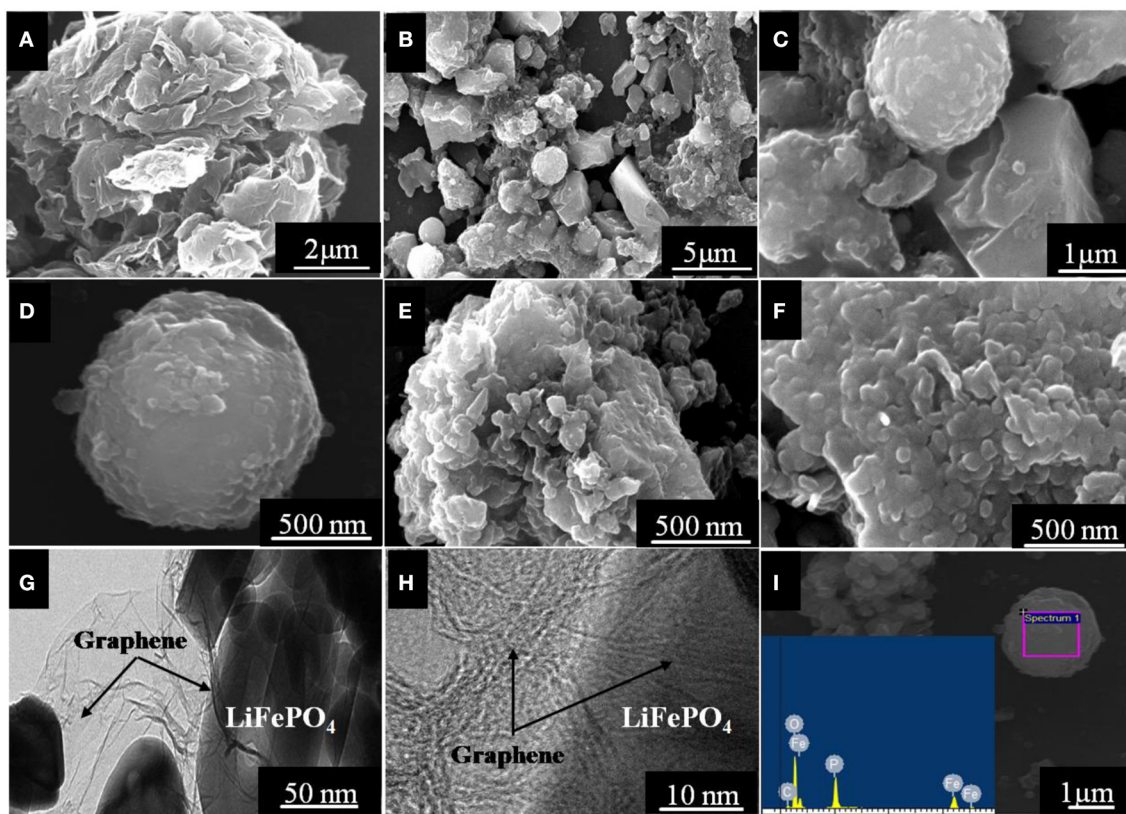


FIGURE 4 | SEM images of the graphene oxide (A) and LiFePO₄/graphene (B–F); TEM and HRTEM images of the LiFePO₄/graphene composites (G,H); EDS spectra of the LiFePO₄/graphene composites (I).

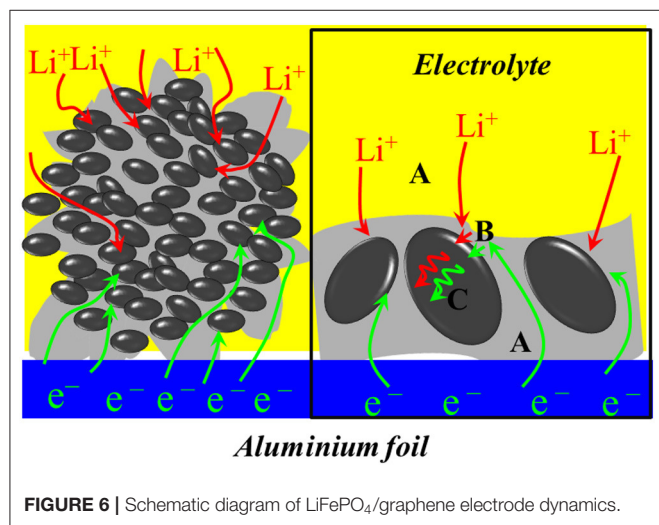
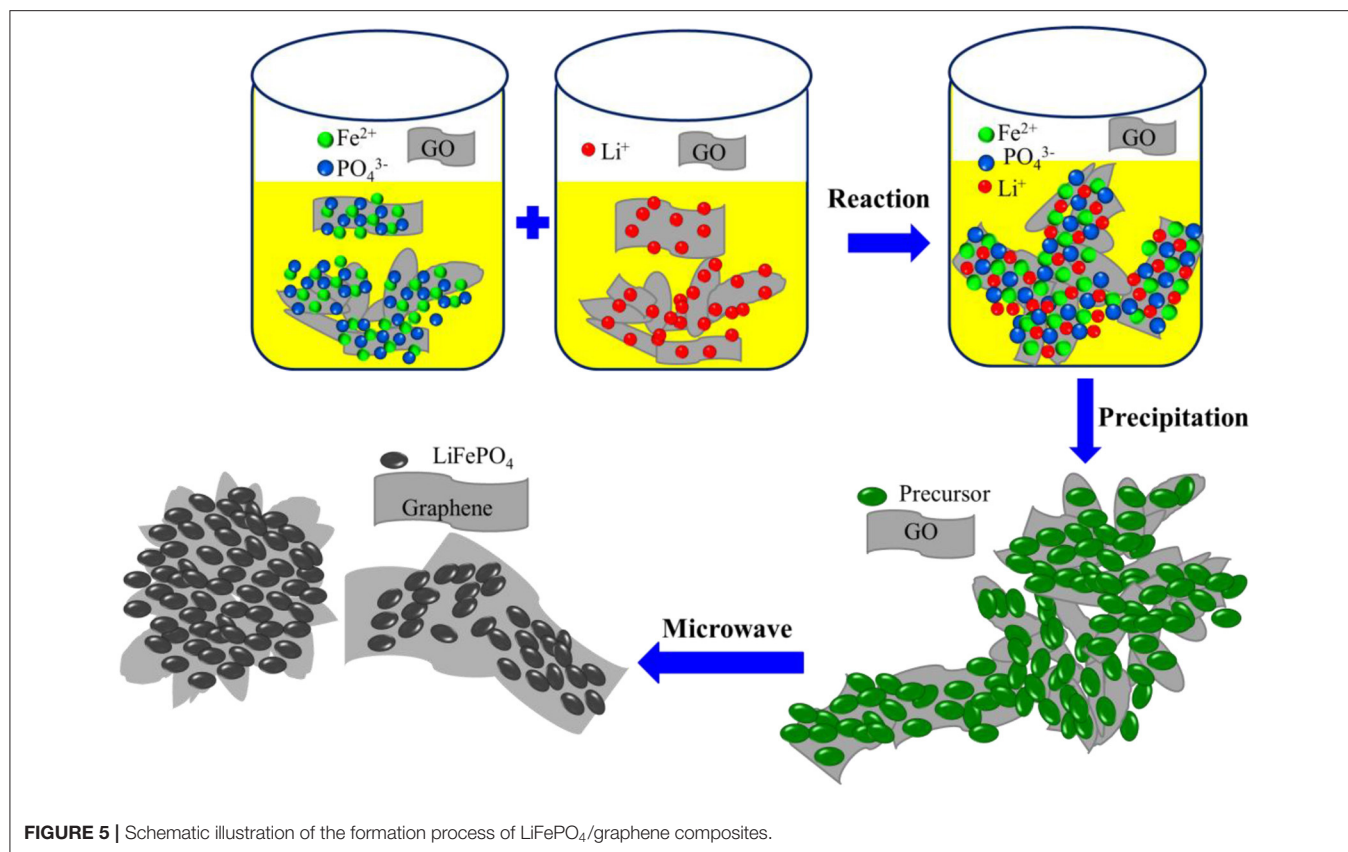
the active functional groups, being polar molecules, can absorb microwave easily, and electromagnetic energy is converted into heat and molecular kinetic energy. The temperature increase quickly, the reactive oxygen groups are exfoliated, and, finally, the graphene oxide is restored into graphene. Meanwhile, the precipitated particles adsorbed on the surface of reduced graphene sheets become hot and absorb microwaves quickly, the particles interact with each other, and then crystal nuclei are formed quickly under the action of the microwave electromagnetic field. Finally, under the influence of micron graphene sheets, the crystal nuclei grow, agglomerate, and form microspheres and micron blocks.

Electrochemical Properties Analysis

A schematic diagram of LiFePO₄/graphene electrode dynamics is shown in **Figure 6**. Transportation of electrons and ions (e⁻ and Li⁺) from their “reservoirs” toward the LiFePO₄ particles (Gaberscek et al., 2007; Gaberscek, 2009) is shown as step A. A charge incorporation reaction that involves the transfer of e⁻ and Li⁺ from the outside into the interior of active particles is shown as step B, and the transport of the lithium component inside the solid active particles (solid-state diffusion) is shown as step C. It can be seen that graphene can provide a high-speed channel for the rapid diffusion of electrons and cause the electrons to reach the reactive site quickly,

thus increasing the electronic conductivity of the materials. Meanwhile, the nanoparticles can shorten the transport path of Li⁺ from the surface to the interior of solid active particles and improve the diffusion coefficient of lithium ions. Moreover, the nanoparticles are surrounded by the micron graphene sheets, and the micron structure guards the stability of the material. Therefore, LiFePO₄/graphene composites are expected to have excellent electrochemical performance.

Cyclic voltammetry was performed to investigate the electrochemical kinetics of LiFePO₄/graphene and LiFePO₄/C cathode materials. **Figure 7** shows the CV spectra of the LiFePO₄/graphene and LiFePO₄/C composites. In the first scan, there is a pair of redox peaks corresponding to the Fe²⁺/Fe³⁺ couple (Ding et al., 2010; Zhou et al., 2011). The shapes of redox peaks are low and asymmetrical; this is because, in the first charging and discharging cycle, active materials are not completely saturated by electrolyte, and the pathways of lithium ion insertion and extraction were not completely formed. In the second scan, the current intensity increases, and the shape of the redox peaks becomes more symmetrical and sharper. For LiFePO₄/graphene, the potential difference between the oxidation and reduction peaks decreases from 0.27 to 0.26 V, which means that the phase is stabilized in subsequent cycles. **Figure 7B** shows the CV spectra of LiFePO₄/C composites. During the second scan, the potential difference increases

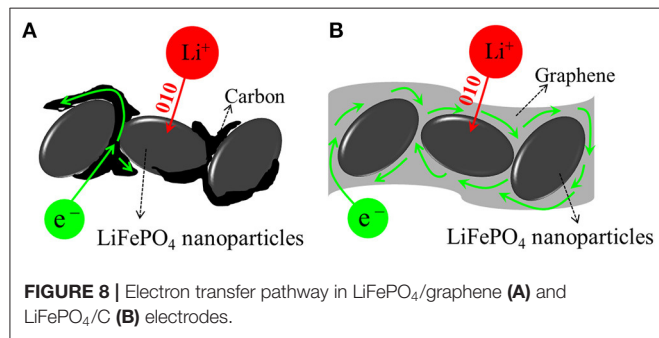
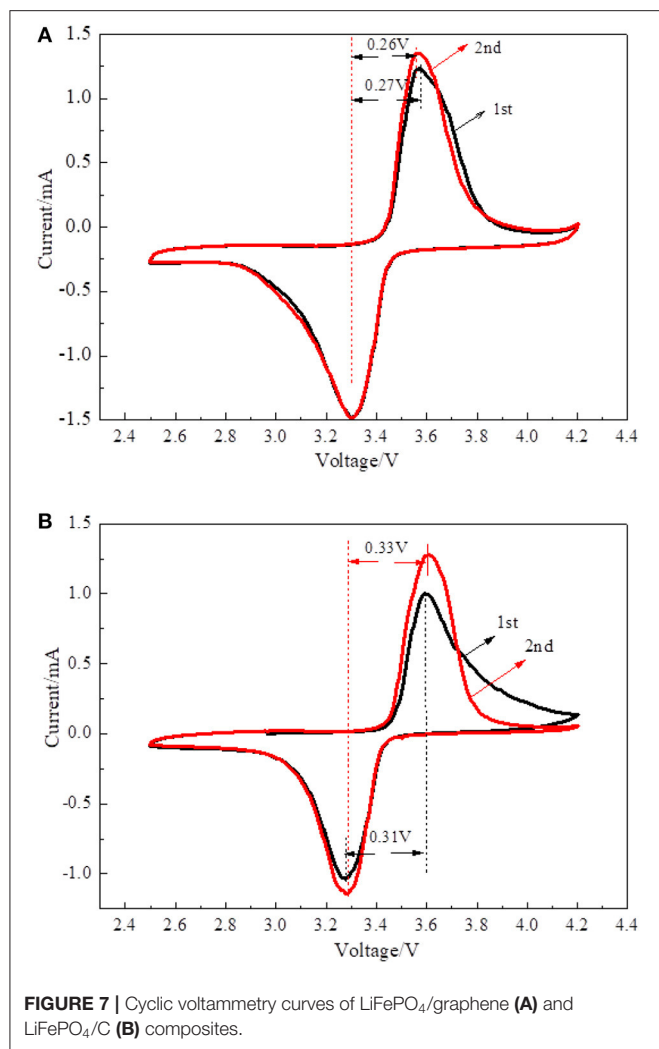


from 0.31 to 0.33 V, which proves that detrimental polarization becomes more and more serious. The results show that LiFePO₄/graphene composites have very high reversibility and better electrochemical activity.

The polarization of the LiFePO₄/C electrode is explained by the electron transfer pathway, as shown in **Figure 8A**. The carbon is dispersed unevenly, so the electrons cannot reach the

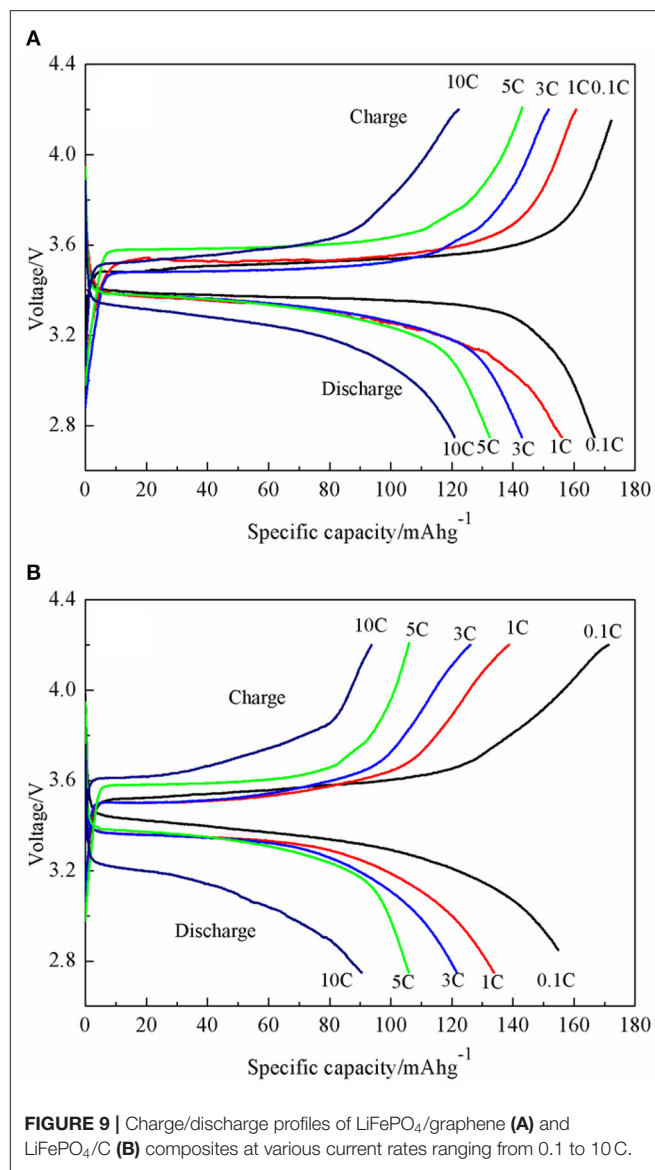
entire reactive site where the Li⁺ ions intercalate. In contrast, for LiFePO₄/graphene, due to the one-dimensional Li⁺ ion mobility in the framework, the graphene can ensure that electrons reach particles from all directions and alleviate the polarization, as shown in **Figure 8B**. Therefore, the LiFePO₄/graphene composites, with well-defined peaks and smaller potential difference, have higher electrochemical reactivity.

The charging and discharging capacity profiles of the LiFePO₄/graphene and LiFePO₄/C at progressively increasing C rates from 0.1 to 10 C are shown in **Figure 9**. The cells are cycled in the voltage window of 2.7–4.2 V at room temperature. For LiFePO₄/graphene composites, the initial discharge capacity is 166.3 mAhg⁻¹ at 0.1 C, and the discharge capacity decreases to 156.1 mAhg⁻¹ with an increase in the discharge rate to 1 C. At a higher discharge rate of 5 C, the cell delivers a capacity of 132.4 mAhg⁻¹. Even at a 10 C rate, the capacities can reach 120.9 mAhg⁻¹, and a good voltage plateau remains above 3 V. For LiFePO₄/C, the discharge capacity is 154.8, 133.8, 121.6, 105.9, and 86.4 mAh g⁻¹ at 0.1, 1, 3, 5, and 10 C rates, respectively. The cycling performances of the LiFePO₄/graphene and LiFePO₄/C from 0.1 to 10 C are shown in **Figure 10**. Although for LiFePO₄/graphene, the specific capacity decreases with increasing current rate, the capacity retention remains very good for all of the different rates; the discharge capacity retentions are, respectively, 99.5, 99.2, 99.4, 99.1, and 97.1% at 0.1, 1, 3, 5, and 10 C current rates after being cycled 10 times. While for LiFePO₄/C, the discharge capacity retentions



are, respectively, 97.7, 96.9, 93.0, 87.1, and 79.5% at 0.1, 1, 3, 5, and 10 C current rates. All of the results demonstrate that LiFePO₄/graphene composites have better rate performance and cycling stability. This can be attributed to the excellent electrical conductivity of graphene, which can improve the conductivity and stability of materials.

Electrochemical impedance spectroscopy was used to investigate the electrochemical behaviors of LiFePO₄/graphene



and LiFePO₄/C cathodes. **Figure 11A** shows the Nyquist plots of the LiFePO₄/graphene and LiFePO₄/C cathodes. The experimental EIS data is simulated by Zview2.1 software according to the equivalent circuit as shown in **Figure 11B**. It can be found that all the Nyquist plots present a high-frequency quasi-semicircle, which is related to the migration of the Li⁺ ions at the electrode/electrolyte interface and the charge transfer process. Meanwhile, a low-frequency sloping line is related to the Warburg impedance of the lithium-ion diffusion in the electrode (Zhang et al., 2011). R_s is the internal resistance of the cell and corresponds to the electrodes, electrolyte, and the separator resistance, R_{ct} is associated with the charge-transfer resistance, CPE is associated with the capacitance contributed by the surface of the active material (Guo et al., 2010). The simulation results show that the R_{ct} value of the LiFePO₄/graphene cathode is 79 Ω, which is smaller than the

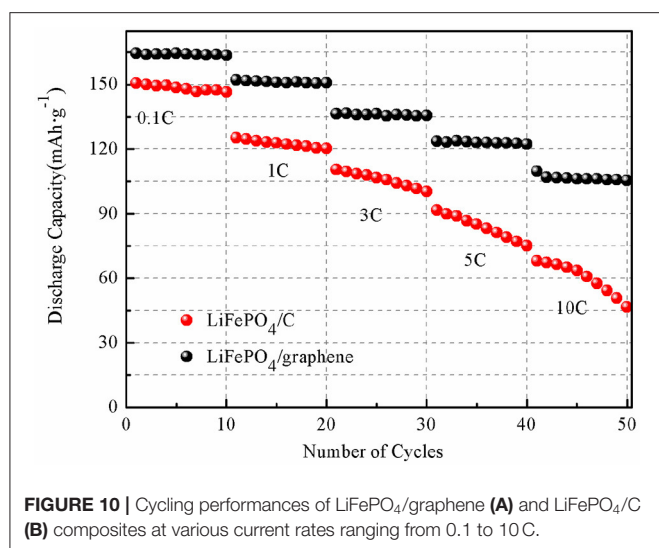


FIGURE 10 | Cycling performances of LiFePO₄/graphene (A) and LiFePO₄/C (B) composites at various current rates ranging from 0.1 to 10 C.

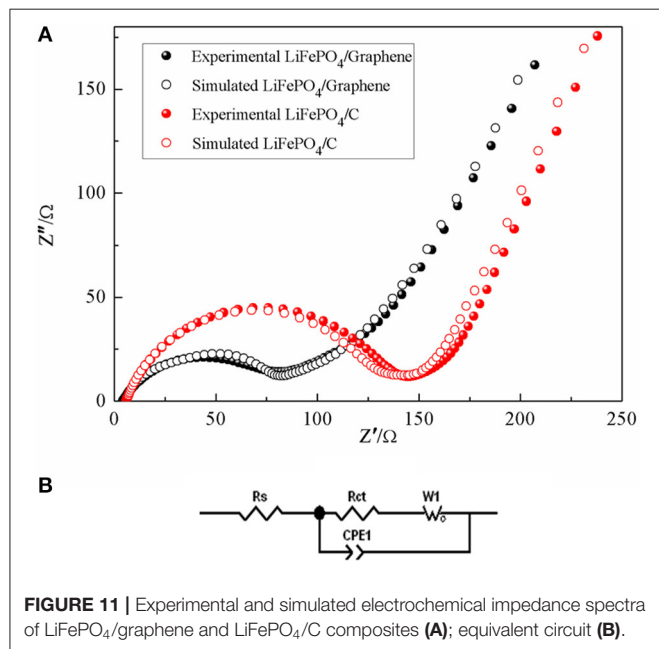


FIGURE 11 | Experimental and simulated electrochemical impedance spectra of LiFePO₄/graphene and LiFePO₄/C composites (A); equivalent circuit (B).

129 Ω value of the LiFePO₄/C cathode. The result shows that graphene can reduce the charge transfer resistance of Li-ion insertion and extraction between the electrode/electrolyte

REFERENCES

- Ahn, W., Seo, M. H., Pham, T. K., Nguyen, Q. H., Luu, V. T., Cho, Y., et al. (2019). High lithium ion transport through rGO-wrapped LiNi_{0.6}Co_{0.2}Mn_{0.2}O₂ cathode material for high-rate capable lithium ion batteries. *Front. Chem.* 7:361. doi: 10.3389/fchem.2019.00361
- Bai, N. B., Chen, H., Zhou, W., Xiang, K. X., Zhang, Y. L., and Li, C. L. (2015). Preparation and electrochemical performance of LiFePO₄/C microspheres by a facile and novel co-precipitation. *Electrochim. Acta* 167, 172–178. doi: 10.1016/j.electacta.2015.03.163
- Belharouak, I., Johnson, C., and Amine, K. (2005). Synthesis and electrochemical analysis of vapor-deposited carbon-coated LiFePO₄. *Electrochem. Commun.* 7, 983–988. doi: 10.1016/j.elecom.2005.06.019
- Beninati, S., Damen, L., and Mastragostino, M. (2008). MW-assisted synthesis of LiFePO₄ for high power applications. *J. Power Sources* 180, 875–879. doi: 10.1016/j.jpowsour.2008.02.066
- Burba, C. M., and Frech, R. (2004). Raman and FTIR spectroscopic study of Li_xFePO₄ (0 ≤ x ≤ 1). *J. Electrochem. Soc.* 151, A1032–A1038. doi: 10.1149/1.1756885
- Chang, M., Wang, H., Zheng, Y., Li, N., Chen, S., Wan, Y., et al. (2019). Surface modification of hollow microsphere Li_{1.2}Ni_{1/3}Co_{1/3}Mn_{1/3}O₂ and increase the conductivity of the LiFePO₄/graphene cathode.

CONCLUSION

A LiFePO₄/graphene composite was successfully prepared as cathode material through one-step microwave heating. The graphene oxide, which has excellent microwave-absorbing properties, can react with microwaves quickly and be restored into high-quality graphene directly without any reducing agent or atmosphere. The introduction of graphene does not impact the structure of LiFePO₄, and LiFePO₄ nanoparticles are packed into micron graphene sheets. The graphene network, which has a high degree of graphitization, can provide a high-speed channel for the rapid transfer of electrons and thus increase the electronic conductivity of materials. Meanwhile, the nanoparticles can improve the diffusion coefficient of lithium ions. Moreover, because the nanoparticles are surrounded by the graphene sheets, the micron structure guards the stability of the material. The electrochemical analyses reveal that the LiFePO₄/graphene composites have excellent high-rate performance and cycling life. The outstanding electrochemical performance, as well as the fast and efficient method, make this technology commercially viable.

DATA AVAILABILITY STATEMENT

The datasets generated for this study are available on request to the corresponding author.

AUTHOR CONTRIBUTIONS

SL, PY, and WS performed the experiments. SL, PY, HL, and XZ performed the data analysis. SL and PY wrote the paper. All authors contributed to the theoretical analysis and the general discussion.

FUNDING

This work was supported by the Program for Quality Engineering at School Level (2017jxcg01), Natural Science Foundation of Anhui Province (1708085QE119), Natural Science Foundation of Anhui Higher Education Institutions of China (KJ2015A314, KJ2017A393), and Collaborative Innovation Center of Advanced Functional Materials (XTZX103732016005).

- cathode by coating with CoAl₂O₄. *J. Solid State Electrochem.* 23, 607–613. doi: 10.1007/s10008-018-4157-y
- Chang, Y. C., Hung, I. M., and Peng, C. T. (2014). Effects of particle size and carbon coating on electrochemical properties of LiFePO₄/C prepared by hydrothermal method. *J. Mater. Sci.* 49, 6907–6916. doi: 10.1007/s10853-014-8395-9
- Chen, H., Zhang, B., Zhang, J., Yu, W., Zheng, J., Ding, Z., et al. (2018). *In-situ* grown SnS₂ nanosheets on rGO as an advanced anode material for lithium and sodium ion batteries. *Front. Chem.* 6:629. doi: 10.3389/fchem.2018.00629
- Dathar, G. K. P., Sheppard, D., Stevenson, K. J., and Henkelman, G. (2011). Calculations of Li ion diffusion in olivine phosphates. *Chem. Mater.* 23, 4032–4037. doi: 10.1021/cm201604g
- Ding, Y., Jiang, Y., Xu, F., Yin, J., Ren, H., Zhuo, Q., et al. (2010). Preparation of nano-structured LiFePO₄/graphene composites by co-precipitation method. *Electrochem. Commun.* 12, 10–13. doi: 10.1016/j.elecom.2009.10.023
- Fan, Q., Lei, L. X., Xu, X. Y., Yin, G., and Sun, Y. M. (2014). Direct growth of FePO₄/graphene and LiFePO₄/graphene hybrids for high rate Li-ion batteries. *J. Power Sources* 257, 65–69. doi: 10.1016/j.jpowsour.2014.01.044
- Fathollahi, F., Javanbakht, M., Omidvar, H., and Ghaemi, M. (2015). Improved electrochemical properties of LiFePO₄/graphene cathode nanocomposite prepared by one-step hydrothermal method. *J. Alloy Compd.* 627, 146–152. doi: 10.1016/j.jallcom.2014.12.025
- Gaberscek, M. (2009). Towards optimized preparation of cathode materials: how can modeling and concepts be used in practice. *J. Power Sources* 189, 22–27. doi: 10.1016/j.jpowsour.2008.12.041
- Gaberscek, M., Dominko, R., and Jamnik, J. (2007). Is small particle size more important than carbon coating? an example study on LiFePO₄ cathodes. *Electrochem. Commun.* 9, 2778–2783. doi: 10.1016/j.elecom.2007.09.020
- Goodenough, J. B., and Kim, Y. (2010). Challenges for rechargeable Li batteries. *Chem. Mater.* 22, 587–603. doi: 10.1021/cm901452z
- Guo, X. F., Zhang, Y. T., Zhan, H., and Zhou, Y. H. (2010). Investigation on the microwave-derived LiFePO₄/C cathode material. *Solid State Ion.* 181, 1757–1763. doi: 10.1016/j.ssi.2010.10.008
- Hai, Y., Zhang, Z., Liu, H., Liao, L., Fan, P., Wu, Y., et al. (2019). Facile controlled synthesis of spinel LiMn₂O₄ porous microspheres as cathode material for lithium ion batteries. *Front. Chem.* 7:437. doi: 10.3389/fchem.2019.00437
- Han, Q. G., Zhang, W. Q., Han, Z. W., Wang, F. X., Geng, D., Li, X., et al. (2019). Preparation of PAN-based carbon fiber@MnO₂ composite as an anode material for structural lithium ion batteries. *J. Mater. Sci.* 54, 11972–11982. doi: 10.1007/s10853-019-03751-x
- Jang, B. Z., Liu, C. G., Neff, D., Yu, Z. Y., Wang, M. C., Xiong, W., et al. (2011). Graphene surface-enabled lithium ion-exchanging cells: next-generation high-power energy storage devices. *Nano. Lett.* 11, 3785–3791. doi: 10.1021/nl2018492
- Kiyoshi, K., Shohei, K., and Kaoru, D. (2008). Hydrothermal synthesis of LiFePO₄ as a cathode material for lithium batteries. *J. Mater. Sci.* 43, 2138–2142. doi: 10.1007/s10853-007-2011-1
- Kovtyukhova, N. I., Ollivier, P. J., Martin, B. R., Mallouk, T. E., Chizhik, S. A., Buzaneva, E. V., et al. (1999). Layer-by-layer assembly of ultrathin composite films from micron-sized graphite oxide sheets and polycations. *Chem. Mater.* 11, 771–778. doi: 10.1021/cm981085u
- Li, Y., Zhang, H., Xiao, Z., and Wang, R. (2019). Flexible Li[Li_{0.2}Ni_{0.13}Co_{0.13}Mn_{0.54}]O₂/carbon nanotubes/nanofibrillated celluloses composite electrode for high-performance lithium-ion battery. *Front. Chem.* 7:555. doi: 10.3389/fchem.2019.00555
- Lim, S., Yoon, C. S., and Cho, J. (2008). Synthesis of nanowire and hollow LiFePO₄ cathodes for high-performance lithium batteries. *Chem. Mater.* 20, 4560–4564. doi: 10.1021/cm8006364
- Ma, F., Wu, Y. H., Wei, G., Qiu, S., and Qu, J. (2019). Enhanced electrochemical performance of LiNi_{0.8}Co_{0.1}Mn_{0.1}O₂ cathode via wet-chemical coating of MgO. *J. Solid State Electrochem.* 23, 2213–2224. doi: 10.1007/s10008-019-04308-3
- Markevich, E., Sharabi, R., Haik, O., Borgel, V., Salitra, G., Aurbach, D., et al. (2011). Raman spectroscopy of carbon-coated LiCoPO₄ and LiFePO₄ olivines. *J. Power Sources* 196, 6433–6439. doi: 10.1016/j.jpowsour.2011.03.059
- Padhi, A. K., Nanjundaswamy, K. S., and Goodenough, J. B. (1997a). Phospho-olivines as positive electrode materials for rechargeable lithium batteries. *J. Electrochem. Soc.* 144, 1188–1194. doi: 10.1149/1.1837571
- Padhi, A. K., Nanjundaswamy, K. S., Masquelier, C., and Goodenough, J. B. (1997b). Mapping of transition metal redox energies in phosphates with NASICON structure by lithium intercalation. *J. Electrochem. Soc.* 144, 2581–2586. doi: 10.1149/1.1837868
- Park, K.-S., Son, J. T., Chung, H. T., Kim, S. J., Lee, C. H., and Kim, H. G. (2003). Synthesis of LiFePO₄ by co-precipitation and microwave heating. *Electrochem. Commun.* 5, 839–842. doi: 10.1016/j.elecom.2003.08.005
- Proisini, P. P., Carewska, M., Scaccia, S., Wisniewski, P., and Pasquali, M. (2003). Long-term cyclability of nanostructured LiFePO₄. *Electrochim. Acta* 48, 4205–4211. doi: 10.1016/S0013-4686(03)00606-6
- Shi, Y., Chou, S. L., Wang, J. Z., Wexler, D., Li, H. J., Liu, H. K., et al. (2012). Graphene wrapped LiFePO₄/C composites as cathode materials for lithium-ion batteries. *J. Mater. Chem.* 22, 16465–16470. doi: 10.1039/c2jm32649c
- Song, L., Tang, F., Xiao, Z., Cao, Z., and Zhu, H. (2018). Energy storage and thermostability of Li₃VO₄-coated LiNi_{0.8}Co_{0.1}Mn_{0.1}O₂ as cathode materials for lithium ion batteries. *Front. Chem.* 6:546. doi: 10.3389/fchem.2018.00546
- Stankovich, S., Dikin, D. A., Piner, R. D., Kohlhaas, K. A., Kleinhammes, A., Jia, Y. Y., et al. (2007). Synthesis of graphene-based nanosheets via chemical reduction of exfoliated graphite oxide. *Carbon* 45, 1558–1565. doi: 10.1016/j.carbon.2007.02.034
- Tang, Y. F., Huang, F. Q., Bi, H., Liu, Z. Q., and Wan, D. Y. (2012). Highly conductive three-dimensional graphene for enhancing the rate performance of LiFePO₄ cathode. *J. Power Sources* 203, 130–134. doi: 10.1016/j.jpowsour.2011.12.011
- Tao, Y., Cao, Y. B., Hu, G. R., Chen, P. W., Peng, Z. D., Du, K., et al. (2019). Effects of vanadium oxide coating on the performance of LiFePO₄/C cathode for lithium-ion batteries. *J. Solid State Electrochem.* 23, 2243–2250. doi: 10.1007/s10008-019-04319-0
- Tuinstra, F., and Koenig, J. L. (1970). Raman spectrum of graphite. *J. Chem. Phys.* 53, 1126–1130. doi: 10.1063/1.1674108
- Wang, G. X., Shen, X. P., Yao, J., and Park, J. (2009). Graphene nanosheets for enhanced lithium storage in lithium ion batteries. *Carbon* 47, 2049–2053. doi: 10.1016/j.carbon.2009.03.053
- Wang, L., Huang, Y. D., Jiang, R. R., and Jia, D. Z. (2007). Preparation and characterization of nano-sized LiFePO₄ by low heating solid-state coordination method and microwave heating. *Electrochim. Acta* 52, 6778–6783. doi: 10.1016/j.electacta.2007.04.104
- Wang, L., Wang, H. B., Liu, Z. H., Xiao, C., Dong, S. M., Han, P. X., et al. (2010). A facile method of preparing mixed conducting LiFePO₄/graphene composites for lithium-ion batteries. *Solid State Ion.* 181, 1685–1689. doi: 10.1016/j.ssi.2010.09.056
- Wang, S. P., Yang, H. X., Feng, L. J., Sun, S. M., Guo, J. X., Yang, Y. Z., et al. (2013). A simple and inexpensive synthesis route for LiFePO₄/C nanoparticles by co-precipitation. *J. Power Sources* 233, 43–46. doi: 10.1016/j.jpowsour.2013.01.124
- Wang, Y., Zhen, M., Liu, H., and Wang, C. (2018). Interlayer-expanded MoS₂/graphene composites as anode materials for high-performance lithium-ion batteries. *J. Solid State Electrochem.* 22, 3069–3076. doi: 10.1007/s10008-018-4018-8
- Wu, J., Dathar, G. K. P., Sun, C. W., Theivanayagam, M. G., Applestone, D., Dylla, A. G., et al. (2013). *In situ* Raman spectroscopy of LiFePO₄: size and morphology dependence during charge and self-discharge. *Nanotechnology* 24:424009. doi: 10.1088/0957-4484/24/42/424009
- Xiao, H., Huang, X., Ren, Y., Ding, X., and Zhou, S. (2019). Fabrication of Li₄Ti₅O₁₂@CN composite with enhanced rate properties. *Front. Chem.* 7:432. doi: 10.3389/fchem.2019.00432
- Zhang, Y., Du, P. P., Wang, L. Z., Zhang, A. Q., Song, Y. H., Li, X. F., et al. (2011). Synthesis and electrochemical properties of gyroscope-like lithium iron phosphate/multiwalled carbon nanotubes composites by microwave-assisted sol-gel method. *Synthetic Metals* 161, 548–551. doi: 10.1016/j.synthmet.2011.01.008
- Zhao, N. N., Li, Y. S., Zhao, X. X., Zhi, X. K., and Liang, G. C. (2016). Effect of particle size and purity on the low temperature electrochemical performance of LiFePO₄/C cathode material. *J. Alloys Compd.* 683, 123–113. doi: 10.1016/j.jallcom.2016.04.070

- Zheng, J. C., Li, X. H., Wang, Z. X., Guo, H. J., and Zhou, S. Y. (2008). LiFePO₄ with enhanced performance synthesized by a novel synthetic route. *J. Power Sources* 184, 574–577. doi: 10.1016/j.jpowsour.2008.01.016
- Zhou, P., Zhang, M., Wang, L., Huang, Q., Su, Z., Li, L., et al. (2019). Synthesis and electrochemical performance of ZnSe electrospinning nanofibers as an anode material for lithium ion and sodium ion batteries. *Front. Chem.* 7:569. doi: 10.3389/fchem.2019.00569
- Zhou, X. F., Wang, F., Zhu, Y. M., and Liu, Z. P. (2011). Graphene modified LiFePO₄ cathode materials for high power lithium ion batteries. *J. Mater. Chem.* 21, 3353–3358. doi: 10.1039/c0jm03287e

Conflict of Interest: The authors declare that the research was conducted in the absence of any commercial or financial relationships that could be construed as a potential conflict of interest.

Copyright © 2020 Liu, Yan, Li, Zhang and Sun. This is an open-access article distributed under the terms of the Creative Commons Attribution License (CC BY). The use, distribution or reproduction in other forums is permitted, provided the original author(s) and the copyright owner(s) are credited and that the original publication in this journal is cited, in accordance with accepted academic practice. No use, distribution or reproduction is permitted which does not comply with these terms.



Facile and Efficient Fabrication of Bandgap Tunable Carbon Quantum Dots Derived From Anthracite and Their Photoluminescence Properties

Jianbo Jia^{1,2}, Yue Sun¹, Yaojie Zhang¹, Quanrun Liu^{1*}, Jianliang Cao¹, Guangxu Huang^{1,2}, Baolin Xing^{1,2}, Chuanxiang Zhang^{1,2*}, Lina Zhang¹ and Yijun Cao²

¹ Henan Key Laboratory of Coal Green Conversion, College of Chemistry and Chemical Engineering, Henan Polytechnic University, Jiaozuo, China, ² Henan Province Industrial Technology Research Institute of Resources and Materials, Zhengzhou University, Zhengzhou, China

OPEN ACCESS

Edited by:

Kezhen Qi,
Shenyang Normal University, China

Reviewed by:

Yongsheng Yang,
Shenyang Normal University, China
Qingrui Zhang,
Yanshan University, China

*Correspondence:

Quanrun Liu
qrliu@163.com
Chuanxiang Zhang
zcx223@hpu.edu.cn

Specialty section:

This article was submitted to
Nanoscience,
a section of the journal
Frontiers in Chemistry

Received: 10 January 2020

Accepted: 10 February 2020

Published: 28 February 2020

Citation:

Jia J, Sun Y, Zhang Y, Liu Q, Cao J, Huang G, Xing B, Zhang C, Zhang L and Cao Y (2020) Facile and Efficient Fabrication of Bandgap Tunable Carbon Quantum Dots Derived From Anthracite and Their Photoluminescence Properties. *Front. Chem.* 8:123. doi: 10.3389/fchem.2020.00123

Low-cost and earth-abundant coal has been considered to have a unique structural superiority as carbon sources of carbon quantum dots (CQDs). However, it is still difficult to obtain CQDs from raw coal due to its compactibility and lower reactivity, and the majority of the current coal-based CQDs usually emit green or blue fluorescence. Herein, a facile two-step oxidation approach (K_2FeO_4 pre-oxidation and H_2O_2 oxidation) was proposed to fabricate bandgap tunable CQDs from anthracite. The K_2FeO_4 pre-oxidation can not only weaken the non-bonding forces among coal molecules which cause the expansion of coal particles, but also form a large number of active sites on the surface of coal particles. The above effects make the bandgap tunable CQDs (blue, green, or yellow fluorescence) can be quickly obtained from anthracite within 1 h in the following H_2O_2 oxidation by simply adjusting the concentration of H_2O_2 . All the as-prepared CQDs contain more than 30 at% oxygen, and the average diameters of which are <10 nm. The results also indicate that the high oxygen content only can create new energy states inside the band gap of CQDs with average diameter more than 3.2 ± 0.9 nm, which make the as-prepared CQDs emit green or yellow fluorescence.

Keywords: carbon quantum dots, coal, photoluminescent, anthracite, bandgap engineering

INTRODUCTION

Carbon quantum dots (CQDs), new zero-dimensional carbon nanomaterials whose size are similar with conventional semiconductor quantum dots but the skeleton is based on carbon, have attracted tremendous research interest after been found (Jaleel and Pramod, 2018; Kaur et al., 2018; Riyanto et al., 2019; Wang et al., 2019; Zhou et al., 2019). And CQDs have been expected to have large potential application in biomedicine (Jaleel and Pramod, 2018), photovoltaic device (Li X. et al., 2015; Kaur et al., 2018), ion detection (Wu et al., 2014; Arumugam and Kim, 2018; Li et al., 2018; Wang et al., 2018; Zhang et al., 2018; Omer et al., 2019), photocatalysis (Yu et al., 2014; Azimirad et al., 2017; Zhang B. et al., 2017; Syed et al., 2019), and other fields due to their fascination optical and electro-optical properties (Shao et al., 2016; Pramanik et al., 2018).

Coal is consist of angstrom-sized or nanometer-sized crystalline carbon linked by amorphous carbon and polymerized aromatic hydrocarbon (Thiyagarajan et al., 2016). These crystalline carbon

domains are abundant in coal and the size of them meet requirements of CQDs (Dong et al., 2014; Hoang et al., 2018). Additionally, the cheapest price and substantial deposits of coal, in contrast to crystalline carbon such as graphene, carbon tubes and fullerenes, have attracted tremendous interest and efforts in developing preparation methods of CQDs from coal. Up to now, CQDs have been successfully prepared from coal by different methods (Ye et al., 2013; Dong et al., 2014; Hu et al., 2015, 2016; Li M. et al., 2015; Sasikala et al., 2016; Li et al., 2017; Liu X. et al., 2018; Saikia et al., 2019). Ye et al. (2013) employed concentrated sulfuric acid and nitric acid to exfoliate CQDs from coal at 100° or 120°C for 24 h. Similarly, CQDs were obtained through refluxing coal in 5 M HNO₃ at 120°C for 12 h (Dong et al., 2014). However, there are some drawbacks to the above methods, such as the longer reaction time and the inherent difficulty in separation of CQDs from the mixture which contains a large amount of inorganic salts that formed during the neutralization phase via the addition of bases. Hence, in order to optimizing the preparation conditions of CQD from coal, selective depolymerization of coal in an oxidizing supercritical fluid was proposed by Sasikala et al. (2016). They isolated CQDs in supercritical water under the conditions of 400°C and 25 MPa within 2 h. Although this way could observably shorten the time to prepare CQDs, the unattainable reaction conditions hampered the large scale preparation of CQDs. Whereupon, greener oxidants (H₂O₂, O₃) were utilized to produce CQDs from coal under milder reaction conditions (Hu et al., 2016; Liu X. et al., 2018).

Despite these efforts, most current CQDs prepared from coal show green or blue fluorescent. And the difficulties in obtaining a defined and desired bandgap have largely hindered the applications of CQDs for a particular purpose (Yan et al., 2018). Hence, in order to obtain narrow bandgap CQDs (yellow to red fluorescent) from coal, there have been more efforts to tailor bandgap of CQDs. The bandgap of CQDs opening is due to the quantum confinement effect (Pan et al., 2010). Consequently, tuning the lateral size of CQD is one of the common strategies for narrowing bandgap of CQD. Different nanometer-sized CQDs were prepared from various coal or coke which possess different-sized graphene domains by strong acidic oxidation (Ye et al., 2013; Hu et al., 2015). In addition, different nanometer-sized CQDs can also be prepared solely from anthracite in concentrated H₂SO₄ and HNO₃, and the size control of CQDs was achieved through cross-flow ultrafiltration, controlling the reaction temperature of the oxidation process or conjugating pristine CQDs with poly aromatic rings (Ye et al., 2015; Yan et al., 2018). Another approach for narrowing the bandgap is forming intramolecular Z-schemes structure via functionalization of pristine CQDs with electron-donating chemical groups (Yan et al., 2018). Much progress has been made, but many more problems need solving before CQDs with varying bandgaps can be feasibly produced from coal in large-scale, such as long production phases, critical synthesis conditions or expensive reagents. Therefore, a simple, fast and facile synthesis method is still highly desirable.

Here we report a two-step, facile and fast method to fabricate CQDs with varying bandgaps solely from anthracite. In the

first step, which is called pre-oxidation stage, anthracite was oxidized with potassium ferrate K₂Fe^{VI}O₄ as an oxidant in H₂SO₄ medium to obtain the oxidized coal. The sp³-hybridized carbon atoms can be selectively oxidized and abundant oxygen-containing groups were produced after K₂FeO₄/H₂SO₄ treatment (Zhang and Xu, 2015). This can substantially improve the chemical reaction activity and wet ability of anthracite. In the second step, CQDs with varying bandgaps can be fast fabricated from the oxidative coal using H₂O₂ as an oxidant by simply controlling the concentration of H₂O₂.

EXPERIMENTAL

Materials

Anthracite collected from Taixi (Inner Mongolia Province, China) without pretreatment was crushed and ground to powder (about 200 mesh). H₂O₂ (30 wt.%) and H₂SO₄ (98%) were purchased from Sinopharm Chemical Reagent Co., Ltd., China. K₂FeO₄ was purchased from Shanghai Mecoxlane International MailorderCo., Ltd., China. Polyethersulfone filter membranes(0.22 μm) were purchased from Jinteng Experimental Equipment Co., Ltd., China. All reagents were used as received unless otherwise noted. Deionized water was used for all experiments.

Pre-oxidation of Anthracite

Two gram anthracite and 100 ml of concentrated H₂SO₄ were mixed in a 250 ml flask. Then 2.5 g potassium ferrate was slowly added in small doses to avoid overheating. The reaction mixture was kept at 40°C for 1 h under magnetic stirring. Once the reaction had finished, the mixture was centrifuged to recycle the concentrated H₂SO₄. The precipitate was poured in to 100 ml water and stand for 30 min. The oxidized coal was obtained by repeated centrifugation and washing with water until the pH of the supernatant approached 7.

Synthesis of CQDs

One gram oxidized coal was mixed with 50 ml H₂O₂ solution, then the obtained mixture was stirred and reacted at 100°C for 1 h. Subsequently, the unreacted coal was removed via centrifugation at 8,000 rpm for 5 min. The supernatant was then filtered through a 0.22 μm filter membrane to remove the larger fragments and the filtrate was dialyzed in 1,000 Da dialysis bag. After purification, the filtrate was freeze-dried to obtain solid CQDs. In order to adjust the bandgap of CQDs, only the concentration of H₂O₂ was changed from 30 to 10%, and the other experimental conditions remain unchanged.

Characterization

Transmission electron microscopy (TEM) images were conducted with a Tecnai G2 F20 instrument (FEI, USA) operated at 200 kV. The scanning electron microscope (SEM) was performed on a Quanta FEG 250 field-emission SEM system (FEI, USA). The fluorescence spectra were measured by a Cary Eclipse spectrophotometer (Varian, USA). X-ray photoelectron spectroscopy (XPS) measurement was performed on an ESCALAB250 Xi photoelectron spectrometer

(Thermo Fisher Scientific, USA). The Fourier-transform infrared spectroscopy (FT-IR) and Ultraviolet-visible (UV-Vis) absorption spectroscopy were obtained from a VERTEX 70 FTIR spectrometer (Bruker, Germany) and a Pgeneral TU-1810 spectrometer (Pgeneral, China), respectively. Raman

spectra were recorded using a microscopic confocal raman spectrometer (Renishaw, UK) with an argon ion laser ($\lambda = 514 \text{ nm}$) at ambient temperature. The X-ray diffraction (XRD) patterns of all samples were recorded on a Bruker D8 Advance (Bruker, Germany) with a $\text{Cu K}\alpha$ X-ray radiation source

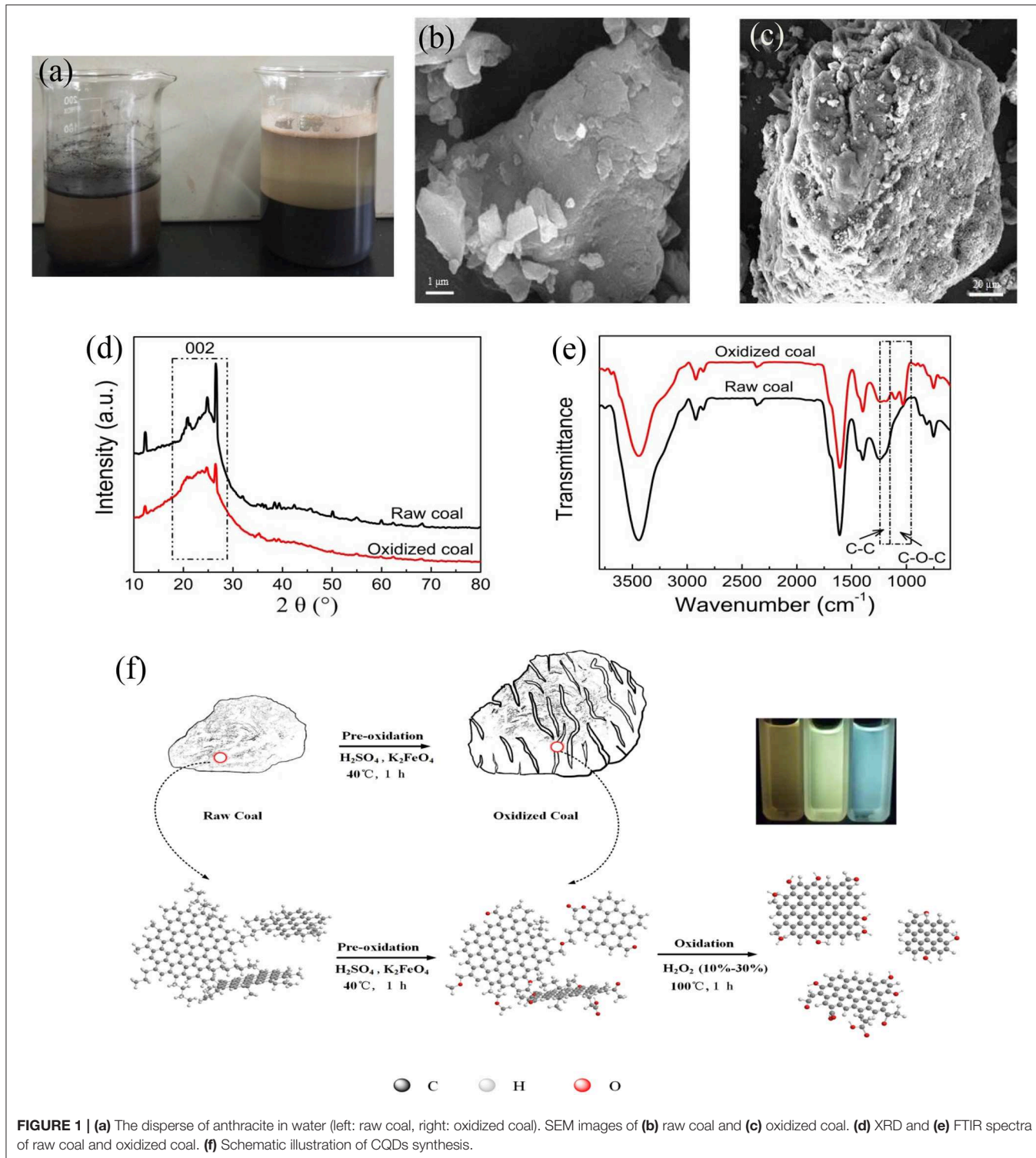


FIGURE 1 | (a) The disperse of anthracite in water (left: raw coal, right: oxidized coal). SEM images of (b) raw coal and (c) oxidized coal. (d) XRD and (e) FTIR spectra of raw coal and oxidized coal. (f) Schematic illustration of CQDs synthesis.

($\lambda = 0.15418$ nm), and the scattering angles (2θ) range from 10° to 80° .

RESULTS AND DISCUSSION

Characterization of Oxidized Coal and Preparation Principle Analysis of Bandgap Tunable CQDs

Raw anthracite was oxidized with K_2FeO_4/H_2SO_4 to improve its surface reactivity. As shown in **Figure 1a**, the wet ability of

pulverized coal is very poor, and most of which floated on the surface of water before oxidized. However, pulverized coal could be very well-moistened with water and the volume of raw coal expanded significantly after the pre-oxidation, indicating that the pre-oxidation has the powerful influence on the structure and properties of anthracite. SEM was used to observe the microscopic morphology change of anthracite before and after the pre-oxidation (**Figures 1b,c**). Compared with the compact structure of raw coal, there are lots of crevices or pores on the surface of the oxidized coal, which may offer much more

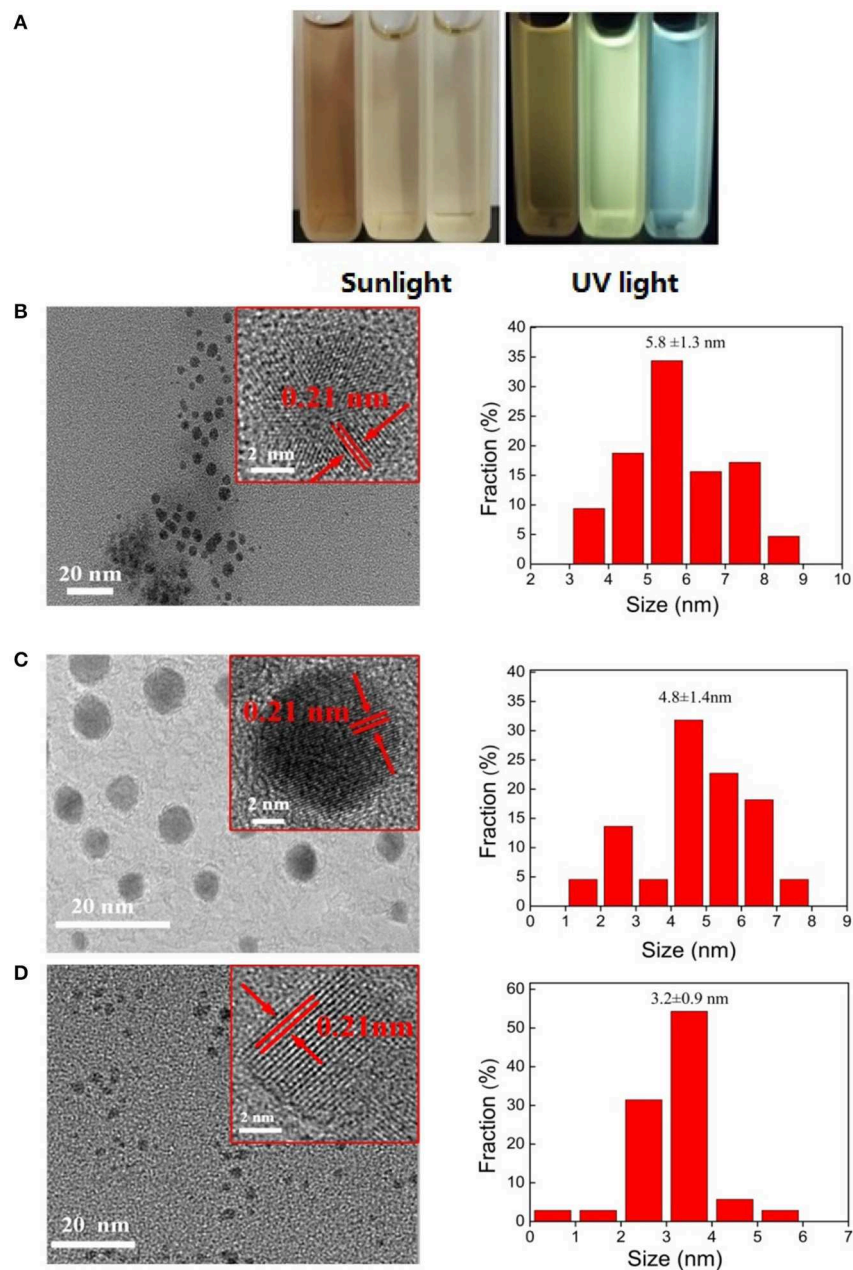


FIGURE 2 | (A) Aqueous solution of CQDs under sunlight and UV light (the left cuvette is CQDs-N10-Y solution, the middle cuvette is CQDs-N20-G solution and the right cuvette is CQDs-N20-G solution). The TEM images, HRTEM images, and size distributions of **(B)** CQDs-N10-Y, **(C)** CQDs-N20-G, and **(D)** CQDs-N30-B.

active sites to react with H_2O_2 reactant used subsequently for fabrication of CQDs. To obtain more information about the structure change of anthracite after the pre-oxidation, original and oxidized samples were analyzed by the X-ray diffraction (XRD) and Fourier transform infrared spectroscopy (FTIR). The XRD spectra (Figure 1d) show that one broad peak observed at 24.5° is attributed to the 002 plane of graphite lattice for both original and oxidized samples (Duraia et al., 2018; Liu Y. et al., 2018). The position and full width at half maximum intensity of 002 peak have little change before and after the pre-oxidation, indicating that the crystalline carbon domains of anthracite were not corrupted in the process of pre-oxidation. The FTIR spectra are shown in Figure 1e. Major structural changes during pre-oxidation for anthracite mainly occurred around $1,000$ and $1,300\text{ cm}^{-1}$ region. The intensity of $1,150\text{--}1,250\text{ cm}^{-1}$ assigned to saturated aliphatic skeletal C-C vibration was found to be weaker and there was a group of peaks in the region $1,150\text{--}950\text{ cm}^{-1}$ due to stretching vibration of C-O (C-O-C or phenolic) for oxidized coal (Okolo et al., 2015; Xing et al., 2017; Qiu et al., 2020), suggesting that a large number of oxygen-containing functional groups were formed and a part of aliphatic carbon atoms were consumed during the pre-oxidation process.

The above results can be interpreted as the selective oxidation of $\text{K}_2\text{FeO}_4/\text{H}_2\text{SO}_4$, namely the sp^3 C-C bonds were oxidized while the C=C bonds remained intact (Zhang and Xu, 2015). H_2SO_4 and K_2FeO_4 can quickly intercalate into the coal molecule interval. The aliphatic portions were oxidized while the oxidant reacts with H^+ or water to produce a lot of oxygen gas (Peng et al., 2015), these results can break the non-covalent interactions (hydrogen bonds, $\pi\text{-}\pi$ interactions, van der Waals interactions and electrostatic interactions) (Niekerk et al., 2010) and cause the significant swelling bulk of powdered coal. Overall, compared to original coal, the oxidized coal possesses higher reactivity in reaction with H_2O_2 . The entire fabrication process of CQDs requires only 1 h, and the as-prepared CQDs with varying bandgaps were obtained by solely controlling the concentration of H_2O_2 . The CQDs formation mechanism is shown in Figure 1f.

Characterization of Bandgap Tunable CQDs

The CQDs synthesized with different concentration of H_2O_2 at 100°C are denoted as CQDs-N_x-y where “N” signifies “Concentration,” “x” signifies the concentration of H_2O_2 and “y” signifies the fluorescent color of CQDs solution under UV lamp (365 nm) irradiation, such as yellow, green, and blue are represented by Y, G and B, respectively. The change of CQDs in bandgap is visualized in Figure 2A, where the as-prepared CQDs solutions emit from blue to yellow under UV lamp (365 nm) irradiation. An of the interesting finding was that the bandgap of CQDs is red-shifted from blue to yellow with decreasing of H_2O_2 concentration from 30 to 10%. The production yields of CQDs-N10-Y, CQDs-N20-G, and CQDs-N30-B are 18.9, 12.6, and 4.3%, respectively. The production yield of CQDs is the ratio between the obtained CQDs solid powder and the amount of coal.

The microstructure of the as-prepared CQDs was investigated by transmission electron microscopy (TEM). The TEM images and the size distributions of the as-prepared CQDs are shown

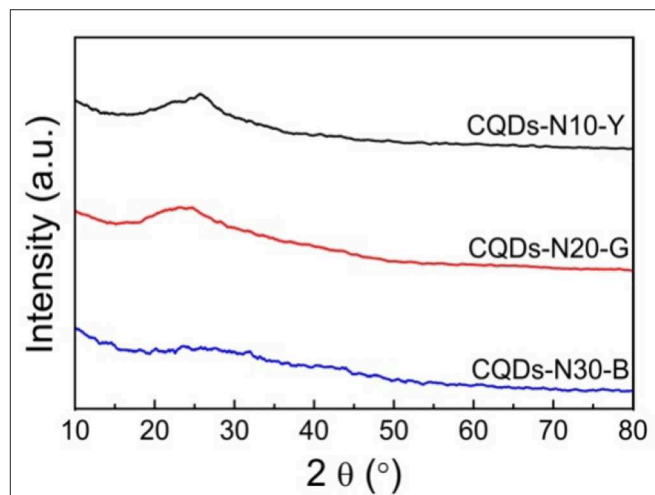


FIGURE 3 | XRD patterns of CQDs-N10-Y, CQDs-N20-G, and CQDs-N30-B.

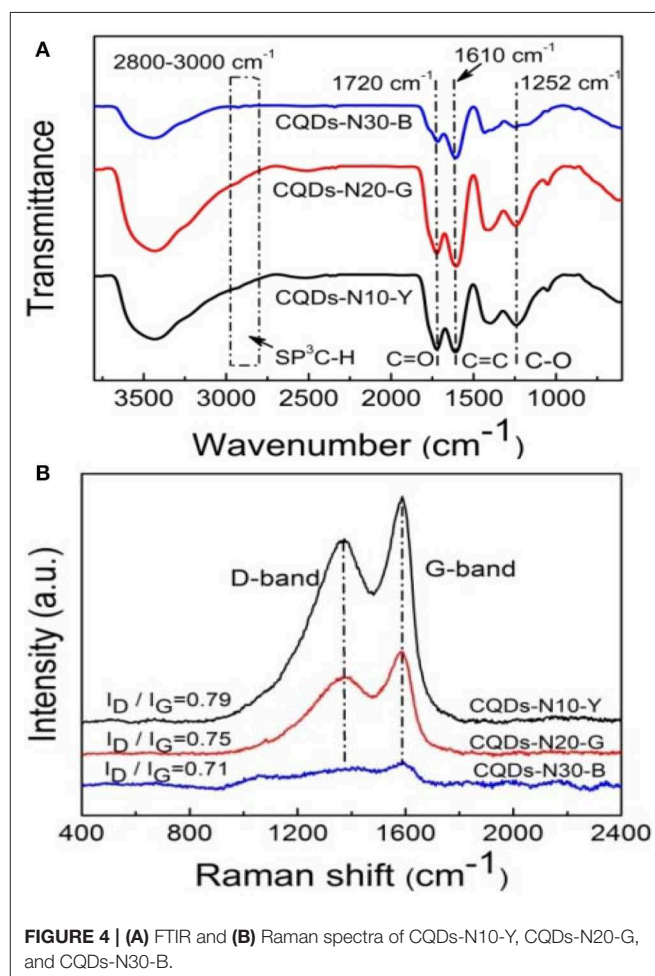


FIGURE 4 | (A) FTIR and (B) Raman spectra of CQDs-N10-Y, CQDs-N20-G, and CQDs-N30-B.

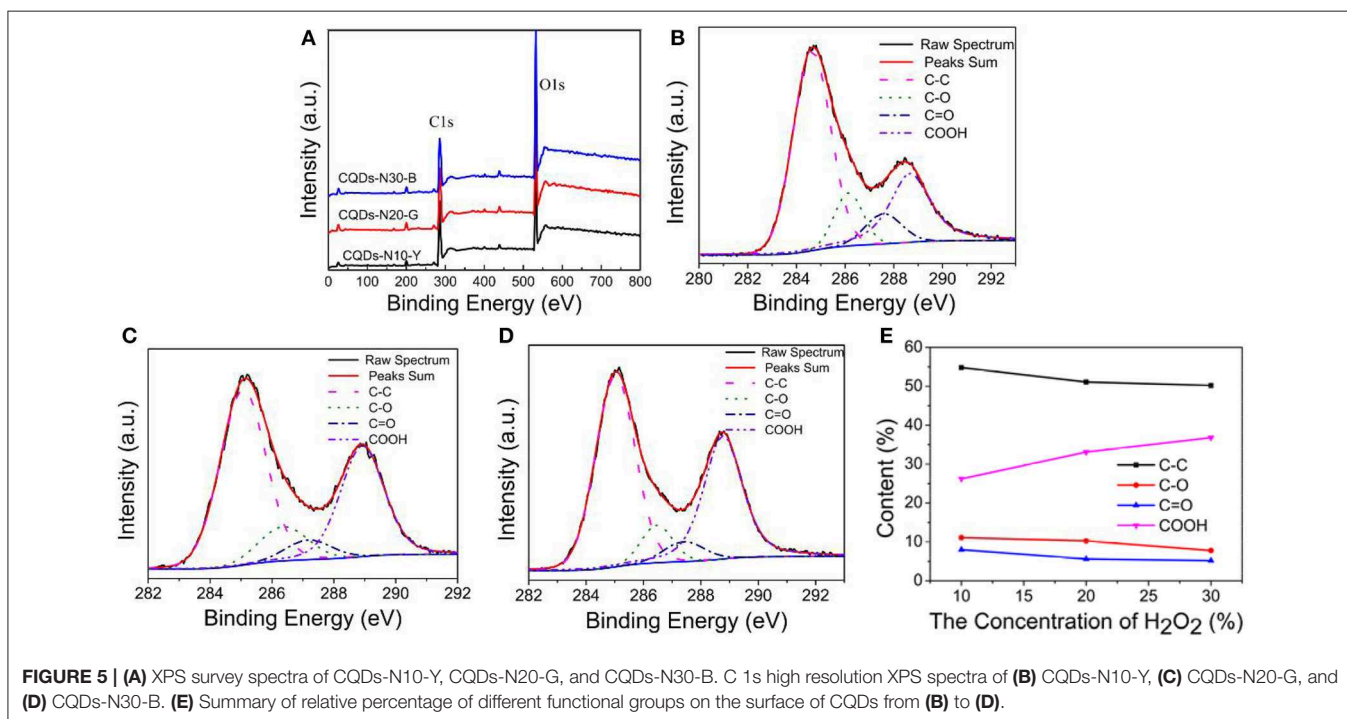
in **Figures 2B–D** and the high-resolution TEM (HRTEM) of the as-prepared CQDs is inset in the corresponding TEM. It was found that the diameters of the as-prepared CQDs were relatively uniform and all the as-prepared CQDs have a quasi-spherical shape. The HRTEM images reveal that the as-prepared CQDs have highly crystalline structure with a lattice spacing of ca. 0.21 nm, which is corresponding to the (100) diffraction facets of graphite carbon (Tian et al., 2017). The size distributions of CQDs-N10-Y, CQDs-N20-G, and CQDs-N30-B are 5.8 ± 1.3 , 4.8 ± 1.4 , and 3.2 ± 0.9 nm, respectively.

The XRD patterns of the as-prepared CQDs (**Figure 3**) show that one broad peak (about 25°) ascribed to the 002 plane of graphite lattice is observed, and this peak of CQDs-N30-B is almost unseeable due to its smaller size. The CQDs could also be prepared by directly oxidation of anthracite with H_2O_2 , but the diameters of which are mainly distributed from 1 to 3 nm significantly smaller than that of the CQDs prepared in this work and they emit blue under UV light (Hu et al., 2016). This indicates the pre-oxidation of anthracite plays a key role in the bandgap adjustment of CQDs which can shorten the oxidative time to avoid the excessive oxidation of crystalline carbon domains of anthracite. In general, as the size of CQDs increases, the bandgap narrows. Therefore, at least initially, this work was designed to tune the bandgap by changing the size of CQDs, however the average diameters of the as-prepared CQDs in this work are all <10 nm. In the literature (Pan et al., 2010), the CQDs with 9.6 nm average diameter were fabricated from graphene oxide by hydrothermal treatment at 200°C , and they emit bright blue under UV light, indicating that the major factor adjusting the bandgap of the as-prepared CQDs isn't the size.

To further understand the effect of reaction conditions on the functional groups, FTIR, Raman and X-ray photoelectron spectroscopy (XPS) and were applied to investigate the structure of CQDs. The FTIR spectra of CQDs are shown in **Figure 4A**. The absorption peaks at $2,800\text{--}3,000\text{ cm}^{-1}$ are assigned to stretching vibrations of aliphatic C-H. The strong absorption peak at $1,610\text{ cm}^{-1}$ are in associated with stretching vibration of aromatic C=C. Compared to the oxidized coal, absorption peaks ($2,800\text{--}3,000\text{ cm}^{-1}$) almost disappear in the FTIR spectra of CQDs, indicating the aliphatic carbon chains which link the crystalline carbon domains of coal have been selectively oxidized into CO_2 and H_2O by H_2O_2 (Hu et al., 2016). Besides, the peaks at $1,720\text{ cm}^{-1}$ and $1,252\text{ cm}^{-1}$ are attributed to the C=O stretching, the O-H deformation and C-O stretching of carboxylic acid, respectively, which make CQDs hydrophilic and stable dispersion in water. The Raman spectra of the as-prepared CQDs (**Figure 4B**) reveal a D band at $1,367\text{ cm}^{-1}$ and a G band at $1,587\text{ cm}^{-1}$, which correspond to disordered structures and graphitic structures, respectively, of carbon materials (Ding et al., 2015; Huang et al., 2020). The intensity ratio for the D to G bands can be used to reflect the level of disorder in carbon materials

TABLE 1 | Element content of the as-prepared CQDs calculated based on XPS analysis (atom %).

Samples	C	O
CQDs-N10-Y	63.8	34.4
CQDs-N20-G	57.1	40.9
CQDs-N30-B	55.9	42.6



(Ma et al., 2019). The values of I_D/I_G for CQDs-N10-Y, CQDs-N20-G, and CQDs-N30-B are 0.79, 0.75, and 0.71, respectively, suggesting the as-prepared CDQs possess much more ordered graphite structures with decreasing of size of CQDs.

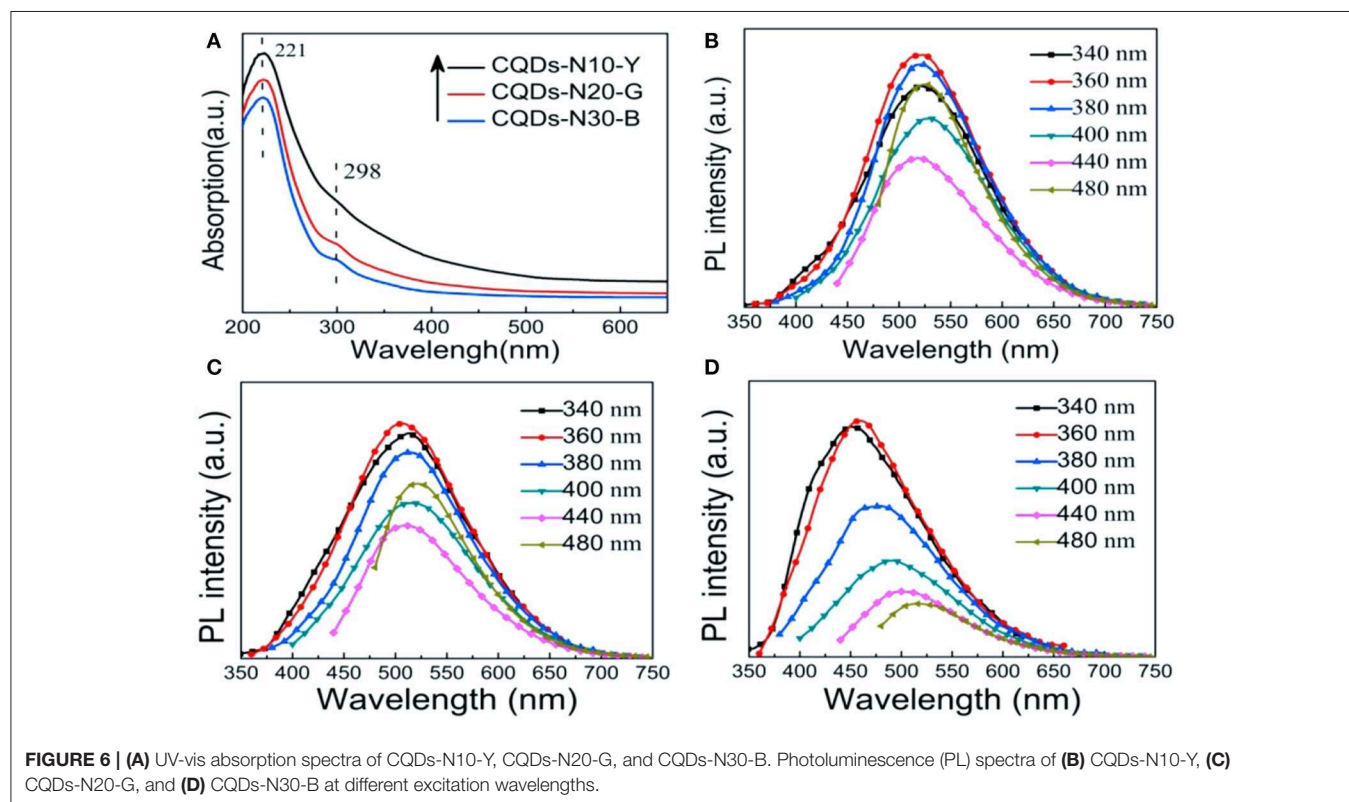
The chemical structures at the surface of the as-prepared CQDs were further investigated by X-ray photoelectron spectroscopy (XPS) analyses. The XPS survey spectra of CQDs (Figure 5A) show that the as-prepared CQDs primarily consist of carbon and oxygen (Zhang Q. et al., 2017, 2019; Zeng et al., 2020). It can be seen that the oxygen content gradually increases from 34.4 to 42.6% with the increasing of the H_2O_2 concentration in Table 1, indicating the higher the concentration of H_2O_2 , the stronger the oxidation ability, due to the increase of the number of-OH radical. As shown in Figures 5B–D, the high resolution C 1s spectra of CQDs can be conceived into four peaks at 285 eV (C-C/C = C/C-H), 286.3 eV (C-O), 287.4 eV (C = O), and 288.8 eV (COOH) (Roy et al., 2014; Shi et al., 2015; Moonrinta et al., 2018; Pacquiao et al., 2018), suggesting the presence of large quantities of oxygen-containing functional groups, especially carboxyl groups. The relative abundances of these components are summarized in Figure 5E.

Optical Properties of Bandgap Tunable CQDs

The optical properties of as-prepared CQDs were explored by UV-vis absorption and photoluminescence (PL) spectroscopy. The UV-vis absorption spectra of as-prepared CQDs are shown in Figure 6A. It is clear that there are a strong peak and a weak

peak at 221 and 298 nm corresponding to π - π^* transition of C=C and n - π^* transition of C=O, respectively (Dehghani et al., 2018; Yang et al., 2018). Apparently, the shoulder peak at 298 nm is almost invisible in the spectrum of CQDs-N10-Y, indicating that the surface content of COOH is relatively lower in CQDs-N10-Y (Zhang et al., 2016). This phenomenon is consistent with the results of XPS analysis. The adsorption of CQDs-N30-G occurs mainly in the UV region (< 400 nm). However, the absorption regions of YCQDs-N10-Y and CQDs-N20-G extend to the visible region (400–650 nm), and the adsorption is more prominent for CQDs-N10-Y, suggesting more narrowing of the bandgap (Choi et al., 2018).

The photoluminescence (PL) spectra of the as-prepared CQDs excited at the different wavelengths are shown in Figures 6B–D. The maximum emission peak shifts from ~ 525 to ~ 450 nm as the concentration of H_2O_2 increases from 10 to 30%. Moreover, it is worth noting that like most CQDs (Zhu et al., 2013; Liu Q. et al., 2018; Chen et al., 2020), the PL behavior of CQDs-N30-B exhibits the emission wavelength is dependence of the excitation wavelength and the intensity of PL decreases with increase of excitation wavelength. But the emission peaks lie in almost the same wavelength (~ 510 or ~ 525 nm) with increasing excitation wavelength for both CQDs-N10-Y and CQDs-N20-G. Two distinct emission modes were proposed to interpret the PL mechanism of CQDs, i.e., intrinsic emission mode and extrinsic emission mode (Liu et al., 2013). The emission peak near 450 nm when excited near 325 nm is considered as the intrinsic emission of sp^2 carbon hexagons. The emission peak



near 500 nm when excited with 325 nm and above is attribute to the extrinsic emission due to the defects of CQDs including oxygen-containing functional groups or sp^3 carbon. The work of Yoon et al. (2016) indicated that oxygen-containing functional groups may create new energy states (extrinsic state) inside the band gap of CQDs resulting in the red shift of PL emission. The results of FTIR and XPS analysis show quantities of oxygen-containing functional groups exist on the surfaces of CQDs-N10-Y, CQDs-N20-G and CQDs-N10-B, but the amount of sp^3 carbon is very low. Therefore, the emission peaks near 520 nm of CQDs-N10-Y and CQDs-N20-G can be attributed to extrinsic emission mode due to the new energy states created by oxygen-containing functional groups. But it is interesting to note that although the oxygen content of CQDs-N30-B is the highest in all the as-prepared CQDs, the emission peak of which is still near 450 nm excited near 325 nm. We propose that this is because in the case of smaller size of CQDs-N30-B (3.2 ± 0.9 nm) the emission is likely dominated by the intrinsic transitions rather than the extrinsic, oxygen defects related transitions. So, our results suggest that for small CQDs prepared by the method described here both intrinsic and extrinsic transitions contribute to the observed CQDs PL, where the former dominate the PL in CQDs-N30-B and the latter dominate the PL in CQDs-N10-Y and CQDs-N20-G.

CONCLUSIONS

In conclusion, we have developed a facile, fast, and green method to prepare bandgap tunable CQDs solely from anthracite. The emission color of CQDs can be adjusted from yellow to blue

REFERENCES

- Arumugam, N., and Kim, J. (2018). Synthesis of carbon quantum dots from broccoli and their ability to detect silver ions. *Mater. Lett.* 219, 37–40. doi: 10.1016/j.matlet.2018.02.043
- Azimirad, R., Safa, S., Ebrahimi, M., Yousefzadeh, S., and Moshfegh, A. Z. (2017). Photoelectrochemical activity of graphene quantum dots/hierarchical porous TiO_2 photoanode. *J. Alloy. Compd.* 721, 36–44. doi: 10.1016/j.jallcom.2017.05.301
- Chen, Y., Sun, X., Pan, W., Yu, G., and Wang, J. (2020). Fe^{3+} -sensitive carbon dots for detection of Fe^{3+} in aqueous solution and intracellular imaging of Fe^{3+} inside fungal cells. *Front. Chem.* 7:911. doi: 10.3389/fchem.2019.00911
- Choi, J., Kim, N., Oh, J., and Kim, F. S. (2018). Bandgap engineering of nanosized carbon dots through electron-accepting functionalization. *J. Ind. Eng. Chem.* 65, 104–111. doi: 10.1016/j.jiec.2018.04.018
- Dehghani, A., Ardekani, S. M., Hassan, M., and Gomes, V. G. (2018). Collagen derived carbon quantum dots for cell imaging in 3D scaffolds via two-photon spectroscopy. *Carbon* 131, 238–245. doi: 10.1016/j.carbon.2018.02.006
- Ding, H., Yu, S., Wei, J., and Xiong, H. (2015). Full-color light-emitting carbon dots with a surface-state-controlled luminescence mechanism. *ACS Nano* 10, 484–491. doi: 10.1021/acsnano.5b05406
- Dong, Y., Lin, J., Chen, Y., Fu, F., Chi, Y., and Chen, G. (2014). Graphene quantum dots, graphene oxide, carbon quantum dots and graphite nanocrystals in coals. *Nanoscale* 6, 7410–7415. doi: 10.1039/C4NR01482K
- Duraia, E. M., Niu, S., Beall, G. W., and Rhodes, C. P. (2018). Humic acid-derived graphene- SnO_2 nanocomposites for high capacity lithium-ion battery anodes. *J. Mater. Sci.* 29, 8456–8464. doi: 10.1007/s10854-018-8858-x
- Hoang, V. C., Hassan, M., and Gomes, V. G. (2018). Coal derived carbon nanomaterials—recent advances in synthesis and applications. *Appl. Mater. Today* 12, 342–358. doi: 10.1016/j.apmt.2018.06.007
- Hu, C., Yu, C., Li, M., Wang, X., Yang, J., Zhao, Z., et al. (2015). Chemically tailoring coal to fluorescent carbon dots with tuned size and their capacity for Cu(II) detection. *Small* 10, 4926–4933. doi: 10.1002/smll.201401328
- Hu, S., Wei, Z., Chang, Q., Trinchì, A., and Yang, J. (2016). A facile and green method towards coal-based fluorescent carbon dots with photocatalytic activity. *Appl. Surf. Sci.* 378, 402–407. doi: 10.1016/j.apsusc.2016.04.038
- Huang, G., Geng, Q., Xing, B., Liu, Y., Li, Y., Liu, Q., et al. (2020). Manganous nitrate -assisted potassium hydroxide activation of humic acid to prepare oxygen-rich hierarchical porous carbon as high-performance supercapacitor electrodes. *J. Power Sources* 449:227506. doi: 10.1016/j.jpowsour.2019.227506
- Jaleel, J. A., and Pramod, K. (2018). Artful and multifaceted applications of carbon dot in biomedicine. *J. Control. Release* 269, 302–321. doi: 10.1016/j.jconrel.2017.11.027
- Kaur, M., Kaur, M., and Sharma, V. K. (2018). Nitrogen-doped graphene and graphene quantum dots: a review on synthesis and applications in energy, sensors and environment. *Adv. Colloid Interfac.* 259, 44–64. doi: 10.1016/j.cis.2018.07.001
- Li, M., Hu, C., Yu, C., Wang, S., Zhang, P., and Qiu, J. (2015). Organic amine-grafted carbon quantum dots with tailored surface and enhanced photoluminescence properties. *Carbon* 91, 291–297. doi: 10.1016/j.carbon.2015.04.083
- Li, M. Y., Yu, C., Hu, C., Yang, W. B., Zhao, C. T., Wang, S., et al. (2017). Solvothermal conversion of coal into nitrogen-doped carbon dots with singlet oxygen generation and high quantum yield. *Chem. Eng. J.* 320, 570–575. doi: 10.1016/j.cej.2017.03.090

under UV light. The bandgap change of as-prepared CQDs can be achieved by simply controlling the concentration of H_2O_2 . The morphology, size and PL properties of the as-prepared CQDs indicate that the blue luminescence may originate from the intrinsic emission, but the yellow and green luminescence may originate from the extrinsic emission due to the new energy states created by the oxygen-containing functional groups inside the band gap of CQDs. This novel strategy for fabricating optically tunable CQDs from coal is highly promising for the high-end application of coal.

DATA AVAILABILITY STATEMENT

The datasets generated for this study are available on request to the corresponding author.

AUTHOR CONTRIBUTIONS

QL, CZ, and JJ conceived and designed the experiments. YS, JC, YZ, and GH fabricated and characterized the sample. BX, LZ, GH, and YC analyzed the data. All authors discussed the experiment results and contributed to the writing of the paper.

FUNDING

This work was funded by the National Natural Science Foundation of China (21646006, U1704255, U1704146, 21805071, 41472127) and the Natural Science Foundation of Henan province (162300410115).

- Li, X., Rui, M., Song, J., Shen, Z., and Zeng, H. (2015). Carbon and graphene quantum dots for optoelectronic and energy devices: a review. *Adv. Funct. Mater.* 25, 4929–4947. doi: 10.1002/adfm.201501250
- Li, Y., Liu, Y., Shang, X., Chao, D., Zhou, L., and Zhang, H. (2018). Highly sensitive and selective detection of Fe³⁺ by utilizing carbon quantum dots as fluorescent probes. *Chem. Phys. Lett.* 705, 1–6. doi: 10.1016/j.cplett.2018.05.048
- Liu, F., Jang, M., Ha, H. D., Kim, J., Cho, Y., and Seo, T. S. (2013). Facile synthetic method for pristine graphene quantum dots and graphene oxide quantum dots: origin of blue and green luminescence. *Adv. Mater.* 25, 3657–3662. doi: 10.1002/adma.201300233
- Liu, Q., Zhang, J., He, H., Huang, G., Xing, B., Jia, J., et al. (2018). Green preparation of high yield fluorescent graphene quantum dots from coal-tar-pitch by mild oxidation. *Nanomaterials* 8, 844–853. doi: 10.3390/nano8100844
- Liu, X., Hao, J., Liu, J., and Tao, H. (2018). Green synthesis of carbon quantum dots from lignite coal and the application in Fe³⁺ detection. *IOP Conf. Ser.* 113, 12063–12069. doi: 10.1088/1755-1315/113/1/012063
- Liu, Y., Zhu, Y., Liu, S., Chen, S., Li, W., and Wang, Y. (2018). Molecular structure controls on micropore evolution in coal vitrinite during coalification. *Int. J. Coal Geol.* 199, 19–30. doi: 10.1016/j.coal.2018.09.012
- Ma, Z., Yang, J., Zhang, J., Chen, G., Miao, C., Shi, L., et al. (2019). Layer-opened graphene paper with carbon nanotubes as support in a flexible electrode material for supercapacitors. *J. Alloy. Compd.* 775, 982–989. doi: 10.1016/j.jallcom.2018.10.135
- Moonrinta, S., Kwon, B., In, I., Kladsomboon, S., Sajomsang, W., and Paoprasert, P. (2018). Highly biocompatible yogurt-derived carbon dots as multipurpose sensors for detection of formic acid vapor and metal ions. *Opt. Mater.* 81, 93–101. doi: 10.1016/j.optmat.2018.05.021
- Niekerk, D. V., Halleck, P. M., and Mathews, J. P. (2010). Solvent swelling behavior of Permian-aged South African vitrinite-rich and inertinite-rich coals. *Fuel* 89, 19–25. doi: 10.1016/j.fuel.2009.06.028
- Okolo, G. N., Neomagus, H. W. J. P., Everson, R. C., Roberts, M. J., Bunt, J. R., Sakurovs, R., et al. (2015). Chemical-structural properties of South African bituminous coals: insights from wide angle XRD-carbon fraction analysis, ATR-FTIR, solid state ¹³C NMR, and HRTEM techniques. *Fuel* 158, 779–792. doi: 10.1016/j.fuel.2015.06.027
- Omer, K. M., Tofiq, D. I., and Ghafoor, D. D. (2019). Highly photoluminescent label free probe for Chromium (II) ions using carbon quantum dots co-doped with nitrogen and phosphorous. *J. Lumin.* 206, 540–546. doi: 10.1016/j.jlumin.2018.10.100
- Pacquiao, M. R., de Luna, M. D. G., Thongsai, N., Kladsomboon, S., and Paoprasert, P. (2018). Highly fluorescent carbon dots from enokitake mushroom as multi-faceted optical nanomaterials for Cr⁶⁺ and VOC detection and imaging applications. *Appl. Surf. Sci.* 453, 192–203. doi: 10.1016/j.apsusc.2018.04.199
- Pan, D., Zhang, J., Li, Z., and Wu, M. (2010). Hydrothermal route for cutting graphene sheets into blue-luminescent graphene quantum dots. *Adv. Mater.* 22, 734–738. doi: 10.1002/adma.200902825
- Peng, L., Xu, Z., Liu, Z., Wei, Y., Sun, H., Li, Z., et al. (2015). An iron-based green approach to 1-h production of single-layer graphene oxide. *Nat. Commun.* 6, 5716–5725. doi: 10.1038/ncomms6716
- Pramanik, A., Biswas, S., and Kumbhakar, P. (2018). Solvatochromism in highly luminescent environmental friendly carbon quantum dots for sensing applications: conversion of bio-waste into bio-asset. *Spectrochim. Acta Part A* 191, 498–512. doi: 10.1016/j.saa.2017.10.054
- Qiu, H., Ni, W., Zhang, H., Chen, K., and Yu, J. (2020). Fabrication and evaluation of a regenerable HFO-doped agricultural waste for enhanced adsorption affinity towards phosphate. *Sci. Total Environ.* 703:135493. doi: 10.1016/j.scitotenv.2019.135493
- Riyanto, S. I., Bindumadhavan, K., Chang, P., and Doong, R. (2019). Boron doped graphene quantum structure and MoS₂ nanohybrid as anode materials for highly reversible lithium storage. *Front. Chem.* 7:116. doi: 10.3389/fchem.2019.00116
- Roy, S., Das, T., Ming, Y., Chen, X., Yue, C. Y., and Hu, X. (2014). Specific functionalization and polymer grafting on multiwalled carbon nanotubes to fabricate advanced nylon 12 composites. *J. Mater. Chem. A* 2, 3961–3970. doi: 10.1039/c3ta14528j
- Saikia, B. K., Saikia, M., Hower, J. C., Das, T., and Dutta, T. (2019). Feasibility study of preparation of carbon quantum dots from *Pennsylvania anthracite* and *Kentucky bituminous* coals. *Fuel* 243, 433–440. doi: 10.1016/j.fuel.2019.01.151
- Sasikala, S. P., Henry, L., Yesilbag Tonga, G., Huang, K., Das, R., Giroire, B., et al. (2016). High yield synthesis of aspect ratio controlled graphenic materials from anthracite coal in supercritical fluids. *ACS Nano* 10, 5293–5303. doi: 10.1021/acsnano.6b01298
- Shao, X., Wu, W., Wang, R., Zhang, J., Li, Z., Wang, Y., et al. (2016). Engineering surface structure of petroleum-coke-derived carbon dots to enhance electron transfer for photooxidation. *J. Catal.* 344, 236–241. doi: 10.1016/j.jcat.2016.09.006
- Shi, W., Fan, H., Ai, S., and Zhu, L. (2015). Preparation of fluorescent graphene quantum dots from humic acid for bioimaging application. *N. J. Chem.* 39, 7054–7059. doi: 10.1039/C5NJ00760G
- Syed, N., Huang, J., Feng, Y., Wang, X., and Cao, L. (2019). Carbon-based nanomaterials via heterojunction serving as photocatalyst. *Front. Chem.* 7:713. doi: 10.3389/fchem.2019.00713
- Thiyagarajan, S. K., Raghupathy, S., Palanivel, D., Raji, K., and Raghupathy, P. (2016). Fluorescent carbon nano dots from lignite: unveiling the impeccable evidence for quantum confinement. *Phys. Chem. Chem. Phys.* 18, 12062–12073. doi: 10.1039/C6CP00867D
- Tian, Z., Zhang, X., Li, D., Zhou, D., Jing, P., Shen, D., et al. (2017). Full-color inorganic carbon dot phosphors for white-light-emitting diodes. *Adv. Opt. Mater.* 5, 1700416–1700424. doi: 10.1002/adom.201700416
- Wang, F., Lu, Y., Chen, Y., Sun, J., and Liu, Y. (2018). Colorimetric nanosensor based on the aggregation of AuNP triggered by carbon quantum dots for detection of Ag⁺ ions. *ACS Sustain. Chem. Eng.* 6, 3706–3713. doi: 10.1021/acssuschemeng.7b04067
- Wang, X., Feng, Y., Dong, P., and Huang, J. (2019). A mini review on carbon quantum dots: preparation, properties, and electrocatalytic application. *Front. Chem.* 7:671. doi: 10.3389/fchem.2019.00671
- Wu, M., Wang, Y., Wu, W., Hu, C., Wang, X., Zheng, J., et al. (2014). Preparation of functionalized water-soluble photoluminescent carbon quantum dots from petroleum coke. *Carbon* 78, 480–489. doi: 10.1016/j.carbon.2014.07.029
- Xing, B., Yuan, R., Zhang, C., Huang, G., Guo, H., Chen, Z., et al. (2017). Facile synthesis of graphene nanosheets from humic acid for supercapacitors. *Fuel Process. Technol.* 165, 112–122. doi: 10.1016/j.fuproc.2017.05.021
- Yan, Y., Chen, J., Li, N., Tian, J., Li, K., Jiang, J., et al. (2018). Systematic bandgap engineering of graphene quantum dots and applications for photocatalytic water splitting and CO₂ reduction. *ACS Nano* 12, 3523–3532. doi: 10.1021/acsnano.8b00498
- Yang, Q., Yang, W., Yang, P., Duan, J., Li, X., Mo, J., et al. (2018). Nitrogen-doped carbon quantum dots from biomass via simple one-pot method and exploration of their application. *Appl. Surf. Sci.* 434, 1079–1085. doi: 10.1016/j.apsusc.2017.11.040
- Ye, R., Peng, Z., Metzger, A., Lin, J., Mann, J. A., Huang, K., et al. (2015). Bandgap engineering of coal-derived graphene quantum dots. *ACS Appl. Mater. Inter.* 7, 7041–7048. doi: 10.1021/acami.5b01419
- Ye, R., Xiang, C., Lin, J., Peng, Z., Huang, K., Yan, Z., et al. (2013). Coal as an abundant source of graphene quantum dots. *Nat. Commun.* 4, 2943–2948. doi: 10.1038/ncomms3943
- Yoon, H., Chang, Y. H., Song, S. H., Lee, E., Jin, S. H., Park, C., et al. (2016). Intrinsic photoluminescence emission from subdomained graphene quantum dots. *Adv. Mater.* 28, 5255–5261. doi: 10.1002/adma.201600616
- Yu, X., Liu, J., Yu, Y., Zuo, S., and Li, B. (2014). Preparation and visible light photocatalytic activity of carbon quantum dots/TiO₂ nanosheet composites. *Carbon* 68, 718–724. doi: 10.1016/j.carbon.2013.11.053
- Zeng, H., Xing, B., Zhang, C., Chen, L., Zhao, H., Han, X., et al. (2020). *In situ* synthesis of MnO₂/porous graphitic carbon composites as high-capacity anode materials for lithium-ion batteries. *Energ. Fuel.* 34, 2480–2491. doi: 10.1021/acs.energyfuels.9b04325
- Zhang, B., Maimaiti, H., Zhang, D., Xu, B., and Wei, M. (2017). Preparation of coal-based C-dots/TiO₂ and its visible-light photocatalytic characteristics for degradation of pulping black liquor. *J. Photochem. Photobiol.* 345, 54–62. doi: 10.1016/j.jphotochem.2017.05.031

- Zhang, F., Liu, F., Wang, C., Xin, X., Liu, J., Guo, S., et al. (2016). Effect of lateral size of graphene quantum dots on their properties and application. *ACS Appl. Mater. Inter.* 8, 2104–2110. doi: 10.1021/acsami.5b10602
- Zhang, L., Wang, Z., Zhang, J., Jia, J., Zhao, D., and Fan, Y. (2018). Phenanthroline-derivative functionalized carbon dots for highly selective and sensitive detection of Cu^{2+} and S^{2-} and imaging inside live cells. *Nanomaterials* 8, 1071–1081. doi: 10.3390/nano8121071
- Zhang, Q., Bolisetty, S., Cao, Y., Handschin, S., Adamcik, J., Peng, Q., et al. (2019). Selective and efficient removal of fluoride from water by in-situ engineered amyloid fibrils-ZrO₂ hybrid membranes. *Angew. Chem. Int. Edn.* 58, 6012–6016. doi: 10.1002/anie.201901596
- Zhang, Q., Yang, Q., Phanlavong, P., Li, Y., Wang, Z., Jiao, T., et al. (2017). Highly efficient lead(II) sequestration using size-controllable polydopamine microspheres with superior application capability and rapid capture. *ACS Sustain. Chem. Eng.* 5, 4161–4170. doi: 10.1021/acssuschemeng.7b00129
- Zhang, Z., and Xu, X. (2015). Nondestructive covalent functionalization of carbon nanotubes by selective oxidation of the original defects with K_2FeO_4 . *Appl. Surf. Sci.* 346, 520–527. doi: 10.1016/j.apsusc.2015.04.026
- Zhou, L., Qiao, M., Zhang, L., Sun, L., Zhang, Y., and Liu, W. (2019). Green and efficient synthesis of carbon quantum dots and their luminescent properties. *J. Lumin.* 206, 158–163. doi: 10.1016/j.jlumin.2018.10.057
- Zhu, S., Meng, Q., Wang, L., Zhang, J., Song, Y., Jin, H., et al. (2013). Highly photoluminescent carbon dots for multicolor patterning, sensors, and bioimaging. *Angew. Chem. Int. Edn.* 52, 3953–3957. doi: 10.1002/anie.201300519

Conflict of Interest: The authors declare that the research was conducted in the absence of any commercial or financial relationships that could be construed as a potential conflict of interest.

Copyright © 2020 Jia, Sun, Zhang, Liu, Cao, Huang, Xing, Zhang, Zhang and Cao. This is an open-access article distributed under the terms of the Creative Commons Attribution License (CC BY). The use, distribution or reproduction in other forums is permitted, provided the original author(s) and the copyright owner(s) are credited and that the original publication in this journal is cited, in accordance with accepted academic practice. No use, distribution or reproduction is permitted which does not comply with these terms.



Fabrication and Characterization of Calcium-Phosphate Lipid System for Potential Dental Application

Ningxin Zhu¹, Dan Wang¹, Fei Xie¹, Man Qin¹, Zhiqiang Lin^{2*} and Yuanyuan Wang^{1*}

¹ Department of Pediatric Dentistry, School and Hospital of Stomatology, Peking University, Beijing, China, ² Beijing Key Laboratory of Tumor Systems Biology, School of Basic Medical Sciences, Institute of Systems Biomedicine, Peking University Health Science Center, Beijing, China

OPEN ACCESS

Edited by:

Kezhen Qi,

Shenyang Normal University, China

Reviewed by:

Desheng Liang,

University of Michigan, United States

Jijun Fu,

Guangzhou Medical University, China

*Correspondence:

Zhiqiang Lin

zhiqiang_lin@bjmu.edu.cn

Yuanyuan Wang

cwyd@126.com

Specialty section:

This article was submitted to

Nanoscience,

a section of the journal

Frontiers in Chemistry

Received: 09 February 2020

Accepted: 24 February 2020

Published: 25 March 2020

Citation:

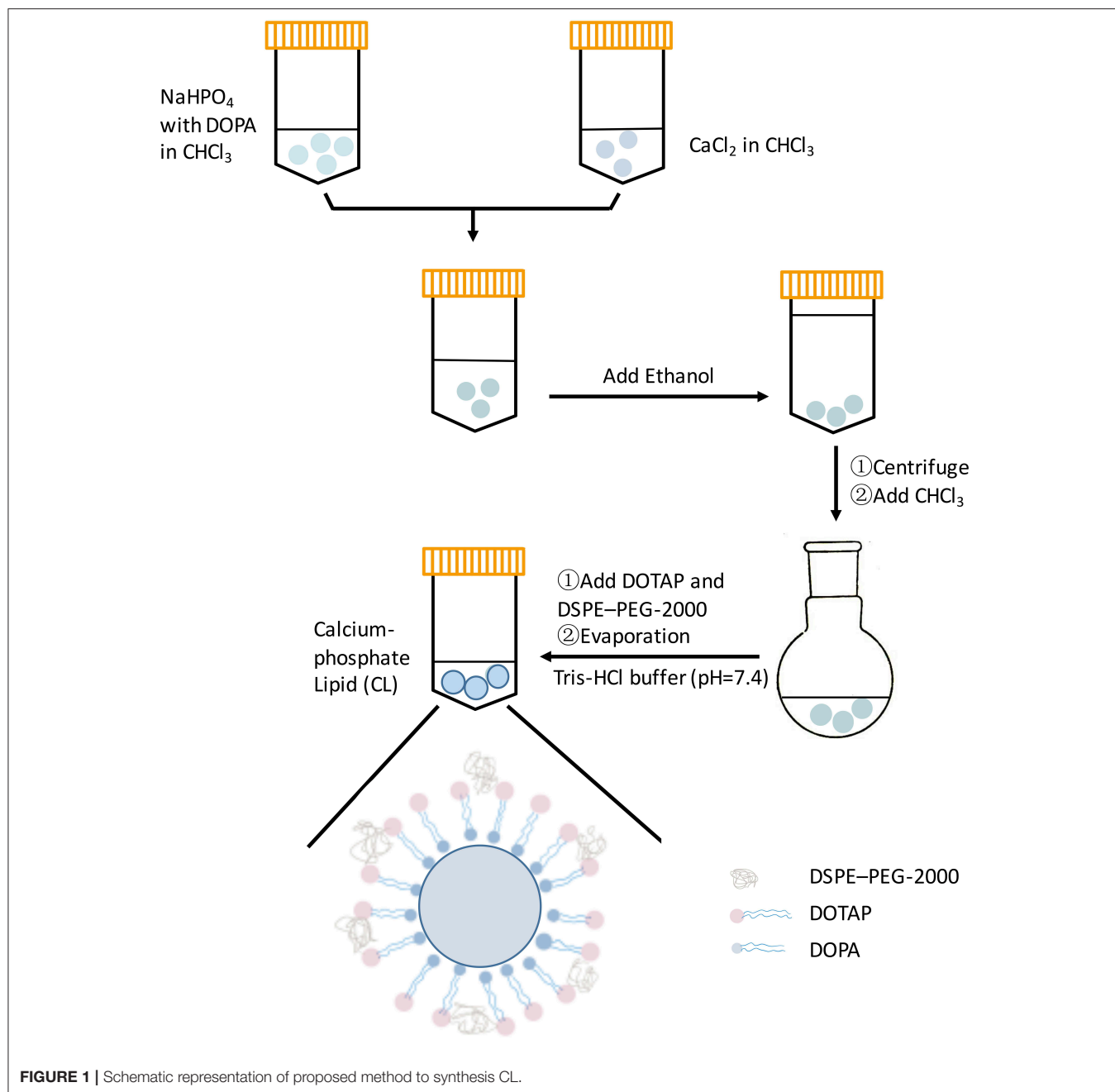
Zhu N, Wang D, Xie F, Qin M, Lin Z and Wang Y (2020) Fabrication and Characterization of Calcium-Phosphate Lipid System for Potential Dental Application. *Front. Chem.* 8:161. doi: 10.3389/fchem.2020.00161

Lipid has been widely studied as a vehicle and loading vector, but there have been no reports of any such related application in the dental field. The purpose of this research was to fabricate and characterize a nano-size calcium-phosphate lipid (CL) system as a potential vehicle in dental regeneration study, wherein the biocompatibility with dental pulp stem cells (DPSCs) was evaluated. The effect of CL on DPSCs proliferation was analyzed by a CCK-8 assay, and the anti-inflammatory effect was investigated by quantitative polymerase chain reaction (qPCR). Moreover, the effect of CL on odontogenic differentiation of inflamed DPSCs (iDPSCs) was studied by Alizarin red staining, tissue-non-specific alkaline phosphatase (TNAP) staining, qPCR, and western blot analyses. The results of this study showed that CL did not affect the proliferation of DPSCs, it down-regulated the inflammatory-associated markers (*IL-1 β* , *IL-6*, *TNF- α* , *COX-2*) of DPSCs treated with *Escherichia coli* lipopolysaccharide (LPS), and enhanced the *in-vitro* odontogenic differentiation potential of iDPSCs. This novel biomaterial has a broad application prospect for its bioactivity and flexible physical property, and thus represents a promising pulpal regeneration material.

Keywords: calcium-phosphate lipid, dental pulp stem cells, biocompatibility, LPS, anti-inflammation

INTRODUCTION

The calcium-phosphate lipid system has shown success in a wide range of treatment strategies due to its multiple properties, such as an efficient encapsulating ability and its antimicrobial properties (Verderosa et al., 2019), many of which were yet unexplored (Satterlee and Huang, 2016). Since 1970s, an attempt to characterize the calcium-phosphate complex to increase transfection efficiency and allow delivery has been made (Graham and van der Eb, 1973; Maitra, 2005; Sokolova et al., 2006; Xu et al., 2019). Lipids have broad application prospects since they were easily designed, synthesized, and characterized (Zhi et al., 2018; Williams and Grant, 2019). Many factors on the surface of the nanoparticle can influence blood residence time and organ-specific accumulation (Alexis et al., 2008; Nuti et al., 2018; Tyo et al., 2019). The length and type of aliphatic chain determine the phase transition temperature and the fluidity of the bilayer, resulting in the stability, and transfection efficiency of a given lipid (Zhi et al., 2018; Li et al., 2019). In 2010, calcium phosphate nanoparticles were successfully coated with a lipid bilayer (Li et al., 2010), and these so-called Lipid-Calcium-Phosphate (LCP) nanoparticles showed efficient gene silencing ability *in vivo* (Li et al., 2012) as well as versatility in encapsulating various therapeutic compounds, such as small molecule drugs (Zhang et al., 2014), siRNA (Yang et al., 2012; Yao et al., 2013), and peptides



(Xu et al., 2013). In consideration of its latent capacity, there is a great application possibility to tissue engineering. The DNA-lipid film was studied as a bone-guiding scaffold in craniofacial tissue (Fukushima et al., 2004), however, there has been little research concerning lipid-based pulp tissue regeneration.

Pulpal vitality of the young immature tooth is essential for root development and reparative dentin formation, which is easily affected, when exposed to external cues. Irreversible pulpitis in an immature permanent tooth will interrupt root development, causing worse function, and shorter survival time of the tooth. Dental pulps with pulpitis suffer higher expressions of pro-inflammatory cytokines (IL-1 α , IL-1 β , IL-6, and TNF- α) and innate immune response (TLR2, TLR4) than pulps without

pulpitis (Zhai et al., 2019). It is a great challenge to find a bioactive and anti-inflammatory material for dental pulp regeneration if failed to preserve vital pulp tissue. The purpose of this novel study is to fabricate the calcium-phosphate lipid (CL) suspension and evaluate its biocompatibility as a composition of dental pulp tissue engineering material.

MATERIALS AND METHODS

Synthesis of Calcium-Phosphate Lipid (CL) and Structural Characterization

The fabrication of CL was performed as previously reported (Li et al., 2012). Briefly, 300 μ L of 500 mM CaCl₂ was

dispersed in 15 mL Cyclohexane/Igepal CO-520 (71/29 v/v) solution to form a very well-dispersed water-in-oil reverse micro-emulsion. Three hundred microliter of 25 mM Na₂HPO₄ (pH = 9.0) in chloroform was dispersed in the same solution to form the phosphate phase, and 200 μL (20 mg/mL) dioleoylphosphatidic acid (DOPA) in chloroform was added. The amphiphilic DOPA could stay at the interface of micro-emulsions and interact with the precipitated CaP core through binding with the surface Ca²⁺ (Kord Forooshani et al., 2019). The above two solutions were mixed adequately for 20 min, then 30 mL ethanol was used to wash the cyclohexane and surfactant 2–3 times (centrifuging at 12,000 g for 15 min each time). The pellets were dissolved in 1 mL chloroform forming CaP core suspension. Then 500 μL of CaP core was mixed with 50 μL of 10 mM DOTAP/Cholesterol (1:1) and 50 μL of 3 mM DSPE-PEG-2000 to encapsulate the core. After evaporating the chloroform, the residual lipid was dispersed in 400 μL of 5 mM Tris-HCl buffer (pH = 7.4) to form calcium-phosphate lipid (Figure 1). The CL suspension was diluted with α-modified minimum essential medium (α-MEM, GIBCO/BRL, USA) to obtain the gradient solutions (50 μg/mL, 5 μg/mL, 500 ng/mL).

The surface morphology of CL was investigated by scanning electron microscopy (SEM) analysis (JSM 7900F, Japan). The hydrodynamic diameter of CL was determined at room temperature using a dynamic light scattering device (DLS, Zetasizer Nano, Malvern, UK). The calcium content was determined through Inductively Coupled Plasma-Atomic Emission Spectrometry (ICP-AES) and the sample was diluted with distilled de-ionized water (DD water) and phosphate buffer saline (PBS) in 1:1 v/v.

Cell Culture

This research had been reviewed and approved by the Ethics Committee of the Peking University Health Science Center. The human dental pulp stem cells (DPSCs) were collected from 14- to 18-year-old patients who were undergoing dental extraction as part of orthodontic treatment. DPSCs were isolated from the pulp tissue derived from the root canal and then digested in 4 mg/mL dispase (Sigma-Aldrich, St. Louis, MO, USA) and 3 mg/mL type-I collagenase (Sigma-Aldrich, St. Louis, MO, USA) for 1 h at 37°C. Single-cell suspensions were obtained by passing cells through a 70-μm strainer (Falcon; BD Biosciences, San Jose, CA). The cell suspensions (0.5–1.0 × 10³/well) were seeded on 12-well plates containing α-MEM supplemented with 10% fetal bovine serum (FBS, GIBCO, USA), 100 U/mL penicillin, and 100 μg/mL streptomycin and then incubated at 37°C in 5% CO₂. DPSCs were identified by our previously published method (Wang et al., 2013). DPSCs between the fourth and sixth passage were used for this research.

Quantitative Polymerase Chain Reaction Analysis (qPCR)

The qPCR analysis was taken out by following a previously published method. In brief, *Escherichia coli* lipopolysaccharide (LPS) (Sigma Aldrich, St Louis, MO, USA) powder was dissolved in sterile distilled water to a final concentration

of 1 μg/mL. According to the results of our previous work (Zhu et al., 2019), after stimulation of LPS within 6 h, mRNA level of inflammatory cytokines of DPSCs will increase significantly. DPSCs were treated with 1 μg/mL LPS for 1 h to trigger inflammatory reaction, and termed LPS-induced DPSCs (inflamed dental pulp stem cells, iDPSCs). iDPSCs were co-cultured with CL dilutions for 3 h. Untreated DPSCs were used as a control group. iDPSCs group and CL group (iDPSCs + CL dilution) were compared with control group at 3 h. Total RNA were extracted from the treated iDPSCs using TRIzol (Introgen, Carlsbad, CA, USA), then converted to cDNA with Moloney murine leukemia virus reverse transcriptase (M-MLV RTase, Promega, Madison, WI, USA). qPCR analysis was performed on a total volume of 20 μL in SYBR[®] Green master mix (Rox, Roche Applied Science, IN, USA), with 0.5 μL cDNA and 200 nM of the primers. Specific primers (listed as Table 1) for Glyceraldehyde-3-phosphate dehydrogenase (GAPDH), dentin sialophosphoprotein (DSPP), interleukin-1β (IL-1β), interleukin-6 (IL-6), interleukin-8 (IL-8), tumor necrosis factor-α (TNF-α), cyclooxygenase-2 (COX-2), alkaline phosphatase (ALP), osteocalcin (OCN), runt-related transcription factor 2 (RUNX2), and bone sialoprotein (BSP) were designed by Primer 3 and synthesized (BGI, China). qPCR amplifications were performed as the following thermal cycling conditions: 50°C for 2 min, then 95°C for 10 min, followed by 40 cycles of 94°C for 15 s, and 60°C for 1 min. ABI PRISM 7500 Sequence Detection System (Applied Biosystems, Foster City, CA, USA) was used for the reaction. All data were analyzed by using PRISM6 software (one-way ANOVA and LSD comparison test).

Western Blot Analysis

According to the results of qPCR, iDPSCs were treated with CL dilutions for seven days, and cells were lysed in RIPA buffer

TABLE 1 | Primers used for quantitative PCR.

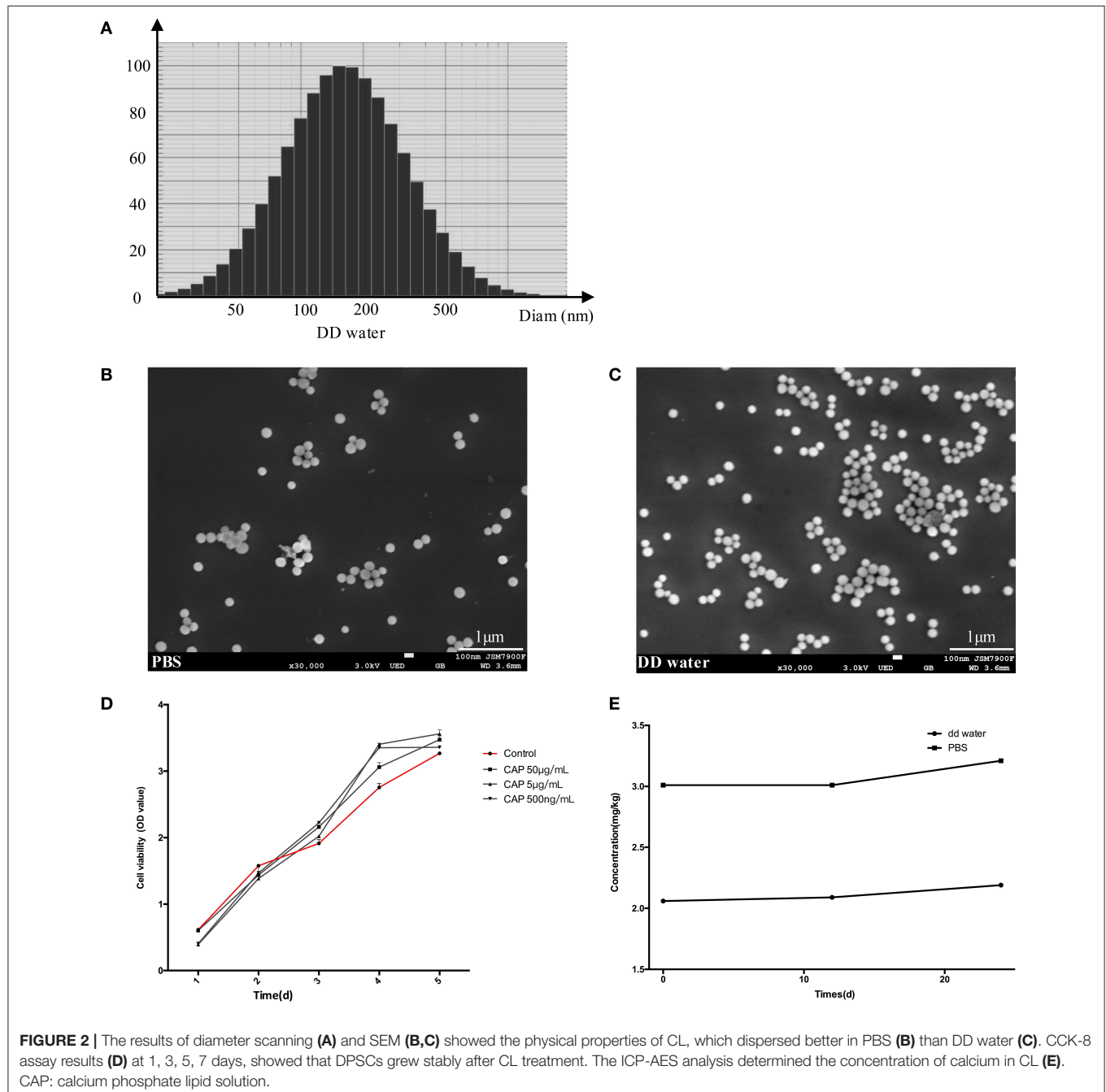
Target gene	Sequence	Product size (bp)
GAPDH	Forward: GCAAATTCATGGCACCGTC	465
	Reverse: GGGGTCATTGATGGCAACAATA	
DSPP	Forward: TCCTAGCAAGATCAAATGTGTCTCAGT	152
	Reverse: CATGCACCAGGACACCACTT	
BSP	Forward: ACCCTGCCAAAAGAATGCAG	281
	Reverse: TGCCACTAACATGAGGACGT	
RUNX2	Forward: CACTGGCGCTGCAACAAGA	157
	Reverse: CATTCCGGAGCTCAGCAGAATAA	
IL-1β	Forward: TGCACGATGCACCTGTACGA	298
	Reverse: AGGCCCAAGGCCACAGGTAT	
IL-6	Forward: ACGAACTCCTTCTCCACAAGC	397
	Reverse: CTACATTTGCCGAAGAGCCC	
COX-2	Forward: CTGGCGCTCAGCCATACAG	401
	Reverse: ACACTCATACATACACCTCGGT	
TNF-α	Forward: CAGAGGGAAGATTTCCCCAG	285
	Reverse: CCTCAGCTTGAGGGTTTGCTAC	

containing protease and phosphatase inhibitors. Proteins were extracted and then quantified by using the BCA Protein Assay (Pierce, USA). Forty micrograms of proteins derived from each sample were separated on 10% SDS-PAGE gels and transferred to PVDF membranes (Millipore, Bedford, MA, USA) at 100 V for 60 min. The membranes were incubated in blocking buffer (5% non-fat dry milk in Tris-buffered saline containing 0.05% Tween-20, pH 7.4) for 1 h and then incubated with antibodies: DSPP (ab216892, Abcam, China), RUNX2 (D1L7F, Cell Signaling Technology, Danvers, MA, USA), OCN (ab13420, Abcam, China), and β -actin (D6A8, 8457T, Cell Signaling Technology,

Danvers, MA, USA) in 1:1000 dilutions at 4°C overnight. The membranes were then incubated with horseradish peroxidase-conjugated secondary antibody (PV9001, PV9002, ZSJK, China) for 1 h at room temperature. The bands were visualized by using Fusin Fx (Vilber Lourmat, France).

Statistical Analysis

ImageJ and PRISM6 were used. Statistical analysis was performed using one-way ANOVA and LSD comparison test. The level of statistical significance was $p < 0.05$.



RESULTS

The Physical Properties and Biocompatibility of CL

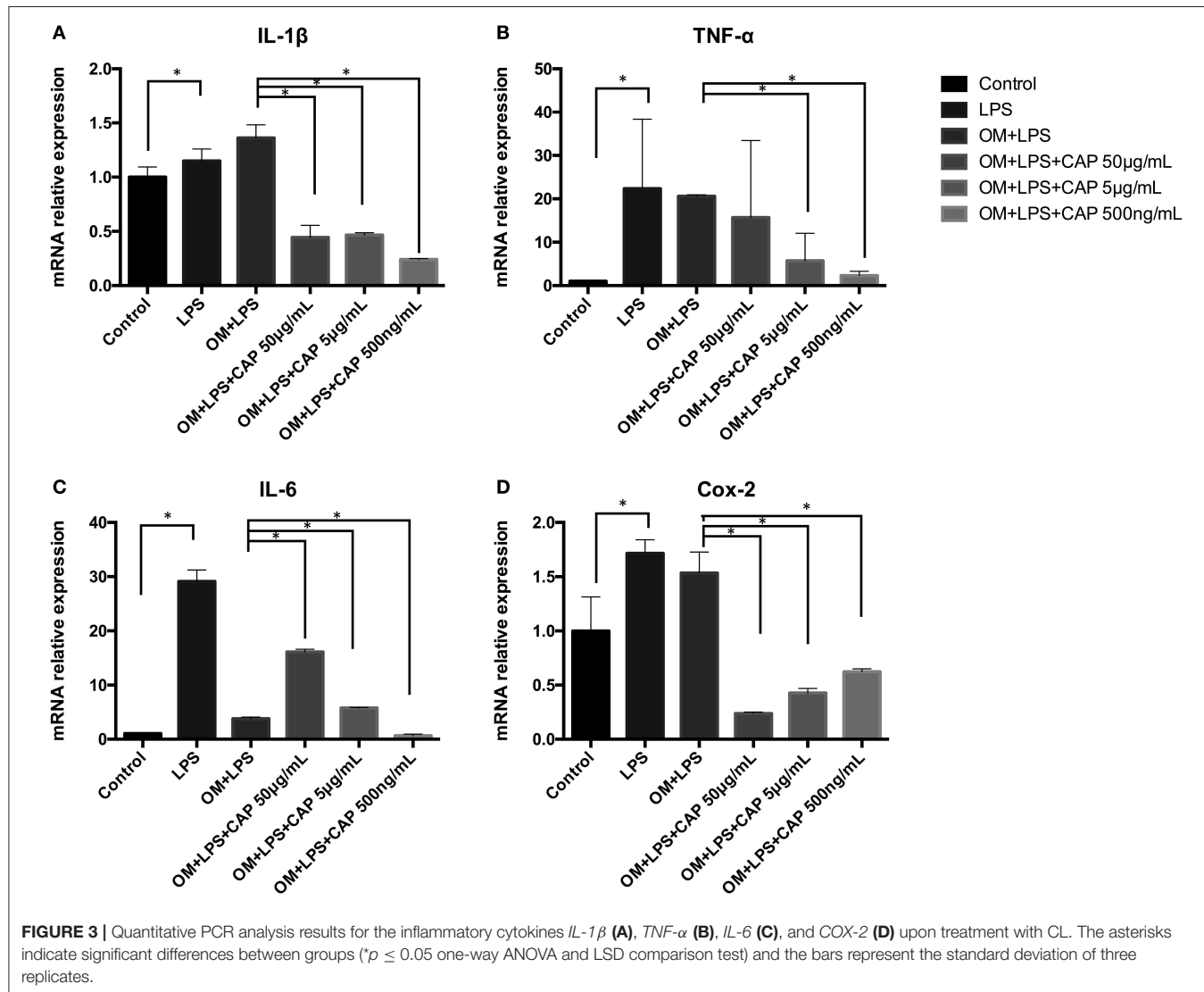
The spherical characteristic of CL could be observed under SEM (Figure 2), the particles dispersed better in PBS (Figure 2B) than DD water, and most of the particles attracted each other and formed larger granules in latter dilution (Figure 2C). The diameters ranged from 100 to 500 nm in DD water, average value was 204.3 nm. The concentration of calcium in the DD water was 2.06 ppm, rising to 2.19 ppm after 24 h. To simulate the body fluid condition, the CL was diluted with PBS, and calcium concentration was 3.02 ppm, but the difference was not significant (Figure 2E). The gradient solutions of CL were used to culture the DPSCs, to examine the biocompatibility. The results of CCK-8 showed that CL had no cellular toxicity (Figure 2D).

Effects of CL on Regulating the Inflammatory Cytokines Expression of iDPSCs

Results of qPCR showed mRNA expression levels of all inflammatory cytokines were up-regulated in iDPSCs. CL had an obvious effect in down-regulating the expression of *IL-1 β* , *TNF- α* , and *IL-6*, with negative correlation of the concentration, while suppressing the expression of *COX-2* dependent with the concentration (Figure 3).

Effects of CL on the Osteo/Odontogenic Differentiation of iDPSCs

The mineralization potential of iDPSCs under CL treatment was examined through Alizarin red staining (Figures 4A–C) and TNAP staining assay (Figures 4B–D). Compared to DPSCs cultured in the osteogenic medium (OM), less mineralized nodules formed in cultured iDPSCs, but CL could significantly

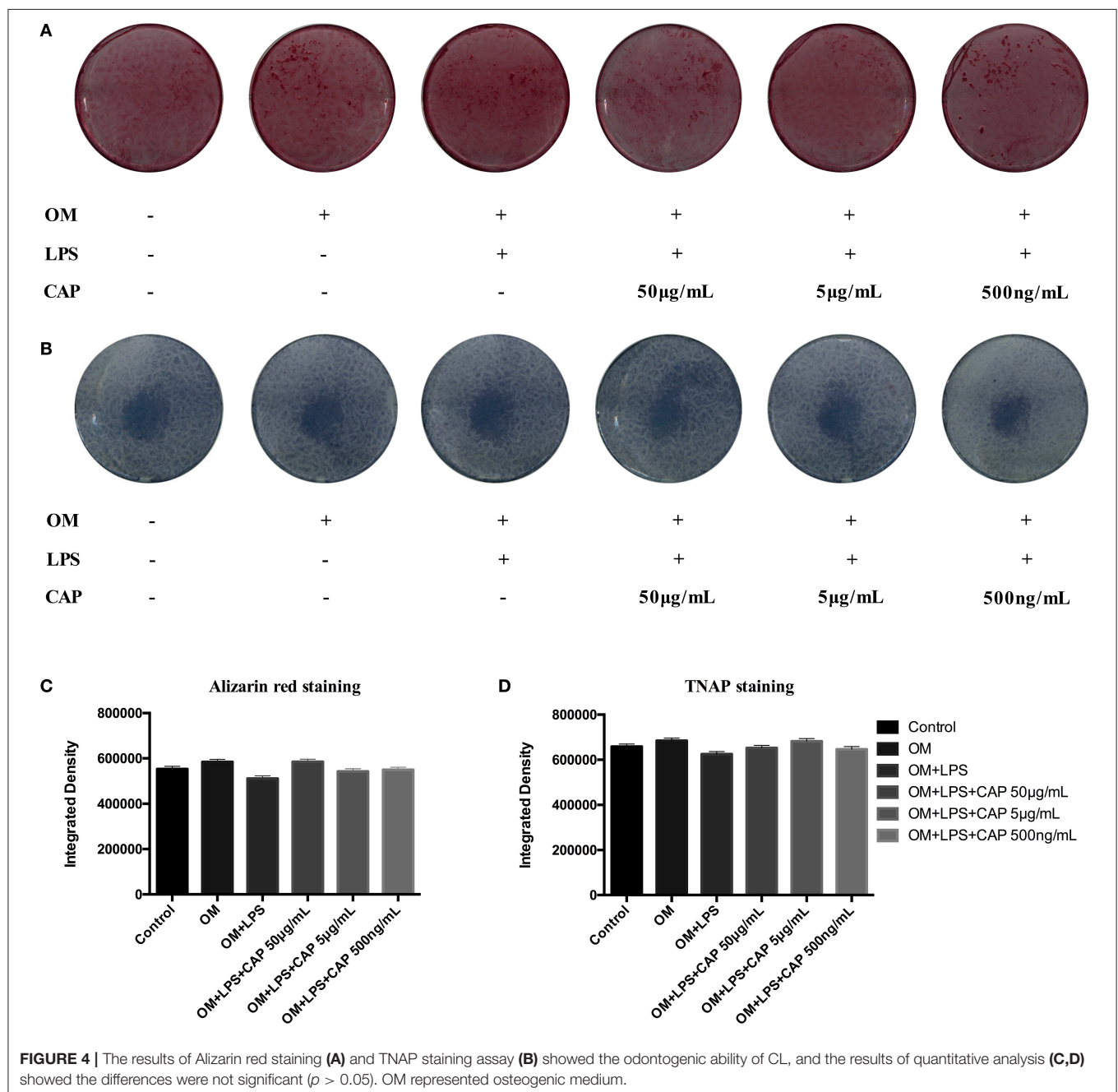


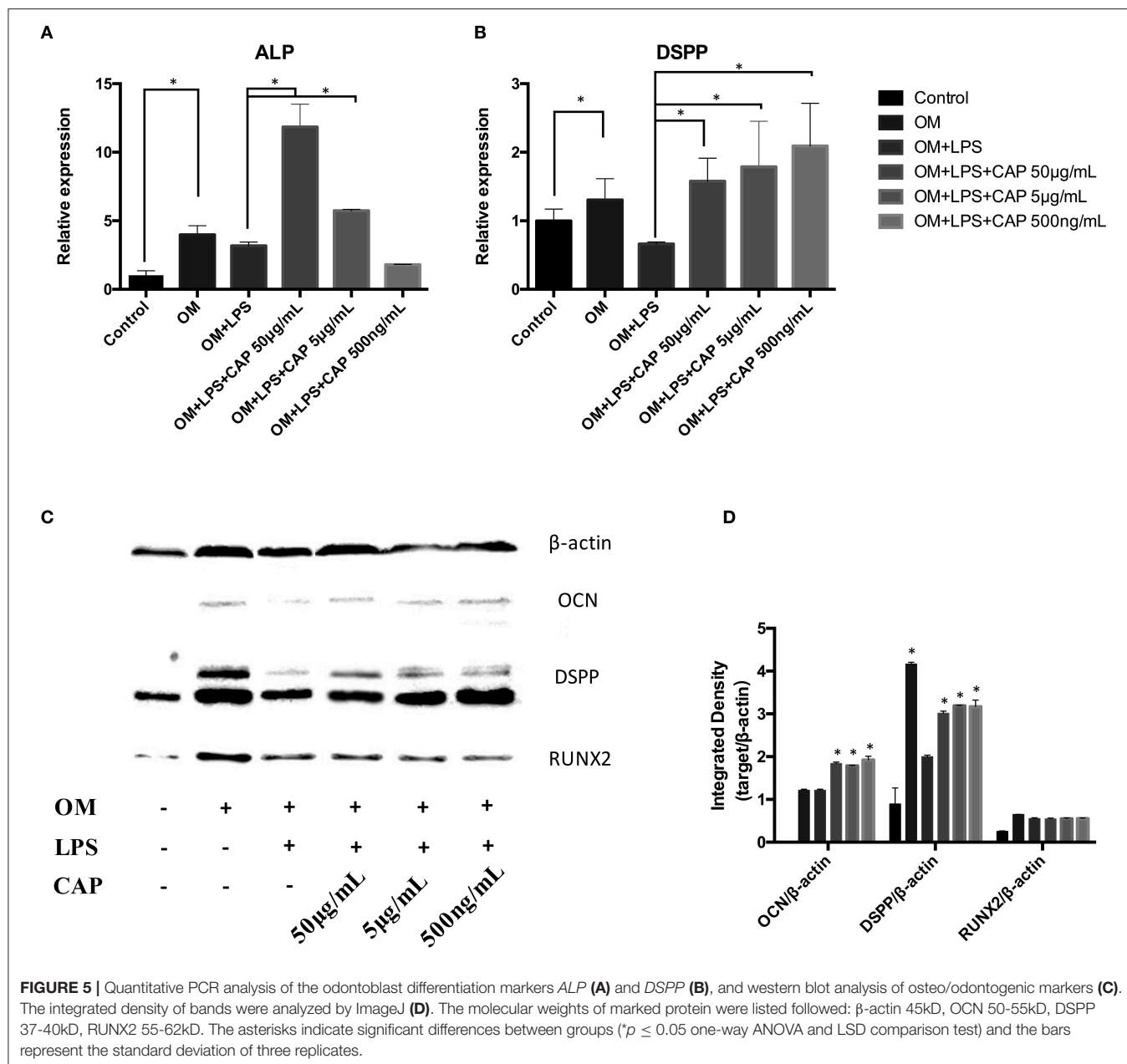
induce the formation of calcium compounds in iDPSCs. The ALP activity varied in the same trend, but the differences were not significant (Figure 4D). The osteo/odontogenic differentiation ability was further investigated by examining related biomarkers and their downstream proteins. The qPCR analysis showed that CL significantly increased the expression of ALP and DSPP at mRNA level ($p < 0.05$) (Figures 5A,B), the expression of ALP was up-regulated most under 50 $\mu\text{g}/\text{mL}$ (Figure 5A), while DSPP increased most under 500 ng/mL (Figure 5B). CL significantly increased the expression of DSPP and OCN at protein level, but the expression of RUNX2 showed no significance (Figures 5C,D,

$p > 0.05$). This result was consistent with previous research, showing DSPP and RUNX2 expressed at the different stages of tooth development (Chen et al., 2009).

DISCUSSION

Calcium-phosphate lipid is formulated using a reverse micro-emulsion system. In separate round-bottom flasks, water droplets containing either calcium or phosphate are stirred in an oil phase containing cyclohexane and the surfactant Igepal. When the two emulsions are mixed and the separate droplets collide, the





soluble calcium and phosphate react to form nanoprecipitates, still suspended in the water droplets. The final nanoparticle is generated by adding free lipids to the cores (Satterlee and Huang, 2016). The formation of asymmetric bilayer occurs when organic solvent is removed from the mixture and exposed to an aqueous solution. The inner leaflet is a cationic lipid to encapsulate negatively charged polynucleotides, and neutral lipid is placed on the outer leaflet to decrease non-specific cellular uptake/toxicity (Li et al., 2012). Till now, calcium-phosphate lipid has been widely considered as a carrier, however, its cellular compatibility has been barely studied. In this study, CL was demonstrated as anti-inflammatory and osteo/odontogenic to iDPSCs, which could be a potential material for vital pulp therapy (VPT).

Lipid mediators are widely appreciated for their important roles in initiating the leukocyte traffic required in host defense (Cotran et al., 1999). Novel families of lipid mediators could actively stimulate cessation of leukocytic infiltration, counterregulation of pro-inflammatory mediators, and the uptake of apoptotic neutrophils and cellular debris (Serhan et al., 2014), probably via cell-cell interactions within inflammatory exudates (i.e., pus), controlling the size, magnitude, and duration of the inflammatory event (Serhan, 2007). It had been demonstrated that specialized lipid mediators which were biosynthesized during self-limited acute inflammatory response (Serhan et al., 2014), called RvD1, RvD5, and PD1, could directly enhance phagocytosis of *E. coli*, counter-regulate a

panel of pro-inflammatory genes, including NF- κ B and TNF- α , and cooperate with antimicrobial process (Chiang et al., 2012; Jia et al., 2019). In the so-called lipid-mediator class switching process, specialized pro-resolving mediators (SPMs) were produced via a prostaglandins and leukotrienes (LTs) switch. SPMs triggered multiple reactions, such as limiting neutrophil tissue infiltration and influencing the translation of mRNAs encoding enzymes, and they were isolated in low-dose and locally active (Serhan et al., 2011), resulting in reducing exudate IL-6 and human neutrophil trans-endothelial migration in response to TNF- α (Dalli et al., 2013). Calcium-phosphate lipid might be able to trigger this reaction due to its similar lipid-bilayer structure, to rescue the inflammatory condition, which was consistent with the results that low-dose CL showed more efficient reduction in IL-1 β , IL-6, and TNF- α (Figures 3A–C). Further mechanisms need to be studied in future research, including macrophage reactions and COX-2 related pathway.

Because calcium-phosphate is acid-sensitive (Ivanets et al., 2019), after the CL is delivered to the cellular endosome, the late endosome's acidic environment will dissolve the calcium-phosphate core (Li et al., 2010). It had been proved that calcium ions of calcium-phosphate lipid released more with a lower pH (Tang et al., 2015). In our study, the pH of DD water was about 7.7 and was freshly prepared (data not shown), with the pH a little bit higher than PBS (pH = 7.4). Calcium released more in PBS (Figure 2E), which was consistent with previous conclusions. Since Ca²⁺ is one of the critical factors in cell differentiation (Maeno et al., 2005; Valerio et al., 2009; Rahmanian et al., 2019), mineralization (Dvorak et al., 2014), and activation of multiple cellular pathways (Yang et al., 2017; Liu et al., 2019), CL might influence iDPSCs differentiation via free Ca²⁺ released. Also, it was reported that lipid membrane behavior upon local application of Ca²⁺ might contribute to several cellular processes, such as cell division and trafficking of proteins (Ali Doosti et al., 2017), and cationic liposomes were reported to be able to inhibit the activation of phosphatidylinositol-3 kinase-Akt (PI3K-Akt) pathway (Inoh et al., 2017). CL was supposed to enhance osteo/odontogenesis for the richness of Ca²⁺; upstream and downstream pathways still need to be further studied.

REFERENCES

- Alexis, F., Pridgen, E., Molnar, L. K., and Farokhzad, O. C. (2008). Factors affecting the clearance and biodistribution of polymeric nanoparticles. *Mol. Pharm.* 5, 505–515. doi: 10.1021/mp800051m
- Ali Doosti, B., Pezeshkian, W., Bruhn, D. S., Ipsen, J. H., Khandelia, H., Jeffries, G. D. M., et al. (2017). Membrane tubulation in lipid vesicles triggered by the local application of calcium ions. *Langmuir* 33, 11010–11017. doi: 10.1021/acs.langmuir.7b01461
- Chen, S., Gluhak-Heinrich, J., Wang, Y. H., Wu, Y. M., Chuang, H. H., Chen, L., et al. (2009). Runx2, osx, and dspp in tooth development. *J. Dent. Res.* 88, 904–909. doi: 10.1177/0022034509342873
- Chiang, N., Fredman, G., Bäckhed, F., Oh, S. F., Vickery, T., Schmidt, B. A., et al. (2012). Infection regulates pro-resolving mediators that lower antibiotic requirements. *Nature* 484, 524–528. doi: 10.1038/nature11042
- Cotran, R. S., Kumar, V., Collins, T., and Robbins, S. L. (1999). *Robbins Pathologic Basis of Disease*. Philadelphia: Saunders.
- Dalli, J., Zhu, M., Vlasenko, N. A., Deng, B., Haeggstrom, J. Z., Petasis, N. A., et al. (2013). The novel 13S,14S-epoxy-maresin is converted by human macrophages to maresin 1 (MaR1), inhibits leukotriene A4 hydrolase (LTA4H), and shifts macrophage phenotype. *FASEB J.* 27, 2573–2583. doi: 10.1096/fj.13-227728
- Dvorak, M., Siddiqua, A., Ward, D., Carter, D., Dallas, S., Nemeth, E. F., et al. (2014). Physiological changes in extracellular calcium concentration directly control osteoblast function in the absence of calciotropic hormones. *Proc. Natl. Acad. Sci. U.S.A.* 101, 5140–5145. doi: 10.1073/pnas.0306141101
- Fukushima, T., Hayakawa, T., Inoue, Y., Miyazaki, K., and Okahata, Y. (2004). Intercalation behavior and tensile strength of DNA-lipid films for the dental application. *Biomaterials* 25, 5491–5497. doi: 10.1016/j.biomaterials.2004.01.006
- Graham, F. L., and van der Eb, A. J. (1973). A new technique for the assay of infectivity of human adenovirus 5 DNA. *Virology* 52, 456–467. doi: 10.1016/0042-6822(73)90341-3
- Inoh, Y., Haneda, A., Tadokoro, S., Yokawa, S., and Furuno, T. (2017). Cationic liposomes suppress intracellular calcium ion concentration increase via

CONCLUSIONS

In the present work, a widely studied vector, calcium-phosphate lipid (CL), was proved to suppress the expression of inflammatory cytokines and promote the osteo/odontogenic differentiation of iDPSCs, demonstrating itself as a biocompatible and anti-inflammatory material. CL has a broad application prospect for its bioactivity and flexible physical property, and thus represents a promising pulpal regeneration material to improve residual dental pulp precursor cells' response. Detailed research of the *in-vivo* biological properties of this material are needed to guide its future clinical applications.

DATA AVAILABILITY STATEMENT

All datasets generated for this study are included in the article/supplementary material.

ETHICS STATEMENT

The studies involving human participants were reviewed and approved by The Ethics Committee of the Peking University Health Science Center. The patients/participants provided their written informed consent to participate in this study.

AUTHOR CONTRIBUTIONS

YW put the hypothesis forward and approved the outcomes. ZL provided the technical support of material fabrication. NZ carried out the experiments with the assistance of DW and FX, then wrote the manuscript draft. MQ revised the final manuscript.

FUNDING

ZL was supported by the Foundation from Science and Technology Bureau of Xinjiang production and Construction Corps (2019BC006).

- inhibition of PI3 kinase pathway in mast cells. *Biochim Biophys Acta Biomembr.* 1859, 2461–2466. doi: 10.1016/j.bbmem.2017.09.025
- Ivanets, A. I., Shashkova, I. L., Kitikova, N. V., Maslova, M. V., and Mudruk, N. V. (2019). New heterogeneous synthesis of mixed Ti-Ca-Mg phosphates as efficient sorbents of ¹³⁷Cs, ⁹⁰Sr and ⁶⁰Co radionuclides. *J Taiwan Inst Chem Engin.* 104, 151–159. doi: 10.1016/j.jtice.2019.09.001
- Jia, B., Ma, Y. M., Liu, B., Chen, P., Hu, Y., and Zhang, R. (2019). Synthesis, antimicrobial activity, structure-activity relationship, and molecular docking studies of indole diketopiperazine alkaloids. *Front. Chem.* 7:837. doi: 10.3389/fchem.2019.00837
- Kord Forooshani, P., Polega, E., Thomson, K., Bhuiyan, M. S. A., Pinnaratip, R., Trought, M., et al. (2019). Antibacterial properties of mussel-inspired polydopamine coatings prepared by a simple two-step shaking-assisted method. *Front. Chem.* 7:631. doi: 10.3389/fchem.2019.00631
- Li, J., Chen, Y.-C., Tseng, Y.-C., Mozumdar, S., and Huang, L. (2010). Biodegradable calcium phosphate nanoparticle with lipid coating for systemic siRNA delivery. *J. Control. Release* 142, 416–421. doi: 10.1016/j.jconrel.2009.11.008
- Li, J., Yang, Y., and Huang, L. (2012). Calcium phosphate nanoparticles with an asymmetric lipid bilayer coating for siRNA delivery to the tumor. *J. Control. Release* 158, 108–114. doi: 10.1016/j.jconrel.2011.10.020
- Li, L., Tian, F., Chang, H., Zhang, J., Wang, C., Rao, W., et al. (2019). Interactions of bacteria with monolithic lateral silicon nanopikes inside a microfluidic channel. *Front. Chem.* 7:483. doi: 10.3389/fchem.2019.00483
- Liu, Q., Li, N., Qiao, Z., Li, W., Wang, L., Zhu, S., et al. (2019). The multiple promotion effects of ammonium phosphate-modified Ag₃PO₄ on photocatalytic performance. *Front. Chem.* 7:866. doi: 10.3389/fchem.2019.00866
- Maeno, S., Niki, Y., Matsumoto, H., Morioka, H., Yatabe, T., Funayama, A., et al. (2005). The effect of calcium ion concentration on osteoblast viability, proliferation and differentiation in monolayer and 3D culture. *Biomaterials* 26, 4847–4855. doi: 10.1016/j.biomaterials.2005.01.006
- Maitra, A. (2005). Calcium phosphate nanoparticles: second-generation nonviral vectors in gene therapy. *Expert Rev. Mol. Diagn.* 5, 893–905. doi: 10.1586/14737159.5.6.893
- Nuti, S., Fernández-Lodeiro, J., Del Secco, B., Rampazzo, E., Rodríguez-González, B., Capelo, J. L., et al. (2018). Engineered nanostructured materials for ofloxacin delivery. *Front. Chem.* 6:554. doi: 10.3389/fchem.2018.00554
- Rahmanian, M., seyfoori, A., Dehghan, M. M., Eini, L., Naghib, S. M., Gholami, H., et al. (2019). Multifunctional gelatin–tricalcium phosphate porous nanocomposite scaffolds for tissue engineering and local drug delivery: *in vitro* and *in vivo* studies. *J. Taiwan Inst. Chem. Engin.* 101, 214–220. doi: 10.1016/j.jtice.2019.04.028
- Satterlee, A. B., and Huang, L. (2016). Current and future theranostic applications of the lipid-calcium-phosphate nanoparticle platform. *Theranostics* 6, 918–929. doi: 10.7150/thno.14689
- Serhan, C. N. (2007). Resolution phase of inflammation: novel endogenous anti-inflammatory and proresolving lipid mediators and pathways. *Annu. Rev. Immunol.* 25, 101–137. doi: 10.1146/annurev.immunol.25.022106.141647
- Serhan, C. N., Chiang, N., Dalli, J., and Levy, B. D. (2014). Lipid mediators in the resolution of inflammation. *Cold Spring Harb. Perspect. Biol.* 7, a016311–a016311. doi: 10.1101/cshperspect.a016311
- Serhan, C. N., Fredman, G., Yang, R., Karamnov, S., Belayev, L. S., Bazan, N. G., et al. (2011). Novel proresolving aspirin-triggered DHA pathway. *Chem. Biol.* 18, 976–987. doi: 10.1016/j.chembiol.2011.06.008
- Sokolova, V. V., Radtke, I., Heumann, R., and Eppler, M. (2006). Effective transfection of cells with multi-shell calcium phosphate-DNA nanoparticles. *Biomaterials* 27, 3147–3153. doi: 10.1016/j.biomaterials.2005.12.030
- Tang, J., Li, L., Howard, C. B., Mahler, S. M., Huang, L., and Xu, Z. P. (2015). Preparation of optimized lipid-coated calcium phosphate nanoparticles for enhanced *in vitro* gene delivery to breast cancer cells. *J. Mater. Chem. B* 3, 6805–6812. doi: 10.1039/C5TB00912J
- Tyo, A., Welch, S., Hennenfent, M., Kord Forooshani, P., Lee, B. P., and Rajachar, R. (2019). Development and characterization of an antimicrobial polydopamine coating for conservation of humpback whales. *Front. Chem.* 7:618. doi: 10.3389/fchem.2019.00618
- Valerio, P., Pereira, M. M., Goes, A. M., and Leite, M. F. (2009). Effects of extracellular calcium concentration on the glutamate release by bioactive glass (BG60S) preincubated osteoblasts. *Biomed. Mater.* 4:045011. doi: 10.1088/1748-6041/4/4/045011
- Verderosa, A. D., Totsika, M., and Fairfull-Smith, K. E. (2019). Bacterial biofilm eradication agents: a current review. *Front. Chem.* 7:824. doi: 10.3389/fchem.2019.00824
- Wang, Y., Zhao, Y., Jia, W., Yang, J., and Ge, L. (2013). Preliminary study on dental pulp stem cell-mediated pulp regeneration in canine immature permanent teeth. *J. Endod.* 39, 195–201. doi: 10.1016/j.joen.2012.10.002
- Williams, D. E., and Grant, K. B. (2019). Metal-assisted hydrolysis reactions involving lipids: a review. *Front. Chem.* 7:14. doi: 10.3389/fchem.2019.00014
- Xu, H., Yang, D., Jiang, D., and Chen, H.-Y. (2019). Phosphate assay kit in one cell for electrochemical detection of intracellular phosphate ions at single cells. *Front. Chem.* 7:360. doi: 10.3389/fchem.2019.00360
- Xu, Z., Ramishetti, S., Tseng, Y.-C., Guo, S., Wang, Y., and Huang, L. (2013). Multifunctional nanoparticles co-delivering Trp2 peptide and CpG adjuvant induce potent cytotoxic T-lymphocyte response against melanoma and its lung metastasis. *J. Control. Release* 172, 259–265. doi: 10.1016/j.jconrel.2013.08.021
- Yang, S., Sun, H., Yan, J., Guo, X., Li, D., and Zhou, D. (2017). Persistent mechanical stretch-induced calcium overload and MAPK signal activation contributed to SCF reduction in colonic smooth muscle *in vivo* and *in vitro* AU - Dong, Fang. *J. Recept. Signal Transduct.* 37, 141–148. doi: 10.1080/10799893.2016.1203939
- Yang, Y., Hu, Y., Wang, Y., Li, J., Liu, F., and Huang, L. (2012). Nanoparticle delivery of pooled siRNA for effective treatment of non-small cell lung cancer. *Mol. Pharm.* 9, 2280–2289. doi: 10.1021/mp300152v
- Yao, J., Zhang, Y., Ramishetti, S., Wang, Y., and Huang, L. (2013). Turning an antiviral into an anticancer drug: nanoparticle delivery of acyclovir monophosphate. *J. Control. Release* 170, 414–420. doi: 10.1016/j.jconrel.2013.06.009
- Zhai, Y., Wang, Y., Rao, N., Li, J., Li, X., Fang, T., et al. (2019). Activation and biological properties of human beta defensin 4 in stem cells derived from human exfoliated deciduous teeth. *Front. Physiol.* 10:1304. doi: 10.3389/fphys.2019.01304
- Zhang, J., Miao, L., Guo, S., Zhang, Y., Zhang, L., Satterlee, A., et al. (2014). Synergistic anti-tumor effects of combined gemcitabine and cisplatin nanoparticles in a stroma-rich bladder carcinoma model. *J. Control. Release* 182, 90–96. doi: 10.1016/j.jconrel.2014.03.016
- Zhi, D., Bai, Y., Yang, J., Cui, S., Zhao, Y., Chen, H., et al. (2018). A review on cationic lipids with different linkers for gene delivery. *Adv. Colloid Interface Sci.* 253, 117–140. doi: 10.1016/j.cis.2017.12.006
- Zhu, N., Chatzistavrou, X., Ge, L., Qin, M., Papagerakis, P., and Wang, Y. (2019). Biological properties of modified bioactive glass on dental pulp cells. *J. Dent.* 83, 18–26. doi: 10.1016/j.jdent.2019.01.017

Conflict of Interest: The authors declare that the research was conducted in the absence of any commercial or financial relationships that could be construed as a potential conflict of interest.

Copyright © 2020 Zhu, Wang, Xie, Qin, Lin and Wang. This is an open-access article distributed under the terms of the Creative Commons Attribution License (CC BY). The use, distribution or reproduction in other forums is permitted, provided the original author(s) and the copyright owner(s) are credited and that the original publication in this journal is cited, in accordance with accepted academic practice. No use, distribution or reproduction is permitted which does not comply with these terms.



Volatile Organic Compounds Gas Sensors Based on Molybdenum Oxides: A Mini Review

Jingxuan Wang¹, Qu Zhou^{1*}, Shudi Peng², Lingna Xu¹ and Wen Zeng^{3*}

¹ College of Engineering and Technology, Southwest University, Chongqing, China, ² Chongqing Electric Power Research Institute, State Grid Chongqing Electric Power Company, Chongqing, China, ³ College of Materials Science and Engineering, Chongqing University, Chongqing, China

OPEN ACCESS

Edited by:

Liwei Wang,
Guangxi University, China

Reviewed by:

Zhaoxiong Yan,
Jiangnan University, China
Zhe Chen,
Jilin Institute of Chemical
Technology, China

*Correspondence:

Qu Zhou
zhouqu@swu.edu.cn
Wen Zeng
wenzeng@cqu.edu.cn

Specialty section:

This article was submitted to
Nanoscience,
a section of the journal
Frontiers in Chemistry

Received: 27 February 2020

Accepted: 01 April 2020

Published: 05 May 2020

Citation:

Wang J, Zhou Q, Peng S, Xu L and
Zeng W (2020) Volatile Organic
Compounds Gas Sensors Based on
Molybdenum Oxides: A Mini Review.
Front. Chem. 8:339.
doi: 10.3389/fchem.2020.00339

As a typical n-type semiconductor, MoO₃ has been widely applied in the gas-detection field due to its competitive physicochemical properties and ecofriendly characteristics. Volatile organic compounds (VOCs) are harmful to the atmospheric environment and human life, so it is necessary to quickly identify the presence of VOCs in the air. This review briefly introduced the application progress of an MoO₃-based sensor in VOCs detection. We mainly emphasized the optimization strategies of a high performance MoO₃, which consists of morphology-controlled synthesis and electronic properties functional modification. Besides the general synthesis methods, its gas-sensing properties and mechanism were briefly discussed. In conclusion, the application status of MoO₃ in gas-sensing and the challenges still to be solved were summarized.

Keywords: MoO₃, gas sensors, volatile organic compounds, functional modification, gas-sensing mechanism

INTRODUCTION

Volatile organic compounds (VOCs) mainly come from the exhaust gases generated by fuel combustion and transportation, as well as emissions from building materials, decorative materials, and furniture. People can suffer headaches, nausea, and even more severe issues such as convulsions and comas when exposed to a certain concentration of VOCs (Chu et al., 2010; Sui et al., 2015). Moreover, many carcinogens that damage the liver, kidneys, brain, and nervous system were found in VOCs. Therefore, the problem of air pollution by VOCs has attracted extensive attention in many countries (Yang et al., 2018; He S. H. et al., 2019). Currently, there are two common techniques—photo ionization detector (PID) and flame ionization detector (FID)—to detect VOCs, however, the application of these methods in industry are limited due to the relatively high cost and complicated maintenance. Considering the characteristics of small size, low cost, and convenient fabrication, semiconductor gas sensor technology plays an important role in many fields (Lu et al., 2018; Xiao et al., 2018; Zhang D. Z. et al., 2018; Zhang Q. Y. et al., 2018; Zhou et al., 2018c, 2019; Wang et al., 2019a; Wei et al., 2020), so it is reasonable to propose the employment of a gas sensor to realize the online monitoring of VOCs.

As a typical n-type semiconductor material with a suitable band gap (2.39–2.9 eV) (Yan et al., 2016), MoO₃ has attracted wide attention because of its distinctive gas sensing performances in the detection of many gases (Liu et al., 2015; Xia et al., 2016; Li, 2017; Zhou et al., 2017; Yang et al., 2018). Researchers have been devoted to designing nanomaterials with more suitable properties, and two methods have proved effective through unremitting efforts. One is to synthesize materials

with larger specific surface areas, which is attributed to the conclusion that the micromorphology features have an impact on the gas-sensitive process (Zhou et al., 2018b; Zhu et al., 2018; Wang et al., 2019b; Wei Z. J. et al., 2019). Considering the changes in the materials that are caused by doping and compounding or the catalytic effect of the introduced material on the sensing process, it is also desirable to improve the properties of the materials by introducing other elements or substances (Mousavi-Zadeh and Rahmani, 2018; Zhou et al., 2018a; Wang et al., 2019c; Xu et al., 2019). Therefore, the optimization strategies of MoO₃ based on controllable morphology synthesis and functional modification were comprehensively summarized in this mini review. Besides, several typical synthesis pathways of MoO₃ nanomaterials, as well as the gas-sensing performances and mechanism to VOCs, were introduced.

SYNTHESIS METHODS OF MoO₃

The preparation of materials with more useful properties has always been a research hotspot in the field of gas detection, and has attracted extensive attention from scholars. In recent years, material preparation craft is constantly updated and developed with the emergence of new technology. At present, solid phase method, liquid phase method, and template method are mainly employed to synthesize MoO₃ materials with admirable performance.

The process of preparing materials by solid phase method is to transform the solid phase raw materials into target powders. Using ammonium molybdate as raw material, Qin et al. (2017) successfully obtained MoO₃ nanoplate arrays in the air through a solid phase chemical synthesis route. By hydrolyzing a mixture of one or more soluble metal salts solution and then evaporating and sublimating them, the liquid phase method adopts a series of processes to separate the solute from the solvent, where finally the nanoparticles with uniform shape are produced by crystallizing metal ions. Nowadays, spray pyrolysis technique, sol-gel route, and hydrothermal method have been reported as common liquid phase methods for the preparation of MoO₃ materials. Sau et al. (2019) used the sol-gel method to heat the solution after the molybdenum source was fully dissolved to a gelatinous state under specific PH (7–8) conditions. Finally they prepared α -MoO₃ nanoparticles through annealing and drying. Pandeeswari and Jeyaprakash (2014) successfully obtained MoO₃ thin films with a thickness of 520 nm on a glass substrate maintained at 250°C by spray pyrolysis route. Zhu et al. (2019) synthesized hollow MoO₃ microcages by a facile one-step hydrothermal process, which had gone through four steps of heating, cooling, centrifugation, and washing. The template method is designed to generate nanomaterials based on the template of appropriate structure, which can effectively influence the growth direction and morphology of the materials. Zhang et al. (2017) deposited MoS₂@MnCO₃ powder based on an MnCO₃ template, and prepared MoS₂ by adding hydrochloric acid to remove MnCO₃. Finally, they obtained hierarchical MoO₃ microboxes by calcining MoS₂ powder.

OPTIMIZATION STRATEGIES OF MoO₃

The sensitivity of the gas sensors is closely related to the changes in the resistance that is attributed to the adsorption and desorption of target gas molecules on the surface of materials, which implies that the gas-sensing properties mainly depend on their own electronic characteristics (carrier concentration, energy band structure, etc.) and morphological characteristics (specific surface area, aperture, etc.). Based on this, the main strategies to enhance the gas-sensing performances of materials are morphology control and electronic properties improvement.

Controllable Synthesis of Diversified MoO₃

In recent years, the production of MoO₃ gas-sensitive materials with high quality morphology has become an important research approach for performance enhancement. In this regard, MoO₃ gas-sensitive materials with different morphologies and dimensions have been prepared through different methods to conduct gas-sensing experiments. In this section, we review and summarize the excellent achievements of MoO₃ morphology control and several typical morphologies are shown in **Figures 1A–C**.

One-dimensional (1D) structures, such as nanofibers, nanorods, and nanoribbons, have limited specific surface areas, but their reaction sites are directly exposed to external environments, leading to the susceptible variation of interface ion transport when some changes occur to environmental factors. Hence, 1D material has the potential to be applied as excellent sensors. The remarkable selectivity and response-recovery characteristics of α -MoO₃ nanorods gas sensors to triethylamine was reported (He S. H. et al., 2019). Besides, the rapid adsorption/desorption processes were confirmed to be the reason for prominent gas-sensing characteristics. By optimizing reaction time and pulse temperature in hydrothermal reaction, Mandal et al. (2019) synthesized uniform MoO₃ nanobelts and MoO₃ nanofibers. The experimental results illustrated that the enhanced ethanol detection performances of nanofibers could be ascribed to the larger specific surface area and surface defects compared with the nanowires.

Materials with two-dimensional structures such as nanoplates and nanosheets have a larger specific surface area, which further improves the gas-sensitive responses. The prominent electron depletion layer that derived from the thin morphologic features of nanoplates was verified as beneficial due to the ultrahigh gas-sensing performances. Moreover, the porous structure caused by the combination of nanoplates could effectively facilitate gas diffusion on the surface of MoO₃, providing convenience for the gas-sensing process (Cho et al., 2014). The study of Jiang et al. (2018) demonstrated that MoO₃ microsheets with a large number of oxygen vacancies exhibit superior sensing properties, and the strong reaction between adsorbed oxygen and target gases to be confirmed was also an important factor to promote the gas-sensing performances.

Three-dimensional structures with large specific surface areas are generally assembled from low-dimensional structures, which have more reaction sites for gas adsorption, leading to better gas-sensitive responses and lower gas detection limits.

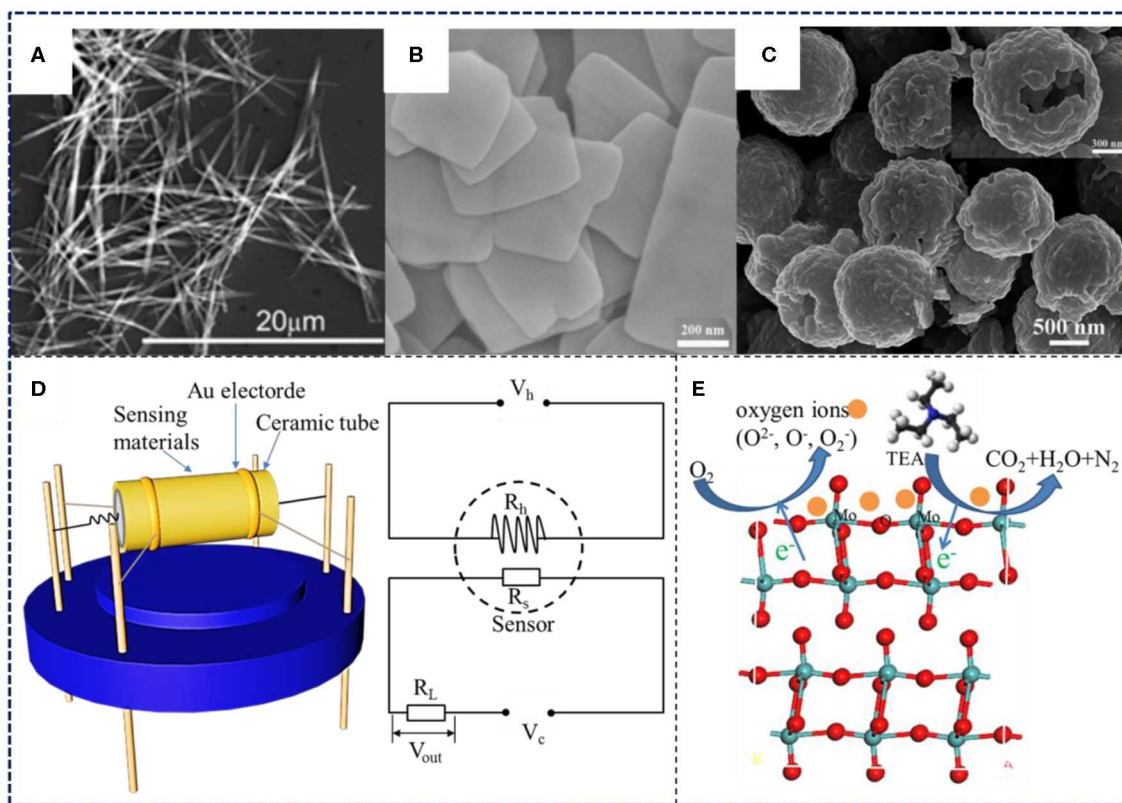


FIGURE 1 | (A) Nanoribbons. Reprinted with permission from Kwak et al. Copyright (2019) American Chemical Society. (B) Nanosheets. Reprinted with permission from Shen et al. Copyright (2019) American Chemical Society. (C) Hollow microspheres. Reprinted with permission from Zhang et al. Copyright (2019) American Chemical Society. (D) Schematic diagram of sensor and detection circuit. (E) Gas sensing mechanism.

Furthermore, more gas diffusion channels are provided by the assembled porous structure, which are conducive to gas sensitivity reaction. Common three-dimensional structures of MoO₃ include nanoarrays, nanoflowers, and nanospheres. For example, Ji et al. (2019a) synthesized three hierarchical MoO₃ flower-like samples with different petal shapes and found that the material with the thinnest petals had the most outstanding gas-sensing performance. Specifically, the thin nanosheets assembled flower-like MoO₃ has a larger specific surface area that provides more potential for gas-sensitive reactions, and the thinness allows electrons to transfer rapidly across the surface, which implied the procedure of gas-sensing became easier. In addition, the curved edges of thin petals make it harder for gas molecules to leave the surface, facilitating the full process of adsorption. Cong et al. (2016) proved the sensors based on MoO₃ nanoarrays assembled from a large number of long nanorods exhibited more reactive sites and more active surface electrical properties than the nanoarrays with fewer nanorods.

Functional Modification Methods

Functional modification is of great significance to improving the properties of gas-sensitive materials. In the present studies, the modification of MoO₃ mainly includes two approaches

of element doping and multi-component compounding, which have been proven to be effective methods in optimizing the electronic properties of materials. In this section, the advances of MoO₃ modification research were briefly summarized.

Metal doping is an alternative approach to acquire the modified characteristics of MoO₃. On the one hand, suitable metal doping can effectively reduce the activation energy of chemisorption reaction for the measured gases. On the other hand, the metal elements play the role of the catalytic activity center, leading to the optimization of the gas-sensing performances. Scholars have studied the influence of different doping elements on the properties of MoO₃ materials. For instance, Cr-doped MoO₃ nanorods had more oxygen vacancy induced by doping, which is meaningful for the promotion of sensitivity (Li et al., 2019). Similar results were obtained when the W element was doped in MoO₃ nanobelts (Li et al., 2017b). As for the dope of Ni, not only did more adsorbed oxygen that can promote the change of resistance in the sensing process appear on the surface of MoO₃, but also the morphology changed with the increase of the doping amount, which is related to the inhibition of lattice growth by the introduction of doped Ni elements (Jiang et al., 2019). Yang et al. (2017) prepared Zn-doped MoO₃ nanobelts using the hydrothermal method. They found that the doped zinc caused the reduction of the band gap of

MoO₃ and increased the amount of adsorbed ethanol molecules, which contributed to the excellent performance.

Many researchers have been devoted to the preparation of hybrid structures that affected properties such as grain boundary barrier, energy band, carrier concentration, and depletion layer, thus improving the performance of gas sensing. For instance, the Au nanoparticle with a larger work function than MoO₃ received electrons from MoO₃ nanosheets, leading to the appearance of electron depletion layer at the Au/MoO₃ Schottky junction, and the enhanced ethanol detection capabilities were attributed to the resulting high resistance (Yan et al., 2016). Considering Pt nanoparticles combined MoO₃ nanobelts, the superior selectivity to formaldehyde was conducted, which was ascribed to the catalytic effect of loaded particles on formaldehyde during the surface gas sensing process (Fu et al., 2019). As for the RuO₂ nanoparticles modified MoO₃ nanobelts, oxygen vacancies produced on the surface, creating more adsorption-desorption sites for gas molecules (Wei Q. et al., 2019). With regard to heterostructure, Li et al. (2018) synthesized the CoMoO₄/MoO₃ nanostructure with p-n heterojunction using the dipping-annealing method. The enhancement of the adsorption to oxygen by p-type CoMoO₄ and the barrier formed at the p-n junction were verified to be favorable to the improved gas response.

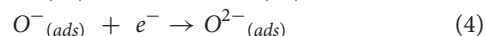
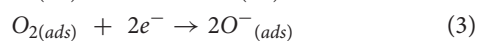
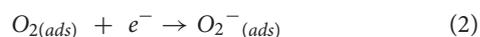
Above all, previous studies have focused on the optimization of MoO₃ through synthesizing different samples with multiple morphologies, the doping of transition metals such as Cr, W, Ag, Au, Fe, Zn, and Ni, and decorating with other nanomaterials (Au nanoparticles, RuO₂ nanoparticles, Fe₂O₃ nanoparticles, CoMoO₄ nanoparticles, NiCo₂O₄ nanosheets, etc.). Thus, in

order to improve the gas sensitivity of MoO₃, many potential materials for the modification of innovative synthesis methods with controllable morphology need to be explored.

GAS-SENSING APPLICATION OF MoO₃

Gas-sensing Mechanism of MoO₃

The theory of sensitivity generated by changes in material resistance during the gas-sensing process has been widely accepted by scholars in the investigation of the gas-sensitive mechanism of metal oxides. As shown in **Figure 1E**, the reaction between the target gas molecules and the adsorbed oxygen ions (O₂⁻, O⁻, O²⁻) on the surface of the gas-sensitive materials leads to the change of the electrical conductivity, which is key to detecting the corresponding response (Li et al., 2015). MoO₃ is an n-type semiconductor with electrons as internal carriers. Mass of oxygen molecules in the air tends to be adsorbed by the MoO₃, forming adsorbed oxygen ions accompanied by the acceptance of electrons from the conduction band of MoO₃. Thus, the electron depletion layer was formed on the surface of MoO₃, which caused the increase of resistance (Ji et al., 2019a). The specific process can be expressed by the following equation:

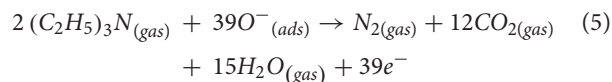


When the MoO₃ sensor was exposed to the atmosphere of the target gas, the adsorbed oxygen ions underwent a reduction

TABLE 1 | Summary of recent researches on MoO₃-based sensors for VOCs detection.

Gas	Sensing material	Concentration (ppm)	Temperature (°C)	Response	References
Formaldehyde	Ni-doped -MoO ₃ nanolamella	100	255	41	Shen et al., 2017
	Pt-decorated MoO ₃ nanobelts	200	27	19.1%	Fu et al., 2019
Methanol	α-MoO ₃ nanorod arrays	500	300	7.8	Cong et al., 2016
	ZnO microcube/MoO ₃ micrograss	500	200	56	Mandal et al., 2018
Ethanol	nanofiber-assembled hierarchical MoO ₃	400	300	32	Ji et al., 2019b
	Au nanoparticles/MoO ₃ nanobelts	500	200	50	Wang et al., 2018
	α-MoO ₃ nanobelts	500	300	80	Mo et al., 2020
	Zn-doped MoO ₃ nanobelts	250	240	52	Yang et al., 2017
Xylene	α-MoO ₃ nanoarrays	1,000	370	83.9	Qin et al., 2017
	Fe-doped α-MoO ₃ nanoarrays	1,000	340	166.3	Wang et al., 2020
	Fe ₂ O ₃ nanoparticles/MoO ₃ nanobelts	100	233.5	22.48	Qu et al., 2019
	Ni-doped MoO ₃ nano-pompon	100	250	62.6	Jiang et al., 2019
Trimethylamine	Ce-doped MoO ₃ nanobelts	50	240	17.4	Li et al., 2017a
	Au nanoparticles/MoO ₃ nanobelts	50	280	70	Zhang et al., 2016
	porous α-MoO ₃ nanosheets	10	133	51.47	Shen et al., 2019
Triethylamine	MoO ₃ nanobelts	50	240	582.3	Yang et al., 2016
	MoO ₃ microsheets	100	275	27.1	Jiang et al., 2018
	α-Fe ₂ O ₃ /α-MoO ₃ nanostructure	50	280	76	Liu et al., 2019
	Cr-doped α-MoO ₃ nanorods	100	200	150.25	Li et al., 2019
	Ag nanoparticles/α-MoO ₃ nanorods	100	200	408.6	He K. et al., 2019

reaction. Further, electrons are released back into the conduction band of MoO₃, and the depletion layer narrows, which results in a decrease in the resistance of the material and completes the whole gas sensing process. Take triethylamine for example, this process can be expressed as the following equation (Wei Q. et al., 2019).



Gas Sensing Properties of MoO₃

Nowadays, many researchers focus on the application of MoO₃ materials in gas sensors, while the ultimate goal of the investigation is to obtain higher performance MoO₃-based sensing materials. Notably, MoO₃ with prominent gas-sensing properties has been proven to be an alternative sensing material to detect VOCs. We summarized the representative research on VOCs detection, which mainly focused on the use of formaldehyde (HCHO), methanol (CH₃OH), ethanol (CH₃CH₂OH), xylene (CH₃C₆H₄CH₃), trimethylamine ((CH₃)₃N), and triethylamine ((C₂H₅)₃N), and listed them in **Table 1**. **Figure 1D** shows the structure diagram of the side heat sensor and the gas-sensing test circuit. The sensing-materials were coated on the alumina ceramic tube. A Ni-Cr resistance wire that could conveniently control the current was inserted in the coating tube and the change of resistances was tested by electrodes. The gas response (S) of MoO₃ based sensors to reducing gas is calculated by $S = R_a/R_g$, while to oxidizing gas it is $S = R_g/R_a$ (Jiang et al., 2019).

CONCLUSION

This mini review focused on the latest advances in synthetic methods, morphological control, functional modification, and gas-sensing application including properties and mechanism of MoO₃ materials in the detection of VOCs. The studies of morphologically-controlled synthesis proved that MoO₃ with a high specific surface area possesses superior gas-sensing

performances and provided reference experience for further MoO₃ gas-sensing material design. Further, appropriate element doping or material hybridization could improve properties of MoO₃, such as energy band gap and adsorbed oxygen content, which is advantageous to the gas sensing process. Scholars have made great efforts to develop more efficient MoO₃-based VOCs sensors and have shown objective achievement, but there are still challenges in practical application. The design of porous structures or hierarchical structures with more reactive gas pathways and reaction sites to further improve the specific surface area of MoO₃ material is an issue that needs to be further explored. In addition, more alternative modification materials should be selected through experimental verification. All of these issues should continue to be addressed to obtain MoO₃-based materials with a higher response, better selectivity, superior stability, and lower operating temperature. Finally, the gas-sensing mechanism was not complete. By combining theoretical calculation and analysis, the changes of electronic properties at the micro level should be analyzed, which will allow for further understanding of the nature of gas sensing and provide guidance for designing MoO₃ materials with better gas-sensing performances in the future.

AUTHOR CONTRIBUTIONS

All authors listed have made a substantial, direct and intellectual contribution to the work, and approved it for publication.

FUNDING

This work has been supported in part by the National Natural Science Foundation of China (No. 51507144), Fundamental Research Funds for the Central Universities (No. XDJJK2019B021), the Chongqing Science and Technology Commission (CSTC) (No. cstc2016jcyjA0400), and the project of China Scholarship Council (CSC).

REFERENCES

- Cho, Y. H., Ko, Y. N., Kang, Y. C., Kim, I. D., and Lee, J. H. (2014). Ultraselective and ultrasensitive detection of trimethylamine using MoO₃ nanoplates prepared by ultrasonic spray pyrolysis. *Sens. Actuat. B Chem.* 195, 189–196. doi: 10.1016/j.snb.2014.01.021
- Chu, X. F., Liang, S. M., Sun, W. Q., Zhang, W. B., Chen, T. Y., and Zhang, Q. F. (2010). Trimethylamine sensing properties of sensors based on MoO₃ microrods. *Sens. Actuat. B Chem.* 148, 399–403. doi: 10.1016/j.snb.2010.05.049
- Cong, S. R., Sugahara, T., Wei, T. T., Jiu, J. T., Hirose, Y., Nagao, S., et al. (2016). Diverse adsorption/desorption abilities originating from the nanostructural morphology of VOC gas sensing devices based on molybdenum trioxide nanorod arrays. *Adv. Mater. Interf.* 3:1600252. doi: 10.1002/admi.201600252
- Fu, X. X., Yang, P. Y., Xiao, X. F., Zhou, D., Huang, R., Zhang, X. H., et al. (2019). Ultra-fast and highly selective room-temperature formaldehyde gas sensing of Pt-decorated MoO₃ nanobelts. *J. Alloy. Compd.* 797, 666–675. doi: 10.1016/j.jallcom.2019.05.145
- He, K., He, S. H., Yang, W., and Tian, Q. F. (2019). Ag nanoparticles-decorated α-MoO₃ nanorods for remarkable and rapid triethylamine-sensing response boosted by pulse-heating technique. *J. Alloy. Compd.* 808:151704. doi: 10.1016/j.jallcom.2019.151704
- He, S. H., Li, W. D., Feng, L., and Yang, W. (2019). Rational interaction between the aimed gas and oxide surfaces enabling high-performance sensor: the case of acidic α-MoO₃ nanorods for selective detection of triethylamine. *J. Alloy. Compd.* 783, 574–582. doi: 10.1016/j.jallcom.2018.12.349
- Ji, H. C., Zeng, W., and Li, Y. Q. (2019a). Assembly of 2D nanosheets into lower-like MoO₃: New insight into the petal thickness affect on gas-sensing properties. *Mater. Res. Bull.* 118:110476. doi: 10.1016/j.materresbull.2019.05.001
- Ji, H. C., Zeng, W., and Li, Y. Q. (2019b). New insight into the gas-sensing properties of nanofiber-assembled and nanosheet-assembled hierarchical MoO₃ structures. *Phys. E.* 114:113646. doi: 10.1016/j.physe.2019.113646
- Jiang, W. H., Meng, L. L., Zhang, S. F., Chuai, X. H., Zhou, Z. J., Hu, C. H., et al. (2019). Design of highly sensitive and selective xylene gas sensor based on Ni-doped MoO₃ nano-pompon. *Sens. Actuat. B Chem.* 299:126888. doi: 10.1016/j.snb.2019.126888

- Jiang, W. H., Wei, D. D., Zhang, S. F., Chuai, X. H., Sun, P., Liu, F. M., et al. (2018). The facile synthesis of MoO₃ microspheres and their excellent gas-sensing performance toward triethylamine: high selectivity, excellent stability and superior repeatability. *New J. Chem.* 42:15111. doi: 10.1039/c8nj03539c
- Kwak, D., Wang, M. J., Koski, K. J., Zhang, L., Sokol, H., Maric, R., et al. (2019). Molybdenum trioxide (α -MoO₃) nanoribbons for ultrasensitive ammonia (NH₃) gas detection: integrated experimental and density functional theory simulation studies. *ACS Appl. Mater. Interf.* 11, 10697–10706. doi: 10.1021/acsami.8b20502
- Li, T. M., Zeng, W., Zhang, Y. Y., and Hussain, S. (2015). Nanobelt-assembled nest-like MoO₃ hierarchical structure: hydrothermal synthesis and gas-sensing properties. *Mater. Lett.* 160, 476–479. doi: 10.1016/j.matlet.2015.08.031
- Li, W. D., He, S. H., Feng, L., and Yang, W. (2019). Cr-doped α -MoO₃ nanorods for the fast detection of triethylamine using a pulse-heating strategy. *Mater. Lett.* 250, 143–146. doi: 10.1016/j.matlet.2019.05.006
- Li, Y. Q. (2017). Morphology-controllable synthesis of three-dimensional α -MoO₃ and their applications in gas sensing. *Phys. E* 94, 22–24. doi: 10.1016/j.physe.2017.07.010
- Li, Z. Q., Song, P., Yang, Z. X., and Wang, Q. (2018). *In situ* formation of one-dimensional CoMoO₄/MoO₃ heterojunction as an effective trimethylamine gas sensor. *Ceram. Int.* 44, 3364–3370. doi: 10.1016/j.ceramint.2017.11.126
- Li, Z. Q., Wang, W. J., Zhao, Z. C., Liu, X. R., and Song, P. (2017a). One-step hydrothermal preparation of Ce-doped MoO₃ nanobelts with enhanced gas sensing Properties. *RSC Adv.* 7:28366. doi: 10.1039/c7ra02893h
- Li, Z. Q., Wang, W. J., Zhao, Z. C., Liu, X. R., and Song, P. (2017b). Facile synthesis and enhanced trimethylamine sensing performances of W doped MoO₃ nanobelts. *Mat. Sci. Semicond. Proc.* 66, 33–38. doi: 10.1016/j.mssp.2017.04.002
- Liu, C. Y., Xu, H. Y., Chen, Z. R., Ye, Q., Wu, X. W., Wang, J. Q., et al. (2019). Enhanced triethylamine sensing properties by designing an α -Fe₂O₃/ α -MoO₃ nanostructure directly grown on ceramic tubes. *ACS Appl. Nano Mater.* 2, 6715–6725. doi: 10.1021/acsanm.9b01630
- Liu, Y. L., Yang, S., Lu, Y., Podval'naya, N. V., Chen, W., and S., et al. (2015). Hydrothermal synthesis of h-MoO₃ microrods and their gas sensing properties to ethanol. *Appl. Surf. Sci.* 359, 114–119. doi: 10.1016/j.apsusc.2015.10.071
- Lu, Z. R., Zhou, Q., Wang, C. S., Wei, Z. J., Xu, L. N., and Gui, Y. G. (2018). Electrospun ZnO–SnO₂ composite nanofibers and enhanced sensing properties to SF₆ decomposition byproduct H₂S. *Front. Chem.* 6:540. doi: 10.3389/fchem.2018.00540
- Mandal, B., Aaryashree, D., as, M., Htay, M. T., and Mukherjee, S. (2019). Architecture tailoring of MoO₃ nanostructures for superior ethanol sensing performance. *Mater. Res. Bull.* 109, 281–290. doi: 10.1016/j.materresbull.2018.09.041
- Mandal, B., Aaryashree, Singh, R., and Mukherjee, S. (2018). Highly selective and sensitive methanol sensor using rose-like ZnO microcube and MoO₃ micrograss-based composite. *IEEE Sens. J.* 18, 2659–2666. doi: 10.1109/JSEN.2018.2803682
- Mo, Y. F., Tan, Z. P., Sun, L. P., Lu, Y. B., and Liu, X. Z. (2020). Ethanol-sensing properties of α -MoO₃ nanobelts synthesized by hydrothermal method. *J. Alloy. Compd.* 812:152166. doi: 10.1016/j.jallcom.2019.152166
- Mousavi-Zadeh, S. H., and Rahmani, M. B. (2018). Synthesis and ethanol sensing characteristics of nanostructured MoO₃: Zn thin films. *Surf. Rev. Lett.* 25:11850046. doi: 10.1142/S0218625X18500464
- Pandeeswari, R., and Jeyaprakash, B. G. (2014). Nanostructured α -MoO₃ thin film as a highly selective TMA sensor. *Biosens. Bioelectron.* 53, 182–186. doi: 10.1016/j.bios.2013.09.057
- Qin, H. Y., Cao, Y. L., Xie, J., Xu, H., and Jia, D. Z. (2017). Solid-state chemical synthesis and xylene-sensing properties of α -MoO₃ arrays assembled by nanoplates. *Sens. Actuat. B Chem.* 242, 769–776. doi: 10.1016/j.snb.2016.11.081
- Qu, F. D., Zhou, X. X., Zhang, B. X., Zhang, S. D., Jiang, C. J., Ruan, S. P., et al. (2019). Fe₂O₃ nanoparticles-decorated MoO₃ nanobelts for enhanced chemiresistive gas sensing. *J. Alloy. Compd.* 782, 672–678. doi: 10.1016/j.jallcom.2018.12.258
- Sau, S., Chakraborty, S., Das, T., and Pal, M. (2019). Ethanol sensing properties of nanocrystalline α -MoO₃. *Front. Mater.* 6:285. doi: 10.3389/fmats.2019.00285
- Shen, J. L., Guo, S. J., Chen, C., Sun, L., Wen, S. P., Chen, Y., et al. (2017). Synthesis of Ni-doped-MoO₃ nanolamella and their improved gas sensing properties. *Sens. Actuat. B Chem.* 252, 757–763. doi: 10.1016/j.snb.2017.06.040
- Shen, S. K., Zhang, X. F., Cheng, X. L., Xu, Y. M., Gao, S., Zhao, H., et al. (2019). Oxygen-vacancy-enriched porous α -MoO₃ nanosheets for trimethylamine sensing. *ACS Appl. Nano Mater.* 2, 8016–8026. doi: 10.1021/acsanm.9b02072
- Sui, L. L., Xu, Y. M., Zhang, X. F., Cheng, X. L., Gao, S., Zhao, H., et al. (2015). Construction of three-dimensional flower-like-MoO₃ with hierarchical structure for highly selective triethylamine sensor. *Sens. Actuat. B Chem.* 208, 406–414. doi: 10.1016/j.snb.2014.10.138
- Wang, J. X., Zhou, Q., Lu, Z. R., Wei, Z. J., and Zeng, W. (2019a). Gas sensing performances and mechanism at atomic level of Au-MoS₂ microspheres. *Appl. Surf. Sci.* 490, 124–136. doi: 10.1016/j.apsusc.2019.06.075
- Wang, J. X., Zhou, Q., Lu, Z. R., Wei, Z. J., and Zeng, W. (2019b). The novel 2D honeycomb-like NiO nanoplates assembled by nanosheet arrays with excellent gas sensing performance. *Mater. Lett.* 255:26523. doi: 10.1016/j.matlet.2019.12.6523
- Wang, J. X., Zhou, Q., and Zeng, W. (2019c). Competitive adsorption of SF₆ decompositions on Ni-doped ZnO (100) surface: computational and experimental study. *Appl. Surf. Sci.* 479, 185–197. doi: 10.1016/j.apsusc.2019.01.255
- Wang, L. W., Wang, S. P., Fu, H., Wang, Y. H., and Yu, K. F. (2018). Synthesis of Au nanoparticles functionalized 1D α -MoO₃ nanobelts and their gas sensing properties. *NANO: Brief Rep. Rev.* 13:1850115. doi: 10.1142/S1793292018501151
- Wang, S. Q., Xie, J., Hu, J. D., Qin, H. Y., and Cao, Y. L. (2020). Fe-doped α -MoO₃ nanoarrays: Facile solid-state synthesis and excellent xylene-sensing performance. *Appl. Surf. Sci.* 512:145722. doi: 10.1016/j.apsusc.2020.145722
- Wei, Q., Song, P., Li, Z. Q., Yang, Z. X., and Wang, Q. (2019). Enhanced triethylamine sensing performance of MoO₃ nanobelts by RuO₂ nanoparticles decoration. *Vacuum* 162, 85–91. doi: 10.1016/j.vacuum.2019.01.028
- Wei, Z. J., Zhou, Q., Wang, J. X., Lu, Z. R., Xu, L. N., and Zeng, W. (2019). Hydrothermal synthesis of SnO₂ nanoneedle-anchored NiO microsphere and its gas sensing performances. *Nanomaterials* 9:1015. doi: 10.3390/nano9071015
- Wei, Z. J., Zhou, Q., and Zeng, W. (2020). Hierarchical WO₃-NiO microflower for high sensitivity detection of SF₆ decomposition byproduct H₂S. *Nanotechnology* 31:215701. doi: 10.1088/1361-6528/ab73bd
- Xia, Y. C., Wu, C. S., Zhao, N. Y., and Zhang, H. (2016). Spongy MoO₃ hierarchical nanostructures for excellent performance ethanol sensor. *Mater. Lett.* 171, 117–120. doi: 10.1016/j.matlet.2015.12.159
- Xiao, S. H., Liu, B., Zhou, R., Liu, Z. W., Li, Q. H., and Wang, T. H. (2018). Room-temperature H₂ sensing interfered by CO based on interfacial effects in palladium-tungsten oxide nanoparticles. *Sens. Actuat. B Chem.* 254, 966–972. doi: 10.1016/j.snb.2017.07.169
- Xu, K., Wei, W. Y., Sun, Y., Lu, W. H., Yu, T., Yang, Y., et al. (2019). Design of NiCo₂O₄ porous nanosheets/ α -MoO₃ nanorods heterostructures for ppb-level ethanol detection. *Powder Technol.* 345, 633–642. doi: 10.1016/j.powtec.2019.01.051
- Yan, H. H., Song, P., Zhang, S., Zhang, J., Yang, Z. X., and Wang, Q. (2016). Au nanoparticles modified MoO₃ nanosheets with their enhanced properties for gas sensing. *Sens. Actuat. B Chem.* 236, 201–207. doi: 10.1016/j.snb.2016.05.139
- Yang, S. A., Liu, Y. L., Chen, T., Jin, W., Yang, T. Q., Cao, M. C., et al. (2017). Zn doped MoO₃ nanobelts and the enhanced gas sensing properties to ethanol. *Appl. Surf. Sci.* 393, 377–384. doi: 10.1016/j.apsusc.2016.10.021
- Yang, S. A., Liu, Y. L., Chen, W., Jin, W., Zhou, J., Zhang, H., et al. (2016). High sensitivity and good selectivity of ultralong MoO₃ nanobelts for trimethylamine gas. *Sens. Actuat. B Chem.* 226, 478–485. doi: 10.1016/j.snb.2015.12.005
- Yang, S. L., Wang, Z., Hu, Y. M., Cai, Y. X., Huang, R., Li, X. X., et al. (2018). Defect-original room-temperature hydrogen sensing of MoO₃ nanoribbon: experimental and theoretical studies. *Sens. Actuat. B Chem.* 260, 21–32. doi: 10.1016/j.snb.2017.12.166
- Zhang, D. Z., Jiang, C. X., and Wu, J. F. (2018). Layer-by-layer assembled In₂O₃ nanocubes/flower-like MoS₂ nanofilm for room temperature formaldehyde sensing. *Sens. Actuat. B Chem.* 273, 176–184. doi: 10.1016/j.snb.2018.06.044
- Zhang, F. D., Dong, X., Cheng, X. L., Xu, Y. M., Zhang, X. F., and Huo, L. H. (2019). Enhanced gas-sensing properties for trimethylamine at low temperature based on MoO₃/Bi₂MO₃O₁₂ hollow microspheres. *ACS Appl. Mater. Interfaces* 11, 11755–11762. doi: 10.1021/acsami.8b22132
- Zhang, J., Song, P., Li, J., Yang, Z. X., and Wang, Q. (2017). Template-assisted synthesis of hierarchical MoO₃ microboxes and their high

- gas-sensing performance. *Sens. Actuat. B Chem.* 249, 458–466. doi: 10.1016/j.snb.2017.04.137
- Zhang, J., Song, P., Li, Z. Q., Zhang, S., Yang, Z. X., and Wang, Q. (2016). Enhanced trimethylamine sensing performance of single-crystal MoO₃ nanobelts decorated with Au nanoparticles. *J. Alloy. Compd.* 685, 1024–1033. doi: 10.1016/j.jallcom.2016.06.257
- Zhang, Q. Y., Zhou, Q., Lu, Z. R., Wei, Z. J., Xu, L. N., et al. (2018). Recent advances of SnO₂-based sensors for detecting fault characteristic gases extracted from power transformer oil. *Front. Chem.* 6:364. doi: 10.3389/fchem.2018.00364
- Zhou, Q., Chen, W. G., Xu, L. N., Kumar, R., Gui, Y. G., Zhao, Z. Y., et al. (2018a). Highly sensitive carbon monoxide (CO) gas sensors based on Ni and Zn doped SnO₂ nanomaterials. *Ceram. Int.* 44, 4392–4399. doi: 10.1016/j.ceramint.2017.12.038
- Zhou, Q., Umar, A., Sodki, E., Amine, A., Xu, L. N., and Gui, Y. G. (2018b). Fabrication and characterization of highly sensitive and selective sensors based on porous NiO nanodisks. *Sens. Actuat. B Chem.* 259, 604–615. doi: 10.1016/j.snb.2017.12.050
- Zhou, Q., Xu, L. N., Umar, A., Chen, W. G., and Kumar, R. (2018c). Pt nanoparticles decorated SnO₂ nanoneedles for efficient CO gas sensing applications. *Sens. Actuat. B Chem.* 256, 656–664. doi: 10.1016/j.snb.2017.09.206
- Zhou, Q., Zeng, W., Chen, W. G., Xu, L. N., Kumar, R., and Umar, A. (2019). High sensitive and low-concentration sulfur dioxide (SO₂) gas sensor application of heterostructure NiO-ZnO nanodisks. *Sens. Actuat. B Chem.* 298:126870. doi: 10.1016/j.snb.2019.126870
- Zhou, Q., Zhang, Q. Y., Liu, H. C., Hong, C. X., Wu, G. L., Peng, S. D., et al. (2017). Research on gas sensing properties of orthorhombic molybdenum oxide based sensor to hydrogen sulfide. *J. Nanoelectr. Optoelectr.* 12, 1072–1076. doi: 10.1166/jno.2017.2119
- Zhu, L., Zeng, W., Li, Y. Q., and Yang, J. D. (2019). Enhanced ethanol gas-sensing property based on hollow MoO₃ microcages. *Phys. E* 106, 170–175. doi: 10.1016/j.physe.2018.10.038
- Zhu, L., Zeng, W., Li, Y. Q., and Zhang, H. (2018). Novel hollow MoO₃ cage structure and its gas sensing property. *Mater. Lett.* 229, 269–271. doi: 10.1016/j.matlet.2018.07.054

Conflict of Interest: The authors declare that the research was conducted in the absence of any commercial or financial relationships that could be construed as a potential conflict of interest.

Copyright © 2020 Wang, Zhou, Peng, Xu and Zeng. This is an open-access article distributed under the terms of the Creative Commons Attribution License (CC BY). The use, distribution or reproduction in other forums is permitted, provided the original author(s) and the copyright owner(s) are credited and that the original publication in this journal is cited, in accordance with accepted academic practice. No use, distribution or reproduction is permitted which does not comply with these terms.



Metal Oxides-Based Semiconductors for Biosensors Applications

Ionel Șerban and Alexandru Enesca*

Product Design, Mechatronics and Environmental Department, Transilvania University of Brasov, Brasov, Romania

The present mini review contains a concessive overview on the recent achievement regarding the implementation of a metal oxide semiconductor (MOS) in biosensors used in biological and environmental systems. The paper explores the pathway of enhancing the sensing characteristics of metal oxides by optimizing various parameters such as synthesis methods, morphology, composition, and structure. Four representative metal oxides (TiO_2 , ZnO , SnO_2 , and WO_3) are presented based on several aspects: synthesis method, morphology, functionalizing molecules, detection target, and limit of detection (LOD).

Keywords: metal oxides, semiconductors, nanostructures, energy bands, biosensors

INTRODUCTION

Biosensors represent key components in medical care, environmental processes, energy efficient systems, food safety, chemical, and agricultural industries. The necessity of using continuous onsite monitoring with flexible and reliable characteristics have recommended biosensors as an efficient tool for rapid measurement and analysis. Adapting the biosensors materials to various applications (quality control, screening methods, safety equipment, environmental evaluation) represents an important research topic with difficult challenges to overcome. In the last decade there were many papers presenting materials such as photonic crystals (Hocini et al., 2019), polymers (Gupta et al., 2020), graphene (Yuan et al., 2019), metals (Rezaei et al., 2019), transition metal dichalcogenides (Wang et al., 2017), and metal organic frameworks (Osman et al., 2019) as suitable for biosensors applications. Some of these materials require significant improvement regarding morphologic optimization, chemical stability, compatibility with different biomolecules, and increase of LOD.

A particular case is represented by MOS materials. These have a high potential to become highly competitive materials in the biosensors market, based on their morphologic versatility (Song et al., 2020), chemical stability (Hernández-Cancel et al., 2015), physicochemical interfacial properties (Scognamiglio et al., 2019), and their ability to combine in composite structures (Zheng et al., 2020). Among others, TiO_2 (Wang M. et al., 2019), WO_3 (Liu et al., 2015), SnO_2 (Dong and Zheng, 2014), and ZnO (Zhang et al., 2019) have attracted considerable attention due to their electrochemical sensitive properties (Enesca et al., 2012a) and energy band alignment (Enesca et al., 2012b) suitable for enzyme based biosensors. Another advantage of these materials is represented by a large number of cost effective synthesis methods such as co-precipitation (Dong and Zheng, 2014), sonochemical precipitation (Zhou et al., 2013), thermal oxidation (Li et al., 2010), chemical etching (Liu et al., 2010), polyol (Elahi et al., 2019), hydrothermal (Zhou et al., 2017), or sol-gel (Rathinamala et al., 2019) allowing the formation of various morphologies such as porous quasi-nanospheres (Liu H. et al., 2017), hollow nano-spheres (Santos et al., 2016), nanorods (Dong et al., 2017), nanosheets (Zhang et al., 2020), or flower-like particles (Feng et al., 2018). Additionally, these materials can be combined between them or with others to form tandem heterostructures (Enesca et al., 2015), hybrid structures (Mihaly et al., 2008), or composite structures (Visa et al., 2016) with advanced electrochemical properties which can be adapted to a specific biosensor application.

OPEN ACCESS

Edited by:

Liwei Wang,
Guangxi University, China

Reviewed by:

Zhongqiu Hua,
Hebei University of Technology, China

Liping Gao,
Chuzhou University, China

*Correspondence:

Alexandru Enesca
aenesca@unitbv.ro

Specialty section:

This article was submitted to
Nanoscience,
a section of the journal
Frontiers in Chemistry

Received: 04 February 2020

Accepted: 06 April 2020

Published: 19 May 2020

Citation:

Șerban I and Enesca A (2020) Metal
Oxides-Based Semiconductors for
Biosensors Applications.
Front. Chem. 8:354.
doi: 10.3389/fchem.2020.00354

MOS with multifunctional properties able to monitor molecules from biological systems represent a step forward in the development of more complex autonomous medical decision-making systems. Enzyme-based biosensors containing MOS have several advantages such as: (1) chemical stability in various environments (Zheng et al., 2020), (2) high energy efficiency (Solaimuthu et al., 2020), (3) good sensitivity (Yi et al., 2020), and (4) adaptability to specific working conditions (Han et al., 2019). There are several issues to overcome in order to implement MOS in biosensing applications: organic/inorganic interface compatibility, increasing the carrier charge mobility, decreasing electron-hole recombinations, and finding facile synthesis techniques.

The present mini review represents a synthesis of the recent achievement of the implementation and optimization of MOS used as biosensor components in biological and environmental systems. The paper is focused on various methods of enhancing the metal oxides' sensing characteristics by optimizing parameters such as synthesis methods, morphology, composition, and structure.

THE MECHANISM OF ENZYME-BASED BIOSENSORS

A biosensor structure (see **Figure 1**) can be broken down in a biotransducer and its auxiliary signal processing elements (Yin et al., 2018). The biotransducer is made up of a biocompatible layer that has biological recognition entities (enzymes, probe molecules, proteins, etc.) attached to the transducer surface. These entities induce a physicochemical interaction between the target analyte and the transducer, sending signal impulses to the signal processor. An important challenge represents the compatibility between metal oxide inorganic materials with the organic material Wang Q. et al., 2019; Yilmaz et al., 2020. In this sense MOS (i.e., TiO_2 , WO_3 , SnO_2 , ZnO) functionalization in order to increase the compatibility with the organic materials has attracted much interest. The metal oxide semiconductors present some advantages regarding biomolecule immobilizations, such as: (a) high isoelectric point (IEP) which induces electrostatic attraction forces with many lower electrostatic point biomolecules (Ramon-Marquez et al., 2018; Zhao et al., 2019) and (b) morphological versatility exhibited by a high surface area-to-volume ratio characteristic for nanomaterials and favorable for enzyme immobilization, (Fiorani et al., 2019).

Most of the metal oxides materials used in biosensors are wide band gap semiconductors (see **Figure 1**) consisting of various crystalline structures, unique electrochemical, optical, electronic, gravimetric, pyroelectric, and piezoelectric properties (Huang et al., 2016). Surface potential represents an important property in the biosensor application. The space charge effect is a result of native and imposed semiconductor potential. The bulk chemical composition, crystallization degree, and chemical interaction between semiconductor surface and the analyte will influence the displacement of Fermi energy and induced depletion (Cao et al., 2020). Consequently, the surface

potential inducing the space charge double layer is directly dependent on the adsorbed layer characteristics of the electrode surface (Chen et al., 2019). Additionally, some of these materials may exhibit super hydrophobicity/phobicity, self-cleaning and antimicrobial activity. Other factors such as light exposure at certain wavelengths (~ 380 nm for TiO_2 and ZnO , ~ 320 nm for SnO_2 and ~ 443 nm for WO_3) induce an increase of charge carrier mobility. During the light irradiation, oxygen vacancies are formed at the semiconductor surface, which can forward develop oxidative species (Ge et al., 2019).

An important advantage in the metal oxides semiconductor functionalization for biosensor application is represented by the low toxicity and low probability of negative interference with the common pharmaceutical compounds (Soldatkina et al., 2018). The major functionalization methodologies are based on covalent interactions (Feizabadi et al., 2019) but non-covalent interactions have been used as well (Ortiz et al., 2019). The covalent conjugation can be done using different molecules such as dimercaptosuccinic acid (DMSA), 1-ethyl-3-(3-dimethylaminopropyl) carbodiimide, (EDC), N-(15-carboxypentadecanoyloxy) succinimide, 16-(2-pyridyldithiol) hexadecanoic acid, etc. During the functionalization the MOS became more stable and reduced the nanoparticles aggregation, (Xu et al., 2020). After functionalization many analytes can be used as detecting materials for: urea, immunoglobulin, DNA, RNA, dopamine, cancer cells, viruses, etc.

The interactions between the bio-transducer and the analytes will alter the physico-chemical surface semiconductor characteristics. The surface potential, impedance or current characteristics can be correlated with the specific chemical stimuli induced by the analytes (Yoo et al., 2019). Various techniques are based on these characteristics, such as cyclic voltametry, impedimetric, differential pulse voltametry, etc.

The fidelity of the results from such a biosensor are however heavily influenced by the environmental factors of the experiment, such as temperature, humidity, pH, presence of oxygen, and foreign organic compounds, all of which can affect the stability of the interface. The applications of such biosensors spread across all domains, depending on the possible interactions between the immobilized biomolecules (enzymes, antibodies, DNA) and the analytes of interest.

METAL OXIDE SEMICONDUCTORS FOR ENZYME-BASED BIOSENSORS

There are various MOS's used in biosensor applications. The majority part use mono-component semiconductors but there are many papers (Oh et al., 2013; Kao et al., 2015) presenting multi-component semiconductors or coupled semiconductors (composite, tandem, heterostructures, etc.). Additionally, in order to enhance certain properties these materials have been coupled with metals nanoparticles or doped with other metal ions. The MOS exhibit a multitude of morphologies such as: rods, stars, flowers, cone, porous or dense films, etc. This mini review will consider only four metal oxides (TiO_2 , SnO_2 , ZnO ,

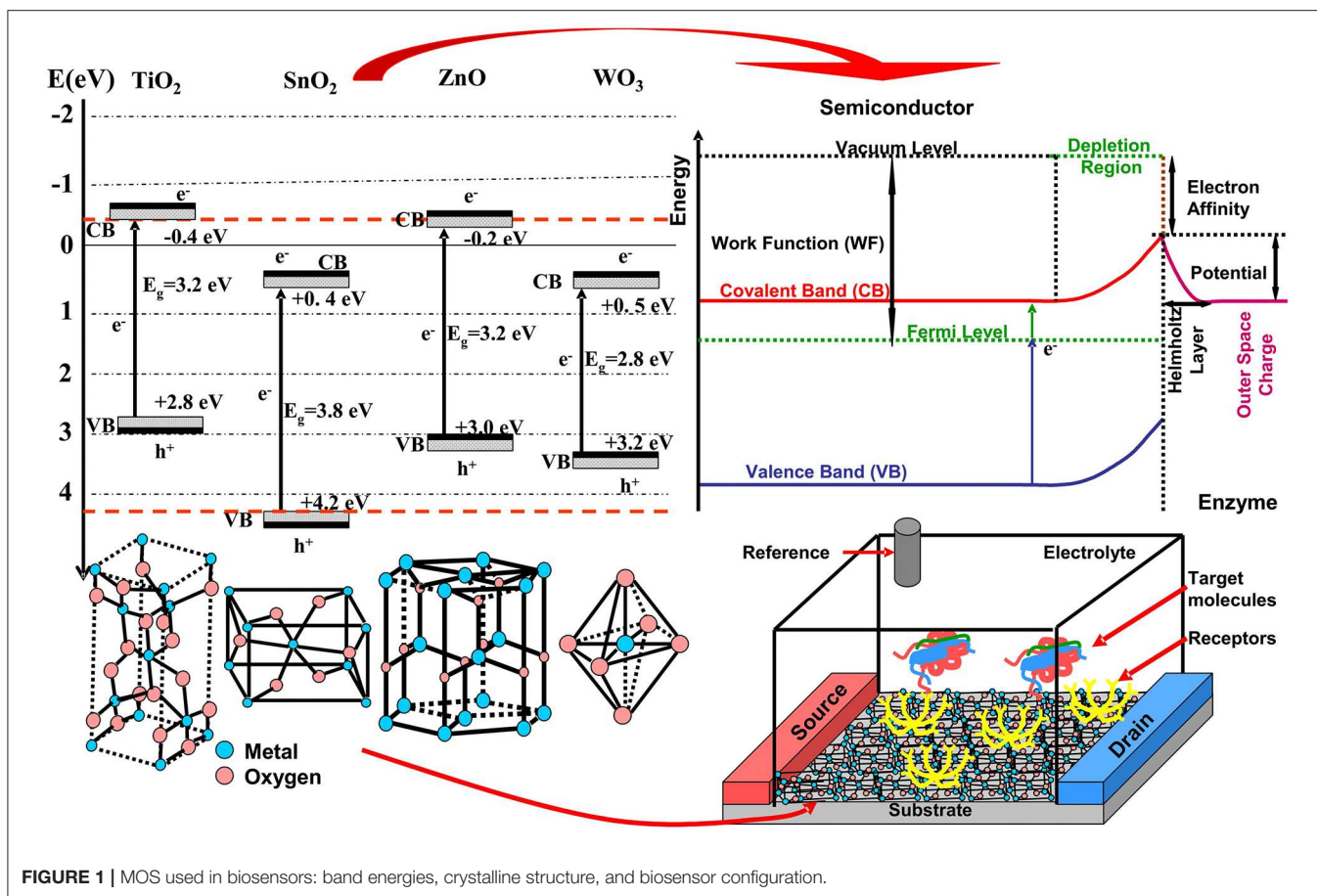


FIGURE 1 | MOS used in biosensors: band energies, crystalline structure, and biosensor configuration.

and WO_3) as representative for biosensor applications. Many other papers which are not included here have the potential to contain highly innovative work. A summarized data collection containing the four metal oxides is presented in **Table 1**.

TiO₂-based Biosensors

TiO₂ is an n-type semiconductor considered as a key material in many applications like photocatalysis, biosensors, photovoltaics, or energy storage due to his properties such as high chemical stability, biocompatibility, morphological versatility, etc.

Dip-coating technique was employed to obtain TiO₂ films serving as sensors for microRNA (Wang M. et al., 2019), heme (Çakiroglu and Özacar, 2019), or glucose (Rajendran et al., 2018). The microRNA sensor is based on black TiO₂ deposited on indium tin oxide (ITO) substrate and improved with Au nanoparticles. The semiconductor was functionalized with histostar antibodies and based on photocurrent measurements the LOD was established at 0.13 fM. Photocurrent was used for LOD evaluation of heme using TiO₂/ITO sensitized with CdS quantum dots, and the result was 19 μM . The glucose detector based on TiO₂ film was functionalized with glucose oxidase (GOx) and the LOD was 0.7 μM . A better LOD value (0.5 μM) in glucose detection was obtained by replacing the TiO₂ films with TiO₂ nanotubes (Zhu et al., 2015). The nanotubes were developed using the hydrothermal method and functionalized

with GOx. TiO₂ nanorods (Yang et al., 2014) and nanosheets (Liu P. et al., 2017) were tested as glucose sensors after functionalizing with GO. Better LOD was obtained for nanorods morphology (0.002 mM) comparing with nanosheets (0.01 mM) mostly due to higher surface coverage, which was 3.32×10^{-11} mol/cm. Concluding, the LOD depends mostly on the active surface, which explains why nanotubes give better results compared with TiO₂ films.

TiO₂ was used for H₂O₂ detection in the form of microspheres (Liu H. et al., 2017) or macro-mesoporous film (Wu et al., 2018). The TiO₂ microspheres with a bag-like structure were hydrothermally obtained and functionalized with hemoglobin (Hem). The amperometric measurements indicate a LOD of 10 nM. This value is considerably lower compared with TiO₂ mesoporous films (1.65 μM LOD) obtained by doctor blade technique and functionalized with horseradish peroxidase (HPOx).

Anodization of titanium was intensively used to obtain TiO₂ nanotubes for H₂O₂ (Kafi et al., 2011), cholesterol (Khaliq et al., 2020) and breast cancer cell (Safavipour et al., 2020) detection. When the TiO₂ nanotubes were functionalized with Hem the LOD evaluated by amperometry was 0.08 μM . Better LOD value was obtained for cholesterol detection (0.05 μM) based on a non-enzymatic approach to the oxidation process. Finally, TiO₂ nanotubes were

TABLE 1 | Representative studies on metal oxide semiconductors used in biosensors.

Synthesis method/morphology	Target detecting substance	Testing method/LOD	References
TiO₂			
Dip-coating/Porous thin film	microRNA	Photocurrent/0.13 fM	Wang M. et al., 2019
	Heme	Photocurrent/19 µM	Çakiroglu and Özacar, 2019
	Glucose	Amperometric/0.7 µM	Rajendran et al., 2018
Dip-coating/nanorods	Glucose	CV/0.002 mM	Yang et al., 2014
Solvothermal/nanosheets		Photocurrent/0.01 mM	Liu P. et al., 2017
Hydrothermal/nanotube		DPV/0.5 µM	Zhu et al., 2015
Doctor blade/porous film	H ₂ O ₂	CV/1.65 µM	Wu et al., 2018
Hydrothermal/microsphere		Amperometric/10 nM	Liu H. et al., 2017
Anodization/nanotubes	H ₂ O ₂	Amperometric/0.08 µM	Kafi et al., 2011
	Cholesterol	CV/0.05 µM	Khaliq et al., 2020
	Cancer cells	Impedance/40 cells/mL	Safavipour et al., 2020
SnO₂			
Precipitation/nanoparticles	L-cysteine	Chronoamperometric/ 0.03 µM	Dong and Zheng, 2014
Sonication/nanoparticles	Methyl parathion	CV/ 5 × 10 ⁻¹⁴ M	Zhou et al., 2013
	Carbofuran	5 × 10 ⁻¹³ M	
Thermal evaporation/nanowires	H ₂ O ₂	Impedance/0.8 µM	Li et al., 2010
Microwave irradiation/nanoparticles		DPV/43 nM	Lavanya et al., 2012
Electrospinning/nanowires	Glucose	Amperometry/1.8 µM	Alim et al., 2019
	Acetaminophen	DPV/ 0.086 µM	Hu et al., 2019
	pHydroxyacetophenone	0.033 µM	
Physical vapor deposition/nanobelt	Cardiac troponin	Fluorescence microscopy/100 pM	Cheng et al., 2011
Hydrothermal/nanosheets	Amyloid β-protein	Photocurrent/ 0.17 pg/mL	Wang et al., 2018
ZnO			
Chemical bath deposition/nanostars	microRNA-21	CV/18.6 aM	Zhang et al., 2019
Chemical bath deposition/nanoparticles	Zika virus	CV/1.00 pg/mL	Faria and Mazon, 2019
Hydrothermal/nanocones	Dopamine	CV/0.04 µM	Yuea et al., 2020
Hydrothermal/nanorods	Phosphate	CV/0.5 µM	Ahmad et al., 2017
	G Immunoglobuline	DPV/0.03 ng/mL	Dong et al., 2017
	Glucose	DPV/1.0 µM	Zong and Zhu, 2018
Hydrothermal/nanoparticles	Glucose	CV/50 µM	Lei et al., 2011
WO₃			
Simple casting/nanowires	Nitrite	Amperometry/ 0.28 µM	Liu et al., 2015
Hydrothermal/nanoparticles		CV/5 µM	Santos et al., 2016
Simple reversible redox/nanosheets	Epididymal protein 4	Colorimetric/ 1.56 pg/mL	Zhang et al., 2020
Ultrasonic/nanosheets	Xanthine	Colorimetric/ 1.24 µmol/L	Li et al., 2019
Hydrothermal/Flower-like	Aflatoxin B1	Photoelectrochemical/0.28 pg/mL	Feng et al., 2018
Hydrothermal/nanorods	Bisphenol A	DPV/0.028 µM	Zhou et al., 2017
Hydrothermal/nanocomposite	Cardiac biomarker Troponin I (cTnI)	DPV/0.01 ng/mL	Sandil et al., 2018

functionalized with human mucin-1 aptamers, inducing sensitive electrochemical detection of breast cancer cells (MCF-7). In this case the 40 cells/mL LOD represent an encouraging result for future biomedical TiO₂ application in breast cancer detection.

SnO₂-based Biosensors

Due to features such as high surface area, good biocompatibility, nontoxicity, excellent chemical stability, and catalytic activity, SnO₂ was used in many applications such as light energy conversion, biosensors, smart windows, and electrochemistry.

Tin oxide is an n-type semiconductor with a wide band gap of 3.8 eV and rutile structure (see **Figure 1**).

SnO₂ nanoparticles were synthesized by precipitation (Dong and Zheng, 2014), sonication (Zhou et al., 2013) and microwave irradiation (Lavanya et al., 2012). By using precipitation method, the SnO₂ nanoparticles have an average diameter of 4 nm and were used for L-cysteine detection. In order to employ the chronoamperometric detection method, the SnO₂ surface was coated with multiwall carbon nanotubes giving a LOD of 0.03 μM. The SnO₂ nanoparticles obtained by sonication methods were used for pesticide detection based on acetylcholinesterase as a functionalize agent. The LOD evaluated by cyclic voltammetry (CV) was 5×10^{-14} for methyl parathion and 5×10^{-13} for carbofuran. The microwave irradiation method was employed to obtain SnO₂ nanoparticles with application for H₂O₂ detection. SnO₂ surface was functionalized with HPOx and, based on differential pulse voltammetry (DPV), a LOD of 43 nM was obtained.

An H₂O₂ sensor was developed using SnO₂ nanowires synthesized by the thermal evaporation method (Li et al., 2010). Using the same functionalizing molecule as SnO₂ nanoparticles, the LOD measured by CV was 0.8 μM. SnO₂ nanowires were also obtained by the electrospinning method (Alim et al., 2019) for glucose amperometric detection. In this case the functionalizing procedure was done with both HPOx and GOx, giving a LOD of 1.8 μM. SnO₂ nanobelts (Cheng et al., 2011) and nanosheets (Wang et al., 2018) were obtained by physical evaporation deposition, respectively using hydrothermal methods. The nanobelts functionalized with D-biotin molecules were successfully used as a troponin I detector, a protein marker for myocardial infarction (100 pM LOD). The nanosheets were used for amyloid β-protein (Aβ) detection after a previous functionalizing procedure with anti-Aβ antibody. Based on photocurrent measurements the LOD value was 0.17 pg/mL, considered as promising for applications in the detection of disease-related biomarkers.

ZnO-based Biosensors

ZnO is a direct wide band gap semiconductor which under UV radiation exhibits n-type conductivity. During the crystallization forms a hexagonal wurtzite structure (see **Figure 1**) which has particular piezoelectric properties based on noncentrosymmetric crystal structures. The major part of the ZnO synthesis procedures are wet techniques. Compared with tin oxide, ZnO has a better binding ability with biological entities, which is a prerequisite for future biosensor applications in medicine. Due to its nontoxicity and compatibility with human skin, ZnO can be adapted as a permanent human sensor in chronic diseases such as diabetes.

Chemical bath deposition (CBD) has been used (Zhang et al., 2019) to obtain ZnO nanostars for detecting microRNA-21 in cancer cells. Previously, the surface was functionalized using thiol-modified hairpin and hybridization chain reactions, considering the development of electrochemiluminescence (ECL) biosensors. The LOD was evaluated at 18.6 aM, which makes this material a good candidate for clinical bioassay. The same technique was also employed (Faria and Mazon, 2019)

to develop ZnO nanoparticles for detection of Zika virus in undiluted urine. The Zika virus is transmitted through mosquito bites and gives symptoms such as headaches, arthralgia, myalgia, or conjunctivitis (Faria and Mazon, 2019). The ZIKV-NS1 antibody was immobilized using cystamine and glutaraldehyde on the ZnO nanoparticles. The LOD was evaluated using CV and the result was 1.00 pg/mL. This MOS biosensor can be used in early detection of the Zika virus.

Another technique that has been extensively used for ZnO synthesis with biosensing application is the hydrothermal procedure. Both ZnO nanorods (Zong and Zhu, 2018) and nanoparticles (Lei et al., 2011) hydrothermally obtained were used in biosensors for glucose detection. The ZnO nanorods where functionalized with GOx by simple immersion and the LOD via DPV was 1.0 μM. These results are significantly better compared with ZnO nanopowder functionalized with GOx, where LOD was 50 μM. ZnO nanorods where hydrothermally obtained and used as sensors for phosphate (Ahmad et al., 2017) and G Immunoglobuline (Dong et al., 2017) detection. For phosphate detection the ZnO was functionalized with pyruvate oxidase by immersion, and the LOD was 0.5 μM. In order to develop a G Immunoglobuline sensor with 0.03 ng/mL LOD, the ZnO surface was functionalized with myoglobin by immersion and cold drying. ZnO nanocone arrays were developed using the hydrothermal technique (Yuea et al., 2020) for dopamine detection. The nanocones were functionalized using Au nanoparticles with carboxyl groups obtaining a sensor with high sensitivity (4.36 μA/μM) and low LOD (0.04 μM).

WO₃-based Biosensors

WO₃ is an n-type semiconductor with a band gap of 2.8 eV and a versatile crystalline structure varying from cubic to octahedral, depending on the synthesis temperature. High surface to volume ratio WO₃-based materials can be developed using physical and chemical techniques with well-controlled dimensionality, sizes, and crystal structure for sensors research.

A WO₃ nitrite-based sensor was prepared by a simple casting (Liu et al., 2015) and hydrothermal (Santos et al., 2016) methods. In the first case WO₃ has nanowire morphology and was functionalized with hemoglobin, while WO₃ nanoparticles were obtained and functionalized with cytochrome c nitrite reductase using the hydrothermal procedure. The LOD value in the case of WO₃ nanowire is significantly lower (0.28 μM) compared with WO₃ nanopowder (5 μM) underlining the significance of semiconductor morphology, synthesis and functionalizing procedures. The hydrothermal method has been used to produce WO₃ sensors with different morphologies: flower-like for aflatoxin B1 (Feng et al., 2018), nanorods for bisphenol A (Zhou et al., 2017), and nanosheets for cardiac biomarker Troponin I (Sandil et al., 2018). The WO₃ flower-like morphology was functionalized with bovine serum albumin and the LOD corresponding to aflatoxin B1 was very low (0.28 pg/mL). The nanorods were doped with Na⁺ ions, giving a LOD value of 0.028 μM. Finally, the nanosheets were functionalized with 3-aminopropyl tri-ethoxy saline for the activation of amino groups and the LOD value was 0.01 ng/mL. In the case of WO₃-based biosensors the nanosheets morphology gives a better LOD for

cardiac biomarker Troponin I compared with the flower-like morphology used for aflatoxin B1 detection.

Other techniques were used to obtain WO₃ nanosheets, such as simple reversible redox (Zhang et al., 2020) and ultrasonic exfoliation (Li et al., 2019) processes. Using the reversible redox process makes it possible to develop WO₃ nanosheets with an average width of 150 nm, and LOD for human epididymal protein 4 detection of 1.56 pg/mL. Ultrasonic exfoliation of bulk WO₃ in water allows the preparation of WO₃ nanosheets in the range of 20 to 40 nm. These nanosheets were functionalized with 3, 3', 5, 5'-tetramethylbenzidine and the LOD for xanthine in urine (based on colorimetric evaluation) was 1.24 μmol/L.

CONCLUSIONS

Metal oxides are considered as versatile materials that can be successfully integrated in biosensor technology. Based on features such as chemical stability, light excitation/light conversion, and high surface-to-volume ratio, these materials are highly competitive in the biosensors market. This mini review has outlined that the biosensors' LOD depends on many

parameters such as: morphology (active surface), functionalizing molecule, evaluation procedure, and detecting target. The same material with similar morphology and detecting targets can give different LOD depending on surface functionalization and evaluation procedures. Even if most of the biosensors are used for glucose (H₂O₂, uric acid) there are encouraging results for cancer cell or virus detection. Recent advancements indicate a promising future for MOS in applications such as skin bioelectronics, neural interfaces, and smart biosensing devices. However, much effort is required to overcome important issues related to optimizing organic/inorganic interface compatibility, the enzyme electrochemistry at the MOS interface, and LOD improvement. To achieve this goal, facile MOS synthesis technologies allowing good interface control must be implemented.

AUTHOR CONTRIBUTIONS

IŞ was responsible for article database regarding TiO₂, SnO₂, and WO₃, including **Table 1**. AE has coordinated the writing, introduction, biosensors mechanism (including **Figure 1**), and article database for ZnO.

REFERENCES

- Ahmad, R., Ahn, M. S., and Hahn, Y. B. (2017). ZnO nanorods array based field-effect transistor biosensor for phosphate detection. *J. Colloid Interf. Sci.* 498, 292–297. doi: 10.1016/j.jcis.2017.03.069
- Alim, S., Kafi, A. K. M., Rajan, J., and Yusoff, M. M. (2019). Application of polymerized multiporous nanofiber of SnO₂ for designing a bienzyme glucose biosensor based on HRP/Gox. *Int. J. Biol. Macromol.* 123, 1028–1034. doi: 10.1016/j.ijbiomac.2018.11.171
- Çakiroglu, B., and Özacar, M. (2019). A self-powered photoelectrochemical biosensor for H₂O₂, and xanthine oxidase activity based on enhanced chemiluminescence resonance energy transfer through slow light effect in inverse opal TiO₂. *Biosens. Bioelectron.* 141:111385. doi: 10.1016/j.bios.2019.111385
- Cao, S. P., Hu, H. M., Liang, R. P., and Qiu, J. D. (2020). An ultrasensitive electrochemiluminescence resonance energy transfer biosensor for divalent mercury monitoring. *J. Electroanal. Chem.* 856:113494. doi: 10.1016/j.jelechem.2019.113494
- Chen, D., Lv, L., Peng, L., Peng, J., and Tu, J. (2019). Controlled synthesis of mesoporous zinc oxide containing oxygen vacancies in low annealing temperature for photoelectrochemical biosensor. *Ceram. Int.* 45, 18044–18051. doi: 10.1016/j.ceramint.2019.06.024
- Cheng, Y., Chen, K. S., Meyer, N. L., Yuan, J., Hirst, L. S., Chase, P. B., et al. (2011). Functionalized SnO₂ nanobelt field-effect transistor sensors for label-free detection of cardiac troponin. *Biosens. Bioelectron.* 26, 4538–4544. doi: 10.1016/j.bios.2011.05.019
- Dong, S., Tong, M., Zhang, D., and Huang, T. (2017). The strategy of nitrite and immunoassay human IgG biosensors based on ZnO@ZIF-8 and ionic liquid composite film. *Sens. Actuat. B-Chem.* 251, 650–657. doi: 10.1016/j.snb.2017.05.047
- Dong, Y., and Zheng, J. (2014). A nonenzymatic L-cysteine sensor based on SnO₂-MWCNTs nanocomposites. *J. Mol. Liq.* 196, 280–284. doi: 10.1016/j.molliq.2014.03.046
- Elahi, N., Kamali, M., Baghersad, M. H., and Amini, B. (2019). A fluorescence nano-biosensors immobilization on iron (MNPs) and gold (AuNPs) nanoparticles for detection of *Shigella* spp. *Mater. Sci. Eng. C* 105:110113. doi: 10.1016/j.msec.2019.110113
- Enesca, A., Andronic, L., and Duta, A. (2012a). Optimization of opto-electrical and photocatalytic properties of SnO₂ thin films using Zn²⁺ and W⁶⁺ dopant ions. *Catal. Lett.* 142, 224–230. doi: 10.1007/s10562-011-0762-4
- Enesca, A., Andronic, L., and Duta, A. (2012b). The influence of surfactants on the crystalline structure, electrical and photocatalytic properties of hybrid multi-structured (SnO₂, TiO₂ and WO₃) thin films. *Appl. Surf. Sci.* 258, 4339–4346. doi: 10.1016/j.apsusc.2011.12.110
- Enesca, A., Isac, L., and Duta, A. (2015). Charge carriers injection in tandem semiconductors for dyes mineralization. *Appl. Catal. B Environ.* 162, 352–363. doi: 10.1016/j.apcatb.2014.06.059
- Faria, A. M., Mazon, T. (2019). Early diagnosis of zika infection using a ZnO nanostructures-based rapid electrochemical biosensor. *Talanta* 203, 153–160. doi: 10.1016/j.talanta.2019.04.080
- Feizabadi, M., Soleymannpour, A., Faridnouri, H., and Ajloo, D. (2019). Improving stability of biosensor based on covalent immobilization of horseradish peroxidase by γ-aminobutyric acid and application in detection of H₂O₂. *Int. J. Biol. Macromol.* 136, 597–606. doi: 10.1016/j.ijbiomac.2019.06.103
- Feng, J., Li, Y., Gao, Z., Lv, H., Zhang, H., Dong, Y., et al. (2018). A competitive-type photoelectrochemical immunosensor for aflatoxin B1 detection based on flower-like WO₃ as matrix and Ag₂S-enhanced BiVO₄ for signal amplification. *Sens. Actuat. B-Chem.* 270, 104–111. doi: 10.1016/j.snb.2018.05.015
- Fiorani, A., Merino, J. P., Zanuti, A., Criado, A., and Paolucci, F. (2019). Advanced carbon nanomaterials for electrochemiluminescent biosensor applications. *Curr. Opin. Electrochem.* 16, 66–74. doi: 10.1016/j.coelec.2019.04.018
- Ge, L., Liu, Q., Jiang, D., Ding, L., and Wang, K. (2019). Oxygen vacancy enhanced photoelectrochemical performance of Bi₂MoO₆/B, N co-doped graphene for fabricating lincomycin aptasensor. *Biosens. Bioelectron.* 135, 145–152. doi: 10.1016/j.bios.2019.04.022
- Gupta, S., Sharma, A., and Verma, R. S. (2020). Polymers in biosensor devices for cardiovascular applications. *Curr. Opin. Biomed. Eng.* 13, 69–75. doi: 10.1016/j.cobme.2019.10.002
- Han, S., Zhang, Q., Zhang, X., Liu, X., and Zheng, G. (2019). A digital microfluidic diluter-based microalgal motion biosensor for marine pollution monitoring. *Biosens. Bioelectron.* 143:111597. doi: 10.1016/j.bios.2019.111597
- Hernández-Cancel, G., Suazo-Dávila, D., Medina-Guzmán, J., Rosado-González, M., and Griebenow, K. (2015). Chemically glycosylation improves the stability of an amperometric horseradish peroxidase biosensor. *Anal. Chim. Acta* 854, 129–139. doi: 10.1016/j.aca.2014.11.008

- Hocini, A., Temmar, M. N., Khedrouche, D., and Zamani, M. (2019). Novel approach for the design and analysis of a terahertz microstrip patch antenna based on photonic crystals. *Photonics Nanostruct.* 36:100723. doi: 10.1016/j.photonics.2019.100723
- Hu, W., Zhang, Z., Li, L., Ding, Y., and An, J. (2019). Preparation of electrospun SnO₂ carbon nanofiber composite for ultrasensitive detection of APAP and p-Hydroxyacetophenone. *Sens. Actuat. B.* 299:127003. doi: 10.1016/j.snb.2019.127003
- Huang, Q., Wang, Y., Lei, L., Xu, Z., and Zhang, W. (2016). Photoelectrochemical biosensor for acetylcholinesterase activity study based on metal oxide semiconductor nanocomposites. *J. Electroanal. Chem.* 781, 377–382. doi: 10.1016/j.jelechem.2016.07.007
- Kafi, A. K. M., Wu, G., Benvenuto, P., and Chen, A. (2011). Highly sensitive amperometric H₂O₂ biosensor based on hemoglobin modified TiO₂ nanotubes. *J. Electroanal. Chem.* 662, 64–69. doi: 10.1016/j.jelechem.2011.03.021
- Kao, C. H., Chen, H., Yao, F., Hou, S., Chang, S. W., and Lin, M. H. (2015). Fabrication of multianalyte CeO₂ nanograin electrolyte–insulator–semiconductor biosensors by using CF₄ plasma treatment, sensing and biosensing. *Res.* 5, 71–77. doi: 10.1016/j.sbsr.2015.07.001
- Khalique, N., Rasheed, M. A., Cha, G., Khan, M., Karim, S., Schmuki, P., et al. (2020). Development of non-enzymatic cholesterol bio-sensor based on TiO₂ nanotubes decorated with Cu₂O nanoparticles. *Sens. Actuat. B.* 302:127200. doi: 10.1016/j.snb.2019.127200
- Lavanya, N., Radhakrishnan, S., and Sekar, C. (2012). Fabrication of hydrogen peroxide biosensor based on Ni doped SnO₂ nanoparticles. *Biosens. Bioelectron.* 36, 41–47. doi: 10.1016/j.bios.2012.03.035
- Lei, Y., Yan, X., Zhao, J., Liu, X., Song, Y., Luo, N., et al. (2011). Improved glucose electrochemical biosensor by appropriate immobilization of nano-ZnO. *Colloid. Surface. B.* 82, 168–172. doi: 10.1016/j.colsurfb.2010.08.034
- Li, L., Huang, J., Wang, Y., Zhang, H., Liu, Y., and Li, J. (2010). An excellent enzyme biosensor based on Sb-doped SnO₂ nanowires. *Biosens. Bioelectron.* 25, 2436–2441. doi: 10.1016/j.bios.2010.03.037
- Li, Z., Liu, X., Liang, X. H., Zhong, J., Guo, L., and Fu, F. (2019). Colorimetric determination of xanthine in urine based on peroxidase-like activity of WO₃ nanosheets. *Talanta* 204, 278–284. doi: 10.1016/j.talanta.2019.06.003
- Liu, C. H., Hong, M. H., Lum, M. C., Flotow, H., Ghadessy, F., and Zhang, J. B. (2010). Large-area micro/nanostructures fabrication in quartz by laser interference lithography and dry etching. *Appl. Phys. A.* 101, 237–241. doi: 10.1007/s00339-010-5807-9
- Liu, H., Duan, C., Yang, C., Chen, X., Shen, W., and Zhu, Z. (2015). A novel nitrite biosensor based on the direct electron transfer hemoglobin immobilized in the WO₃ nanowires with high length–diameter ratio. *Mater. Sci. Eng. C.* 53, 43–49. doi: 10.1016/j.msec.2015.04.016
- Liu, H., Guo, K., Duan, C., Dong, X., and Gao, J. (2017). Hollow TiO₂ modified reduced graphene oxide microspheres encapsulating hemoglobin for a mediator-free biosensor. *Biosens. Bioelectron.* 87, 473–479. doi: 10.1016/j.bios.2016.08.089
- Liu, P., Huo, X., Tang, Y., Xu, J., Liu, X., and Wong, K. Y. (2017). A TiO₂ nanosheet-g-C₃N₄ composite photoelectrochemical enzyme biosensor excitable by visible irradiation. *Anal. Chim. Acta* 984, 86–95. doi: 10.1016/j.aca.2017.06.043
- Mihaly, M., Lacatusu, I., Enesca, A., and Meghea, A. (2008). Hybrid nanomaterials based on silica coated C-60 clusters obtained by microemulsion technique. *Mol. Cryst. Liq. Cryst.* 483, 205–215. doi: 10.1080/15421400801906885
- Oh, J., Yoo, G., Chang, Y. W., Kim, H. J., and Yoo, K. H. (2013). A carbon nanotube metal semiconductor field effect transistor-based biosensor for detection of amyloid-beta in human serum. *Biosens. Bioelectron.* 50, 345–350. doi: 10.1016/j.bios.2013.07.004
- Ortiz, E., Gallay, P., Galicia, L., Eguilaz, M., and Rivas, G. (2019). Nanoarchitectures based on multi-walled carbon nanotubes non-covalently functionalized with Concanavalin A: a new building-block with supramolecular recognition properties for the development of electrochemical biosensors. *Sens. Actuat. B-Chem.* 292, 254–262. doi: 10.1016/j.snb.2019.04.114
- Osman, D. I., El-Sheikh, S. M., Sheta, S. M., Ali, O. I., and Shawky, S. M. (2019). Nucleic acids biosensors based on metal-organic framework (MOF): paving the way to clinical laboratory diagnosis. *Biosens. Bioelectron.* 141:111451. doi: 10.1016/j.bios.2019.111451
- Rajendran, S., Manoj, D., Raju, K., Dionysiou, D. D., Naushad, M., Gracia, F., et al. (2018). Influence of mesoporous defect induced mixed-valent NiO (Ni²⁺/Ni³⁺)-TiO₂ nanocomposite for non-enzymatic glucose biosensors. *Sens. Actuat. B.* 264, 27–37. doi: 10.1016/j.snb.2018.02.165
- Ramon-Marquez, T., Medina-Castillo, A. L., Fernandez-Gutierrez, A., and Fernandez-Sanchez, J. F. (2018). Evaluation of two sterically directed attachments of biomolecules on a coaxial nanofibre membrane to improve the development of optical biosensors. *Talanta* 187, 83–90. doi: 10.1016/j.talanta.2018.05.004
- Rathinamala, I., Jeyakumar, N., and Prithivikumar, N. (2019). Sol-gel assisted spin coated CdS/PS electrode based glucose biosensor. *Vacuum* 161, 291–296. doi: 10.1016/j.vacuum.2018.12.045
- Rezaei, H., Motovali-bashi, M., and Radfar, S. (2019). An enzyme-free electrochemical biosensor for simultaneous detection of two hemophilia A biomarkers: Combining target recycling with quantum dots-encapsulated metal-organic frameworks for signal amplification. *Anal. Chim. Acta* 1092, 66–74. doi: 10.1016/j.aca.2019.09.037
- Safavipour, M., Kharaziha, M., Amjadi, E., Karimzadeh, F., and Allafchian, A. (2020). TiO₂ nanotubes/reduced GO nanoparticles for sensitive detection of breast cancer cells and photothermal performance. *Talanta* 208:120369. doi: 10.1016/j.talanta.2019.120369
- Sandil, D., Srivastava, S., Malhotra, B. D., Sharma, S. C., and Puri, N. K. (2018). Biofunctionalized tungsten trioxide-reduced graphene oxide nanocomposites for sensitive electrochemical immunosensing of cardiac biomarker. *J. Alloy. Compd.* 763, 102–110. doi: 10.1016/j.jallcom.2018.04.293
- Santos, L., Silveira, C. M., Elangovan, E., Neto, J. P., Nunes, D., Pereira, L., et al. (2016). Synthesis of WO₃ nanoparticles for biosensing applications. *Sens. Actuat. B-Chem.* 223, 186–194. doi: 10.1016/j.snb.2015.09.046
- Scognamiglio, V., Antonacci, A., Arduini, F., Moscone, D., and Paleschi, G. (2019). An eco-designed paper-based algal biosensor for nanoformulated herbicide optical detection. *J. Hazard. Mater.* 373, 483–492. doi: 10.1016/j.jhazmat.2019.03.082
- Solaimuthu, A., Vijayan, A. N., Murali, P., and Korrapati, P. S. (2020). Nano-biosensors and their relevance in tissue engineering. *Curr. Opin. Biomed. Eng.* 13, 84–93. doi: 10.1016/j.cobme.2019.12.005
- Soldatkina, O. V., Soldatkin, O. O., Velychko, T. P., Prilipko, V. O., and Dzyadevych, S. V. (2018). Conductometric biosensor for arginine determination in pharmaceuticals. *Bioelectrochemistry* 124, 40–46. doi: 10.1016/j.bioelechem.2018.07.002
- Song, H., Zhang, Y., Wang, S., Huang, K., and Xu, W. (2020). Label-free polygonal-plate fluorescent-hydrogel biosensor for ultrasensitive microRNA detection. *Sens. Actuat. B-Chem.* 306:27554. doi: 10.1016/j.snb.2019.127554
- Visa, M., Andronic, L., and Enesca, A. (2016). Behavior of the new composites obtained from fly ash and titanium dioxide in removing of the pollutants from wastewater. *Appl. Surf. Sci.* 388, 359–369. doi: 10.1016/j.apsusc.2015.12.154
- Wang, M., Yin, H., Zhou, Y., Sui, C., Wang, Y., Meng, X., et al. (2019). Photoelectrochemical biosensor for microRNA detection based on a MoS₂/g-C₃N₄/black TiO₂ heterojunction with Histostar@AuNPs for signal Amplification. *Biosens. Bioelectron.* 128, 137–143. doi: 10.1016/j.bios.2018.12.048
- Wang, Q., Zhao, Y., Yang, Q., Du, D., and Lin, Y. (2019). Amperometric sarcosine biosensor with strong anti-interference capabilities based on mesoporous organic-inorganic hybrid materials. *Biosens. Bioelectron.* 141:111431. doi: 10.1016/j.bios.2019.111431
- Wang, Y., Fan, D., Zhao, G., Feng, J., Wei, D., Zhang, N., et al. (2018). Ultrasensitive photoelectrochemical immunosensor for the detection of amyloid β-protein based on SnO₂/SnS₂/Ag₂S nanocomposites. *Biosens. Bioelectron.* 120, 1–7. doi: 10.1016/j.bios.2018.08.026
- Wang, Y. H., Huang, K. J., and Wu, X. (2017). Recent advances in transition-metal dichalcogenides based electrochemical biosensors: a review. *Biosens. Bioelectron.* 97, 305–316. doi: 10.1016/j.bios.2017.06.011
- Wu, X., Zhang, H., Huang, K., Zeng, Y., and Zhu, Z. (2018). Rose petal and P123 dual-templated macro-mesoporous TiO₂ for a hydrogen peroxide biosensor. *Bioelectrochemistry* 120, 150–156. doi: 10.1016/j.bioelechem.2017.12.009
- Xu, B., Huang, J., Ding, L., and Cai, J. (2020). Graphene oxide-functionalized long period fiber grating for ultrafast label-free glucose biosensor. *Mater. Sci. Eng. C* 107:110329. doi: 10.1016/j.msec.2019.110329

- Yang, Z., Tang, Y., Li, J., Zhang, Y., and Hu, X. (2014). Facile synthesis of tetragonal columnar-shaped TiO₂ nanorods for the construction of sensitive electrochemical glucose biosensor. *Biosens. Bioelectron.* 54, 528–533. doi: 10.1016/j.bios.2013.11.043
- Yi, Y., Xie, B., Zhao, T., Qian, Z., and Liu, H. (2020). The effect of anode hydrodynamics on the sensitivity of microbial fuel cell based biosensors and the biological mechanism. *Bioelectrochemistry* 132:107351. doi: 10.1016/j.bioelechem.2019.107351
- Yilmaz, Y. Y., Yalcinkaya, E. E., Demirkol, D. O., and Timur, S. (2020). 4-aminothiophenol-intercalated montmorillonite: Organic-inorganic hybrid material as an immobilization support for biosensors. *Sens. Actuat. B-Chem.* 307:127665. doi: 10.1016/j.snb.2020.127665
- Yin, M.-J., Gu, B., An, Q.-F., Yang, C., and Yong, K.-T. (2018). Recent development of fiber-optic chemical sensors and biosensors: Mechanisms, materials, micro/nano-fabrications and applications. *Coordin. Chem. Rev.* 376, 348–392. doi: 10.1016/j.ccr.2018.08.001
- Yoo, T., Lim, K., Sultan, M. T., Lee, J. S., and Jang, M. (2019). The real-time monitoring of drug reaction in HeLa cancer cell using temperature/impedance integrated biosensors. *Sens. Actuat. B-Chem.* 291, 17–24. doi: 10.1016/j.snb.2019.03.145
- Yuan, Y., Wang, Y., Wang, H., and Hou, S. (2019). Gold nanoparticles decorated on single layer graphene applied for electrochemical ultrasensitive glucose biosensor. *J. Electroanal. Chem.* 855:113495. doi: 10.1016/j.jelechem.2019.113495
- Yuea, H. Y., Zhanga, H. J., Huang, S., Lua, X. X., Gao, X., Song, S. S., et al. (2020). Highly sensitive and selective dopamine biosensor using Au nanoparticles-ZnO nanocone arrays/graphene foam electrode. *Mater. Sci. Eng. C* 108:110490. doi: 10.1016/j.msec.2019.110490
- Zhang, B., Wang, H., Xi, J., Zhao, F., and Zeng, B. (2020). *In situ* formation of inorganic/organic heterojunction photocatalyst of WO₃/Au/ polydopamine for immunoassay of human epididymal protein 4. *Electrochim. Acta* 331:135350. doi: 10.1016/j.electacta.2019.135350
- Zhang, X., Li, W., Zhou, Y., Chai, Y., and Yuan, R. (2019). An ultrasensitive electrochemiluminescence biosensor for MicroRNA detection based on luminol-functionalized Au NPs@ZnO nanomaterials as signal probe and dissolved O₂ as coreactant. *Biosens. Bioelectron.* 135, 8–13. doi: 10.1016/j.bios.2019.04.004
- Zhao, D., Liu, Y., Zhang, Q., Zhang, Y., and Sang, S. (2019). Surface stress-based biosensor with stable conductive AuNPs network for biomolecules detection. *Appl. Surf. Sci.* 491, 443–450. doi: 10.1016/j.apsusc.2019.06.178
- Zheng, H., Liu, M., Yan, Z., and Chen, J. (2020). Highly selective and stable glucose biosensor based on incorporation of platinum nanoparticles into polyaniline-montmorillonite hybrid composites. *Microchem. J.* 152:104266. doi: 10.1016/j.microc.2019.104266
- Zhou, Q., Yang, L., Wang, G., and Yang, Y. (2013). Acetylcholinesterase biosensor based on SnO₂ nanoparticles-carboxylic graphene-nafion modified electrode for detection of pesticides. *Biosens. Bioelectron.* 49, 25–31. doi: 10.1016/j.bios.2013.04.037
- Zhou, Y., Yang, L., Li, S., and Dang, Y. (2017). A novel electrochemical sensor for highly sensitive detection of bisphenol A based on the hydrothermal synthesized Na-doped WO₃ nanorods. *Sens. Actuat. B-Chem.* 245, 238–246. doi: 10.1016/j.snb.2017.01.034
- Zhu, J., Liu, X., Wang, X., Huo, X., and Yan, R. (2015). Preparation of polyaniline-TiO₂ nanotube composite for the development of electrochemical biosensors. *Sens. Actuat. B* 221, 450–457. doi: 10.1016/j.snb.2015.06.131
- Zong, X., and Zhu, R. (2018). ZnO nanorod-based FET biosensor for continuous glucose monitoring. *Sens. Actuat. B-Chem.* 255, 2448–2453. doi: 10.1016/j.snb.2017.09.037

Conflict of Interest: The authors declare that the research was conducted in the absence of any commercial or financial relationships that could be construed as a potential conflict of interest.

Copyright © 2020 Şerban and Enesca. This is an open-access article distributed under the terms of the Creative Commons Attribution License (CC BY). The use, distribution or reproduction in other forums is permitted, provided the original author(s) and the copyright owner(s) are credited and that the original publication in this journal is cited, in accordance with accepted academic practice. No use, distribution or reproduction is permitted which does not comply with these terms.



Study on Preparation and Properties of InN Films on Self-Supporting Diamond Substrates Under Different Nitrogen Flows

Shuaijie Wang^{1,2}, Fuwen Qin^{1*}, Yizhen Bai¹ and Dong Zhang²

¹ School of Physics, Dalian University of Technology, Dalian, China, ² School of Renewable Energy, Shenyang Institute of Engineering, Shenyang, China

OPEN ACCESS

Edited by:

Kezhen Qi,
Shenyang Normal University, China

Reviewed by:

Guoqiang Liu,
Northeastern University, China
Chunqiang Zhuang,
Beijing University of
Technology, China

*Correspondence:

Fuwen Qin
qfw@dlut.edu.cn

Specialty section:

This article was submitted to
Thin Solid Films,
a section of the journal
Frontiers in Materials

Received: 31 March 2020

Accepted: 29 April 2020

Published: 10 June 2020

Citation:

Wang S, Qin F, Bai Y and Zhang D
(2020) Study on Preparation and
Properties of InN Films on
Self-Supporting Diamond Substrates
Under Different Nitrogen Flows.
Front. Mater. 7:154.
doi: 10.3389/fmats.2020.00154

Several InN film samples with superb properties were prepared on a self-supporting diamond substrate for different nitrogen flow rates using an electron cyclotron resonance plasma-enhanced metal-organic chemical vapor deposition (ECR-PEMOCVD) system. After the InN film samples were obtained, the samples were characterized via reflected high-energy electron diffraction (RHEED), X-ray diffraction (XRD), scanning electron microscopy (SEM), atomic force microscope (AFM), and electron probe micro-analysis (EPMA) to study the effect of the nitrogen flow on the quality of the InN films. The experimental results show that the variation in the nitrogen flow has a great impact on the preferential growth of the (0002) crystal plane of the InN thin film. By increasing the nitrogen flow moderately, the crystal quality of the film is improved. Under the growth condition of appropriate nitrogen flow, InN thin films with a preferred orientation along the c-axis can be obtained, and the surface of the resulting InN thin films is relatively flat. However, a high nitrogen flow does not improve the film crystal quality. The results of the experiment and of the analysis show that the InN films prepared with a nitrogen flow rate of 80 sccm have an excellent preferential orientation. The result of the EPMA test shows that the percentages of the In and N atoms in the prepared film samples are close to a ratio of 1:1, and a small amount of metal In droplets is present. In addition, the InN thin films prepared in such condition have an excellent surface morphology and composition.

Keywords: InN thin film, nitrogen flow, self-supporting diamond substrate, ECR-PEMOCVD, low temperature

INTRODUCTION

Indium nitride (InN) has become an important semiconductor material due to its narrow band gap (0.7 eV) and excellent physical properties (Bashir et al., 2018; Dwivedi et al., 2018; Madapu et al., 2018; Polanco and Lindsay, 2018). InN can bind with GaN and AlN (semiconductors of the same group) to form the ternary alloys InGaN and InAlN. These ternary alloys have wide band gaps that cover the entire spectrum of visible light. They are excellent materials for producing LEDs of different colors and high-efficiency photovoltaic cells. In addition to its wide band gap, InN has some special properties, such as a high breakdown voltage, a high saturation electron drift speed, and a high thermal stability, making it a promising material in the development and production of solid-state optoelectronic devices, high-performance semiconductor devices, and high-quality

infrared detectors (Akasaka et al., 2018; Bashir et al., 2018; Buzynin et al., 2018; Ke et al., 2018; Madapu and Dhara, 2018; Madapu et al., 2018; Polanco and Lindsay, 2018). In fact, the quantum efficiency of photovoltaic cells, which are based on GaN/InGaN prepared on a sapphire substrate via the metal-organic chemical vapor deposition method, reaches 60% (Ke et al., 2018). Therefore, researchers are trying various new methods to prepare high-quality InN thin films (Darakchieva et al., 2011; Zhou et al., 2017; Anjum et al., 2018; Bi et al., 2018; Kobayashi et al., 2018; Liu et al., 2018; Peng et al., 2018) to expand the applications of InN. The emission wavelength of InN-based materials can reach the long-wavelength communication band of 1.55 μm . This increases the number of candidate materials for developing optical communication devices and provides new opportunities to make breakthroughs in the development of optical communication devices. Theoretical studies have shown that InN has both a superb steady state and transient electron transport characteristics. Moreover, it has a higher mobility and a spike rate similar to other materials (its low-field mobility reaches 14,000 $\text{cm}^2/\text{V}\cdot\text{s}$, the peak rate reaches 4.3×10^7 cm/s), and its electron transport rate is not affected by the temperature. Compared with extensive application of ZnO thin film materials (Lucarelli and Brown, 2019; Marikutsa et al., 2019; Pereira and Hatton, 2019; Qi et al., 2019, 2020a,b; Tharsika et al., 2019; Yu et al., 2019), all these properties endow InN unique advantages in the development and production of devices, such as high-frequency, high-speed transistors.

Although InN has unique optoelectronic properties and a great potential in various applications, the research on the growth method and on the physical properties of high-quality InN films lags behind the research on other nitride materials of the III group. This is mainly attributable to the following scientific problems that need to be solved urgently: (1) The InN-based materials are difficult to prepare due to the high decomposition pressure of nitrogen and the low InN decomposition temperature. (2) There is a lack of substrate materials with well-matching lattice constant and thermal expansion coefficient for growing the films. (3) High-power, high-frequency devices present high requirements on durability and heat dissipation. However, it is difficult to find a substrate with excellent heat dissipation. With the improvement in the film growth methods in recent years, researchers have successfully grown InN thin films on heterogeneous substrates, such as $\alpha\text{-Al}_2\text{O}_3$ via magnetron sputtering, metal-organic chemical vapor deposition (MOCVD), atomic layer deposition (ALD), molecular beam epitaxy (MBE), and plasma-enhanced MBE. However, heterogeneous substrates, such as $\alpha\text{-Al}_2\text{O}_3$, do not have excellent heat dissipation. Therefore, finding suitable substrate materials is still a challenge to fabricating high-quality InN thin film for high-power, high-frequency devices.

It is well-known that diamond has very a high thermal conductivity and an excellent heat resistance, ideal for producing high-power, high-frequency devices. The high thermal conductivity and excellent heat resistance can greatly improve the durability of the devices. Due to these properties, high-power, high-frequency devices incorporating diamond components have become a focus of research. The CVD

technique for preparing diamond films has made great progress in recent years, and high-quality, large-area diamond films can be grown on silicon or metal substrates via deposition. Therefore, achieving a low-temperature growth of high-quality InN films on a self-supporting diamond thick film substrate is key to foster the application of InN in optoelectronic devices and high-frequency, high-power electronic devices. In this study, high-quality InN films were successfully prepared on a self-supporting diamond substrate via the ECR-PEMOCVD system.

EXPERIMENTAL DETAILS

In this study, a number of InN thin film samples was prepared using the ECR-PEMOCVD system at low temperature on a self-supporting diamond substrate for different nitrogen reaction source flows. ECR-PEMOCVD is a new thin film growth technique that combines advanced MBE and MOCVD techniques with a program-controlled coupled ECR microwave plasma source, capable of generating high-density charges and stimulating particles at low pressures. Under this condition, the particles can easily undergo a chemical reaction on the substrate and accumulate into the thin film. Therefore, ECR-PEMOCVD has more advantages when compared to traditional plasma-enhanced chemical vapor deposition methods.

In this study, a self-supporting diamond film was used as the substrate, and the InN thin film samples were prepared under different nitrogen flow rates. Prior to the preparation of the thin film samples, the surface of the self-supporting diamond substrate was ultrasonically cleaned with the aim of removing the contaminants, such as stains on the surface. The steps are the following: (1) The self-supporting diamond substrate was immersed in an acetone solution and ultrasonically cleaned for 10 min. (2) The substrate in the ethanol solution was ultrasonically cleaned for 10 min. (3) The substrate in the deionized water was ultrasonically cleaned for 10 min. (4) The substrate was dried with nitrogen gas. Then, the self-supporting diamond substrate was cleaned via plasma gas discharging. During the process, a flow of hydrogen gas with a flow rate of 60 sccm was supplied; the microwave power was 650 W. The hydrogen electrically discharged via the microwave system, and the substrate was cleaned in the hydrogen plasma environment at room temperature for 30 min. Thus, a substrate with a clean surface was obtained.

In this study, trimethylindium (TMIn) and high-purity N_2 were used as the sources of indium and nitrogen, respectively. A semiconductor cold trap was used to maintain the temperature of TMIn precisely within the $20^\circ\text{C} \pm 1^\circ\text{C}$ range, and H_2 was used as the carrier gas. The N_2 ionization reaction was greatly improved by ECR. Under the enhancement effect of ECR, a large number of activated nitrogen ions accumulated onto the substrate (Zhang et al., 2012). This is crucial for forming the InN thin film. In order to effectively alleviate the lattice mismatch between the InN thin film and the self-supporting diamond substrate, it was necessary to introduce a buffer layer. After the self-supporting diamond substrate was cleaned, the next step was to prepare the buffer layer film. The preparation of the buffer layer film

was accomplished at room temperature, the nitrogen flow rate was 60 sccm, the flow rate of reaction source trimethylindium (TMIn) was 0.3 sccm, and the preparation process lasted 30 min. A mass flow controller was used to maintain the TMIn flow rate at 0.6 sccm, the temperature was maintained at 400°C, the microwave power was 650 W, and the film growth lasted 180 min. The effect of the nitrogen flow rate on the structure and on the properties of the resulting film was studied by shifting the flow rate of the reaction source nitrogen from 60 to 100 sccm, and the thickness of InN films were 500 nm, which were tested by a step meter system.

The structural properties and preferred orientation of the prepared thin film samples were determined by XRD at D/Max-2400 (CuK α 1: $\lambda = 0.154056$ nm) and reflected high-energy electron diffraction (RHEED). The surface morphology of the InN thin film was tested and analyzed via the scanning electron microscopy (SEM), atomic force microscopy (AFM), and electron probe microanalysis (EPMA) methods.

RESULTS AND DISCUSSION

RHEED Analysis

After the experiment was completed, the InN thin film samples prepared with different nitrogen flow rates were characterized by using the (RHEED) method. The results are shown in **Figure 1**. As the nitrogen flow rate increases from 60 to 80 sccm, the RHEED pattern of the InN film gradually changes from a continuous ring to a broken ring, and the definition of the RHEED pattern increases. However, when the nitrogen flow rate continues to increase from 80 to 100 sccm, the RHEED pattern of the prepared thin film gradually changes from a broken ring to a continuous ring. The test results show that the nitrogen flow has a great influence on the RHEED test results of the thin film samples. When the nitrogen flow rate is fixed to the value of 80 sccm, an excellent RHEED pattern can be obtained from the prepared thin film. With this nitrogen flow rate, the RHEED pattern shows a clear broken ring. A further analysis

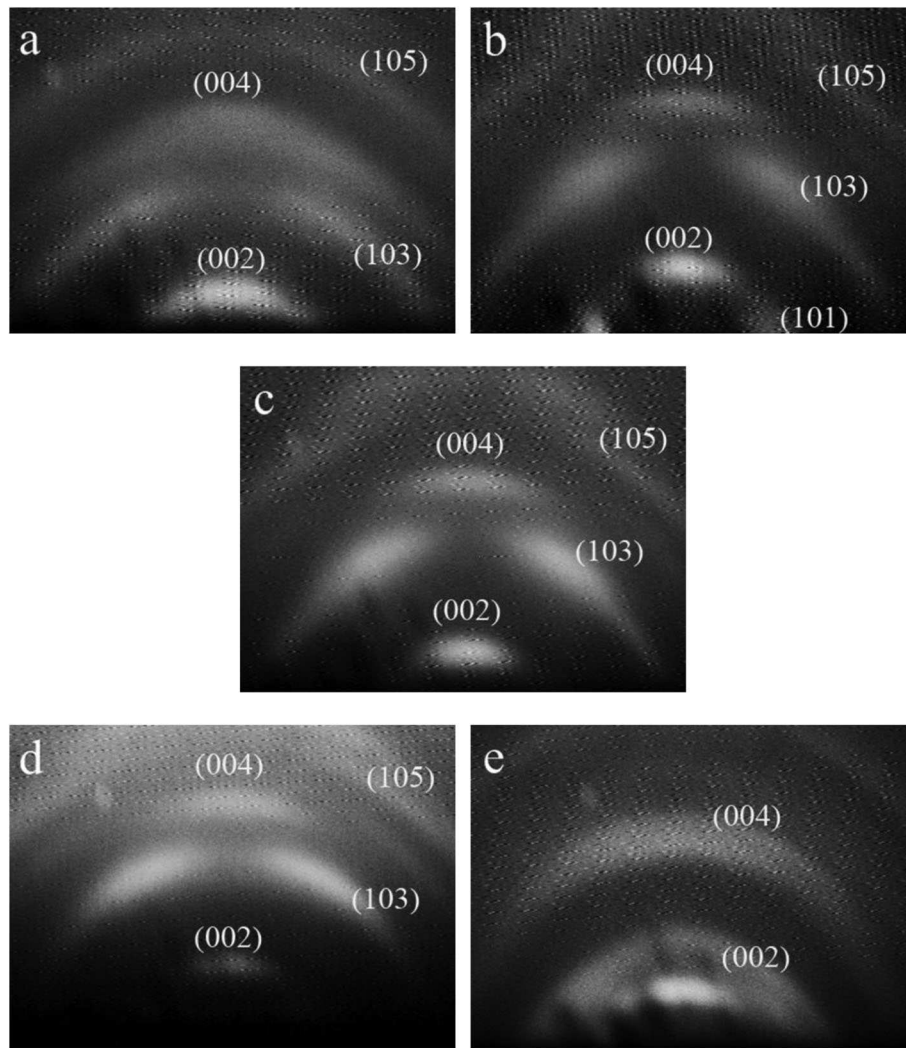


FIGURE 1 | The RHEED patterns of InN (0002) plane films at various N₂ flux for (a) 60 sccm, (b) 70 sccm, (c) 80 sccm, (d) 90 sccm, and (e) 100 sccm, respectively.

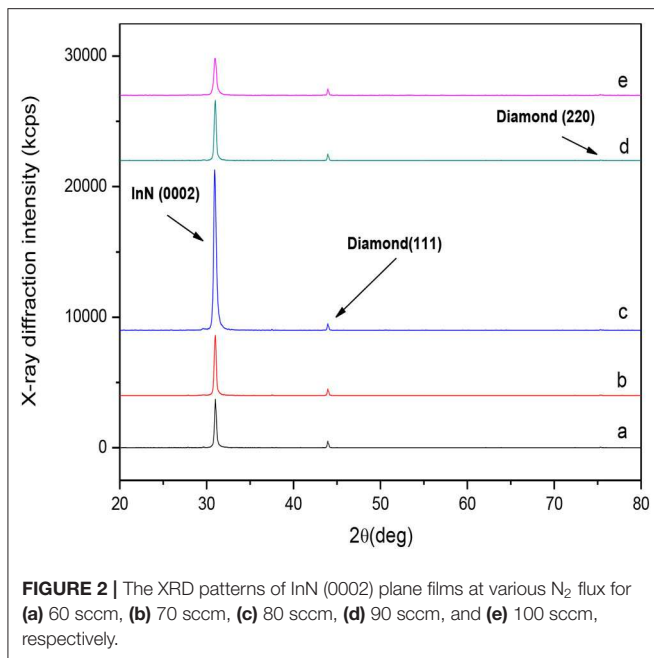


TABLE 1 | The InN (0002) diffraction peak position, FWHM, lattice parameter of c-axis, and grain size.

Sample	Nitrogen flow rate (sccm)	2θ (°)	Half peak width (°)	Size (nm)	Lattice constant C ₀ (nm)
A	60	31.27	0.24	36	0.5721
b	70	31.28	0.22	42	0.5716
c	80	31.31	0.17	51	0.5708
d	90	31.26	0.23	41	0.5727
e	100	31.24	0.25	34	0.5731

of the RHEED pattern reveals that only the InN (002) and (004) crystal plane family diffractions occur at the middle of the pattern, and the pattern has a high definition. The crystal plane families InN (101) and (103) can also be clearly observed at other positions in the diffraction image. The results of RHEED pattern analysis show that, under a nitrogen flow rate of 80 sccm, the prepared InN thin film sample has excellent crystallization properties, the growth direction is perpendicular to the substrate, and a high c-axis preferred orientation is achieved. Moreover, the film samples prepared under other nitrogen flow conditions have poor crystallization properties, indicating that the optimal nitrogen flow rate for film preparation is 80 sccm.

XRD Analysis

After the experiment was over, the InN thin film samples prepared for different nitrogen flow rates were characterized by XRD to reveal their crystallization properties. **Figure 2** shows that the lattice orientations 43.9° and 75.4° correspond to the (111) and (220) diffraction peaks of the self-supporting diamond substrate. The highest diffraction peak at 31.3° in **Figure 2** is the diffraction peak of the prepared InN thin film and corresponds

to the diffraction peak of InN (002). The XRD pattern shows that the InN thin film samples prepared on the self-supporting diamond substrate have an excellent preferred orientation: The film material grows perpendicularly to the substrate, and a high c-axis preferred orientation is achieved. The analysis of the XRD pattern reveals that the InN thin film samples prepared in this study have excellent crystallization properties. The effect of the nitrogen flow on the crystallization properties of the thin film samples was further studied. The following equation can be derived from Scherrer's formula:

$$d = 0.94\lambda / B \cos \theta \quad (1)$$

where d is the size of the crystal grains, λ is the wavelength of the Cu K α rays and is equal to 0.15406 nm, θ is the Bragg diffraction angle, and B is the half-peak width of the film. The measured degrees of the c-axis diffraction peaks, the half-peak widths, the crystal grain sizes, and the c-axis lattice constants of the InN thin film samples prepared under different nitrogen flow rates as well as the calculated stress of each thin film sample are listed in **Table 1**. When the nitrogen flow rate increases from 60 to 80 sccm, the c-axis lattice constant of the prepared film gradually decreases, the crystal grain size gradually increases, and the FWHM gradually decreases. When the nitrogen flow rate further increases from 80 to 100 sccm, the c-axis lattice constant gradually increases, the crystal grain size gradually decreases, and the FWHM gradually increases. The results show that the film sample prepared under a nitrogen flow rate of 80 sccm has a larger crystal grain size and a smaller FWHM. This can be explained in the following way: The InN thin film samples are prepared by using the ECR-PEMOCVD system, and the nitrogen reaction source is nitrogen gas. During the preparation process, the nitrogen molecules are difficult to ionize, and they decompose because the nitrogen gas is an inert gas. When the nitrogen flow rate is low, the insufficient nitrogen decomposition keeps the supply of the nitrogen reaction source at a low level, resulting in a large number of nitrogen vacancies. Consequently, the reaction with trimethylindium is not sufficient. Therefore, a large number of indium particles are present, leading to the poor crystallization quality of the prepared thin film samples. As the nitrogen flow rate continues to increase, the efficiency of the N₂ ionization reaction improves, producing more nitrogen ions. However, because not enough indium reacts with the nitrogen ions at this time, the quality of the prepared film deteriorates. The analysis shows that the InN film samples prepared at a nitrogen flow rate of 80 sccm have excellent crystallization properties. This is consistent with the results of the RHEED analysis.

SEM Analysis

Considering that the lattice constant of the prepared InN thin film differs significantly from that of the self-supporting diamond substrate, the InN film samples prepared on the self-supporting diamond substrate were tested via SEM and analyzed. The test results show that, as the nitrogen flow rate increases from 60 to 80 sccm, the surface island density of the prepared InN film increases, and grain boundaries are clearly visible. As the

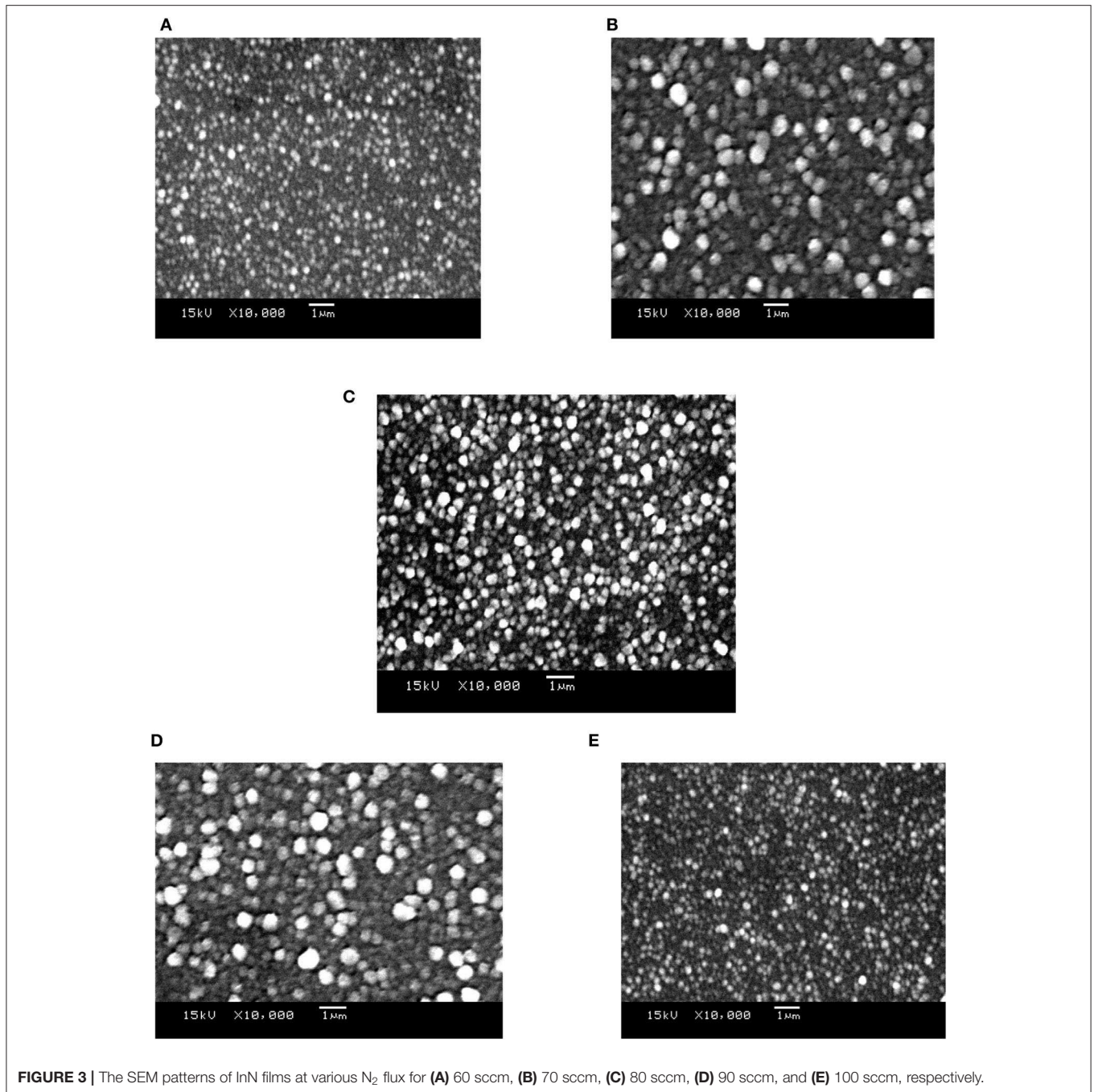


FIGURE 3 | The SEM patterns of InN films at various N_2 flux for (A) 60 sccm, (B) 70 sccm, (C) 80 sccm, (D) 90 sccm, and (E) 100 sccm, respectively.

nitrogen flow rate increases, the competitive growth mechanism of “large islands annexing small islands” takes place, and the island growth mode gradually triggers the layer-island hybrid growth mode. **Figure 3** shows that the grain boundaries of the thin film samples prepared under a nitrogen flow rate of 80 sccm tend to become larger, the number of grain boundaries reduces significantly, and the grain boundaries become more stable. The deposited atoms are stacked onto the surface of the substrate in coherent and semi-coherent forms, and the film always spreads out along the surface of the substrate in a two-dimensional

expansion mode, showing an excellent layered growth mode. However, as the nitrogen flow rate continues to increase from 80 to 100 sccm, the surface island density of the prepared InN film decreases, the crystal grains become disordered, and the grain boundaries become blurred. As the nitrogen flow rate further increases, the island growth mode of “large islands annexing small islands” does not appear. However, the layer-island hybrid growth mode gradually triggers the island growth mode. The explanation for this growth mode is the following: In the initial stage of the film formation, some gaseous atoms/molecules begin

to condense onto the surface of the substrate, thus initiating the nucleation process. When the gaseous atoms reach the surface of the substrate, the atoms adhere to the substrate at first, and then aggregate to form uniform, fine, and mobile atomic clusters called “islands.” These small bead-like islands continue to accept new deposited atoms and merge with other islands to form bigger islands. The number of islands quickly reaches its saturation level. Although the islands continue to merge, new islands emerge in the vacant areas of the substrate surface. The formation and merging of such small islands take place continuously, and larger islands constantly annex adjacent smaller islands. With the progressing of such phenomenon, the isolated islands are interconnected and form a big piece, and only some isolated holes and channels are left. These holes and channels are continuously filled, forming an initial film with a continuous morphology and a complete coverage.

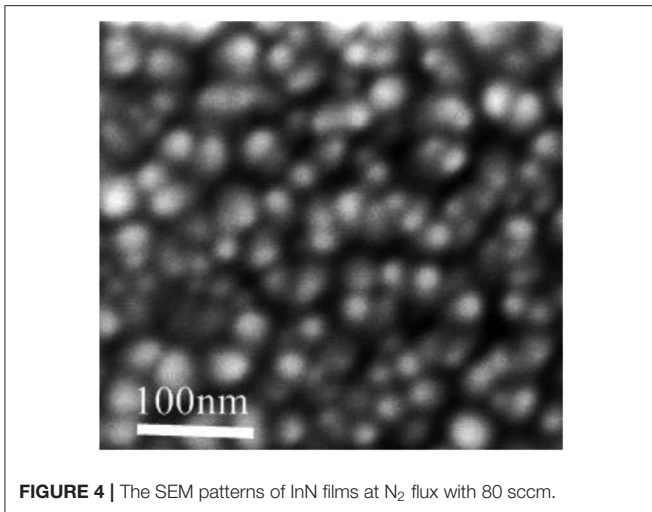


FIGURE 4 | The SEM patterns of InN films at N_2 flux with 80 sccm.

In order to further study the morphology of the InN thin film samples prepared under a nitrogen flow rate of 80 sccm, these thin film samples were tested via SEM once again with a precision of 100 nm. As can be seen from **Figure 4**, the grain boundaries of the prepared samples are clearly visible, and the crystal grains densely arrange with the same nucleation direction, indicative of an excellent preferential orientation. This analysis result is consistent with the XRD analysis result.

AFM Analysis of the InN Thin Films

By considering that the lattice constant of the prepared InN thin film samples differs significantly from that of a self-supporting diamond substrate, the surface morphology of the InN thin film samples prepared on a self-supporting diamond substrate was analyzed by using the AFM method. To pave the way for the subsequent development of optoelectronic devices based on InN thin films, the surface flatness of the InN thin films needs to be on the order of nanometers. The test result shown in **Figure 5** indicates that the surface roughness of the prepared InN thin film samples is 3 nm, which fully meets the requirements of the devices concerning the surface flatness. A further analysis of the AFM pattern reveals that when the nitrogen flow rate is 80 sccm, the surface island density of the prepared InN film increases, and the crystal grain boundaries are clearly visible, forming a uniform two-dimensional plane.

EPMA Analysis

The above analysis shows that the prepared films have excellent crystallization properties and surface morphology when the nitrogen source flow rate is 80 sccm. To study the composition of the prepared thin film, the thin film samples were analyzed via EPMA. It can be seen from **Figure 6** and **Table 2** that, as the nitrogen flow rate increases from 60 to 80 sccm, the In:N atomic ratio of the prepared InN films gradually increases. Actually, the In:N atomic ratio should be 1:1 given the chemical composition of InN. However, when the nitrogen flow rate continues to

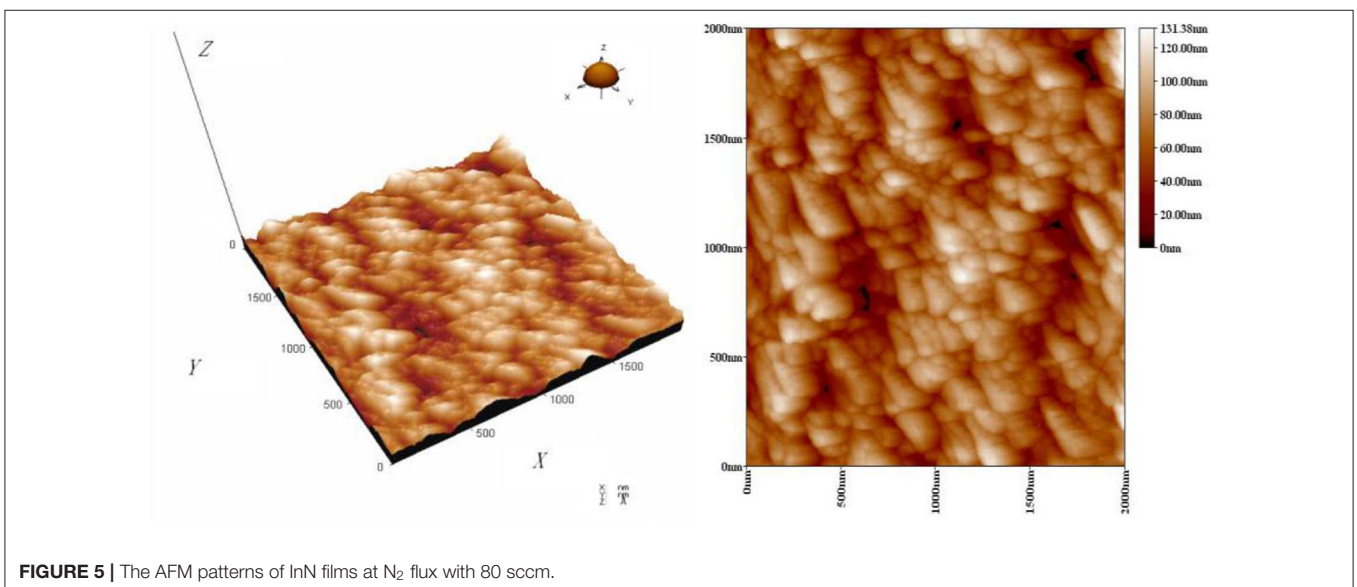


FIGURE 5 | The AFM patterns of InN films at N_2 flux with 80 sccm.

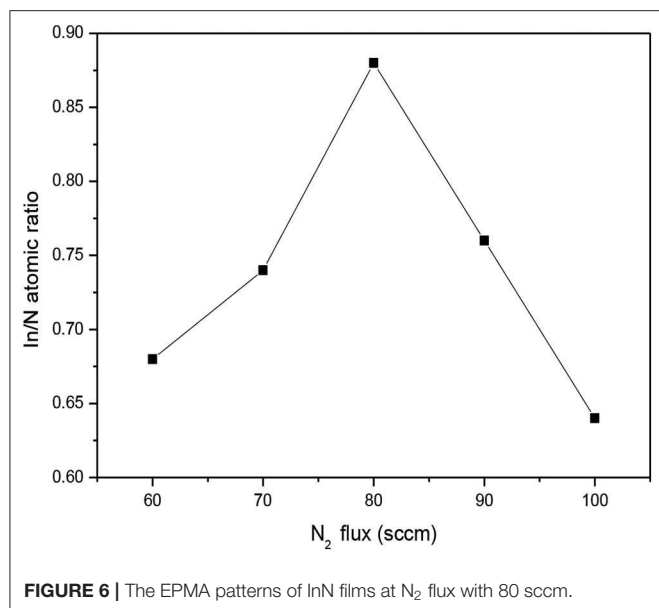


FIGURE 6 | The EPMA patterns of InN films at N₂ flux with 80 sccm.

TABLE 2 | The content of InN films deposited at different N₂ flux.

Sample	N ₂ flux (sccm)	In/N atomic ratio
A	60	0.68
B	70	0.74
C	80	0.88
D	90	0.76
E	100	0.64

increase from 80 to 100 sccm, the In:N atomic ratio of the prepared InN film gradually decreases. When the flow rate of the N₂ source is 80 sccm, the In:N atomic ratio of the prepared InN thin film sample is 0.88, which is the highest value. This indicates that several nitrogen atoms escape in the process of the thin film growth, which results in a large number of nitrogen vacancies and in an incomplete reaction. The generation of nitrogen vacancies leads to the formation of indium particles, which leads to the

formation of metal indium droplets. In this case, the In:N atomic ratio is not close to 1:1.

CONCLUSION

A number of InN film samples with superb properties were prepared on a self-supporting diamond substrate under different nitrogen flows using an ECR-PEMOCVD system. The experimental results show that the variation in the nitrogen flow has a great impact on the preferential growth of the (0002) crystal plane of the InN thin film. By increasing the nitrogen flow moderately, the crystal quality of the film can be improved. With an appropriate nitrogen flow, InN thin films with a high c-axis preferential orientation can be obtained, and their surface thin film is relatively flat. However, a too high nitrogen flow does not improve the crystallization quality of the thin films. The EPMA analysis shows that the In:N atomic ratio of the prepared InN film samples is close to 1:1 and that a small amount of metal indium droplets are present. The results of the experiment and of the analysis show that InN thin films prepared under a nitrogen flow rate of 80 sccm have excellent preferential orientation, surface morphology, and atomic ratio.

DATA AVAILABILITY STATEMENT

The original contributions presented in the study are included in the article/supplementary materials, further inquiries can be directed to the corresponding authors.

AUTHOR CONTRIBUTIONS

SW: the total master planning and film preparation. FQ: experimental data analysis. YB: theoretical study of different test results. DZ: film structure test and analysis.

FUNDING

This work was supported by the National Natural Science Foundation of China under Grant No. 51872036, the fund of Science and Technology Project of Liaoning, China under Grant No. 20180510049.

REFERENCES

- Akasaka, T., Schied, M., and Kumakura, K. (2018). N-face (0001) GaN/InN/GaN double heterostructures emitting near-infrared photoluminescence grown by metalorganic vapor phase epitaxy. *Appl. Phys. Exp.* 8:081001. doi: 10.7567/APEX.11.081001
- Anjum, F., Ahmad, R., and Afzal, N. (2018). Characterization of InN films prepared using magnetron sputtering at variable power. *Mater. Lett.* 219, 23–28. doi: 10.1016/j.matlet.2018.02.058
- Bashir, U., Hassan, Z., and Ahmed, N. (2018). Structural, electrical and optical properties of sputtered-grown InN films on ZnO buffered silicon, bulk GaN, quartz and sapphire substrates. *J. Electr. Mater.* 8, 4875–4881. doi: 10.1007/s11664-018-6386-3
- Bi, Z., Ek, M., and Stankevici, T. (2018). Self-assembled InN quantum dots on side facets of GaN nanowires. *J. Appl. Phys.* 16:164302. doi: 10.1063/1.5022756
- Buzynin, Y., Khrykin, O., and Yunin, P. (2018). InN layers grown by MOCVD on a-Plane Al₂O₃. *Phys. Status Solidi*. 11:1700919. doi: 10.1002/pssa.201700919
- Darakchieva, V., Xie, M., and Rogalla, D. (2011). Free electron properties and hydrogen in InN grown by MOVPE. *Phys. Status Solidi*. 208, 1179–1182. doi: 10.1002/pssa.201001151
- Dwivedi, S., Ghosh, A., and Ghadi, H. (2018). Oblique angle deposited InN quantum dots array for infrared detection. *J. Alloys Compound*. 25, 297–304. doi: 10.1016/j.jallcom.2018.06.346
- Ke, W., Chiang, C., and Son, W. (2018). InGaN-based light-emitting diodes grown on various aspect ratios of concave nanopattern sapphire substrate. *Appl. Surface Sci.* 456, 967–972. doi: 10.1016/j.apsusc.2018.06.223
- Kobayashi, A., Oseki, M., and Ohta, J. (2018). Epitaxial growth of thick polar and semipolar inn films on yttria-stabilized zirconia using pulsed sputtering deposition. *Phys. Status Solidi* 255:1700320. doi: 10.1002/pssa.201700320

- Liu, H., Wang, X., and Chen, Z. (2018). High-electron-mobility InN epilayers grown on silicon substrate. *Appl. Phys. Lett.* 112:162102. doi: 10.1063/1.5017153
- Lucarelli, G., and Brown, T. M. (2019). Development of highly bendable transparent window electrodes based on MoO_x, SnO₂, and Au dielectric/metal/dielectric stacks: application to indium tin Oxide (ITO)-free perovskite solar cells. *Front. Mater.* 6:310. doi: 10.3389/fmats.2019.00310
- Madapu, K., and Dhara, S. (2018). Surface-enhanced raman spectroscopy using 2D plasmons of InN nanostructures. *Appl. Phys. A.* 6:435. doi: 10.1007/s00339-018-1845-5
- Madapu, K., Sivadasan, A., and Baral, M. (2018). Observation of surface plasmon polaritons in 2D electron gas of surface electron accumulation in InN nanostructures. *Nanotechnology* 27:275707. doi: 10.1088/1361-6528/aabe60
- Marikutsa, A., Romyantseva, M., Gaskov, A., Batuk, M., Hadermann, J., Sarmadian, N., Saniz, R., et al. (2019). Effect of zinc oxide modification by indium oxide on microstructure, adsorbed surface species, and sensitivity to CO. *Front. Mater.* 6:43. doi: 10.3389/fmats.2019.00043
- Peng, H., Feng, X., and Gong, J. (2018). Low temperature growth of polycrystalline InN films on non-crystalline substrates by plasma-enhanced atomic layer deposition. *Appl. Surf. Sci.* 30, 830–834. doi: 10.1016/j.apsusc.2018.08.093
- Pereira, H. J., and Hatton, R. A. (2019). High figure-of-merit transparent copper-zinc oxide window electrodes for organic photovoltaics. *Front. Mater.* 6:228. doi: 10.3389/fmats.2019.00228
- Polanco, C., and Lindsay, L. (2018). Thermal conductivity of InN with point defects from first principles. *Phys. Rev.* 98:014306. doi: 10.1103/PhysRevB.98.014306
- Qi, K., Lv, W., Iltaf, K., and Liu, S. (2020a). Photocatalytic H₂ generation via CoP quantum-dot-modified g-C₃N₄ from electroless plating. *Chin. J. Catal.* 41, 114–121. doi: 10.1016/S1872-2067(19)63459-5
- Qi, K., Xie, Y., Wang, R., Liu, S., and Zhao, Z. (2019). Electroless plating Ni-P cocatalyst decorated g-C₃N₄ with enhanced photocatalytic water splitting for H₂ generation. *Appl. Surf. Sci.* 466, 847–853. doi: 10.1016/j.apsusc.2018.10.037
- Qi, K., Xing, X., Amir, Z., Li, M., Wang, Q., Liu, S., et al. (2020b). Transition metal doped ZnO nanoparticles with enhanced photocatalytic and antibacterial performances: experimental and DFT studies. *Ceramics Int.* 46, 1494–1502. doi: 10.1016/j.ceramint.2019.09.116
- Tharsika, T., Thanihachelvan, M., Haseeb, A. S. M. A., and Akbar, S. A. (2019). Highly sensitive and selective ethanol sensor based on ZnO nanorod on SnO₂ thin film fabricated by spray pyrolysis. *Front. Mater.* 6:122. doi: 10.3389/fmats.2019.00122
- Yu, Q., Rong, P., Ren, S., Jiang, L., and Li, Y. (2019). Fabrication and electrochemical performance of Al-Doped ZnO nanosheets on graphene-based flexible substrates. *Front. Mater.* 6:208. doi: 10.3389/fmats.2019.00208
- Zhang, D., Qin, F., Bai, Y., and Bian, J. (2012). Effect of buffer layer on the structural and morphological properties of GaN films grown with ECR-PEMOCVD. *Diamond Related Mater.* 21, 88–91. doi: 10.1016/j.diamond.2011.10.016
- Zhou, J., Li, J., and Lu, S. (2017). Characteristics of InN epilayers grown with H₂-assistance. *Aip Adv.* 11:115207. doi: 10.1063/1.5001546

Conflict of Interest: The authors declare that the research was conducted in the absence of any commercial or financial relationships that could be construed as a potential conflict of interest.

Copyright © 2020 Wang, Qin, Bai and Zhang. This is an open-access article distributed under the terms of the Creative Commons Attribution License (CC BY). The use, distribution or reproduction in other forums is permitted, provided the original author(s) and the copyright owner(s) are credited and that the original publication in this journal is cited, in accordance with accepted academic practice. No use, distribution or reproduction is permitted which does not comply with these terms.



Flower-Like ZnO Nanorods Synthesized by Microwave-Assisted One-Pot Method for Detecting Reducing Gases: Structural Properties and Sensing Reversibility

Abdullah Aljaafari^{1*}, Faheem Ahmed^{1*}, Chawki Awada¹ and Nagih M. Shaalan^{1,2*}

¹ Department of Physics, College of Science, King Faisal University, Al-Ahsa, Saudi Arabia, ² Physics Department, Faculty of Science, Assiut University, Assiut, Egypt

OPEN ACCESS

Edited by:

Kezhen Qi,
Shenyang Normal University, China

Reviewed by:

Amir Zada,
Abdul Wali Khan University
Mardan, Pakistan
Enesca Ioan Alexandru,
Transilvania University of
Braşov, Romania

*Correspondence:

Nagih M. Shaalan
nmohammed@kfu.edu.sa
Abdullah Aljaafari
aaljaafari@kfu.edu.sa
Faheem Ahmed
fahmed@kfu.edu.sa

Specialty section:

This article was submitted to
Nanoscience,
a section of the journal
Frontiers in Chemistry

Received: 18 March 2020

Accepted: 01 May 2020

Published: 02 July 2020

Citation:

Aljaafari A, Ahmed F, Awada C and
Shaalan NM (2020) Flower-Like ZnO
Nanorods Synthesized by
Microwave-Assisted One-Pot Method
for Detecting Reducing Gases:
Structural Properties and Sensing
Reversibility. *Front. Chem.* 8:456.
doi: 10.3389/fchem.2020.00456

In this work, flower-like ZnO nanorods (NRs) were successfully prepared using microwave-assisted techniques at a low temperature. The synthesized NRs exhibited a smooth surface and good crystal structure phase of ZnO. The sharp peak of the XRD and Raman spectrum confirmed the high crystallinity of these ZnO NRs with a pure wurtzite structure. The nanorods were $\sim 2 \mu\text{m}$ in length and $\sim 150 \text{nm}$ in diameter, respectively. The electron diffraction pattern confirmed that the single crystal ZnO nanorods aligned along the [001] plane. The NRs were applied to fabricate a gas sensor for reducing gases such as CH_4 , CO , and H_2 . The sensor showed a good performance and sensitivity toward the target gases. However, its response toward CH_4 and CO was higher compared to H_2 gas. Although the operating temperature was varied from room temperature (RT) up to 350°C , the sensor did not show a response toward any of the target gases in the range of RT – 150°C , but dramatic enhancement of the sensor response was observed at 200°C , and up to higher temperatures. This behavior was ascribed to the activity of the smooth surface and the reactivity of surface oxygen species with the targeted gases. The sensor response was measured at various gas concentrations, where the calibration curve was shown. The gas sensing mechanism was described in terms of the reaction of the gases with the transformed oxygen species on the surface of the oxides.

Keywords: nanoflowers, ZnO nanorods, gas sensor, methane, carbon monoxide, hydrogen

INTRODUCTION

Due to their optical and physical properties, ZnO nanostructures have become a suitable material to use in different environmental monitoring applications (Livage, 1981; Roy et al., 2011; Spencer, 2012; Brookes et al., 2014; Kumar et al., 2015; Chen et al., 2019; Zada et al., 2019, 2020; Qi et al., 2020a,b). One of these applications that have attracted the interests of scientific communities is gas-sensing applications that require some specific characteristics such as high surface-to-volume ratio and good chemical and thermal stability (Vomiero et al., 2007; Guo et al., 2012; Pan et al., 2013; Bai et al., 2014; Hosseini et al., 2015; Jin et al., 2015; Mascini et al., 2018; Jingxuan et al., 2020).

In fact, the morphology of materials-based gas sensors is extremely important to the performance of the gas sensor. Thus, since the first use of ZnO nanostructures as gas-sensing

materials (Seiyama et al., 1962), many studies have been reported on the morphology-dependent gas sensor performance (Alam et al., 2015; Zhang et al., 2017; Ridha et al., 2018; Qin et al., 2019; Zhao et al., 2019). Zhang et al. showed that 1D ZnO nano-cones were highly promising for practical application in gas sensors, due to their large surface area per unit mass and unique conical structure (Zhang et al., 2017). Uniform 1D ZnO/ZnCo₂O₄ nanocomposite showed a fast response and good selectivity to acetone gas (Qin et al., 2019). In the same sequence, an intensive investigation on the effects of the lengths and diameters of ZnO nanorods, with regard to the sensing performance of ethanol vapor, was also studied (Ridha et al., 2018). ZnO NRs supported by the complex surfactant showed excellent ethanol sensing properties at an optimal operating temperature of 300 °C, which could be attributed to their large surface to volume ratio, and a high number of surface defects due to oxygen vacancies (Zhao et al., 2019). A new structure, by synthesizing Pd nanocubes (NCs) decorated on vertical ZnO nanorods (NRs) applied to a resistive-type gas sensor, was developed by Bin Alam et al. (2015). The shape control of Pd NCs with close {111} packing effects remarkably enhances the catalytic activity and capacity for H₂ adsorption compared to that of {100}.

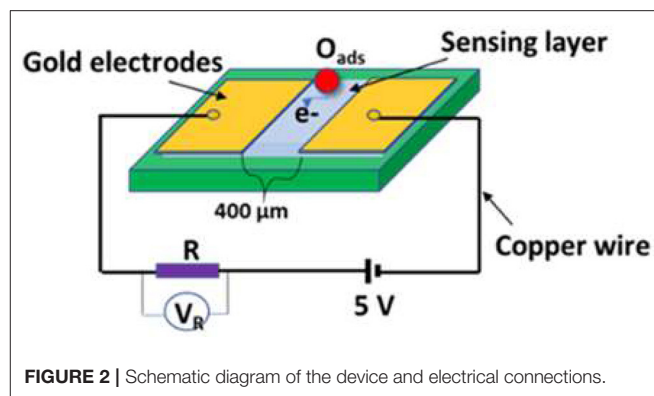
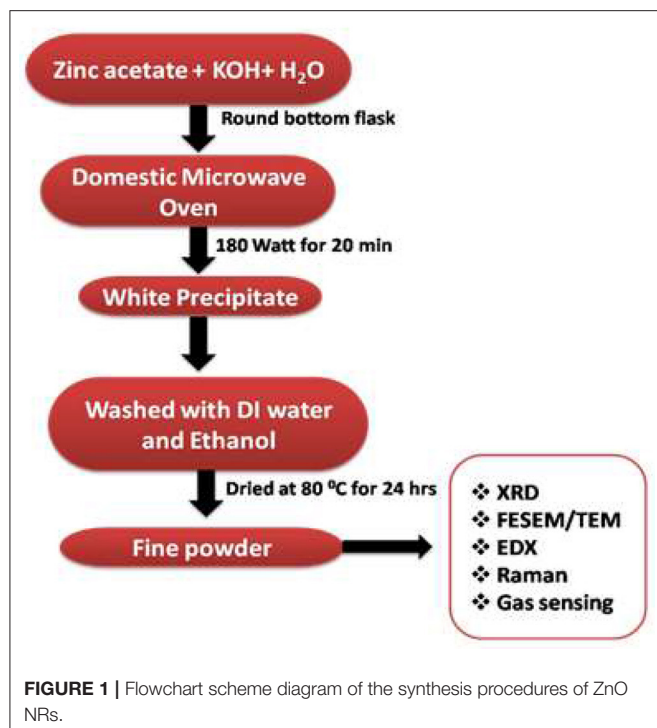
The challenges are not limited to the high-performance gas sensor but also to the synthesis methods, as few of them consider the real working conditions of a sensor during the functional characterizations, especially, when they address complex structures. For example, the electrochemical method (Lee and Tak, 2001), template-based growth (Li et al., 2000), sol-gel processing (Chen and Liu, 2005), and the hydrothermal method (Rakshit et al., 2012) are some of the techniques widely used for growing different morphologies of ZnO nanostructures. More specifically, many methods have the disadvantages of low productivity, long processing times, and low growth rates. Time is invaluable and becoming increasingly important in these manufacturing processes where one has to advance in many trial and error experiments to obtain the best results. In this regard, microwave synthesis methods have unique influences on high reaction rates, short processing times, reaction selectivity, power-saving, and are low cost (Rana et al., 2016).

It is known that gas sensing properties strongly depend on the morphology of the sensing materials. Various ZnO nanostructures, such as nanoparticles, quantum dots, cloudy-like nanoparticles, isotropic nanoparticles, and nanorods were investigated as a sensitive layer for various gasses, and it was found that the morphology of ZnO nanostructures significantly influenced the responses of the sensors to the reducing gases (Jonca et al., 2014; Park et al., 2019). ZnO nanostructures of one-dimension such as rods, wires, tubes, and belts have been attracting increased attention due to their aspect ratio, high surface to volume ratio, high electron mobility, etc.; these parameters play an important role in the gas sensor (Hernandez-Ramirez et al., 2009). While working with the 1D structure, we might observe a considerable diversity in geometric parameters of this nanostructure. Thus, if the 1D nanostructure has been used as a sensitive layer, specific geometrical parameters

are considered. Shaalan et al. (2011) found that the sensing properties of oxide gas sensors were well-controlled by the 1D nanostructure, and although the high surface-to-volume ratio of the sensing layer was an important parameter to enhance the sensing response, the low density of the potential barrier at interconnected grains was required and had better be considered in the proposal of sensors. The results expressed that the 1D structure has many advantages in reliability and high response.

It was reported that the flower-like structure of random branches was helpful for avoiding agglomeration as well as showed good electron transportation. This structure has been reported for ZnO with high performance in photocatalysts (Bohle and Spina, 2009), chemical sensors (Wan et al., 2004), etc. The high performance is ascribed to the surface defects, species, and surface adsorption. Wang et al. developed flower-like ZnO on GaN using the electro-deposition technique and its application as ethanol gas sensors at room temperature (Wang et al., 2019). Fan et al. combined the hydrothermal method with electrospinning to produce flower-like ZnO hierarchical structures that showed high sensitivity toward H₂S gas (Fan et al., 2019). Agarwal et al. showed that nanorods-like ZnO structures synthesized using the hydrothermal method were very selective and sensitive toward NO₂, but not CO (Agarwal et al., 2019). Although the improvement carried-out on the gas sensor performance due to the morphologies effects presented in the previous studies, the morphology and structure geometry in gas-sensing properties for developing reliable and sensitive gas sensors are still highly considered.

In this work, flower-like ZnO nanorods (NRs) are fabricated in a microwave oven. Low growth temperature and a short time are used in the current work for growing polycrystalline ZnO nanorods. The procedures used in this method are simpler than the traditional method. The structure and morphology of the synthesized ZnO NRs were studied by XRD, FE-SEM, TEM, and Raman spectroscopy. These NRS are applied in fabricating gas sensors for testing its sensitivity in detecting different reducing gases at different operating temperatures. The gas sensor was applied to investigate the reversible behavior toward CH₄, CO, and H₂ reducing gases with repeated cycles and various gas concentrations. Carbon monoxide (CO) gas is generally regarded as one of the most dangerous air pollutants among greenhouse gases and is produced from exhausts of factories, and vehicles. It is odorless, colorless, and regarded as a silent killer gas. CH₄ is highly combustible and can form an explosive mixture with ambient air. Thus, it is important to monitor CH₄ escaping into the atmosphere for both industrial process control and reduction of environmental pollution. Hydrogen gas is used as a potential fuel in vehicles and fuel cells to be transformed into electricity. It is also used in the production of some industrial chemicals and food products. An explosion can occur if hydrogen leaks into the air at a specific level (4%). Therefore, there is a need to develop a reliable sensor based on metal oxide reducing gas with improved performance. Our work demonstrates the developing possibility of a ZnO-nanostructure based gas sensor for reducing gases.



electron microscopy (HRTEM) of the samples were performed by Transmission electron microscopy (TEM) [FE-TEM (JEOL/JEM-2100F version)] operated at 200 kV. The Raman spectra were measured using a LabRAM HR800 confocal micro-Raman spectrometer equipped with a multichannel charge-coupled detector. A He-Cd laser (wavelength 442 nm, 20 mW) was used as a source of excitation. The number of gratings in the Raman spectrometer was 1,800 l/mm. The Raman spectra were collected in a backscattering geometry with a spectral resolution of 0.8 cm^{-1} at ambient temperature. **Figure 1** shows the flow diagram for the synthesis of ZnO nanostructures.

MATERIALS AND METHODS

Preparation and Characterization of ZnO Nanorods

All reagents used in this research were of analytical grade and used as received. The synthesis was performed in a simple microwave oven (Samsung, 750 W). For the synthesis of nanorods, a reaction solution in 100 ml deionized water was prepared to contain a 1:20 molar ratio of zinc acetate dihydrate [$\text{Zn}(\text{CH}_3\text{COO})_2 \cdot 2\text{H}_2\text{O}$; 99.99%, Sigma Aldrich] and potassium hydroxide (KOH; 99.99%, Sigma Aldrich), and then transferred into a commercial microwave oven. The reaction was carried out at a microwave power of 180 W for 20 min (Ahmed et al., 2011). Subsequent to microwave reaction, the resulted solution was cooled to room temperature and the precipitate was obtained. The resulted precipitate was separated by centrifugation, followed by thorough washing in the presence of deionized water and ethanol numerous times, and the collected samples were finally dried in an oven at 80°C for 24 h. The sample was calcined at 400°C for 2 h and then used for the gas sensing measurements.

X-ray diffraction [Phillips X'pert (MPD 3040)] was used to study the crystal structure and phase purity of the samples. Morphologies of the samples were studied by Field emission scanning electron microscopy (FESEM) (TESCAN; MIRA II LMH microscope). To find the elemental composition of ZnO, energy dispersive X-ray spectroscopy (EDX, Inca Oxford, attached to the FESEM) was used. Further morphological characterization including micrographs, selected area electron diffraction (SAED) pattern, and high-resolution transmission

Preparation and Characterizations of Gas Sensor

Since the sensing materials are in powder form, the sensor fabrication was carried out in a sequence of two gold electrodes with $400 \mu\text{m}$ -gap deposited by DC-sputtering on a substrate of glass. The sensing layer of $10 \mu\text{m}$ was deposited by the screen-printing method on the top of the electrodes, as shown in **Figure 2**. The sensing layer was then treated for 30 min at 400°C in the air ambient before testing the target gases in order to avoid any recrystallization during the testing. The operating temperature starting from 200 up to 350°C was well-controlled. Dry synthetic air (21% O_2 , and 79% N_2) mixed with a gas such as H_2 , CO, and CH_4 flowed into the chamber at a flow rate of 200 SCCM, which was controlled by Horiba MFCs (SEC-N112 MGM-Horiba). A computerized data acquisition instrument (Multi-channel- LXI-Agilent 34972A) was used to record the electrical measurements. The sensing response calculated from the electrical data is defined as $S = R_a/R_g$, where R_a and R_g are the sensor resistances in the air and gas, respectively.

RESULTS AND DISCUSSIONS

Structure and Morphology

The XRD pattern of the as-prepared ZnO powder is shown in **Figure 3**. The chart is indexed in the hexagonal phase with the lattice-matched parameters ($a = 3.254 \text{ \AA}$ and $c = 5.197 \text{ \AA}$), which are very close to the standard data reported in the JCPDS, 89-0501 card. The recorded XRD pattern exhibits a single-phase nature for the wurtzite-ZnO structure. The XRD pattern does

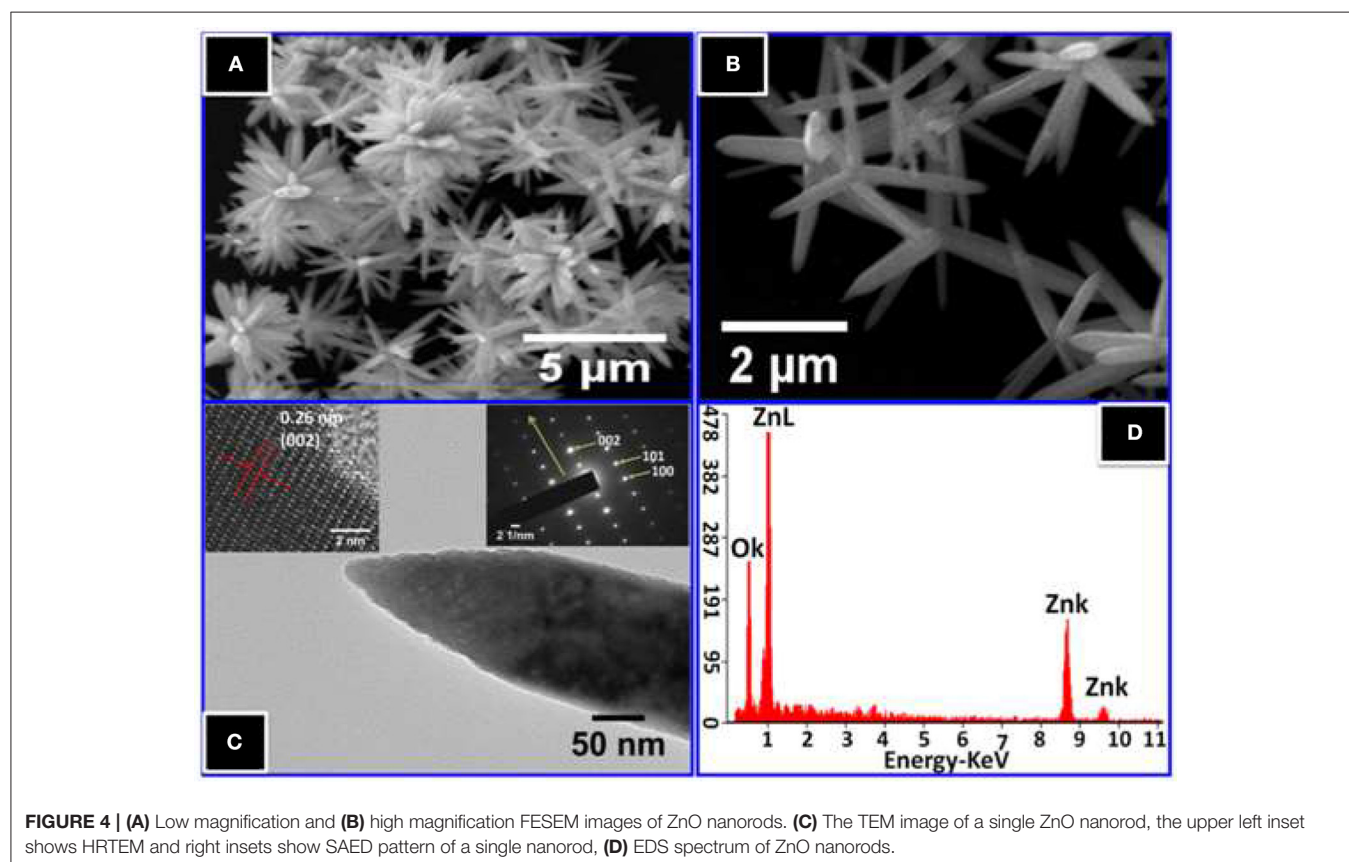
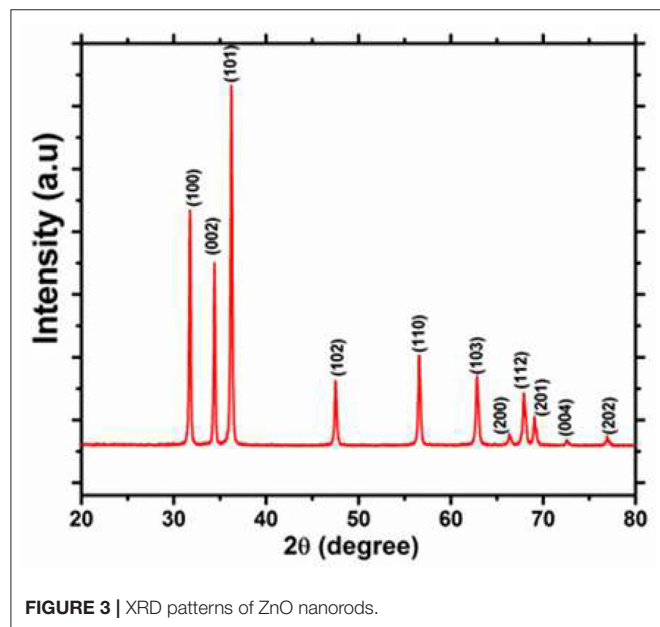
not show any diffraction peaks for other impurities, and the high crystallinity is shown from the sharpness of the peaks of the as-prepared ZnO nanorods.

Figures 4A,B show FESEM images of ZnO nanostructures. The images exhibit flower-like clusters for the synthesized ZnO

nanorods on a large-scale with high dispersion, and more or less uniform morphologies. From the high magnification image shown in Figure 4B of flower-like ZnO, numerous symmetric taper arms composed of a number of aggregative nanorods can be observed.

Figure 4C shows a complementary morphological description obtained by TEM with SAED. From this figure, the TEM micrograph of a typical individual ZnO nanorod confirms the crystal quality and growth direction. The diameters of the NRs range from 145 to 185 nm with a tip diameter of ~ 15 nm, while the length is approximately $2\ \mu\text{m}$. Further, the TEM image clarifies, that the ZnO nanorod has a sharp tip at the end. In addition, HRTEM shows a well-resolved d-spacing of 0.265 nm, which corresponds to the plane (002) of wurtzite ZnO, indicating single crystallinity for the ZnO NRs in nature with and preferentially growth direction of [001] in c-axis, which was confirmed in SAED pattern. For further confirmation, the EDS spectrum of the elemental analysis of ZnO NRs is shown in Figure 4D. The only Zinc and oxygen signals are detected in the spectrum, which confirms that the NRs are pure ZnO.

A LabRAM HR800 confocal micro-Raman spectrometer is used to measure the Raman spectra. As one of the simplest uniaxial crystals, ZnO with a wurtzite structure belongs to the C_{6v}^4 ($P6_3\ mc$) space group. For the perfect ZnO crystal, only the optical phonons at Γ point of the Brillouin zone are involved in first-order Raman scattering. We can see different optical modes



in the group theory: $\Gamma_{\text{opt}} = A_1 + 2B_1 + E_1 + 2E_2$. The two first modes, A_1 and E_1 , are polar and can be divided into transverse optical (A_1^{TO} and E_1^{TO}) and longitudinal optical (A_1^{LO} and E_1^{LO}) components. E_2 mode is composed of two modes, a low and a high-frequency phonon (E_2^{low} and E_2^{high}), which correspond to the vibration of the heavy Zn sublattice and oxygen atoms, respectively. According to the Raman selection rule, the modes mentioned above are first-order Raman-active modes (Zhang

et al., 2005, 2009). For the B_1 mode, it is silent and has two frequencies which are the B_1^{low} and B_1^{high} modes, located at 260 and 540 cm^{-1} , respectively (Damen et al., 1966; Calleja and Cardona, 1977).

In our geometry of excitation and collection, the E_2 , A_1 (TO), and E_1 (TO) modes are active when the incident light is perpendicular to the c -axis (Decremps et al., 2002). As the c -axis is oriented in space, most of the modes can appear. For example, the E_2^{low} mode is observed at 99.5 cm^{-1} and the E_2^{high} mode at 438 cm^{-1} has a high intensity in the Raman spectrum (Figure 5), confirming perfect crystallinity of the sample. The peak located at 384 cm^{-1} is assigned to the A_1 (TO) mode. By performing the Gaussian-Lorentz fitting, we can observe a weak shoulder peak located at 425 cm^{-1} that corresponds to the E_1 (TO) mode. The E_1 (LO) mode is observed at 583 cm^{-1} ; this peak can be observed with the c -axis of nanorods which is normal on the surface of the sample. Moreover, we can also observe another optical phonon mode near the A_1 symmetry, located at 333 cm^{-1} (Rajalakshmi et al., 2000). The acoustic combination of A_1 and E_2 was observed around 1,101 cm^{-1} (Wang et al., 2004). Our results show a large band located between 1,060 and 1,200 cm^{-1} , which are in good agreement with previous literature's report. The broad peak at 663 and 1,152 cm^{-1} are due to the multi-phonon process (Calleja and Cardona, 1977). We can also clearly see one of the silent modes, B_1 (high), which is located at 540 cm^{-1} .

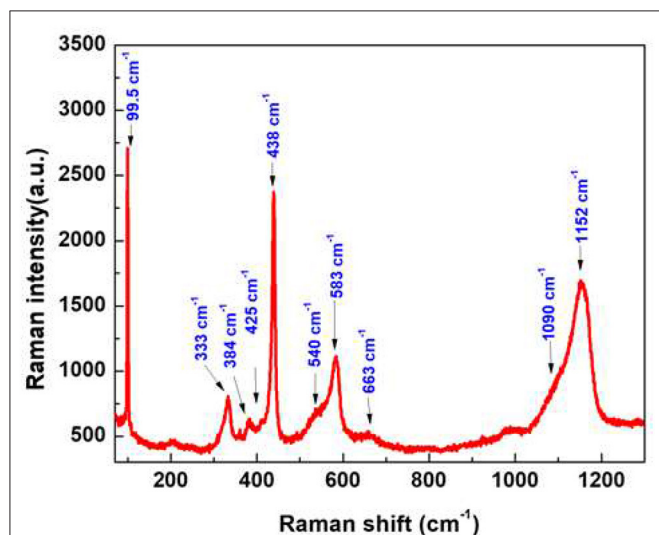


FIGURE 5 | Room temperature Raman spectrum of ZnO nanorods.

Sensing Properties

The sensing properties of ZnO flower-like NRs sensors are systematically studied at various operating temperatures toward

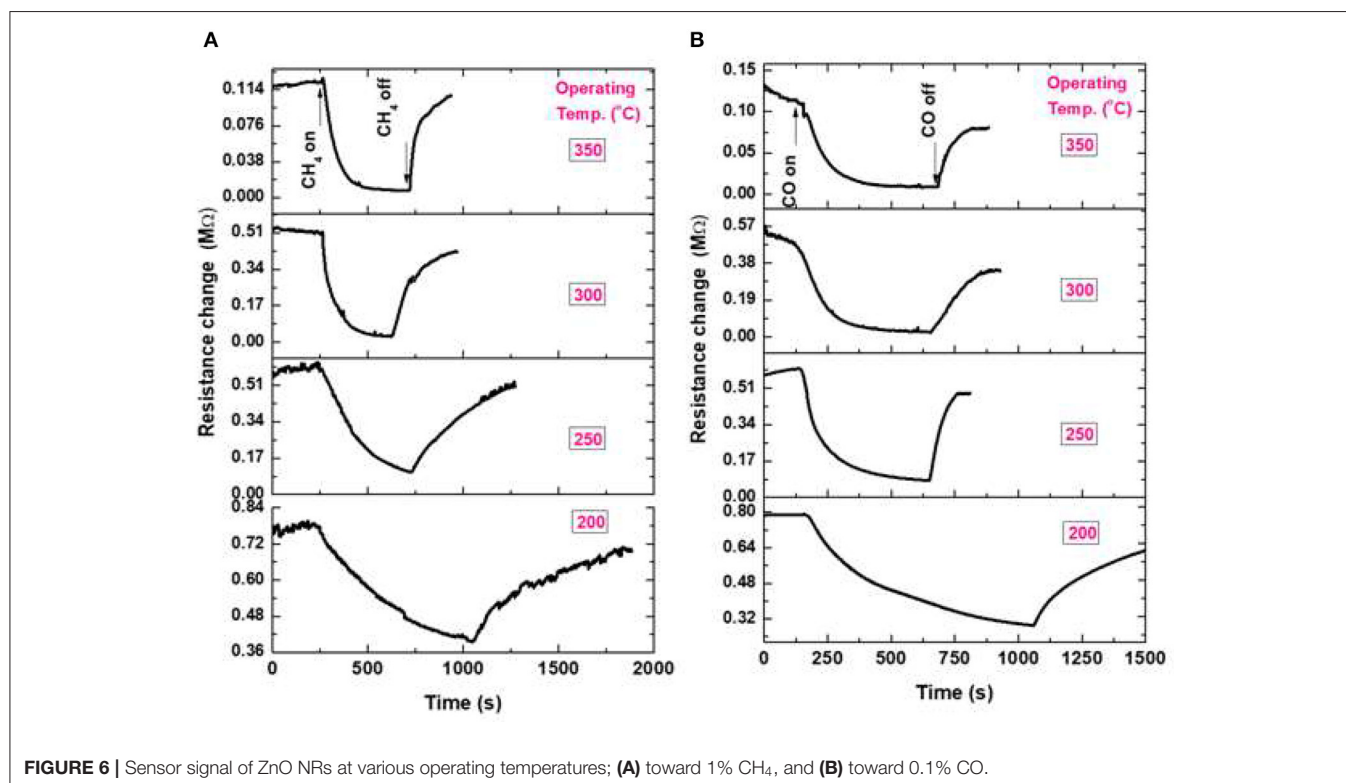


FIGURE 6 | Sensor signal of ZnO NRs at various operating temperatures; (A) toward 1% CH_4 , and (B) toward 0.1% CO .

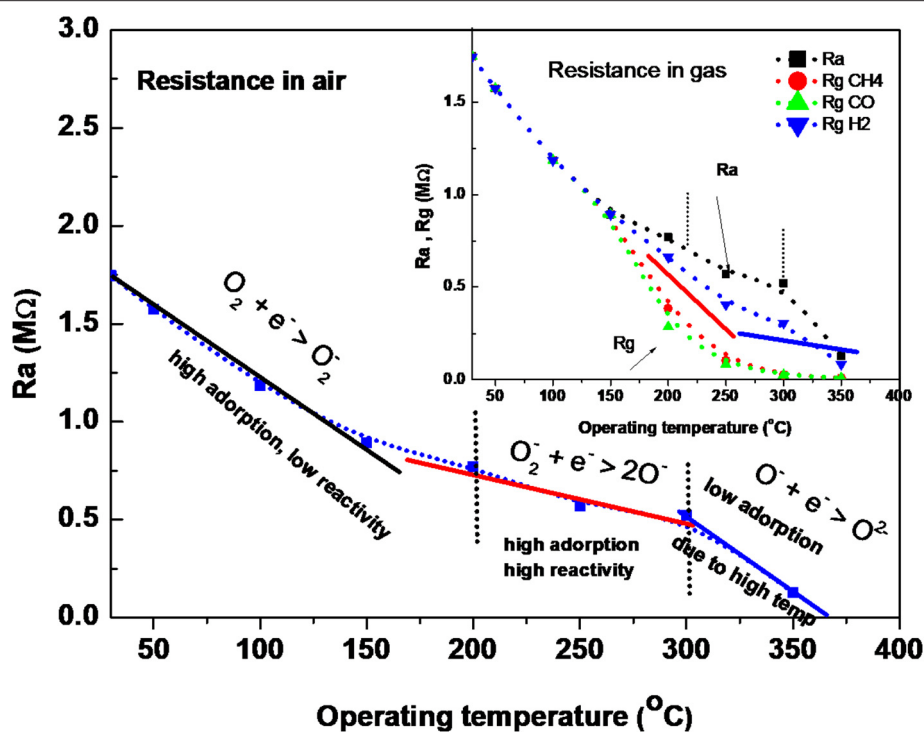


FIGURE 7 | The change in resistance in air and in air having gas as a function of temperature.

reducing gases of CH_4 , CO , and H_2 . The variation of resistance in the presence of gases for the fabricated NRs sensor toward 1.0% CH_4 , 0.1% CO , and 1.0% H_2 is shown in Figure 6. It can be seen that the resistance of the sensor decreases if the gas is introduced to the sensor surface, suggesting that the prepared ZnO nanostructure is an n-type semiconductor-like material. According to the band theory (Yamazoe et al., 1979) in gas sensors, the target gas interacts with the surface of the metal oxide semiconductor through surface adsorbed oxygen ions. The interaction causes a change in the charge carrier concentrations of the oxide, resulting in a resistivity change. The majority of carriers of n-type semiconductors, such as ZnO, are electrons. Upon exposure to the reducing gas, a decrease in resistivity occurs because the electrons are injected back to the conduction band of the oxide. This explanation is in good agreement with the presented results in this work. The operating temperature of the sensor is varied from RT up to 350°C , however, the sensor did not show any response in the range of RT- 150°C (not shown here). On the contrary, a dramatic change in the sensor response is observed at 200°C , which is ascribed to the increase of the surface activity of NRs at higher temperatures, since the gas reacts with the active sites on the oxide surface. Although ZnO NRs have a high surface area compared to the bulk, the surface of ZnO NRs presented here is smooth, which has a low surface activity to the gas reaction at the low temperature.

To explain the surface activity, we must clarify the reaction of surface species (adsorbed molecules) in air and in air containing gas. It is well-known that ZnO is an n-type semiconductor,

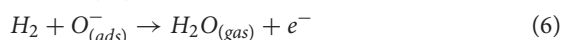
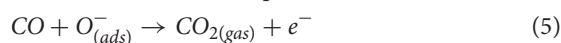
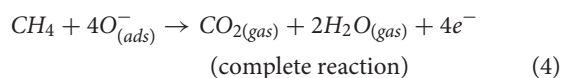
and its gas-sensing mechanism belongs to the surface-controlled type (Ruhland et al., 1998; Koziej et al., 2007; Haridas and Gupta, 2012; Shaalan et al., 2019a,b), and the change in conductivity is dependent on the species type and the amount of chemisorbed oxygen on the surface. The intrinsic resistance of the semiconductor decreases when increasing the temperature; however, we have to consider the transformation of physisorbed oxygen molecules into various oxygen ions when increasing the surface temperature. Ruhland et al. (1998), have supposed the transformation of oxygen molecules with surface temperature as shown in the following equations:



Thus, studying the behavior of oxide in the air with these transformations compared to the intrinsic behavior of the semiconductor, we may be able to understand the surface activity at various temperatures. Figure 7 shows the change in the ZnO conductivity (based resistance change) in air and in gas (inset figure) as a function of the operating temperature. It indicates that the charge exchange reactions of ZnO NRs with the oxygen species are dependent on the surface temperature. Three regions can clearly distinguish the reaction of oxygen species with ZnO electronic surface in air. The first region shows that ZnO conductivity increased with an increasing temperature, although O_2 molecules transform to O_2^- , which picked up some electrons from the conduction band of the oxide. However, the

electron transport in the conduction band due to thermal energy, dominates the conduction, indicating a low reactivity of oxygen onto the ZnO surface at these low temperatures of RT-150°C. In this temperature range, the resistance of the ZnO NRs sensor (in the air) decreased with the large slope with an increasing surface temperature. In the second range of 200–300°C, it decreases with a low slope, which is expected to be due to the high reactivity of the dissociation of O^{2-} to $2O^-$ with the surface of ZnO. The third region shows, again, a large decrease in ZnO resistance, although $2O^-$ transforms to O^{2-} . This is attributed to the low adsorption and diffusion of oxygen molecules into the grains of ZnO at this high temperature, which allows for more conduction electrons to thermally transport.

It is well-known that reducing gas prefers to react with atomic oxygen ions O^- rather than O_2^- ions on the surface, which causes the sensor to be active at 200°C (Ruhland et al., 1998; Koziej et al., 2007; Haridas and Gupta, 2012; Shaalan et al., 2019a,b). Thus, at low temperatures of RT-150°C, the chance of reaction is very low. However, it is highest at 200–300°C when O^- ions are the most available species. This reactivity decreases again at higher temperatures of 350°C due to the formation of O_2^- . Thus, the dramatic improvement in the response at 200–300°C can be attributed to the light of the formation of oxygen species. As a result of the forming oxygen ions on the oxide, the reducing gas reacts with O^- ions and produces neutral compounds (such as H_2O , and CO_2 depending on the gas type Koziej et al., 2007; Haridas and Gupta, 2012; Shaalan et al., 2019a,b) and injects electron charges back to the oxide conduction band, causing a decrease in the resistance due to the increase in the conduction electron density, as follows:



The sensor response measured for ZnO NRs at various operating temperatures of 200–350°C with exposure to 1% of CH_4 is shown in **Figure 6A**. When the temperature increased from 200 up to 350°C, the sensing performance enhanced, as well as the response/recovery times constants. The decrease in resistance upon exposure to CH_4 was assumed by Haridas and Gupta (Haridas and Gupta, 2012) to be due to the dissociation of methane molecules, which react with the surface O^- species, liberating the trapped charges to the oxide, reducing its resistance. The gas sensing signal of ZnO NRs at a temperature of 200–350°C with exposure to 0.1% CO gas is shown in **Figure 6B**. With the increase in operating temperature, an enhancement in the sensing response behavior is observed. Koziej et al. (2007) have predicted a reaction mechanism for the reducing gas such as CO with oxygen ions on the oxide. Upon the reaction of CO with the O^- ions, an electron was released to the conduction band of the oxide, increased the oxide conductivity. Reviewing the basic reaction between H_2 gas and oxide surface is described in terms of the reaction of

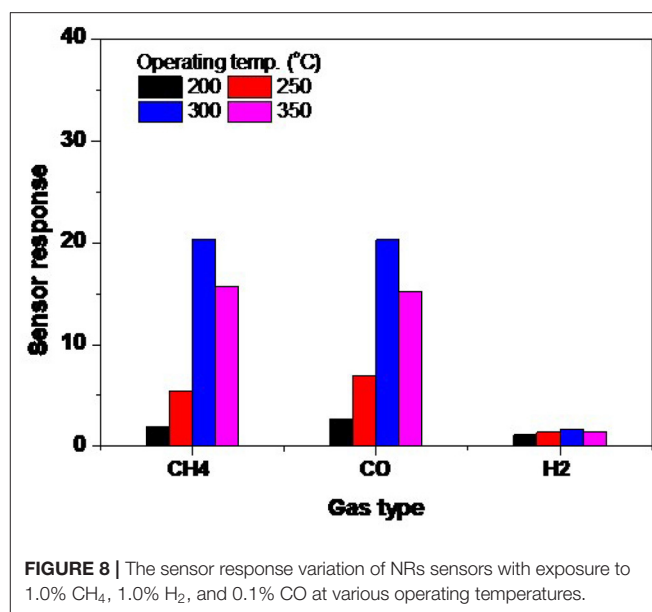


FIGURE 8 | The sensor response variation of NRs sensors with exposure to 1.0% CH_4 , 1.0% H_2 , and 0.1% CO at various operating temperatures.

H_2 with the oxygen species as the following single-step process (Koziej et al., 2007). In this reaction, H_2O (gas) is produced as a final product, followed by the accumulation of electron charges at the oxide surface causing the conductance increase (*not shown here*).

Operating Temperature Control

The dependence of sensing behavior on the operating temperature is a very important parameter to describe the gas sensor, in order to obtain the highest performance of this sensor. **Figure 8** shows the response of the fabricated sensor at various operating temperatures, starting from 200 up to 350°C. The response was well-calculated for CH_4 , H_2 , and CO gases. The response of the sensors fabricated from NRs is shown in **Figure 8**. It seems that the sensing layer is more active when increasing the operating temperature, while in the NRs sample the maximum response occurs at a high temperature of 300°C. When the temperature was increased further, a weaker response was observed. The sensor gains the same behavior for all gases; however, it is less sensitive toward H_2 gas. The maximum responses are recorded as high as 20.2 for CH_4 and CO gases, while it is 1.7 for H_2 gas at 300°C. We may ascribe the low sensitivity of ZnO NRs toward H_2 to the low reactivity of H_2 with the smooth surface of the oxide. To react H_2 with the surface in a better way, the surface catalytic is favorably introduced to assist the dissociation of H_2 as in the case of the Spillover effect.

The decrease in response at higher temperatures is possible due to the quantity of the diffused oxygen and gas into the oxide. The diffusion and adsorption are exothermic phenomena, so at high temperatures the amount of the diffused species into the surface decreases, which leads to a lower response. In addition, at high temperatures, the O^- ions mostly transform into O^{2-} ions, which is unlikely to react with reducing gases. However, we may

consider that O^- ions are still there with in low amounts, which reduces the sensing response.

Gas Sensing Evaluation

Figure 9 shows the sensor evaluation toward the targeted gases at different operating temperatures. As mentioned above that the sensor of NRs is highly responsive toward the reducing gases, however, it is recommended for the high-temperature sensor.

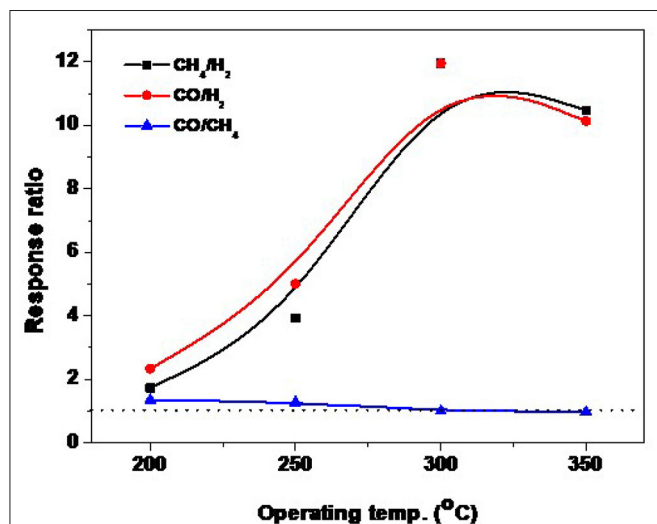


FIGURE 9 | Temperature dependence of the response ratio for 1.0% CH₄, 0.1% CO and 1.0% H₂ for ZnO NRs.

Figure 9 shows the evaluation curve of the response ratio of ZnO-NRs for CO and CH₄ against H₂, and CO against CH₄ gas, respectively. The response ratio is expressed as the ratio of the gas response value to another gas (e.g., CO response value to H₂ response value, $\alpha_{CO/H_2} = S_{CO}/S_{H_2}$). The sensor showed a ratio higher than >1 for CO and CH₄ against H₂ gas at all temperature ranges. The maximum response ratio of ZnO-NRs for either CO or CH₄ gas is ~11.7 at 300°C. For CO against CH₄, it is higher than >1.0 at 200, and 250°C, while it is ~1.0 at 300°C and <1.0 at 350°C. The sensor showed a high ratio for either CO or CH₄ gases compared to H₂ gas. It can be concluded that ZnO NRs is the optimum composition for the CO and CH₄ gas sensor. The temperature dependence of the detection of both CO and CH₄ gases by NRs is closely related to the surface activation at different sensing temperatures.

Calibration Curve and Reversibility

The sensor signal of ZnO NRs for CH₄, CO, and H₂ measured a few months later at various concentrations at an operating temperature of 300°C is shown in Figure 10. The sensor response depends on gas concentration. The response to different gas concentrations was repeated, confirming the reliability of these sensors. It can be observed that the sensor is responding promptly to the change in the gas concentration. The sensor still responds to the lower concentrations of the gas even with fair sensitivity, especially for H₂ gas, which exhibits the lower sensitivity compared to CH₄ and CO gases. This measurement was carried out a few months later from the first measurement, thus, we may be able to state that the sensor signal is stable, and it is reversible. The sensor also provides almost an identical

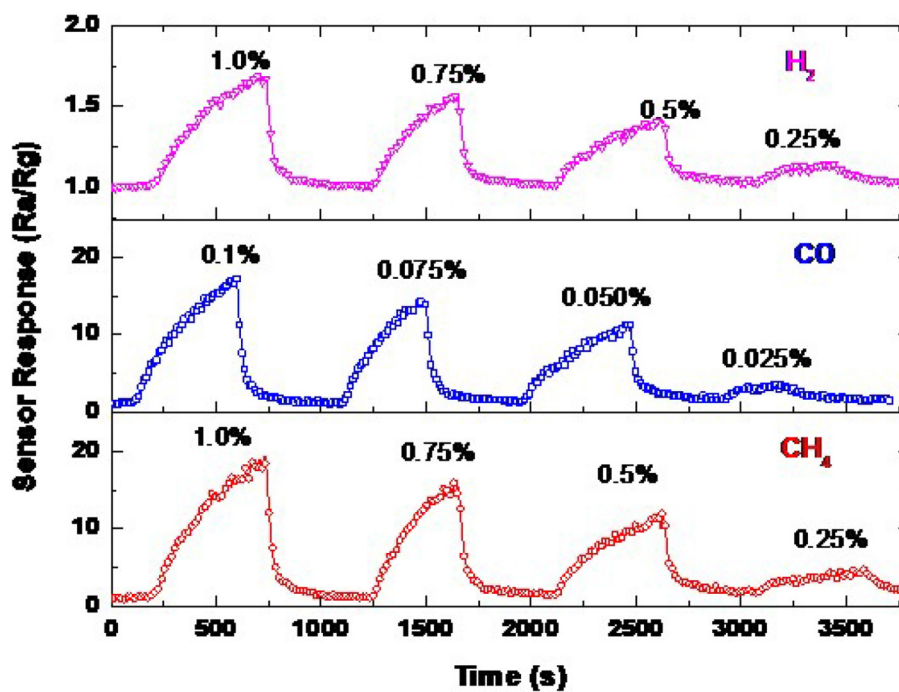


FIGURE 10 | Sensor signals of ZnO NRs toward various concentrations of CH₄, CO, and H₂ at an operating temperature of 300°C.

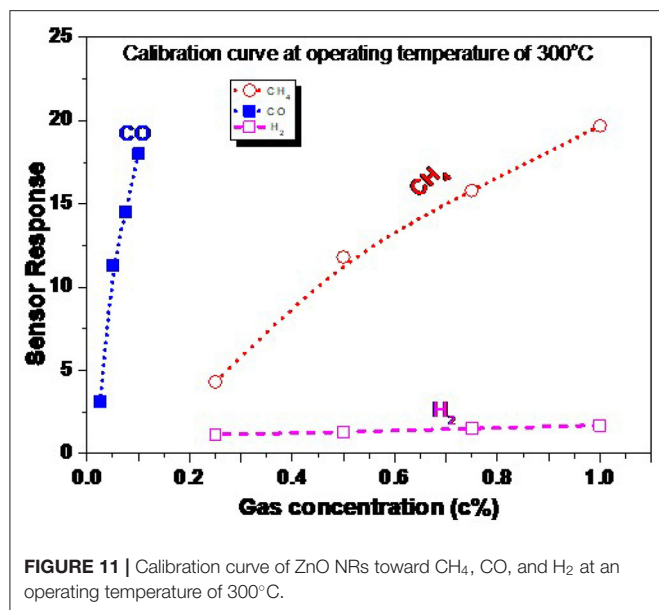


FIGURE 11 | Calibration curve of ZnO NRs toward CH₄, CO, and H₂ at an operating temperature of 300°C.

response value toward 1.0, 0.1, and 1.0% of CH₄, CO, and H₂, respectively, with a drift of <2.5%.

The calibration curve of the ZnO NRs sensor measured at the most highly sensitive operating temperature of 300 °C is presented in **Figure 11**. This figure is extracted from **Figure 10**, where the gas concentration was changed from 1.0 down to 0.25% for CH₄ and H₂, and from 0.1 down to 0.025% for CO gas. The gas concentration was controlled by the adjustment of the flow rate, kept at 200 ml/min, between the synthetic air (21% O₂, and 79% N₂) and the air containing the maximal gas concentration of 1.0% CH₄, 0.1% CO, and 1.0% H₂. The gas concentration was kept much lower than the lower explosive level (LEL) for the targeted gases. The response is curve-like, where a soft increase in the sensor response is observed. There are two stages of the calibration curve of the present sensor, showing the non-linear behavior in general. The sensor responds respectively to the low and high concentration, which may be ascribed to the nature of the NRs shape, which allows the gases to diffuse deeply into the sensing layer to react with more oxygen species. To thoroughly address this behavior, a wide range of higher gas concentrations should be studied. These measurements may be carried out in the future, supported by theoretical bases.

REFERENCES

- Agarwal, S., Rai, P., Gatell, E. N., Llobet, E., Güell, F., Kumar, M., et al. (2019). Gas sensing properties of ZnO nanostructures (flowers/rods) synthesized by hydrothermal method. *Sens. Actuators: B. Chem.* 292, 24–31. doi: 10.1016/j.snb.2019.04.083
- Ahmed, F., Kumar, S., Arshi, N., Anwar, M. S., Koo, B. H., and Lee, C. G. (2011). Rapid and cost effective synthesis of ZnO nanorods using microwave irradiation technique. *Funct. Mater. Lett.* 4, 1–5. doi: 10.1142/S1793604711001531

CONCLUSIONS

In summary, ZnO NRs have been successfully synthesized using a domestic microwave-assisted solution method and showed a smooth surface morphology and wurtzite hexagonal structure. The morphology and structure were studied by XRD, FESEM, and Raman spectroscopy. The sharp peak of Raman and XRD spectra exhibited a good crystallinity of the as-prepared ZnO NRs. When these NRs were applied for the gas sensing testing, they showed good performance toward the targeted gases such as CH₄, CO, and H₂. However, due to the smooth surface of the oxide NRs, the sensor was inactive at the low-temperature range of RT–150°C. Thus, it showed good sensitivity to all targeted gases especially CH₄ and CO compared to H₂, but at a higher temperature of 200–350°C. The advantage of the ZnO NRs sensing performance toward CO and CH₄ compared to H₂ gas was explained in terms of the possible gas sensing mechanisms. Where CO and CH₄ gases can react with the oxide surface species of O²⁻ and O⁻ ions, in contrast with H₂, which likely reacts with O⁻ or dissociates to H⁺. However, surface modification of ZnO nanostructures might be tuned to work at lower temperatures with good stability. Finally, we conclude that the fabricated ZnO NRs using the present method is very sensitive to CH₄ and CO, where the sensitivity toward these two gases was very high compared to H₂ gas. These smooth surface NRs can also be used as a high operating temperature sensor.

DATA AVAILABILITY STATEMENT

The raw data supporting the conclusions of this article will be made available by the authors, without undue reservation.

AUTHOR CONTRIBUTIONS

NS, FA, and CA: data curation and writing—original draft. AA, NS, and FA: formal analysis and methodology. AA: funding acquisition and supervision. AA and NS: writing—review and editing. All authors contributed to the article and approved the submitted version.

FUNDING

This project was funded by the National Plane of Science and Technology, Innovation (MAARIFAH), King Abdul-Aziz City for Science and Technology, the Kingdom of Saudi Arabia, (08-NAN2-06).

- Alam, M. F. B., Phan, D.-T., and Chung, G.-S. (2015). Palladium nanocubes decorated on a one-dimensional ZnO nanorods array for use as a hydrogen gas sensor. *Mater. Lett.* 156, 113–117. doi: 10.1016/j.matlet.2015.05.007
- Bai, S., Guo, T., Zhao, Y., Sun, J., Li, D., Chen, A., et al. (2014). Sensing performance and mechanism of Fe-doped ZnO microflowers. *Sens. Actuators B: Chem.* 195, 657–666. doi: 10.1016/j.snb.2014.01.083
- Bohle, D. S., and Spina, C. J. (2009). Cationic and anionic surface binding sites on nanocrystalline zinc oxide: surface influence on photoluminescence and photocatalysis. *J. Am. Chem. Soc.* 131:4397. doi: 10.1021/ja808663b

- Brookes, C., Wells, P. P., Cibin, G., Dimitratos, N., Jones, W., Morgan, D. J., et al. (2014). Molybdenum oxide on Fe₂O₃ core-shell catalysts: probing the nature of the structural motifs responsible for methanol oxidation catalysis. *ACS Catal.* 4, 243–250. doi: 10.1021/cs400683e
- Calleja, J. M., and Cardona, M. (1977). Resonant raman scattering in ZnO. *Phys. Rev. B* 16:3753. doi: 10.1103/PhysRevB.16.3753
- Chen, G., Liu, F., Ling, Z., Zhang, P., Wei, B., and Zhu, W. (2019). Efficient organic light emitting diodes using solution-processed alkali metal carbonate doped ZnO as electron injection layer. *Front. Chem.* 7:226. doi: 10.3389/fchem.2019.00226
- Chen, Y. W., and Liu, Y. C. (2005). Optical properties of ZnO and ZnO: in nanorods assembled by sol-gel method. *J. Chem. Phys.* 123:134701. doi: 10.1063/1.2009731
- Damen, T. C., Porto, S. P. S., and Tell, B. (1966). Raman effect of zinc oxide. *Phys. Rev.* 142:570. doi: 10.1103/PhysRev.142.570
- Decremps, F., Pellicer-Porres, J., Saitta, A. M., Chervin, J., and Polian, A. (2002). High-pressure raman spectroscopy study of wurtzite ZnO. *Phys. Rev. B* 65:092101. doi: 10.1103/PhysRevB.65.092101
- Fan, C., Sun, F., Wang, X., Huang, Z., Keshvardoostchokami, M., Kumar, P., et al. (2019). Synthesis of ZnO hierarchical structures and their gas sensing properties. *Nanomaterials* 9:1277. doi: 10.3390/nano9091277
- Guo, W., Liu, T., Zhang, H., Sun, R., Chen, Y., Zeng, W., et al. (2012). Gas-sensing performance enhancement in ZnO nanostructures by hierarchical morphology. *Sens. Actuators B: Chem.* 166, 492–499. doi: 10.1016/j.snb.2012.02.093
- Haridas, D., and Gupta, V. (2012). Enhanced response characteristics of SnO₂ thin film based sensors loaded with Pd clusters for methane detection. *Sens. Actuators B* 166–167, 156–164. doi: 10.1016/j.snb.2012.02.026
- Hernandez-Ramirez, F., Prades, J. D., Jimenez-Diaz, R., Fischer, T., Romano-Rodriguez, A., and Mathur, S. (2009). Morante on the role of individual metal oxide nanowires in the scaling down of chemical sensors. *Phys. Chem. Chem. Phys.* 11, 7105–7110. doi: 10.1039/b905234h
- Hosseini, Z. S., Mortezaali, A. I., Zad, A., and Fardindoost, S. (2015). Sensitive and selective room temperature H₂S gas sensor based on Au sensitized vertical ZnO nanorods with flower-like structures. *J. Alloy. Compd.* 628, 222–229. doi: 10.1016/j.jallcom.2014.12.163
- Jin, C., Park, S., Kim, C.-W., Lee, C., Choi, S.-W., Shin, K.-H., et al. (2015). Characterization and gas sensing properties of bead-like ZnO using multi-walled carbon nanotube templates. *Ceram. Int.* 41, 7729–7734. doi: 10.1016/j.ceramint.2015.02.104
- Jingxuan, W., Qu, Z., Shudi, P., Lingna, X., and Wen, Z. (2020). Volatile organic compounds gas sensors based on molybdenum oxides: a mini review. *Front. Chem.* 8:339. doi: 10.3389/fchem.2020.00339
- Jonca, J., Ryzhikova, A., Kahna, M. L., Fajerwerga, K., Chaudret, B., Chapelle, A., et al. (2014). Shape-controlled ZnO nanostructures for gas sensing applications. *Proc. Eng.* 87, 907–910. doi: 10.1016/j.proeng.2014.11.302
- Koziej, D., Thomas, K., Barsan, N., Thibault-Starzyk, F., and Weimar, U. (2007). Influence of annealing temperature on the CO sensing mechanism for tin dioxide based sensors—operando studies. *Catal. Today* 126, 211–218. doi: 10.1016/j.cattod.2007.03.011
- Kumar, R., Al-Dossary, O., Kumar, G., and Umar, A. (2015). Zinc oxide nanostructures for NO₂ gas-sensor applications: a review. *Nanomicro Lett.* 7, 97–120. doi: 10.1007/s40820-014-0023-3
- Lee, J., and Tak, Y. (2001). Electrodeposition of ZnO on ITO electrode by potential modulation method. *Electrochim. Solid State Lett.* 4, C63–C65. doi: 10.1149/1.1388179
- Li, Y., Meng, G. W., Zhang, L. D., and Philipp, F. (2000). Ordered semiconductor ZnO nanowire arrays and their photoluminescence properties. *Appl. Phys. Lett.* 76, 2011–2013. doi: 10.1063/1.126238
- Live, J. (1981). Amorphous transition-metal oxides. *J. Phys.* 42, 981–992. doi: 10.1051/jphyscol:19814215
- Mascini, M., Gaggiotti, S., Della Pelle, F., Di Natale, C., Qakala, S., Iwuoha, E., et al. (2018). Peptide modified ZnO nanoparticles as gas sensors array for volatile organic compounds (VOCs). *Front. Chem.* 6:105. doi: 10.3389/fchem.2018.00105
- Pan, X., Liu, X., Bermak, A., and Fan, Z. (2013). Self-gating effect induced large performance improvement of ZnO nanocomposite gas sensors. *ACS Nano* 7, 9318–9324. doi: 10.1021/nn4040074
- Park, Y., Yoo, R., Park, S., Lee, J. H., Jung, H., Lee, H.-S., et al. (2019). Highly sensitive and selective isoprene sensing performance of ZnO quantum dots for a breath analyzer. *Sens. Actuators: B. Chem.* 290, 258–266. doi: 10.1016/j.snb.2019.03.118
- Qi, K., Liu, S., and Zada, A. (2020b). Graphitic carbon nitride, a polymer photocatalyst. *J. Taiwan Inst. Chem. Eng.* 109, 111–123. doi: 10.1016/j.jtice.2020.02.012
- Qi, K., Xing, X., Zada, A., Li, M., Wang, Q., Liu, S., et al. (2020a). Transition metal doped ZnO nanoparticles with enhanced photocatalytic and antibacterial performances: Experimental and DFT studies. *Ceram. Int.* 46, 1494–1502. doi: 10.1016/j.ceramint.2019.09.116
- Qin, H., Liu, T., Liu, J., Liu, Q., Li, R., Zhang, H., et al. (2019). Fabrication of uniform 1-D ZnO/ZnCo₂O₄ nano-composite and enhanced properties in gas sensing detection. *Mater. Chem. Phys.* 228, 66–74. doi: 10.1016/j.matchemphys.2019.02.051
- Rajalakshmi, M., Arora, A. K., Bendre, B. S., and Mahamuni, S. (2000). Optical phonon confinement in zinc oxide nanoparticles. *J. Appl. Phys.* 87:2445. doi: 10.1063/1.372199
- Rakshit, T., Mandal, S., Mishra, P., Dhar, A., Manna, I., and Ray, S. K. (2012). Optical and bio-sensing characteristics of ZnO nanotubes grown by hydrothermal method. *J. Nanosci. Nanotechnol.* 12, 308–315. doi: 10.1166/jnn.2012.5134
- Rana, A., Kang, M., and Kim, H. (2016). Microwave-assisted facile and ultrafast growth of ZnO nanostructures and proposition of alternative microwave-assisted methods to address growth stoppage. *Sci Rep.* 6:24870. doi: 10.1038/srep24870
- Ridha, N., Alosfur, F. K. M., Jumali, M. H. H., and Radiman, S. (2018). Dimensional effect of ZnO nanorods on gas-sensing performance. *Phys. D: Appl. Phys.* 51:43. doi: 10.1088/1361-6463/aaedcb
- Roy, P., Berger, S., and Schmuki, P. (2011). TiO₂ nanotubes: synthesis and applications. *Angew. Chem. Int. Ed.* 50, 2904–2939. doi: 10.1002/anie.201001374
- Ruhland, B., Becker, T., and Muller, G. (1998). Gas-kinetic interactions of nitrous oxides with SnO₂ surfaces. *Sens. Actuators B* 50, 85–94. doi: 10.1016/S0925-4005(98)00160-9
- Seiyama, T., Kato, A., Fujiishi, K., and Nagatani, M. (1962). A new detector for gaseous components using semiconductive thin films. *Anal. Chem.* 34, 1502–1503. doi: 10.1021/ac60191a001
- Shaalán, N. M., Hamad, D., Aljaafari, A., Abdel-Latif, A. Y., and Abdel-Rahim, M. A. (2019b). Preparation and characterization of developed Cu_xSn_{1-x}O₂ nanocomposite and its promising methane gas sensing properties. *Sensors* 19:2257. doi: 10.3390/s19102257
- Shaalán, N. M., Hamad, D., and Saber, O. (2019a). Co-evaporated CuO-Doped In₂O₃ 1D-nanostructure for reversible CH₄ detection at low temperatures: structural phase change and properties. *Materials* 12:4073. doi: 10.3390/ma12244073
- Shaalán, N. M., Yamazaki, T., and Kikuta, T. (2011). Influence of morphology, and structure geometry on NO₂ gas-sensing characteristics of SnO₂ nanostructures synthesized via a thermal evaporation method. *Sens. Actuators B* 153, 11–16. doi: 10.1016/j.snb.2010.09.070
- Spencer, M. J. S. (2012). Gas sensing applications of 1D-nanostructured zinc oxide: insights from density functional theory calculations. *Prog. Mater. Sci.* 57, 437–486. doi: 10.1016/j.pmatsci.2011.06.001
- Vomiero, A., Bianchi, S., Comini, E., Faglia, G., Ferroni, M., and Sberveglieri, G. (2007). Controlled growth and sensing properties of In₂O₃ nanowires. *Cryst. Growth Des.* 7, 2500–2504. doi: 10.1021/cg070209p
- Wan, Q., Li, Q. H., Chen, Y. J., Wang, T. H., He, X. L., Li, J. P., et al. (2004). Fabrication and ethanol sensing characteristics of ZnO nanowire gas sensors. *Appl. Phys. Lett.* 84:3654. doi: 10.1063/1.1738932
- Wang, G., Wang, Z.-G., Xi, R., Zhang, L., Zhang, S.-H., Wang, L.-J., et al. (2019). In situ synthesis of flower-like ZnO on GaN using electrodeposition and its application as ethanol gas sensor at room temperature. *Sens. Actuators B: Chem.* 292, 270–276. doi: 10.1016/j.snb.2019.04.140
- Wang, P., Xu, G., and Jin, P. (2004). Size dependence of electron-phonon coupling in ZnO nanowires. *Phys. Rev. B* 69:113303. doi: 10.1103/PhysRevB.69.113303
- Yamazoe, N., Fuchigami, J., Kishikawa, M., and Seiyama, T. (1979). Interactions of tin oxide surface with O₂, H₂O AND H₂. *Surf. Sci.* 86, 335–344. doi: 10.1016/0039-6028(79)90411-4

- Zada, A., Khan, M., Qureshi, M. N., Liu, S. Y., and Wang, R. (2020). Accelerating photocatalytic hydrogen production and pollutant degradation by functionalizing g-C₃N₄ with SnO₂. *Front. Chem.* 7:941. doi: 10.3389/fchem.2019.00941
- Zada, A., Muhammad, P., Ahmad, W., Hussain, Z., Ali, S., Khan, M., et al. (2019). Surface plasmonic-assisted photocatalysis and optoelectronic devices with noble metal nanocrystals: design, synthesis, and applications. *Adv. Funct. Mater.* 6:1906744. doi: 10.1002/adfm.201906744
- Zhang, R., Yin, P.-G., Wang, N., and Guo, L. (2009). Photoluminescence and raman scattering of ZnO nanorods. *Solid State Sci.* 11, 865–869. doi: 10.1016/j.solidstatesciences.2008.10.016
- Zhang, S., Nguyen, S. T., Nguyen, T. H., Yang, W., and Noh, J.-S. (2017). Effect of the morphology of solution-grown ZnO nanostructures on gas-sensing properties. *J. Am. Ceram. Soc.* 100, 5629–5637. doi: 10.1111/jace.15096
- Zhang, X. H., Liu, Y. C., and Chen, S. H. (2005). A novel method for measuring distribution of orientation of one-dimensional ZnO using resonance raman spectroscopy. *J. Raman Spectrosc.* 36:1101. doi: 10.1002/jrs.1413
- Zhao, S., Shen, Y., Yan, X., Zhou, P., Yin, Y., Lu, R., et al. (2019). Complex-surfactant-assisted hydrothermal synthesis of one-dimensional ZnO nanorods for high-performance ethanol gas sensor. *Sens. Actuators: B. Chem.* 286, 501–511. doi: 10.1016/j.snb.2019.01.127

Conflict of Interest: The authors declare that the research was conducted in the absence of any commercial or financial relationships that could be construed as a potential conflict of interest.

Copyright © 2020 Aljaafari, Ahmed, Awada and Shaalan. This is an open-access article distributed under the terms of the Creative Commons Attribution License (CC BY). The use, distribution or reproduction in other forums is permitted, provided the original author(s) and the copyright owner(s) are credited and that the original publication in this journal is cited, in accordance with accepted academic practice. No use, distribution or reproduction is permitted which does not comply with these terms.



Mini-Review: Mixed Ionic–Electronic Charge Carrier Localization and Transport in Hybrid Organic–Inorganic Nanomaterials

Mariano Romero*, Dominique Mombrú, Fernando Pignanelli, Ricardo Faccio* and Alvaro W. Mombrú*

Centro NanoMat & Área Física, Departamento de Experimentación y Teoría de la Estructura de la Materia y sus Aplicaciones - DETEMA, Facultad de Química, Universidad de la República, Montevideo, Uruguay

OPEN ACCESS

Edited by:

Rengaraj Selvaraj,
Sultan Qaboos University, Oman

Reviewed by:

Xiaopeng Han,
Tianjin University, China
Guillermo Javier Copello,
Consejo Nacional de Investigaciones
Científicas y Técnicas
(CONICET), Argentina

*Correspondence:

Mariano Romero
mromero@fq.edu.uy
Ricardo Faccio
rfaccio@fq.edu.uy
Alvaro W. Mombrú
amombrú@fq.edu.uy

Specialty section:

This article was submitted to
Nanoscience,
a section of the journal
Frontiers in Chemistry

Received: 16 April 2020

Accepted: 26 May 2020

Published: 14 July 2020

Citation:

Romero M, Mombrú D, Pignanelli F,
Faccio R and Mombrú AW (2020)
Mini-Review: Mixed Ionic–Electronic
Charge Carrier Localization and
Transport in Hybrid Organic–Inorganic
Nanomaterials. *Front. Chem.* 8:537.
doi: 10.3389/fchem.2020.00537

In this mini-review, a comprehensive discussion on the state of the art of hybrid organic–inorganic mixed ionic–electronic conductors (*hOI*-MIECs) is given, focusing on conducting polymer nanocomposites comprising inorganic nanoparticles ranging from ceramic-in-polymer to polymer-in-ceramic concentration regimes. First, a brief discussion on fundamental aspects of mixed ionic–electronic transport phenomena considering the charge carrier transport at bulk regions together with the effect of the organic–inorganic interphase of hybrid nanocomposites is presented. We also make a recount of updated instrumentation techniques to characterize structure, microstructure, chemical composition, and mixed ionic–electronic transport with special focus on those relevant for *hOI*-MIECs. Raman imaging and impedance spectroscopy instrumentation techniques are particularly discussed as relatively simple and versatile tools to study the charge carrier localization and transport at different regions of *hOI*-MIECs including both bulk and interphase regions to shed some light on the mixed ionic–electronic transport mechanism. In addition, we will also refer to different device assembly configurations and *in situ/operando* measurements experiments to analyze mixed ionic–electronic conduction phenomena for different specific applications. Finally, we will also review the broad range of promising applications of *hOI*-MIECs, mainly in the field of energy storage and conversion, but also in the emerging field of electronics and bioelectronics.

Keywords: hybrid organic–inorganic composites, nanomaterials, mixed ionic–electronic conducting materials, semiconductor, Raman micro spectroscopy, impedance spectroscopy

INTRODUCTION

In the last decades, mixed ionic–electronic conductors (MIECs) have been widely studied for energy storage and energy conversion materials, separation membranes, and catalysts (Shao and Haile, 2004; Maier, 2005; Wachsmann and Lee, 2011; Aoki et al., 2014). Both ionic (σ_i) or electronic (σ_e) conduction obey separately and analogously to the following equation:

$$\sigma = qN\mu \quad (1)$$

where q is the charge, N is the number, and μ is the mobility of the charge carrier, the latter being proportional to diffusivity (D). In the particular case of inorganic MIECs, some well-known

examples are semiconducting compounds such as Ag_2X (with $\text{X} = \text{S}, \text{Se}, \text{or Te}$) as mixed silver ion (Ag^+) and electronic conducting materials (Yokota, 1961; Miyatani, 1973; Riess, 2003) and A-doped MO_{2-8} (typically $M = \text{Ce}$ or Zr , and A being different dopants) as mixed oxygen ion (O^{2-}) and electronic transport materials (Goodenough, 2000; Balaguer et al., 2011; Lin et al., 2015). However, one of the most relevant inorganic MIEC materials gaining special attention in the recent years are $\text{A}_x\text{M}_2\text{O}_4$ (with $M = \text{Ni}, \text{Co}, \text{and/or Mn}$ and $A = \text{Li}$ or Na) due to their excellent performance, particularly as cathode materials for lithium (Li^+) and sodium (Na^+) ion batteries (Doeff et al., 1993; Barker et al., 1996; Saïdi et al., 1996; Thackeray, 1997; Dokko et al., 2001; Lu and Dahn, 2001; Cao and Prakash, 2002; Levasseur et al., 2002; Sauvage et al., 2007; Berthelot et al., 2010; Tevar and Whitacre, 2010). For instance, typical electronic conductivities (σ_e) and lithium-ion diffusivities (D_i) for $\text{Li}_x\text{M}_2\text{O}_4$ cathode materials are $\sigma_e \sim 10^{-6}$ - 10^{-1} S cm^{-1} and $D_i \sim 10^{-11}$ - 10^{-8} cm^2s^{-1} , respectively, depending strongly on the transition metal (M), lithiation degree (x), and crystallinity (Park et al., 2010). In the particular case of semiconducting inorganic nanomaterials, both ionic and electronic transport present lower charge carrier resistance at the crystalline bulk regions but are drastically compromised by the poor charge carrier conducting nature of grain boundaries (Park et al., 2010). In the last decades, the addition of conducting coating materials and secondary phases such as mixed ionic–electronic conducting organic materials (e.g., conducting polymers), working as linkers between inorganic nanomaterials, has attracted a lot of attention (Judeinstein and Sanchez, 1996; Gómez-Romero and Lira-Cantú, 1997; Guizard et al., 2001; Le Bideau et al., 2011). It is well-accepted that electronic conducting organic polymers, usually called conjugated polymers, are semiconductors in nature and that the most popular cases such as poly(pyrrrole) (Ppy) (Della Santa et al., 1997), poly(aniline) (PANI) (Zhang K. et al., 2012a; Chatterjee et al., 2013; Zhang Q. et al., 2013a; Roussel et al., 2015), poly(ethylenedioxythiophene) (PEDOT) (Crispin et al., 2006; Udo et al., 2009; Takano et al., 2012; Kim et al., 2013; Mengistie et al., 2013, 2015; Lee et al., 2014; Kumar et al., 2016; Zia Ullah et al., 2016), and poly(3-hexylthiophene) (P3HT) (Zhang Q. et al., 2012; Pingel and Neher, 2013; Glaudell et al., 2015; Jacobs et al., 2016; Qu et al., 2016; Jung et al., 2017; Wang W. et al., 2017; Lim et al., 2018) generally exhibit an electronic donor behavior. In this case, the most common procedure to enhance the electronic conduction, where charge carriers will be mostly holes rather than electrons, is by doping these polymers with electronic acceptor species (p-type doping) such as halide and sulfonate salts, yielding a decrease in the electronic band gap and an increase of the electronic conductivity up to $\sigma_e \sim 10^{-1}$ - 10^3 S cm^{-1} values (Della Santa et al., 1997; Crispin et al., 2006; Udo et al., 2009; Takano et al., 2012; Zhang K. et al., 2012; Zhang Q. et al., 2012, 2013; Chatterjee et al., 2013; Kim et al., 2013; Mengistie et al., 2013, 2015; Pingel and Neher, 2013; Lee et al., 2014; Glaudell et al., 2015; Roussel et al., 2015; Jacobs et al., 2016; Kumar et al., 2016; Qu et al., 2016; Zia Ullah et al., 2016; Jung et al., 2017; Wang W. et al., 2017; Lim et al., 2018). The mere presence of the dopant, typically halide, or sulfonate salts with relatively high degree of

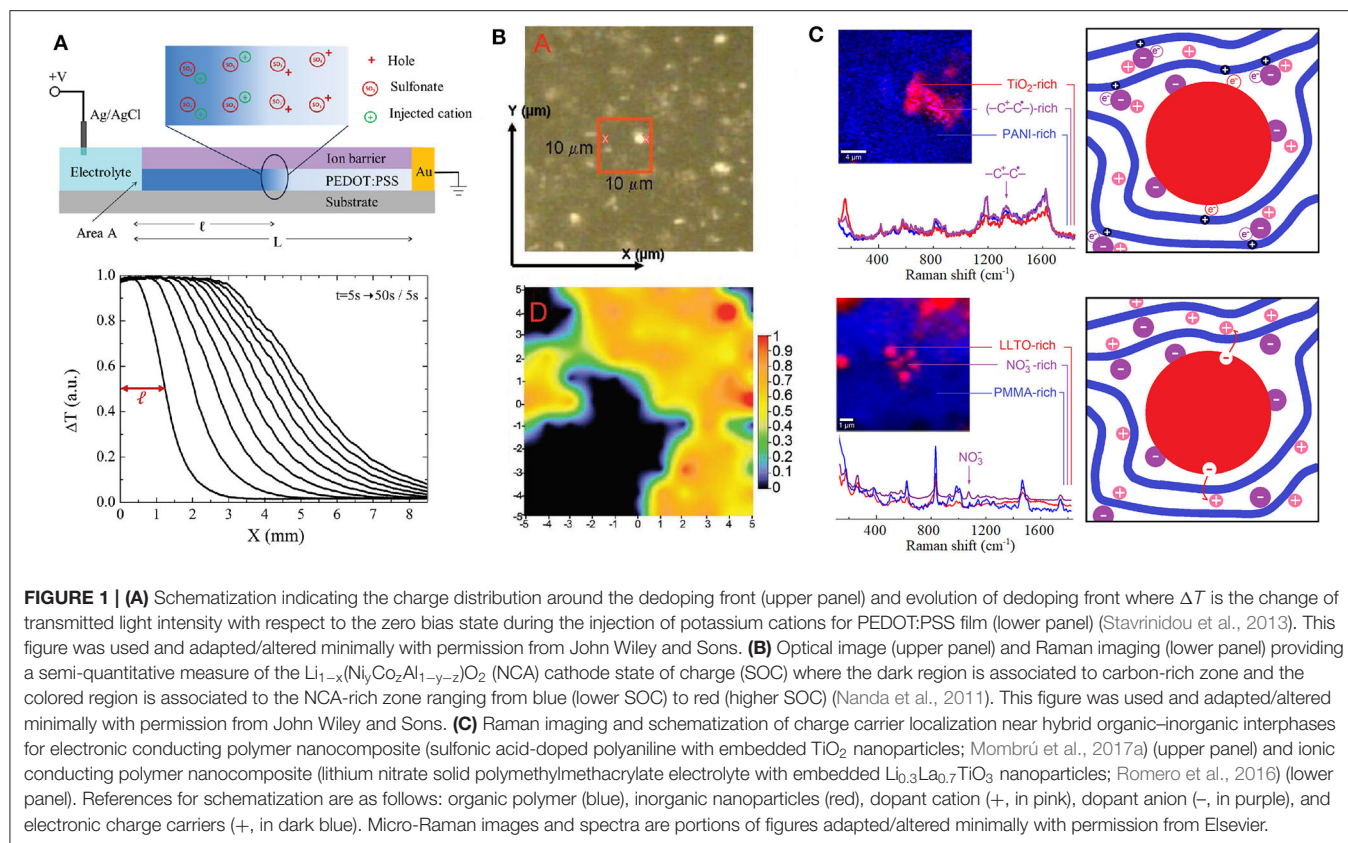
dissociation, will trigger a non-negligible ionic conduction in addition to the electronic transport (Riess, 2000). It is important to mention that there are other “non-dissociable” excellent dopants such as the case of tetracyanoquinodimethane (TCNQ) in all of its fluorinated forms, but as it does not provide highly mobile ionic carriers, it will not be considered in this review. It was long observed that protons (H^+), lithium (Li^+), sodium (Na^+), or potassium (K^+) cations yielded a considerable ionic contribution to the total mixed ionic–electronic transport of conjugated polymers (Nigrey et al., 1978; Aldebert et al., 1986; Barthet and Guglielmi, 1995; Watanabe, 1996). The voluminous dopant anions are generally more fixed to the polymer chain, allowing the electronic exchange process (doping) to take place but contributing in a lesser extent to the ionic conductivity except for a few particular cases (Cheng et al., 2005). Pursuing an increase in the ionic conduction of MIECs, blending and co-polymerization (including functionalization of side chains) of electronic conducting polymers with good ionic conducting polymers [e.g., poly(ethylene oxide) (PEO)], has shown enhancement of ionic conductivities up to $\sigma_i \sim 10^{-5}$ - 10^{-4} S cm^{-1} (Li and Khan, 1991; Barthet et al., 1997; Ghosh and Inganäs, 2000; Zhang et al., 2002; Patel et al., 2012; Ju et al., 2014; Kang et al., 2014; Dong et al., 2019; Sengwa and Dhatarwal, 2020). Another strategy includes the simultaneous doping and blending of electronic conducting polymers with polymeric dopants, particularly observed for protons and lithium-ion charge carriers (Murthy and Manthiram, 2011; Fu and Manthiram, 2012; Liu et al., 2012). However, it is important to remark that the inclusion of electronic-insulating polymers inevitably leads to the declining of the electronic conductivity ($\sigma_e \sim 10^{-5}$ S cm^{-1} , i.e., several orders of magnitude less than the isolated conducting polymer in its doped form), and thus, electronic-conducting polymer/ionic-conducting polymer/dopant concentrations need to be rationally balanced (Li and Khan, 1991; Barthet et al., 1997; Ghosh and Inganäs, 2000; Zhang et al., 2002; Murthy and Manthiram, 2011; Fu and Manthiram, 2012; Liu et al., 2012; Patel et al., 2012; Ju et al., 2014; Kang et al., 2014; Dong et al., 2019; Sengwa and Dhatarwal, 2020). Recent comprehensive reviews discussing different types of organic MIEC classes, with particular focus on taxonomy and electronic–ionic interactions, are given by Paulsen et al. (2020), and a thorough discussion of morphologic effects on organic polymeric MIEC is given by Onorato and Luscombe (2019). On the other hand, it is well-known that the addition of semiconducting ceramic nanoparticles, even with negligible intrinsic electronic (or ionic) transport ability, can also yield an enhancement of the electronic (or ionic) conduction in conducting polymer nanocomposites. For instance, the presence of inorganic nanoparticles, particularly transition metal oxides, has yielded a notorious increment of electronic conductivity for electronic–conductor polymer nanocomposites in both ceramic-in-polymer (Mombrú et al., 2017a,b; Mombrú et al., 2019) and polymer-in-ceramic concentration regimes (Huguenin et al., 2004; Wang et al., 2010; Mombrú et al., 2017a). In analogy, the presence of inorganic nanoparticles resulted in an enhancement on the ionic conductivity for ionic conductor polymer nanocomposites (Kloster et al., 1996; Scrosati et al., 2000; Shin and Passerini, 2004). The presence

of secondary phases or inorganic nanofillers induces slight structural modifications, altering the degree of order of the conducting polymer chains that could explain the enhancement of the conductivity, without considering direct mediation of charge carriers through the nanoparticle interphase. Although it is accepted that the electronic conduction in polymer nanocomposites is usually related to higher crystallinity (or higher degree of order), the enhancement of the ionic conduction is mostly associated to lower crystallinity (or lower degree of order), but the latter case is still under recent debate (Onorato and Luscombe, 2019). Furthermore, in the case of ceramic nanoparticles' interaction with conducting polymers, the presence of an interphase between both organic and inorganic materials adds a particular complexity to the system and can eventually lead to important consequences in both ionic and electronic transport properties. Leaving out drastic effects such as voids, poor contact, or the presence of decomposition phases due to eventual chemical reactions, it is extremely difficult to obtain well-defined interphases between such different materials. For instance, the presence of defects, mainly in the inorganic nanoparticle boundaries, can lead to the presence of charge localization at the interphase and the presence of different crystallographic surfaces of the inorganic nanoparticle at the interphase can exhibit different electronic interactions with the polymer phase. Up to now, to the best of our knowledge, there are only a few reviews of MIEC materials with particular focus on their applications such as energy (Sengodu and Deshmukh, 2015), bioelectronics (Han S. et al., 2019), and sensing (Inal et al., 2018), but no further insights into *hOI*-MIECs. In this mini-review, charge carrier localization and transport at different regions of *hOI*-MIECs including both bulk and interphase regions is revised, focusing on the use of some powerful and versatile instrumental techniques.

CHARGE CARRIER LOCALIZATION

There are a lot of instrumentation techniques that can provide particularly rich information about structural features of *hOI*-MIECs such as Nuclear Magnetic Resonance (NMR), X-ray diffraction (XRD), and wide-/small-angle X-ray scattering (WAXS/SAXS) in both transmission or grazing incidence configurations (Sanjeeva Murthy, 2016). However, it is important to remark that X-ray scattering techniques are relatively accessible but generally give indirect information about charge carrier localization and on the other hand, although NMR could be very powerful to monitor charge carrier's location, it is particularly less versatile than other optical spectroscopies techniques. For instance, a relatively simple and powerful method to monitor not only charge localization but also drift mobility in organic MIECs is the "moving front" experiment, which is based on visible light transmission monitoring through an electrochromic film as it is dedoped due to lateral injection of H^+ , Na^+ , or K^+ ions from a planar junction with an electrolyte, as shown in **Figure 1A** (Stavrinidou et al., 2013; Rivnay et al., 2016). Nonetheless, one of the most popular but no less powerful and versatile technique to study structural features of *hOI*-MIECs

is vibrational spectroscopy. Raman spectroscopy is particularly interesting for inorganic materials characterization as it does not exclude highly amorphous systems in comparison with XRD and provides accessibility to vibrational modes with lower wavenumbers (typically $\nu_{\min} \sim 80\text{--}100\text{ cm}^{-1}$) in comparison to infrared spectroscopy (typically $\nu_{\min} \sim 200\text{--}400\text{ cm}^{-1}$). Raman spectroscopy also has the remarkable advantage of needing little sample preparation, allowing the study of materials in its native conditions, as well as permitting collection of *in situ* and *in operando* measurements. For instance, *in situ/operando* Raman spectroscopy has allowed the study of the state of charge of $(Li, Na, K)_xM_2O_4$ electrodes by monitoring the broadening and shifting of Raman peaks when lowering Li, Na, or K content from nominal $X = 1$ (full charged cathode), particularly associated to the loss of ions from the interlayer of the MO_2 layered structure (Dokko et al., 2003; Nanda et al., 2011; Nishi et al., 2013; Chen et al., 2015; Flores et al., 2018). An example on the use of Raman imaging to monitor the state of charge for a $Li_{1-x}(Ni_yCo_zAl_{1-y-z})O_2$ cathode is shown and described briefly in **Figure 1B** (Nanda et al., 2011). In addition, the use of micro-Raman imaging technique is highly powerful to study simultaneously both compositional and microstructural features, especially for hybrid inorganic-organic materials, as the characteristic Raman signals for inorganic and organic compounds generally lie well-separated at lower ($\nu < 800\text{ cm}^{-1}$) and higher ($\nu > 800\text{ cm}^{-1}$) wavenumbers, respectively (Romero et al., 2016; Mombrú et al., 2017a,b,c; Pignanelli et al., 2018, 2019a,b). Furthermore, although Raman spectroscopy is quite sensitive to diluted effects such as doping processes of inorganic materials, it is on the other hand, extremely sensitive to doping effects of organic materials such as conducting polymers (Furukawa, 1996). Briefly, the doping process of conducting polymers yields to drastic modifications of the Raman signature in relation to the charge carrier formation, typically in the form of positive polarons ($-C^+-C^{\bullet-}$) or bipolarons ($-C^+-C^{+}-$), particularly altering both Raman frequency and activity of vibrational modes associated to carbon-to-carbon ($C=C$) molecular bonds in conjugated polymers (Furukawa, 1996; Kumar et al., 2012; Yamamoto and Furukawa, 2015; Francis et al., 2017; Mombrú et al., 2018; Nightingale et al., 2018). For instance, micro-Raman imaging has evidenced the presence of these types of charge carriers particularly localized near the interphase with inorganic nanoparticles; [e.g., MX_2 with M being different transition metals and $X = O$ (for oxides) or S (for sulfides) (Mombrú et al., 2017a,b,c; Mombrú et al., 2019)]. The increment of conducting polymer electronic charge carriers near the interphase could be discussed in view of at least two eventual scenarios: (one or *passive*) the dopant stabilizes at the interphase due to strong polar or coulombic interactions with nanoparticles surface, or/and (two or *active*) the nanoparticles are also good electronic acceptors, producing in both cases an enhancement on the doping of nearby polymer chains, as schematized in **Figure 1C** (upper panel). On the other hand, micro-Raman imaging has also been useful to evidence the enhancement of ionic-pair dissociation occurring near the interphase with inorganic nanoparticles, in agreement with the increment of ionic conductivity (Romero et al., 2016; Pignanelli et al., 2018,



Pignaneli et al., 2019a). Analogously, two different scenarios could be discussed for ionic charge carriers: (one or *passive*) the counter-ion (in analogy to the dopant anion) stabilizes at the interphase due to strong polar or coulombic interactions with nanoparticles surface yielding an enhancement on the ionic-pair dissociation, or/and (two or *active*) the nanoparticles may also possess mobile ionic carriers at the surface (e.g., active filler) that can be injected into the polymer, as schematized in **Figure 1C** (lower panel). Whatever the case, the previous micro-Raman imaging studies revealed that the interphase of organic-inorganic nanocomposites, to a greater or lesser extent, always play an important role in the charge carrier transport mechanism.

CHARGE CARRIER CONDUCTION

There are several electrochemical methodologies to study the charge carrier conduction in MIECs, but one of the most powerful techniques to access both electronic and ionic transport simultaneously is impedance spectroscopy (Jamnik and Maier, 1999; Vorotyntsev et al., 1999; Huggins, 2002; Atkinson et al., 2004; Lee et al., 2009). Briefly, the impedance response as a function of the frequency (typically 10^{-3} - 10^6 Hz) of an oscillating voltage (typically 10–100 mV amplitude) can provide information about different charge carriers with different relaxation times (τ) depending on their q/m ratio; [i.e., the higher

the q/m ratio, the lower τ and the higher associated frequencies ($f = 2\pi/\tau$)]. In this case, the Nyquist representation of impedance (imaginary impedance vs. real impedance, $-Z''$ vs. Z') for a single electronic semiconductor in a continuous medium will show a single semicircle arc. The semicircle arc associated to the electronic carrier transport can be typically modeled using the parallel combination of a resistor (R_e) and a capacitor (C_e). In analogy, but with probably higher associated τ (lower f), a single ionic conductor in a continuous medium will also show a similar single semicircle arc associated to the ionic carrier transport that can also be modeled using the parallel combination of a resistor (R_i) and a capacitor (C_i), whose associated charge carrier pathway is represented with a straight line in **Figure 2A**. If an additional pathway is mediating the electronic (or ionic) transport (e.g., the presence of grain boundaries or depletion regions in less crystalline solids), a second $R_e C_e'$ (or $R_i C_i'$) parallel combination connected in series with the previous one is usually necessary to fit the total impedance response, whose associated charge carrier pathway is represented with a zig-zag line in **Figure 2A**. For simplicity, from now on, we will only consider the charge carrier transport of ionic and electronic conductor samples assembled in a symmetric cell configuration using ideal metallic ion-blocking electrodes. This means that only electronic carriers will be short-circuited and ionic species will be blocked at the interphase with the ion-blocking metallic electrodes but the opposite will apply in the case of using electronic-blocking electrodes. In the case of using metallic ion-blocking electrodes, in addition to

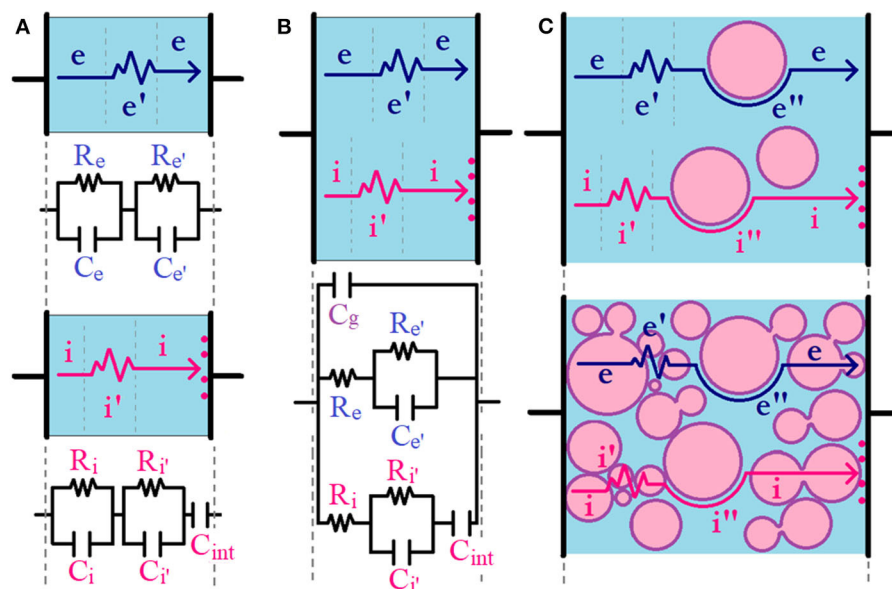


FIGURE 2 | Circuit model schematization for **(A)** separated electronic and ionic transport in a single phase, **(B)** mixed ionic–electronic transport in a single phase, and **(C)** mixed ionic–electronic transport in *hOI*-MIECs ranging from ceramic-in-polymer (upper panel) to polymer-in-ceramic (lower panel). Electronic and ionic hypothetical pathways are shown with dark blue and pink arrows. The zigzag part of the arrows indicates the presence of eventual grain boundaries or depleted regions [with associated ionic (i') or electronic (e') contributions] and the curved part of the arrows indicates the presence of eventual transport pathway mediated through organic–inorganic interfacial regions [with associated ionic (i'') and electronic (e'') contributions].

the semicircle arc observed at higher frequencies, the Nyquist plots of single ionic conductors will also show an additional capacitive tail at low frequencies (C_{int}), which is associated to the polarization of blocked ions at the sample/electrode interphase, as shown in **Figure 2A**. If now we consider the simplest case of a MIEC material, the bi-continuous ionic and electronic channels can be strategically represented by the parallel combination of ionic and electronic resistances (R_i and R_e , respectively) together with a global geometrical capacitance (C_g), with the associated pathway represented by a straight line in **Figure 2B**. It is important to remark that the C_{int} element only appears connected in series with the ionic resistance as we are working with ideal ion-blocking electrodes, but the opposite will occur (i.e., an analogous C_{int} element will only appear connected in series with the electronic resistance) if we are working with electronic-blocking electrodes. The origin of this circuit model simplification is described thoroughly by Jamnik and Maier and is only applicable for macroscopically thick samples considering ideal selectively ion-blocking electrodes and chemical capacitance much larger than the interfacial capacitance of the blocked carriers (Jamnik and Maier, 1999; Lee et al., 2009). In the case that any of the electronic or ionic transport is mediated by the presence of a secondary pathway in a MIEC, generally associated to grain boundaries or depleted regions, as we discuss before, a second $R_e C_e'$ (or $R_i C_i'$) parallel combination connected in series with R_e (or R_i), respectively, could be useful to fit the total impedance response, with associated pathway represented by a zig-zag line in **Figure 2B** (Huggins, 2002). In the recent literature, both the inclusion and exclusion of

this second $R_e C_e'$ (or $R_i C_i'$) parallel combination in biphasic polymeric MIECs have been observed, depending mainly on the electronic- and ionic-conducting phase concentration or microstructural differences (Patel et al., 2012; Renna et al., 2017). In the particular case of *hOI*-MIECs, the second contribution (and probably a third contribution) to ionic or electronic transport could be present due to the mere existence of the organic–inorganic interphase, as shown in **Figure 2C**. However, even for a simplified experiment configuration, (e.g., using symmetric ion-blocking electrodes), it is important to rationalize the number of elements in a given circuit model to avoid over-parametrization. For instance, in the extreme case of *hOI*-MIECs based on a continuous organic semiconductor, [e.g., conducting polymer with diluted inorganic nanoparticle additives (ceramic-in-polymer)], both electronic and ionic carriers will be mainly transported through the organic matrix. For instance, $R_e C_e'$ and $R_i C_i'$ elements could be eventually excluded from the circuit model in the presence of homogeneous (full crystalline or amorphous) polymeric phase. However, in consonance with the non-homogeneous localization of charge carriers discussed in the previous section, the presence of an organic–inorganic interphase can eventually activate another electronic or/and ionic pathway mediated through the interphase that could be passive or active (Irvine et al., 1990). For instance, solid polymer electrolytes with active inorganic nanofillers are the typical case of organic–inorganic interphase-mediated ionic transport (Zheng et al., 2016; Yang et al., 2017; Pignanelli et al., 2019a), and a similar behavior will be observed for the electronic counterpart, if there are electronic interactions at the organic–inorganic interphase

(Chen et al., 2010; Nowy et al., 2010; Cai et al., 2012; Mombrú et al., 2017b). This effect, whose associated charge carrier pathway is represented by a curved line in **Figure 2C**, can also be eventually modeled with $R_{e''}C_{e''}$ (or $R_{i''}C_{i''}$) elements connected in series with the electronic (or ionic) part of the mixed ionic–electronic circuit, in analogy to R_eC_e (or R_iC_i), respectively. However, as mentioned earlier in the previous section, even when the inorganic nanoparticles are passive or non-interacting in nature with charge carriers, the concentration of both electronic or ionic charge carriers at the vicinities of the organic–inorganic interphase could also be activating a second pathway to the charge carrier transport. Nonetheless, in the case of passive interphases, this effect could be rather weak and both charge carrier transport pathways are expected to be mainly through the organic phase without interphase mediation; thus, only a global contribution to the charge carrier transport is usually observed and additional $R_{e''}C_{e''}$ (or $R_{i''}C_{i''}$) elements are not necessary to fit the global impedance response. In the other extreme case, [i.e., *hOI*-MIECs based on inorganic semiconductor nanoparticles with diluted organic polymeric additives (polymer-in-ceramic)], both electronic and ionic carriers are mainly transported through the inorganic matrix. In this case, due to the inevitable presence of grain boundaries in inorganic semiconductor nanoparticles, R_eC_e (or R_iC_i) elements should always be considered, as this contribution practically governs the global electronic (or ionic) transport. In this case, the polymeric additions usually act as fillers of empty spaces between nanoparticles, resulting in an enhancement of the electronic (or ionic) conductivity, and this is usually evaluated directly on R_eC_e (or R_iC_i) elements. However, in the case of simultaneous presence of particle-to-particle and particle–polymer–particle interphases, there will be at least two different pathways to electronic (or ionic) transport and additional $R_{e''}C_{e''}$ (or $R_{i''}C_{i''}$) elements could be necessary to fit the polymer-mediated transport contribution, as depicted in **Figure 2C**.

APPLICATIONS

The successful synergistic properties between organic and inorganic MIECs have yielded excellent performances, especially in the field of energy storage and particularly for lithium- and sodium-ion battery electrode materials (Sengodu and Deshmukh, 2015). In this sense, active cathode or anode materials embedded in polymeric hosts not only increase the mixed ionic–electronic conduction but also act as a sort of protection to the decomposition of active materials (Sengodu and Deshmukh, 2015). For instance, in the case of lithium-ion battery cathode materials: hybrid P3HT-co-PEO/LiFePO₄ has improved the delivery of both ionic and electronic charge to active centers (Javier et al., 2011); Ppy/LiFePO₄ with different hierarchical structures promoted both electronic and ionic transport (Fedorkova et al., 2010; Shi et al., 2017); PEDOT/LiFePO₄ offers excellent discharge capacity (Vadivel Murugan et al., 2008); Ppy/ α -LiFeO₂ has improved the reversible capacity and cycling stability (Zhang et al., 2013); PPy/MoO₃, PPy/V₂O₅, PPy/LiCoO₂, and PPy/LiV₃O₈ yielded a reduction of charge

transfer resistance of the Li⁺ ion intercalation/deintercalation process (Wang et al., 2010; Tian et al., 2011; Tang et al., 2012a,b; Liu et al., 2013); and PEDOT-co-PEG/LiNi_{0.6}Co_{0.2}Mn_{0.2}O₂ showed high discharge capacity and enhanced transport of Li⁺ ions as well as electrons (Ju et al., 2014). Furthermore, in the case of lithium-ion anode materials, only to mention some examples, hybrid Ppy/SnO₂ yielded a more controlled Li⁺ diffusion (Yuan et al., 2007; Cui et al., 2011) and hybrid PANI-graphene/TiO₂ yielded fast charge-to-discharge rate and high enhanced cycling performance (Zhang F. et al., 2012). In the case of sodium-ion battery cathode materials, inorganic Na_xMO₂ oxides, NaMPO₄ phosphates, and Na[M'(CN)₆] hexacyanometalates (commonly known as Prussian blue analogs) have been tested (Xiang et al., 2015; Liu et al., 2020), and to a lesser extent, some organic MIEC polymers such as the case of Ppy (Zhou et al., 2012; Zhou et al., 2013; Zhu et al., 2013). However, in recent literature, *hOI*-MIECs started to be studied thoroughly as cathode materials for sodium-ion batteries, (e.g., Ppy/NaMnFe(CN)₆ (Li et al., 2015), PANI/NaNiFe(CN)₆ (Wang Z. et al., 2017), PEDOT/NaMnFe(CN)₆ (Wang et al., 2020), and Ppy/NaMnO₂ Lu et al., 2020). In the case of sodium-ion battery anode materials, the most frequent *hOI*-MIECs are based on metallic oxides such as PANI/SnO₂ (Zhao et al., 2015) and Ppy/SnO₂ (Yuan et al., 2018) and sulfides such as PANI/Co₃S₄ (Zhou et al., 2016) and Ppy/ZnS (Hou et al., 2017). It is interesting to mention that *hOI*-MIECs are also extensively used as cathodes of lithium-sulfur (Li-S) batteries such as PEDOT:PSS/S (Yang et al., 2011), Ppy/S (Han et al., 2019), and PANI/S (Wei et al., 2019). The study of MIECs as electrochemical transistors was reported long ago for typically doped Ppy (White et al., 1984), PANI (Paul et al., 1985), and PEDOT (Thackeray et al., 1985) conducting polymers, but the exploration of conducting polymers (principally PEDOT) doped with biocompatible materials such as hyaluronic acid, dextran sulfonate, heparin, pectin, guar gum, and deoxyribonucleic acid is rising fast in recent years, especially for bioelectronics purposes (Mantione et al., 2017; Tekoglu et al., 2019). In addition, a very recent report has shown that the preparation of an organic mixed-conducting particulate composite material based on PEDOT: PSS and chitosan enabled facile and effective electronic bonding between soft and rigid electronics, permitting recording of neurophysiological data at the resolution of individual neurons (Jastrzebska-Perfect et al., 2020). However, to the best of our knowledge, up to now, only carbon nanotubes (but no biocompatible inorganic nanoparticles) have been tested with organic MIECs to be evaluated for bioelectronics applications (Nie et al., 2015; Liu et al., 2019; Reddy et al., 2019; Yu et al., 2019).

CONCLUSIONS AND PERSPECTIVES

Herein, the state of the art of *hOI*-MIECs with special focus on charge carrier localization and transport at different regions including both bulk and interphase regions was discussed. In this particular case, we have mainly based our discussion by means of useful and versatile instrumental techniques such as micro-Raman and impedance spectroscopy, but other instrumental

techniques can be very useful and should be considered to gain more insight into the *hOI*-MIECs transport mechanism. There is no doubt that *hOI*-MIECs have shown to be very promising for different applications, ranging from more developed applications (e.g., lithium- and sodium-ion batteries) to more emerging applications (e.g., bioelectronics), as mentioned in the previous section. However, more work is still needed to understand the charge carrier transport mechanism of such complicated systems, in order to pursue the filling of the existent gap between fundamental knowledge and applications. In our opinion, *in situ/operando* monitoring of *hOI*-MIECs during working conditions is the ideal strategy to gain more insight into this field. However, as we have discussed in this mini-review, the complexity of these particular systems (biphasic by definition and sometimes intrinsically inhomogeneous) requires the rational design of more simple devices in order to make them accessible to a broader range of *in situ* characterization experiments. We think that the oncoming focus on these experiments is crucial to shed

some light on the structural and microstructural correlations of *hOI*-MIECs with the charge carrier transport mechanism.

AUTHOR CONTRIBUTIONS

MR, RF, and AM contributed to the conception and design of the study. DM and FP selected, compiled, and organized the literature references database. MR created the schematizations, adaptation of figure artwork, and wrote the first draft of the manuscript. DM, FP, RF, and AM wrote sections of the manuscript. All authors contributed to manuscript revision, read, and approved the submitted version.

ACKNOWLEDGMENTS

The authors wish to thank the support of Uruguayan CSIC, ANII, and PEDECIBA institutions as well as the Fondo Vaz Ferreira FVF-188 (D2C2-MEC) research project.

REFERENCES

- Aldebert, P., Audebert, P., Armand, M., Bidan, G., and Pineri, M. (1986). New chemical synthesis of mixed conductivity polymers. *J. Chem. Soc. Chem. Commun.* 1636–1638. doi: 10.1039/c39860001636
- Aoki, Y., Wiemann, C., Feyer, V., Kim, H.-S., Schneider, C. M., Ill-Yoo, H., et al. (2014). Bulk mixed ion electron conduction in amorphous gallium oxide causes memristive behavior. *Nat. Commun.* 5:473. doi: 10.1038/ncomms4473
- Atkinson, A., Baron, S. A., and Brandon, N. P. (2004). AC impedance spectra arising from mixed ionic electronic solid electrolytes. *J. Electrochem. Soc.* 151, E1E86–E1E93. doi: 10.1149/1.1690291
- Balaguer, M., Solís, C., and Serra, J. M. (2011). Study of the transport properties of the mixed ionic electronic conductor $Ce_{1-x}Tb_xO_{2-\delta}+Co(x = 0.1,0.2)$ and evaluation as oxygen-transport membrane. *Chem. Mater.* 23, 2333–2343. doi: 10.1021/cm103581w
- Barker, J., Pynenburg, R., Koksang, R., and Saidi, M. Y. (1996). An electrochemical investigation into the lithium insertion properties of Li_xCoO_2 . *Electrochim. Acta* 41, 2481–2488. doi: 10.1016/0013-4686(96)00036-9
- Barthet, C., and Guglielmi, M. (1995). Mixed electronic and ionic conductors: a new route to Nafion®-doped polyaniline. *J. Electroanal. Chem.* 388, 35–44. doi: 10.1016/0022-0728(94)03759-V
- Barthet, C., Guglielmi, M., and Baudry, P. (1997). A polyaniline + polyethylene oxide mixture as a composite polymer positive electrode in solid-state secondary batteries. *J. Electroanal. Chem.* 431, 145–152. doi: 10.1016/S0022-0728(97)00174-5
- Berthelot, R., Carlier, D., and Delmas, C. (2010). Electrochemical investigation of the $P_2-Na_xCoO_2$ phase diagram. *Nat. Mater.* 10, 74–80. doi: 10.1038/nmat2920
- Cai, S. D., Gao, C. H., Zhou, D. Y., Gu, W., and Liao, L. S. (2012). Study of hole-injecting properties in efficient, stable, and simplified phosphorescent organic light-emitting diodes by impedance spectroscopy. *ACS Appl. Mater. Interfaces* 4, 312–316. doi: 10.1021/am2013568
- Cao, F., and Prakash, J. (2002). A comparative electrochemical study of $LiMn_2O_4$ spinel thin-film and porous laminate. *Electrochim. Acta* 47, 1607–1613. doi: 10.1016/S0013-4686(01)00884-2
- Chatterjee, K., Mitra, M., Kargupta, K., Ganguly, S., and Banerjee, D. (2013). Synthesis, characterization and enhanced thermoelectric performance of structurally ordered cable-like novel polyaniline-bismuth telluride nanocomposite. *Nanotechnology* 24:215703. doi: 10.1088/0957-4484/24/21/215703
- Chen, C.-C., Huang, B.-C., Lin, M.-S., Lu, Y.-J., Cho, T.-Y., Chang, C.-H., et al. (2010). Impedance spectroscopy and equivalent circuits of conductively doped organic hole-transport materials. *Org. Electron.* 11, 1901–1908. doi: 10.1016/j.orgel.2010.09.005
- Chen, D., Ding, D., Li, X., Waller, G., Xiong, X., El-Sayed, M., et al. (2015). Probing the charge storage mechanism of a pseudocapacitive MnO_2 electrode using in operando Raman spectroscopy. *Chem. Mater.* 27, 6608–6619. doi: 10.1021/acs.chemmater.5b03118
- Cheng, C. H. W., Lin, F., and Lonergan, M. C. (2005). Charge transport in a mixed ionically/electronically conducting, cationic, polyacetylene ionomer between ion-blocking electrodes. *J. Phys. Chem. B* 109, 10168–10178. doi: 10.1021/jp0505431
- Crispin, X., Jakobsson, F. L. E., Crispin, A., Grim, P. C. M., Andersson, P., Volodin, A., et al. (2006). The origin of the high conductivity of poly(3,4-ethylenedioxythiophene)-poly(styrenesulfonate) (PEDOT-PSS) plastic electrodes. *Chem. Mater.* 18, 4354–4360. doi: 10.1021/cm061032+
- Cui, L., Shen, J., Cheng, F., Tao, Z., and Chen, J. (2011). SnO_2 nanoparticles/poly pyrrole nanowires composite as anode materials for rechargeable lithium-ion batteries. *J. Power Sources* 196:2195. doi: 10.1016/j.jpowsour.2010.09.075
- Della Santa, A., De Rossi, D., and Mazzoldi, A. (1997). Performance and work capacity of a polypyrrole conducting polymer linear actuator. *Synthetic Metals* 90, 93–100. doi: 10.1016/S0379-6779(97)81256-8
- Doeff, M. M., Ma, Y., Visco, S. J., and De Jonghe, L. C. (1993). Electrochemical insertion of sodium into carbon. *J. Electrochem. Soc.* 140, L1L69–L1L70. doi: 10.1149/1.2221153
- Dokko, K., Mohamedi, M., Fujita, Y., Itoh, T., Nishizawa, M., Umeda, M., et al. (2001). Kinetic characterization of single particles of $LiCoO_2$ by AC impedance and potential step methods. *J. Electrochem. Soc.* 148, A4A22–A4A26. doi: 10.1149/1.1359197
- Dokko, K., Shi, Q., Stefan, I. C., and Scherson, D. A. (2003). *In situ* Raman spectroscopy of single microparticle Li^+ -intercalation electrodes. *J. Phys. Chem. B* 107, 12549–12554. doi: 10.1021/jp034977c
- Dong, B. X., Nowak, C., Onorato, J. W., Strzalka, J., Escobedo, F. A., Luscombe, C. K., et al. (2019). Influence of side-chain chemistry on structure and ionic conduction characteristics of polythiophene derivatives: a computational and experimental study. *Chem. Mater.* 31, 1418–1429. doi: 10.1021/acs.chemmater.8b05257
- Fedorokova, A., Alejos, A. N., Romero, P. G., Orinakovic, R., and Kaniansky, D. (2010). Structural and electrochemical studies of PPy/PEG-LiFePO₄ cathode material for Li-ion batteries. *Electrochim. Acta* 55, 943–947. doi: 10.1016/j.electacta.2009.09.060
- Flores, E., Novák, P., and Berg, E. J. (2018). *In situ* and operando Raman spectroscopy of layered transition metal oxides for Li-ion battery cathodes. *Front. Energy Res.* 6:82. doi: 10.3389/fenrg.2018.00082
- Francis, C., Fazzi, D., Grimm, S. B., Paulus, F., Beck, S., Hillebrandt, S., et al. (2017). Raman spectroscopy and microscopy of electrochemically and

- chemically doped high-mobility semiconducting polymers. *J. Mater. Chem. C* 5, 6176–6184. doi: 10.1039/C7TC01277B
- Fu, Y., and Manthiram, A. (2012). Enhanced cyclability of lithium–sulfur batteries by a polymer acid-doped polypyrrole mixed ionic–electronic conductor. *Chem. Mater.* 24, 3081–3087. doi: 10.1021/cm301661y
- Furukawa, Y. (1996). Electronic absorption and vibrational spectroscopies of conjugated conducting polymers. *J. Phys. Chem.* 100, 15644–15653. doi: 10.1021/jp960608n
- Ghosh, S., and Inganäs, O. (2000). Networks of electron-conducting polymer in matrices of ion-conducting polymers applications to fast electrodes. *Electrochem. Solid-State Lett.* 3, 213–215. doi: 10.1149/1.1391005
- Glaudell, A. M., Cochran, J. E., Patel, S. N., and Chabiny, M. L. (2015). Impact of the doping method on conductivity and thermopower in semiconducting polythiophenes. *Adv. Energy Mater.* 5:1401072. doi: 10.1002/aenm.201401072
- Gómez-Romero, P., and Lira-Cantú, M. (1997). Hy. (brid organic-inorganic electrodes: the molecular material formed between polypyrrole and the phosphomolybdate anion. *Adv. Mater.* 9, 144–147. doi: 10.1002/adma.19970090210
- Goodenough, J. B. (2000). Oxide-ion conductors by design. *Nature* 404, 821–823. doi: 10.1038/35009177
- Guizard, C., Bac, A., Barboiu, M., and Hovnanian, N. (2001). Hybrid organic-inorganic membranes with specific transport properties: applications in separation and sensors technologies. *Separat. Purification Technol.* 25, 167–180. doi: 10.1016/S1383-5866(01)00101-0
- Han, P., Chung, S.-H., and Manthiram, A. (2019). Designing a high-loading sulfur cathode with a mixed ionic–electronic conducting polymer for electrochemically stable lithium–sulfur batteries. *Energy Storage Mater.* 17, 317–324. doi: 10.1016/j.ensm.2018.11.002
- Han, S., Ul Hassan Alvi, N., Granlöv, L., Granberg, H., Berggren, M., Fabiano, S., et al. (2019). A multiparameter pressure–temperature–humidity sensor based on mixed ionic–electronic cellulose aerogels. *Adv. Sci.* 6:1802128. doi: 10.1002/advs.201802128
- Hou, T., Tang, G., Sun, X., Cai, S., Zheng, C., and Hu, W. (2017). Perchlorate ion doped polypyrrole coated ZnS sphere composites as a sodium-ion battery anode with superior rate capability enhanced by pseudocapacitance. *RSC Adv.* 7, 43636–43641. doi: 10.1039/C7RA07901J
- Huggins, R. A. (2002). Simple method to determine electronic and ionic components of the conductivity in mixed conductors, a review. *Ionics* 8, 300–313. doi: 10.1007/BF02376083
- Huguenin, F., Ferreira, M., Zucolotto, V., Nart, F. C., Torresi, R. M., Oliveira, J. R., et al. (2004). Molecular-level manipulation of V₂O₅/polyaniline layer-by-layer films to control electrochromogenic and electrochemical properties. *Chem. Mater.* 16, 2293–2299. doi: 10.1021/cm035171s
- Inal, S., Rivnay, J., Suii, A.-O., Malliaras, G. G., and McCulloch, I. (2018). Conjugated polymers in bioelectronics. *Acc. Chem. Res.* 51, 1368–1376. doi: 10.1021/acs.accounts.7b00624
- Irvine, J. T. S., Sinclair, D. C., and West, A. R. (1990). Electroceramics: characterization by impedance spectroscopy. *Adv. Mater.* 2, 132–138. doi: 10.1002/adma.19900020304
- Jacobs, I. E., Aasen, E. W., Oliveira, J. L., Fonseca, T. N., Roehling, J. D., Li, J., et al. (2016). Comparison of solution-mixed and sequentially processed P3HT:F4TCNQ films: effect of doping-induced aggregation on film morphology. *J. Mater. Chem. C* 4, 3454–3466. doi: 10.1039/C5TC04207K
- Jamnik, J., and Maier, J. (1999). Treatment of the impedance of mixed conductors, equivalent circuit model and explicit approximate solutions. *J. Electrochem. Soc.* 146, 4183–4188. doi: 10.1149/1.1392611
- Jastrzebska-Perfect, P., Spyropoulos, G. D., Cea, C., Zhao, Z., Rauhala, O. J., Viswanathan, A., et al. (2020). Mixed-conducting particulate composites for soft electronics. *Sci. Adv.* 6:eaa26767. doi: 10.1126/sciadv.aaz6767
- Javier, A. E., Patel, S. N., Hallinan, Jr D. T., Srinivasan, V., and Balsara, N.P. (2011). Simultaneous electronic and ionic conduction in a block copolymer: application in lithium battery electrodes. *Angew. Chem. Int. Ed.* 50:9848. doi: 10.1002/anie.201102953
- Ju, S. H., Kang, I. S., Lee, Y. S., Shin, D. K., Kim, S., Shin, K., et al. (2014). Improvement of the cycling performance of LiNi_{0.6}Co_{0.2}Mn_{0.2}O₂ cathode active materials by a dual-conductive polymer coating. *ACS Appl. Mater. Interfaces* 6, 2546–2552. doi: 10.1021/am404965p
- Judeinstein, P., and Sanchez, C. (1996). Hybrid organic-inorganic materials: a land of multidisciplinary. *J. Mater. Chem.* 6, 511–525. doi: 10.1039/JM9960600511
- Jung, I. H., Hong, C. T., Lee, U.-H., Kang, Y. H., Jang, K.-S., and Cho, S. Y. (2017). High thermoelectric power factor of a diketopyrrolopyrrole-based low bandgap polymer via finely tuned doping engineering. *Sci. Rep.* 7:44704. doi: 10.1038/srep44704
- Kang, I. S., Lee, Y. S., and Kim, D. W. (2014). Improved cycling stability of lithium electrodes in rechargeable lithium batteries. *J. Electrochem. Soc.* 161, A5A3–A5A7. doi: 10.1149/2.029401jes
- Kim, G. H., Shao, L., Zhang, K., and Pipe, K. P. (2013). Engineered doping of organic semiconductors for enhanced thermoelectric efficiency. *Nat. Mater.* 12:719. doi: 10.1038/nmat3635
- Kloster, G. M., Thomas, J. A., Brazis, P. W., Kannewurf, C. R., and Shriver, D. F. (1996). Synthesis, characterization, and transport properties of new mixed ionic–electronic conducting V₂O₅-polymer electrolyte xerogel nanocomposites. *Chem. Mater.* 8, 2418–2420. doi: 10.1021/cm9603361
- Kumar, R., Pillai, R. G., Pekas, N., Wu, Y., and McCreery, R. L. (2012). Spatially resolved raman spectroelectrochemistry of solid-state polythiophene/violon memory devices. *J. Am. Chem. Soc.* 134, 14869–14876. doi: 10.1021/ja304458s
- Kumar, S. R. S., Kurra, N., and Alshareef, H. N. (2016). Enhanced high temperature thermoelectric response of sulphuric acid treated conducting polymer thin films. *J. Mater. Chem. C* 4, 215–221. doi: 10.1039/C5TC03145A
- Le Bideau, J., Viau, L., and Vioux, A. (2011). Ionogels, ionic liquid based hybrid materials. *Chem. Soc. Rev.* 40, 907–925. doi: 10.1039/C0CS00059K
- Lee, J. S., Jamnik, J., and Maier, J. (2009). Generalized equivalent circuits for mixed conductors: silver sulfide as a model system. *Monatshfte für Chemie* 140, 1113–1119. doi: 10.1007/s00706-009-0130-x
- Lee, S. H., Park, H., Kim, S., Son, W., Cheong, I. W., and Kim, J. H. (2014). Transparent and flexible organic semiconductor nanofilms with enhanced thermoelectric efficiency. *J. Mater. Chem. A* 2, 7288–7294. doi: 10.1039/C4TA00700J
- Levasseur, S., Ménétrier, M., and Delmas, C. (2002). On the dual effect of Mg doping in LiCoO₂ and Li1+ δ CoO₂: structural, electronic properties, and 7Li MAS NMR Studies. *Chem. Mater.* 14 3584–3590. doi: 10.1021/cm021107j
- Li, J., and Khan, I. M. (1991). Mixed (electronic and ionic) conductive solid polymer matrix, synthesis and properties of poly(2,5,8,11,14,17,20,23-octaaxapentacosylmethacrylate)-block-poly(4-vinylpyridine). *Makromol. Chem.* 192, 3043–3050. doi: 10.1002/macp.1991.021921219
- Li, W.-J., Chou, S.-L., Wang, J.-Z., Wang, J.-L., Gu, Q.-F., Liu, H.-K., et al. (2015). Multifunctional conducting polymer coated Na1+xMnFe(CN)6 cathode for sodium-ion batteries with superior performance via a facile and one-step chemistry approach. *Nano Energy* 13, 200–207. doi: 10.1016/j.nanoen.2015.02.019
- Lim, E., Peterson, K. A., Su, G. M., and Chabiny, M. L. (2018). Thermoelectric properties of poly(3-hexylthiophene) (P3HT) doped with 2,3,5,6-tetrafluoro-7,8-tetracyanoquinodimethane (F4TCNQ) by vapor-phase infiltration. *Chem. Mater.* 30, 998–1010. doi: 10.1021/acs.chemmater.7b04849
- Lin, Y., Fang, S., Su, D., Brinkman, K. S., and Chen, F. (2015). Enhancing grain boundary ionic conductivity in mixed ionic–electronic conductors. *Nat. Commun.* 6:6824. doi: 10.1038/ncomms7824
- Liu, C., Wang, W., Li, Y., Cui, F., Xie, C., Zhu, L., et al. (2019). PMWCNT/PVDF ultrafiltration membranes with enhanced antifouling properties intensified by electric field for efficient blood purification. *J. Membr. Sci.* 576, 48–58. doi: 10.1016/j.memsci.2019.01.015
- Liu, J., Davis, N. R., Liu, D. S., and Hammond, P. T. (2012). Highly transparent mixed electron and proton conducting polymer membranes. *J. Mater. Chem.* 22:15534. doi: 10.1039/c2jm32296j
- Liu, L. L., Wang, X. J., Zhu, Y. S., Hu, C. L., Wu, Y. P., and Holze, R. (2013). Polypyrrole-coated LiV₃O₈-nanocomposites with good electrochemical performance as anode material for aqueous rechargeable lithium batteries. *J. Power Sources* 224, 290–294. doi: 10.1016/j.jpowsour.2012.09.100
- Liu, Q., Hu, Z., Chen, M., Zou, C., Jin, H., Wang, S., et al. (2020). The cathode choice for commercialization of sodium-ion batteries: layered transition metal oxides versus prussian blue analogs. *Adv. Funct. Mater.* 30:1909530. doi: 10.1002/adfm.201909530
- Lu, D., Yao, Z. J., Li, Y. Q., Zhong, Y., Wang, X. L., Xie, D., et al. (2020). Sodium-rich manganese oxide porous microcubes with polypyrrole coating as a superior

- cathode for sodium ion full batteries. *J. Colloid Interface Sci.* 565, 218–226. doi: 10.1016/j.jcis.2020.01.023
- Lu, Z., and Dahn, J. R. (2001). *In situ* X-ray diffraction study of $P_2\text{-Na-}2/3[\text{Ni}_{1/3}\text{Mn}_{2/3}]\text{O-}2$. *J. Electrochem. Soc.* 148, A1A225–A1A229. doi: 10.1149/1.1407247
- Maier, J. (2005). Nanoionics: ion transport and electrochemical storage in confined systems. *Nature Materials* 4, 805–815. doi: 10.1038/nmat1513
- Mantione, D., del Agua, I., Sanchez-Sanchez, A., and Mecerreyes, D. (2017). Poly(3,4-ethylenedioxythiophene) (PEDOT) derivatives: innovative conductive polymers for bioelectronics. *Polymers* 9:354. doi: 10.3390/polym9080354
- Mengistie, D. A., Chen, C.-H., Boopathi, K. M., Pranoto, F. W., Li, L.-J., and Chu, C.-W. (2015). Enhanced thermoelectric performance of pedot:pss flexible bulky papers by treatment with secondary dopants. *ACS Appl. Mater. Interfaces* 7, 94–100. doi: 10.1021/am507032e
- Mengistie, D. A., Wang, P.-C., and Chu, C.-W. (2013). Effect of molecular weight of additives on the conductivity of pedot:pss and efficiency for ito-free organic solar cells. *J. Mater. Chem. A* 1, 9907–9915. doi: 10.1039/c3ta11726j
- Miyatani, S. (1973). Electronic and ionic conduction in $(\text{AgxCu}_{1-x})_2\text{Se}$. *J. Phys. Soc. Jap.* 34, 423–432. doi: 10.1143/JPSJ.34.423
- Mombrú, D., Romero, M., Faccio, R., Castiglioni, J., and Mombrú, A. W. (2017a). *In situ* growth of ceramic quantum dots in polyaniline host via water vapor flow diffusion as potential electrode materials for energy applications. *J. Solid State Chem.* 250, 60–67. doi: 10.1016/j.jssc.2017.03.016
- Mombrú, D., Romero, M., Faccio, R., and Mombrú, A. W. (2017b). Raman and impedance spectroscopy under applied dc bias insights on the electrical transport for donor:acceptor nanocomposites based on poly(vinyl carbazole) and TiO_2 quantum dots. *J. Phys. Chem. C* 121, 23383–23391. doi: 10.1021/acs.jpcc.7b08400
- Mombrú, D., Romero, M., Faccio, R., and Mombrú, A. W. (2017c). From positive to negative magnetoresistance behavior at low applied magnetic fields for polyaniline:titania quantum dot nanocomposites. *J. Appl. Phys.* 121:245106. doi: 10.1063/1.4989831
- Mombrú, D., Romero, M., Faccio, R., and Mombrú, A. W. (2018). Raman microscopy insights on the out-of-plane electrical transport of carbon nanotube-doped PEDOT:PSS electrodes for solar cell applications. *J. Phys. Chem. B* 122, 2694–2701. doi: 10.1021/acs.jpcc.8b00317
- Mombrú, D., Romero, M., Faccio, R., and Mombrú, A. W. (2019). Transition from positive to negative electrical resistance response under humidity conditions for PEDOT:PSS- MoS_2 nanocomposite thin films. *J. Mater. Sci.* 30, 5959–5964. doi: 10.1007/s10854-019-00895-z
- Murthy, A., and Manthiram, A. (2011). Highly water-dispersible, mixed ionic-electronic conducting, polymer acid-doped polyanilines as ionomers for direct methanol fuel cells. *Chem. Commun.* 47, 6882–6884. doi: 10.1039/c1cc11473e
- Nanda, J., Remillard, J., O'Neill, A., Bernardi, D., Ro, T., Nietering, K. E., et al. (2011). Local state-of-charge mapping of lithium-ion battery electrodes. *Adv. Funct. Mater.* 21, 3282–3290. doi: 10.1002/adfm.201100157
- Nie, C., Ma, L., Xia, Y., He, C., Deng, J., Wang, L., et al. (2015). Novel heparin mimicking polymer brush grafted carbon nanotube/PES composite membranes for safe and efficient blood purification. *J. Membr. Sci.* 475, 455–468. doi: 10.1016/j.memsci.2014.11.005
- Nightingale, J., Wade, J., Moia, D., Nelson, J., and Kim, J.-S. (2018). Impact of molecular order on polaron formation in conjugated polymers. *J. Phys. Chem. C* 122, 29129–29140. doi: 10.1021/acs.jpcc.8b09706
- Nigrey, P. J., Macdiarmid, A. G., and Heeg, A. J. (1978). Electrochemistry of polyacetylene, (CH): electrochemical doping of $(\text{CH})_x$ films to the metallic state. *J. Chem. Soc. Chem. Commun.* 594–595. doi: 10.1039/c39790000594
- Nishi, T., Nakai, H., and Kita, A. (2013). Visualization of the state-of-charge distribution in a LiCoO_2 cathode by *in situ* raman imaging. *J. Electrochem. Soc.* 160, A1A785–A1A788. doi: 10.1149/2.061310jes
- Nowy, S., Ren, W., Elschner, A., Lovenich, W., and Brutting, W. (2010). Impedance spectroscopy as a probe for the degradation of organic light-emitting diodes. *J. Appl. Phys.* 107:054501. doi: 10.1063/1.3294642
- Onorato, J. W., and Luscombe, C. K. (2019). Morphological effects on polymeric mixed ionic/electronic conductors. *Mol. Syst. Des. Eng.* 4, 310–324. doi: 10.1039/C8ME00093J
- Park, M., Zhang, X., Chung, M., Less, G. B., and Sastry, A. M. (2010). A review of conduction phenomena in Li-ion batteries. *J. Power Sources* 195, 7904–7929. doi: 10.1016/j.jpowsour.2010.06.060
- Patel, S. N., Javier, A. E., Stone, G. M., Mullin, S. A., and Balsara, N. P. (2012). Simultaneous conduction of electronic charge and lithium ions in block copolymers. *ACS Nano* 6, 1589–1600. doi: 10.1021/nn2045664
- Paul, E. W., Ricco, A. J., and Wrighton, M. S. (1985). Resistance of polyaniline films as a function of electrochemical potential and the fabrication of polyaniline-based microelectronic devices. *J. Phys. Chem.* 1985, 1441–1447. doi: 10.1021/j100254a028
- Paulsen, B. D., Tybrandt, K., Stavrinidou, E., and Rivnay, J. (2020). Organic mixed ionic–electronic conductors. *Nat. Mater.* 19, 13–26. doi: 10.1038/s41563-019-0435-z
- Pignanelli, F., Romero, M., Castiglioni, J., Faccio, R., and Mombrú, A. W. (2019b). Novel synergistic *in situ* synthesis of lithium-ion poly(ethylene citrate)- TiO_2 nanocomposites as promising fluorine-free solid polymer electrolytes for lithium batteries. *J. Phys. Chem. Solids* 135:109082. doi: 10.1016/j.jpcc.2019.109082
- Pignanelli, F., Romero, M., Estéves, M., Fernández-Werner, L., Faccio, R., and Mombrú, A. W. (2019a). Lithium titanate nanotubes as active fillers for lithium-ion polyacrylonitrile solid polymer electrolytes. *Ionics* 25, 2607–2614. doi: 10.1007/s11581-018-2768-z
- Pignanelli, F., Romero, M., Faccio, R., Fernández-Werner, L., and Mombrú, A. W. (2018). Enhancement of lithium-ion transport in poly(acrylonitrile) with hydrogen titanate nanotube fillers as solid polymer electrolytes for lithium-ion battery applications. *J. Phys. Chem. C* 122, 1492–1499. doi: 10.1021/acs.jpcc.7b10725
- Pingel, P., and Neher, D. (2013). Comprehensive picture of p-type doping of P3HT with the molecular acceptor F4TCNQ. *Phys. Rev. B* 87:115209. doi: 10.1103/PhysRevB.87.115209
- Qu, S., Yao, Q., Shi, W., Wang, W., and Chen, L. (2016). The influence of molecular configuration on the thermoelectrical properties of poly(3-hexylthiophene). *J. Electron. Mater.* 45:8. doi: 10.1007/s11664-015-4045-5
- Reddy, S., Xiao, Q., Liu, H. Q., Li, C. P., Chen, S. F., Wang, C., et al. (2019). Bionanotube/poly(3,4-ethylenedioxythiophene) nanohybrid as an electrode for the neural interface and dopamine sensor. *ACS Appl. Mater. Interfaces* 11, 18254–18267. doi: 10.1021/acsami.9b04862
- Renna, L. A., Lenef, J. D., Bag, M., and Venkataraman, D. (2017). Mixed ionic–electronic conduction in binary polymer nanoparticle assemblies. *Adv. Mater. Interfaces* 1700397, 10397–8. doi: 10.1002/admi.201700397
- Riess, I. (2000). Polymeric mixed ionic electronic conductors. *Solid State Ionics* 136–137, 1119–1130. doi: 10.1016/S0167-2738(00)00607-X
- Riess, I. (2003). Mixed ionic-electronic conductors-material properties and applications. *Solid State Ionics* 157, 1–17. doi: 10.1016/S0167-2738(02)00182-0
- Rivnay, J., Inal, S., Collins, B. A., Sessolo, M., Stavrinidou, E., Strakosas, X., et al. (2016). Structural control of mixed ionic and electronic transport in conducting polymers. *Nat. Commun.* 7:11287. doi: 10.1038/ncomms11287
- Romero, M., Faccio, R., Vázquez, S., and Mombrú, A. W. (2016). Enhancement of lithium conductivity and evidence of lithium dissociation for LLTO-PMMA nanocomposite electrolyte. *Mater. Lett.* 172, 1–5. doi: 10.1016/j.matlet.2016.02.128
- Roussel, F., Chen, Yu King, R., Kuriakose, M., Depriester, M., Hadj-Sahraoui, A., Gors, C., et al. (2015). Electrical and thermal transport properties of polyaniline/silver composites and their use as thermoelectric materials. *Synth. Met.* 199, 196–204. doi: 10.1016/j.synthmet.2014.11.020
- Saïdi, M. Y., Barker, J., and Koksang, R. (1996). Thermodynamic and kinetic investigation of lithium insertion in the $\text{Li}_{1-x}\text{Mn}_2\text{O}_4$ spinel phase. *J. Solid State Chem.* 122, 195–199. doi: 10.1006/jssc.1996.0101
- Sanjeeva Murthy, N. (2016). “Chapter 2: x-ray diffraction from polymers,” in *Polymer Morphology: Principles, Characterization, and Processing, 1st Edn*, ed Qipeng Guo (Hoboken, NJ: John Wiley & Sons, Inc), 14–36. doi: 10.1002/9781118892756.ch2
- Sauvage, F., Laffont, L., Tarascon, J. M., and Baudrin, E. (2007). Study of the insertion/deinsertion mechanism of sodium into $\text{Na}_{0.44}\text{MnO}_2$. *Inorg. Chem.* 46, 3289–3294. doi: 10.1021/ic0700250
- Scrosati, B., Croce, F., and Persi, L. (2000). Impedance spectroscopy study of PEO-based nanocomposite polymer electrolytes. *J. Electrochem. Soc.* 147, 1718–1721. doi: 10.1149/1.1393423

- Sengodu, P., and Deshmukh, A. (2015). Conducting polymers and their inorganic composites for advanced Li-ion batteries: a review. *RSC Adv.* 5, 42109–42130. doi: 10.1039/C4RA17254J
- Sengwa, R. J., and Dhatwarwal, P. (2020). Predominantly chain segmental relaxation dependent ionic conductivity of multiphase semicrystalline PVDF/PEO/LiClO₄ solid polymer electrolytes. *Electrochim. Acta* 338:135890. doi: 10.1016/j.electacta.2020.135890
- Shao, Z., and Haile, S. M. (2004). A high-performance cathode for the next generation of solid-oxide fuel cells. *Nature* 431, 170–173. doi: 10.1038/nature02863
- Shi, Y., Zhou, X., Zhang, J., Bruck, A. M., Bond, A. C., Marschilok, A. C., et al. (2017). Nanostructured conductive polymer gels as a general framework material to improve electrochemical performance of cathode materials in Li-ion batteries. *Nano Lett.* 17, 1906–1914. doi: 10.1021/acs.nanolett.6b05227
- Shin, J. H., and Passerini, S. (2004). PEO- LiN(SO₂CF₂CF₃)₂ polymer electrolytes V. Effect of fillers on ionic transport properties. *J. Electrochem. Soc.* 151, A2A38–A2A45.
- Stavrinidou, E., Leleux, P., Rajaona, H., Khodagholy, D., Rivnay, J., Lindau, M., et al. (2013). Direct measurement of ion mobility in a conducting polymer. *Adv. Mater.* 25, 4488–4493. doi: 10.1002/adma.201301240
- Takano, T., Masunaga, H., Fujiwara, A., Okuzaki, H., and Sasaki, T. (2012). Pedot nanocrystal in highly conductive pedot:pss polymer films. *Macromolecules* 45, 3859–3865. doi: 10.1021/ma300120g
- Tang, W., Gao, X. W., Zhu, Y. S., Yue, Y. B., Shi, Y., Wu, Y. P., et al. (2012b). A hybrid of V₂O₅ nanowires and MWCNTs coated with polypyrrole as an anode material for aqueous rechargeable lithium batteries with excellent cycling performance. *J. Mater. Chem.* 22, 20143–20145. doi: 10.1039/c2jm34563c
- Tang, W., Liu, L., Zhu, Y., Sun, H., Wu, Y., and Zhu, K. (2012a). An aqueous rechargeable lithium battery of excellent rate capability based on a nanocomposite of MoO₃ coated with PPy and LiMn₂O₄. *Energy Environ. Sci.* 5, 6909–6913. doi: 10.1039/c2ee21294c
- Tekoglu, S., Wielend, D., Scharber, M. C., Sariciftci, N. S., and Yumusak, C. (2019). Conducting polymer-based biocomposites using deoxyribonucleic acid (DNA) as counterion. *Adv. Mater. Technol.* 5:1900699. doi: 10.1002/admt.201900699
- Tevar, A. D., and Whitacre, J. F. (2010). Relating synthesis conditions and electrochemical performance for the sodium intercalation compound Na₄Mn₉O₁₈ in aqueous electrolyte. *J. Electrochem. Soc.* 157, A8A70–A8A75. doi: 10.1149/1.3428667
- Thackeray, J. W., White, H. S., and Wrighton, M. S. (1985). Poly(3-methylthiophene)-coated electrodes: optical and electrical properties as a function of redox potential and amplification of electrical and chemical signals using poly(3-methylthiophene)-based microelectrochemical transistors. *J. Phys. Chem.* 1985, 5133–5140. doi: 10.1021/j100269a048
- Thackeray, M. M. (1997). Manganese oxides for lithium batteries. *Prog. Solid State Chem.* 25, 1–71. doi: 10.1016/S0079-6786(97)81003-5
- Tian, F., Liu, L., Yang, Z., Wang, X., Chen, Q., and Wang, X. (2011). Electrochemical characterization of a LiV₃O₈-polypyrrole composite as a cathode material for lithium ion batteries. *Mater. Chem. Phys.* 127, 151–155. doi: 10.1016/j.matchemphys.2011.01.051
- Udo, L., Elisabeth, M., Nicola, N., and Jurg, D. (2009). Microscopical investigations of pedot:pss thin films. *Adv. Funct. Mater.* 19, 1215–1220. doi: 10.1002/adfm.200801258
- Vadivel Murugan, A., Muraliganth, T., and Manthiram, A. (2008). Rapid microwave-solvothermal synthesis of phospho-olivine nanorods and their coating with a mixed conducting polymer for lithium ion batteries. *Electrochem. Commun.* 10, 903–906. doi: 10.1016/j.elecom.2008.04.004
- Vorotyntsev, M. A., Deslouis, C., Musiani, M. M., Tribollet, B., and Aoki, K. (1999). Transport across an electroactive polymer film in contact with media allowing both ionic and electronic interfacial exchange. *Electrochim. Acta* 44, 2105–2115. doi: 10.1016/S0013-4686(98)00318-1
- Wachsman, E. D., and Lee, K. T. (2011). Lowering the temperature of solid oxide fuel cells. *Science* 334, 935–939. doi: 10.1126/science.1204090
- Wang, G. J., Yang, L. C., Qu, Q. T., Wang, B., Wu, Y. P., and Holze, R. (2010). An aqueous rechargeable lithium battery based on doping and intercalation mechanisms. *J. Solid State Electrochem.* 14:865. doi: 10.1007/s10008-009-0869-3
- Wang, W., Chen, C., Tollan, C., Yang, F., Qin, Y., and Knez, M. (2017). Efficient and controllable vapor to solid doping of the polythiophene P3HT by low temperature vapor phase infiltration. *J. Mater. Chem. C* 5, 2686–2694. doi: 10.1039/C6TC05544C
- Wang, X., Wang, B., Tang, Y., Xu, B. B., Liang, C., Yana, M., et al. (2020). Manganese hexacyanoferrate reinforced by PEDOT coating towards high-rate and long-life sodium-ion battery cathode. *J. Mater. Chem. A* 8, 3222–3227. doi: 10.1039/C9TA12376H
- Wang, Z., Liu, Y., Wu, Z., Guan, G., Zhang, D., Zheng, H., et al. (2017). A string of nickel hexacyanoferrate nanocubes coaxially grown on a CNT@bipolar conducting polymer as a high-performance cathode material for sodium-ion batteries. *Nanoscale* 9, 823–831. doi: 10.1039/C6NR08765E
- Watanabe, M. (1996). Molecular design of ion and ion/electron mixed conducting polymers. *Macromol. Symp.* 105, 229–233. doi: 10.1002/masy.19961050133
- Wei, Y., Yan, Y., Zou, Y., Shi, M., Deng, Q., Zhao, N., et al. (2019). The ternary conductive polymer coated S/BDPC composite cathode for enhancing the electrochemical prospects in Li-S batteries. *Surface Coatings Technol.* 358, 560–566. doi: 10.1016/j.surfcoat.2018.11.038
- White, H. S., Kittleson, G. P., and Wrighton, M. S. (1984). Chemical derivatization of an array of three gold microelectrodes with polypyrrole: fabrication of a molecule-based transistor. *J. Am. Chem. Soc.* 11, 5375–5377. doi: 10.1021/ja00330a070
- Xiang, X., Zhang, K., and Chen, J. (2015). Recent advances and prospects of cathode materials for sodium-ion batteries. *Adv. Mater.* 27, 5343–5364. doi: 10.1002/adma.201501527
- Yamamoto, J., and Furukawa, Y. (2015). Electronic and vibrational spectra of positive polarons and bipolarons in regioregular poly(3-hexylthiophene) doped with ferric chloride. *J. Phys. Chem. B* 119, 4788–4794. doi: 10.1021/jp512654b
- Yang, T., Zheng, J., Cheng, Q., Hu, Y.-Y., and Chan, C. K. (2017). Composite polymer electrolytes with 6th Li₇La₃Zr₂O₁₂ garnet-type nanowires as ceramic fillers: mechanism of conductivity enhancement and role of doping and morphology. *ACS Appl Mater Interfaces* 9, 21773–21780. doi: 10.1021/acsami.7b03806
- Yang, Y., Yu, G., Cha, J. J., Wu, H., Vosgueritchian, M., Yao, Y., et al. (2011). Improving the performance of lithium-sulfur batteries by conductive polymer coating. *ACS Nano* 5, 9187–9193. doi: 10.1021/nn203436j
- Yokota, I. (1961). On the theory of mixed conduction with special reference to conduction in silver sulfide group semiconductors. *J. Phys. Soc. Jap.* 16, 2213–2223. doi: 10.1143/JPSJ.16.2213
- Yu, X., Zhu, Y., Cheng, C., Zhang, T., Wang, X., and Hsiao, B. S. (2019). Novel thin-film nanofibrous composite membranes containing directional toxin transport nanochannels for efficient and safe hemodialysis application. *J. Membr. Sci.* 582, 151–163. doi: 10.1016/j.memsci.2019.04.006
- Yuan, J., Hao, Y., Zhang, X., and Li, X. (2018). Sandwiched CNT@SnO₂@PPy nanocomposites enhancing sodium storage. *Colloids Surfaces A* 555, 795–801. doi: 10.1016/j.colsurfa.2018.07.023
- Yuan, L., Wang, J., Chew, S. Y., Chen, J., Guo, Z. P., Zhao, L., et al. (2007). Synthesis and characterization of SnO₂-polypyrrole composite for lithium-ion battery. *J. Power Sources* 174, 1183–1187. doi: 10.1016/j.jpowsour.2007.06.179
- Zhang, F., Cao, H., Yue, D., Zhang, J., and Qu, M. (2012). Enhanced anode performances of polyaniline-TiO₂-reduced graphene oxide nanocomposites for lithium ion batteries. *Inorg. Chem.* 2012, 9544–9551. doi: 10.1021/ic301378j
- Zhang, K., Davis, M., Qiu, J., Hope-Weeks, L., and Wang, S. (2012). Thermoelectric properties of porous multi-walled carbon nanotube/polyaniline core/shell nanocomposites. *Nanotechnology* 23:385701. doi: 10.1088/0957-4484/23/38/385701
- Zhang, Q., Sun, Y., Xu, W., and Zhu, D. (2012). Thermoelectric energy from flexible P3HT films doped with a ferric salt of triflimide anions. *Energy Environ. Sci.* 5, 9639–9644. doi: 10.1039/c2ee23006b
- Zhang, Q., Wang, W., Li, J., Zhu, J., Wang, L., Zhu, M., et al. (2013). Preparation and thermoelectric properties of multi-walled carbon nanotube/polyaniline hybrid nanocomposites. *J. Mater. Chem. A* 1, 12109–12114. doi: 10.1039/c3ta12353g
- Zhang, X. W., Wang, C., Appleby, A. J., and Little, F. E. (2002). Composite doped emeraldine-polyethylene oxide-bonded lithium-ion nano-tin anodes with electronic-ionic mixed conduction. *Solid State Ionics* 150, 383–389. doi: 10.1016/S0167-2738(02)00522-2
- Zhang, Z. J., Wang, J. Z., Chou, S. L., Liu, H. K., Ozawa, K., and Li, H. (2013). Polypyrrole-coated α-LiFeO₂O nanocomposite with enhanced

- electrochemical properties for lithium-ion batteries. *Electrochim. Acta* 108, 820–826. doi: 10.1016/j.electacta.2013.06.130
- Zhao, X., Zhang, Z., Yang, F., Fu, Y., Lai, Y., and Li, J. (2015). Core-shell structured SnO₂ hollow spheres-polyaniline composite as an anode for sodium-ion batteries. *RSC Adv.* 5, 31465–31471. doi: 10.1039/C5RA02834E
- Zheng, J., Tang, M., and Hu, Y. Y. (2016). Lithium ion pathway within Li₇La₃Zr₃O₁₂-polyethylene oxide composite electrolytes. *Angew. Chem. Int. Ed.* 55, 12538–12542. doi: 10.1002/anie.201607539
- Zhou, M., Xiong, Y., Cao, Y., Ai, X., and Yang, H. (2013). Electroactive organic anion-doped polypyrrole as a low cost and renewable cathode for sodium-ion batteries. *J. Polym. Sci. B* 51:114. doi: 10.1002/polb.23184
- Zhou, M., Zhu, L. M., Cao, Y. L., Zhao, R. R., Qian, J. F., Ai, X. P., et al. (2012). Fe(CN)₆⁴⁻-doped polypyrrole: a high-capacity and high-rate cathode material for sodium-ion batteries. *RSC Adv.* 2, 5495–5498. doi: 10.1039/c2ra20666h
- Zhou, Q., Liu, L., Huang, Z., Yi, L., Wang, X., and Cao, G. (2016). Co₃S₄@polyaniline nanotubes as high-performance anode materials for sodium ion batteries. *J. Mater. Chem. A* 4, 5505–5516. doi: 10.1039/C6TA01497F
- Zhu, L. M., Shen, Y. F., Sun, M. Y., Qian, J. F., Cao, Y., Ai, X., et al. (2013). Self-doped polypyrrole with ionizable sodium sulfonate as a renewable cathode material for sodium ion batteries. *Chem. Commun.* 49, 11370–11372. doi: 10.1039/c3cc46642f
- Zia Ullah, K., Jesper, E., Mahiar Max, H., Roger, G., Hjalmar, G., Lars, W., et al. (2016). Thermoelectric polymers and their elastic aerogels. *Adv. Mater.* 28, 4556–4562. doi: 10.1002/adma.201505364

Conflict of Interest: The authors declare that the research was conducted in the absence of any commercial or financial relationships that could be construed as a potential conflict of interest.

Copyright © 2020 Romero, Mombrú, Pignanelli, Faccio and Mombrú. This is an open-access article distributed under the terms of the Creative Commons Attribution License (CC BY). The use, distribution or reproduction in other forums is permitted, provided the original author(s) and the copyright owner(s) are credited and that the original publication in this journal is cited, in accordance with accepted academic practice. No use, distribution or reproduction is permitted which does not comply with these terms.



ZnO Nanomaterials: Current Advancements in Antibacterial Mechanisms and Applications

Shengjie Jiang^{1,2,3}, Kaili Lin^{1,2,3*} and Ming Cai^{1,2,3*}

¹ Department of Oral and Cranio-Maxillofacial Surgery, Shanghai Ninth People's Hospital, College of Stomatology, Shanghai Jiao Tong University School of Medicine, Shanghai, China, ² National Clinical Research Center for Oral Diseases, Shanghai, China, ³ Shanghai Key Laboratory of Stomatology and Shanghai Research Institute of Stomatology, Shanghai, China

The prevalence of various diseases caused by bacteria has been increasing, and some traditional antibiotics have been reported to have varying degrees of resistance. ZnO nanomaterials (ZnO-NMs), due to their excellent broad-spectrum antibacterial properties, lasting antibacterial effects, and excellent biocompatibility, have quickly become the research focus of new antibacterial agents. While the narrow light response range of ZnO-NMs has limited the antibacterial performance to some extent and modifying it by various means to improve its response under visible light, such as doping metal/non-metal atoms, depositing noble metals and coupling carbon materials, which is a new research hotspot. Herein, the current mainstream claims about the antibacterial mechanisms and applications of ZnO-NMs are reviewed.

Keywords: ZnO nanomaterials, antibacterial activity, mechanism, applications, review

INTRODUCTION

Till now, the bacterial infection is still an urgent problem to be solved. The emergence and development of antibiotics have provided a simple and effective treatment for complex and severe diseases. However, the widespread production and abuse of antibiotics in recent decades have led to some “super bacteria” that have apparent resistance to antibiotics. Conventional antibiotic treatment has little effect on the increase of such bacteria.

Recently, nanotechnology, especially some nanomaterials with antibacterial activity such as metal nanoparticles, metal oxide nanoparticles, and carbon nanotubes, are considered as a new defense method against bacterial infections. The nanoscale surface effect and small size effect give these materials a unique antibacterial mechanism, mainly including three viewpoints: generate reactive oxygen species (ROS) or release metal ions to destroy bacterial DNA and protein; nanoparticles gather on the surface of the bacterial cell membrane and destroy the cell membrane (Qi et al., 2020) and interrupt transmembrane electron transfer (Li et al., 2008).

Compared with other antibacterial materials, as a traditional wide bandgap semiconductor, ZnO possesses excellent biocompatibility, safety, and long-term effectiveness, making it suitable for various biomedical applications (Liu et al., 2019). Moreover, the nanoscale gives it a unique antibacterial mechanism and significant antibacterial potential. ZnO nanoparticles (NPs) show significant bactericidal potential against various Gram-positive bacteria and Gram-negative bacteria such as *Escherichia coli*, *Staphylococcus aureus*, *Pseudomonas aeruginosa*, and *Klebsiella pneumoniae* (Luo et al., 2013). However, knowledge of the exact antibacterial mechanism of ZnO-NPs is still limited, and a correct understanding of its antibacterial mechanism is a prerequisite for effectively exerting its antibacterial potential. First, we review the latest research progress of the

OPEN ACCESS

Edited by:

Kezhen Qi,

Shenyang Normal University, China

Reviewed by:

Shu-Yuan Liu,

Shenyang Medical College, China

Yuanyuan Wang,

Peking University Hospital of

Stomatology, China

*Correspondence:

Kaili Lin

lklecnu@aliyun.com

Ming Cai

zidanecm500@126.com

Specialty section:

This article was submitted to

Nanoscience,

a section of the journal

Frontiers in Chemistry

Received: 15 April 2020

Accepted: 05 June 2020

Published: 21 July 2020

Citation:

Jiang S, Lin K and Cai M (2020) ZnO

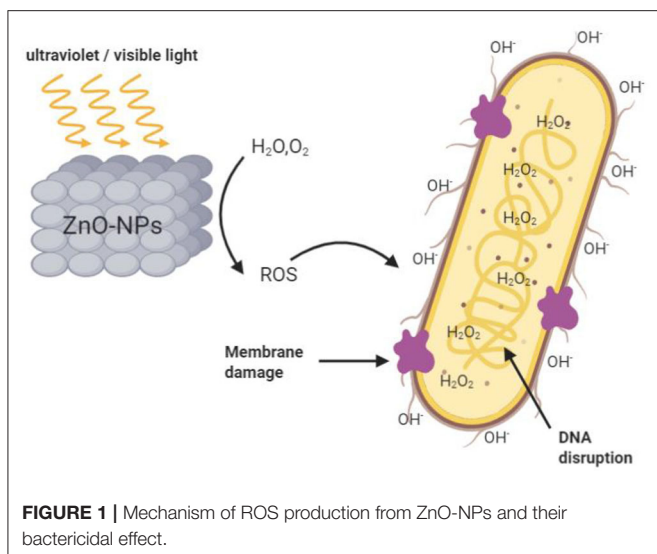
Nanomaterials: Current

Advancements in Antibacterial

Mechanisms and Applications.

Front. Chem. 8:580.

doi: 10.3389/fchem.2020.00580



antibacterial mechanism of ZnO-NPs and the factors affecting its antibacterial activity. Then the applications of ZnO-NPs in antibacterial and antifungal are summarized.

ANTIBACTERIAL MECHANISM OF ZnO-NPs

Generation of Reactive Oxygen Species (ROS)

Reactive oxygen species (ROS) is the most common and widely accepted mechanism for the antibacterial activity of ZnO-NPs (Kumar et al., 2017). Active oxygen is a type of single-electron reduction product of oxygen, such as superoxide anion O_2^- , hydroxyl radical OH^\cdot and hydrogen peroxide H_2O_2 . ZnO is a wide bandgap semiconductor material. The electrons (e^-) in its valence band transition under ultraviolet/visible light, leaving positively charged holes (h^+). e^- and h^+ undergo a series of redox reactions with oxygen and water on the surface of ZnO particles to generate ROS with extreme chemical activity (Miao et al., 2017; **Figure 1**).

ROS can cut off the chemical bonds of bacteria's organic matter, to achieve the bactericidal effect. Among them, the negatively charged peroxide cannot pass through the cell membrane, OH^- aggregates on the surface of bacterial cell membranes and causes cell membrane destruction, and H_2O_2 can penetrate the cell membrane, causing damage to the cell membrane and the destruction of DNA and protein in the membrane, which plays a bactericidal role (Kumar et al., 2017). However, it is worth noting that some studies have also found that ZnO also shows prominent antibacterial ability in the dark, and it is more significant when the bacterial concentration is low (Leung et al., 2016). In the study of Jeong et al. (2020) an array of ZnO nanorods was prepared by hydrothermal method and wrapped with an atomic layer of aluminum oxide to reduce the generation of active oxygen and the release of Zn^{2+} . The results showed that in the dark, the mechanical damage to the

cell membrane of *E. coli* accounted for 56.4% of the sterilization efficiency, while the chemical damage caused by the generation of reactive oxygen species and the release of Zn^{2+} accounted for only 37.8%. Hirota et al. (2010) also demonstrated that ZnO NPs have sustainable antibacterial activity against *E. coli* in the absence of light. These results indicate that in the absence of light, there may be additional mechanisms for generating active oxygen or other antibacterial mechanisms not related to light, as shown in **Figure 2**.

Zn^{2+} Release Induced Damage

This theory holds that ZnO can slowly release Zn^{2+} in aqueous solution. Zn^{2+} can penetrate through the cell membrane and result in protein denaturation and loss of cell proliferation. Besides, Zn^{2+} can also destroy the electron transport system, leading to a cellular respiratory disorder. Joe et al. (2017) studied the antibacterial effects of various ZnO-NPs with different particle sizes and the number of oxygen vacancies in the dark state, and found that ZnO and Zn^{2+} adsorbed on the cell surface were the primary mode of action of antibacterial.

Although some studies attribute the antibacterial potential of ZnO to the release of Zn^{2+} , no significant improvement in antibacterial effect was obtained with the increasing of Zn^{2+} concentration (Sawai, 2003). In the antibacterial experiment of Elena et al. (2016) on ZnO nanorod-modified graphene nanosheets (ZNGs) against *Streptococcus mutans*, the negligible dissolution of Zn^{2+} was observed, indicating high cell mortality in suspension is not related to Zn^{2+} release. It indicates that the release of Zn^{2+} should not be the primary mechanism of ZnO antibacterial.

Interaction of ZnO-NPs With the Cell Membrane

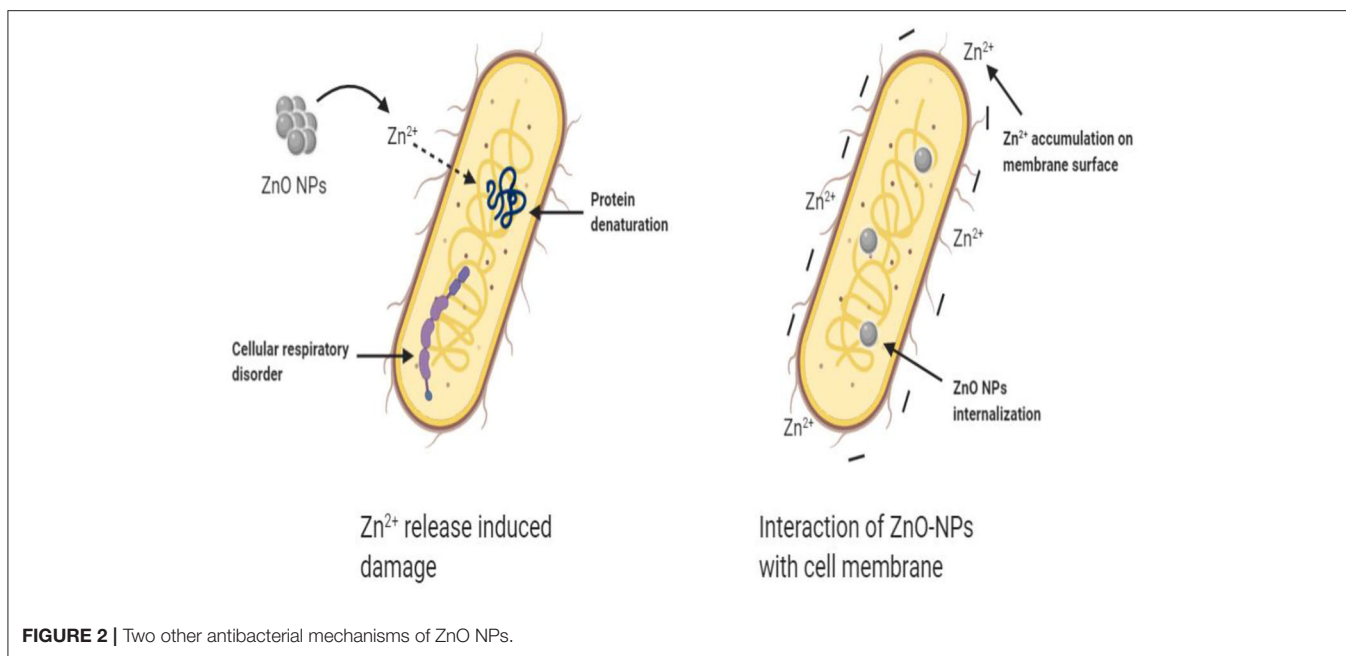
The Interaction of ZnO-NPs with bacteria and subsequent destruction of the bacterial surface has been proposed to explain the antibacterial activity of ZnO-NPs. This mainly includes membrane dysfunction caused by the accumulation of positively charged Zn^{2+} on the surface of the cell membrane and the disorder of energy metabolism of bacterial substances caused by the internalization of ZnO-NPs.

Membrane Dysfunction

As shown in **Figure 2**, some studies suggest that Zn^{2+} will be electrostatically attracted to the negatively charged bacterial cell membrane surface, thereby interfering with the charge balance on the cell membrane surface, resulting in severe cell deformation, and finally leading to bacterial lysis (Wang et al., 2014). Zhang et al. (2007) showed that ZnO-NPs caused damage to the cell membrane of *E. coli*, and further research found that this damage may be caused by the direct interaction between ZnO-NPs and the cell membrane.

Cell Internalization

Particles with sizes <10 nm can pass through the cell plasma membrane, called particle internalization (Kumar et al., 2017). Moreover, ZnO-NPs can be transported into the cytoplasm



(Manna, 2012). In addition, the interaction between ZnO and bacterial cell membranes can enhance the permeability of cell membranes. Once the ZnO-NPs are internalized by the cells, it will inhibit or cut off the metabolic exchange of substances and energy between bacteria and environment, resulting in the death of bacteria (Zhang et al., 2007).

As a photocatalytic antibacterial agent, many researchers attribute their antibacterial mechanism to the cell damage mediated by ROS generated on the surface of ZnO after photocatalysis. However, some studies are showing that ZnO-NPs also have prominent antibacterial activity under dark conditions (Hirota et al., 2010; Leung et al., 2016). Other factors, including size, surface structure and morphology of ZnO-NPs also bring essential impacts on antibacterial activity (Padmavathy and Vijayaraghavan, 2008; Ansari et al., 2013; Ma et al., 2013; Qi et al., 2013, 2014, 2017) and also the bacteria type (Premanathan et al., 2011). Under different light conditions, the primary antibacterial mechanism of ZnO-NPs is different for different types of bacteria. Therefore, to study the primary antibacterial mechanism of ZnO-NPs under different circumstances and the synergistic effects with other mechanisms is the direction of future research.

APPLICATION PROSPECTS OF ZnO-NPs

ZnO-NPs is considered as a relatively safe metal oxide with the inherent ability to induce ROS production and lead to apoptosis, and possesses antibacterial, antifungal, and wound healing activities. We summarize the latest application progress of ZnO-NPs based on antibacterial and antifungal properties, including wound healing, antifungal activity, and prevention of caries.

Wound Healing

Anti-infection ability and skin regeneration are essential aspects of the wound healing process. The excellent antibacterial property of ZnO-NPs and epithelial stimulation effect of Zn^{2+} have been successfully applied in wound dressings (Lansdown et al., 2007). The traditionally used wound dressings of cellulose, chitosan and alginate cannot be used alone due to their low mechanical properties, which can be improved by addition ZnO-NPs (Alavi and Nokhodchi, 2020). The incorporation of ZnO-NPs into electrospinning collagen/chitosan nanofibers apparently improve antibacterial activity and accelerate wound healing process (Sun et al., 2019). The study of Hu et al. (2018) further suggested that ZnO-NPs showed better biocompatibility than that of silver NPs. These preliminary findings provide new drug candidates for the treatment of increasing antimicrobial resistance and infections.

Antifungal Ability

In addition to its excellent antibacterial activity, ZnO-NPs also have a significant inhibitory effect on fungus. It has been confirmed that ZnO-NPs can significantly inhibit the growth and reproduction of penicillium and mucor, and the morphologies of ZnO-NPs play critically role in inhibition activity (Zeng et al., 2016). In another study, the decoration of ZnO nanorods on graphene nanoplatelets (ZNGs) can affect the development of the primary virulence factor hyphae of fungus and the formation of biofilms, inducing significant fungal death (Graziella et al., 2018).

Prevent Caries

Streptococcus mutans is the leading cause of caries. During the killing of *Streptococcus mutans*, conventional antibiotics and fungicides also harm the healthy flora of the mouth and intestines (Jarvinen et al., 1993). So, agents characterized by a notable antibacterial activity and do not develop resistance are

now highly requested. The ZnO-NPs has attracted more and more attentions due to their significant antibacterial properties. It is revealed that ZnO NPs could inhibit biofilm formation of *Streptococcus mutans* (Eshed et al., 2012). The inhibition activity derived from the relevant mechanical damages exerted by ZNGs and showed a ZnO dose-dependent effect (Elena et al., 2016). Therefore, ZnO-NPs has a promising application as a nano-bactericide for dental pathogens, and maybe a very effective method for controlling the growth of *Streptococcus mutans* and the development of dental caries.

CONCLUSION

Herein, we summarize the main antibacterial mechanisms and application prospects of ZnO-NPs. The excellent biocompatibility, photochemical stability, and other characteristics of ZnO-NPs make it suitable for antibacterial. However, there is still a lack of understanding of its antimicrobial mechanism and toxicity issues. Therefore, researchers should focus on the exactly antibacterial mechanism of ZnO-NPs and adopt more advanced biotechnology to obtain more information on the mechanism. On the other hand, the microstructure

of ZnO has a significant influence on its photocatalytic and antibacterial properties. We should develop environmentally friendly synthesis methods and surface modification strategies to improve the antibacterial property of ZnO-NPs. Besides, doping with other metals or non-metallic materials to enhance the selectivity for pathogenic microorganisms and reduce the toxic effect of tissue cells might exert the more extensive biomedical potentials for ZnO-NPs.

AUTHOR CONTRIBUTIONS

SJ wrote the manuscript. KL and MC conceived the concept of this review. All authors discussed and commented on the manuscript.

ACKNOWLEDGMENTS

The authors gratefully acknowledge the support of the National Natural Science Foundation of China (81871490), Program of Shanghai Academic/Technology Research Leader (19XD1434500), and Two-Hundred Talent (20191819).

REFERENCES

- Alavi, M., and Nokhodchi, A. (2020). An overview on antimicrobial and wound healing properties of ZnO nanobiofilms, hydrogels, and bionanocomposites based on cellulose, chitosan, and alginate polymers. *Carbohydr. Polym.* 227:115349. doi: 10.1016/j.carbpol.2019.115349
- Ansari, S. A., Khan, M. M., Ansari, M. O., Lee, J., and Cho, M. H. (2013). Biogenic Synthesis, Photocatalytic, and Photoelectrochemical Performance of Ag-ZnO Nanocomposite. *J. Physical Chem. C* 117, 27023–27030. doi: 10.1021/jp410063p
- Elena, Z., Chandrakanth, C., Giovanni, D. B., Maria, M., Giovanna, A., Paolo, B., et al. (2016). Zinc oxide nanorods-decorated graphene nanoplatelets: a promising antimicrobial agent against the cariogenic bacterium *Streptococcus mutans*. *Nanomaterials* 6:179. doi: 10.3390/nano6100179
- Eshed, M., Lellouche, J., Matalon, S., Gedanken, A., and Banin, E. (2012). Sonochemical coatings of ZnO and CuO nanoparticles inhibit streptococcus mutans biofilm formation on teeth model. *Langmuir Acs Jf Surf. Colloids* 28, 12288–12295. doi: 10.1021/la301432a
- Graziella, F., Maria, G., De, C. Caris, and G., Trill, ò, D. C. (2018). Anticandidal activity and *in vitro* cytotoxicity assessment of graphene nanoplatelets decorated with zinc oxide. *Nanorods*. 8:E752. doi: 10.3390/nano8100752
- Hirota, K., Sugimoto, M., Kato, M., Tsukagoshi, K., Tanigawa, T., and Sugimoto, H. (2010). Preparation of zinc oxide ceramics with a sustainable antibacterial activity under dark conditions. *Ceramics Intern.* 36, 497–506. doi: 10.1016/j.ceramint.2009.09.026
- Hu, M., Li, C., Li, X., Zhou, M., Sun, J., Sheng, F., et al. (2018). Zinc oxide/silver bimetallic nanoencapsulated in PVP/PCL nanofibres for improved antibacterial activity. *Artif. Cells Nanomed. Biotechnol.* 46, 1248–1257. doi: 10.1080/21691401.2017.1366339
- Jarvinen, H., Tenovu, J., and Huovinen, P. (1993). *In vitro* susceptibility of *Streptococcus mutans* to chlorhexidine and six other antimicrobial agents. *Antimicrob. Agents Chemother* 37, 1158–1159. doi: 10.1128/AAC.37.5.1158
- Jeong, E., Ul Kim, C., Byun, J., Lee, J., Kim, H. E., Kim, E. J., et al. (2020). Quantitative evaluation of the antibacterial factors of ZnO nanorod arrays under dark conditions: physical and chemical effects on *Escherichia coli* inactivation. *Sci. Total Environ.* 712, 136574. doi: 10.1016/j.scitotenv.2020.136574
- Joe, A., Park, S. H., Shim, K. D., Kim, D. J., Jhee, K. H., Lee, H. W., et al. (2017). Antibacterial mechanism of ZnO nanoparticles under dark conditions. *J. Indus. Eng. Chem.* 45, 430–439. doi: 10.1016/j.jiec.2016.10.013
- Kumar, R., Umar, A., Kumar, G., and Nalwa, H. S. (2017). Antibacterial properties of ZnO nanomaterials: a review. *Ceramics Intern.* 43, 3940–3961. doi: 10.1016/j.ceramint.2016.12.062
- Lansdown, A. B. G., Mirastschijski, U., Stubbs, N., Scanlon, E., and Agren, M. S. (2007). Zinc in wound healing: Theoretical, experimental, and clinical aspects. *Wound Repair Regen.* 15, 2–16. doi: 10.1111/j.1524-475X.2006.00179.x
- Leung, Y. H., Xu, X., Ma, A. P. Y., Liu, F., Ng, A. M. C., Shen, Z., et al. (2016). Toxicity of ZnO and TiO₂ to *Escherichia coli* cells. *Sci. Rep.* 6:35243. doi: 10.1038/srep35243
- Li, Q., Mahendra, S., Lyon, D. Y., Brunet, L., Liga, M. V., Li, D., et al. (2008). Antibacterial nanomaterials for water disinfection and microbial control: potential applications and implications. *Water Res.* 42, 4591–4602. doi: 10.1016/j.watres.2008.08.015
- Liu, Y., Wang, R., Li, N., Liu, M., and Zhang, Q. (2019). Preparation of zinc oxide mesocrystal filler and its properties as dental composite resin. *J. Inorganic Mat.* 10, 1077–1084. doi: 10.15541/jim20180598
- Luo, Z., Wu, Q., Xue, J., and Ding, Y. (2013). Selectively enhanced antibacterial effects and ultraviolet activation of antibiotics with ZnO nanorods against *Escherichia Coli*. *J. Biomed. Nanotechnol.* 9, 69–76. doi: 10.1166/jbn.2013.1472
- Ma, J., Liu, J., Bao, Y., Zhu, Z., Wang, X., and Zhang, J. (2013). Synthesis of large-scale uniform mulberry-like ZnO particles with microwave hydrothermal method and its antibacterial property. *Ceramics Intern.* 39, 2803–2810. doi: 10.1016/j.ceramint.2012.09.049
- Manna, A. C. (2012). *Synthesis, Characterization, and Antimicrobial Activity of Zinc Oxide Nanoparticles*. Berlin: Springer. doi: 10.1007/978-3-642-24428-5_5
- Miao, L. G., Shi, B. M., Stanislaw, N., Mu, C. M., and Qi, K. Z. (2017). Facile synthesis of hierarchical ZnO microstructures with enhanced photocatalytic activity. *Mat. Sci. Poland* 35, 45–49. doi: 10.1515/msp-2017-0007
- Padmavathy, N., and Vijayaraghavan, R. (2008). Enhanced bioactivity of ZnO nanoparticles-an antimicrobial study. *Sci. Technol. Adv. Mat.* 9:035004. doi: 10.1088/1468-6996/9/3/035004
- Premanathan, M., Karthikeyan, K., Jeyasubramanian, K., and Manivannan, G. (2011). Selective toxicity of ZnO nanoparticles toward Gram-positive bacteria and cancer cells by apoptosis through lipid peroxidation. *Nanomed. Nanotechnol. Biol. Med.* 7, 184–192. doi: 10.1016/j.nano.2010.10.001

- Qi, K., Qin, Q., Duan, X., Wang, G., Wu, L., and Zheng, W. (2014), Geometric matching principle for adsorption selectivity of ionic liquids: a simple method into the fascinating world of shape-controlled chemistry. *Chem. Eur. J.* 20, 9012–9017. doi: 10.1002/chem.201400409
- Qi, K., Xing, X., Zada, A., Li, M., Wang, Q., Liu, S., et al. (2020). Transition metal doped ZnO nanoparticles with enhanced photocatalytic and antibacterial performances: experimental and DFT studies. *Ceramics Intern.* 46, 1494–1502. doi: 10.1016/j.ceramint.2019.09.116
- Qi, K., Yang, J., Fu, J., Wang, G., Zhu, L., Liu, G., et al. (2013). Morphology-controllable ZnO rings: ionic liquid-assisted hydrothermal synthesis, growth mechanism and photoluminescence properties. *Cryst. Eng. Comm.* 15, 6729–6735. doi: 10.1039/c3ce27007f
- Qi, K., Cheng, B., Yu, J., and Ho, W. (2017). Review on the improvement of the photocatalytic and antibacterial activities of ZnO. *J. Alloys Comp.* 727, 792–820. doi: 10.1016/j.jallcom.2017.08.142
- Sawai, J. (2003). Quantitative evaluation of antibacterial activities of metallic oxide powders (ZnO, MgO and CaO) by conductimetric assay. *J. Microbiol. Methods* 54, 177–182. doi: 10.1016/S0167-7012(03)00037-X
- Sun, L., Han, J., Liu, Z., Wei, S., Su, X., and Zhang, G. (2019). The facile fabrication of wound compatible anti-microbial nanoparticles encapsulated Collagenous Chitosan matrices for effective inhibition of poly-microbial infections and wound repairing in burn injury care: exhaustive *in vivo* evaluations. *J. Photochem. Photobiol. B Biol.* 197:111539. doi: 10.1016/j.jphotobiol.2019.111539
- Wang, Y. W., Cao, A., Jiang, Y., Zhang, X., and Wang, H. (2014). Superior antibacterial activity of ZnO/graphene oxide composites originated from high zinc concentration localized around bacteria. *ACS Appl. Mat. Interf.* 6, 2791–2798. doi: 10.1021/am4053317
- Zeng, X., Zhang, F., He, N., Zhang, B., Liu, X., and Li, X. (2016). ZnO Nanoparticles of Different Shapes and Their Antimycotic Property Against Penicillium and Mucor. *Nanosci. Nanotechnol. Lett.* 8, 688–694. doi: 10.1166/nnl.2016.2206
- Zhang, L., Jiang, Y., Ding, Y., Povey, M., and York, D. (2007). Investigation into the antibacterial behaviour of suspensions of ZnO nanoparticles (ZnO nanofluids). *J. Nano. Res.* 9, 479–489. doi: 10.1007/s11051-006-9150-1

Conflict of Interest: The authors declare that the research was conducted in the absence of any commercial or financial relationships that could be construed as a potential conflict of interest.

Copyright © 2020 Jiang, Lin and Cai. This is an open-access article distributed under the terms of the Creative Commons Attribution License (CC BY). The use, distribution or reproduction in other forums is permitted, provided the original author(s) and the copyright owner(s) are credited and that the original publication in this journal is cited, in accordance with accepted academic practice. No use, distribution or reproduction is permitted which does not comply with these terms.



Study and Analysis of Removing the Carbon Deposition on the Inner Surface of a Turbo-Shaft by Chemically Assisted Magnetic Grinding

Hui Xu^{1,2*}, Renke Kang¹, Xianglong Zhu¹, Lijuan Liu³, Leilei Wang³ and Yan Chen^{2*}

¹ Key Laboratory for Precision and Non-traditional Machining Technology of Ministry of Education, Dalian University of Technology, Dalian, China, ² School of Mechanical Engineering and Automation, University of Science and Technology, Liaoning, Anshan, China, ³ Shaft Center, Xi'an Aero-Engine Plc, Xi'an, China

OPEN ACCESS

Edited by:

Kezhen Qi,
Shenyang Normal University, China

Reviewed by:

Xu Wang,
Zhejiang University of Technology,
China

Yu Liu,
Dalian Jiaotong University, China

Chaofeng Li,
Northeastern University, China

*Correspondence:

Hui Xu
xuhui04120412@126.com

Yan Chen
laochen412@gmail.com

Specialty section:

This article was submitted to
Thin Solid Films,
a section of the journal
Frontiers in Materials

Received: 15 May 2020

Accepted: 25 June 2020

Published: 28 July 2020

Citation:

Xu H, Kang R, Zhu X, Liu L,
Wang L and Chen Y (2020) Study
and Analysis of Removing the Carbon
Deposition on the Inner Surface of a
Turbo-Shaft by Chemically Assisted
Magnetic Grinding.
Front. Mater. 7:232.
doi: 10.3389/fmats.2020.00232

Removing carbon deposition (CD) has always been a challenging problem. On the inner surface of a turbo shaft, CD is observed by scanning electron microscopy (SEM) to analyze its microstructure and composition, and its formation mechanism is analyzed by X-ray diffraction (XRD), infrared spectroscopy, and Raman spectroscopy. Considering the physical and chemical properties of deposited carbon, chemically assisted magnetic grinding (CAMG) is proposed and tested by a translational permanent magnet grinding device. By analyzing the removing mechanism of CAMG, response surface analysis is adopted to analyze the influence law of surface roughness based on the interactions between pairs of the three following parameters: the rotational speed of the rotating magnetic field, needle type, and grinding time. The optimal process parameters can be obtained with a rotational speed of the rotating magnetic field of 600 r/min, a needle type of $\Phi 1.0 \times 5$ mm, and a grinding time of 60 min. The surface quality of the workpiece processed by CAMG can be comprehensively appraised by observing the microstructure, calculating the carbon deposit removal ratio and testing the surface stress. Compared to single magnetic grinding, CAMG is more environmentally friendly and has a higher removal ratio and better surface quality with an obvious decrease in residual stress. By professional tests, the remaining deposited carbon is less than the specified value required by the technology, which satisfies the requirements of enterprises.

Keywords: carbon deposition, chemically assisted magnetic grinding, surface roughness, aluminum alloy tube, oscillator frequency

INTRODUCTION

A turbo shaft is the main driving part of an aeroengine. Since the engine often runs at a temperature greater than 500 degrees, under catalysis of metal, carbon deposition (CD) can be produced on the inner surface of a turbo shaft after a series of oxidation reactions, pyrolysis, cracking, dehydrogenation, coking, and polymerization from the fuel in the engine (Tumuluri et al., 2017).

In a real working environment, in a single flight when the temperature exceeds 400 degrees and in multiple flights when the temperature exceeds 300 degrees, CD can be visually observed on the engine fuel system parts (Li et al., 2014). Dr. Robert E. Kauffman (Kauffman et al., 2000) discovered that aero fuel can produce deposited carbon particles at a temperature of 225 degrees after 7 h without antioxidants. When the temperature exceeds 325 degrees, the antioxidants in the aero fuel can be consumed quickly. Carbon deposition can occur more quickly when no antioxidant exists. Carbon deposition in the turbo shaft can impact the dynamic balance of the plane, which substantially influences flight safety. Therefore, when an aeroengine turbo shaft runs more than 300 h, it must be cleaned (Jia, 2005).

Carbon deposition in engines has obtained an increasing amount of attention from aviation industry countries. Although a considerable amount of domestic and international research has addressed the formation mechanism of CD, excellent methods of removing carbon deposits are scarce. Jiang et al. (2017) analyzed the impact and harm of CD in car engines, introduced its formation mechanism, and proposed a high-purity hydrogen removing method and tested its effect. Huang et al. (2011) conducted a characteristics analysis of the coking CD on the surface of a Nickel-base-alloy nozzle of an aeroengine by scanning electron microscopy (SEM), transmission electron microscopy, X-ray diffraction (XRD), and other methods. A graphite-like structure and bonding phenomenon between the alloy metal and carbon in the aeroengine were observed. Liu et al. (2014) analyzed the reason and mechanism of CD on the valve of a gasoline engine and suggested ways to optimize engine design and reduce CD. Wang et al. (2017) proposed the utilization of fused salts to eliminate CD on the valve of an automation engine after analyzing its microstructure and formation mechanism. The removal of deposited carbon has been studied previously. To study the molten salt cleaning process for removing carbon deposited on a remanufacturing engine valve, Yao et al. (2015) applied sodium hydroxide, sodium nitrate, and sodium nitrite as a molten salt system and binary nitrate $\text{NaNO}_3\text{-NaNO}_2$ as a cleaning medium under the alkaline condition of 250–380°C. A quadratic model was simultaneously established to predict the cleaning cycle. After a series of optimization tests, it was concluded that the best cleaning conditions were 30% NaOH, at least 40% NaNO_2 , a cleaning temperature of 330–360°C, and a maximum cleaning cycle of 5 min. According to the principle of ultrasonic cleaning and related research of the low-vortex axial parts cleaning process via the design of aeroengine large, low-pressure turbine small parts, low-pressure turbine shaft parts, and low-vortex axial parts cleaning process simulation test, Hao (2016) determined the ultrasonic cleaning technology of these parts based on the design for large-scale ultrasonic cleaning equipment, which is used for aviation engine low vortex axial parts cleaning problems.

Currently, carbon deposited on the inner surface of an aeroengine is mainly eliminated by disassembling parts, manual scrubbing parts, degreasing parts with hot water, rinsing parts with warm water, and soaking parts with alkali solution. The entire period is so long that the parts' surfaces may become scratched and damaged, which causes poor effects and low

efficiency. Additionally, the workers' labor intensity is very high, and the working environment is full of poisonous and harmful gases. Since the engine is often running at high temperature and high pressure, the deposited carbon has been graphitized and even absorbs some metal atoms. In some military plane aeroengines, where the temperature exceeds 1,600 degrees, permeation and dissociation of the stubborn carbon adhered to the alloy surface by alkali solution is difficult. Therefore, the traditional cleaning process cannot have a better effect or satisfy the service demand.

For these problems of the removing technology, chemically assisted magnetic grinding (CAMG) is proposed to remove the carbon deposited on the inner surface of an aeroengine turbo shaft to enable the process to satisfy the cleaning requirements.

FORMATION MECHANISM OF CD

Analysis of the Microstructure of CD

A titanium-alloy aeroengine turbo shaft, which was disassembled and provided by an enterprise, is selected in this experiment. In the environment of high temperature and high pressure, a large amount of deposited carbon gathers on the inner surface of the turbo shaft. **Figure 1A** shows the microstructure of the workpiece. It is observed that there are many cracks on the surface of the CD, which is mainly composed of black blocks and flakes. As shown in **Figure 1B**, irregularity is observed on the surface of the CD, and white, shiny solid particles of different shapes and sizes are distributed unevenly in the cracks between the blocks. As shown in **Figures 1C,D**, the particles are accumulated and embedded in a disorderly manner. In the formation of a CD, disorderly cracks and pits appear, which will increase the possibility of a new CD. Thus, the CD will consist of coke and will deteriorate gradually.

Composition of Carbon Deposits

As shown in **Figure 2**, in a carbon deposit, there are many elements, such as carbon, oxygen, silica, aluminum, titanium, iron, and manganese, among which carbon has the highest mass percentage and atomic percentage of 53.2 and 72.1%, respectively, and oxygen has the second highest mass percentage and atomic percentage of 18.6 and 19.3%, respectively. Metal elements, such as Ti, Fe, Al, and Mn, from the base material of the turbo shaft, account for a small proportion of the total mass. In the high-temperature and high-pressure environment, carbon is deposited on the inner surface of the turbo shaft, and after a reaction, the deposited carbon gradually permeates into the metal layer, which causes a transfer of metal atoms from the base into the metal (Zhang et al., 2018).

Spectrum of CD

An infrared spectrum analysis, as shown in **Figure 3**, reveals that the macromolecular compounds in the carbon deposit include hydroxyl, methyl, carbonyl, and olefin. An energy spectrum analysis of the composition of the carbon deposit reveals that some of the carbon exists in the form of methylene, which constitutes long-chain hydrocarbons, whereas some exists in the

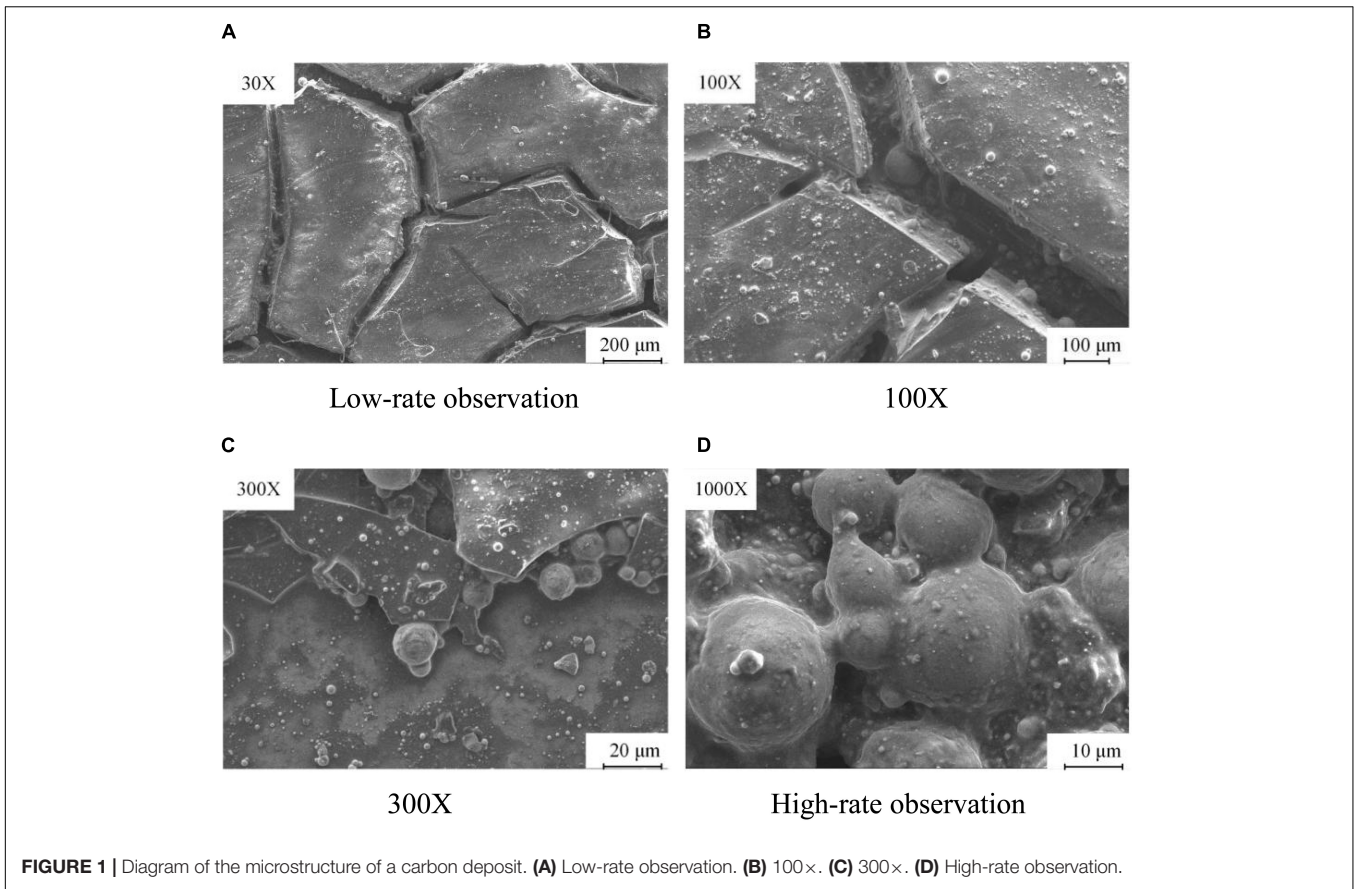


FIGURE 1 | Diagram of the microstructure of a carbon deposit. (A) Low-rate observation. (B) 100×. (C) 300×. (D) High-rate observation.

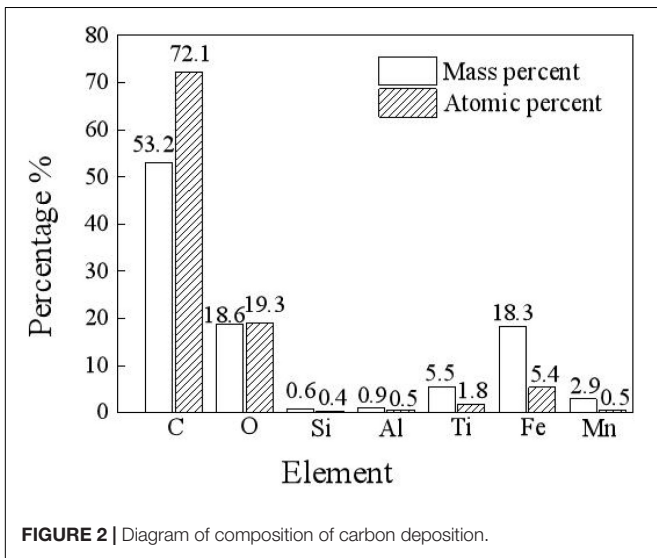


FIGURE 2 | Diagram of composition of carbon deposition.

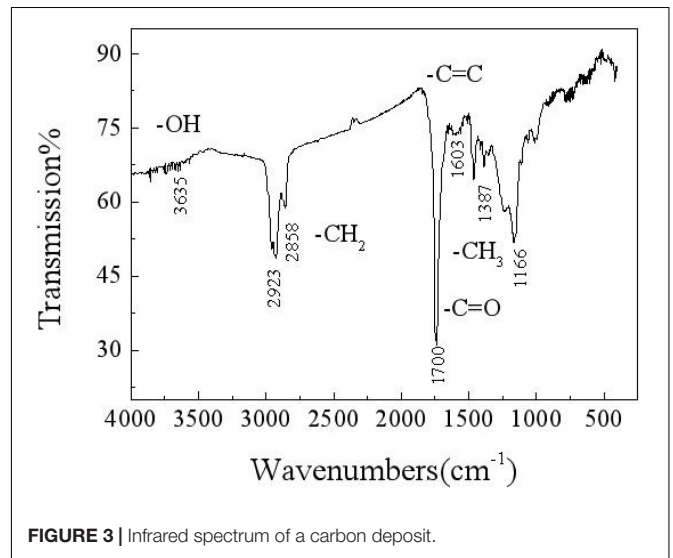


FIGURE 3 | Infrared spectrum of a carbon deposit.

form of a carbon–carbon double bond, carbon–oxygen double bond, and methyl. Oxygen exists in the forms of hydroxyl, carbonyl, and metallic oxides. Therefore, it can be estimated that there are some functional groups, which mainly include hydroxyl, methylene, olefin, methyl, and metallic oxides. This finding suggests that, in the formation of a carbon deposit,

organic chemical reactions form complex and varied substances (Wu, 2018).

X-ray diffraction is adopted to analyze the composition of the carbon deposit. **Figure 4** shows that main peaks appear when 2θ is equal to 22.36° , 27.8° , 44.2° , 54.8° , and so on. The main peak of 2θ , which is equal to 22.36° , is similar to the characteristic

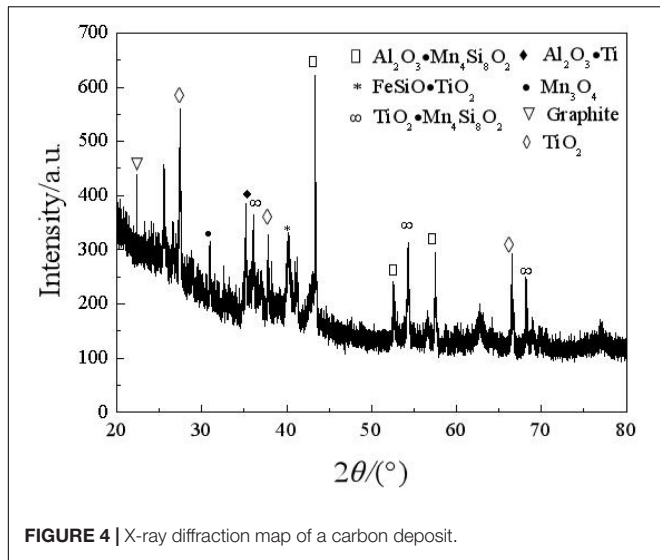


FIGURE 4 | X-ray diffraction map of a carbon deposit.

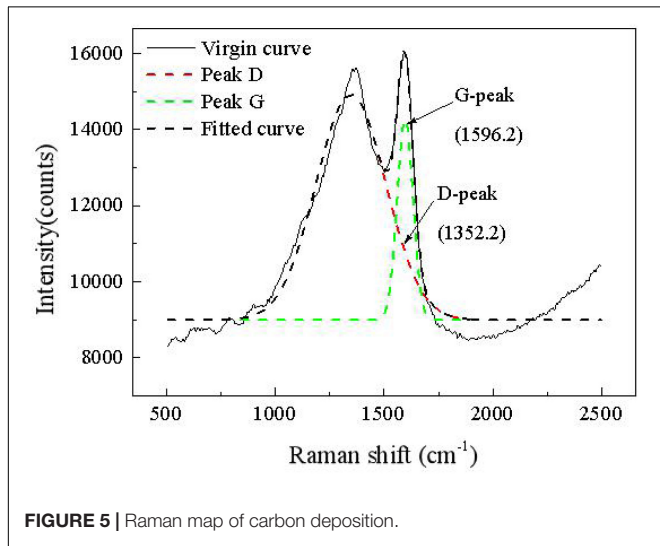


FIGURE 5 | Raman map of carbon deposition.

main peak of graphite; thus, there is a graphite-like structure in the carbon deposit. In this situation (Yoshiya et al., 2016; Zhang et al., 2020), the carbon substance is hexagonal and composed of a six-member ring. It is predicted that, in the carbon deposit, a lamella graphite structure with a hexagonal carbon ring is formed according to a certain crystallographic vector direction (Husnawan et al., 2009; Qi et al., 2020b).

Figure 5 shows a Raman map of a carbon deposit. There are two obvious peaks in the areas of 1,352 and 1,596 cm^{-1} , which, respectively, represent the D vibration peak and the G vibration peak of the carbon-based material. The D vibration peak indicates the disorder and defect of element carbon material, whereas the G vibration peak represents the in-plane vibration. The ratio of D to G can be applied to evaluate the graphitization degree of the carbon substance. As shown on the map, I_D/I_G is equal to 0.85, which means that many defects exist in the grapheme. Coupled with the XRD map, a graphitization structure that exists in the carbon deposit is further corroborated.

Comprehensively considering the composition of the carbon deposit and when performing a maps analysis, oxidation reactions occur in the formation process, among which the oxidation of hydrocarbons dominates, where metallic particles are the catalyst.

THEORY OF REMOVING CD BY CHEMICALLY AIDED MAGNETIC GRINDING

Working Mechanism of Magnetic Grinding

Because of the consistently changing magnetic field force, in the grinding container, numerous free tiny magnetic needles flip and are bound violently to grind the workpiece (Jayswal et al., 2008). By the vortex effect caused by the changing magnetic force and the CD detergent, two movement forms exist for every needle: around the axis of the grinding container and around its gravity center. When a needle bumps the workpiece at an angle, there is a scratch effect. When numerous needles collide with the workpiece many times, there will be a superposition of many plastic deformations. When the allowable plastic deformation of the material is surpassed, small chips will fall off. Thus, microgrinding is realized with a reduction in the surface roughness. When the needles are rolling on the surface of the workpiece, a tiny deformation will occur on the micropeaks of the surface, which reduces the surface roughness, whereas the surface can be hardened with improved wear resistance and fatigue strength (Jiao et al., 2015).

Figure 6 shows three kinds of contact: colliding, scratching, and rolling. When the needles contact the surface of the workpiece at a certain speed, plastic deformations will occur on the top layer of the carbon deposit. After a number of contacts, the carbon deposit will be peeled off when many contacts allow the deformation degree to exceed the plastic deformation limit. The removing effect has been obtained (Chen et al., 2018). The forces that are well distributed everywhere on the workpiece can be guaranteed by rotating the magnetic field clockwise and counterclockwise. Regarding the magnetic intensity, there exists the point effect, which means that the protruding carbon deposits will be the first to be removed by needles. When the protruding

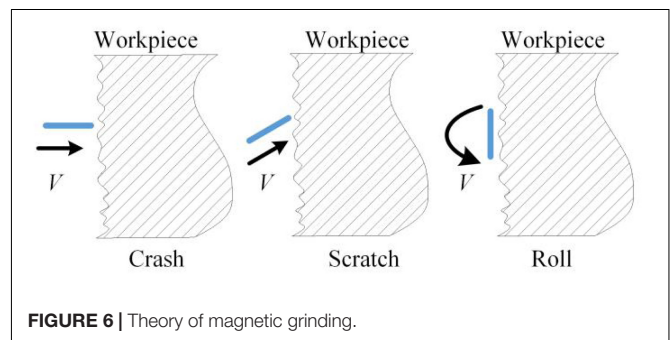


FIGURE 6 | Theory of magnetic grinding.

carbon deposits are peeled off gradually, the point effect will fade, which gives homogeneity (Zhou et al., 2019).

Function of CD Detergent

Generally, metal detergents can be divided into two types: solvent detergent and water-based detergent. In recent years, ozone-depleting substance detergent has faced strict international restrictions because of its contamination and harmfulness; traditional petroleum detergent cannot satisfy the requirements of cleaning an aircraft surface because of its harmfulness to humans, contamination of the environment, and low flash point (Zhang and Han, 2014; Guo et al., 2019). Conversely, water-based detergent has many advantages due to its nonharmfulness, noncontamination, high flash point, strong cleaning ability, and wide range of application. Water-based detergent causes no damage or corrosion of the cleaned item and is suitable for high-pressure and ultrasonic cleaning and cleaning an engine compressor offline and online (Abdallah et al., 2018; Qi et al., 2020a).

As shown in **Figure 7**, in certain conditions, when water-based detergent contacts dirt, the amphiphilic surfactants in the detergent, which adhere to the surface of the grease dirt, reduce the interfacial tension between grease and water. The surfactants rise to the interface and reduce the adhesion between grease and metal via oriented absorption. By a series of actions, such as madefaction, emulsification, dispersion, and solubilization, combining physical ways, such as heating, scrubbing, flushing, and ultrasonic wave, the dirt can be more quickly removed and

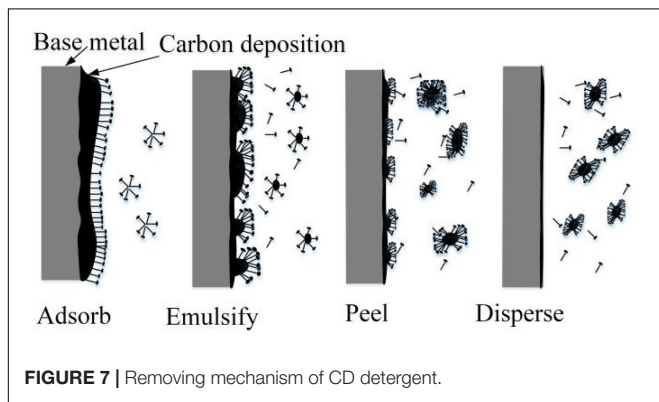


FIGURE 7 | Removing mechanism of CD detergent.

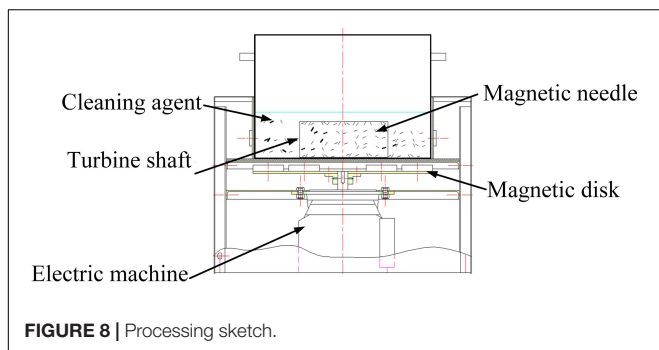


FIGURE 8 | Processing sketch.

dispersed into the detergent from the workpiece (Stancu et al., 2016; Li et al., 2020; Liu et al., 2020).

Removing Mechanism of Chemically Aided Magnetic Grinding

The carbon deposit on the inner surface of the turbo shaft, which is cemented and hardened, sticks to the base metal with a thickness of 1–2 mm and cannot be removed completely with detergent. Therefore, CAMG is proposed to remove the compacted carbon deposit with high efficiency. By drenching the turbo shaft into the detergent, the cohesion between the carbon deposit and the base metal can be reduced by actions of the surfactants, which soften the top layer of the carbon deposit via madefaction, emulsification, dispersion, and solubilization. The carbon deposit, which is collided, scratched, and rolled by the magnetic needles driven by the rotating magnetic field, will be peeled off the base metal at a faster rate (Liu et al., 2015). Combined with magnetic grinding, the detergent will also saturate the deeper layers, which causes emulsification of the deeper carbon deposit. By the interaction of magnetic grinding and the detergent, the carbon deposit will be removed entirely and more quickly (Inagaki et al., 2005; Garnweitner and Niederberger, 2006).

EXPERIMENT RESEARCH

Experiment Equipment

As shown in **Figure 8**, a translational permanent magnetic grinding machine, which is researched and developed independently, which is composed of a grinding container, magnetic disk, spring, motor controlling system, and so on, is selected for the experiment. On the rotating plate, neodymium magnets are placed according to a certain rule. The magnetic disk is driven by the motor to form the changing magnetic force. On the pole plate, the N-pole and S-pole are distributed alternatively using the same circumference. The workpiece is put into the grinding container with the CD detergent submerging it. Parameters, such as the rotating speed of the poles on the disk, process time, reciprocating speed of the magnetic disk, and so on, can be adjusted. The grinding effect can be affected by many factors, among which the needle type, process time, and processing space are the major factors.

In the experiment, the adopted needles are fabricated of 304 stainless steel and are cylindrical and magnetized. There are many different types of needles in terms of diameter. With a constant magnetic field intensity, the type of magnetic needle determines the magnetic force. If the type is too small, the magnetic force is correspondingly weak. The collision, scratches, and rolling on the surface of the workpiece are not enough to present the grinding effect. If the type is too big, the magnetic force is accordingly strong. When the material of the workpiece is soft, the surface of the workpiece will be damaged by overgrinding.

When the processing time is too short, the collision, scratches, and rolling on the surface of the workpiece by the needles is insufficient. As a result, the microstructure of the workpiece

will be seldom improved, and the surface undergoes minimal intensification due to an insufficient number of microplastic deformations. When the processing time is too long, energy will be wasted, and the processing efficiency will be low. Sometimes there may be unnecessary damage to the workpiece (Li et al., 2010; Wu et al., 2015).

The changing frequency of the magnetic field is determined by the rotating speed of the magnetic disk. When other parameters remain constant, the movement track of a needle grows more complex as the disk's rotating speed increases. Better surface quality can be ensured by increasing the frequency of contact between the needles and the workpiece (Zou et al., 2011; Xu et al., 2020b).

The processing magnetic distance, which is the distance between the magnetic disk and the grinding container, determines the forces of the needles generated by the magnetic field. According to experience, the processing distance is set to 20 mm (Zhou et al., 2015).

Table 1 shows the parameters for the experiment.

Experiment Conditions

(1) Test of surface features. VHX-500F (a super field three-dimensional electron microscope) and JB-08E (a surface roughness meter) are adopted to observe the microstructure and measure the surface roughness before and after grinding. HV-1000 (a microhardness tester), and X-ray stress analyzer is selected to test the surface microhardness and residual stress before and after grinding.

(2) Evaluation method for the carbon deposit removal ratio. There are numerous ways to estimate the surface clearness of a metal part. Based on its property and the contaminations on it, the selected testing method should be accurate and easily operational, scientific and reasonable. Currently, the main testing method is Blue-Ray detection combined with visual inspection. However, the whole process is neither objective nor accurate (Lee et al., 2015). In this article, the area

percentage of the carbon deposit on the inner surface before and after grinding is selected to estimate the surface clearness. A single lens reflex camera is employed to take pictures in

TABLE 1 | Experiment parameters.

Parameter	Value
Needle type (mm)	$\Phi 0.8 \times 5$ $\Phi 1.0 \times 5$ $\Phi 1.2 \times 5$
Needle number (g)	500
Rotating speed (r/min)	400 600 800
Feed rate (mm/min)	120
Time (min)	40 60 80
Workpiece (mm)	Turbo shaft $115 \times 130 \times 314$
Cleaning agent (mL)	Carbon cleaner 200
Processing space (mm)	20

TABLE 2 | Group parameters of response surface.

Needle type (mm)	Rotation speed (r/min)	Time (min)
$\Phi 0.8 \times 5$	400	40
$\Phi 1.0 \times 5$	600	60
$\Phi 1.2 \times 5$	800	80

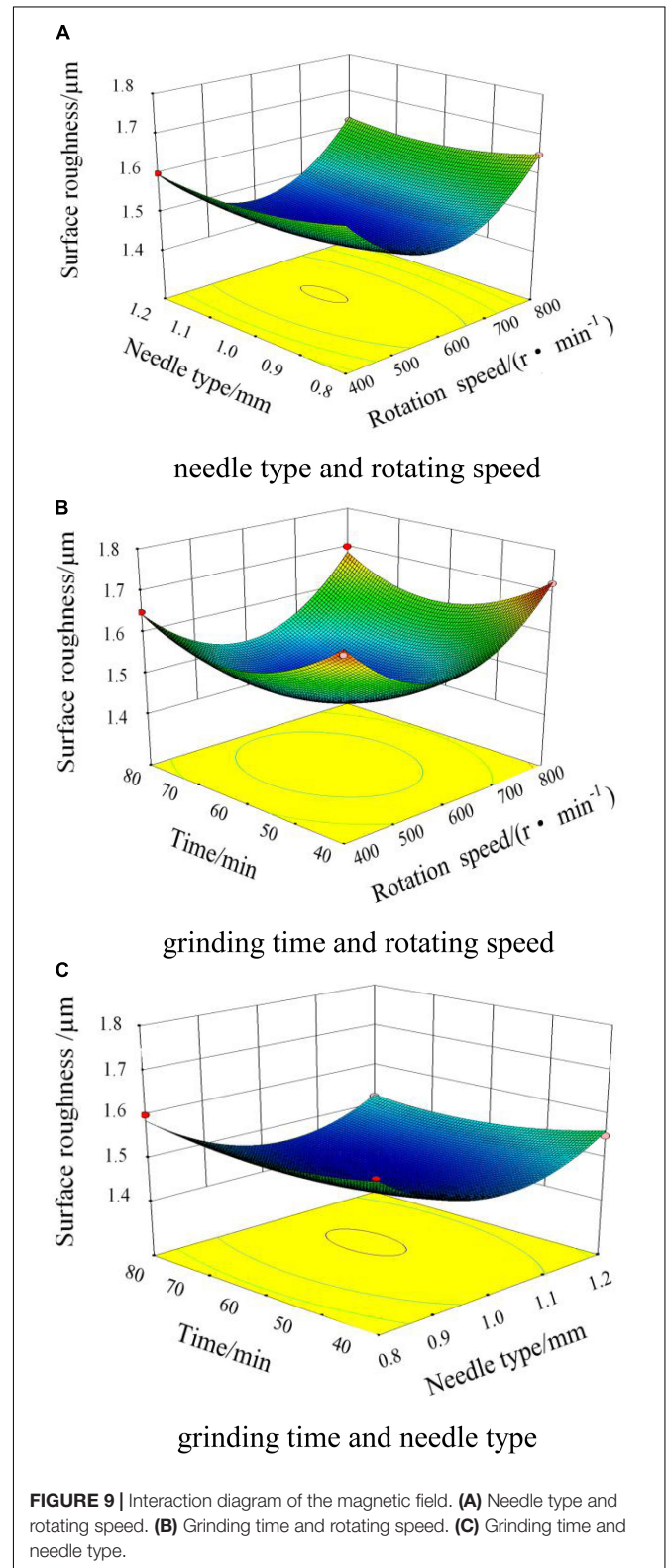


FIGURE 9 | Interaction diagram of the magnetic field. (A) Needle type and rotating speed. (B) Grinding time and rotating speed. (C) Grinding time and needle type.

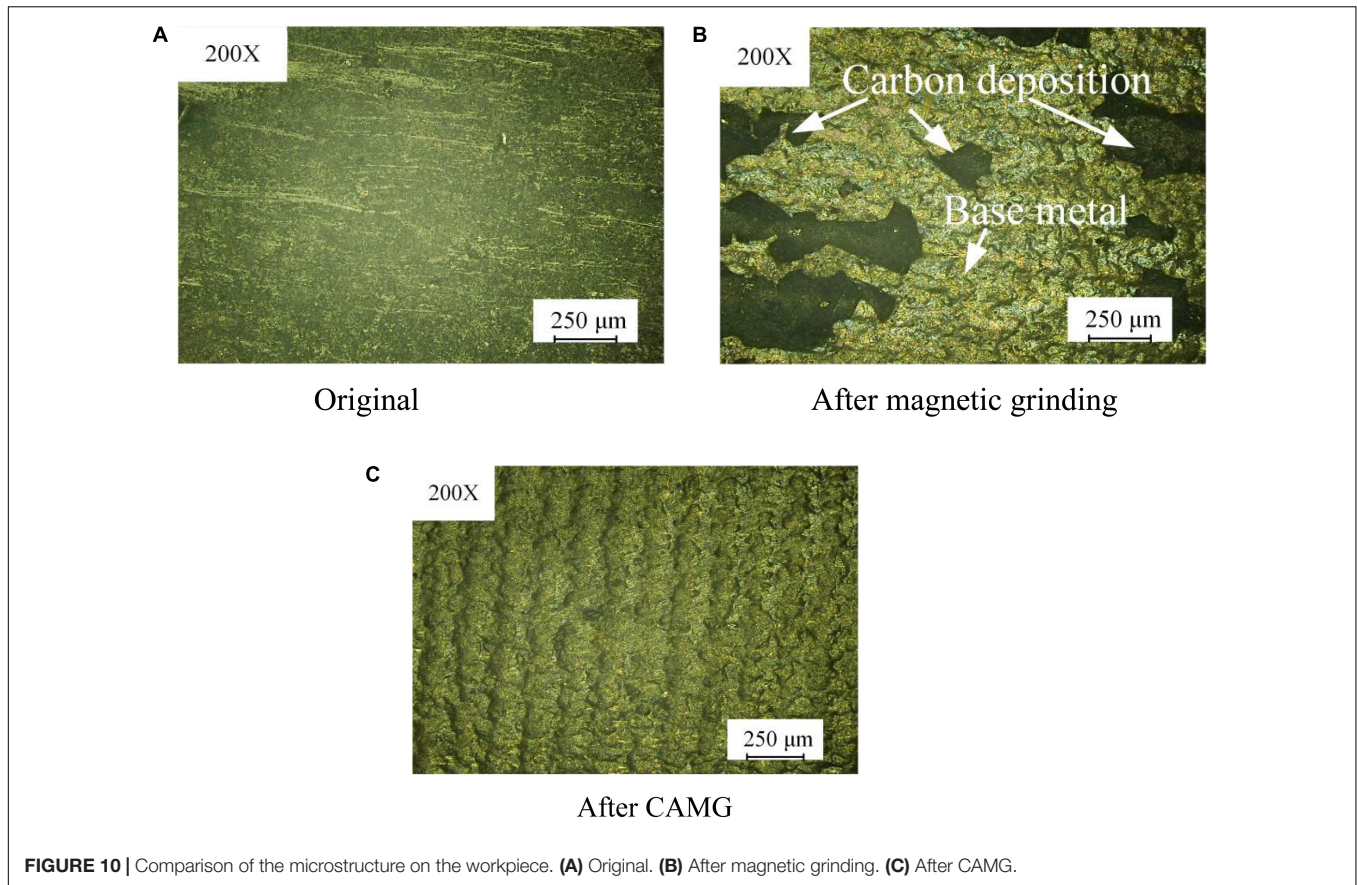


FIGURE 10 | Comparison of the microstructure on the workpiece. **(A)** Original. **(B)** After magnetic grinding. **(C)** After CAMG.

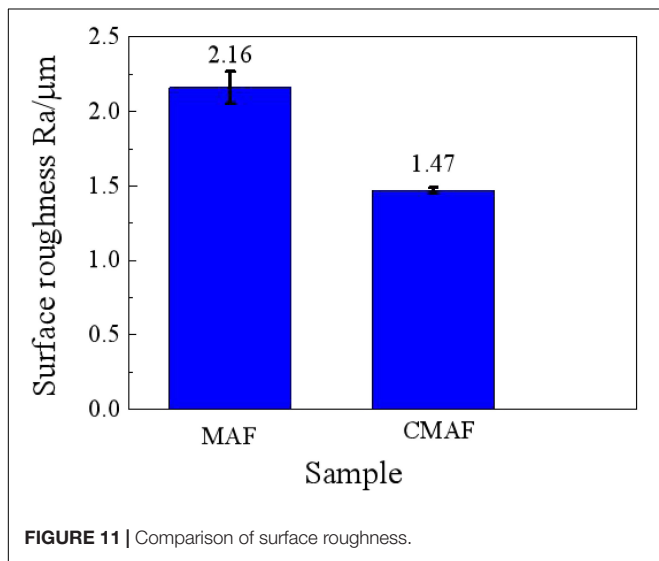


FIGURE 11 | Comparison of surface roughness.

the shaft before and after grinding. MATLAB is utilized to quantize the carbon deposit in the image and separate it from the base metal by conducting clustering segmentation, image enhancement, image binarization, expansion and corrosion, and calculation of the area of CD (Du and Zhao, 2016; Xu et al., 2020a).

OPTIMIZING PROCESS PARAMETERS

Process Parameters

To investigate the optimum process parameters for magnetic grinding, based on the preceding work, response surface analysis is adopted with the speed of the magnetic field, process time, and needle type as the main influence factors. A three-factor and three-level experiment plan is designed. Each of the factors has the value range shown in **Table 2**.

Response surface analysis is employed to fit values of the experimental points. Combining Design-Expert modeling and linear regression equation, the interactive influence relationship between every two factors can be obtained. The linear regression equation is expressed as follows:

$$Y = 1.45 + 0.015A - 0.024B - 0.011C + (5.000E - 0.003)$$

$$AB - (7.500E - 0.003)BC + 0.15A^2$$

$$+0.091B^2 + 0.026C^2 \tag{1}$$

The value of R^2 is 0.9859, which is approaching 1.0; that is, the reliability of the mathematical model fitted by Design-Expert for the surface roughness is excellent with a high fitting degree. The value of $Pr > F$ is 0.0001, which is much less than 0.5 and means that the three selected factors have significant impacts on the surface roughness.

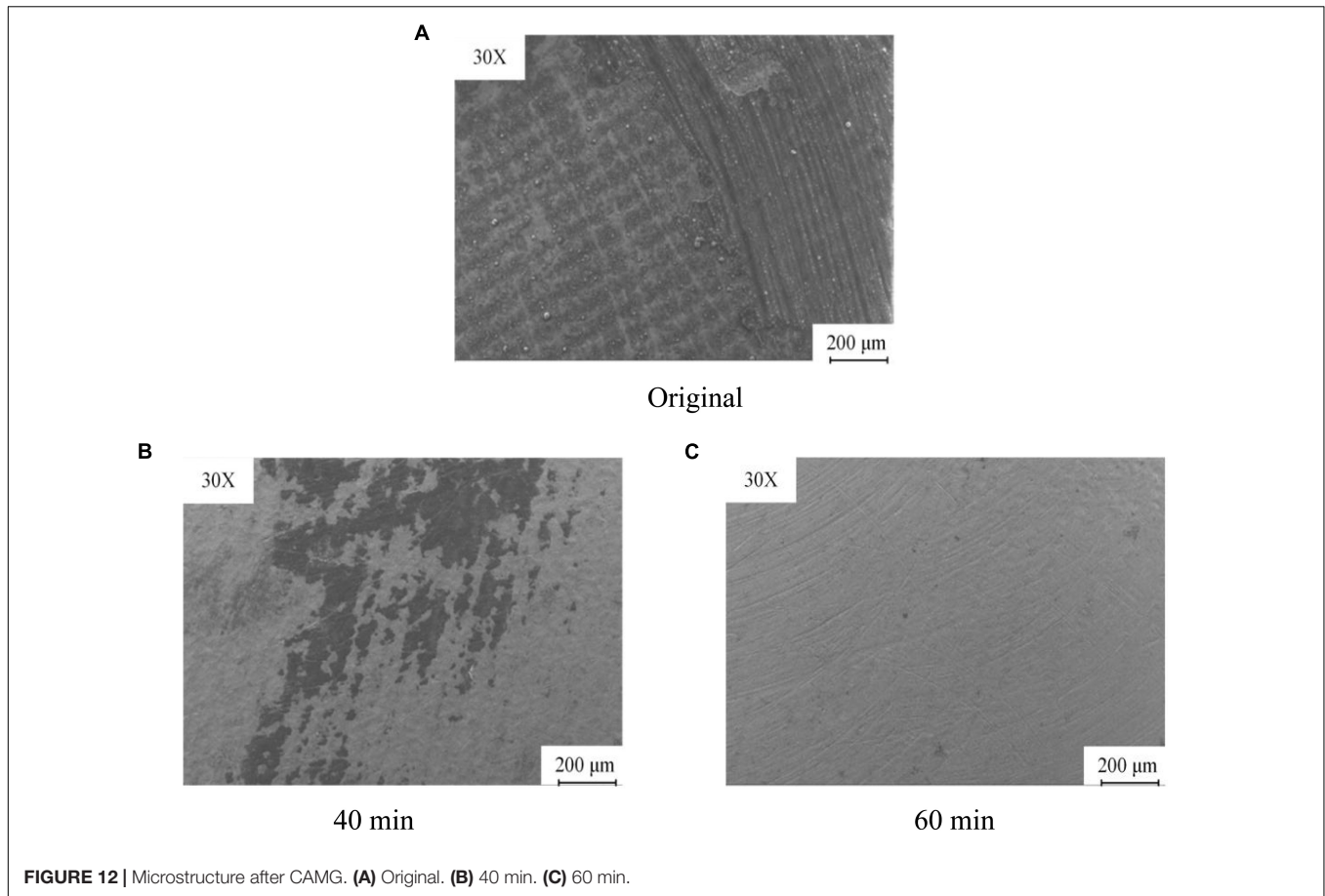


FIGURE 12 | Microstructure after CAMG. **(A)** Original. **(B)** 40 min. **(C)** 60 min.

Interaction Between Needle Type and Rotating Speed of the Magnetic Field

Figure 9A shows the interaction diagram of the needle type and rotating speed of the magnetic field when the grinding time is 60 min. When the needle type and rotating speed of the magnetic field are both increasing, the surface roughness will initially decrease and then increase. When the rotating speed of the magnetic field is 400 r/min, the needles move slowly relative to the cylinder wall. Within the unit time, the amounts of collision, scratching, and rolling are insufficient, which produces a low-quality surface and decreases the surface roughness. When the rotating speed of the magnetic field increases to 800 r/min, the needles move much more violently per unit time. The actions on the workpiece by the needles increase to make the movement tracks of the needles repeatedly and iteratively act on the surface, which produces deep scratches with high surface roughness. By experiments, the best effect can be obtained when the rotating speed is 600 r/min, and the type of needle is $\Phi 1.0 \times 5$ mm.

Interaction Between Grinding Time and Rotating Speed of the Magnetic Field

Figure 9B shows the interaction between the grinding time and the rotating speed of the magnetic field when the needle type is $\Phi 1.0 \times 5$ mm. When the grinding time is

in the range of 0–60 min, the surface roughness decreases very quickly. When the grinding time increases to 60 min, the surface roughness reaches the lowest value. As the grinding time increases continuously, on the surface of the workpiece, the scratches exacerbate with an increase in surface roughness.

Interaction Between Grinding Time and Needle Type

Figure 9C shows the interaction between the grinding time and the needle type when the rotating speed of the magnetic field is 600 r/min. As the grinding time and the diameter of the needle increase, and the surface roughness decreases and then increases. When the needle type is $\Phi 1.0 \times 5$ mm and the grinding time is 60 min, the lowest surface roughness is obtained. Comprehensively analyzing the influence factors, the optimum combination of process parameters can be obtained: the rotating speed of the magnetic field is 600 r/min, the needle type is $\Phi 1.0 \times 5$ mm, and the grinding time is 60 min.

Microstructure and Surface Roughness

Figure 10 shows comparison pictures of the microstructure on the workpiece after magnetic grinding and CAMG. **Figure 10A** shows the original microstructure. **Figure 10B** shows the microstructure after magnetic grinding. **Figure 10C** shows the microstructure after CAMG. The original surface, which

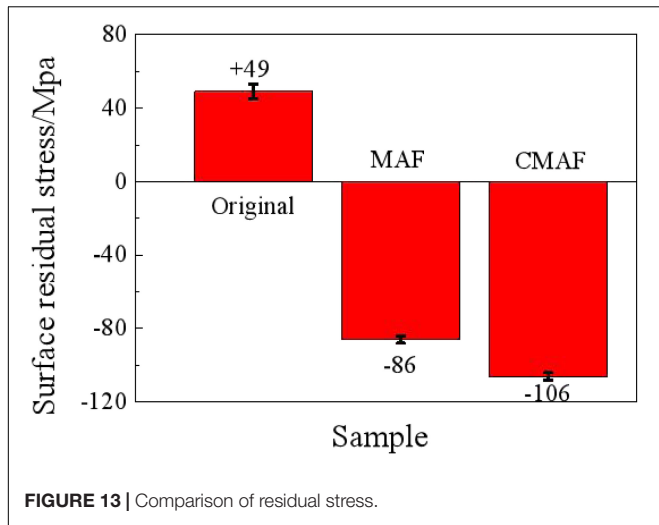


FIGURE 13 | Comparison of residual stress.

is almost covered by carbon, is so uneven that the surface roughness cannot be measured. After 60 min of magnetic grinding, which is shown in Figure 10B, most of the deposited carbon has been removed, and the base metal appears. As shown in Figure 10C, by 60 min, CAMG not only causes the base metal to appear but also obviously increases the removing efficiency.

Figure 11 shows the comparison curves of the surface roughness after magnetic grinding and CAMG. With the same grinding time of 60 min, the surface roughness after CAMG is 1.47, whereas that after magnetic grinding is 2.16. By CAMG, in addition to the increase in the removing efficiency, the surface quality has been improved obviously.

Scanning electron microscopy is employed to observe the surface of the workpiece shown in Figure 12. As shown in Figure 12A, on the surface of the base metal before grinding, there is thick carbon deposit. After 40 min of grinding, part of the carbon deposit is removed, as shown in Figure 12B. As shown in Figure 12C, after 60 min, the carbon deposit has been removed entirely, and metal luster presents with few scratches on the surface.

Residual Stress

On the surface of the workpiece, six points are selected to test the stress interplanar spacing. The residual stress can be calculated as follows:

$$\sigma = \frac{E}{(1 + \nu)} \sin^2 \psi \left[\frac{d_\phi - d_n}{d_n} \right] \quad (2)$$

In the formula, σ is residual stress, MPa; ν is Poisson ratio the material; ψ is tilting angle; E is modulus of elasticity of the material, GPa; ϕ is diffraction angle; d_ϕ is tilting interplanar spacing, μm ; d_n is the plastic deformation spacing of the initial surface on the crystal material at the initial tilting angle due to preliminary processing, μm .

As shown in Figure 13, the residual stress on the material original surface, which is affected by the plastic deformation and

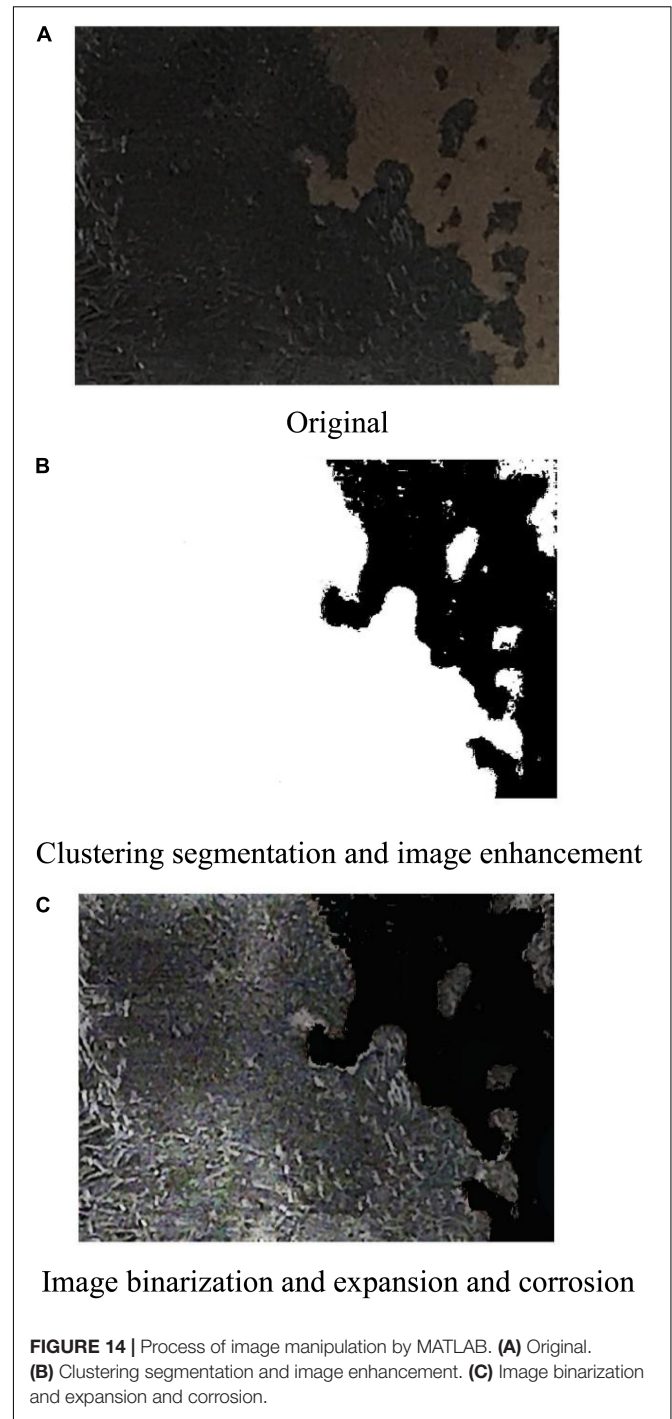
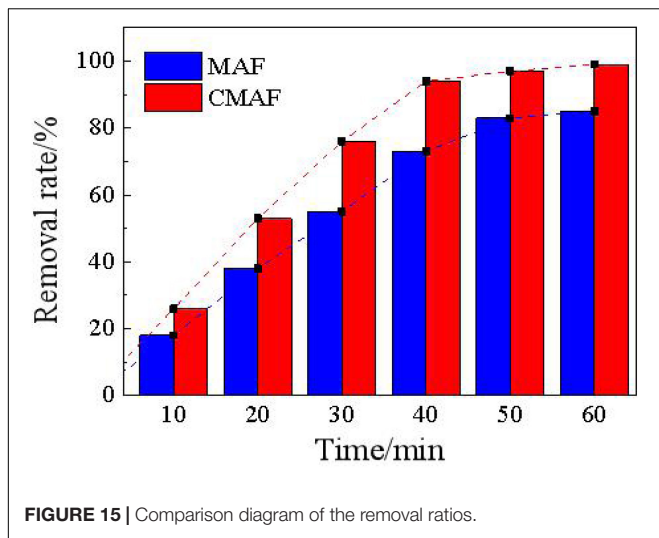


FIGURE 14 | Process of image manipulation by MATLAB. (A) Original. (B) Clustering segmentation and image enhancement. (C) Image binarization and expansion and corrosion.

processing temperature during preliminary processing, is tensile with a value of +49 MPa. After magnetic grinding, the residual stress decreases obviously to -86 MPa, which means compressive stress, as the residual stress has been released after the surface is repeatedly impacted by the magnetic needles when the carbon deposit is removed.

On the surface processed by CAMG, the residual stress decreases significantly to -106 MPa and is also compressive



due to the frictions of the magnetic needles and lubrication of the detergent. The residual compressive stress can effectively improve the ability to resist fatigue, stress corrosion, and creep cracking. The surface has been improved obviously (Zhu and Zhang, 2014).

Carbon Deposition Removal Ratio

Figure 14 shows the comparison pictures taken by a camera and processed by MATLAB via a series of operations, namely, clustering segmentation, image enhancement, image binarization, and expansion and corrosion. **Figure 14A** shows the original picture after grinding. **Figure 14B** shows the picture after clustering segmentation and intensification by the Retinex algorithm. Binarization is performed to turn the carbon deposit black and turn the base metal and background white by setting the gray value of the pixel to 0 or 255. Binarization enables the number of black pixels that represent deposited carbon to be calculated more easily. In the morphological calculation for images, image expanding and corroding are performed to increase and decrease the number of pixels around the objective area based on the structure factors and dimensions. Image expanding can make the objective area expand to some extent. **Figure 14C** shows that the picture is divided into two parts: the first part is black and represents deposited carbon with the gray value of pixels set to 0, whereas the second part is white and represents the background and the base metal with the gray value of pixels set to 1. By calculating the number of black pixels in the images of the workpiece before and after cleaning, the carbon deposition removal ratio can be obtained.

Figure 15 shows a comparison diagram of the removal ratios between magnetic grinding and CAMG. After 60 min, both methods can effectively remove deposited carbon with removal ratios greater than 80%. CAMG has a higher efficiency with a removal ratio of 98% and satisfies the reapplication requirements.

CONCLUSION

1. For the problem of removing carbon deposited on the inner surface of a large-scale turbo shaft of an aeroengine with high efficiency and low damage, chemically aided magnetic grinding is proposed. By magnetic force, the magnetic needles collide, scratch, and roll on the workpiece with high frequency to achieve the purpose of microcutting. Thus, the removing effect is obtained.
2. SEM, XRD, FTIR, and Raman spectroscopy are adopted to analyze carbon deposits, in which, by preliminary judgment, there exist functional groups such as hydroxyl, methylene, alkene, methyl, and sulfur compounds, which are formed by a series of actions, such as fracture, oxidation, and accumulation. In the production of the carbon deposit, many organic chemical reactions occur, in which aromatics and cycloalkanes have been oxidized, cracked, pyrolyzed, coked, and polymerized on the inner surface of the turbo shaft. Thus, complex and diverse substances, which are mainly composed of graphitized carbon, colloids, and oxides, are produced.
3. A translational permanent magnet grinding machine, which is designed and developed independently, is adopted to conduct an experiment for removing the carbon deposited on the inner surface of the turbo shaft. By experiments and interaction analysis, the best removing effect can be obtained with a rotating speed of the magnetic field of 600 r/min, a needle type of $\Phi 1.0 \times 5$ mm, a grinding time of 60 min, and a surface roughness of Ra 1.8 μm .
4. Chemically aided magnetic grinding is adopted to conduct the research. Amphiphilic surfactant in the detergent can reduce the adhesion between the carbon deposit and the surface of the base metal. By a series of chemical actions, such as madeaction, emulsification, dispersion, and solubilization, and combining physical actions of collision, scratching, and rolling, the carbon deposit can be peeled off the metal surface at a faster rate.
5. The comparison experiments verify that, against the single magnetic grinding, chemically aided magnetic grinding can remove the stubborn carbon deposit with a higher efficiency. After 60 min of grinding, 98% of the carbon deposit has been removed, and the residual stress is -106 MPa. The surface quality has been improved obviously and satisfies the requirements of reapplication.

DATA AVAILABILITY STATEMENT

All datasets generated for this study are included in the article.

AUTHOR CONTRIBUTIONS

HX did experiments, wrote the manuscript, and participated in the experimental design. RK did experimental design. XZ did the

spectrum test which include XRD, Raman, and gave some writing guidance. LL was involved in research guidance and test results discussion and demonstration. LW participated in the workpiece measurement and test plan design. YC was the leader of project and participated in the experimental design. All authors contributed to the article and approved the submitted version.

REFERENCES

- Abdallah, M., Hegazy, M. A., Alfakeer, M., and Ahmed, H. (2018). Adsorption and inhibition performance of the novel cationic gemini surfactant as a safe corrosion inhibitor for carbon steel in hydrochloric acid. *Green Chem. Lett. Rev.* 11, 457–468. doi: 10.1080/17518253.2018.1526331
- Chen, Y., Zeng, J., Hu, Y., and Wu, C. (2018). Ultrasonic assisted magnetic abrasive finishing special-shaped pipe of nickel based alloy GH4169. *China Surf. Eng.* 31, 118–124.
- Du, M., and Zhao, X. (2016). Face enhancement algorithm with variable illumination based on improved retinex. *Comput. Sci.* 43, 105–108, 112.
- Garnweitner, G., and Niederberger, M. (2006). Nonaqueous and surfactant-free synthesis routes to metal oxide nanoparticles. *J. Am. Ceram. Soc.* 89, 1801–1808. doi: 10.1111/j.1551-2916.2006.01005.x
- Guo, J., Au, K. H., Sun, C., Goh, M. H., Kum, C. W., Liu, K., et al. (2019). Novel rotating-vibrating magnetic abrasive polishing method for double-layered internal surface finishing. *J. Mater. Process. Technol.* 264, 422–437. doi: 10.1016/j.jmatprotec.2018.09.024
- Hao, L. (2016). *Research on the Ultrasonic Cleaning Technology of Aero-Engine Low Pressure Turbine Shaft*. Ph.D. thesis, Dalian university of technology, Dalian.
- Huang, Y., Zhu, Y., Xiong, C., and Pan, Y. (2011). The nature of the aeroengine nozzle coking carbon. *J. Beijing Univ. Aeronaut. Astronaut.* 5, 753–756. doi: 10.13700/j.bh.1001-5965.2011.06.015
- Husnawan, M., Masjuki, H. H., Mahlia, T. M. I., and Saifullah, M. G. (2009). Thermal analysis of cylinder head carbon deposits from single cylinder diesel engine fueled by palm oil-diesel fuel emulsions. *Appl. Energy* 86, 2107–2113. doi: 10.1016/j.apenergy.2008.12.031
- Inagaki, Y., Suzumura, A., Lkeshoji, T. T., and Yamazaki, T. (2005). Cleaning effect of interlayer metal on the joining surface during braze pressure welding. *JSME Int. J. Ser. A* 48, 413–419. doi: 10.1299/jsmea.48.413
- Jayswal, S. C., Jain, V. K., and Dixit, P. M. (2008). Magnetic abrasive finishing process—a parametric analysis. *J. Adv. Manuf. Syst.* 4, 131–150. doi: 10.1142/S0219686705000655
- Jia, W. (2005). *The Study of the Remanufacturing Cleaning Technology for a Fighter's Parts*. Ph.D. thesis, Dalian University of Technology, Dalian.
- Jiang, J., Shen, H., and He, Y. (2017). The discuss of carbon deposition treatment new technology method about car engines. *Equip. Manuf. Technol.* 4, 155–157.
- Jiao, A. Y., Quan, H. J., Li, Z. Z., and Chen, Y. (2015). Study of magnetic abrasive finishing in seal ring groove surface operations. *Int. J. Adv. Manuf. Technol.* 85, 1195–1205. doi: 10.1007/s00170-015-8029-7
- Kauffman, R. E., Feng, A. S., and Karasek, K. R. (2000). Coke formation from aircraft engine oils: part II-effects of oil formulation and surface composition. *Tribol. Trans.* 43, 677–680. doi: 10.1080/10402000008982395
- Lee, Y., Wu, K., Bai, C., Liao, C., and Yan, B. (2015). Planetary motion combined with two-dimensional vibration-assisted magnetic abrasive finishing. *Int. J. Adv. Manuf. Technol.* 76, 1865–1877. doi: 10.1007/s00170-014-6370-x
- Li, F., Zhu, Y., Huang, Y., and Liu, Y. (2014). Anti-coking performance of nozzle material's surface chemical modification. *J. Beijing Univ. Aeronaut. Astronaut.* 40, 564–568. doi: 10.13700/j.bh.1001-5965.2013.0326
- Li, H., Zou, X., Wei, H., Li, Q., Gao, Q., Liu, Q., et al. (2020). SiO₂ coated on ZnO nanorod arrays with UV-durable superhydrophobicity and highly transmittance on glass. *Front. Chem.* 8:101. doi: 10.3389/fchem.2020.00101

FUNDING

This study was co-supported by the National Natural Science Foundation of China (51775258) and the Key Laboratory of Precision and Special Processing Ministry of Education (201703).

- Li, L., Wang, Z., Huang, T., Xie, J., and Qi, L. (2010). Porous gold nanobelts templated by metal-surfactant-complex nanobelts. *Langmuir* 26, 12330–12335. doi: 10.1021/la1015737
- Liu, S., Yan, P., Li, H., Zhang, X., and Sun, W. (2020). One-step microwave synthesis of micro/nanoscale LiFePO₄/graphene cathode with high performance for lithium-ion batteries. *Front. Chem.* 8:104. doi: 10.3389/fchem.2020.00104
- Liu, W., Li, M., Short, T., Qing, X., He, Y., Li, Y., et al. (2015). Supercritical carbon dioxide cleaning of metal parts for remanufacturing industry. *J. Clean. Prod.* 93, 339–346. doi: 10.1016/j.jclepro.2015.01.014
- Liu, Z., Wang, J., and Lin, Y. (2014). Study on the causes and countermeasures of intake valve deposit of gasoline direct injection engine. *Int. Combust. Eng.* 3, 54–57.
- Qi, K., Lv, W., Khan, I., and Liu, S. (2020a). Photocatalytic H₂ generation via CoP quantum-dot-modified g-C₃N₄ from electroless plating. *Chin. J. Catal.* 41, 114–121. doi: 10.1016/S1872-2067(19)63459-5
- Qi, K., Xing, X., Zada, A., Li, M., Wang, Q., Liu, S., et al. (2020b). Transition metal doped ZnO nanoparticles with enhanced photocatalytic and antibacterial performances: experimental and DFT studies. *Ceram. Int.* 46, 1494–1502. doi: 10.1016/j.ceramint.2019.09.116
- Stancu, C., Alegre, D., Ionita, E. R., Mitua, B., Grisoliar, C., Tabares, F. L., et al. (2016). Cleaning of carbon materials from flat surfaces and castellations gaps by an atmospheric pressure plasma jet. *Fusion Eng. Des.* 103, 38–44. doi: 10.1016/j.fusengdes.2015.12.024
- Tumuluri, S., Murugesan, P., Mishra, R. K., and Subrahmanyam, V. V. (2017). Application of direct metal deposition process for failure prevention of oil pump gear shaft in an aero engine. *J. Fail. Anal. Prevent.* 17, 788–795. doi: 10.1007/s11668-017-0289-0
- Wang, X., Jia, X., Li, F., Yang, M., Zhang, J., and Sun, Y. (2017). The research on formation mechanism of carbon deposition in remanufacturing engines. *Chin. J. Mech. Eng.* 53, 69–75. doi: 10.3901/JME.2017.05.069
- Wu, J., Zou, Y., and Sugiyama, H. (2015). Study on ultra-precision magnetic abrasive finishing process using low frequency alternating magnetic field. *J. Magn. Magn. Mater.* 386, 50–59. doi: 10.1016/j.jmmm.2015.03.041
- Wu, Y. (2018). *Pyrolysis and Coking Kinetics and the Effects Mechanism During the Pyrolysis Process of n-Heptane*. Ph.D. thesis, University of Chinese Academy of Sciences, Huairou District.
- Xu, H., Kang, R., and Chen, Y. (2020a). Experimental study on removing carbon from fuel nozzles by magnetic grinding. *Acta Aeronaut. Astronaut. Sin.* 41:623505. doi: 10.7527/S1000-6893.2019.23505
- Xu, H., Kang, R., Liu, D., and Chen, Y. (2020b). Experimental analysis of removal inner surface carbon from aero-engine turboshaft by magnetic grinding. *Surf. Technol.* 49, 336–342. doi: 10.16490/j.cnki.issn.1001-3660.2020.01.040
- Yao, S., Jia, X., Wang, X., Li, J., and Li, J. (2015). Molten salt cleaning process of carbon deposition on engine valve. *China Surf. Eng.* 28, 121–126. doi: 10.11933/j.issn.1007-9289.2015.04.016
- Yoshiya, M., Ono, K., Dewa, K., Watanabe, A., Saito, Y., Matsushita, Y., et al. (2016). Reaction pathway for nascent soot in ethylene pyrolysis. *Combust. Flame* 167, 248–258. doi: 10.1016/j.combustflame.2016.02.008
- Zhang, S., Khan, I., Qin, X., Qi, K., Liu, Y., and Bai, S. (2020). Construction of 1D Ag-AgBr/AlOOH plasmonic photocatalyst for degradation of tetracycline hydrochloride. *Front. Chem.* 8:117. doi: 10.3389/fchem.2020.00117
- Zhang, Y., Ni, D., Lee, I., Lin, D., and Yang, Z. (2018). Test on hot jet noise of scaled engine nozzle. *Acta Aeronaut. Astronaut. Sin.* 39, 145–155. doi: 10.7527/S1000-6893.2018.22446
- Zhang, Z., and Han, L. (2014). Application of component-remanufactured cleaning technology. *Clean. World* 30, 42–45.

- Zhou, C., Han, B., Xiao, C., Chen, Y., and Liu, X. (2019). Application of magnetic abrasive particle aided magnetic needles grinding. *Surf. Technol.* 48, 275–282. doi: 10.16490/j.cnki.issn.1001-3660.2019.03.037
- Zhou, K., Chen, Y., Du, Z. W., and Niu, F. L. (2015). Surface integrity of titanium part by ultrasonic magnetic abrasive finishing. *Int. J. Adv. Manuf. Technol.* 80, 997–1005. doi: 10.1007/s00170-015-7028-z
- Zhu, A., and Zhang, X. (2014). Application of MATLAB in underwater laser line scan image processing. *J. Atmos. Environ. Opt.* 9, 391–396. doi: 10.3969/j.issn.1673-6141.2014.05.009
- Zou, Y., Liu, J., and Shinmura, T. (2011). Study on internal magnetic field assisted finishing process using a magnetic machining jig for thick non-ferromagnetic tube. *Adv. Mater. Res.* 325, 530–535. doi: 10.4028/www.scientific.net/amr.325.530

Conflict of Interest: LL and LW were employed by the company AECC XI'AN AERO-ENGINE LTD.

The remaining authors declare that the research was conducted in the absence of any commercial or financial relationships that could be construed as a potential conflict of interest.

Copyright © 2020 Xu, Kang, Zhu, Liu, Wang and Chen. This is an open-access article distributed under the terms of the Creative Commons Attribution License (CC BY). The use, distribution or reproduction in other forums is permitted, provided the original author(s) and the copyright owner(s) are credited and that the original publication in this journal is cited, in accordance with accepted academic practice. No use, distribution or reproduction is permitted which does not comply with these terms.



Hydrothermal Synthesis of Flake-Flower NiO and Its Gas Sensing Performance to CO

Guochao Qian^{1,2*}, Qingjun Peng¹, Dexu Zou¹, Shan Wang¹ and Bing Yan¹

¹ Electric Power Science Research Institute of Yunnan Power Grid Co., Ltd., Kunming, China, ² State Key Laboratory of Power Transmission Equipment & System Security and New Technology, Chongqing University, Chongqing, China

In this work, flake-flower NiO was successfully prepared via a facile hydrothermal method. The microstructure of the synthesized sample was characterized by X-ray powder diffraction (XRD), scanning electron microscopy (SEM), and transmission electron microscopy (TEM). We find that the hierarchical flake-flower structure was assembled by numerous nanosheets with different size and shape. The fabricated sensor based on the obtained microstructure exhibited excellent gas sensing performance including high response, outstanding selectivity and stability toward 5 ppm CO at the optimal working temperature of 250°C. A plausible gas sensing mechanism was given out to explain how the nanosheet assembly morphology affects the gas sensing performance of the flake-flower structure.

OPEN ACCESS

Edited by:

Kezhen Qi,
Shenyang Normal University, China

Reviewed by:

Matteo Tonezzer,
Italian National Research Council, Italy
S. V. Prabhakar Vattikuti,
Yeungnam University, South Korea

*Correspondence:

Guochao Qian
164688847@qq.com

Specialty section:

This article was submitted to
Thin Solid Films,
a section of the journal
Frontiers in Materials

Received: 13 May 2020

Accepted: 12 June 2020

Published: 07 August 2020

Citation:

Qian G, Peng Q, Zou D, Wang S
and Yan B (2020) Hydrothermal
Synthesis of Flake-Flower NiO and Its
Gas Sensing Performance to CO.
Front. Mater. 7:216.
doi: 10.3389/fmats.2020.00216

Keywords: hydrothermal, NiO, flake-flower, gas sensor, CO

INTRODUCTION

Dissolved Gas in Oil Analysis (DGA) is one of the most convenient and effective methods to judge the early latent faults of oil immersed high-voltage electrical equipment at present (Gui et al., 2019; Yang et al., 2019a; Zhou et al., 2019; Wang et al., 2020; Wei et al., 2020a). As one of the most important fault characteristic gases of oil immersed transformer, carbon monoxide (CO), has received considerable attention for its application to provide vital help for judging the operation state of transformer (Zhou et al., 2015, 2018a,b; Yang et al., 2019b). In this respect, to detect and analyze the dissolved gases, many strategies have been proposed, for instance, gas chromatography, photoacoustic spectrometry and gas sensor (Qu et al., 2016; Liu et al., 2017; Wei et al., 2019b). Among these methods, the design of gas sensor has attracted numerous interest, owing to its low cost, facile route and simple structure (Wang et al., 2019a; Zargouni et al., 2019). However, to ensure the normal operation of transformer and power system, the fabrication of high-performance gas sensors is still a still a challenging work (Wei et al., 2019c; Zhou et al., 2018c; Zhang et al., 2019).

In order to fabricate high-performance gas sensors among various metal oxide semiconductors, which includes ZnO (Zhou et al., 2013; Zhu et al., 2017, 2018a), SnO₂ (Zhang et al., 2014, 2017; Ahmed et al., 2019), WO₃ (Park et al., 2014; Du et al., 2018; Li et al., 2018), TiO₂ (Zeng et al., 2012; Zhang Y. X. et al., 2018), and NiO (Zhang H. et al., 2018; Zhou et al., 2018d; Devarayapalli et al., 2019), Nickel oxide (NiO) has gained increasing attention for its wide band gap energy (3.6–4.0 eV) and stable physical and chemical properties (Sun et al., 2016; Zhang Y. et al., 2016; Wang et al., 2017; Nagajyothi et al., 2019). Besides, a lot of studies have confirmed that NiO is a promising nanomaterial to detect the fault characteristic gas in transformer oil (Dang et al., 2015; Li et al., 2015; Beroual and Haddad, 2017).

Considering that the morphology of the nanomaterials plays an important role in the gas sensing performance of NiO sensors, there have been considerable efforts in the synthesis of different NiO nanostructures for instance nanoparticle (0-D) (Cao et al., 2016; Kruefu et al., 2016), nanorod (1-D) (Choi et al., 2016; Feng et al., 2017), nanosheet (2-D) (Yu et al., 2015; Sta et al., 2016) and nanoflower (3-D) (Wang et al., 2016; Miao et al., 2017). Compared with low dimensional nanostructures, hierarchical nanostructures have made great progress because of their complicated and beneficial structures (Cao et al., 2015; Wang et al., 2015). For example, Wei et al. (2019a) designed and synthesized 2-D NiO porous nanosheet via a facile hydrothermal method, the gas sensor based on which had excellent gas sensing performance toward 30 ppm H₂ at the optimal working temperature of 225°C benefited from the special porous nanostructure. Wang et al. (2019b) synthesized hierarchical structure assembled with NiO nanosheets and the sensor based on the nanostructure exhibited excellent gas sensing performance due to its high special surface area. Reasonable design of hierarchical structure of NiO is a challenging but meaningful work to enhance the performance of NiO based sensor to detect the fault characteristic gas in transformer oil (Zhang D. Z. et al., 2016; Balamurugan et al., 2017; Cui et al., 2019).

In this work, hierarchical flake-flower NiO has been prepared with a facile hydrothermal method. The obtained sample was characterized by XRD, SEM, TEM, HRTEM, and SAED and fabricated into gas sensing device. Gas sensing test toward CO was carried out to demonstrate the high-performance of the special hierarchical NiO structure. The gas sensing results indicated that the fabricated sensor showed excellent performances including high response, prominent stability and outstanding selectivity toward 5 ppm CO at the optimal working temperature of 250°C. A plausible gas sensing mechanism was proposed, demonstrating that the excellent performance might be caused by the hierarchical 3-D structure with high special surface area.

EXPERIMENTAL

Synthesis of Flake-Flower NiO

All reagents in this work used to prepare the hierarchical flake-flower NiO were of analytical grade and used without any further purification. In a typical hydrothermal procedure, 0.475 g NiCl₂·6H₂O was added into 20 ml mixed solution composed of 10 ml of pure water and 10 ml of ethanol. Then, 0.2 g PVP and 10 ml of EG were added into the mixture under stirring. The pH value of the solution was adjusted to about 10 by dropping NH₃·H₂O. After that, the mixture was magnetically stirred for 5 min to form a homogeneous solution and then poured into a 50 mL Teflon-lined stainless autoclave which was kept at 140°C for 10 h. After the autoclave cooled to room temperature, the green sample was harvested by centrifugation and washing with pure water and ethanol for several times. After drying at 60°C for 10 h, the expected product was obtained by calcination at 600°C for 1 h.

Materials Characterization

The structure and phase purity of the product were characterized by X-ray diffraction (XRD) with a Rigaku D/Max-2550 diffractometry (Cu-K α radiation, $\lambda = 0.15418$ nm, $2\theta = 30-85^\circ$). The morphology of the flake-flower NiO was observed by a Nova 400 scanning electronic microscope (SEM). The high-magnification structure of the flake-flower morphology was investigated by a JEM-2100F field-emission transmission electron microscope including transmission electron microscope (TEM), high resolution transmission electron microscope (HRTEM) and selected area electron diffraction (SAED).

Gas Sensor Measurements

In order to fabricate high-performance CO sensing sensor based on the flake-flower NiO, the device was designed with a side-heated structure as shown in **Figure 1A**. Concretely, the prepared sample was mixed with pure water and ethanol in a ratio of 8:1:1 to obtain a homogeneous solution which was used to form a

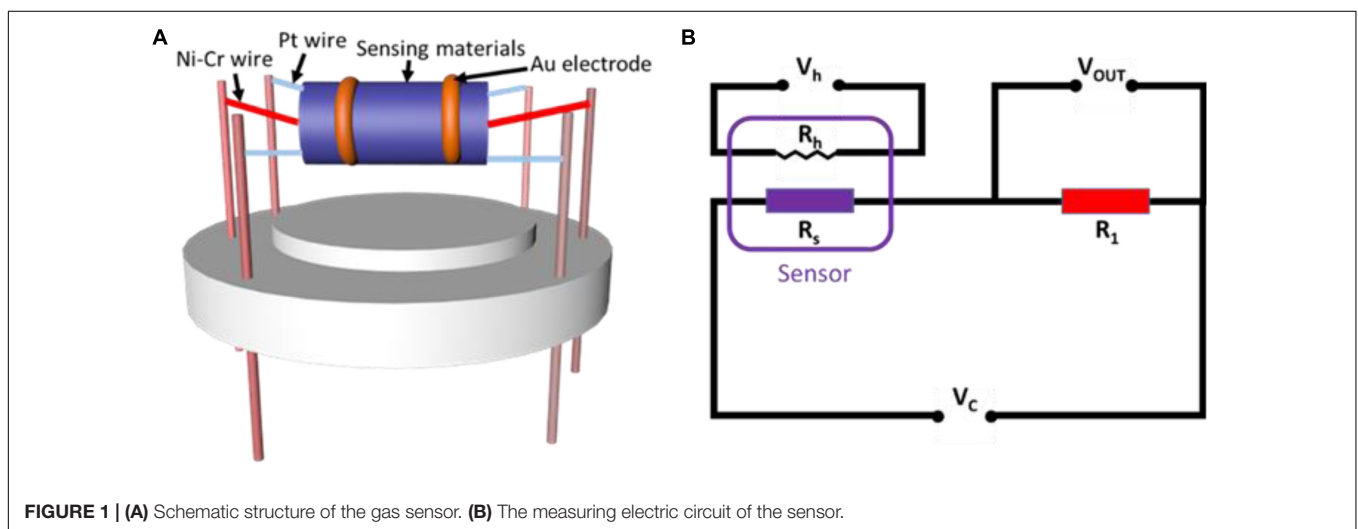
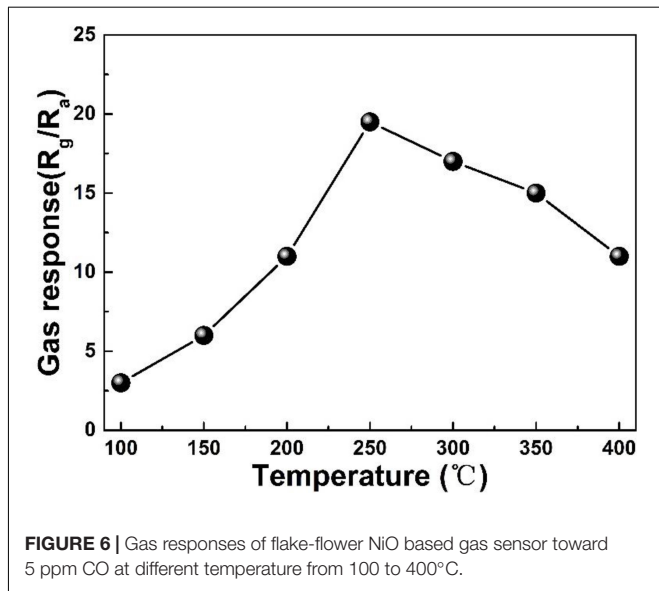
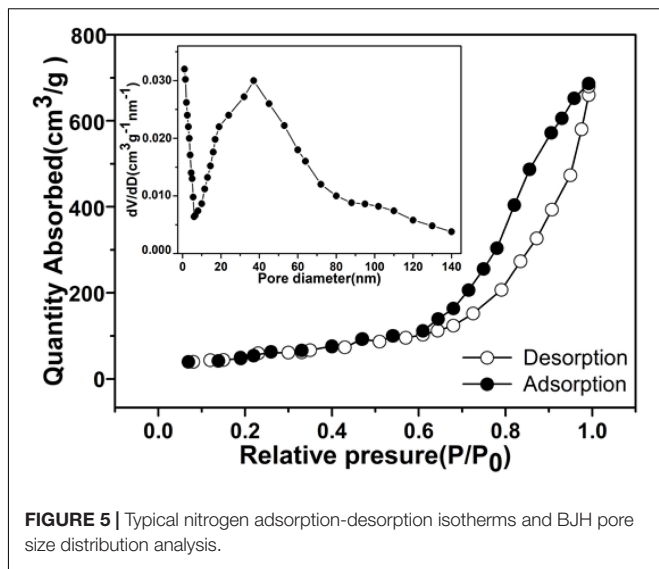
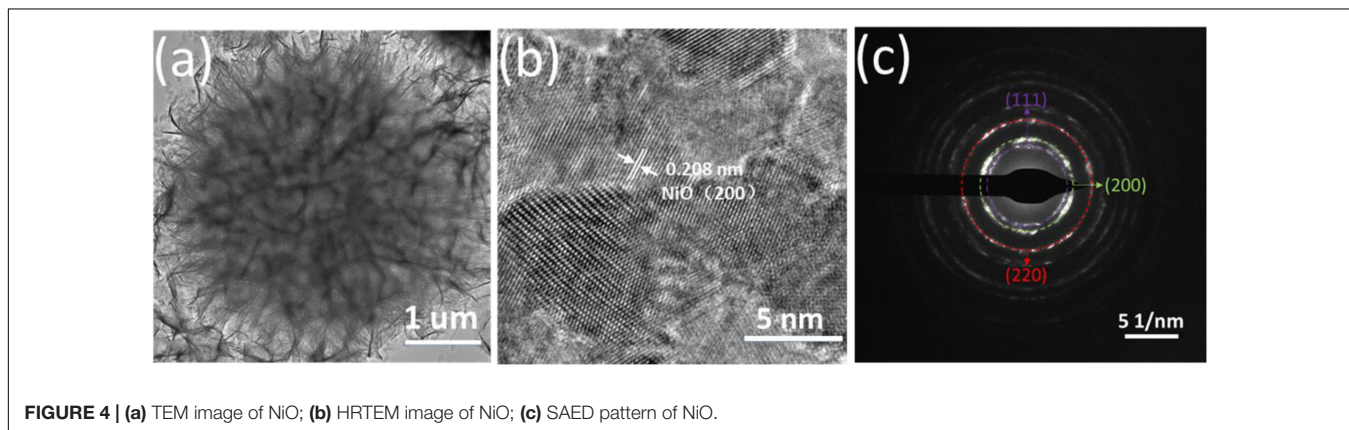
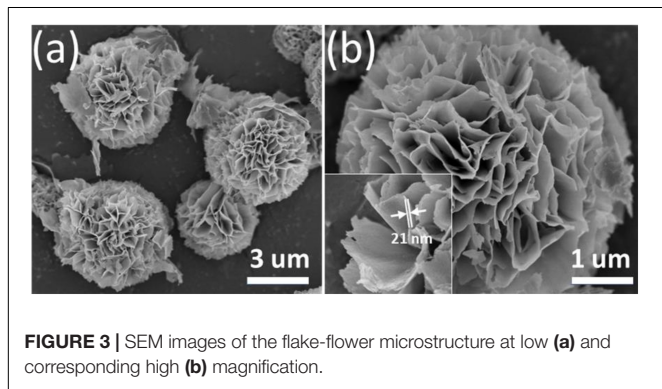
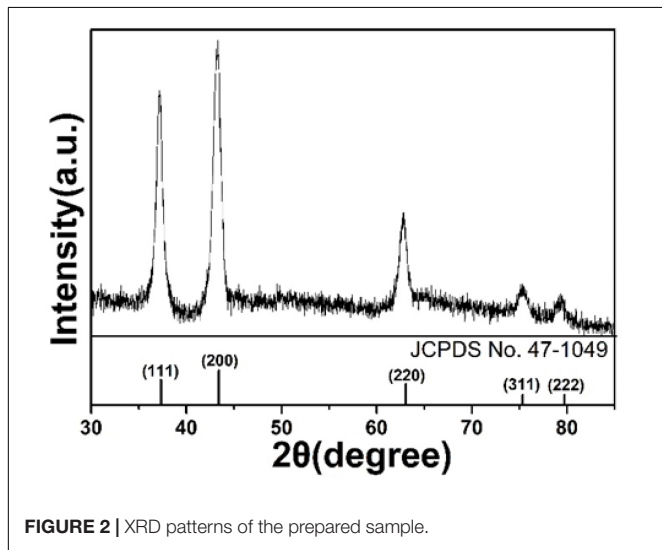


FIGURE 1 | (A) Schematic structure of the gas sensor. (B) The measuring electric circuit of the sensor.

sensing film. Then, the formed film was coated onto a ceramic tube which has been designed with a pair of Au electrodes and two pairs of Pt wires. Next, a Ni-Cr wire was inserted into the tube to control the working temperature of the sensor (Zhang et al., 2015; Zhu et al., 2018b). **Figure 1B** gives out the theoretic diagram of the test circuit, from which one can find that V_{out} represents the output voltage to calculate the resistance and V_h represents



the heating voltage to change the working temperature (Wei et al., 2019b). To ensure the long-term stability and repeatability of the fabricated CO sensor, the device was aged at 300°C for 1 week in air (Lu et al., 2018). The gas sensing performance of the fabricated sensor was measured with a static analysis system using a Chemical Gas Sensor-8 intelligent system (Beijing Elite Tech Co., Ltd.). Besides, the volume of the test chamber is 20 L and the flux of the test gases was set to 20 ml/min. Gas response in this work were defined as $S = R_g/R_a$, in which R_g and R_a represent the resistances in target gases and in air (Wei et al., 2020b).

RESULTS AND DISCUSSION

Morphology and Structure

The structure and phase purity of the synthesized flake-flower sample were characterized by XRD as shown in **Figure 2**. From

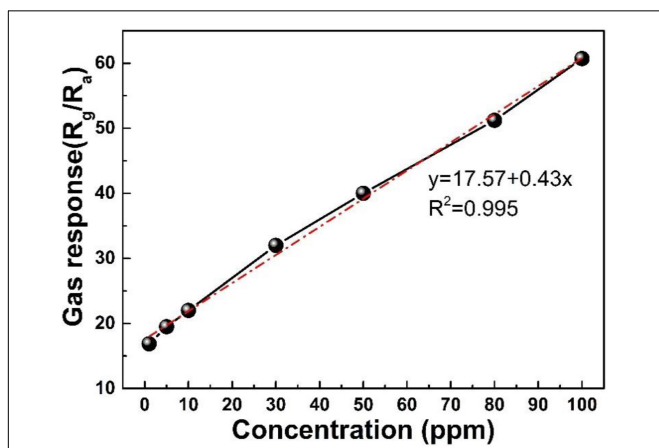


FIGURE 7 | Gas responses of flake-flower NiO based gas sensor toward different concentration of CO from 1 to 100 ppm at the optimal working temperature of 250°C.

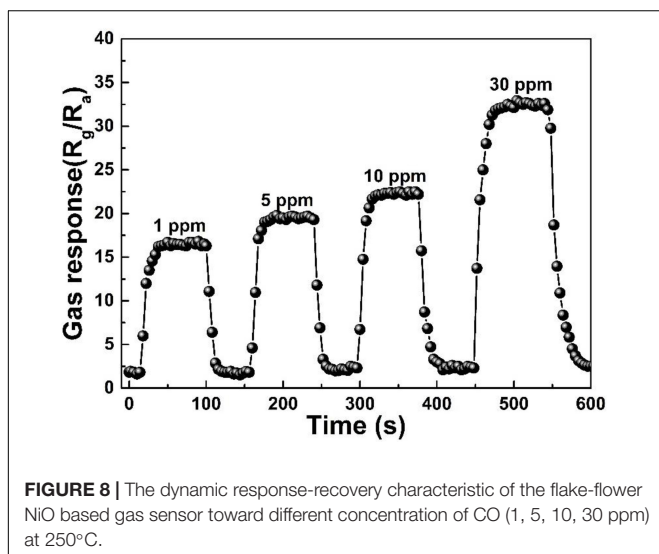


FIGURE 8 | The dynamic response-recovery characteristic of the flake-flower NiO based gas sensor toward different concentration of CO (1, 5, 10, 30 ppm) at 250°C.

the XRD pattern, it is obvious that there are five clear diffraction peaks at 37.1°, 43.3°, 63.1°, 75.1°, and 79.5°, which can be well indexed with (1 1 1), (2 0 0), (2 2 0), (3 1 1), and (2 2 2) lattice planes of cubic NiO (JCPDS Card no. 47-1049). Besides, no other diffraction peaks were observed in the spectrum, indicating that the prepared product must be pristine NiO with high-purity.

Figure 3 displays the SEM micrographs of the flake-flower NiO with different magnification. As shown in **Figure 3a**, it can be seen that the synthesized sample has a flower-like microstructure with a relatively uniform distribution and a diameter of about 5 μm. From the higher magnification image of the flower-like microstructure (**Figure 3b**), it is intuitive that the flake-flower structure was assembled by a lot of thin nanosheets. The numerous nanosheets with different shape and size make the NiO structure exhibit a flake-flower shape and hierarchy which will possess large surface sites and abundant reaction rooms for gas molecules.

To observe a more detailed structural information of the flake-flower microstructure, the sample was analyzed by transmission electron microscope with the characterization of TEM, HRTEM and SAED (**Figure 4**). As presented in **Figure 4a**, the structure was confirmed to be assembled by numerous irregular and random nanosheets which have been mentioned in **Figure 3b**. A clear HRTEM image of NiO is displayed in **Figure 4b**, demonstrating the existence of crystalline NiO. From the clear lattice stripes, the lattice spacing can be calculated to be 0.208 nm which corresponded to the (200) plane of the cubic NiO. Moreover, **Figure 4c** depicts the SAED image of synthesized NiO sample, from which one can observe that there are a group of diffraction rings, namely (1 1 1), (2 0 0), and (2 2 0) lattice planes of cubic NiO. To confirm the potential impact of the specific surface area on gas sensing properties, the typical nitrogen adsorption-desorption isotherm was calculated. The BET analysis (**Figure 5**) indicated that the specific surface area of the synthesized flake-flower NiO is 176.5 m²g⁻¹ and the average pore size is 27.6 nm, suggesting that the flake-flower microstructure provided a large surface area.

Gas Sensing Performance

As we all know, the working temperature of gas sensor has a great influence on the reaction in the process of gas sensing. To obtain the optimal working temperature of the fabricated CO sensor based on the flake-flower NiO, the device was tested at different temperatures from 100 to 400°C toward 5 ppm CO. It can be seen from **Figure 6** that the response of the flake-flower NiO based sensor toward CO of 5 ppm increased first and then decreased with the increase of temperature, suggesting that the response of the sensor is strongly dependent on the working temperature. This is because the low activation energy at low temperature is not enough to support the gas reaction, and the increased temperature will lead to the higher desorption rate. Given this, the gas response will reach a maximum at a specific temperature, which is the optimum working temperature. In this work, the optimum working temperature of the CO sensor is 250°C, at which the highest response is 19.5. And subsequent gas sensing experiments will be carried out at this optimal operating temperature.

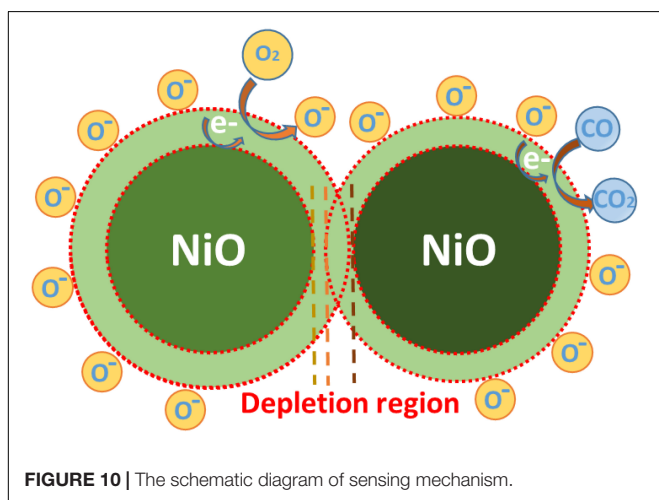
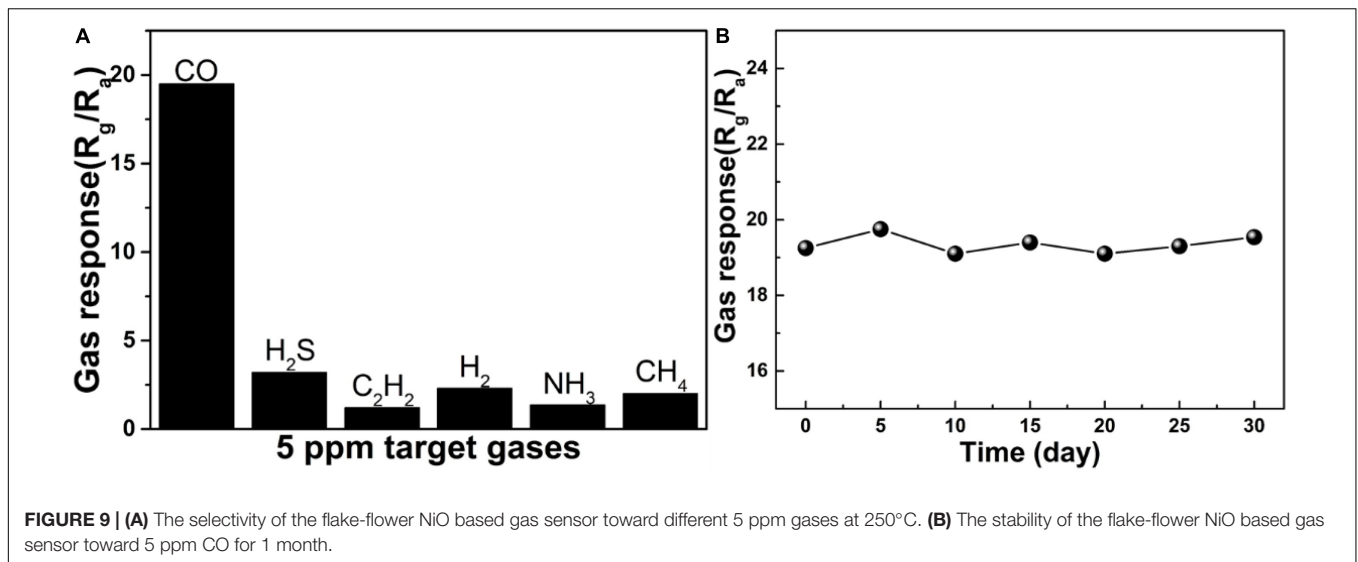


FIGURE 10 | The schematic diagram of sensing mechanism.

Figure 7 presents the response of the flake-flower NiO based sensor toward different concentration of CO at the optimal working temperature of 250°C. Obviously, the response of the fabricated sensor increased almost linearly with the increase

of the concentration of CO from 1 to 100 ppm. Besides, the linear fitting function and the linear correlation coefficient were calculated as $y = 17.57 + 0.43x$ and 0.995, respectively. It can be found that the responses of flake-flower NiO based sensor increased obviously linearly with the increasing CO from 1 to 100 ppm at the optimal working temperature of 250°C.

Figure 8 demonstrates the response and recovery characteristic of the prepared sensor with different concentrations of CO (1, 5, 10, 30 ppm) at the optimal working temperature of 250°C. It is obvious the gas response curve of the sensor increases sharply when CO in, while the gas response curve of the sensor quickly returns to the original state when CO out. The CO responses of the sensor were tested to be 16.9, 19.5, 22.8, and 32.7 under 1, 5, 10, and 30 ppm, respectively. The dynamic response-recovery result indicated that the fabricated sensor possessed excellent reversibility which is an important property for the application of gas sensors.

Considering that selectivity and stability are two important indexes to evaluate the performance of gas sensors, further gas sensing experiments were carried out based on the gas concentration of 5 ppm and the optimal working temperature of 250°C. As shown in **Figure 9A**, the sensor based on the

TABLE 1 | Summary of recent researches on NiO based sensors for sensing of toward different reducing gases.

Sensing material	Gas	Concentration (ppm)	Temp. (°C)	Response	References
NiO nanowires	H ₂	1000	400	100%	Hoa et al., 2018
NiO nanowires	H ₂	1000	250	106.9%	Tonezzer et al., 2017
NiO nanofibers	CO	10	300	1.78	Choi et al., 2016
NiO nanowires	H ₂	1000	250	107%	Tonezzer et al., 2016
Hollow NiO hemisphere	C ₂ H ₅ OH	200	300	5	Cho et al., 2011
NiO nanoparticles	CO	100	350	90	Aslani et al., 2011
Porous NiO microspheres	H ₂ S	20	200	27.2	Trung et al., 2019
NiO nanoplates	CO	10	275	16.39	Wang et al., 2019b
NiO nanosheet	H ₂	30	225	20.47	Wei et al., 2019a
Flake-flower NiO	CO	30	250	32.7	This work

flake-flower NiO was exposed toward hydrogen sulfide (H₂S), acetylene (C₂H₂), hydrogen (H₂), ammonia (NH₃), methane (CH₄), and CO. It can be calculated that the response toward CO is at least 6 times higher than that of other gas, indicating that the NiO based sensor has good selectivity for 5 ppm CO at the optimal working temperature of 250°C, and can be applied for the effective detection of CO. The long-term stability experiment of fabricated CO sensor was carried out for 1 month. The performance of the sensor toward 5 ppm CO at 250°C was tested every 5 day. **Figure 9B** confirms that the prepared device possessed outstanding stability with slight change for 1 month, suggesting the fabricated sensor could be a promising choice for the application to the effective detection of CO.

Sensing Mechanism

As we all know, the basic gas sensing mechanism is demonstrated by the resistance change caused by the reaction between the adsorbed oxygen molecules and the measured gas molecules. Before injecting the CO gases, the oxygen molecules in the air were adsorbed on the surface of the NiO material due to its strong electronegativity (Cao et al., 2015; Chen et al., 2018, 2019). The oxygen molecules captured the electrons from the surface of NiO material and then were reduced to oxygen ions (O⁻). For a typical p-type oxide, since the main carrier of NiO is hole, the electrons captured by oxygen mainly come from valence band. This process results in the formation of a hole aggregation layer on the surface of the material, which has a lower resistance compared with the core region (**Figure 10**). The oxygen adsorption mechanism can be expressed as follows:

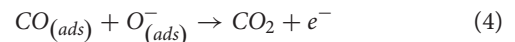


When the reducing gas CO is introduced, it will react with the oxygen ion adsorbed on the NiO surface to produce CO₂ and release electrons at the same time. This process make the released electrons combine with the holes, leading to the increase of the resistance compared with previous state. The process can be described as follows:



REFERENCES

- Ahmed, A., Siddique, M. N., Ali, T., and Tripathi, P. (2019). Defect assisted improved room temperature ferromagnetism in Ce doped SnO₂ nanoparticles. *Appl. Surf. Sci.* 483, 463–471. doi: 10.1016/j.apsusc.2019.03.209
- Aslani, A., Oroojpour, V., and Fallahi, M. (2011). Sonochemical synthesis, size controlling and gas sensing properties of NiO nanoparticles. *Appl. Surf. Sci.* 257, 4056–4061. doi: 10.1016/j.apsusc.2010.11.174
- Balamurugan, C., Jeong, Y. J., and Lee, D. W. (2017). Enhanced H₂S sensing performance of a p-type semiconducting PdO-NiO nanoscale heteromixture. *Appl. Surf. Sci.* 420, 638–650. doi: 10.1016/j.apsusc.2017.05.166
- Beroual, A., and Haddad, A. (2017). Recent advances in the quest for a new insulation gas with a low impact on the environment to replace sulfur hexafluoride (SF₆) gas in high-voltage power network applications. *Energies* 10:1216. doi: 10.3390/en10081216



Besides, for typical p-type NiO based sensing materials, various strategies have been used to synthesize different nanostructures for the detection of various reducing gases. The gas sensing characteristics of the NiO based sensors of the recently published investigations were listed in **Table 1**, from which we can find that various NiO based sensors possessed excellent gas sensing performances toward different reducing gases.

CONCLUSION

To summarize, hierarchical flake-flower NiO was successfully synthesized via a facile hydrothermal method. The prepared sample was tested by various structural and morphological characterization, demonstrating that the flake-flower microstructure was assembled by numerous nanosheets with different shape and size. Further CO sensing experiments indicated that the sensor based on the flake-flower NiO exhibited excellent gas sensing performance including high response, outstanding selectivity and stability. A plausible mechanism suggested that the excellent performance was caused by the flake-flower morphology with complicated microstructure and large special surface area. Therefore, the results suggested that flake-flower NiO based CO sensor might be considered as a promising candidate for detecting the fault characteristic gases dissolved in transformer oil.

DATA AVAILABILITY STATEMENT

The raw data supporting the conclusions of this article will be made available by the authors, without undue reservation, to any qualified researcher.

AUTHOR CONTRIBUTIONS

All authors listed have made a substantial, direct and intellectual contribution to the work, and approved it for publication.

- Cao, J., Zhang, H. M., and Yan, X. Q. (2016). Facile fabrication and enhanced formaldehyde gas sensing properties of nanoparticles-assembled chain-like NiO architectures. *Mater. Lett.* 185, 40–42. doi: 10.1016/j.matlet.2016.08.099
- Cao, S. K., Zeng, W., Long, H. W., and Zhang, H. (2015). Hydrothermal synthesis of novel flower-needle NiO architectures: structure, growth and gas response. *Mater. Lett.* 159, 385–388. doi: 10.1016/j.matlet.2015.07.045
- Chen, K. W., Tsai, J. H., and Chen, C. H. (2019). NiO functionalized Co₃O₄ hetero-nanocomposites with a novel apple-like architecture for CO gas sensing applications. *Mater. Lett.* 255:126508. doi: 10.1016/j.matlet.2019.126508
- Chen, Y., Qin, H., and Hu, J. (2018). CO sensing properties and mechanism of Pd doped SnO₂ thick-films. *Appl. Surf. Sci.* 428, 207–217. doi: 10.1016/j.apsusc.2017.08.205
- Cho, N. G., Hwang, I. S., Kim, H. G., Lee, J. H., and Kim, I. D. (2011). Gas sensing properties of p-type hollow NiO hemispheres prepared by polymeric colloidal

- templating method. *Sens. Actuators B: Chem.* 155, 366–371. doi: 10.1016/j.snb.2010.12.031
- Choi, J. M., Byun, J. H., and Kim, S. S. (2016). Influence of grain size on gas-sensing properties of chemiresistive p-type NiO nanofibers. *Sens. Actuators B: Chem.* 227, 149–156. doi: 10.1016/j.snb.2015.12.014
- Cui, H., Zhang, X. X., Zhang, G. Z., and Tang, J. (2019). Pd-doped MoS₂ monolayer: a promising candidate for DGA in transformer oil based on DFT method. *Appl. Surf. Sci.* 470, 1035–1042. doi: 10.1016/j.apsusc.2018.11.230
- Dang, T. T. L., Tonezzer, M., and Nguyen, V. H. (2015). Hydrothermal Growth and Hydrogen Selective Sensing of Nickel Oxide Nanowires. *J. Nanomater.* 2015:785856. doi: 10.1155/2015/785856
- Devarayapalli, K. C., Vattikuti, S. V. P., Sreekanth, T. V. M., Yoo, K. S., Nagajyothi, P. C., and Shim, J. (2019). Facile synthesis of Ni-MOF using microwave irradiation method and application in the photocatalytic degradation. *Mater. Res. Express* 6:1150h3. doi: 10.1088/2053-1591/ab5261
- Du, Q., Wang, L., Yang, J., Liu, J. F., Yuan, Y. K., Wang, M. Z., et al. (2018). Enhancing gas sensing performances and sensing mechanism at atomic and molecule level of WO₃ nanoparticles by hydrogenation. *Sens. Actuators B: Chem.* 273, 1786–1793. doi: 10.1016/j.snb.2018.07.099
- Feng, C. B., Kou, X. Y., Chen, B., Qian, G. B., Sun, Y. F., and Lu, G. Y. (2017). One-pot synthesis of In doped NiO nanofibers and their gas sensing properties. *Sens. Actuators B: Chem.* 253, 584–591. doi: 10.1016/j.snb.2017.06.115
- Gui, Y. G., Li, T., He, X., Ding, Z. Y., and Yang, P. G. (2019). Pt cluster modified h-BN for gas sensing and adsorption of dissolved gases in transformer oil: a Density Functional Theory Study. *Nanomaterials* 9:1746. doi: 10.3390/nano9121746
- Hoa, N. D., Tong, P. V., Hung, C. M., Duy, N. V., and Hieu, N. V. (2018). Urea mediated synthesis of Ni(OH)(2) nanowires and their conversion into NiO nanostructure for hydrogen gas-sensing application. *Int. J. Hydrogen Energ.* 43, 9446–9453. doi: 10.1016/j.ijhydene.2018.03.166
- Kruefu, V., Wisitsoraat, A., Phokharatkul, D., Tuantranont, A., and Phanichphant, S. (2016). Enhancement of p-type gas-sensing performances of NiO nanoparticles prepared by precipitation with RuO₂ impregnation. *Sens. Actuators B: Chem.* 236, 466–473. doi: 10.1016/j.snb.2016.06.028
- Li, F., Ruan, S. P., Zhang, N., Yin, Y. Y., Guo, S. J., Chen, Y., et al. (2018). Synthesis and characterization of Cr-doped WO₃ nanofibers for conductometric sensors with high xylene sensitivity. *Sens. Actuators B: Chem.* 265, 355–364. doi: 10.1016/j.snb.2018.03.054
- Li, G. H., Wang, X. W., Liu, L., Liu, R., Shen, F. P., Cui, Z., et al. (2015). Controllable Synthesis of 3D Ni(OH)(2) and NiO Nanowalls on Various Substrates for High-Performance Nanosensors. *Small* 11, 731–739. doi: 10.1002/smll.201400830
- Liu, H. C., Zhou, Q., Zhang, Q. Y., Hong, C. X., Xu, L. N., Jin, L. F., et al. (2017). Synthesis, characterization and enhanced sensing properties of a NiO/ZnO p-n junctions sensor for the SF₆ decomposition byproducts SO₂, SO₂F₂, and SOF₂. *Sensors* 17:913. doi: 10.3390/s17040913
- Lu, Z., Zhou, Q., Xu, L., Gui, Y., Zhao, Z., Tang, C., et al. (2018). Synthesis and characterization of highly sensitive hydrogen (H₂) sensing device based on Ag doped SnO₂ nanospheres. *Materials* 11:492. doi: 10.3390/ma11040492
- Miao, R. Y., Zeng, W., and Gao, Q. (2017). Hydrothermal synthesis of novel NiO nanoflowers assisted with CTAB and SDS respectively and their gas-sensing properties. *Mater. Lett.* 186, 175–177. doi: 10.1016/j.matlet.2016.09.127
- Nagajyothi, P. C., Deyarayapalli, K. C., Tettey, C. O., Vattikuti, S. V. P., and Shim, J. (2019). Eco-friendly green synthesis: catalytic activity of nickel hydroxide nanoparticles. *Mater. Res. Express* 6: 055036. doi: 10.1088/2053-1591/ab04e4
- Park, S., Park, S., Jung, J., Hong, T., Lee, S., Kim, H. W., et al. (2014). H₂S gas sensing properties of CuO-functionalized WO₃ nanowires. *Ceram. Int.* 40, 11051–11056. doi: 10.1016/j.ceramint.2014.03.120
- Qu, Z., Fu, Y., Yu, B., Deng, P., Xing, L., and Xue, X. (2016). High and fast H₂S response of NiO/ZnO nanowire nanogenerator as a self-powered gas sensor. *Sens. Actuators B: Chem.* 222, 78–86. doi: 10.1016/j.snb.2015.08.058
- Sta, I., Jlassi, M., Kandyla, M., Hajji, M., Koralli, P., Krout, F., et al. (2016). Surfacefunctionalization of sol-gel grown NiO thin films with palladium nanoparticles for hydrogen sensing. *Int. J. Hydrogen Energ.* 41, 3291–3298. doi: 10.1016/j.ijhydene.2015.12.109
- Sun, G.-J., Kheel, H., Lee, J. K., Choi, S., Lee, S., and Lee, C. (2016). H₂S gas sensing properties of Fe₂O₃ nanoparticle-decorated NiO nanoplate sensors. *Surf. Coat. Tech.* 307, 1088–1095. doi: 10.1016/j.surfcoat.2016.06.066
- Tonezzer, M., Le, D. T. T., Huy, T. Q., and Iannotta, S. (2016). Dual-selective hydrogen and ethanol sensor for steam reforming systems. *Sens. Actuators B: Chem.* 236, 1011–1019. doi: 10.1016/j.snb.2016.04.150
- Tonezzer, M., Le, D. T. T., Tran, Q. H., Nguyen, V. H., and Iannotta, S. (2017). Selective hydrogen sensor for liquefied petroleum gas steam reforming fuel cell systems. *Int. J. Hydrogen Energ.* 42, 740–748. doi: 10.1016/j.ijhydene.2016.11.102
- Trung, D. D., Cuong, N. D., Quang, P. L., Anh, N. T. N., Quang, D. T., Nam, P. C., et al. (2019). Facile post-synthesis and gas sensing properties of highly porous NiO microspheres. *Sens. Actuators A: Phys.* 296, 110–120. doi: 10.1016/j.sna.2019.07.014
- Wang, C., Liu, J. Y., Yang, Q. Y., Sun, P., Gao, Y., Liu, F. M., et al. (2015). Ultrasensitive and low detection limit of acetone gas sensor based on W-doped NiO hierarchical nanostructure. *Sens. Actuators B: Chem.* 220, 59–67. doi: 10.1016/j.snb.2015.05.037
- Wang, C., Zeng, W., and Chen, T. (2017). Facile synthesis of thin nanosheet assembled flower-like NiO-ZnO composite and its ethanol-sensing performance. *J. Mater. Sci-Mater. El.* 28, 222–227. doi: 10.1007/s10854-016-5514-1
- Wang, J., Zeng, W., and Wang, Z. C. (2016). Assembly of 2D nanosheets into 3D flower-like NiO: synthesis and the influence of petal thickness on gas-sensing properties. *Ceram. Int.* 42, 4567–4573. doi: 10.1016/j.ceramint.2015.11.150
- Wang, J. X., Zhou, Q., Lu, Z. R., Wei, Z. J., and Zeng, W. (2019a). Gas sensing performances and mechanism at atomic level of Au-MoS₂ microspheres. *Appl. Surf. Sci.* 490, 124–136. doi: 10.1016/j.apsusc.2019.06.075
- Wang, J. X., Zhou, Q., Lu, Z. R., Wei, Z. J., and Zeng, W. (2019b). The novel 2D honeycomb-like NiO nanoplates assembled by nanosheet arrays with excellent gas sensing performance. *Mater. Lett.* 255:126523. doi: 10.1016/j.matlet.2019.126523
- Wang, J. X., Zhou, Q., Xu, L. N., Gao, X., and Zeng, W. (2020). Gas sensing mechanism of dissolved gases in transformer oil on Ag-MoS₂ monolayer: a DFT study. *Physica E* 118:113947. doi: 10.1016/j.physe.2019.113947
- Wei, Z. J., Zhou, Q., Wang, J. X., Gui, Y. G., and Zeng, W. (2019a). A novel porous NiO nanosheet and its H₂ sensing performance. *Mater. Lett.* 245, 166–169. doi: 10.1016/j.matlet.2019.03.013
- Wei, Z. J., Zhou, Q., Wang, J. X., Lu, Z. R., Xu, L. N., and Zeng, W. (2019b). Hydrothermal synthesis of SnO₂ nanoneedle-anchored NiO microsphere and its gas sensing performances. *Nanomaterials* 9:1015. doi: 10.3390/nano9071015
- Wei, Z. J., Zhou, Q., Lu, Z. R., Xu, L. N., Gui, Y. G., and Tang, C. (2019c). Morphology controllable synthesis of hierarchical WO₃ nanostructures and C₂H₂ sensing properties. *Physica E* 109, 253–260. doi: 10.1016/j.physe.2019.01.006
- Wei, Z. J., Zhou, Q., and Zeng, W. (2020a). Hierarchical WO₃-NiO microflower for high sensitivity detection of SF₆(decomposition)byproduct H₂S. *Nanotechnology* 31:215701. doi: 10.1088/1361-6528/ab73bd
- Wei, Z. J., Zhou, Q., Wang, J. X., and Zeng, W. (2020b). Hydrothermal synthesis of hierarchical WO₃/NiO porous microsphere with enhanced gas sensing performances. *Mater. Lett.* 264:127383. doi: 10.1016/j.matlet.2020.127383
- Yang, Z., Zhou, Q., Wu, X. D., Zhao, Z. Y., Tang, C., and Chen, W. G. (2019a). Detection of water content in transformer oil using multi frequency ultrasonic with PCA-GA-BPNN. *Energies* 12:1379. doi: 10.3390/en12071379
- Yang, Z., Zhou, Q., Wu, X. D., and Zhao, Z. Y. (2019b). A novel measuring method of interfacial tension of transformer oil combined PSO optimized SVM and multi frequency ultrasonic technology. *IEEE Access* 7, 182624–182631. doi: 10.1109/ACCESS.2019.2954899
- Yu, F., Xu, X. L., Peng, H. G., Yu, H. J., Dai, Y. F., Liu, W. M., et al. (2015). Porous NiO nano-sheet as an active and stable catalyst for CH₄ deep oxidation. *Appl. Catal. A* 507, 109–118. doi: 10.1016/j.apcata.2015.09.023
- Zargouni, S., Derbali, L., Ouadhour, M., Rigon, M., Martucci, A., and Ezzaouia, H. (2019). Elaboration and characterization of PVP-assisted NiO thin films for enhanced sensitivity toward H₂ and NO₂ gases. *Ceram. Int.* 45, 5779–5787. doi: 10.1016/j.ceramint.2018.12.044
- Zeng, W., Liu, T. M., and Wang, Z. C. (2012). Enhanced gas sensing properties by SnO₂ nanosphere functionalized TiO₂ nanobelts. *J. Mater. Chem.* 22, 3544–3548. doi: 10.1039/c2jm15017d
- Zhang, H., Zeng, W., Zhang, Y., Li, Y. Q., Miao, B., Chen, W. G., et al. (2014). Synthesis and gas sensing properties of novel SnO₂ nanorods. *J. Mater. Sci-Mater. El.* 25, 5006–5012. doi: 10.1007/s10854-014-2264-9

- Zhang, Q. Y., Zhou, Q., Yin, X. T., Liu, H. C., Xu, L. N., Tan, W. M., et al. (2017). The effect of PMMA pore-forming on hydrogen sensing properties of porous SnO₂ thick film sensor. *Sci. Adv. Mater.* 9, 1350–1355. doi: 10.1166/sam.2017.3111
- Zhang, W. L., Zeng, W., Miao, B., and Wang, Z. C. (2015). Effect of the sheet thickness of hierarchical SnO₂ on the gas sensing performance. *Appl. Surf. Sci.* 355, 631–637. doi: 10.1016/j.apsusc.2015.07.149
- Zhang, X. X., Fang, R. X., Chen, D. C., and Zhang, G. Z. (2019). Using Pd-doped gamma-graphyne to detect dissolved gases in transformer oil: a density functional theory investigation. *Nanomaterials* 9:1490. doi: 10.3390/nano9101490
- Zhang, Y., Wang, J., Wei, H., Hao, J., Mu, J., Cao, P., et al. (2016). Hydrothermal synthesis of hierarchical mesoporous NiO nanourchins and their supercapacitor application. *Mater. Lett.* 162, 67–70. doi: 10.1016/j.matlet.2015.09.123
- Zhang, D. Z., Chang, H. Y., Li, P., and Liu, R. (2016). Characterization of nickel oxide decorated-reduced graphene oxide nanocomposite and its sensing properties toward methane gas detection. *J. Mater. Sci-Mater. El.* 27, 3723–3730. doi: 10.1007/s10854-015-4214-6
- Zhang, Y. X., Zeng, W., Ye, H., and Li, Y. Q. (2018). Enhanced carbon monoxide sensing properties of TiO₂ with exposed (001) facet: a combined first-principle and experimental study. *Appl. Surf. Sci.* 442, 507–516. doi: 10.1016/j.apsusc.2018.02.036
- Zhang, H., Chen, W. G., Li, Y. Q., Jin, L. F., Cui, F., and Song, Z. H. (2018). 3D Flower-like NiO hierarchical structures assembled with size-controllable 1D blocking units: gas sensing performances towards acetylene. *Front. Chem.* 6:472. doi: 10.3389/fchem.2018.00472
- Zhou, Q., Chen, W. G., Xu, L. N., and Peng, S. D. (2013). Hydrothermal synthesis of various hierarchical ZnO nanostructures and their methane sensing properties. *Sensors* 13, 6171–6182. doi: 10.3390/s130506171
- Zhou, Q., Tang, C., Zhu, S. P., and Chen, W. G. (2015). NiO doped SnO₂ p-n heterojunction microspheres: preparation, characterisation and CO sensing properties. *Mater. Technol.* 30, 349–355. doi: 10.1179/1753555715y.0000000010
- Zhou, Q., Chen, W. G., Xu, L. N., Kumar, R., Gui, Y. G., Zhao, Z. Y., et al. (2018a). Highly sensitive carbon monoxide (CO) gas sensors based on Ni and Zn doped SnO₂ nanomaterials. *Ceram. Inter.* 44, 4392–4399. doi: 10.1016/j.ceramint.2017.12.038
- Zhou, Q., Lu, Z. R., Wei, Z. J., Xu, L. N., Gui, Y. G., and Chen, W. G. (2018b). Hydrothermal synthesis of hierarchical ultrathin NiO nanoflakes for high-performance CH₄ sensing. *Front. Chem.* 6:194. doi: 10.3389/fchem.2018.00194
- Zhou, Q., Umar, A., Sodki, E., Amine, A., Xu, L. N., Gui, Y. G., et al. (2018c). Fabrication and characterization of highly sensitive and selective sensors based on porous NiO nanodisks. *Sens. Actuator. B Chem.* 259, 604–615. doi: 10.1016/j.snb.2017.12.050
- Zhou, Q., Xu, L. N., Umar, A., Chen, W. G., and Kumar, R. (2018d). Pt nanoparticles decorated SnO₂ nanoneedles for efficient CO gas sensing applications. *Sens. Actuator. B Chem.* 256, 656–664. doi: 10.1016/j.snb.2017.09.206
- Zhou, Q., Zeng, W., Chen, W. G., Xu, L. N., Kumar, R., and Umar, A. (2019). High sensitive and low-concentration sulfur dioxide (SO₂) gas sensor application of heterostructure NiO-ZnO nanodisks. *Sens. Actuator. B Chem.* 298, 126870. doi: 10.1016/j.snb.2019.126870
- Zhu, L., Li, Y. Q., and Zeng, W. (2017). Enhanced ethanol sensing and mechanism of Cr-doped ZnO nanorods: experimental and computational study. *Ceram. Int.* 43, 14873–14879. doi: 10.1016/j.ceramint.2017.08.003
- Zhu, L., Li, Y. Q., and Zeng, W. (2018a). Hydrothermal synthesis of hierarchical flower-like ZnO nanostructure and its enhanced ethanol gas-sensing properties. *Appl. Surf. Sci.* 427, 281–287. doi: 10.1016/j.apsusc.2017.08.229
- Zhu, L., Zeng, W., Ye, H., and Li, Y. Q. (2018b). Volatile organic compound sensing based on coral rock-like ZnO. *Mater. Res. Bull.* 100, 259–264. doi: 10.1016/j.materresbull.2017.12.043

Conflict of Interest: GQ, QR, DZ, SW, and BY were employed by the company Electric Power Science Research Institute of Yunnan Power Grid Co., Ltd.

Copyright © 2020 Qian, Peng, Zou, Wang and Yan. This is an open-access article distributed under the terms of the Creative Commons Attribution License (CC BY). The use, distribution or reproduction in other forums is permitted, provided the original author(s) and the copyright owner(s) are credited and that the original publication in this journal is cited, in accordance with accepted academic practice. No use, distribution or reproduction is permitted which does not comply with these terms.



Fluorescence Resonant Energy Transfer-Based Quantum Dot Sensor for the Detection of Calcium Ions

Shreya Ghosh^{1*}, Yinghua Chen², Anne George², Mitra Dutta^{3,4} and Michael A. Stroschio^{3,4,5}

¹ Micro and Nanotechnology Laboratory, University of Illinois at Urbana-Champaign, Urbana, IL, United States, ² Department of Oral Biology, University of Illinois at Chicago, Chicago, IL, United States, ³ Department of Electrical and Computer Engineering, University of Illinois at Chicago, Chicago, IL, United States, ⁴ Department of Physics, University of Illinois at Chicago, Chicago, IL, United States, ⁵ Department of Bioengineering, University of Illinois at Chicago, Chicago, IL, United States

A simple optical aptasensor has been synthesized for the detection of calcium ions. This sensing approach employs a semiconductor quantum dot (QD)–gold nanoparticle as the donor–quencher pair and operates on the principle of fluorescence resonant energy transfer (FRET). On binding with calcium ions, the DNA aptamer undergoes a conformational change, which changes the distance between the quantum dot and the gold nanoparticle, conjugated on the 5' terminal and 3' terminal of the aptamer, respectively. This phenomenon results in the quenching of the quantum dot emission. In this sensor, a maximum quenching of $22.42 \pm 0.71\%$ has been achieved at 35 nM calcium ion concentration while the limit of detection has been determined to be 3.77 pM. The sensor has been found to have high specificity for calcium ions in comparison to other metal ions like sodium, magnesium, and potassium. The molecular apta-beacons also demonstrated successful endocytosis and FRET-based calcium ion detection in osteocyte cells when conjugated with a cell-penetrating peptide (DSS).

Keywords: aptamer, biosensor, calcium detection, FRET, quantum dot, optical sensor

INTRODUCTION

Calcium ions (Ca^{2+}) are an essential component of the physiological system. They play a significant role as an intracellular messenger, which regulates several cellular functions like secretion, contraction, excitability, and gene expression (Russell, 2011). An increased Ca^{2+} release can contribute to diseases like HIV, schizophrenia, and Alzheimer's disease (Wojda et al., 2008). The review by Feske et al. throws light on the role of Ca^{2+} signaling in congenital immunodeficiency syndromes along with autoimmunity and inflammatory conditions (Feske, 2007). For instance, in systemic lupus erythematosus (SLE), it has been observed that signaling through the B-cell receptor in B cells is abnormal and results in increased Ca^{2+} signals. Chung et al. reported that with an elevation in the Ca^{2+} concentration, there was a greater risk of long-term mortality after an acute ischemic stroke (Chung et al., 2015). Hence, owing to the significance of this metal ion in the physiological system, the objective of this study is to design a sensor, which rapidly detects Ca^{2+} . Asif et al. reported a zinc oxide nanorod-extended gate field-effect transistor (MOSFET), which detected Ca^{2+} linearly between 1 μM and 1 mM (Asif et al., 2009). Several analytical techniques for Ca^{2+} sensing have been published in literature.

OPEN ACCESS

Edited by:

Kezhen Qi,
Shenyang Normal University, China

Reviewed by:

Yongsheng Yang,
Shenyang Normal University, China
Enesca Ioan Alexandru,
Transilvania University of
Braşov, Romania

*Correspondence:

Shreya Ghosh
shreyaghosh215@gmail.com

Specialty section:

This article was submitted to
Nanoscience,
a section of the journal
Frontiers in Chemistry

Received: 15 April 2020

Accepted: 08 June 2020

Published: 11 August 2020

Citation:

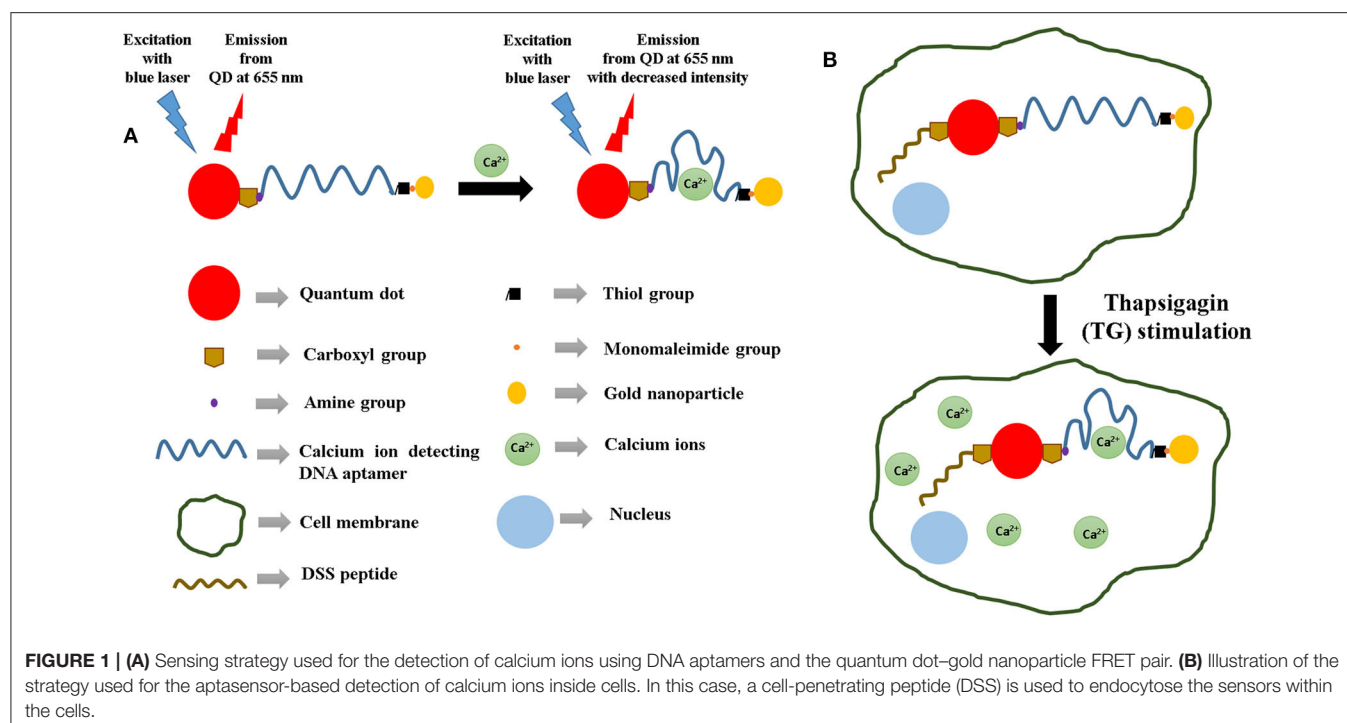
Ghosh S, Chen Y, George A, Dutta M
and Stroschio MA (2020) Fluorescence
Resonant Energy Transfer-Based
Quantum Dot Sensor for the Detection
of Calcium Ions. *Front. Chem.* 8:594.
doi: 10.3389/fchem.2020.00594

Ankireddy designed an optical sensor consisting of highly fluorescent ethylenediaminetetraacetic acid (EDTA)-CDs (ECDs) to detect Ca^{2+} in human serum with a detection limit of 77 pM (Ankireddy and Kim, 2018). Calcein- Ca^{2+} complex was used by Kim et al. to detect Ca^{2+} colorimetrically in human serum (Kim et al., 2009). Asadnia et al. used an AlGaIn/GaN transistor functionalized with poly(vinylchloride) (PVC)-based membranes as a sensing platform for Ca^{2+} (Asadnia et al., 2017). Other methods include potentiometric detection (Ganjali et al., 2005; Singh and Mehtab, 2007), microfluidic chips (Caglar et al., 2006), and ion-selective electrodes (Schefer et al., 1986). Although in the last few years the development of aptamer-based sensors for various kinds of target detection has attracted huge interest, they have been hardly explored in the field of Ca^{2+} detection. Aptasensors utilize short single-stranded DNA/RNA oligonucleotides to bind to a specific target molecule. The binding affinity can be transduced using various methods and therefore can be employed as a primary sensing component in several types of sensors. In this manuscript, we have designed a DNA aptamer-based optical sensor for the detection of calcium ions. This sensor is based on the principle of FRET, which changes the photoluminescence (PL) intensity of the semiconductor quantum dot crystal depending on its distance with the gold nanoparticle quencher (Figure 1A).

The phenomenon of fluorescence resonance energy transfer (FRET) facilitates transfer of energy from a “donor” to an “acceptor.” In the process of FRET, the efficiency is proportional to $1/\{1 + (d/d_0)^6\}$, where d is the distance between the donor and the acceptor and d_0 has been determined to be approximately

5 nm (Markvart, 2000; Yun et al., 2005; Shu et al., 2013). This distance-dependent behavior occurs due to dipole–dipole interactions between the donor and the acceptor. The effect of FRET is relatively strong when d is less than about 5 nm and starts getting weaker when d is greater than about 5 nm. This study incorporates a quantum dot as the donor and a gold nanoparticle as the acceptor. Variation of distance between the QD and the nanoparticle quencher causes a transfer of energy from the QD to the nanoparticle. When d between QD and the nanoparticle acceptor is less than 5 nm, there is less energy available in the QD to emit as photons because of a strong transfer of energy from it to the quencher. Consequently, the QD light emission decreases significantly. The sensor design involves the QD donor and the gold nanoparticle acceptor conjugated to opposite ends of a DNA aptamer, which functions as the primary sensing element here. This is because the aptamer has the ability to change its conformation on binding to the target analyte. As a result of the change in the conformational shape of the aptamer, there is a variation in d , which further causes a change in the intensity of the light emitted by the QD. Therefore, this change in QD emission can be considered as an indicator of d as well as the binding between the aptamer and the target. This phenomenon has been used as the principle of Ca^{2+} detection in this molecular beacon-based sensing platform.

In the recent years, quantum dots of various types of composition (Qi et al., 2016; Jia et al., 2020) have attracted huge attention because of their applicability in a wide variety of biomedical applications (Wegner et al., 2019; Song et al., 2020). We have successfully detected biomarker proteins like glycated albumin (Ghosh et al., 2017) and tumor necrosis factor-



alpha (Ghosh et al., 2018) using this design strategy. Apart from biomarker proteins, our group has also used this sensing strategy to detect metal ions like potassium (Wu et al., 2011; Meshik et al., 2014), lead (Brenneman et al., 2013; Meshik et al., 2014), and mercury (Brenneman et al., 2010). The innovation of this study lies in the design of the sensor, which has a cell-penetrating peptide conjugated to the aptamer-based FRET sensor. Such a sensor for the detection of calcium ions has not been reported in literature previously. Therefore, this paper also investigates the response of a cell-penetrating peptide (DSS)-conjugated aptasensor inside a cellular environment and its effectiveness in detecting intracellular Ca^{2+} (Figure 1B). Such aptasensors have the potential of being incorporated in point-of-care setups for clinical applications.

MATERIALS AND METHODS

Materials Used for Synthesis and Testing of Molecular Beacon

The calcium-detecting DNA aptamer was purchased from Biosearch Technologies (Petaluma, CA). Calcium chloride dihydrate ($\text{CaCl}_2 \cdot 2\text{H}_2\text{O}$), 2 M magnesium chloride (MgCl_2) solution, and 5 M sodium chloride (NaCl) solution were purchased from Sigma-Aldrich (St. Louis, MO) while 4.6 M potassium chloride (KCl) solution was obtained from Fischer Chemicals (Fairlawn, NJ). 1-Ethyl-3-(3-dimethylaminopropyl)-carbodiimide (EDC) and tris(2-carboxyethyl)phosphine (TCEP) were purchased from Pierce Biotechnology (Rockford, IL). Monomaleimide-functionalized nanogold particles (diameter = 1.4 nm) were obtained from Nanoprobes (Yaphank, NY). Carboxyl-coated CdSe/ZnS QDs e-flour ITK 655NC (diameter = 20 nm) was obtained from Life Technologies (Carlsbad, CA). Nanosep molecular weight cutoff (MWCO) filters of 3 and 100 k pore sizes were purchased from Pall Life Sciences (Ann Arbor, MI).

Aptamer Structure and Preparation of Aptamer Stock Solution

The calcium-detecting DNA aptamer consisted of 12 bases and had been modified with an amine group on the 5' terminal and a thiol functional group on the 3' terminal (5'-amino C6/GGGGTTTTGGGG/thiol C6 SS 3'). The aptamer was dissolved into 654 μl of tris ethylenediamine tetraethyl acetate (EDTA) buffer to obtain 100 μM aptamer stock solution in order to prevent cation-induced degradation.

Preparation of Molecular Beacon

The molecular beacon was synthesized based on the protocol reported by Ghosh et al. (2017, 2018). Briefly, 9 μl of TCEP was added to 20 μl of the 100 μM calcium-detecting aptamer. The mixture was allowed to incubate for 30 min at room temperature so that the dithiol groups in the aptamer get reduced. One vial of gold nanoparticles (6 nmol) was added to 100 ml of deionized water to form a solution, which was further added to the aptamer-TCEP mixture (quencher: aptamer = 3:1 approximately). This mixture was then incubated for 2 h at room temperature, after which it was centrifuged [Fisher Scientific accuSpin Micro (Fisher Scientific, USA)] twice at 5,000 rpm

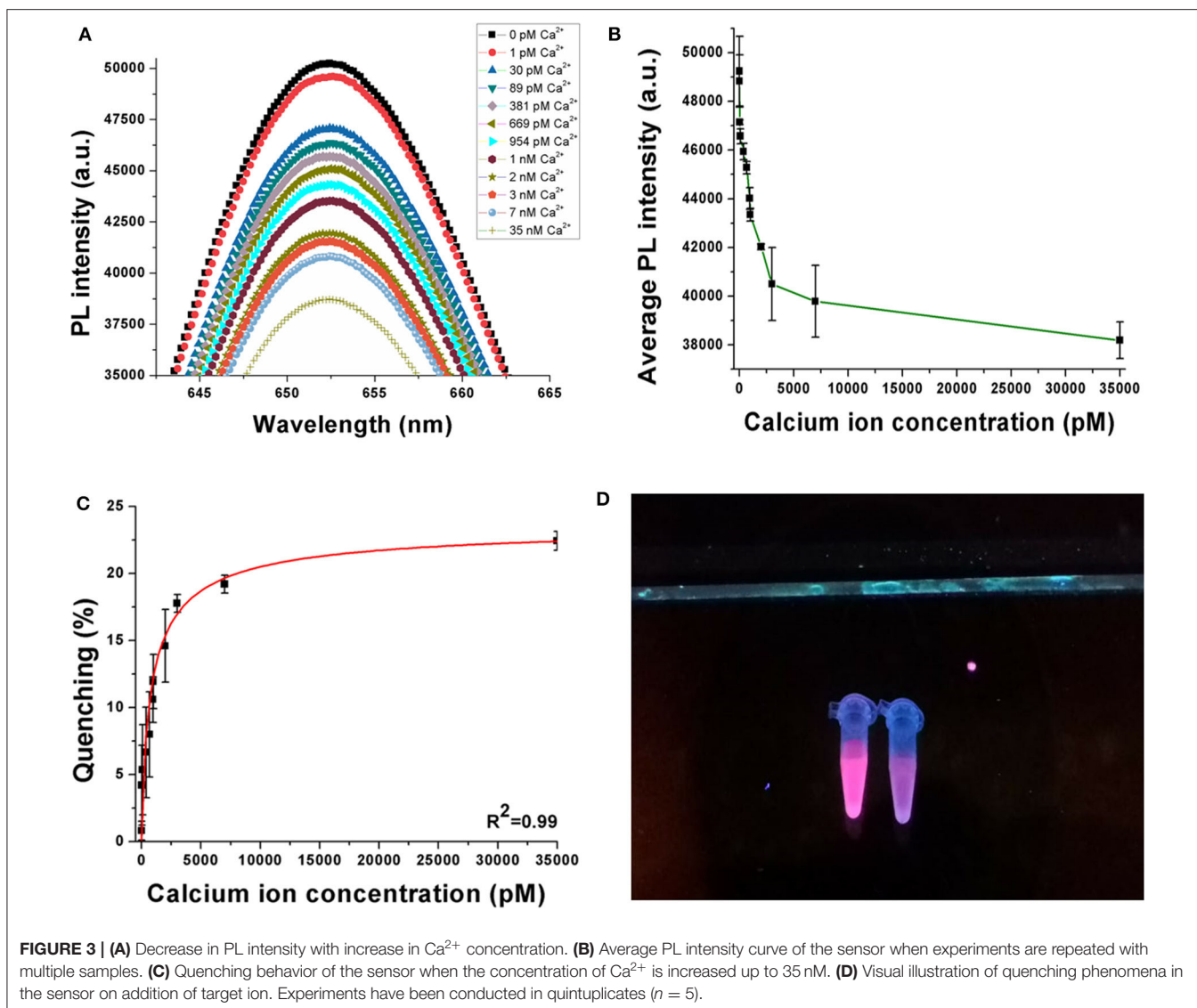
for 15 min each using a 3 k MWCO filter. This step ensured the removal of excess unbound gold nanoparticles from the mixture. The supernatant after each centrifugation was washed with 50 μl of deionized water. 13 μl of carboxylated CdSe/ZnS QDs (0.1 nmol) was mixed with 87 μl of 10 mM borate buffer (pH 7.4) to form a 100 μl QD solution, which was further added to the filtered DNA aptamer/gold nanoparticle solution in the presence of 23 μl of 4 $\mu\text{g}/\mu\text{l}$ EDC/Sulfo-NHS solution. The resulting mixture was then allowed to shake gently for 2 h at room temperature, following which the samples were centrifuged five times at 7,000 rpm for 5 min each using a 100 k MWCO filter in 50 mM borate buffer (pH 8.3). The supernatant left after each centrifugation was washed with 50 μl of the 50 mM borate buffer (pH 8.3). This resulted in the removal of unbound aptamers and EDC from the sensor solution.

Preparation of DSS Peptide-Conjugated Molecular Beacons for Calcium ion Sensing

9 μl of TCEP was added to 20 μl of the 100 μM calcium-detecting aptamer. The mixture was allowed to incubate for 30 min at room temperature so that the dithiol groups in the aptamer get reduced. One vial of gold nanoparticles (6 nmol) was added to 100 ml of deionized water to form a solution, which was further added to the aptamer-TCEP mixture (quencher: aptamer = 3:1 approximately). This mixture was then incubated for 2 h at room temperature, after which it was centrifuged (Fisher Scientific accuSpin Micro [Fisher Scientific, USA]) twice at 5,000 rpm for 15 min each using a 3 k MWCO filter. The supernatant after each centrifugation was washed with 50 μl of deionized water. 13 μl of carboxylated CdSe/ZnS QDs (0.1 nmol) was mixed with 87 μl of 10 mM borate buffer (pH 7.4) to form a 100 μl QD solution. A 10-mg/ml DSS peptide solution was prepared by adding 2.3 mg of the DSS peptide to 230 μl of deionized water. 30 μl of 4 $\mu\text{g}/\mu\text{l}$ EDC/Sulfo-NHS solution was added to a mixture of 100 μl of the QD solution, 230 μl of the DSS peptide, and the filtered calcium aptamer/gold nanoparticle solution in order to facilitate binding. Subsequently, this mixture was allowed to shake for 2 h at room temperature, following which the samples were centrifuged five times at 7,000 rpm for 5 min each using a 100 k MWCO filter in 50 mM borate buffer (pH 8.3). The supernatant obtained after each centrifugation cycle was washed with 50 μl of the 50 mM borate buffer (pH 8.3).

DNA Secondary Structure Determination

The secondary structure of the calcium ion-detecting DNA aptamer was predicted using the M-fold web server (SantaLucia, 1998; Peyret, 2000; Zuker, 2003). The predicted secondary structures were compared at different temperatures and sodium ion (Na^+) concentrations. The temperatures used are as follows: (1) 20°C: This has been considered as the room temperature and the temperature in which the optical characterization experiments were conducted (2) 37°C: This is the temperature under physiological conditions. There were three different ionic conditions considered: (1) 1.37 mM Na^+ , (2) 10 mM Na^+ , and (3) 150 mM Na^+ . These sodium ion concentrations were chosen because the Na^+ concentration for this aptasensor is approximately 1.37 mM while the concentration of Na^+ in a



loop was composed of 5 single-strand bases along with 1 closing helix. On the other hand, the hairpin loop had a closing pair at $\text{G}^1\text{-T}^7$. As shown in **Table 1**, Gibb's free energy was observed to increase with an increase in temperature while no such pattern was observed for the sodium ion concentration. The aptamer was chosen from the work reported by Miyoshi et al. (2003). They determined that the DNA aptamer underwent a structural transition from antiparallel to parallel G-quadruplex in the presence of Ca^{2+} . This characteristic was utilized to induce FRET in the proposed sensor here.

Sensitivity Determination of Sensor

A decrease in photoluminescence intensity was observed with an increase in the concentration of the calcium ions. This phenomenon is shown in **Figure 3A**, where the PL spectra indicate a decrease when Ca^{2+} is progressively added between 0 pM and 35 nM. A consistent repetition of this behavior is

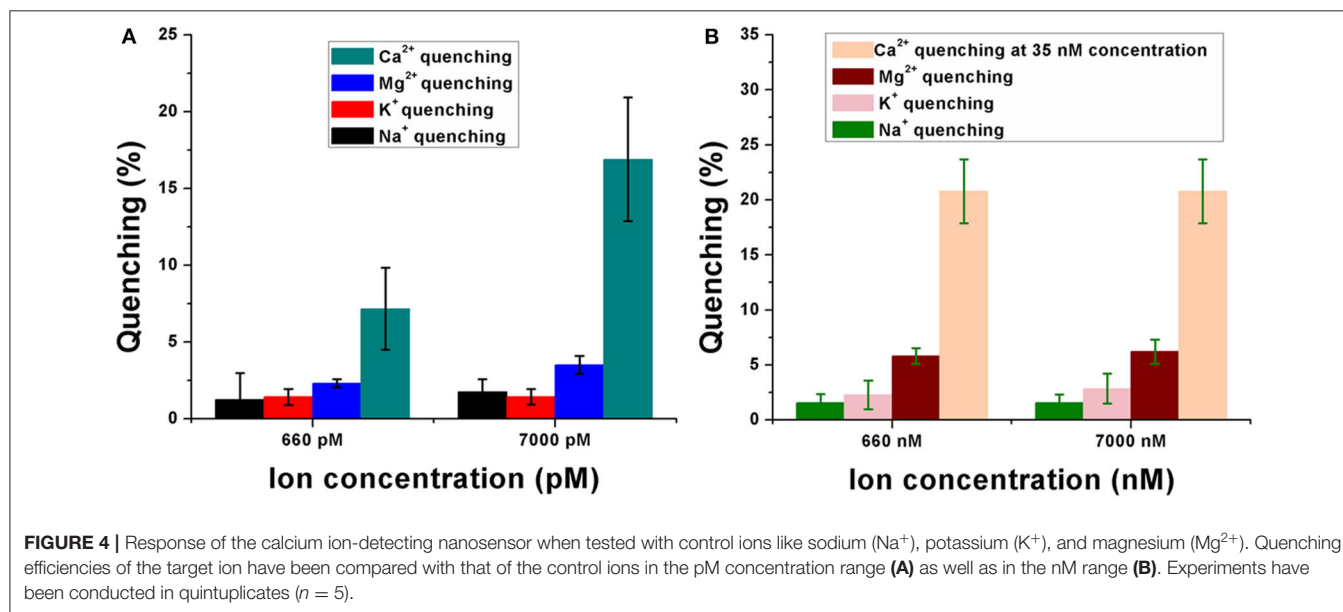
observed in **Figure 3B** when the experiments are repeated in quintuplicates ($n = 5$), where the average PL intensity decreases with an increase in the target ion concentration. **Figure 3C** shows the quenching behavior of the sensor samples. Quenching (%) has been calculated using Equation (1), where I_{blank} is the peak photoluminescence intensity before the addition of target, I_{Ca} is the peak photoluminescence intensity after the addition of Ca^{2+} , and quenching (%) is the quenching efficiency of the sensor. The quenching efficiency is an indicator of the occurrence of FRET in the sensor while detecting the target analyte (Held, 2005).

$$\text{Quenching (\%)} = \frac{(I_{\text{blank}} - I_{\text{Ca}})}{I_{\text{Ca}}} \times 100 \quad (1)$$

According to **Figure 3C**, the sensor achieves average quenching efficiencies of $4.2 \pm 2.97\%$ and $22.42 \pm 0.71\%$ at 30 pM and 35 nM Ca^{2+} concentrations, respectively. This behavior can be

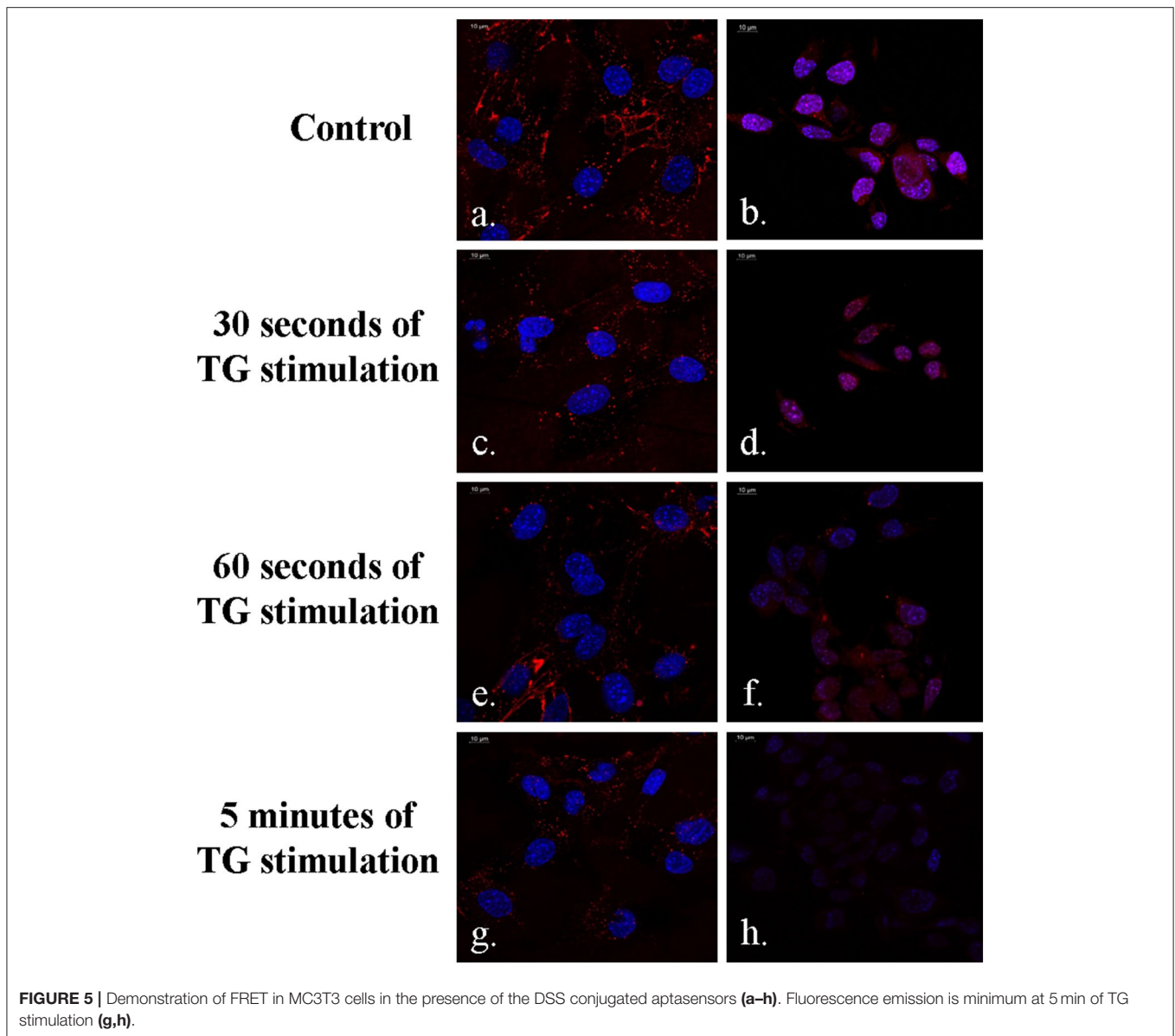
TABLE 2 | Comparative summary of various sensing platforms reported in literature for calcium ion detection.

Sensing element	Sensor type	Limit of detection	References
Calmodulin (CaM)	Fiber-optic sensor	5×10^{-8} M	Blair et al., 1994
Carboxylic polyether antibiotic A23187	Fiber-optic sensor	1×10^{-7} M	Suzuki et al., 1989
Ionophore N,N,N',N'-tetracyclohexyl-3-oxapentanediamide	Calcium-selective electrode	100 pM	Schefer et al., 1986
Sensing membrane consisting of modified merocyanine photoacid polymer and a calcium ionophore in plasticized poly(vinyl chloride)	Optical sensor	5×10^{-4} M	Johns et al., 2014
NiCO ₂ O ₄ nanostructures on 3-dimensional graphene foam	Electrochemical sensor	4.45 μ M	Wu et al., 2015
α -Furildioxime ionophore	Potentiometric sensor	1.25×10^{-7} M	Singh and Mehtab, 2007
Arsenazo III (1,8-dihydroxynaphthalene-3,6-disulfonic acid-2,7-bis[(azo-2)-phenyl arsenic acid])	Microfluidic fiber-optic sensor	2.68×10^{-5} M	Caglar et al., 2006
2-[(2-Hydroxyphenyl)imino]-1,2-diphenylethanone (HD)	Potentiometric sensor	8.0×10^{-7} M	Ganjali et al., 2005
Ethylenediaminetetraacetic acid (EDTA)-carbon dots	Optical sensor	77 pM	Ankireddy and Kim, 2018
Hexametaphosphate-capped CdS QDs	Optical sensor	4 μ M	Liu et al., 2016
4,4',4'',4'''-(3,6-Dicyanobenzene-1,2,4,5-tetrayl)tetrakis(sulfanediy))tetra-benzoic acid	Optical sensor	0.6 μ M	Chen et al., 2019
DNA aptamer	Optical sensor	3.77 pM	This work



attributed to the phenomenon of FRET, where the DNA aptamer binds to the target analyte and changes its conformation, because of which the donor (QD) and the quencher (gold nanoparticles) are driven closer to each other. Consequently, owing to a dipole–dipole interaction between the FRET pair, there is an intersystem transfer of energy from the donor to the quencher. This reduces the resulting emission from the QDs, causing a decrease in PL intensity. As the concentration of the target ion is increased, a greater number of DNA aptamers bind to them and hence a higher number of QDs participate in FRET. In this case, the DNA aptamer has been reported to have an

antiparallel G-quadruplex structure initially. Addition of Ca²⁺ induces the formation of a parallel G-quadruplex structure and finally to a G-wire structure. The parallel G-quadruplex has been found to be unstable, and hence, the aptamer rapidly transitions to the G-wire structure. The visual illustration shown in **Figure 3D** shows reduced fluorescence emission from the sample on the right compared to that on the left because the latter has no target analyte added to it while the former has 100 nM Ca²⁺ added. This further establishes the successful occurrence of FRET in the sensor on the addition of the target ion.



According to **Figure 3C**, the quenching behavior of the nanosensor follows the Hill chemical kinetics. In the Hill formalism, the quenching efficiency can be expressed as:

$$Quenching = 23.765 \times \frac{x^{0.765}}{(906.703^{0.765} + x^{0.765})} \quad (2)$$

Based on the definition of Hill's equation, 906.703 pM refers to the concentration at which half of the receptors are occupied by the target. The Hill coefficient of 0.765 is the slope of the Hill curve and also refers to negative cooperativity with respect to substrate binding. Also, from the equation theory, the average binding constant (K_D) can be estimated as 183 pM.

$$LOD = \frac{3 \times SD_0}{Sensitivity_{Ca}} \quad (3)$$

From the results obtained in Equation (3), where the SD_0 is the normalized standard deviation of the blank sensor sample while $Sensitivity_{Ca}$ is the slope of the quenching curve (**Figure 3C**), the limit of detection (LOD) was calculated to be 3.77 pM or 0.55 pg/ml (assuming molecular weight of the $CaCl_2 \cdot 2H_2O = 147$ g/mol). The LOD obtained from this sensor has been compared with several other sensing platforms for Ca^{2+} in **Table 2**.

Specificity Determination of Sensor

The sensor was observed to have significant selectivity toward Ca^{2+} when compared to the control metal ions like Na^+ , Mg^{2+} , and K^+ . These cations were specifically chosen because of their importance and abundance in the physiological system. **Figure 4** shows the quenching behavior of the control ions in the picomolar (pM) and nanomolar (nM) concentration range.

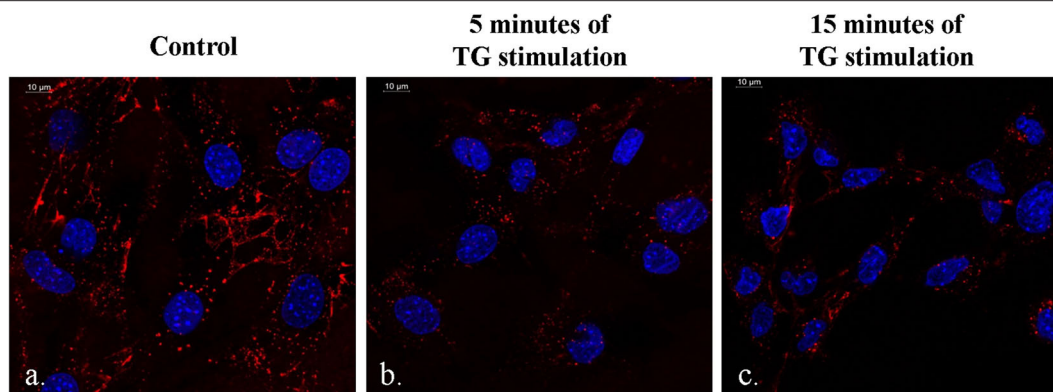


FIGURE 6 | Difference in the quantum dot emission from the DSS-conjugated molecular beacon in the presence of no TG stimulation (a), 5 min of TG stimulation (b), and 15 minutes of TG stimulation (c).

In **Figure 4A**, the quenching efficiencies have been compared between all the four ions while keeping their concentrations the same (660 pM and 7 nM). Ca^{2+} was shown to have a significantly high quenching efficiency compared to Na^+ , Mg^{2+} , and K^+ at both 660 pM and 7 nM concentrations, respectively (**Figure 4B**), indicating a high selectivity of the sensor toward calcium in the pM concentration range. A similar response was observed even when the concentration of the control ions is much higher (660 nM and 7 μM) in the sensor solution. Their quenching efficiencies were significantly lower than that of Ca^{2+} at 35 nM concentration in the sensor. This further established the specificity of the aptasensor toward Ca^{2+} .

FRET Determination in an Intracellular Environment

The DSS peptide is a cell-penetrating peptide, which is composed of amino acids like aspartic acid and serine. It allows successful endocytosis of the DNA aptamer-based molecular beacons, and this has been shown in **Figures 5a–h**, which clearly indicates the red emission from the 655 nm QDs in the DSS-conjugated molecular beacons. A higher-intensity QD emission from the MC3T3 cells was observed in **Figures 5a,b** in the absence of TG stimulation. This sample has been indicated in the figure as control. TG stimulation increases intracellular calcium release, during which a greater number of aptasensors bind to the higher concentration of Ca^{2+} , causing greater reduction in the fluorescence emission. As can be seen in **Figures 5c–h**, with an increase in the duration of TG stimulation, there was an elevation in the concentration of intracellular Ca^{2+} . This decreased the fluorescence emission from the QDs with the progression of time and resulted in successful quenching in the presence of the target ion.

It was observed that there was a slight increase in the QD emission from the DSS-conjugated molecular beacon when the duration of TG stimulation reached 15 min (**Figures 6a–c**). This phenomenon could be attributed to the structure of the DNA aptamer, which reorganizes itself to a G-wire formation. During this process, there is a possibility that the donor–quencher pair

is driven away, causing a slight decrease in quenching. However, the difference in QD emission is not very high between 5 and 15 min (**Figures 6b,c**). Additionally, the phenomenon of FRET is still evident between the control sample and the sample with 15 min of TG stimulation (**Figures 6a,c**).

CONCLUSION

This study reports a simple DNA aptamer-based optical sensor, which detects Ca^{2+} between 0 pM and 35 nM. It employs a DNA aptamer as the primary Ca^{2+} sensing element and operates on the principle of FRET. It has the ability to detect the target ion up to a lower limit of 3.77 pM. Primary advantages of this sensor lie in its ability to successfully detect Ca^{2+} in an intracellular environment when used in conjunction with a cell-penetrating peptide (DSS). Additionally, it has very low sample requirement (5 μl) and is quite flexible, i.e., the same sensing strategy can be used to detect other analytes by replacing the sensing element with a DNA aptamer specific to the analyte.

DATA AVAILABILITY STATEMENT

The original contributions presented in the study are included in the article/supplementary materials, further inquiries can be directed to the corresponding author/s.

AUTHOR CONTRIBUTIONS

MS and MD conceived and advised on the overall project idea. AG conceived the cell culture experiments. SG and YC performed the experiments and wrote the manuscript. All authors read and edited the manuscript.

FUNDING

This work was supported, in part, by the Army Research Office (subcontract FPO67468-01-PR to W911NF-18-1-0042) and the National Institutes of Health grant DE028531 (AG).

REFERENCES

- Ankireddy, S.R., and Kim, J. (2018). Chemical highly selective and sensitive detection of calcium (II) ions in human serum using novel fluorescent carbon dots. *Sensor. Actuat. B-Chem.* 255, 3425–3433. doi: 10.1016/j.snb.2017.09.172
- Asadnia, M., Myers, M., Umama-membreno, G. A., Sanders, T. M., Mishra, U. K., Nener, B. D., et al. (2017). Analytica chimica Acta Ca²⁺ detection utilising AlGaIn/GaN transistors with ion-selective polymer membranes. *Anal. Chim. Acta.* 987, 105–110. doi: 10.1016/j.aca.2017.07.066
- Asif, M.H., Nur, O., Willander, M., and Danielsson, B. (2009). Selective calcium ion detection with functionalized ZnO nanorods-extended gate MOSFET. *Biosens. Bioelectron.* 24, 3379–3382. doi: 10.1016/j.bios.2009.04.011
- Blair, T.L., Yang, S., Smith-palmer, T., and Bachas, L.G. (1994). Fiber optic sensor for Ca²⁺ based on an induced change in the conformation of the protein calmodulin. *Anal. Chem.* 66, 300–302. doi: 10.1021/ac00074a019
- Brenneman, K.L., Poduri, S., Stroschio, M.A., and Dutta, M. (2013). Optical detection of lead (II) ions using DNA-based nanosensor. *IEEE Sens. J.* 13, 1783–1786. doi: 10.1109/JSEN.2013.2241757
- Brenneman, K.L., Sen, B., Stroschio, M.A., and Dutta, M. (2010). Aptamer-based optical bionano sensor for mercury (II) ions. *Nanotechnol. Mater. Devices Conf. (NMDC), IEEE 2010*, 221–224. doi: 10.1109/NMDC.2010.5652331
- Caglar, P., Tuncel, S. A., Malcik, N., Landers, J. P., and Ferrance, J. P. (2006). A microchip sensor for calcium determination. *Anal. Bioanal. Chem.* 386, 1303–1312. doi: 10.1007/s00216-006-0776-8
- Chen, G., Zhou, Z., and Feng, H. (2019). An aggregation-induced phosphorescence probe for calcium ion-specific detection and live-cell imaging in *Arabidopsis thaliana*. *Chem. Commun.* 55, 4841–4844. doi: 10.1039/C9CC01580A
- Chung, J., Ryu, W., Kim, J., and Yoon, B. (2015). Elevated calcium after acute ischemic stroke : association with a poor short-term outcome and long-term mortality. *J. Stroke* 17, 54–59. doi: 10.5853/jos.2015.17.1.54
- Feske, S. (2007). Calcium signalling in lymphocyte activation and disease. *Nat. Rev. Immunol.* 7, 690–702. doi: 10.1038/nri2152
- Ganjali, M. R., Zamani, H. A., Norouzi, P., Adib, M., and Accedy, M. (2005). Novel calcium sensor based on [2-(2-Hydroxyphenyl)amino]-1, 2-diphenylethanone. *Acta Chim. Slov.* 52, 309–316. Available online at: <http://acta-arhiv.chem-soc.si/52/52-3-309.pdf>
- Ghosh, S., Datta, D., Cheema, M., Dutta, M., and Stroschio, M. A. (2017). Aptasensor based optical detection of glycated albumin for diabetes mellitus diagnosis. *Nanotechnology* 28:aa893a. doi: 10.1088/1361-6528/aa893a
- Ghosh, S., Datta, D., Chaudhry, S., Dutta, M., and Stroschio, M. A. (2018). Rapid detection of tumor necrosis factor-alpha using quantum dot based optical aptasensor. *IEEE Trans. Nanobiosci.* 17, 417–423. doi: 10.1109/TNB.2018.2852261
- Held, P. (2005). *An Introduction to Fluorescence Resonance Energy Transfer (FRET) Technology and its Application in Bioscience*, BioTek. Available online at: <https://www.biotek.com/resources/white-papers/an-introduction-to-fluorescence-resonance-energy-transfer-fret-technology-and-its-application-in-bioscience/>
- Jia, J., Sun, Y., Zhang, Y., Liu, Q., Cao, J., Huang, G., et al. (2020). Facile and efficient fabrication of bandgap tunable carbon quantum dots derived from anthracite and their photoluminescence properties. *Front. Chem.* 8:123. doi: 10.3389/fchem.2020.00123
- Johns, V. K., Patel, P. K., Hassett, S., Calvo-marzal, P., Qin, Y., and Chumbimunitorres, K. Y. (2014). Visible light activated ion sensing using a photoacid polymer for calcium detection. *Anal. Chem.* 86, 23–26. doi: 10.1021/ac500956j
- Kim, S., Park, J. W., Kim, D., Kim, D., Lee, I., and Jon, S. (2009). Bioinspired colorimetric detection of calcium (II) ions in serum using calsequestrin-functionalized gold nanoparticles. *Angew. Chem. Int. Ed.* 48, 4138–4141. doi: 10.1002/anie.200900071
- Liu, S., Wang, H., Cheng, Z., and Liu, H. (2016). Hexametaphosphate-capped quantum dots as fluorescent probes for detection of calcium ion and fluoride. *Sensor. Actuat. B-Chem.* 232, 306–312. doi: 10.1016/j.snb.2016.03.077
- Lodish, H., Berk, A., Zipursky, S. L., Matsudaira, P., Baltimore, D., and Darnell, J. (2000). *Intracellular Ion Environment and Membrane Electric Potential*. *Mol. Cell Biol. 4th Edn.* New York, NY: WH Freeman.
- Markvart, T. (2000). Light harvesting for quantum solar energy conversion. *Prog. Quantum. Electron.* 24, 107–186. doi: 10.1016/S0079-6727(00)00003-3
- Meshik, X., Xu, K., Dutta, M., and Stroschio, M. A. (2014). Optical detection of lead and potassium ions using a quantum-dot-based aptamer nanosensor. *IEEE Trans. Nanobiosci.* 13, 161–164. doi: 10.1109/TNB.2014.2317315
- Miyoshi, D., Nakao, A., and Sugimoto, N. (2003). Structural transition from antiparallel to parallel G-quadruplex of d (G 4 T 4 G 4) induced by Ca²⁺. *Nucleic Acids Res.* 31, 8–9. doi: 10.1093/nar/gkg211
- Peyret, N. (2000). *Prediction of Nucleic Acid Hybridization: Parameters and Algorithms*. Detroit, MI: Wayne State University Detroit.
- Qi, K., Wang, Y., Wang, R., Wu, D., and Li, G.D. (2016). Facile synthesis of homogeneous CuInS₂ quantum dots with tunable near-infrared emission. *J. Mater. Chem. C.* 4, 1895–1899. doi: 10.1039/C5TC04232A
- Russell, J. T. (2011). Imaging calcium signals *in vivo*: a powerful tool in physiology and pharmacology. *Br. J. Pharmacol.* 163, 1605–1625. doi: 10.1111/j.1476-5381.2010.00988.x
- SantaLucia, J. (1998). A unified view of polymer, dumbbell, and oligonucleotide DNA nearest-neighbor thermodynamics. *Proc. Natl. Acad. Sci. U.S.A.* 95, 1460–1465. doi: 10.1073/pnas.95.4.1460
- Schefer, U., Ammann, D., Pretsch, E., Oesch, U., and Simon, W. (1986). Neutral carrier based Ca²⁺-selective electrode with detection limit in the sub-nanomolar range. *Anal. Chem.* 58, 2282–2285. doi: 10.1021/ac00124a036
- Shu, G. W., Chiu, C. H., Huang, L. T., Lin, T. N., Yang, C. C., Wang, J. S., et al. (2013). Efficient energy transfer from InGaIn quantum wells to Ag nanoparticles. *Phys. Chem. Chem. Phys.* 15, 3618–3362. doi: 10.1039/c3cp43894e
- Singh, A. K., and Mehtab, S. (2007). Calcium (II) -selective potentiometric sensor based on-furildioxime as neutral carrier, *Sensor. Actuat. B-Chem.* 123, 429–436. doi: 10.1016/j.snb.2006.09.016
- Song, C., Haoyue, L., Xiaogang, L., Zhijia, P., Lingdong, W., Xiaosheng, T., et al. (2020). Study on AgInZnS-graphene oxide non-toxic quantum dots for biomedical sensing. *Front. Chem.* 8:331. doi: 10.3389/fchem.2020.00331
- Suzuki, K., Tohda, K., Tanda, Y., Ohzora, H., Nishihama, S., and Inoue, H. (1989). Fiber-optic magnesium and calcium ion sensor based. *Anal. Chem.* 384, 382–384. doi: 10.1021/ac00179a018
- Wegner, K. D., Dussert, F., Truffier-Boutry, D., Benayad, A., Beal, D., Mattered, L., et al. (2019). Influence of the core/shell structure of indium phosphide based quantum dots on their photostability and cytotoxicity. *Front. Chem.* 7:466. doi: 10.3389/fchem.2019.00466
- Wojda, U., Salinska, E., and Kuznicki, J. (2008). Calcium ions in neuronal degeneration. *Critical Rev.* 60, 575–590. doi: 10.1002/iub.91
- Wu, T.-C., Biswas, S., Dutta, M., and Stroschio, M. A. (2011). Quantum-dot-based aptamer beacon for the detection of potassium ions. *IEEE Trans. Nanotechnol.* 10, 991–995. doi: 10.1109/TNANO.2010.2091967
- Wu, M., Meng, S., Wang, Q., Si, W., Huang, W., and Dong, X. (2015). Nickel – cobalt oxide decorated three-dimensional graphene as an enzyme mimic for glucose and calcium detection. *ACS Appl. Mater. Interfaces.* 7, 3–8. doi: 10.1021/acsami.5b06299
- Yun, C. S., Javier, A., Jennings, T., Fisher, M., Hira, S., Peterson, S., et al. (2005). Nanometal surface energy transfer in optical rulers, breaking the FRET barrier. *J. Am. Chem. Soc.* 127, 3115–3119. doi: 10.1021/ja043940i
- Zuker, M. (2003). Mfold web server for nucleic acid folding and hybridization prediction. *Nucleic Acids Res.* 31, 3406–3415. doi: 10.1093/nar/gkg595

Conflict of Interest: The authors declare that the research was conducted in the absence of any commercial or financial relationships that could be construed as a potential conflict of interest.

Copyright © 2020 Ghosh, Chen, George, Dutta and Stroschio. This is an open-access article distributed under the terms of the Creative Commons Attribution License (CC BY). The use, distribution or reproduction in other forums is permitted, provided the original author(s) and the copyright owner(s) are credited and that the original publication in this journal is cited, in accordance with accepted academic practice. No use, distribution or reproduction is permitted which does not comply with these terms.



Formulation of Mesoporous Silica Nanoparticles for Controlled Release of Antimicrobials for Stone Preventive Conservation

Alessandro Presentato¹, Francesco Armetta¹, Alberto Spinella²,
Delia Francesca Chillura Martino^{1,2}, Rosa Alduina^{1*} and Maria Luisa Saladino^{1*}

¹ Department of Biological, Chemical, and Pharmaceutical Sciences and Technology (STEBICEF), University of Palermo, Palermo, Italy, ² Advanced Technologies Network (ATeN) Center, University of Palermo, Palermo, Italy

OPEN ACCESS

Edited by:

Kezhen Qi,
Shenyang Normal University, China

Reviewed by:

Saurabh Kulshrestha,
Shoolini University of Biotechnology
and Management Sciences, India
Zafar Hussain Ibupoto,
University of Sindh, Pakistan

*Correspondence:

Rosa Alduina
valeria.alduina@unipa.it
Maria Luisa Saladino
marialuisa.saladino@unipa.it

Specialty section:

This article was submitted to
Nanoscience,
a section of the journal
Frontiers in Chemistry

Received: 25 April 2020

Accepted: 07 July 2020

Published: 21 August 2020

Citation:

Presentato A, Armetta F, Spinella A,
Chillura Martino DF, Alduina R and
Saladino ML (2020) Formulation of
Mesoporous Silica Nanoparticles for
Controlled Release of Antimicrobials
for Stone Preventive Conservation.
Front. Chem. 8:699.
doi: 10.3389/fchem.2020.00699

The biotic deterioration of artifacts of archaeological and artistic interest mostly relies on the action of microorganisms capable of thriving under the most disparate environmental conditions. Thus, to attenuate biodeterioration phenomena, biocides can be used by the restorers to prevent or slow down the microbial growth. However, several factors such as biocide half-life, its wash-out because of environmental conditions, and its limited time of action make necessary its application repeatedly, leading to negative economic implications. Sound and successful treatments are represented by controlled release systems (CRSs) based on porous materials. Here, we report on the design and development of a CRS system based on mesoporous silica nanoparticles (MSNs), as a carrier, and loaded with a biocide. MSNs, with a diameter of 55 nm and cylindrical pores of ca. 3–8 nm arranged as parallel arrays concerning the NP diameter, and with 422 m²/g of specific surface area were synthesized by the sol-gel method assisted by oil in water emulsion. Biocide loading and release were carried out in water and monitored by UV-Vis Spectroscopy; in addition, microbiological assay was performed using as control the MCM-41 mesoporous silica loaded with the same biocide. The role of specific supramolecular interaction in regulating the release is discussed. Further, we demonstrated that this innovative formulation was useful in inhibiting the *in vitro* growth of *Kocuria rhizophila*, an environmental Gram-positive bacterial strain. Besides, the CRS here prepared reduced the bacterial biomass contaminating a real case study (i.e., stone derived from the Santa Margherita cave located in Sicily, Italy), after several months of treatment thus opening for innovative treatments of deteriorated stone artifacts.

Keywords: mesoporous silica nanoparticles, controlled release systems, condensation in emulsion, biocides, biodeterioration, stone conservation, cultural heritage

INTRODUCTION

Mesoporous silica nanoparticles (MSNs) are one of the most interesting recent findings in the field of materials chemistry (Farjadian et al., 2019). Thanks to the high percentage of hydroxyl groups in the inner walls of the pores and the high thermal and chemical stability and biocompatibility, MSNs have been used as nanoreactors for catalytic applications (Zhu et al., 2019)

and as controlled release systems (CRSs) in the biological medicine (Slowing et al., 2008; Niu et al., 2014; Niculescu, 2020). Furthermore, MSNs have a high adsorption capacity guaranteed by the high value of pore volume and surface area, being their surface properties easily modifiable. Other interesting features of MSNs are their inert and biodegradable nature (Barbé et al., 2004; Lu et al., 2007; Trewyn et al., 2008; Lin and Haynes, 2009). As far as the drug delivery issue is concerned, MSNs are considered very promising because of their capacity in loading larger amounts of drugs as compared to conventional mesoporous materials (Du et al., 2013; Ma et al., 2013; Niu et al., 2014; Lu et al., 2015; Bernardos et al., 2019).

The development of alternative strategies based on either metal or metal-oxide nanoparticles (Russo et al., 2015, 2016; Qi et al., 2017, 2019, 2020; Cusimano et al., 2020; Yaqoob et al., 2020), as well as mesoporous ones (Cavallaro et al., 2018) and natural biocides (Fidanza and Caneva, 2019) has gained momentum mainly when it comes to the prevention of manufacture goods belonging to cultural heritage from chemical- or bio-deterioration phenomena (Artesani et al., 2020; David et al., 2020). Particularly, CRSs based on mesoporous materials have been developed to protect both environment and artifacts of archaeological and artistic interest (Popat et al., 2012; Ruggiero et al., 2019). Recent studies showed that the mesoporous silica can release biocides “on-demand” (Böttcher et al., 1999; Chan et al., 2017; Ruggiero et al., 2018). In this regard, the long-term actions of MSNs on paper (Michaelsen et al., 2013), woods (Liu et al., 2001), and stones (Allsopp et al., 2004; Eyssautier-Chuine et al., 2018) have been already assessed.

The development of CRSs of biocide for the preventive conservation of artifacts derives from the need to control the deteriorative action of microorganisms on them. Indeed, bacteria and fungi contaminating artifacts can determine the rise of detrimental phenomena of the work of arts themselves, as microorganisms can release a vast array of metabolites (i.e., oxalic, citric, and sulphuric acids), extracellular enzymes, biological pigments, carotenoids, to name a few (Warscheid and Braams, 2000; Urzi, 2004). Thus, the interaction occurring between these biotic compounds and artifacts can lead to physicochemical and aesthetic alterations of the latter, demanding their treatment with expensive procedures. During a restoration work aimed to restrain the action of deteriorative microorganisms, the restorers apply products whose efficacy would depend on the species to be contained, the artifacts' features, as well as physicochemical properties of the chosen product and its mode of application. Nowadays, most biocides feature high toxicity against both environment and operator, resulting in potentially noxious for human health especially in the case of museum environments. In this context, CRSs are of utmost interest as they could reduce the number of treatments over time concurrently guaranteeing the artifact protection.

With all this in mind, here, a new system consisting of mesoporous silica nanoparticles (MSNs) for the controlled release of biocides, long-term preventing and preserving both archaeological sites and museum environments from biodeterioration phenomena, is proposed. Specifically, the CRS was designed for the preventive conservation of stone material.

MSNs were prepared through the method of condensation in an emulsion and characterized by several physicochemical and biological analyses. Preventol RI-80 is a commercial biocide commonly used by restorers constituted by a mixture of quaternary ammonium salts, where the main component is benzyldimethyltridecylazanium chloride. In this study, it was chosen as a biocide, since it is active against a wide variety of fungi, algae, and bacteria contaminating stone materials, plasters, wood, and ceramics. Preventol RI-80 loading on and its release from MSNs were performed in water; further, the efficiency of the best CRS obtained was compared to that of mesoporous silica MCM-41 (Dresler et al., 2017). The validity of this formulation was supported by the application of the best CRS, in terms of the biocide release performance, on a real case study consisting of stone fragments deriving from a cave (named as *Grotta di Santa Margherita*) located in Castellammare del Golfo (Trapani, Italy). The ability of the system to locally kill microorganisms once applied on the stone materials was evaluated over 12 months, evaluating the microbial proliferation every 3 months, strengthening the suitable application of such material for the prevention of work of arts.

MATERIALS AND METHODS

Materials

Tetraethyl ortosilicate (TEOS, $d = 0.934$ g/mL 99%, Aldrich), cetyl-trymethyl ammonium bromide (CTAB 98%, Aldrich), ethanol ($d = 0.789$ g/mL $\geq 99.8\%$, Fluka), *n*-heptane ($d = 0.688$ g/mL 99%, Aldrich), ammonium hydroxide ($d = 0.90$ g/mL, 30%, Carlo Erba), and hydrochloric acid (37%, Aldrich) were used without further purification. The synthesis of the MCM-41 was performed as reported elsewhere (Caponetti et al., 2010; Saladino et al., 2011; Lavall et al., 2012). MCM-41 had highly ordered hexagonal structures with toroidal particles of few microns. The specific surface area S_{BET} and the average pore size w_{BJH} were 931 m²/g and 2.4 nm, respectively. Preventol RI-80 was supplied by C.T.S. s.r.l. (Altavilla Vicentina (VI), Italy), being no information provided about the purity of the formulation. Aqueous solutions were prepared by weight, using conductivity grade water having 1.5 μ S/m of conductivity.

MSNs Synthesis

MSNs were synthesized following the emulsion-condensation route reported by Cao et al. (2016), which involves the hydrolysis of alkoxysilanes followed by the reaction of polycondensation of the resulting silanol on a template consisting of CTAB surfactant molecules (Ma et al., 2011; Xu et al., 2014; Cao et al., 2016; Farjadian et al., 2019; Zhu et al., 2019). The oil phase (*n*-heptane) determines the size of the nanopores by swelling the micelles and regulating the rate of hydrolysis of alkoxysilanes through the partitioning of the latter among the oil and aqueous phases. Besides, a stabilization of the emulsion either by the surfactant or the formed silica nanoparticles could occur. First, in a Nalgene bottle 70 mL of distilled water, 0.80 mL of ammonium hydroxide, 15 mL of *n*-heptane, 5 mL of ethanol and 0.5 g of CTAB were mixed at room temperature. Once the mixture became homogeneous, 2.6 mL of TEOS were added. The mixture

was stirred at room temperature for 4 h. To block the base-catalyzed reaction, 1.0 mL of hydrochloric acid was added to the formed suspension, which was then allowed to stand for 24 h. The obtained product was thus filtered, washed with a mixture 1:1 of water and ethanol to remove CTAB and ammonium chloride formed as byproduct and dried at 60°C for about 72 h, until the weight of the obtained white powder was constant.

Characterization Techniques

X-ray Diffraction (XRD) patterns were obtained using Philips PW 1050/39 diffractometer in Bragg–Brentano geometry (source Cu K α , $\lambda = 1.54056 \text{ \AA}$, voltage 40 kV, current 30 mA) in the range 2–60°, steps of 0.05° and acquisition time 5 s/step.

The FT-IR spectra were acquired by using FT-IR Bruker Vertex 70 v spectrophotometer with Platinum ATR, with 2 cm⁻¹ steps and 60 scans in the acquisition range 4,000–400 cm⁻¹. The measure was carried out at 2 hPa. A base line correction of the scattering was made.

NMR spectra were acquired by using a Bruker Advance II 400 spectrometer operating at the frequency of 400.15, 100.62, and 79.49 MHz for the ¹H, ¹³C, and ²⁹Si nuclide, respectively. All samples were placed in 4 mm zirconia rotors equipped with Kel-f caps. ¹³C CPMAS NMR spectrum was acquired with a MAS rotation speed of 7 kHz, at a temperature of 300 K using a 90° pulse on ¹H of 4.5 μ s, a contact time during cross polarization of 2 ms, a delay time of 3 s and 400 scans. ²⁹Si CPMAS NMR spectrum was acquired with a MAS rotation speed of 5 kHz, at a temperature of 300 K using a 90° pulse on ¹H of 4.5 μ s, a contact time during cross polarization of 8 ms, a delay time of 5 s and 400 scans. Hartman-Hahn's conditions were optimized by standard samples of adamantane and of tetramethylsilane for ¹³C and ²⁹Si nuclei, respectively. The two compounds were also used as external chemical shift reference.

Transmission Electron Microscopy (TEM) investigation was performed by using a JEOL-2100 microscope operating at an accelerating voltage of 200 kV. The powders were dispersed in water and deposited on a copper grid. The observation of the samples was performed after complete evaporation of the solvent. The particle size distribution was determined by linear intercept method based on the TEM micrographs (Dai et al., 2018).

The N₂ adsorption and desorption isotherms were recorded at 77 K using a Quantachrome Nova 2200 Multi-Station High Speed Gas Sorption Analyzer after degassing of the samples for 24 h at 23°C in the degas station. Adsorbed nitrogen volumes were normalized to the standard temperature and pressure. The specific surface area (S_{BET}) was calculated according to the standard BET method in the relative absorption pressure (P/P_0) range from 0.045 to 0.250 (Brunauer et al., 1938). The total pore volume (V_t) was obtained from the nitrogen amount adsorbed in correspondence of P/P_0 equal to 0.99. The cylinder diameter size (w_{BJH}) was calculated by the BJH method (Kruk et al., 1999).

UV–vis spectra were recorded in the range 200–500 nm using a double beam Beckman DU-800 spectrophotometer with a resolution of 1.0 nm. To avoid the effect of instrumental errors and of particle diffusion, the value of absorbance at 500 nm was subtracted to each spectrum. A typical spectrum of the Preventol RI-80 is reported in **Figure S1**.

Biological Test

The efficiency of the CRS was evaluated by means of disc diffusion antibiotic sensitivity assay, as reported elsewhere (Giardina et al., 2010; Ciabocco et al., 2018), using the Gram-positive bacterial strain *Kocuria rhizophila* ATCC® 9341™ (*K. rhizophila*) since this species is frequently found on works of art and the stone materials (Warscheid, 2003; Randazzo et al., 2015). Briefly, a dense bacterial suspension ($\sim 10^7$ cells) was prepared in the Luria Bertani growth medium (hereinafter named as LB and composed of 10 g/L of sodium chloride, 5 g/L of yeast extract, and 10 g/L of tryptone) and spread onto LB-agar—20% w/v of bacteriological agar—plates. Aqueous suspension aliquots containing different amounts of MSNs and biocides were directly spotted on sterile paper discs (6 mm diameter), which were deposited onto the bacterial overlay present in the LB-agar plate, as previously described (Rubino et al., 2018a). After overnight incubation at 30°C, the diameter of the growth inhibition halos was registered. The antimicrobial activity was calculated as a mean of three replicates and standard deviations were calculated.

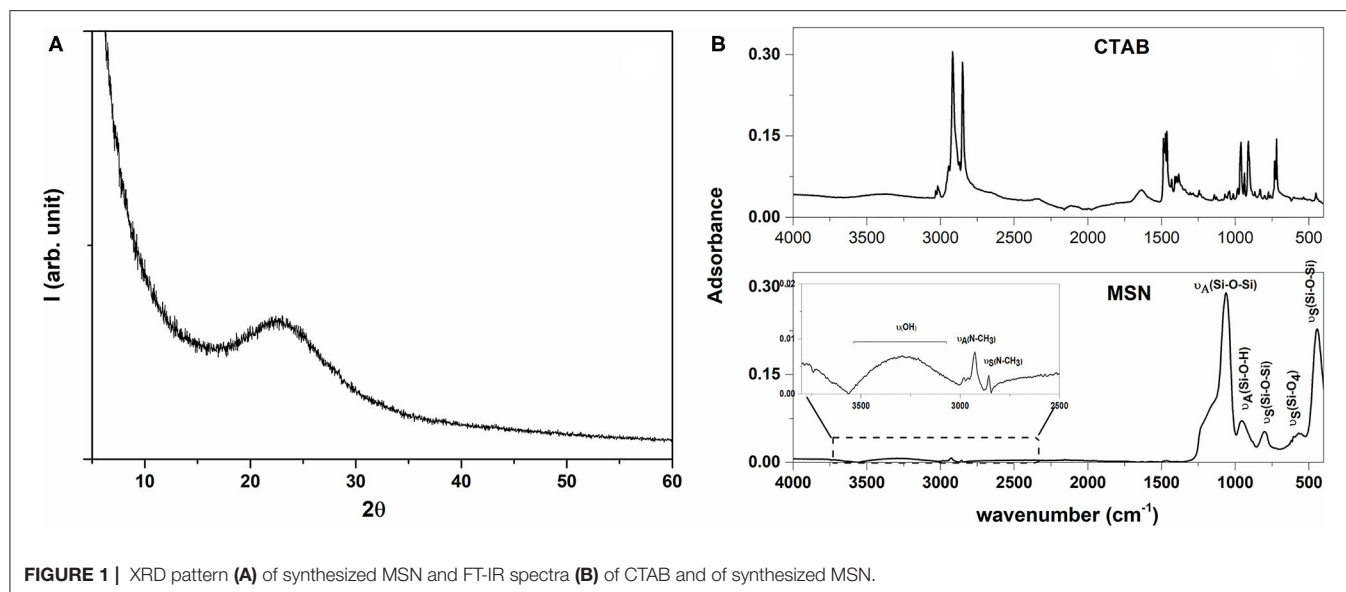
The release of biocides from the loaded MSN was followed over time (after 1, 3, 6, 24, and 48 h) by collecting aliquots of the solution in which the CRS was immersed. The aliquots of solution were directly spotted on sterile paper discs and tested as aforementioned to detect antibacterial activity. Twenty microliters of Preventol RI-80 and the dispersions of the two mesoporous materials (0.1_{w/v}% MSN and 0.1%_{w/v} MCM-41) were tested as controls.

To test the performance of the CRS based on MSNs loaded with Preventol RI-80, total viable bacterial count was measured, as previously described (Piacenza et al., 2018; Poma et al., 2019). Briefly, samples of 1 g of both untreated and treated stones were vigorously vortexed in 10 mL of LB to detach bacteria from the stone material. Serial dilutions of these suspensions were prepared using LB, being 100 μ l of each dilution spread onto LB-agar to allow bacterial growth. Plates were incubated at 30°C until colonies appeared. Data are reported as mean ($n = 3$) of the colony forming units (CFU) per g of stone and standard deviations were calculated.

After 1 year, the metagenomic DNA was extracted from these samples using the method reported in Presentato et al. (2020). PCR was carried out with primers and conditions used in Arizza et al. (2019).

Loading Procedure and Experiments of Release

The biocide loading was performed following the procedure reported elsewhere (Saladino et al., 2016; Dresler et al., 2017; Rubino et al., 2018b). One milligram/millilitre of the mesoporous powder was immersed in the aqueous solutions containing different biocide concentrations (range of the nominal concentration 0.012–0.64_{v/v}%) for 24 h under continuous magnetic stirring in the dark. The values of concentration were chosen based on the restorer's suggestions. The suspension was centrifuged at appropriate RCF for the separation of the powder. Then, the supernatant was carefully removed and the loaded samples dried under vacuum



overnight. The loaded MSNs were white and similar to those unloaded. The yield of loading—which was evaluated by UV-vis spectroscopy—was of 100% for all systems. The loaded MSN are called Preventol RI-80 x @NP SiO₂ where x is the initial concentration ($v/v\%$) of the biocide in which MSNs were immersed. Preventol RI-80 loading within the MSNs was successful, as highlighted by the decreased MSN specific surface area (41 m²/g) as compared to that of the unloaded material (422.8 m²/g).

The following procedure was carried out to study the release of biocides from the MSN: 20 mg of each biocide-loaded MSN were placed in a closed 3.5 kDa dialysis membrane tube (Spectra/Por 3 Dialysis membrane) and then in a Nalgene-flask filled with 20 mL of water. The flask was kept at room temperature under continuous shaking during all the experiments. The UV-vis spectra were registered on 2.5 mL of solution collected at the scheduled time (1, 3, 6, 24, and 48 h). The release profile was obtained plotting the values of concentration (obtained by Lambert Beer's law) vs. time and evaluating the antibacterial activity by disc diffusion antibiotic sensitivity assays, as described above. Each experiment was performed in triplicate.

RESULTS AND DISCUSSION

MSNs Characterization

The physicochemical characterization of the synthesized MSNs was performed to ascertain the goodness of the material used as a carrier in this study. MSNs showed a broad band centered at 22° in the XRD pattern (Figure 1A), which is ascribable to a silica amorphous material (Dubey et al., 2015; Jiang et al., 2019). The ATR spectrum (Figure 1B) of the sample did exhibit the trademark signs of silica (Mourhly et al., 2015). The most intense absorption bands, in the range between 1,000 and 1,300 cm⁻¹

are due to the asymmetrical stretching of the Si-O-Si groups (i.e., 1,060 and 1,232 cm⁻¹). The signal at 966 cm⁻¹ is due to the Si-O symmetric stretching, as well as the ones at 797 and 451 cm⁻¹ (Mourhly et al., 2015). The broad band centered at 3,216 cm⁻¹ (highlighted in the inset of the Figure 1B) is due to the stretching of O-H groups, which are indicative of the presence of hydrogen bonds resultant from the interaction occurring between the silanol groups (Si-OH) and the adsorbed water molecules. Accordingly, the signal observed in the ²⁹Si CP-MAS NMR spectrum (Figure 2) is due to the convolution of three peaks. The first peak (i.e., Q2; centered at ca. 90 ppm) was due to the geminal silanols, the second peak (i.e., Q3; centered at 100 ppm) highlighted silicon atoms bearing one hydroxyl group, while Q4 peak (centered at around 109 ppm) is due to each Si atom, which is linked over oxygen atoms with 4 Si neighbors (Saladino et al., 2008), which, overall, are contributions of mesoporous silica materials. Other than silica signals, IR spectra revealed vibration bands attributable to CTAB (Viana et al., 2012), as it is evident by comparing the spectrum of the MSN with that of CTAB (upper part of the Figure 1B). The signals falling between 1,250 and 1,500 cm⁻¹ were due to the bending vibrational modes of CH₂ groups, while those at 2,920 and 2,848 cm⁻¹ were due to the asymmetric and symmetric stretching of the methyl and methylene groups. CTAB signals were also present in the ¹³C CPMAS NMR spectrum (Figure 2). The resonance of the N-CH₂ and N-CH₃ groups was visible at 68 and 58 ppm respectively, while the strong resonance at 30 ppm derived from the methylene chain. Finally, the signals of the CH₂ and CH₃ end groups of the CTAB aliphatic chain were clearly visible at 27 and 23 ppm (Xu et al., 2014). These findings evidenced that the CTAB was still present in the material, although several washing steps of MSNs were performed. Indeed, since the bands of ¹³C nuclei were broad, it is reasonable to assert that the mobility of the molecule was low, likely indicating that the residual CTAB was located

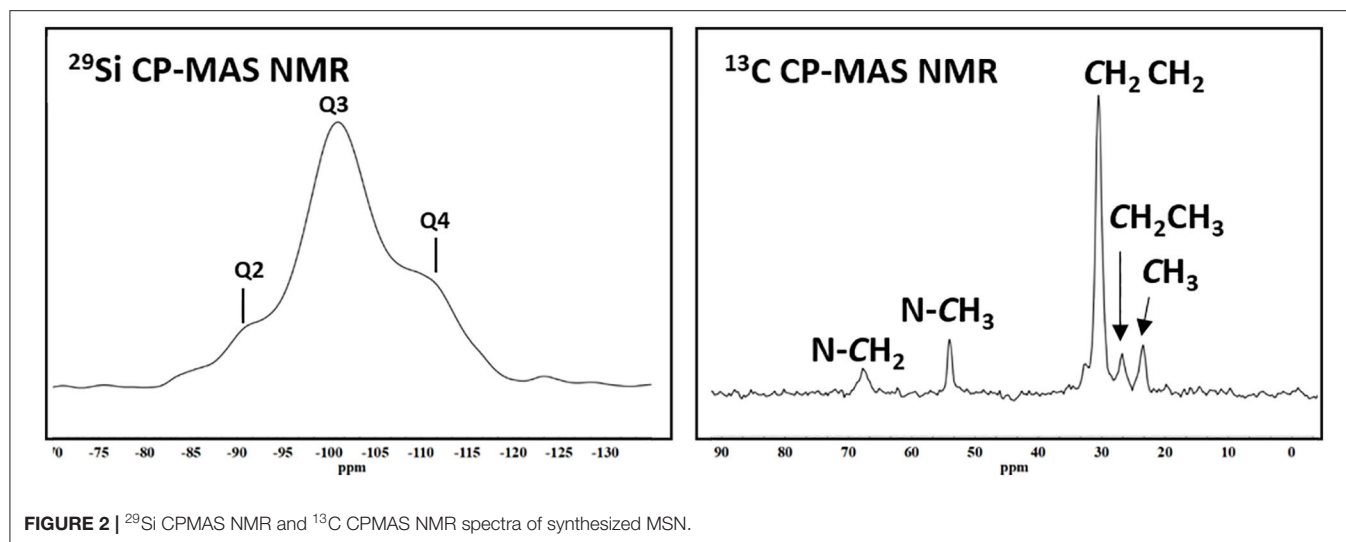


FIGURE 2 | ^{29}Si CP-MAS NMR and ^{13}C CP-MAS NMR spectra of synthesized MSN.

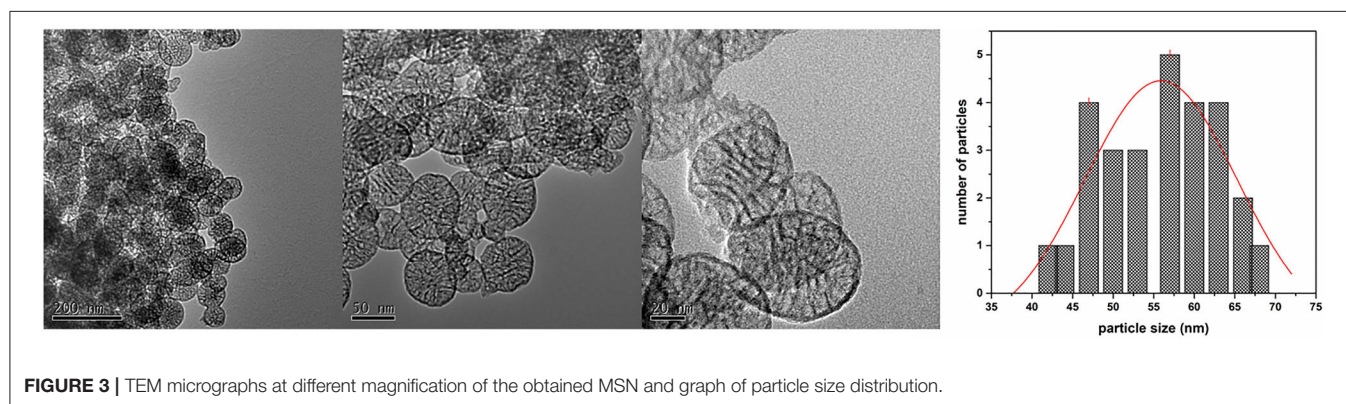


FIGURE 3 | TEM micrographs at different magnification of the obtained MSN and graph of particle size distribution.

within the pores of the mesoporous structure (Xu et al., 2014), therefore explaining the reason why it did not remove during the washing steps.

The isotherms of the sample were of Type IV-isotherm, and the hysteresis-type E of “ink-bottle” shape (Figure S2), according to IUPAC classification (Sing et al., 2008; Kraveva et al., 2011). The specific surface area, pore width, and the total pore volume of the synthesized MSN were $422 \pm 8 \text{ m}^2/\text{g}$, $3.7 \pm 0.1 \text{ nm}$, and $0.90 \pm 0.02 \text{ cm}^3/\text{g}$, respectively. The observed high values of specific surface area are in line with those reported elsewhere (Nandiyanto et al., 2009), being also an indication of the mesoporous nature of the obtained silica, which can be used as a carrier because it should load high amount of biocide.

Some of the MSN's TEM micrographs at different magnification are reported in Figure 3 together with its size distribution, highlighting how the sample was composed of spherical nanoparticles of $55 \pm 10 \text{ nm}$ (Figure 3), having also cylindrical pores of ca. three to eight nanometers, which were arranged as parallel arrays concerning the NP diameter. This morphology of MSNs is in good agreement with that of mesoporous nanoparticles investigated elsewhere (Slowing et al., 2008; Cao et al., 2016).

Maintenance of the Antibacterial Activity of Preventol RI-80 After Loading

Microbiological assays using decreasing percentages (0.2–0.0002 v/v%) of Preventol RI-80 demonstrated that 0.0002 v/v% was sufficient to inhibit the growth of *K. rhizophila* (data not shown). Also, the maintenance of the antibacterial activity of the MSN system differently loaded with Preventol RI-80 was compared to that of MCM-41. Microbiological assays showed a large inhibition halo around Preventol RI-80 0.2@MSN than Preventol RI-80 0.1@MSN. Differently, 0.2% of Preventol RI-80 loaded on MCM-41 barely inhibited the bacterial growth, while MCM-41 carrying 0.1% Preventol RI-80 did not exert any antibacterial effect (Figure 4A). This finding demonstrated that the Preventol RI-80 loaded on MSN was more effective than the MCM-41-based system in maintaining the activity against *K. rhizophila*. When we tested the antibacterial activity of 0.2 v/v% Preventol RI-80 and either unloaded 0.1% MCM-41 or 0.1% MSN as controls, we found that MCM-41 was completely inactive, while MSN produced a small halo, probably due to the CTAB presence inside the pore structure (Figure 4B). Thus, we surmise that Preventol RI-80@MSN works better than Preventol RI-80@MCM-41 since the antibacterial activity derives from both Preventol RI-80 and, even if at little extent, CTAB.

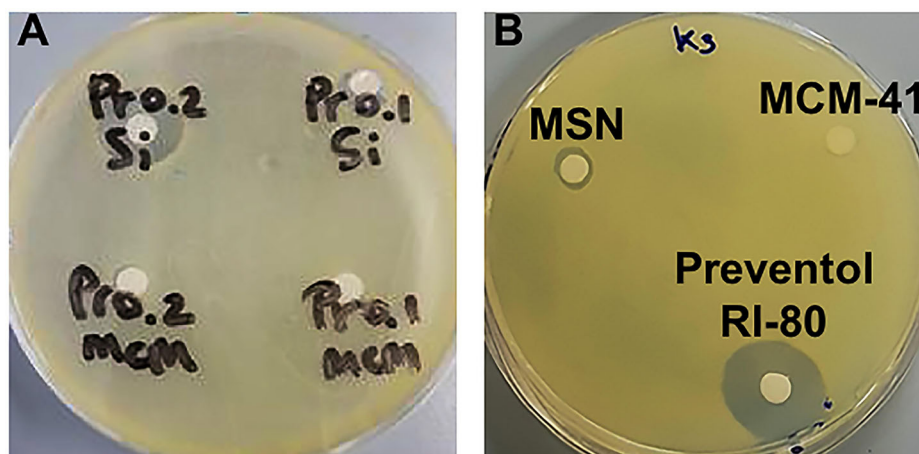


FIGURE 4 | Microbiological assays using *K. rhizophila* as a tester strain. Antibacterial activity **(A)** of Preventol RI-80 0.2@MCM-41 (Pr0.2MCM), Preventol RI-80 0.1@MCM-41 (Pr0.1MCM), Preventol RI-80 0.2@MSN (Pr0.2Si), and Preventol RI-80 0.1@MSN (Pr0.1Si), while in **(B)** is highlighted the effect of either unloaded MSN or MCM-41 systems, as well as Preventol RI-80.

Release Studies

To evaluate biocide's release, MSNs loaded with various amounts of Preventol RI-80 were placed in the water and aliquots of the solution were collected at different sampling times. The release kinetics of Preventol RI-80 (**Figure 5**, **Figure S3A**) into the water solution was followed by recording intensities at two diverse wavelengths (210 and 260 nm) to determine differences, if any, in the release of the different compounds present within the commercial formulation. Indeed, benzyldimethyltridecylazanium chloride, the main active compound of the quaternary ammonium salts mixture, has the maximum absorbance centered at ca. 260 nm. Preventol RI-80 release was evaluated at the two wavelengths and, although the observed trends were similar, the equilibrium state was reached after either 1 or 3 h for benzyldimethyltridecylazanium chloride or the other components, which have the maximum absorbance at 210 nm, respectively. Accordingly to the literature (Wang, 2009; Bruschi, 2015), the model of Higuchi was applied to the outcomes. The two-step regimes were observed suggesting that the load and then the release is controlled by both chemical and physical entrapping of the active compounds within the pores. The Higuchi constant was in the order Preventol RI-80@MSN (260 nm), $K_H = 0.37 \pm 0.01 \text{ s}^{-0.5} >$ Preventol RI-80@MSN (210 nm), $K_H = 0.25 \pm 0.01 \text{ s}^{-0.5}$, while differences in terms of the amount of biocide release were not observed. Similar results were observed in our previous studies regarding the loading of Biotin-T (constituted by the quaternary ammonium salt didecyldimethylammonium chloride and 2-octyl-2H-isothiazole) (Dresler et al., 2017). This behavior can be explained by a different physicochemical interaction between the hydroxyl groups of the silica and the biocide components and, accordingly to previous study (Dresler et al., 2017), could be ascribed to ion (charged head groups of quaternary salts)—dipole (Si-O-H surface groups) interactions strengthened by the Lewis acid-base interaction among the phenyl group of benzyldimethyltridecylazanium

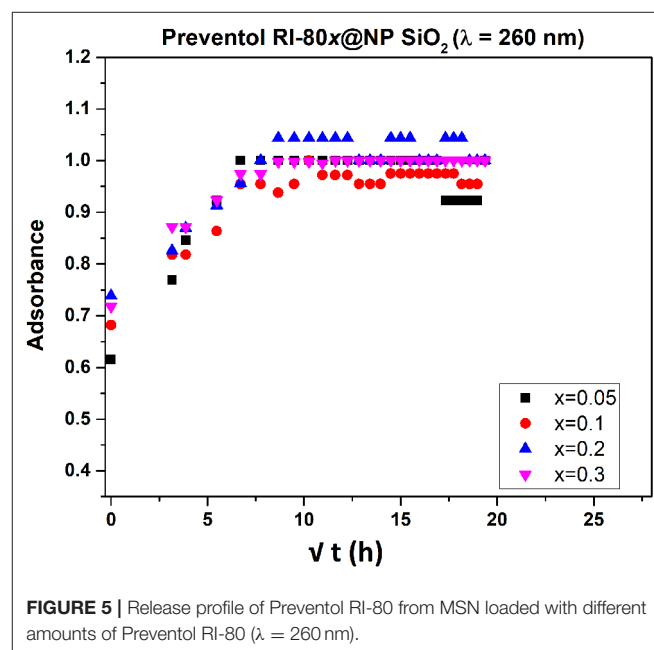


FIGURE 5 | Release profile of Preventol RI-80 from MSN loaded with different amounts of Preventol RI-80 ($\lambda = 260 \text{ nm}$).

chloride and the acidic sites (electropositive Si) in the MSN structure (Chauhan et al., 2020).

The release efficiency of Preventol RI-80-loaded within MSN was compared with Preventol RI-80 loaded within MCM-41. It is worth mentioning that also MCM41 was efficiently loaded (100%) with Preventol RI-80 as confirmed by the decrease of the specific surface area up to $50 \text{ m}^2/\text{g}$. The release kinetics of Preventol RI-80@MCM-41 followed the Higuchi model (**Figures S3B,C**); however, the Higuchi constant was in the opposite order as compared to MSNs (i.e., Preventol RI-80@MCM-41 (210 nm), $K_H = 0.43 \pm 0.02 \text{ s}^{-0.5} >$ Preventol RI-80@MCM-41 (260 nm), $K_H = 0.26 \pm 0.03 \text{ s}^{-0.5}$ and, regardless

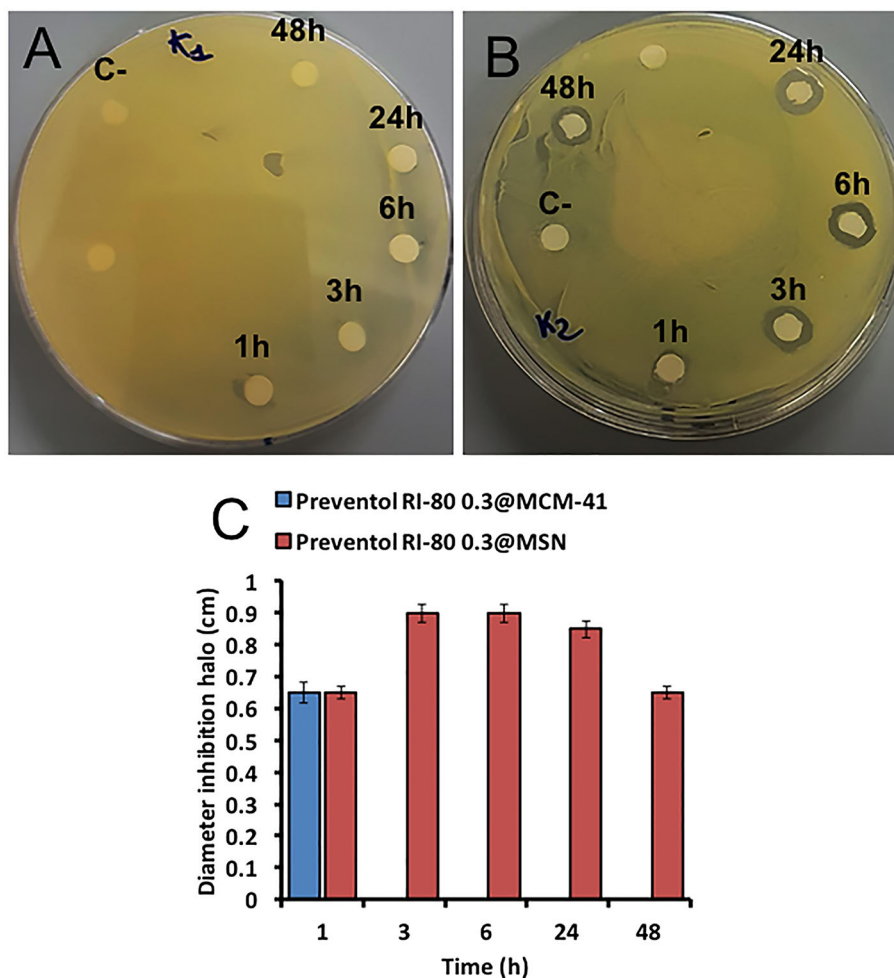


FIGURE 6 | Microbiological assays using *K. rhizophila* as tester strain. Antimicrobial activity of both Preventol RI-80 0.3@MCM-41 (A) and Preventol RI-80 0.3@MSN (B) CRSs, while the bar graph in (C) shows the actual diameter size of the inhibition halos, over time, ascribed to Preventol RI-80 0.3@MCM-41 (blue) and Preventol RI-80 0.3@MSN (red) systems activity.

the wavelength, the state of equilibrium was reached roughly after 1 h.

These outcomes suggest a higher efficiency in releasing benzyldimethyltridecylazanium chloride by the Preventol RI-80@MSN as compared with Preventol RI-80@MCM-41 probably due to a higher amount of acidic sites on the surface of MSN thus suggesting that the role of Lewis acid-base interaction is pivotal in regulating the release of biocides. On this basis, the MSN system was judged to be more suitable, in terms of release kinetics, for its application in a real case study; therefore, the biological activity of the Preventol RI-80 0.3@MSN system was compared to that of Preventol RI-80 0.3@MCM-41.

The biocide release was also studied by microbiological assays for the Preventol RI-80 0.3@MSN system over time (i.e., 1, 3, 6, 24, 48 h), being Preventol RI-80 0.3@MCM-41 one used as a comparison. The system Preventol RI-80 0.3@MSN maintained the antibacterial activity for a longer time than that based on MCM-41; indeed, the latter lost its activity after 1 h of application (Figure 6A), while the system Preventol RI-80 0.3@MSN resulted

to be active up to 48 h (Figure 6B). Thus, the MSN-based system resulted to be more suitable as a carrier to achieve both biocide loading and release over time as compared to MCM-41 one, as also indicated by the inhibition halo values (Figure 6C). The difference could be due to CTAB traces in the system, as well as the different size and organization of the mesoporous pore structure. The release of 0.3% Preventol RI-80 was completed within 1 h when MCM-41 was used, while we had previously obtained the complete release of 0.75% Biotin T from MCM-41 within 6 h (Dresler et al., 2017). Besides the diverse concentrations of biocides used, the difference could be ascribed to the different mechanism of interactions of benzyldimethyltridecylazanium chloride (Preventol RI-80) or 2-octyl-2H-isothiazole (Biotin T) and silica, even it could be influenced by the relative composition of the product (unknown). Therefore, Preventol RI-80 loaded within MSN was the most efficient CRS we designed so far. The release efficiency was in line to that observed for similar silica based CRS developed for the preventive conservation of artifacts (Sorensen et al., 2010;

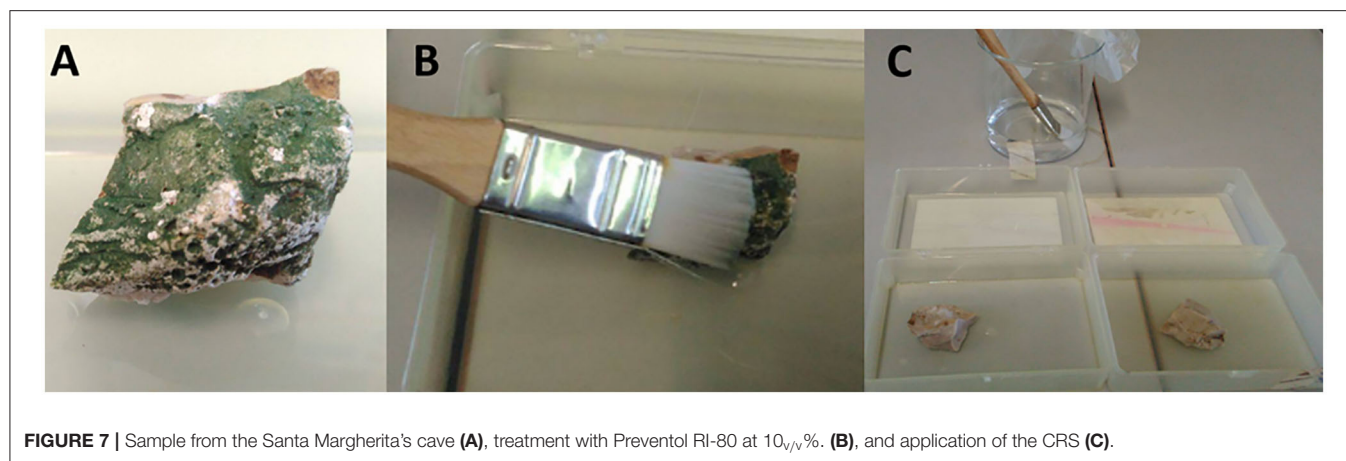


FIGURE 7 | Sample from the Santa Margherita's cave (A), treatment with Preventol RI-80 at 10_{v/v}%. (B), and application of the CRS (C).

TABLE 1 | Evaluation of the alive microbial biomass retrieved from either untreated or differently treated stone material.

Sample	Days of treatment			
	2 (days)	10 (days)	6 (months)	12 (months)
Untreated stone	5 ± 2	13 ± 3	10 ± 4	15 ± 2
Preventol RI-80 treated stone	0	0	1 ± 1	3 ± 2
Preventol RI-80@MSN-treated stone	0	0	0	0

Borisova et al., 2011). On the other hand, it is well-known that the release could be triggered by external stimuli by proper functionalization of silica surface or that the use of layered double hydroxides (LDH) could give a dual role also acting in the capture of specific ions (Giuliani et al., 2020). It has to keep in mind that for applicative purposes, the balance among costs and benefits have to be accounted and, in some cases, low cost materials as natural clays (Cavallaro et al., 2018) could be advantageous.

Test on Real Case Study: The Stone of the Castellammare Del Golfo's Cave

The Santa Margherita's cave in Castellammare del Golfo (Trapani, Italy) is a natural cave, containing the remains of paintings belonging to an ancient church dated back to the middle age (Purpura, 1999)¹. The cave is in a poor state of conservation and most of the paintings and the stone are contaminated by biodeteriogens. The identification of biodeteriogenic bacterial strains has been performed (data not shown), as well as the monitoring of environmental conditions (i.e., temperature and humidity), which demonstrated that in a full year there are the proper conditions allowing microbial

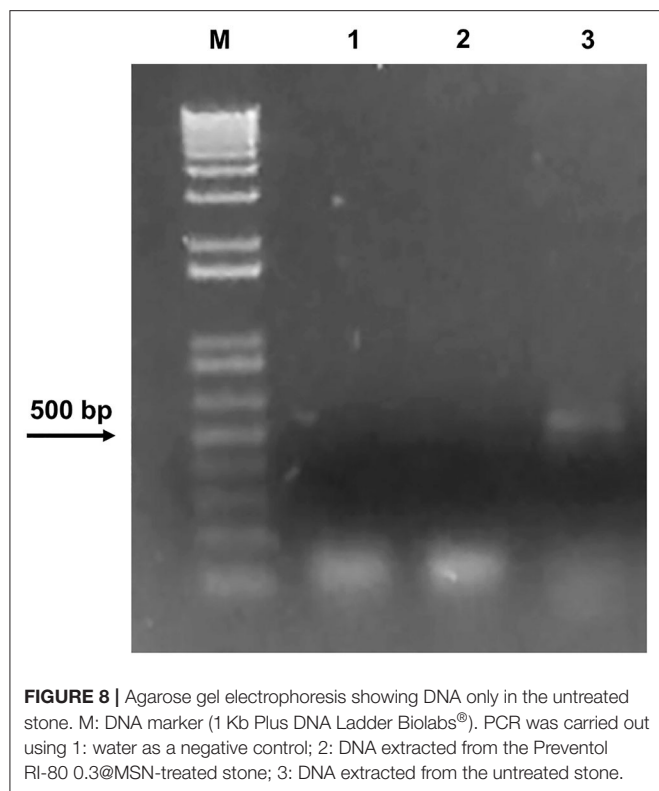
¹Trapani oggi (2019). Gli affreschi della grotta di Santa Margherita. <https://www.trapanioggi.it/gli-affreschi-della-grotta-di-santa-margherita> (accessed April 25, 2020).

growth. Thus, fragments of the stone support represent a good case study to test the performances of the MSN system developed to treat damaged stone materials.

The Preventol RI-80 0.3@MSN system was applied to a sample taken from the west wall of the cave. The surface of the sample was covered by a green biopatina (Figure 7A), likely representing a microbial biofilm, as microorganisms growing in a sessile life form are more prone in handling harsh environmental conditions and stressors of various nature (i.e., antimicrobials) deriving from the surrounding ecological niche (Piacenza et al., 2017). To simulate a real treatment during the restoration works, the sample was treated with a solution of Preventol RI-80 (10_{v/v}%) for 15 h, being then washed with a water brush (Figure 7B). The green color disappeared after this application. The sample was then divided into two smaller fragments and one of them was used for applying the MSN-based CRS by using a brush (Figure 7C).

The presence of bacteria was evaluated by counting the viable cells and by extracting metagenomics DNA from the untreated stone, the sample treated with Preventol RI-80, and that treated with Preventol RI-80 and Preventol RI-80 0.3@MSN. Evaluation of viable bacteria showed that after 12 months no bacteria were present in samples treated with Preventol RI-80 and additionally with Preventol RI-80 0.3@MSN; differently, from the untreated stone, a mean of 15 ± 2 CFU/g was found at the end of the timeframe considered, while Preventol RI-80 treated samples highlighted the presence of lower microbial contamination after 12 months (Table 1).

We cannot rule out that the initial treatment was so strong to completely inhibit bacterial growth for such a long time or that the conditions in which stones were stored did not allow further bacterial proliferation. Since a minority of environmental microorganisms (ca. 10%) can be isolated through conventional cultivable-dependent methods (Soffritti et al., 2019), to further confirm the absence of bacteria on Preventol RI-80 0.3@MSN-treated stone, metagenomic DNA was extracted from the latter, which was used as a template to amplify a 464-base pair DNA internal fragment of the gene coding for the 16S bacterial ribosomal subunit (Arizza et al., 2019). Agarose gel electrophoresis showed the amplicon of the correct size (~500



bp) only in the untreated stone (**Figure 8**), thus confirming the efficacy of the treatment.

CONCLUSIONS

This study highlights new avenues in developing controlled release systems directed to a specific target (i.e., stone material) to reduce the frequency of antibacterial treatments of cultural heritage. The mesoporous silica nanoparticles were synthesized by condensation in emulsion method.

The MSNs, spherical in shape featuring having average diameter of 55 nm, show cylinder pores of 3–8 nm in diameter. CRSs based on mesoporous silica nanoparticles with a high yield in loading the biocides Preventol RI-80 were developed and tested as a smart tool against the biodeterioration phenomenon of the material of archaeological and artistic interest.

Preventol RI-80 loaded on MSN showed a high approximation to a more efficient drug delivery system, even higher with respect to the MCM-41.

The antibacterial test showed that all systems are efficient against microbial blooming with MSN more active than MCM-41.

REFERENCES

Allsopp, D., Seal, K., and Gaylarde, C. (2004). *Introduction to Biodeterioration*. Cambridge: Cambridge University Press. 233. doi: 10.1017/CBO9780511617065

Finally, Preventol RI-80 0.3@MSN system was applied on a stone sample from the Santa Margherita cave in Castellammare del Golfo (Trapani, Italy). The bacterial growth was inhibited for 12 months after treatment. This work demonstrates that it is possible to use the CRSs against the deterioration and that, knowing the kind of biodeteriogens, it is possible to develop *ad hoc* systems to prevent the degradation of artifacts based on stone material. The use of the systems could be extended to other kinds of artifacts based on paper, woods, or metals.

DATA AVAILABILITY STATEMENT

The raw data supporting the conclusions of this article will be made available by the authors, without undue reservation.

AUTHOR CONTRIBUTIONS

RA and MS: Conceptualization and methodology. FA: preparation of samples. RA and AP: biological test. MS: XRD and FT-IR data. AS: NMR data. RA, DC, MS, and AP: writing–review and editing. All authors contributed to the article and approved the submitted version.

FUNDING

This work is part of the project Development and Application of Innovative Materials and processes for the diagnosis and restoration of Cultural Heritage—DELIAS—PON03PE 00214-2 (Programma Operativo Nazionale Ricerca e Competitività 2017–2013). Grants of AP and FA were from the MIUR for the Project PON Ricerca e Innovazione 2014-2020—Avviso DD 407/2018 AIM Attrazione e Mobilità Internazionale (AIM1808223).

ACKNOWLEDGMENTS

We thank Leonardo Borgioli of C.T.S. s.r.l. for providing the biocides. We would like to express our gratitude to Soprintendenza di Trapani (Italy) and Prof. Sebastiano Tusa for the permission to perform the experiments on the samples collected at Santa Margherita Cave. NMR and TEM experimental data were provided by ATeN Center—University of Palermo (<https://www.unipa.it/servizi/atcenter/>).

SUPPLEMENTARY MATERIAL

The Supplementary Material for this article can be found online at: <https://www.frontiersin.org/articles/10.3389/fchem.2020.00699/full#supplementary-material>

Arizza, V., Vecchioni, L., Caracappa, S., Sciarba, G., Berlinghieri, F., Gentile, A., et al. (2019). New insights into the gut microbiome in loggerhead sea turtles *Caretta caretta* stranded on the Mediterranean coast. *PLoS ONE* 14:e0220329. doi: 10.1371/journal.pone.0220329

- Artesani, A., Di Turo, F., Zucchelli, M., and Traviglia, A. (2020). Recent advances in protective coatings for cultural heritage—an overview. *Coatings* 10:217. doi: 10.3390/coatings10030217
- Barbé, C., Bartlett, J., Kong, L., Finnie, K., Linn, H. Q., Larkin, M., et al. (2004). Silica particles: a novel drug-delivery system. *Adv. Mater.* 16, 1959–1966. doi: 10.1002/adma.200400771
- Bernardos, A., Piacenza, E., Sanceón, F., Hamadi, M., Maleki, A., Turner, R. J., et al. (2019). Mesoporous silica-based materials with bacterial properties. *Small* 15:1900669. doi: 10.1002/smll.201900669
- Borisova, D., Mohwald, H., and Shchukin, D. G. (2011). Mesoporous silica nanoparticles for active corrosion protection. *ACS Nano* 5, 1939–1946. doi: 10.1021/nn102871v
- Böttcher, H., Jagota, C., Treppe, J., Kallies, K. H., and Haufe, H. (1999). Sol-gel composite films with controlled release of biocides. *J. Control. Release* 60, 57–65. doi: 10.1016/S0168-3659(99)00053-X
- Brunauer, S., Emmett, P. H., and Teller, E. (1938). Adsorption of gases in multimolecular layers. *J. Am. Chem. Soc.* 60, 309–319. doi: 10.1021/ja01269a023
- Bruschi, M. L. (2015). “Mathematical and physicochemical models of drug release,” in *Strategies to Modify the Drug Release From Pharmaceutical Systems*, ed M. L. Bruschi (Cambridge: Woodhead Publishing), 63–86. doi: 10.1016/B978-0-08-100092-2.00005-9
- Cao, N., Zhao, Y., Sang, B., Wang, Z., Cao, L., Sun, L., et al. (2016). Fabrication of autofluorescent porous silica nanoparticles for redox-responsive drug release. *Mater. Sci. Eng. C* 69, 330–336. doi: 10.1016/j.msec.2016.06.096
- Caponetti, E., Pedone, L., Saladino, M. L., Chillura Martino, D. F., and Nasillo, G. (2010). MCM-41-CdS nanoparticles composite material: preparation and characterization. *Microporous Mesoporous Mater.* 128, 101–107. doi: 10.1016/j.micromeso.2009.08.010
- Cavallaro, G., Lazzara, G., and Fakhruddin, R. (2018). Mesoporous inorganic nanoscale particles for drug adsorption and controlled release. *Ther. Delivery* 9, 287–301. doi: 10.4155/tde-2017-0120
- Chan, A. C., Cadena, M. B., Townley, H. E., Fricker, M. D., and Thompson, I. P. (2017). Effective delivery of volatile biocides employing mesoporous silicates for treating biofilms. *J. R. Soc. Interface* 14:650. doi: 10.1098/rsif.2016.0650
- Chauhan, M., Saini, V. K., and Suthar, S. (2020). Ti-pillared montmorillonite clay for adsorptive removal of amoxicillin, imipramine, diclofenac-sodium, and paracetamol from water. *J. Hazard. Mater.* 399:122832. doi: 10.1016/j.jhazmat.2020.122832
- Ciabocco, M., Cancemi, P., Saladino, M. L., Caponetti, E., Alduina, R., and Berrettoni, M. (2018). Synthesis and antibacterial activity of iron-hexacyanocobaltate nanoparticles. *J. Biol. Inorg. Chem.* 23, 385–398. doi: 10.1007/s00775-018-1544-x
- Cusimano, M. G., Ardizzone, F., Nasillo, G., Gallo, M., Sfriso, A., Chillura Martino, D., et al. (2020). Biogenic silver nanoparticles inhibit bacterial biofilm formation due to Ag⁺ release as determined by a novel phycoerythrin-based assay. *Appl. Microbiol. Biotechnol.* 104, 6325–6336. doi: 10.1007/s00253-020-10686-w
- Dai, Z., Liu, Q., Hreniak, D., Dai, J., Wang, W., and Li, J. (2018). Fabrication of Yb:Sc₂O₃ transparent ceramics from co-precipitated nanopowders: the effect of ammonium hydrogen carbonate to metal ions molar ratio. *Opt. Mater.* 75, 673–679. doi: 10.1016/j.optmat.2017.11.035
- David, M. E., Ion, R. -M., Grigorescu, R. M., Iancu, L., and Andrei, E. R. (2020). Nanomaterials used in conservation and restoration of cultural heritage: an up-to-date overview. *Materials* 13:2064. doi: 10.3390/ma13092064
- Dresler, C., Saladino, M. L., Demirbag, C., Caponetti, E., Chillura Martino, D. F., and Alduina, R. (2017). Development of controlled release systems of biocides for the conservation of cultural heritage. *Int. Biodeterior. Biodegrad.* 125, 150–156. doi: 10.1016/j.ibiod.2017.09.007
- Du, X., Shi, B., Liang, J., Bi, J., Dai, S., and Qiao, S. Z. (2013). Developing functionalized dendrimer-like silica nanoparticles with hierarchical pores as advanced delivery nanocarriers. *Adv. Mater.* 25, 5981–5985. doi: 10.1002/adma.201302189
- Dubey, R. S., Rajesh, Y. B. R. D., and More, M. A. (2015). Synthesis and characterization of SiO₂ nanoparticles via sol-gel method for industrial applications. *Mater. Today Proc.* 2, 3575–3579. doi: 10.1016/j.matpr.2015.07.098
- Eyssautier-Chuine, S., Calandra, I., Vaillant-Gaveau, N., Fronteau, G., Thomachot-Schneider, C., Hubert, J., et al. (2018). A new preventive coating for building stones mixing a water repellent and an eco-friendly biocide. *Prog. Org. Coat.* 120, 132–142. doi: 10.1016/j.porgcoat.2018.03.022
- Farjadian, F., Roointan, A., Mohammadi-Samani, S., and Hosseini, M. (2019). Mesoporous silica nanoparticles: synthesis, pharmaceutical applications, biodistribution, and biosafety assessment. *Chem. Eng. J.* 359, 684–705. doi: 10.1016/j.ccej.2018.11.156
- Fidanza, M. R., and Caneva, G. (2019). Natural biocides for the conservation of stone cultural heritage: a review. *J. Cult. Heritage* 38, 271–286. doi: 10.1016/j.culher.2019.01.005
- Giardina, A., Alduina, R., Gottardi, E., Di Caro, V., Süßmuth, R. D., and Puglia, A. M. (2010). Two heterologously expressed *Planobispora rosea* proteins cooperatively induce *Streptomyces lividans* thiostrepton uptake and storage from the extracellular medium. *Microb. Cell Fact.* 9:44. doi: 10.1186/1475-2859-9-44
- Giuliani, G., Messina, E., Stacioli, M. P., Pascucci, M., Riccucci, C., Liotta, L. F., et al. (2020). On-demand release of protective agents triggered by environmental stimuli. *Front. Chem.* 8:304. doi: 10.3389/fchem.2020.00304
- Jiang, X., Tang, X., Tang, L., Zhang, B., and Mao, H. (2019). Synthesis and formation mechanism of amorphous silica particles via sol-gel process with tetraethylorthosilicate. *Ceram. Int.* 45, 7673–7680. doi: 10.1016/j.ceramint.2019.01.067
- Kraljeva, E., Saladino, M. L., Spinella, A., Nasillo, G., and Caponetti, E. (2011). H₃PW₁₂O₄₀ supported on mesoporous MCM-41 and Al-MCM-41 materials: preparation and characterization. *J. Mat. Sci.* 46, 7114–7120. doi: 10.1007/s10853-011-5505-9
- Kruk, M., Antchshuk, V., Jaroniec, M., and Sayari, A. (1999). New approach to evaluate pore size distributions and surface areas for hydrophobic mesoporous solids. *J. Phys. Chem. B* 103, 10670–10678. doi: 10.1021/jp992264h
- Lavall, R. L., Ferrari, S., Tomasi, C., Marzantowicz, M., Quartarone, E., Fagnoni, M., et al. (2012). MCM-41 silica effect on gel polymer electrolytes based on thermoplastic polyurethane. *Electrochim. Acta* 60, 359–365. doi: 10.1016/j.electacta.2011.11.073
- Lin, Y. S., and Haynes, C. L. (2009). Synthesis and characterization of biocompatible and size-tunable multifunctional porous silica nanoparticles. *Chem. Mater.* 21, 3979–3986. doi: 10.1021/cm901259n
- Liu, Y., Yan, L., Heiden, P., and Laks, P. (2001). Use of nanoparticles for controlled release of biocides in solid wood. *J. Appl. Polym. Sci.* 79, 458–465. doi: 10.1002/1097-4628(20010118)79:3<458::AID-APP80>3.0.CO;2-H
- Lu, J., Liong, M., Zink, J. I., and Tamanoi, F. (2007). Mesoporous silica nanoparticles as delivery system for hydrophobic anticancer drugs. *Small* 8, 1341–1346. doi: 10.1002/smll.200700005
- Lu, J., Shen, H. H., Wu, Z., Wang, B., Zhao, D., and He, L. (2015). Self-assembly of bi-functional peptides on large pores mesoporous silica nanoparticles formiRNA binding and delivery. *J. Mater. Chem. B* 3, 7653–7657. doi: 10.1039/C5TB01133G
- Ma, S., Wang, Y., and Zhu, Y. (2011). A simple room temperature synthesis of mesoporous silica nanoparticles for drug storage and pressure pulsed delivery. *J. Porous Mater.* 18, 233–239. doi: 10.1007/s10934-010-9375-3
- Ma, X., Zhao, Y., Ng, K. W., and Zhao, Y. (2013). Integrated hollow mesoporous silica nanoparticles for target drug/siRNA co-delivery. *Chem. Eur. J.* 19, 15593–15603. doi: 10.1002/chem.201302736
- Michaelsen, A., Pinzari, F., Barbabietola, N., and Piñar, G. (2013). Monitoring of the effects of different conservation treatments on paper infecting fungi. *Int. Biodeterior. Biodegrad.* 84, 333–341. doi: 10.1016/j.ibiod.2012.08.005
- Mourhly, A., Khachani, M., El Hamidi, A., Kacimi, M., Halim, M., and Arsalane, S. (2015). The synthesis and characterization of low-cost mesoporous silica SiO from local pumice rock. *Nanomater. Nanotechnol.* 5:35. doi: 10.5772/62033
- Nandiyanto, A. B. D., Kim, S. G., Iskandar, F., and Okuyama, K. (2009). Synthesis of spherical mesoporous silica nanoparticles with nanometer-size controllable pores and outer diameters. *Microporous Mesoporous Mater.* 120, 447–453. doi: 10.1016/j.micromeso.2008.12.019
- Niculescu, V. C. (2020). Mesoporous silica nanoparticles for bio-applications. *Front. Mater.* 7:36. doi: 10.3389/fmats.2020.00036
- Niu, D., Liu, Z., Li, Y., Luo, X., Zhang, J., Gong, J., et al. (2014). Monodispersed and ordered largepore mesoporous silica nanospheres with tunable pore structure for magnetic functionalization and gene delivery. *Adv. Mater.* 26, 4947–4953. doi: 10.1002/adma.201400815
- Piacenza, E., Presentato, A., Ambrosi, E., Spaghini, A., Turner, R. J., Vallini, G., et al. (2018). Physical-chemical properties of biogenic selenium nanostructures

- produced by *Stenotrophomonas maltophilia* SeITE02 and *Ochrobactrum* sp. MPV1. *Front. Microbiol.* 9:3178. doi: 10.3389/fmicb.2018.03178
- Piacenza, E., Presentato, A., Zonaro, E., Lemire, J. A., Demeter, M., Vallini, G., et al. (2017). Antimicrobial activity of biogenically produced spherical Senanomaterials embedded in organic material against *Pseudomonas aeruginosa* and *Staphylococcus aureus* strains on hydroxyapatite-coated surfaces. *Microb. Biotechnol.* 10, 804–818. doi: 10.1111/1751-7915.12700
- Poma, P., Labbozzetta, M., Zito, P., Alduina, R., Ramarosandrata, A. V., Bruno, M., et al. (2019). Essential oil composition of *Alluaudia procera* and *in vitro* biological activity on two drug-resistant models. *Molecules* 24:2871. doi: 10.3390/molecules24162871
- Popat, A., Liu, J., Hu, Q., Kennedy, M., Peters, B., Lu, G. Q., et al. (2012). Adsorption and release of biocides with mesoporous silica nanoparticles. *Nanoscale* 4, 970–975. doi: 10.1039/C2NR11691J
- Presentato, A., Lampis, S., Vantini, A., Manea, F., Daprà, F., Zuccoli, S., et al. (2020). On the ability of perfluorohexane sulfonate (PFHxS) bioaccumulation by two *Pseudomonas* sp. strains isolated from PFAS-contaminated environmental matrices. *Microorganisms* 8:92. doi: 10.3390/microorganisms8010092
- Purpura, G. (1999). *Le pitture della grotta di Santa Margherita, and Kalos-Larte in Sicilia*. Palermo: Edizioni Kalós.
- Qi, K., Cheng, B., Yu, J., and Ho, W. (2017). Review on the improvement of the photocatalytic and antibacterial activities of ZnO. *J. Alloys Comp.* 727, 792–820. doi: 10.1016/j.jallcom.2017.08.142
- Qi, K., Li, Y., Xie, Y., Liu, S. -Y., Zheng, K., Chen, Z., et al. (2019). Ag loading enhanced photocatalytic activity of g-C₃N₄ porous nanosheets for decomposition of organic pollutants. *Front. Chem.* 7:91. doi: 10.3389/fchem.2019.00091
- Qi, K., Xing, X., Zada, A., Li, M., and Wang, G. (2020). Transition metal doped ZnO nanoparticles with enhanced photocatalytic and antibacterial performances: experimental and DFT studies. *Ceram. Int.* 46, 1494–1502. doi: 10.1016/j.ceramint.2019.09.116
- Randazzo, L., Montana, G., Alduina, R., Quatrini, P., Tsantini, E., and Salemi, B. (2015). *Flos tectorii* degradation of mortars: an example of synergistic action between soluble salts and biodeteriogens. *J. Cult. Heritage* 16, 838–847. doi: 10.1016/j.culher.2015.04.002
- Rubino, S., Pibiri, I., Minacori, C., Alduina, R., Di Stefano, V., Orecchio, S., et al. (2018a). Synthesis, structural characterization, anti-proliferative and antimicrobial activity of binuclear and mononuclear Pt(II) complexes with perfluoroalkyl-heterocyclic ligands. *Inorg. Chim. Acta* 483, 180–190. doi: 10.1016/j.ica.2018.07.039
- Rubino, S., Saladino, M. L., Attanzio, A., Busà, R., Girasolo, M. A., Caponetti, E., et al. (2018b). Loading and release of the complex Pt(II) with the 2,2'-dithiobis(benzothiazole) ligand [Pt(DTBTA)(DMSO)Cl]-CHCl₃ into mesoporous silica and studies of antiproliferative activity. *Polyhedron* 153, 234–239. doi: 10.1016/j.poly.2018.07.006
- Ruggiero, L., Crociani, L., Zendri, E., El Habra, N., and Guerriero, P. (2018). Incorporation of the zosteric sodium salt in silica nanocapsules: synthesis and characterization of new fillers for antifouling coatings. *Appl. Surf. Sci.* 439, 705–711. doi: 10.1016/j.apsusc.2017.12.228
- Ruggiero, L., Di Bartolomeo, E., Gasperi, T., Luisetto, I., Talone, A., Zurlo, F., et al. (2019). Silica nanosystems for active antifouling protection: nanocapsules and mesoporous nanoparticles in controlled release applications. *J. Alloy Comp.* 798, 144–148. doi: 10.1016/j.jallcom.2019.05.215
- Russo, M., Armetta, F., Riela, S., Chillura Martino, D., Lo Meo, P., and Noto, R. (2015). Silver nanoparticles stabilized by a polyaminocyclodextrin as catalysts for the reduction of nitroaromatic compounds. *J. Mol. Catal. A Chem.* 408, 250–261. doi: 10.1016/j.molcata.2015.07.031
- Russo, M., Meli, A., Suter, A., Gallo, G., Chillura Martino, D., Lo Meo, P., et al. (2016). Photosynthesized silver-polyaminocyclodextrin nanocomposites as promising antibacterial agents with improved activity. *RSC Adv.* 6, 40090–40099. doi: 10.1039/C6RA00042H
- Saladino, M. L., Kraveva, E., Todorova, S., Spinella, A., Nasillo, G., and Caponetti, E. (2011). Synthesis, characterization and catalytic activity of mesoporous Mn-MCM-41 materials. *J. Alloy Comp.* 509, 8798–8803. doi: 10.1016/j.jallcom.2011.06.078
- Saladino, M. L., Rubino, S., Colomba, P., Girasolo, M. A., Chillura Martino, D. F., Demirbag, C., et al. (2016). Pt(II) complex @mesoporous silica: preparation, characterization and study of release. *Biointerface Res. Appl. Chem.* 6, 1621–1626.
- Saladino, M. L., Spinella, A., Caponetti, E., and Minoja, A. (2008). Characterization of Nd-MCM41 obtained by impregnation. *Microporous Mesoporous Mat.* 113, 490–498. doi: 10.1016/j.micromeso.2007.12.007
- Sing, K. S. W., Douglas, H., Everett, D. H., Haul, R. A. W., Moscou, L., Pierotti, R. A., et al. (2008). Reporting physisorption data for gas/solid systems. *Pure Appl. Chem.* 57:16. doi: 10.1002/9783527610044.hetcat0065
- Slowing, I. I., Vivero-Escoto, J. L., Wu, C. W., and Lin, V. S. (2008). Mesoporous silica nanoparticles as controlled release drug delivery and gene transfection carriers. *Adv. Drug Deliv. Rev.* 60, 1278–1288. doi: 10.1016/j.addr.2008.03.012
- Soffritti, I., D'Accolti, M., Lanzoni, L., Volta, A., Bisi, M., Mazzacane, S., et al. (2019). The potential use of microorganisms as restorative agents: an update. *Sustainability* 11:3853. doi: 10.3390/su11143853
- Sorensen, G., Nielsen, A. L., Pedersen, M. M., Poulsen, S., Hissen, H., Poulsen, M., and Nygaard, S. D. (2010). Controlled release of biocide from silica microparticles in wood paint. *Prog. Org. Coat.* 68, 299–306. doi: 10.1016/j.porgcoat.2010.03.009
- Trapani oggi (2019). *Gli affreschi della grotta di Santa Margherita*. Available online at: <https://www.trapanioggi.it/gli-affreschi-della-grotta-di-santa-margherita> (accessed April 25, 2020).
- Trewyn, B. G., Nieweg, J. A., Zhao, Y., and Lin, V. S. Y. (2008). Biocompatible mesoporous silica nanoparticles with different morphologies for animal cell membrane penetration. *Chem. Eng. J.* 137, 23–29. doi: 10.1016/j.cej.2007.09.045
- Urzi, C. (2004). Microbial deterioration of rocks and marble monuments of the mediterranean basin: a review. *Corros. Rev.* 22:441. doi: 10.1515/CORRREV.2004.22.5-6.441
- Viana, R. B., da Silva, A. B. F., and Pimentel, A. S. (2012). Infrared spectroscopy of anionic, cationic, and zwitterionic surfactants. *Adv. Phys. Chem.* 2012:903272. doi: 10.1155/2012/903272
- Wang, S. (2009). Ordered mesoporous materials for drug delivery. *Microporous Mesoporous Mat.* 117, 1–9. doi: 10.1016/j.micromeso.2008.07.002
- Warscheid, T. (2003). "The evaluation of biodeterioration processes on cultural objects and approaches for their effective control," in *Art, Biology, and Conservation: Biodeterioration of Works of Art*, eds R. J. Koestler, V. H. Koestler, A. E. Charola, and F. E. Nieto-Fernandez (New York, NY: The Metropolitan Museum of Art), 14–27.
- Warscheid, T., and Braams, J. (2000). Biodeterioration of stone: a review. *Int. Biodeterior. Biodegrad.* 4, 343–368. doi: 10.1016/S0964-8305(00)00109-8
- Xu, D., Feng, J., and Che, S. (2014). An insight into the role of the surfactant CTAB in the formation of microporous molecular sieves. *Dalton Trans.* 43, 3612–3617. doi: 10.1039/C3DT53308E
- Yaqoob, A. A., Ahmad, H., Parveen, T., Ahmad, A., Oves, M., Ismail, I. M. I., et al. (2020). Recent advances in metal decorated nanomaterials and their various biological applications: a review. *Front. Chem.* 8:341. doi: 10.3389/fchem.2020.00341
- Zhu, W., Chen, Z., Pan, Y., Dai, R., Wu, Y., Zhuang, Z., et al. (2019). Functionalization of hollow nanomaterials for catalytic applications: nanoreactor construction. *Adv. Mater.* 31:1800426. doi: 10.1002/adma.201800426

Conflict of Interest: The authors declare that the research was conducted in the absence of any commercial or financial relationships that could be construed as a potential conflict of interest.

Copyright © 2020 Presentato, Armetta, Spinella, Chillura Martino, Alduina and Saladino. This is an open-access article distributed under the terms of the Creative Commons Attribution License (CC BY). The use, distribution or reproduction in other forums is permitted, provided the original author(s) and the copyright owner(s) are credited and that the original publication in this journal is cited, in accordance with accepted academic practice. No use, distribution or reproduction is permitted which does not comply with these terms.



Size Dependent Photocatalytic Activity of ZnO Nanosheets for Degradation of Methyl Red

Abdullah Aljaafari*

Department of Physics, College of Science, King Faisal University, Al-Ahsa, Saudi Arabia

In this work, ZnO nanosheets with a tunable thickness were produced by a microwave-assisted hydrothermal-based method. The product was well characterized by various tools such as XRD, SEM, EDX spectroscopy, TEM, and Raman spectroscopy. ZnO nanosheets were highly crystalline and possessed a single phase with the wurtzite structure. The ZnO nanosheets have a thickness ranging from 20 to 50 nm, as shown by the micrographs of SEM. The SAED pattern inferred that the ZnO nanosheets have a single crystal nature with preferential growth direction along [0001]. ZnO nanosheets with E_2^{high} mode of wurtzite structure were observed by Raman scattering spectra. The photodegradation of methyl red using ZnO nanosheets was measured under UV light irradiation. In comparison with the commercial ZnO, ZnO nanosheets showed higher efficiency in photodegradation of organic dyes. The thinner the nanosheets, the higher their performance, which can be explained based on surface area. The excellent performance of ZnO nanosheets in photodegradable organic dyes might be important in environmental treatment and photocatalysis applications.

OPEN ACCESS

Edited by:

Rengaraj Selvaraj,
Sultan Qaboos University, Oman

Reviewed by:

Sanjay S. Kolekar,
Shivaji University, India
Zinetula Z. Insepov,
Purdue University, United States

*Correspondence:

Abdullah Aljaafari
aaljaafari@kfu.edu.sa

Speciality section:

This article was submitted to
Thin Solid Films,
a section of the journal
Frontiers in Materials

Received: 03 June 2020

Accepted: 29 September 2020

Published: 18 November 2020

Citation:

Aljaafari A (2020) Size Dependent
Photocatalytic Activity of ZnO
Nanosheets for Degradation of
Methyl Red.
Front. Mater. 7:562693.
doi: 10.3389/fmats.2020.562693

Keywords: ZnO, nanosheets (NSs), photocatalysts, XRD, TEM

INTRODUCTION

Recently, environmental pollution of organic pollutants by photolysis of wide-gapped semiconductors, have attracted great attention (Linsebigler et al., 1995; Chatterjee and Dasgupta, 2005; Comparelli et al., 2005; Thompson and Yates, 2006). Moreover, these nanostructures provide enhancement in the functional properties for potential applications in the fabrication of nanodevices. In photocatalytic applications, numerous semiconducting nanostructures, including ZnO and TiO₂, are being used due to their unique properties of low cost, high photosensitivity, non-toxicity and environmentally friendly behavior (Wu and Tseng, 2006; Wang et al., 2007). ZnO has been considered to be a more capable photocatalyst than TiO₂ due to its high surface reactivity resulting from a large number of active surface defect states (Kumar and Rao, 2015). Additionally, the more efficient hydroxyl ion production capability (Carraway et al., 1994) of ZnO provides high reaction and mineralization rates (Poulios et al., 1999; Bohle and Spina, 2009; Wang et al., 2009). The catalytic activity of metal oxide nanostructures is known to depend on surface area and surface defects (Baruah et al., 2008). Among the different dimensions, two-dimensional nanostructures including nanosheets or nanotubes can be considered a new class of nanostructure material due to their high anisotropy, large surface area and nanometer scale thickness, and they have interesting properties (Jang et al., 2006).

The unique structural features of two-dimensional nanomaterials, such as ultrathin thickness and possibly specific open crystal planes, may be useful for a wide range of surface interactions/

interactivity-oriented applications, such as electrodes of dye-sensitive solar cells, gas sensors, supercapacitors, lithium ion batteries, photocatalytic water splitting, photocatalysis, etc. (Hosono et al., 2005; Jing and Zhan, 2008; Liu et al., 2009; Qiu et al., 2010; Zhang et al., 2009a). ZnO crystals are composed of closely packed O^{2-} layers piled alternatively along the c-axis, producing positively charged Zn-terminated (0001) polar surfaces and negatively charged O-terminated (000 $\bar{1}$) polar surfaces (Kong and Wang, 2004). ZnO crystals have a non-central symmetric wurtzite structure. The average surface energy of ZnO for the polar $\pm\{0001\}$ plane is higher than non-polar $\{01\bar{1}0\}$, and $\{2\bar{1}\bar{1}0\}$ planes. It can be expected that the higher-surface-energy $\pm(0001)$ surface has much higher amounts of chemical activity (Kong and Wang, 2004).

Therefore, the development of a synthesis technique for the shape and size of tunable ZnO nanostructures is needed. Numerous reports have shown the growth of ZnO nanostructures in various dimensions including nanowires, nanobelts, nanorods, nanosheets, and nanotubes (Huang et al., 2001; Pan et al., 2001; Wu et al., 2002; Tien et al., 2007; Baruah and Dutta, 2009; Becker et al., 2011). Also, ZnO nanosheets have been synthesized by using different chemical and physical methods such as thermal evaporation, chemical vapor deposition (CVD), physical vapor deposition (PVD), electrochemical processes, hydrothermal or solvothermal methods (Zhang et al., 2003; Zeng et al., 2005; Hu et al., 2008; Li et al., 2008; Qiu et al., 2009). However, these methods have disadvantages due to their high-temperatures, vacuum conditions, or longer reaction times, which make these techniques expensive. Thus, to fulfill economic and industrial necessities, a quick and easy process for the synthesis of ZnO nanostructures under ambient conditions is required. Nevertheless, the controlled growths of ZnO nanosheets with the thickness in quantum confinement range and their thickness dependent photocatalytic properties have not been reported. More recently, microwave radiation has introduced the synthesis of nanomaterials. Compared with conventional heating, microwave heating has unique effects such as fast and homogeneous volumetric heating, high reaction rate, short reaction time, improved reaction selectivity, energy saving and low cost (Ahmed et al., 2011).

In this work, a simple microwave-assisted hydrothermal assisted solution method was used to prepare ZnO nanosheets containing highly reactive (0001) facets and tunable thickness. The dependence of photocatalytic degradation of methyl red dye on the thickness of ZnO nanosheets was investigated. It is worth mentioning that the present products possessed higher specific surface areas and smaller nanosheet thicknesses in quantum confinement range than products from both microwave-assisted processes, and hydrothermal (Zhou et al., 2008; Qiu et al., 2010). Most importantly, there is no requirement of further calcination steps to obtain the final product as is required in earlier reports (Dong et al., 2012). The ZnO nanosheets prepared by the present process possessed single-crystallinity, high surface areas, and ultrathin thicknesses, characteristics which are beneficial for photocatalytic applications.

EXPERIMENTAL DETAILS

The product was synthesized using the microwave hydrothermal method (CEM; MARS 5). Potassium hydroxide (KOH; 99.99%) and Zinc acetate dihydrate ($Zn(CH_3COO)_2 \cdot 2H_2O$; 99.999) were mainly used in experiments. Different molar ratios of 1:2.5 (sample 1), 1:2.75 (sample 2), 1:5 (sample 3) of $Zn(CH_3COO)_2 \cdot 2H_2O$ and KOH were dissolved in a round-bottom flask which included 100 ml water. The mixture was then transferred to a Teflon-lined digestion vessel of 100 ml and operated at 160°C and 100 psi for 20 min in a microwave system. The operating power used was 1200 W. The temperature was observed during irradiation by a thermocouple fixed into the reference vessel. After the process, the product was allowed to cool down to room temperature. Centrifuge was used to separate the precipitate which was washed with deionized water and absolute ethanol several times. The product was then dried in an oven at 80°C for 24 h.

For photocatalysis experiments, methyl red (MR) was used as a test pollutant. An aqueous solution of MR (10 μM) was used corresponding to ZnO (10 mg). To attain an adsorption-desorption equilibrium, the suspension was then stirred in the dark for 30 min. A mercury lamp of high pressure was used as a light source radiation. After the time interval, 5 ml was withdrawn and centrifuged immediately to remove the photocatalyst particles. Then it was analyzed by a UV-Vis spectrophotometer (Agilent 8453) to observe the spectra MR. For the photocatalytic stability of ZnO nanosheets, a time track of photocatalytic degradation of MR using photocatalyst was conducted.

X-ray diffraction (Phillips X'pert (MPD-3040)) was used to investigate the phase purity of the product obtained with Cu K α radiations ($\lambda = 1.5406 \text{ \AA}$). Field emission electron microscopy (FESEM) images were obtained using a MIRA II LMH microscope and initial synthesis of ZnO was obtained by energy dispersing X-ray spectroscopy (EDX, Inca Oxford) attached to FESEM.

The electron microscopy (TEM) and electron diffraction pattern for the selected area (SAED) and high-resolution transmission electron microscopy (HRTEM) micrographs were obtained using FE-TEM (JEOL/JEM-2100F version). ZnO nanosheets were first dispersed in ethanol solution followed by ultrasound treatment for 10 min for TEM analysis. Furthermore, a fine drop of ZnO suspension was cast onto a carbon-covered copper mesh and then dried in the air before being transferred to the microscope. The Micro-Raman spectrometer (NRS-3100) was used to obtain a phonon vibrational of ZnO nanostructures, with a solid 532 nm primary laser as an excitation source in configuring background dispersion at room temperature. Optical absorption spectra of room temperature were recorded in the range of 200–800 nm using the UV-vis optical spectrophotometer (Agilent-8453). Brunauer-Emmett-Teller (BET) surface area measurements were performed by nitrogen adsorption using Autosorb-1 (Quantachrome Instruments, Boynton Beach, FL, United States).

RESULTS AND DISCUSSION

XRD patterns of ZnO nanosheets prepared at different KOH concentrations are shown in **Figures 1A**. The diffraction peaks were indexed to the hexagonal wurtzite ZnO phase (JCPDS 89-1397) with calculated lattice parameters a and c to be 3.249 and 5.207 Å, respectively. It can also be seen that all the samples showed a single-phase nature with a wurtzite structure (Marković et al., 2019). As the molar ratio was increased from 1:2.5 to 1:5, the peak became more intense which signified better crystallinity.

High-resolution transmission electron microscopy (HRTEM) revealed the atomic structures of ZnO nanosheets. The HRTEM image (**Figures 1B**) also shows that the ZnO nanosheets (sample 1) were highly crystalline, having a lattice spacing of about 0.26 nm, corresponding to the distance between the (002) planes in ZnO crystal lattice. Also, selected-area electron diffraction (SAED) patterns of the same ZnO nanosheets (sample 1) were indexed to hexagonal ZnO, which also indicated that the ZnO nanosheets were single crystalline and had growth along the [001] direction. These results are also in good agreement with the XRD results.

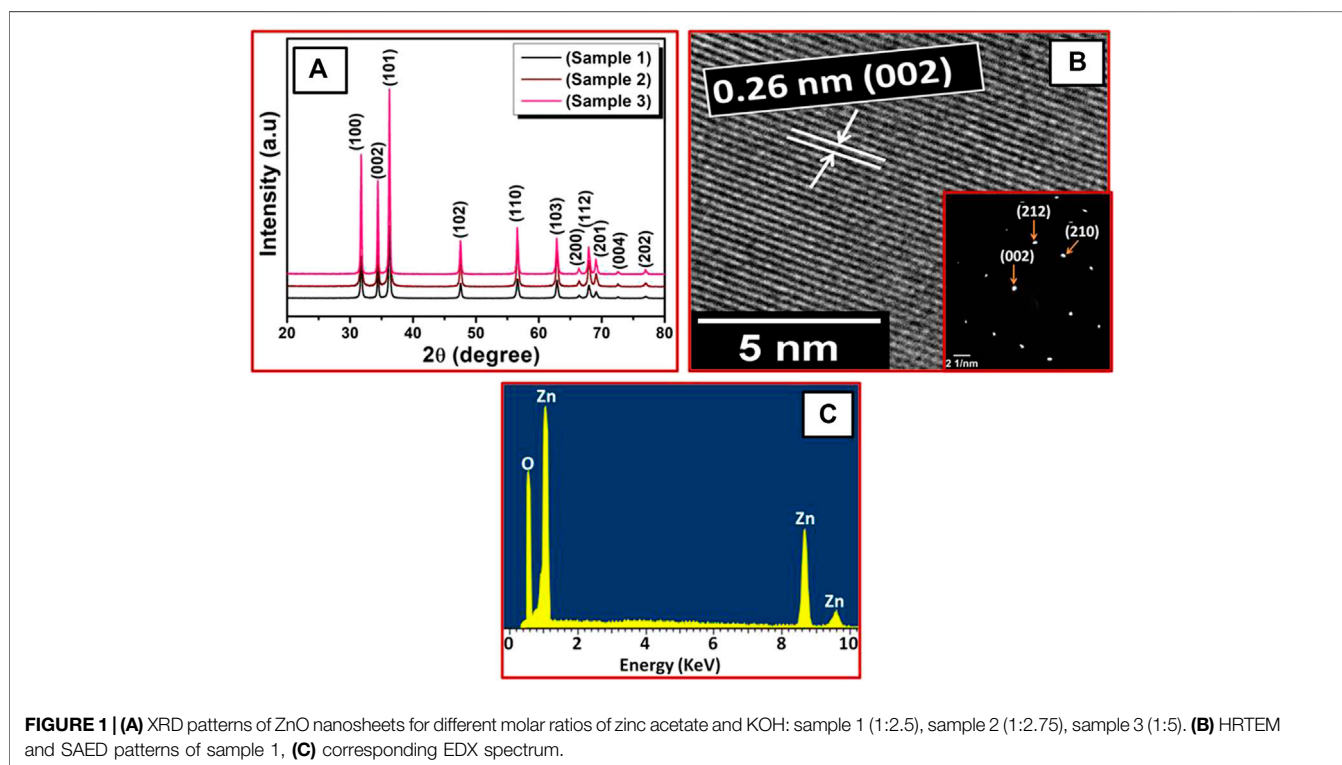
Energy dispersive X-ray spectroscopy (EDX) was used for elemental composition of the ZnO nanosheets. The EDX spectrum (**Figures 1C**) shows peaks of Zn and O for all the ZnO nanosheets, which signifies that the ZnO nanosheets were composed of Zn and O only and no impurity peaks were found, confirming high purity of ZnO nanosheets.

Figure 2 shows FESEM images of the ZnO nanosheets with different thicknesses obtained from the varying concentration of KOH. **Figures 2A** represents the morphology of the ZnO

nanosheets (sample 1) with a lateral dimension of ~500 nm and thickness of ~24 nm, respectively with a molar ratio of 1:2.5. The thickness of the samples was measured by using “Image J” software which is a strong tool for the TEM and SEM analysis. For the measurement, nanosheets in the images were chosen randomly, and the lateral size and thickness were measured accurately. Using ImageJ, one can measure the size in nano-range with more precision, thus the thickness was reported. With the increase of the molar ratio to 1:2.75 (sample 2), the lateral dimension of nanosheets decreased to ~360 nm, with a slight increase in the thickness to ~29 nm (**Figures 2B**). On further increasing the molar ratio to 1:5 (sample 3) (**Figures 2C**), ZnO nanosheets with lateral dimension ~240 nm, thickness ~50 nm; aspect ratio ~37 were obtained. Hence, it can be seen that as the lateral dimension of the nanosheets decreases, the thickness increases with the increasing molar ratio, concluding that ZnO morphology is molar ratio dependent.

Figure 3 depicts the room temperature Raman spectra of ZnO nanosheets for different molar ratios of zinc acetate and KOH. The Raman spectrum (**Figure 3**) of ZnO nanosheets confirms conventional vibration modes (Cusco et al., 2007) of $E_2^{\text{high}}-E_2^{\text{low}}$, A_1 (TO), and E_2^{high} , centered at 332 cm^{-1} , 381 cm^{-1} , and 439 cm^{-1} , respectively. These results commensurate with the XRD results. Further, with the increase in molar ratio the intensity of E_2^{high} mode varies, this change in the intensity of Raman modes is due to increase in supersaturation (Nagy and Casey, 1971).

To study the specific surface area of the nanosheets with various thicknesses, BET analysis was carried out. BET analysis of the sample one showed a surface area of $182\text{ m}^2/\text{g}$,



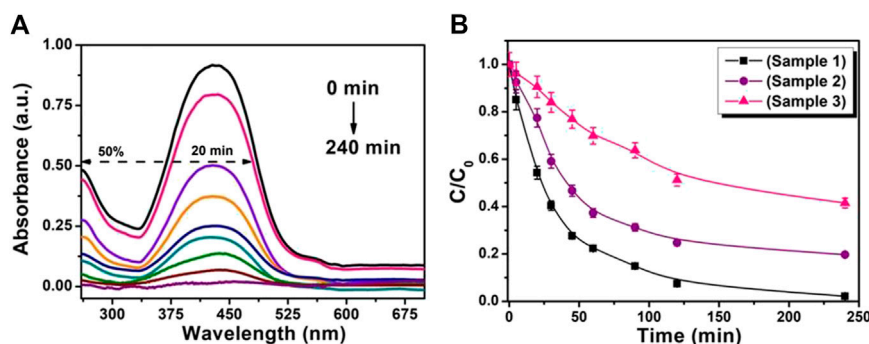


FIGURE 4 | (A) UV-visible absorbance spectra of photodegradation of MR in the presence of ZnO nanosheets (sample 1). **(B)** Temporal evolution of MR absorption spectra with various ZnO nanosheets photocatalysts.

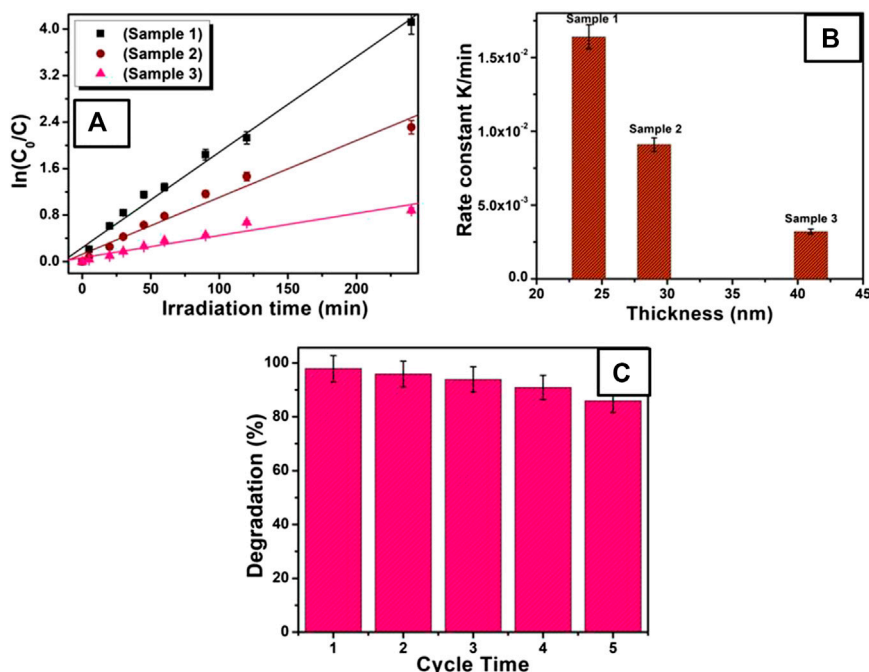


FIGURE 5 | (A) Kinetic relationship of $\ln(C_0/C)$ vs. irradiation time, for various ZnO nanosheet photocatalysts. **(B)** Plot of rate constant vs thickness of nanosheets. **(C)** The stability of ZnO nanosheets (sample 1) for photodegradation of MR.

photocatalytic process can be regarded as a pseudo-first-order reaction with the rate equation $\ln(C_0/C) = Kt$, where, t is reaction time, K is the apparent reaction rate constant, and C_0 and C are the concentration of MR at 0 and t time, respectively. **Figures 5B** gives the relation between reaction rate k and nanosheets with different thickness. The apparent reaction rate constant K for the degradation of MR was calculated to be $1.60 \times 10^{-2} \text{ min}^{-1}$, $9.10 \times 10^{-3} \text{ min}^{-1}$, and $3.18 \times 10^{-3} \text{ min}^{-1}$ for ZnO nanosheets with thicknesses of $\sim 24 \text{ nm}$ (sample 1), $\sim 29 \text{ nm}$ (sample 2), and $\sim 50 \text{ nm}$ (sample 3), respectively. As can be seen from inset of **Figures 5B**, the reaction rate constant is higher for thinner nanosheets (sample 1) than for the thicker one (sample 3), signifying higher photocatalytic activity of thinner ZnO nanosheets.

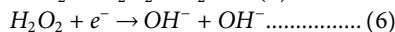
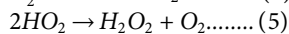
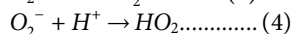
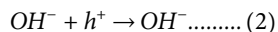
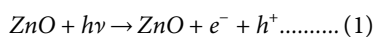
Additionally, comparing the photocatalytic activity of other previously reported nanostructures with the thinner ZnO nanosheets (sample 1) obtained in the present study, it is found that ZnO nanosheets showed better photocatalytic behavior. *Comparelli et al. (2004)* showed the degradation to be 50% of MR with nanosized ZnO, and 90% of MR with nanosized TiO_2 for 140 min under UV irradiation. *Kanjwal et al. (2010)* showed that the hierarchical nanostructure of ZnO- TiO_2 can remove almost all the MR dye within 90 min of irradiation time; moreover, pure ZnO nanoflowers removed less than 30% of MR dye, even after 180 min. However, for pristine TiO_2 nanofibers, up to 50% of the dye was removed after 180 min. In the present work, more than 50% of MR was degraded by ZnO nanosheets (sample 1) within 20 min and

almost completely degraded for 240 min of UV light irradiation. Therefore, thin ZnO nanosheets obtained in the present work are far better photocatalysts than others, taking care that the experimental conditions in the above mentioned previous reports might be different.

The main criterion for the development of photocatalysts for organic dye degradation is its stability. In order to estimate the photocatalytic stability of the ZnO nanosheets, a time track for photocatalytic degradation of MR using thin ZnO nanosheets (sample 1) was recorded as shown in **Figures 5C**. For repeated runs, slight change in the degradation of MR was found for the photocatalytic reaction at 60 min, which shows that thinner ZnO nanosheets are stable. So, it can be used as a potential candidate for practical photocatalysis applications.

Several factors such as carrier recombination, size of the particles, surface area, surface acidity, and presence of higher number of hydroxyl groups are responsible for the photocatalytic activity of a catalytic material. In this work, thinner ZnO nanosheets (sample 1) show a higher percentage of degradation as compared to the thicker nanosheets as well as previously reported work. The enhancement of photocatalytic activity can be attributed to the relative increase of the active morphological surface due to the increased surface to volume ratio and low recombination rate of electron hole pairs, generated by optical exposure, owing to largely available surface states.

Photocatalytic degradation process is due to the action of hydroxyl radicals formed during the reaction (Zhang et al., 2009b). The mechanism is as follows: On illumination of ZnO nanosheets with light, electrons get excited from the valence band to the conduction band of ZnO, leaving a hole in the valence band. The hydroxyl groups present on the surface of the ZnO nanosheets react with the photogenerated hole to produce hydroxyl radicals. Also, dissolved oxygen interacts with photogenerated electrons to form peroxide (O_2^-). This peroxide takes one proton to form a superoxide (HO_2^-) and then hydrogen peroxide (H_2O_2).



A hydroxyl radical was also produced by the attack of a photogenerated electron to the hydrogen peroxide. These

reactive radicals and intermediate species react with dye and degrade them into non-toxic organic compounds.

CONCLUSION

Highly-crystalline ZnO nanosheets with different thicknesses have been prepared by a simple microwave-hydrothermal assisted solution method. XRD, HRTEM, SAED, and Raman analyses explained that ZnO nanosheets are of hexagonal phase structure. FESEM images showed that the thickness of ZnO nanosheets could be efficiently controlled by changing the molar ratio. Increasing the molar ratio increases the thickness of the nanosheets and decreases the lateral dimension. Raman measurements confirmed the characteristic mode E_2^{high} of ZnO nanosheets. Photodegradation results show that the thinner ZnO nanosheet (sample 1) is capable of degrading ~50% of MR within 20 min and degrades MR almost completely on increasing irradiation time to 240 min. This improvement in photocatalytic activity might be due to the easy separation of photogenerated charge carriers in the thinner nanosheets which resulted in the enhanced oxygen chemisorptions. Considering this outstanding photocatalytic performance, and simple preparation method, the prepared ZnO nanosheets are believed to have potential applications in photocatalysis and environmental remediation.

DATA AVAILABILITY STATEMENT

The raw data supporting the conclusions of this article will be made available by the authors, without undue reservation.

AUTHOR CONTRIBUTIONS

AA designed the experiment to execute the concept. AA performed the analyses, and wrote the manuscript.

ACKNOWLEDGMENTS

The author would like to thank the Deanship of Scientific Research at King Faisal University for supporting this research through NASHER track (grant # 186106).

REFERENCES

- Ahmed, F., Kumar, S., Arshi, N., Anwar, M. S., Koo, B. H., and Lee, C. G. (2011). Rapid and cost effective synthesis of zno nanorods using microwave irradiation technique. *Funct. Mater. Lett.* 04, 1–5. doi:10.1142/s1793604711001531
- Baruah, S., and Dutta, J. (2009). Hydrothermal growth of ZnO nanostructures. *Sci. Technol. Adv. Mater.* 10, 013001. doi:10.1088/1468-6996/10/1/013001
- Baruah, S., Rafique, R. F., and Dutta, J. (2008). Visible light photocatalysis by tailoring crystal defects in zinc oxide nanostructures. *Nano* 3, 8.
- Becker, J., Raghupathi, K. R., St. Pierre, J., Zhao, D., and Koodali, R. T. (2011). Tuning of the crystallite and particle sizes of ZnO nanocrystalline materials in solvothermal synthesis and their photocatalytic activity for dye degradation. *J. Phys. Chem. C* 115, 13844. doi:10.1021/jp2038653
- Bohle, D. S., and Spina, C. J. (2009). Cationic and anionic surface binding sites on nanocrystalline zinc oxide: surface influence on photoluminescence and photocatalysis. *J. Am. Chem. Soc.* 131, 4397. doi:10.1021/ja808663b
- Carraway, E. R., Hoffman, A. J., and Hoffmann, M. R. (1994). Photocatalytic oxidation of organic acids on quantum-sized semiconductor colloids, *Environ. Sci. Technol.* 28, 786. doi:10.1021/es00054a007
- Chatterjee, D., and Dasgupta, S. (2005). Visible light induced photocatalytic degradation of organic pollutants, *J. Photochem. Photobiol. C Photochem. Rev.* 6, 186. doi:10.1016/j.jphotochemrev.2005.09.001

- Comparelli, R., Cozzoli, P. D., Curri, M. L., Agostiano, A., Mascolo, G., and Lovecchio, G. (2004). Photocatalytic degradation of methyl-red by immobilised nanoparticles of TiO₂ and ZnO. *Water Sci. Technol.* 49, 183. doi:10.2166/wst.2004.0257
- Comparelli, R., Fanizza, E., Curri, M. L., Cozzi, P. D., Mascolo, G., and Agostiano, A. (2005). Photocatalytic degradation of azo dyes by organic-capped anatase TiO₂ nanocrystals immobilized onto substrates. *Appl. Catal., B* 1, 60.
- Cusco, R., Alarcon-Llado, E., Ibanez, J., Artus, L., Jimenez, J., Wang, B. G., et al. (2007). Temperature dependence of Raman scattering in ZnO. *Phys. Rev. B* 75, 165202. doi:10.1103/physrevb.75.165202
- Dong, J.-Y., Lin, C.-H., Hsu, Y.-J., Lu, S.-Y., and Wong, D. S.-H. (2012). Single-crystalline mesoporous ZnO nanosheets prepared with a green antisolvent method exhibiting excellent photocatalytic efficiencies. *Crystengcomm* 14, 4732–4737. doi:10.1039/c2ce06739k
- Hosono, E., Fujihara, S., Honma, I., and Zhou, H. (2005). The fabrication of an upright-standing zinc oxide nanosheet for use in dye-sensitized solar cells. *Adv. Mater.* 17, 2091–2094. doi:10.1002/adma.200500275
- Hu, J., Zhu, K., Chen, L., Yang, H., Li, Z., Suchopar, A., et al. (2008). Preparation and surface activity of single-crystalline NiO(111) nanosheets with hexagonal holes: a semiconductor nanospanner. *Adv. Mater.* 20, 267–271. doi:10.1002/adma.200701389
- Huang, M. H., Mao, S., Feick, H., Yan, H. Q., Wu, Y. Y., Kind, H., et al. (2001). Room-temperature ultraviolet nanowire nanolasers. *Science* 292, 1897–1899. doi:10.1126/science.1060367
- Jang, E. S., Won, J.-H., Hwang, S.-J., and Choy, J.-H. (2006). Fine tuning of the face orientation of ZnO crystals to optimize their photocatalytic activity. *Adv. Mater.* 18, 3309. doi:10.1002/adma.200601455
- Jing, Z. H., and Zhan, J. H. (2008). Fabrication and gas-sensing properties of porous ZnO nanoplates. *Adv. Mater.* 20, 4547. doi:10.1002/adma.200800243
- Kanjwal, M. A., Barakat, N. A. M., Sheikh, F. A., Park, S. J., and Kim, H. Y. (2010). Photocatalytic activity of ZnO-TiO₂ hierarchical nanostructure prepared by combined electrospinning and hydrothermal techniques. *Macromol. Res.* 18, 233. doi:10.1007/s13233-010-0303-9
- Kong, X. Y., and Wang, Z. L. (2004). Polar-surface dominated ZnO nanobelts and the electrostatic energy induced nanohelices, nanosprings, and nanospirals. *Appl. Phys. Lett.* 84, 975. doi:10.1063/1.1646453
- Kumar, S. G., and Rao, K. S. R. K. (2015). Zinc oxide based photocatalysis: tailoring surface-bulk structure and related interfacial charge carrier dynamics for better environmental applications. *RSC Adv.* 5, 3306. doi:10.1039/c4ra13299h
- Li, G.-R., Lu, X.-H., Zhao, W.-X., Su, C.-Y., and Tong, Y.-X. (2008). Controllable electrochemical synthesis of Ce⁴⁺-doped ZnO nanostructures from nanotubes to nanorods and nanocages. *Cryst. Growth Des.* 8, 1276. doi:10.1021/cg7009995
- Linsebigler, A., Lu, G., and Yates, J. T. (1995). Photocatalysis on TiO₂ surfaces: principles, mechanisms, and selected results. *Chem. Rev.* 95, 735–758. doi:10.1021/cr00035a013
- Liu, J., Guo, Z., Meng, F., Luo, T., Li, M., and Liu, J. (2009). Novel porous single-crystalline ZnO nanosheets fabricated by annealing ZnS(en)0.5(en = ethylenediamine) precursor. Application in a gas sensor for indoor air contaminant detection. *Nanotechnology* 20, 125501. doi:10.1088/0957-4484/20/12/125501
- Marković, S., Simatović, I. S., Ahmetović, S., Veselinović, L., Stojadinović, S., Rac, V., et al. (2019). Surfactant-assisted microwave processing of ZnO particles: a simple way for designing the surface-to-bulk defect ratio and improving photo(electro)catalytic properties. *RSC Adv.* 9, 17165
- Nagy, G. D., and Casey, E. J. (1971). Wiley, 29–36.
- Pan, Z. W., Dai, Z. R., and Wang, Z. L. (2001). Nanobelts of semiconducting oxides. *Science* 291, 1947. doi:10.1126/science.1058120
- Poulios, I., Makri, D., and Prohaska, X. (1999). Photocatalytic treatment of olive milling waste water: oxidation of protocatechuic acid. *Global Nest: Int. J.* 1, 55.
- Qiu, M., Ye, Z., Lu, J., He, H., Huang, J., Zhu, L., et al. (2009). Growth and properties of ZnO nanorod and nanonails by thermal evaporation. *Appl. Surf. Sci.* 255, 3972. doi:10.1016/j.apsusc.2008.10.093
- Qiu, Y. C., Chen, W., and Yang, S. H. (2010). Facile hydrothermal preparation of hierarchically assembled, porous single-crystalline ZnO nanoplates and their application in dye-sensitized solar cells. *J. Mater. Chem.* 20, 1001. doi:10.1039/b917305f
- Thompson, T. L., and Yates, J. T. (2006). Surface science studies of the photoactivation of TiO₂New photochemical processes. *Chem. Rev.* 106, 4428. doi:10.1021/cr050172k
- Tien, L. C., Norton, D. P., Pearton, S. J., Wang, H.-T., and Ren, F. (2007). Nucleation control for ZnO nanorods grown by catalyst-driven molecular beam epitaxy. *Appl. Surf. Sci.* 253, 4620. doi:10.1016/j.apsusc.2006.10.012
- Wang, J., Liu, P., Fu, X., Li, Z., Han, W., and Wang, X. (2009). Relationship between oxygen defects and the photocatalytic property of ZnO nanocrystals in nafion membranes. *Langmuir* 25, 1218. doi:10.1021/la803370z
- Wang, Y. W., Zhang, L. Z., Deng, K. J., Chen, X. Y., and Zou, Z. G. (2007). Low temperature synthesis and photocatalytic activity of rutile TiO₂Nanorod superstructures. *J. Phys. Chem. C* 111, 2709. doi:10.1021/jp066519k
- Wu, J.-J., and Tseng, C.-H. (2006). Photocatalytic properties of nc-Au/ZnO nanorod composites. *Appl. Catal. B Environ.* 66, 51. doi:10.1016/j.apcatb.2006.02.013
- Wu, J.-J., Liu, S.-C., Wu, C.-T., Hen, C. K. H., and Chen, L.-C. (2002). Heterostructures of ZnO-Zn coaxial nanocables and ZnO nanotubes. *Appl. Phys. Lett.* 81, 1312. doi:10.1063/1.1499512
- Zeng, Y.-J., Ye, Z.-Z., Xu, W.-Z., Zhu, L.-P., and Zhao, B.-H. (2005). Well-aligned ZnO nanowires grown on Si substrate via metal-organic chemical vapor deposition. *Appl. Surf. Sci.* 250, 280. doi:10.1016/j.apsusc.2005.03.140
- Zhang, J., Wang, S., Xu, M., Wang, Y., Zhu, B., Zhang, S., et al. (2009a). Hierarchically porous ZnO architectures for gas sensor application. *Cryst. Growth Des.* 9, 3532. doi:10.1021/cg900269a
- Zhang, L.-S., Wong, K.-H., Zhang, D.-Q., Hu, C., Yu, J. C., Chan, C.-Y., et al. (2009b). Zn:In(OH)_ySzSolid solution nanoplates: synthesis, characterization, and photocatalytic mechanism. *Environ. Sci. Technol.* 43, 7883. doi:10.1021/es902013d
- Zhang, Y., Jia, H. B., Wang, R. M., Chen, C. P., Luo, X. H., Yu, D. P., et al. (2003). Low-temperature growth and Raman scattering study of vertically aligned ZnO nanowires on Si substrate. *Appl. Phys. Lett.* 83, 4631. doi:10.1063/1.1630849
- Zhou, X. F., Hu, Z. L., Fan, Y. Q., Chen, S., Ding, W. P., and Xu, N. P. (2008). Hollow microsphere assembly of ZnO nanosheets. *J. Phys. Chem. C* 112, 11722. doi:10.1016/j.matchemphys.2008.06.025

Conflict of Interest: The authors declare that the research was conducted in the absence of any commercial or financial relationships that could be construed as a potential conflict of interest.

Copyright © 2020 Aljaafari. This is an open-access article distributed under the terms of the Creative Commons Attribution License (CC BY). The use, distribution or reproduction in other forums is permitted, provided the original author(s) and the copyright owner(s) are credited and that the original publication in this journal is cited, in accordance with accepted academic practice. No use, distribution or reproduction is permitted which does not comply with these terms.

Advantages of publishing in Frontiers



OPEN ACCESS

Articles are free to read for greatest visibility and readership



FAST PUBLICATION

Around 90 days from submission to decision



HIGH QUALITY PEER-REVIEW

Rigorous, collaborative, and constructive peer-review



TRANSPARENT PEER-REVIEW

Editors and reviewers acknowledged by name on published articles

Frontiers

Avenue du Tribunal-Fédéral 34
1005 Lausanne | Switzerland

Visit us: www.frontiersin.org

Contact us: info@frontiersin.org | +41 21 510 17 00



REPRODUCIBILITY OF RESEARCH

Support open data and methods to enhance research reproducibility



DIGITAL PUBLISHING

Articles designed for optimal readership across devices



FOLLOW US

[@frontiersin](https://twitter.com/frontiersin)



IMPACT METRICS

Advanced article metrics track visibility across digital media



EXTENSIVE PROMOTION

Marketing and promotion of impactful research



LOOP RESEARCH NETWORK

Our network increases your article's readership